
Combustion Characterisation of Compositionally Dynamic Steelworks Gases

Daniel Pugh

A thesis submitted for the degree of Doctor of Philosophy

School of Engineering

Cardiff University

September 2013

Summary

This thesis investigates the combustion of fuel compositions representative of those produced by the integrated steelmaking process. As organisations strive for improvements in utilisation efficiency with increasingly complex technologies, more detailed understanding is required to accurately simulate combustion of the potentially weak and dilute fuels, and thereby aid design processes. Dynamic fuel properties have been characterised through experimentation, in addition to a comparison of numerically simulated results obtained from chemical kinetics. The parameters identified to investigate fuel behaviour were laminar burning velocity and Markstein Length, and characterised with regard to operational instability in practical combustion systems. The design and construction of a suitable experimental rig is detailed, as required to facilitate the accurate determination of burning velocities by quantifying the outward propagation of spherical flames. A regressive analytical technique was developed based on previous studies, nonlinearly relating propagation to change in stretch rate. The developed solution was benchmarked against analogous studies in literature, and ensured experimental performance was accurate and repeatable for the well documented combustion of methane.

Steelworks gases were tested to attain representative burning velocities, with significant attention paid to the change resulting from fluctuation in blast furnace gas H_2 fraction. The study characterised the observed sensitivity to change in flame speed and discussed the implications with regard to practical combustion systems. Several methods of reducing the measured fluctuation are subsequently quantified, including change in ambient condition, and relative humidity. Non-monotonic behaviour was observed for the latter effect, with a suggested trade-off between a chemically catalytic influence on intermediate species, and lowering of flame temperature. Consequently this suggested water addition could be an effective mechanism for the reduction of H_2 induced flame speed variation for blast furnace gas, and influence other synthesised fuels comprising large quantities of CO, including BOS gas. Additional steelworks gases were blended in different ratios to assess dynamic combustive properties relating to fuel flexibility, and the effectiveness of minimising fluctuation in combustion behaviour.

Declaration

This work has not been submitted in substance for any other degree or award at this or any other university or place of learning, nor is being submitted concurrently in candidature for any degree or other award.

Signed (Daniel Pugh) Date

STATEMENT 1

This thesis is being submitted in partial fulfillment of the requirements for the degree of(insert MCh, MD, MPhil, PhD etc, as appropriate)

Signed (Daniel Pugh) Date

STATEMENT 2

This thesis is the result of my own independent work/investigation, except where otherwise stated. Other sources are acknowledged by explicit references. The views expressed are my own.

Signed (Daniel Pugh) Date

STATEMENT 3

I hereby give consent for my thesis, if accepted, to be available for photocopying and for inter-library loan, and for the title and summary to be made available to outside organisations.

Signed (Daniel Pugh) Date

Acknowledgements

I would like to take the opportunity to express my deepest gratitude to the following:

For all of the expert advice and support I'd like to thank; Prof. Tim O'Doherty, Prof. Tony Griffiths, Prof. Phil Bowen, and Dr. Andrew Crayford. In addition, for all the technical assistance provided in undertaking the work I'd like to thank Paul Malpas, Malcolm Seabourne, and the endlessly patient and helpful Gareth Hunt.

For tolerating my mumbled nonsense and constantly reinforcing my suspicion that it might all be worth a damn, I'd like to thank my friends and incredibly supportive parents. There isn't enough space to mention all those that have helped, but I'd like to offer special thanks to the following; Laura Clements, Amy Fitzgerald, John Steggle, Rob Frewin, Dave Webb, Andy Rennison, Mark Panton, Christos Panou and Fergus (making the world a little better with the faint aroma of fox poo). It would be impossible to smile without any of you.

Finally, I'd like to thank Kiri, for being everything that is my wonderful Kiri. I simply could not do without her.

having a little faith baby...

Nomenclature

A	-	Area
A_a	-	Pre-exponential factor
AFR_{act}	-	Actual air-fuel ratio
AFR_{st}	-	Stoichiometric air-fuel ratio
B_{Su}	-	Total bias uncertainty
c	-	Burner constant
c_p	-	Isobaric heat capacity
c_v	-	Isochoric heat capacity
C	-	Capacitance
CV_G	-	Gross calorific value
d_q	-	Quenching distance
d_t	-	Flame thickness
D	-	Mass diffusivity
e	-	Ignition energy
E_a	-	Activation energy
g_f	-	Critical boundary velocity gradient
h	-	specific enthalpy
k	-	Thermal diffusivity
k_f	-	Rate constant
Ka	-	Karlovitz number
L_b	-	Markstein length
Le	-	Lewis number
m_f	-	Mass of fuel
m_o	-	Mass of oxidiser
Ma	-	Markstein number
M	-	Degrees of freedom
M_f	-	Molar mass of fuel
M_o	-	Molar mass of oxidiser
\dot{M}	-	Mass flow rate
n	-	Number of moles
n_f	-	Number of moles fuel
n_o	-	Number of moles oxidiser
n_T	-	Total number of moles
N	-	Number of repeats
P	-	Initial pressure
P_e	-	End pressure
P_i	-	Initial pressure
P_f	-	Fuel partial-pressure
P_o	-	Oxidiser partial-pressure
P_T	-	Total pressure
r_f	-	Flame radius
r_{poly}	-	Polynomial fitted flame radius

r_{Sch}	-	Schlieren flame radius
r_{error}	-	Error in fitted radius
R	-	Universal gas constant
R_c	-	Chamber radius
S_u	-	Unstretched flame speed
S_n	-	Stretched flame speed
SEE	-	Standard error in the estimate
SG_{air}	-	Specific gravity in relation to air
\bar{s}	-	Stretch normalised flame speed
t	-	Time
$t_{M-1,95}$	-	Student t value at 95 % confidence level
T	-	Temperature
T_o	-	Initial temperature
T_f	-	Adiabatic flame temperature
u	-	Velocity
u_L	-	Laminar burning velocity
$u_{LCHEMKIN}$	-	Modelled laminar burning velocity
U_{Su}	-	Uncertainty in unstretched flame speed
V_k	-	Diffusion velocity
Wl_G	-	Gross Wobbe index
\bar{W}	-	Mixture average molecular weight
x	-	Axial distance
x_i	-	mole fraction
x_m	-	Burned mass fraction
y_i	-	Fixed error in variable
Y_k	-	Mass fraction
α_T	-	Temperature exponent
α_P	-	Pressure exponent
α	-	Flame stretch-rate
β	-	Temperature factor
γ_u	-	Isentropic exponent of unburned gas
λ	-	Thermal Conductivity
ρ	-	Density
ρ_b	-	Density of the burned gas
ρ_u	-	Density of the unburned gas
v_i	-	Independent variable
σ	-	Loss parameter
σ_{Su}	-	Standard deviation in S_u
ϕ	-	Equivalence ratio
$\dot{\omega}_k$	-	Net chemical production rate

Contents

Chapter 1.	Introduction	
1.1	Thesis Context	1
	1.1.1 - Emissions and Climate Change	1
	1.1.2 - The Steel Industry Perspective	2
1.2	Operation of an Integrated Steelworks	4
	1.2.1 – Overview	4
	1.2.2 - Coke Ovens and By-Product Plant	5
	1.2.3 - Sinter Plant	6
	1.2.4 - Blast Furnaces	7
	1.2.5 - Basic Oxygen Steelmaking and Continuous Casting	8
	1.2.6 - Hot Rolling Mill and Reheat Furnaces	9
1.3	Indigenous By-Product Steelworks Gases	10
	1.3.1 – Coke Oven Gas	10
	1.3.2 - Blast Furnace Gas	11
	1.3.3 - Basic Oxygen Steelmaking Gas	13
1.4	Aim of this Work	15
Chapter 2.	Background Research and Literature Review	
2.1	Case Study- Tata Steel Strip Products UK Port Talbot Works	16
	2.1.1 - Historical Works Overview	16
	2.1.2 – Generation of Coke Oven Gas at the Port Talbot Works	17
	2.1.3 – Generation of Blast Furnace Gas on the Port Talbot Site	19
	2.1.4 – Generation of BOS Gas on the Port Talbot Site	22
	2.1.5 – Gas Usage at the Port Talbot Works	23
2.2	Overview of Steelworks Gases in Research Literature	27
	2.2.1 – Steelworks Gas Distribution and Usage Optimisation	27
	2.2.2 –Steelworks Gas Usage in Boilers and Furnaces	27
	2.2.3 – Steelworks Gas Usage in Alternative Technologies	28
	2.2.4 – Steelworks Gas Combustion	30
	2.2.5 – Summarising Steelworks Gas Background Research	31
2.3	Fuel Combustion Properties	32
	2.3.1 – Definition of Laminar Burning Velocity and Flame stretch	32
	2.3.2 – Importance of u_L in Characterising Operational Fuel Stability	35
	2.3.3 – Selecting an Experimental Flame Configuration	37
2.4	Analogous Research with Alternative Fuels	40
	2.4.1 – Flame Speed Research with Methane	40
	2.4.2 – Research with Hydrogen and Carbon Monoxide Syngases	42
2.5	Investigation Objectives	44

Chapter 3. Theory and Experimental Method	
3.1 Theory	46
3.1.1 - Flame Configuration and Analysis	46
3.1.2 - Defining Stretch Rate for Spherical Flames	47
3.1.3 - Linear Extrapolation Methodology	48
3.1.4 - Nonlinear Extrapolation Methodology	50
3.1.5 – Accounting for Expansion of Combustion Products	51
3.1.6 – Dynamic Pressure Measurement Approach	51
3.2 Experimental Apparatus	53
3.2.1 - Components of the Experimental Rig	53
3.2.2 - CVCB Design Overview	54
3.2.3 - Schlieren Imaging Setup	55
3.2.4 - Vacuum System	57
3.2.5 - Gas Delivery and Mixing System	58
3.2.6 - Temperature control system	58
3.2.7 - Data Logging System	59
3.2.8 - Ignition System	61
3.3 Experimental Procedure and Data Acquisition	63
3.3.1 - Step-by-step test methodology	63
3.3.2 - Equivalence Ratio Calculation	66
3.3.3 - Video Processing	69
3.3.4 – Image Scaling	74
3.4 Chemical Kinetics Modelling	76
3.4.1 – Software Operation Overview	76
3.4.2 – Reaction Mechanisms Overview	78
Chapter 4. Benchmarking Experimental Performance	
4.1 Numerically Processing Experimental Data	79
4.1.1 - Linear Extrapolation Technique	82
4.1.2 - Nonlinear Extrapolation Technique	83
4.1.3 - Pressure Measurement Technique	86
4.2 Fully Benchmarking CH ₄ Combustion	89
4.2.1 - CH ₄ /air Markstein Length	92
4.2.2 - CH ₄ /air Laminar Burning Velocity	94
4.2.3 - Change in Ambient Temperature	97
4.3 Exploring Experimental Uncertainties	99
4.3.1 - Influences On Total Bias Uncertainty	99
4.3.2 - Example Uncertainty Calculation for Stoichiometric CH ₄	102
4.3.3 - CH ₄ Dataset Uncertainty	102
4.4 Summary	104

Chapter 5. BFG H ₂ Variation - Atmospheric Conditions	
5.1 Chapter Introduction	106
5.1.1 – Defining Experimental Parameters	106
5.1.2 – Adaptations to the Experimental Methodology	107
5.2 Results	107
5.2.1 – Relationship between Flame Speeds, Stretch Rates and Markstein Lengths	109
5.2.2 – Unstretched Flame Speeds, Laminar Burning Velocity	116
5.2.3 – Practical Implication of Obtained Results	120
5.2.4 – Quantifying Experimental Uncertainty	123
5.3 Comparison with Chemical Models	126
5.4 Summary and Conclusions	129
Chapter 6. BFG H ₂ Fluctuation - Variation in Ambient Conditions	
6.1 Chapter Introduction	130
6.1.1 – Defining Experimental Parameters	130
6.1.2 – Considerations for the Experimental Methodology	131
6.2 Results for Variation in Ambient Pressure	132
6.2.1 – Relationship between Flame Speeds, Stretch Rates and Markstein Lengths	132
6.2.2 – Unstretched Flame Speeds, and Laminar Burning Velocity	138
6.2.3 – Experimental and Modelled values of Laminar Burning Velocity	141
6.3 Results for Change in Temperature	143
6.3.1 – Relationship between Flame Speeds, Stretch Rates and Markstein Lengths	143
6.3.2 – Change in Unstretched flame speed	145
6.3.3 – Experimental and modelled values of Laminar Burning Velocity	147
6.3.4 – Practical significance of temperature change	149
6.4 Quantifying Uncertainty and Power Law Correlation	150
6.4.2 – Power Law Association	151
6.5 Summary and Conclusions	153

Chapter 7. BFG H ₂ Fluctuation - Variation in H ₂ O Concentration	
7.1 Chapter Introduction	155
7.1.1 – Defining Experimental Parameters	156
7.1.2 – Considerations for the Experimental Methodology	158
7.2 Stoichiometric BFG/H ₂ O Mixtures	159
7.2.1 – Relationship between Stretch and Flame Speed	160
7.2.2 – Measured and Computational Values of Laminar Burning Velocity	166
7.3 Variation in Equivalence Ratio of BFG/H ₂ O Mixtures	168
7.3.1 – Relationship between Stretch and Flame Speed	168
7.3.2 – Measured and Computational Values of Laminar Burning Velocity	174
7.3.3 – Practical Implication of Obtained Results	177
7.4 Quantifying Experimental Uncertainty	178
7.5 Summary and Conclusions	180
Chapter 8. Further Steelworks Gas Testing	
8.1 Coke Oven Gas	182
8.1.1 – Defining Experimental Parameters	182
8.1.2 – Relationship between Stretch and Flame speed	183
8.1.3 – Measured and Computational Laminar Burning Velocity	187
8.1.4 – Experimental Uncertainties for the COG dataset	188
8.2 BFG blended with COG	189
8.2.1 – Defining Experimental Parameters	190
8.2.2 – Changes to the Experimental Methodology	190
8.2.2 – Relationship between Stretch and Flame speed	191
8.2.3 – Change in Experimental and Modelled Laminar Burning Velocity	199
8.2.4 – Practical Implications of Fuel Property Change	200
8.2.5 – Experimental Uncertainty	203
8.3 BOS Gas Modelling	203
8.3.1 – Fuel Specification	204
8.3.2 – Variable moisture in BOS gas mixtures	205
8.3.3 – Blended BFG and BOS gas mixtures	207
8.4 Summary and Conclusions	209
Conclusions and Outcomes of Work	212
Recommendations for further Work	214
References	215
Appendix A – Ancillary Information	225
Appendix A – Results Tables	240
Appendix A – Thesis Publications	293

List of Figures

Fig. 1.1 - Atmospheric CO₂ concentration change since 1976.

Fig. 1.2 - (a) Percentage share of global anthropogenic greenhouse gas emission sources (2004). (b) Breakdown of greenhouse gases produced in terms of equivalent CO₂ global warming potential.

Fig. 1.3 - Global tonnages of steel and blast furnace iron produced annually from 2001 to 2011.

Fig. 1.4 - Overview of the typical integrated steelmaking process.

Fig. 1.5 – Volumetric breakdown of a typical representative COG composition.

Fig. 1.6 – Diagrammatic overview of material flows in blast furnace operation.

Fig. 1.7 – Dry volumetric breakdown of typical representative BFG composition.

Fig. 1.8 – Volumetric breakdown of typical BOS Gas composition.

Fig. 2.1 – COG compositions attained from analyses performed by Tata central laboratories.

Fig. 2.2 – BFG H₂ fraction and GCI injection rate from furnace 4 at the Port Talbot works.

Fig. 2.3 – Components of BFG sampling system.

Fig. 2.4 – Change in composition of BOS gas throughout blow cycle.

Fig. 2.5 – Average monthly COG distribution at Port Talbot works.

Fig. 2.6 – Average monthly BFG energy distribution at Port Talbot works.

Fig. 2.7 – Average monthly BOS gas energy distribution at Port Talbot works.

Fig. 2.8 – Average monthly natural gas energy distribution at Port Talbot works.

Fig. 2.9 – Average monthly quantities of gaseous energy consumed at the Port Talbot works.

Fig. 2.10 – Diagrammatic representation of fuel velocity gradients for a simple rim burner.

Fig. 2.11 – Flashback and blowoff profiles for the combustion of natural gas.

Fig. 2.12 – Schematic representation of four experimental flame configurations for determination of u_L : a) Bunsen burner flame. b) Flat flame. c) Outwardly propagating spherical flame. d) Counterflow flame.

Fig. 2.13 – Examples of the variation in work undertaken by a) Bradley *et al.* and b) Gu *et al.*

Fig. 2.14 – Variation in u_L (a) and L_b (b) with equivalence ratio (ϕ) for CH₄ with increasing H₂ fraction (X), taken from Hu *et al.*

Fig. 2.15 – Variation in u_L with equivalence ratio for CO with increasing H₂ fraction. (Bouvet *et al.*)

Fig. 2.16 – Variation in u_L with equivalence ratio for an equal H₂-CO blend with N₂ addition. (Prathap *et al.*)

Fig. 3.1 – Outwardly propagating spherical flame configuration.

Fig. 3.2 – Experimental rig schematic.

Fig. 3.3 – CVCB dimensions.

Fig. 3.4 – Outline of the Schlieren imaging principle used in this study.

Fig. 3.5 – Schlieren images of: a) Burning butane. b) Butane release. c) Spherically propagating flame

Fig. 3.6 – Code from temperature data capture system, with live readout expressed on the front panel.

Fig. 3.7 – Code from temperature data capture system, with live readout expressed on the front panel.

Fig. 3.8 – Schematic of the ignition system employed on the CVCB rig.

Fig. 3.9 – Screenshot of the employed MATLAB code.

Fig. 3.10 – Flow chart of employed MATLAB algorithm.

Fig. 3.11 – Schlieren and binary images of a spherical flame.

Fig. 3.12 – Schlieren and binary scaling images.

Fig. 3.13 – CHEMKIN PREMIX operational flow chart.

-
- Fig. 4.1** – Plotted radii of CH₄/air spherical flame propagation.
- Fig. 4.2** – Plotted error in obtained polynomial radius.
- Fig. 4.3** – Plotted change in CH₄/air (a) S_n and (b) α with time as the flame propagates.
- Fig. 4.4** – Plotted CH₄/air values of S_n against α.
- Fig. 4.5** – Stoichiometric CH₄/air values of S_n against α with linear relationship (Eq. 3.6) superimposed.
- Fig. 4.6** – Stoichiometric CH₄/air values of S_n against α with nonlinear relationship (Eq. 3.10) superimposed.
- Fig. 4.7** – Plotted data to emphasise the curvature accounted for by the nonlinear relationship for both; (a) n-butane/air From Kelley and Law, and (b) CH₄/air experimental results obtained for the Cardiff CVCB.
- Fig. 4.8** – Internal chamber pressure trace for the specified test.
- Fig. 4.9** – Internal chamber pressure rise in the range 0.12 to 0.3 MPa.
- Fig. 4.10** – Comparison of radial propagation rates for different equivalence ratios.
- Fig. 4.11** – Samples of plotted CH₄/air S_n against α data, for lean to stoichiometric equivalence ratios.
- Fig. 4.12** – Samples of plotted CH₄/air S_n against α data, for rich equivalence ratios.
- Fig. 4.13** – Experimental scatter seen in obtained values of S_u for each of the optical methodologies.
- Fig. 4.14** – Experimental scatter seen in obtained values of L_b for each of the optical methodologies.
- Fig. 4.15** – Comparison of average L_b values from each optical technique with data from literature.
- Fig. 4.16** – Values of adiabatic density ratio obtained from GRI-Mech 3.0 in CHEMKIN-PRO.
- Fig. 4.17** – Comparison of attained S_u data with selected values published in literature.
- Fig. 4.18** – Comparison of attained u_L data with selected values published in literature.
- Fig. 4.19** – CH₄/air experimental parameters of S_n against α (a), and resultant change in L_b (b) at elevated temperature.
- Fig. 4.20** – Comparison of average u_L values for CH₄/air experiments at elevated temperature.
- Fig. 4.21** – Linear unstretched flame speed of CH₄/air experiments with superimposed uncertainty.
- Fig. 4.22** – Linear unstretched flame speed of CH₄/air experiments with superimposed uncertainty at 358 K.
-
- Fig. 5.1** – Example Schlieren images of BFG flame growth (time-step = 0.01333 s).
- Fig. 5.2** – Examples of BFG radial flame growth.
- Fig. 5.3** – Samples of plotted 1% H₂ BFG/air S_n against α data, for ϕ = 0.7 - 1.1.
- Fig. 5.4** – Samples of plotted 1% H₂ BFG/air S_n against α data, for ϕ = 1.2 - 1.5.
- Fig. 5.5** – Samples of plotted 3% H₂ BFG/air S_n against α data, for ϕ = 0.7 - 1.1.
- Fig. 5.6** – Samples of plotted 3% H₂ BFG/air S_n against α data, for ϕ = 1.2 - 1.5.
- Fig. 5.7** – Samples of plotted 5% H₂ BFG/air S_n against α data, for ϕ = 0.7 - 1.1.
- Fig. 5.8** – Samples of plotted 5% H₂ BFG/air S_n against α data, for ϕ = 1.2 - 1.5.
- Fig. 5.9** – Samples of plotted 7% H₂ BFG/air S_n against α data, for ϕ = 0.7 - 1.1.
- Fig. 5.10** – Samples of plotted 7% H₂ BFG/air S_n against α data, for ϕ = 1.2 - 1.5.
- Fig. 5.11** – Changes in Markstein length with equivalence ratio for each of the tested BFG compositions.
- Fig. 5.12** – Illustrative example of the difference in slope between linear and nonlinear relationships with positive and negative L_b.
- Fig. 5.13** – Changes in S_u with equivalence ratio for each of the tested BFG compositions.
- Fig. 5.14** – Adiabatic density ratios attained using the Li et al. mechanism.

Fig. 5.15 – Variation in average u_L with equivalence ratio for each of the four tested compositions.

Fig. 5.16 – Growth in average BFG u_L with H_2 fraction for $\phi = 1, 1.2$ and 1.5 .

Fig. 5.17 – Theoretical use of temperature profile to obtain flame thickness.

Fig. 5.18 – Calculated flame thicknesses of the 1 and 7% H_2 BFG mixtures.

Fig. 5.19 – Calculated burner independent critical velocity gradients of the 1 and 7% H_2 BFG mixtures.

Fig. 5.20 – Example stoichiometric pressure/time curves for two of the tested BFG compositions.

Fig. 5.21 – Plotted BFG S_u data with superimposed $\pm U_{su}$ and individual data points.

Fig. 5.22 – Plotted BFG L_b data with superimposed $\pm \sigma_{su}$.

Fig. 5.23 – BFG u_L data with superimposed data from chemical models.

Fig. 6.1 – Examples of stoichiometric flame growth for the 7% H_2 BFG mixtures at different initial ambient pressures.

Fig. 6.2 – Samples of plotted 0.15 MPa 1% H_2 BFG/air S_n against α data, for $\phi = 0.8 - 1.4$.

Fig. 6.3 – Samples of plotted 0.15 MPa 3% H_2 BFG/air S_n against α data, for $\phi = 0.8 - 1.4$.

Fig. 6.4 – Samples of plotted 0.15 MPa 5% H_2 BFG/air S_n against α data, for $\phi = 0.8 - 1.4$.

Fig. 6.5 – Samples of plotted 0.15 MPa 7% H_2 BFG/air S_n against α data, for $\phi = 0.8 - 1.4$.

Fig. 6.6 – Samples of plotted 0.2 MPa 1% H_2 BFG/air S_n against α data, for $\phi = 0.8 - 1.4$.

Fig. 6.7 – Samples of plotted 0.2 MPa 3% H_2 BFG/air S_n against α data, for $\phi = 0.8 - 1.4$.

Fig. 6.8 – Samples of plotted 0.2 MPa 5% H_2 BFG/air S_n against α data, for $\phi = 0.8 - 1.4$.

Fig. 6.9 – Samples of plotted 0.2 MPa 7% H_2 BFG/air S_n against α data, for $\phi = 0.8 - 1.4$.

Fig. 6.10 – Plotted values of Markstein length against equivalence ratio for each of the tested BFG compositions at 0.15 MPa.

Fig. 6.11 – Plotted values of Markstein length against equivalence ratio for each of the tested BFG compositions at 0.2 MPa.

Fig. 6.12 – Plotted values of L_b against initial ambient pressure for each tested BFG composition. a) 1, b) 3, c) 5, d) 7 % H_2 .

Fig. 6.13 – Experimental values of S_u against ϕ for each BFG composition at 0.15 MPa

Fig. 6.14 – Experimental values of S_u against ϕ for each BFG composition at 0.2 MPa

Fig. 6.15 – Experimental values of u_L against ϕ for each BFG composition at 0.15 and 0.2 MPa

Fig. 6.16 – Plotted values of u_L against initial ambient pressure for each tested BFG composition, at $\phi = 0.8$ (a), $\phi = 1$ (b), $\phi = 1.2$ (c), $\phi = 1.4$ (d), with modelled values superimposed.

Fig. 6.17 – Examples of stoichiometric flame growth for 7% H_2 BFG at different initial ambient temperatures.

Fig. 6.18 – Examples of plotted 7% H_2 BFG /air S_n against α , for $\phi = 0.8-1.4$, a) $T = 333$ K and b) $T = 393$ K (b).

Fig. 6.19 – Examples of plotted BFG /air S_n against α , for a) 3%, and b) 5% H_2 BFG and variation in Temperature.

Fig. 6.20 – Examples of plotted BFG /air S_n against α , for 3% (a), and 5% (b) H_2 and variation in T.

Fig. 6.21 – BFG /air S_u against ϕ , for a) 333 K, b) 363 K, and c) 393 K.

Fig. 6.22 – Change in density ratio with initial ambient temperature for each BFG mixture.

Fig. 6.23 – Plotted values of u_L against initial ambient temperature for each tested BFG composition, at a) $\phi = 0.8$, b) $\phi = 1$, c) $\phi = 1.2$, d) $\phi = 1.4$, with modelled values superimposed.

Fig. 6.24 – Power law correlations for sample mixtures of αT (a) and αP (b).

Fig. 7.1 – Plotted growth of flame radii for the 1 % (a), 3 % (b), 5 % (c), and 7 % (d) H₂ BFG mixtures, with the four injected masses of H₂O.

Fig. 7.2 – Samples of stoichiometric 1% H₂ BFG/air S_n against α data with increasing water fraction.

Fig. 7.3 – Samples of stoichiometric 3% H₂ BFG/air S_n against α data with increasing water fraction.

Fig. 7.4 – Samples of stoichiometric 5% H₂ BFG/air S_n against α data with increasing water fraction.

Fig. 7.5 – Samples of stoichiometric 7% H₂ BFG/air S_n against α data with increasing water fraction.

Fig. 7.6 – Measured individual (grey), and averaged (coloured) values of L_b for all BFG mixtures with increasing H₂O.

Fig. 7.7 – Measured individual (grey), and averaged (coloured) values of S_u for all BFG mixtures with increasing H₂O.

Fig. 7.8 – Computationally modelled values of: a) Maximum H fraction, b) maximum OH fraction, c) maximum net heat release, and d) adiabatic flame temperature for each tested stoichiometric BFG blend, with rise in injected water fraction.

Fig. 7.9 – Modelled values of adiabatic density ratio for each stoichiometric mixture.

Fig. 7.10 – Experimental and modelled values of u_L for each stoichiometric BFG mixture against water addition.

Fig. 7.11 – Examples of propagating flame radii for 1 and 7 % H₂ BFG mixtures, for a) ϕ = 0.8, b) ϕ = 1.4.

Fig. 7.12 – Samples of a) 1 %, b) 3 %, c) 5 %, d) 7% H₂ BFG/air S_n against α data with increasing water fraction, for ϕ = 0.8.

Fig. 7.13 – Samples of a) 1 %, b) 3 %, c) 5 %, d) 7% H₂ BFG/air S_n against α data with increasing water fraction, for ϕ = 1.4.

Fig. 7.14 – Values of L_b for BFG mixtures with increasing H₂O addition, for ϕ = 0.8.

Fig. 7.15 – Values of L_b for BFG mixtures with increasing H₂O addition, for ϕ = 1.4.

Fig. 7.16 – Plotted values of S_u for BFG mixtures with increasing H₂O addition, for ϕ = 0.8.

Fig. 7.17 – Plotted values of S_u for BFG mixtures with increasing H₂O addition, for ϕ = 1.4.

Fig. 7.18 – Plotted values of density ratio with increasing H₂O addition, for ϕ = 1.4, and ϕ = 0.8.

Fig. 7.19 – Average experimental and modelled BFG u_L with increasing H₂O addition for ϕ = 0.8.

Fig. 7.20 – Average experimental and modelled BFG u_L with increasing H₂O addition for ϕ = 1.4.

Fig. 7.21 – Theoretical g_r/c values that prevent boundary layer flashback, for selected BFG compositions.

Fig. 7.22 – Values of average stoichiometric BFG S_u with increasing H₂O addition and calculated U_{su}.

Fig. 7.23 – Average BFG S_u with increasing H₂O addition and calculated U_{su} for ϕ = 0.8.

Fig. 7.24 – Average BFG S_u with increasing H₂O addition and calculated U_{su} for ϕ = 1.4.

Fig. 8.1 – Samples of COG/air S_n against α relationships, for ϕ = 0.7 – 1.1.

Fig. 8.2 – Samples of COG/air S_n against α relationships, for ϕ = 1.2 – 1.5.

Fig. 8.3 – Individual and average values of COG/air L_b against equivalence ratio.

Fig. 8.4 – Plotted values of COG/air S_u against equivalence ratio.

Fig. 8.5 – Plotted values of COG/air u_L against equivalence ratio.

Fig. 8.6 – Plotted values of COG/air S_u against equivalence ratio with superimposed ±U_{su}

Fig. 8.7 – Plotted values of COG/air L_b against equivalence ratio with superimposed ±σ_{Lb}

Fig. 8.8 – Samples of plotted BFG/COG/air S_n against α relationships, for a) 1, b) 3, c) 5, d) 7 % BFG H₂ Fraction, ϕ = 0.8.

Fig. 8.9 – Samples of plotted BFG/COG/air S_n against α relationships, for a) 1, b) 3, c) 5, d) 7 % BFG H₂ Fraction, ϕ = 1.

-
- Fig. 8.10** – Samples of plotted BFG/COG/air S_n against α relationships, for a) 1, b) 3, c) 5, d) 7 % BFG H_2 Fraction, $\phi = 1.2$.
- Fig. 8.11** – Samples of plotted BFG/COG/air S_n against α relationships, for a) 1, b) 3, c) 5, d) 7 % BFG H_2 Fraction, $\phi = 1.4$.
- Fig. 8.12** – Each plotted BFG/air mixture L_b against COG addition, for a) $\phi = 0.8$, b) $\phi = 1$, c) $\phi = 1.2$, d) $\phi = 1.4$.
- Fig. 8.13** – Each plotted BFG/air mixture S_u against COG addition, for a) $\phi = 0.8$, b) $\phi = 1$, c) $\phi = 1.2$, d) $\phi = 1.4$.
- Fig. 8.14** – Each plotted BFG/COG/air mixture u_L against ϕ , for 1 (a), 3 (b), 5 (c), 7 (d) % BFG H_2 , with equivalent modelled velocities superimposed.
- Fig. 8.15** – Percentage change in u_L resulting from 1-7% BFG H_2 increase with COG addition.
- Fig. 8.16** – g_f/c values that prevent boundary layer flashback, for selected BFG/COG compositions.
- Fig. 8.17** – Actual values and percentage change in CV_G/WI_G resulting from 1-7% BFG H_2 increase with COG addition.
- Fig. 8.18** – Modelled values of u_L for specified BOS/air mixtures against ϕ .
- Fig. 8.19** – Modelled values of u_L for BOS/air mixtures against ϕ , with increasing water fraction.
- Fig. 8.20** – Modelled values of u_L for BOS/air mixtures against water fraction, for three equivalence ratios.
- Fig. 8.21** – Modelled BFG/air/BOS gas u_L against ϕ , for 1(a), 3(b), 5(c), 7(d) % BFG H_2 and increasing BOS fraction.

Chapter 1. Introduction

1.1 Thesis Context

1.1.1 - Emissions and Climate Change

The Earth's climate is warming, creating severe potential threats to the natural environmental ecosystem. The 2007 fourth synthesis report produced by the Intergovernmental Panel on Climate Change [1] stated: "*Most of the observed increase in global average temperatures since the mid-20th century is very likely due to the observed increase in anthropogenic greenhouse gas concentrations*". Natural greenhouse gases such as N_2O , O_3 , CO_2 , and CH_4 participate to the warming of Earth's atmosphere by absorbing and emitting infrared radiation. The concentrations of the latter two examples have increased significantly over the last 250 years [2], and are still rising. The plot given in Fig. 1.1 is a representation of the Keeling curve [3]; showing averaged monthly atmospheric CO_2 concentrations from four remote stations of the ESRL, and NOAA observatory network [4].

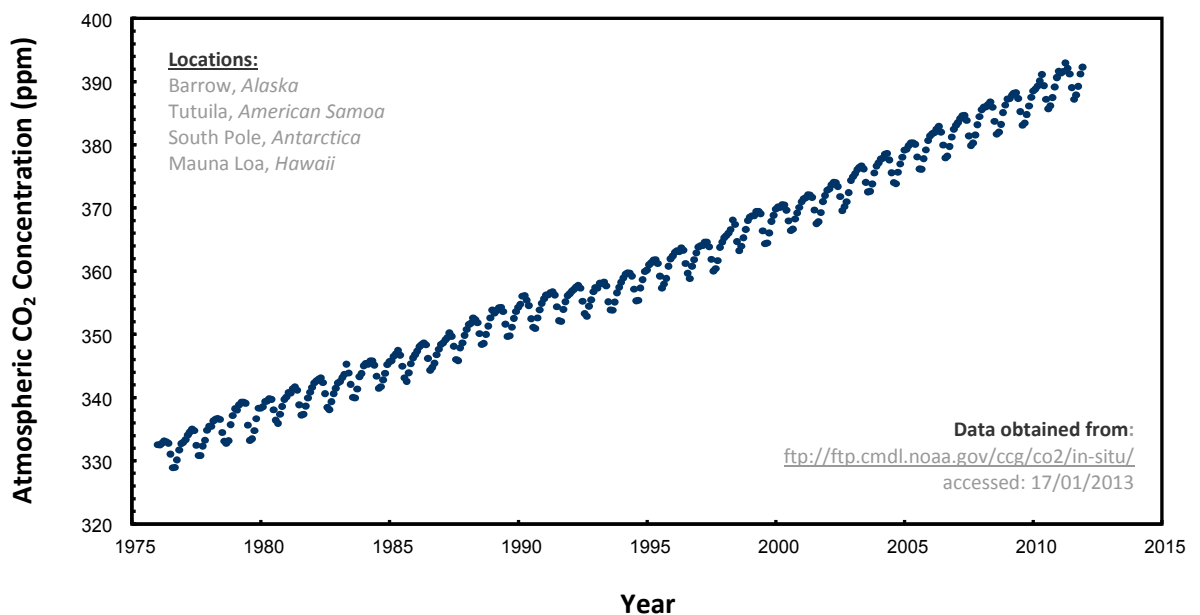


Fig. 1.1 - Atmospheric CO_2 concentration change since 1976. [4]

The threat is not limited simply to a potential rise in sea levels from global warming; with additional adverse effects such as oceanic acidification attributed to atmospheric CO₂ increase [5]. The preponderant reason for the rise in manmade CO₂ production is the increasing demand for energy. It is produced as a by-product from the use of many non-renewable fuels, widely employed to meet a variety of significant requirements such as; domestic heat and power, transportation, and industry [6]. Fig. 1.2 provides breakdowns of (a) global anthropogenic greenhouse gas emission sources (from, 2004 [1]) by sector, in addition to (b) ratios of the CO₂ equivalent warming potential of the gases produced [1].

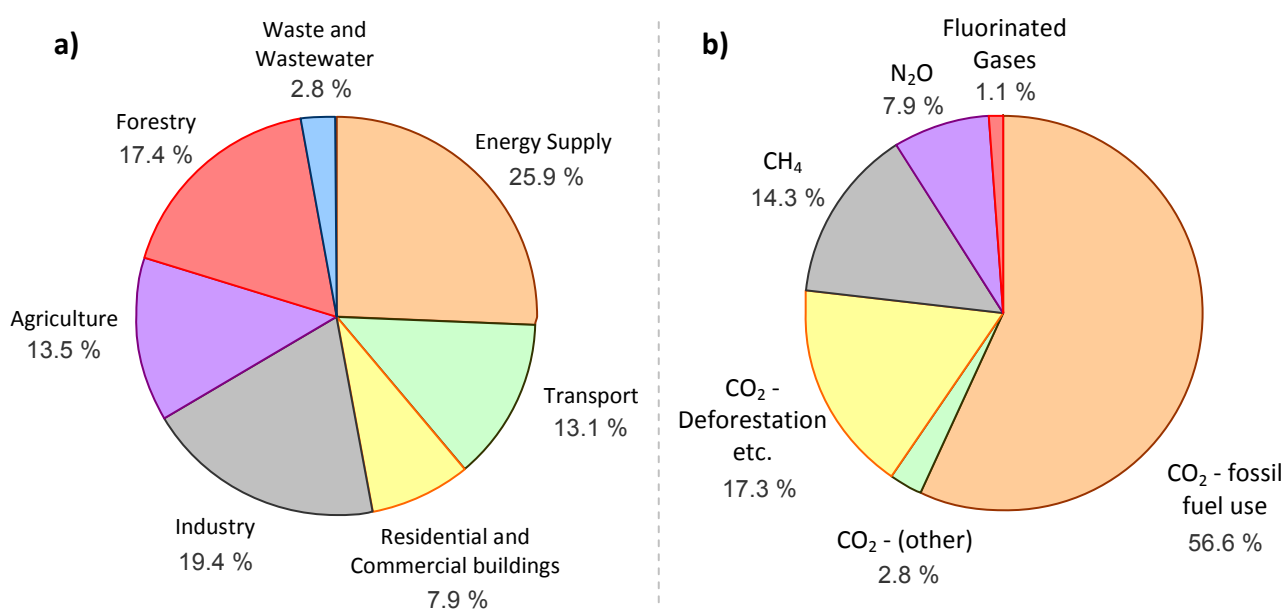


Fig. 1.2 - (a) Percentage share of global anthropogenic greenhouse gas emission sources (2004 [1]). (b) Breakdown of greenhouse gases produced in terms of equivalent CO₂ global warming potential [1].

1.1.2 - The Steel Industry Perspective

The steel producing sector of industry is estimated to emit 1,500-1,600 Mt of CO₂ per year, thereby accounting for 6-7 percent of global anthropogenic emissions [1,7]. Thus, according to the World Steel Association, climate change is the “*biggest issue facing the steel industry in the 21st century*” [8]. The quantity of CO₂ emissions generated per tonne of steel produced varies by country (for example; 1.25t and 3.8 t from Brazil and China respectively [1]), as different techniques are used throughout the world.

The primary method of steelmaking is to reduce iron within a blast furnace using coke, followed by decarburisation as a separate process. This usually happens in one integrated works, and accounts for over 60 percent of global steel production [1]. Other techniques include using an electric arc furnace to process scrap, or employing different materials to directly reduce iron. Although these techniques can lower the amount of CO₂ emissions produced by up to 50 percent, there are limitations on how much they can be currently employed to meet global steel demand [1, 9]. Fig. 1.3 demonstrates the trend for international steel production over the last decade, with annual tonnages plotted alongside quantities of iron produced by the primary integrated works method [10].

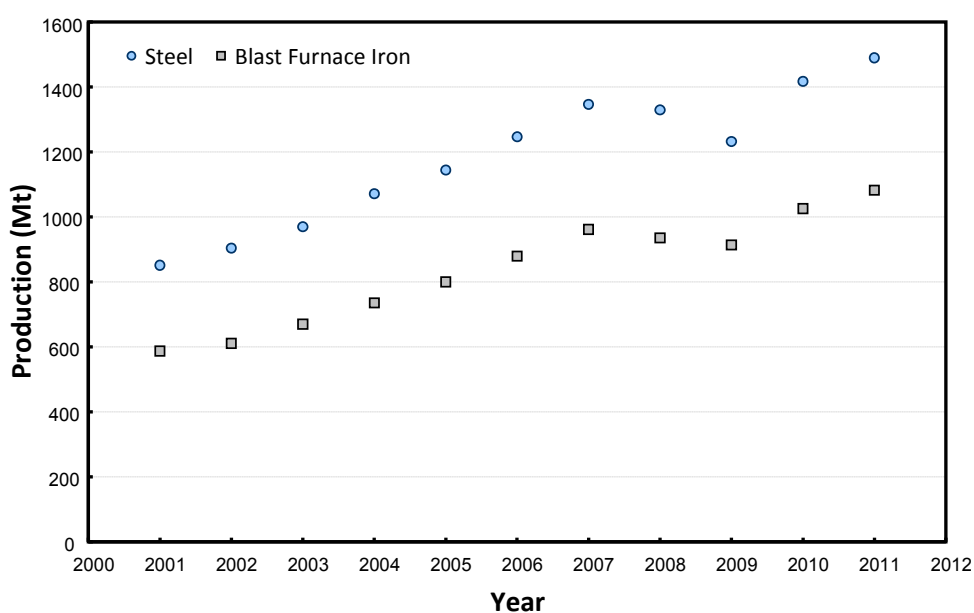


Fig. 1.3 - Global tonnages of steel and blast furnace iron produced annually from 2001 to 2011.
Statistics from World Steel Association [10]

There are parallel trends in growth for production of both steel and blast furnace iron, together with a drop to coincide with the global recession of 2008/9. An overall tendency for increasing manufacture is evident, with a total global steel production figure of 1,490 Mt in 2011. If the world steel statistics are examined closely, the steady rise in values appears largely a result of increasing production in Asia, where the more traditional integrated works have higher relative market share [10]. With global production figures of blast furnace iron surpassing 1,000 Mt for the first time in 2010, it is important that efforts are made to continuously strive for efficiency improvements in the integrated process, with savings available for both fuel cost and emissions [1].

The IPCC recommended approach to improving steelworks efficiency is to utilise a series of options, centred around best available technologies and maximising use of by-products indigenous to the integrated process [1, 11, 12]. Chief amongst these are three gases that form the subject of this research dissertation and are introduced in this chapter, following a steelworks overview.

1.2 Operation of an Integrated Steelworks

1.2.1 - Overview

The function of an integrated steelworks is to utilise raw materials for the multi-stage process of primary steel production at one facility. This practise nominally consists of cokemaking, sintering, ironmaking, steelmaking, casting, and then product rolling. Fig. 1.4 shows the sequential chart for production employed at a typical integrated works, with material flows indicated (adapted from [12]). There can be technological substitutions made to the process, such as pelletising iron ore opposed to sintering, however the raw and produced materials remain largely the same [13].

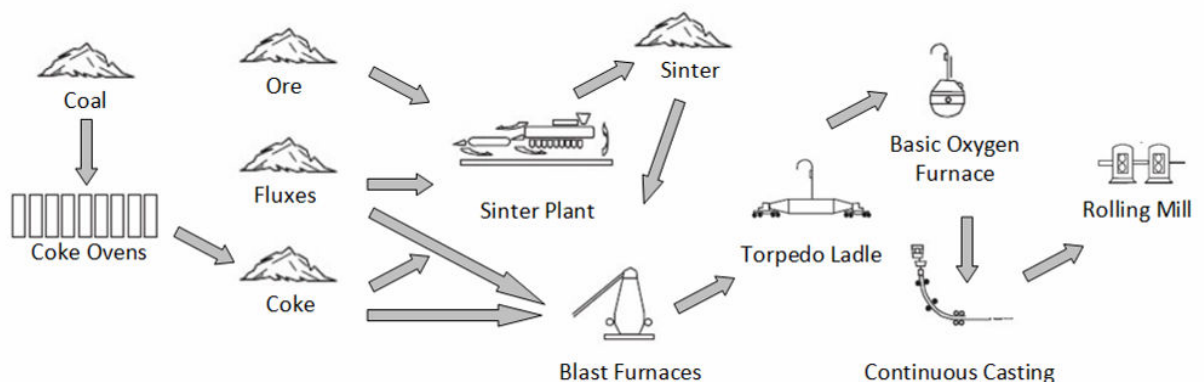


Fig. 1.4 - Overview of the typical integrated steelmaking process. [12]

What follows is a brief sequential guide through each major stage in this typical process, to broadly establish how rolled steel and any subsequent by-products are made. This section will also outline some of the significant energy demands, particularly in the form of heat, required by the process.

1.2.2 - Coke Ovens and By-Product Plant

Metallurgical coke is produced through the carbonisation of coal, a process that requires pyrolysis at elevated temperatures (over 1,250 K) for extended periods of time. The aim of this is to drive off any volatiles within the coal, leaving a permeable carbonaceous material that is utilised by the blast furnaces in three ways; firstly as a fuel to provide additional heat, secondly as a reducing agent in the production of pig iron, and finally as physical support for the *burden* (the bulk of material within the furnace) [14]. As a result of these requirements, metallurgical coke must have a specified composition with adequate physical and reactive properties. These properties are controlled not only by the coking time and temperature, but also by the characteristics of the coals charged into the ovens, typically requiring a low sulphur and ash content. Following carbonisation, a proximate analysis of coke composition would typically yield 94 % fixed carbon, 4 % ash and 1 % volatiles [12].

Volatilised mass released from the coal is normally collected and treated in an adjoining by-product plant. The primary material treated is coke oven gas, which can be cleaned and distributed for use as a gaseous fuel. Additional contaminants can also be sequestered within the plant, and sold as individual products including; benzene, tar, ammonia, naphthalene, and other liquors. Alternatively, non-recovery coke ovens utilise all by-products *in situ* to generate the heat used to drive the process, with any excess used to power ancillary boilers [15].

Following carbonisation, incandescent coke is transported from the ovens, quenched and sized. Any coke fragments diametrically smaller than ~5 mm are treated as 'coke breeze' and are transferred to the sinter plant for use as a fuel [16]. All other remaining coke is conveyed in bulk, for use as a charge material within the blast furnace.

1.2.3 - Sinter Plant

Iron ore is required by the steelworks as a raw material, however it does not have suitable properties to support the burden of matter within a blast furnace, or maintain physical integrity from the *blast* (section 1.2.4) itself. Therefore, the purpose of this stage in the process is to agglomerate this raw material to into a solid, permeable mass [12, 14].

Within a sinter plant this is achieved by blending the fine ores with limestone, coke breeze and recycled iron bearing material. The mixture is typically layered atop a moving grate, with the coke breeze then ignited as it passes under a canopy of burners. Negative pressure is created under the mixture using fans, and draws the combustion front downward through the raw material as the grate travels along. The heat of combustion fuses the mixture together into a porous iron bearing clinker. Typically, as the solidified sinter cake reaches the end of the conveyed grate, it overhangs, and then crumbles onto the *crash desk*, before being cooled and sized. Any sinter fragments that are too fine are recycled back into the mixture before being reprocessed. All useable sinter is then employed in a blast furnace as charge material [14].

Pelletisation plants exist as an alternative method of agglomerating raw material, with both methodologies having their respective advantages. Sintering allows continuous recycling of solid wastes, where as pellets tend to degrade slower, and therefore allow discrete sites to be located away from the integrated works. In Europe volumes of sinter produced typically outnumber pellets three to one [12].

1.2.4 - Blast Furnaces

Blast furnaces operate as closed reactors to which porous quantities of coke, sinter, and limestone are continuously added to produce carbon-saturated *pig-iron*. These components are disseminated in layers at the furnace top to form the burden. Pressurised air, potentially supplemented with additional oxygen and reductants, is preheated to over 1,450 K prior to being blown into the furnace through base-level *tuyeres*. This is referred to as the blast, and is preheated using a series of stoves that behave as reversing regenerators, operating in a periodic shift pattern. Whilst one stove is used to preheat the blast air, others are reheated until the temperature in the stove *on-blast* drops below a set threshold, when functions are then cycled. The gaseous rise of the blast heats the burden, and the subsequent chemical reactions produce vast quantities of gaseous by-product available from atop the furnace. This is a continuous process, with raw materials and blast air interminably supplied to the system [14, 17].

The blast catalyses reactions to reduce iron oxides within the sinter to form molten pig iron alloy, with a typical carbon content of around four percent. The predominant reductant is coke; however additional alternative materials can be used provided the burden temperature, integrity, and porosity are maintained. The added limestone reacts as a flux, removing impurities from the alloy and forming a slag [12].

The overriding result is for stratified pig iron and slag to amalgamate in the section of the furnace below the tuyeres, referred to as the *hearth*. This molten mixture is over 1,700 K, and is periodically withdrawn from the hearth and collected in insulated torpedo ladles, with slag separately cooled and collected for use as a by-product [14, 17].

1.2.5 - Basic Oxygen Steelmaking and Continuous Casting

Basic Oxygen Steelmaking (*BOS*) is the term used to describe a discontinuous method of primary steelmaking, whereby carbon rich pig-iron is decarburised into steel. Pig-iron, transported from the blast furnaces in torpedo ladles, is charged into an LD (Linz-Donawitz) converter; a form of Basic oxygen furnace, or *BOF*. Prior to this stage, a quantity of recyclable scrap steel may have been loaded to the converter to increase yield. A water-cooled lance is then lowered to hover above the surface of the hot metal, before oxygen is blown through at high velocity [17]. The purpose of this is to decarburise the hot metal by oxidising the carbon, together with any other undesirable impurities within the feedstock, such as sulphur or phosphorus. Fluxes, such as Burnt Lime and Dolomite, are added to the vessel to help remove any unwanted constituents by forming an impurity-absorbing slag. Carbon is released and creates an additional gaseous by-product that can be used as a fuel, referred to as BOS gas. The overall reaction is highly exothermic, and increases the temperature within the vessel to over 1,950 K, giving the previously added scrap additional purpose as coolant [12]. The oxygen content within the off-gas is monitored, with a rise taken to be indicative of process completion, leaving the carbon concentration within the steel at 0.01 - 0.4 percent [12].

Samples are taken to ensure the appropriate quality standard is met, prior to which steel is poured from the converter to another refractory lined ladle in a process known as *tapping*. The slag forms an emulsion with the molten steel, which is then scoured from the surface and taken to cool. Further additions can be made for the formation of alloys, and nitrogen potentially used for agitation as required. This stage is referred to as secondary metallurgy, and typically occurs in smaller batches [18].

The final stage is cooling and casting the steel in a *continuous-caster*. Initially the molten steel is transferred from a transportation ladle into a refractory lined *Tundish* [17]. The Tundish has a controllable outlet that feeds into a vertical water-cooled copper mould, which oscillates up and down, and is lubricated with powders or oils to

prevent the material from sticking. Steel is cast into a strand guide that curves it through 90 degrees as it hardens under cooling sprays to form horizontal slabs. The steel is then cut to appropriate slab lengths using torches, and stored prior to further processing [12].

1.2.6 - Hot Rolling Mill and Reheat Furnaces

The job of the rolling mill is to reduce the cast steel slab to the required width and gauge, whilst improving the metallurgical structure and surface quality. Reheat furnaces can be used to uniformly increase slab temperature to over 1,500 K [12] in a reducing atmosphere, thereby controlling surface oxidation or slag formation. Typically the slab then oscillates through the *reversing roughing mill*, reducing the gauge whilst maintaining strip width.

The strand finishing mill is then used to reduce the final thickness, giving the strip the desired shape and metallurgical structure as required. A *coil-box* may be used to ensure temperature uniformity in the product, before the heated strip is passed onto a *run-out table*, where coolant sprays are used to reduce the product temperature. When the slabs leave the reheat furnace oxidation is rapid, and the mills have a secondary task of cracking the scale which forms on the surface of the product [17].

Having outlined some of the major stages in the integrated steelmaking process, and resultant energy demands, production of the aforementioned gaseous by-products are now discussed in further detail.

1.3 Indigenous By-Product Steelworks Gases

1.3.1 – Coke Oven Gas

Coke oven gas (COG) is generated through destructive distillation, as a by-product of the carbonisation process undertaken for the production of metallurgical coke (section 1.2.2). The process requires the pyrolysis of a bituminous coal mixture at high temperatures for extended periods, and must meet the requirements as defined by the Blast Furnaces (section 1.2.4). COG is therefore produced as part of a batch process with volatiles released at different rates as the coal is heated. The mass yield of COG recovery to total coal used is typically 18-19 percent, however this is highly dependent on the employed coal specification. Consequently the composition of COG is also dependent on the raw material, but will typically be a mixture of principally combustible constituents [12, 16, 17]. A representative volumetric COG composition is shown in Fig. 1.5 [12].

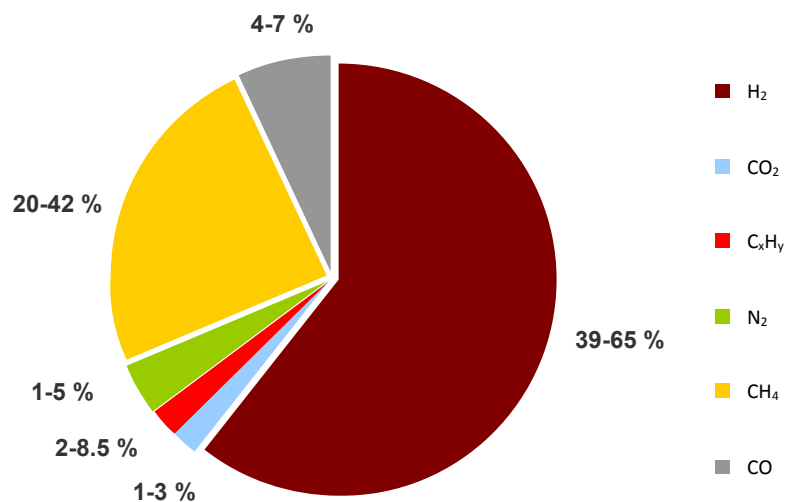


Fig. 1.5 – Volumetric breakdown of a typical representative COG composition. [12]

In the region of $40 \text{ MJ}\cdot\text{kg}^{-1}$, the calorific value of COG is the highest of all steelworks gases, making it an attractive fuel to use. However, there are problems with residual concentrations of aromatic light oils and tars such as Benzole and Naphthalene, together with traces of contaminants like H₂S. This also leads to deposition problems within pipelines if the fuel is supplied over long distances [19].

1.3.2 - Blast Furnace Gas

Blast furnace gas (*BFG*) is the name given to the by-product continuously produced from the upward gaseous rise of blast air through the burden (see section 1.2.4). Fig. 1.6 shows an illustrative view of blast furnace operation, followed by a simplified analysis of the overriding chemistry.

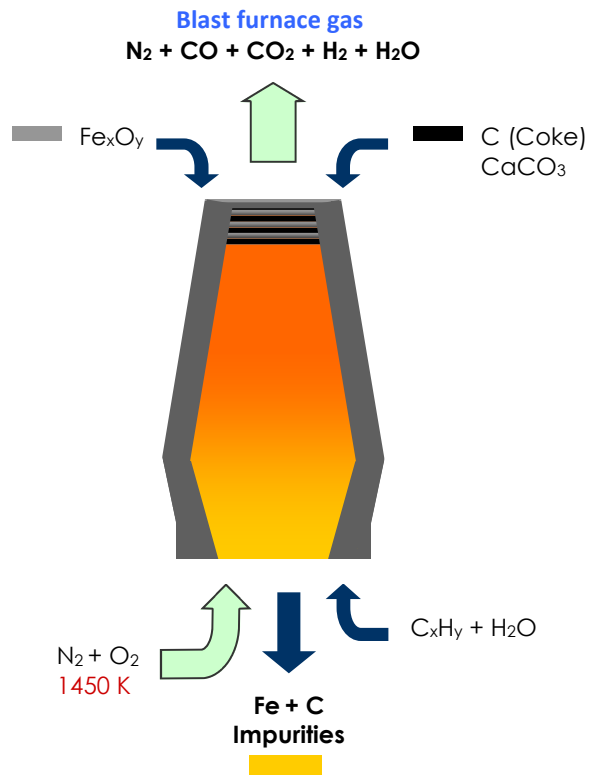


Fig. 1.6 – Diagrammatic overview of material flows in blast furnace operation

Oxygen contained within the preheated blast air reacts with carbon (in the form of coke) to produce CO₂ and CO, thus:



Both coke and CO are reducing agents of sintered Fe(II) and Fe(III) oxides within the burden. These include species such as hematite (Fe₂O₃), wüstite (FeO), and magnetite (Fe₃O₄), and are reduced to form Fe and CO₂. Example reduction mechanisms of hematite are given so;



A further source of gaseous release results from decomposition of limestone as a basic flux to remove impurities, for example CO_2 is generated in silica removal through reaction with calcium oxide [17];



All of these changes are happening in the reaction zone of the furnace, and importantly from the perspective of BFG composition, chemical equilibrium for the gases released is governed by the Boudouard reaction as a set ratio is reached between CO and CO_2 for a given temperature [20];



The operational result is for large quantities of hot CO_2 , CO , and N_2 to ascend through the furnace as fresh burden travels down into the reaction zone. However, there can be further constituents added to the gaseous composition depending on systematic variables. For example, additional reductants can be added in order to reduce coke demand in the burden, such as granulated coal, oil, natural gas, or recycled plastics [12, 21], and thereby improve furnace efficiency. However, burden integrity must be maintained, necessitating the injection of steam or oxygen alongside any additional reductants. These additions lead to fluctuating levels of H_2 and H_2O in the blast, and subsequently affect the water-gas shift reaction chemistry [22];



The overall chemical composition of BFG is therefore dynamic and dependent on furnace specifications, with a dry volumetric breakdown representative of typical operation given in Fig. 1.7 [12, 14, 17].

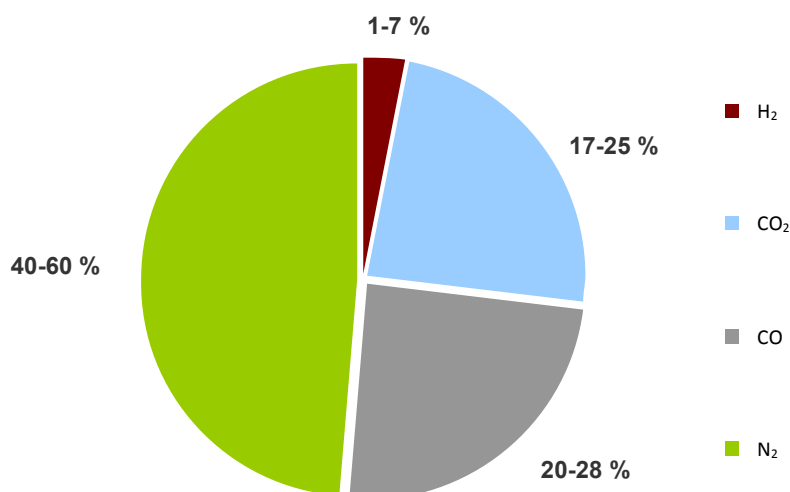


Fig. 1.7 – Dry volumetric breakdown of typical representative BFG composition [12, 14, 17].

Prior to utilisation as a fuel, the warm by-product will typically be cleaned by *wet-scrubbers*, or electrostatic precipitators. The former can lower the temperature and saturate the gas with water vapour. This moisture condenses as the temperature of the gas drops, meaning the absolute humidity depends on the where the gas is used, and how much opportunity there is for it to cool [23].

The relatively high proportion of diluent components leads to BFG having a weak calorific value, in the order of $2\text{-}3 \text{ MJ}\cdot\text{kg}^{-1}$ [12]. However, its value as fuel results from constant production in large volumes through continuous operation of the furnace.

1.3.3 - Basic Oxygen Steelmaking Gas

Basic oxygen steelmaking gas, (sometimes referred to as BOS, BOF or converter gas) is produced as a result of the basic decarburisation process, whereby carbon rich pig-iron is made into steel. High velocity oxygen agitates the molten blast furnace product, ultimately resulting in carbon oxidation within the alloy. This produces large quantities of CO, and CO₂, with a water-cooled hood lowered over the converter to collect the gas as it is generated [12]. This process is periodic and controlled by both CO and O₂ concentrations, with fuel only collected with enough combustible gas in the mixture, and little enough O₂ to allow for safe transportation and storage. Collection of BOS gas

as a distinct fuel is not universally employed, with the possibility of partial or full combustion in the collection duct, for sensible heat recovery in boilers [24].

The temporal degree of variation in BOS gas composition is significant, with ratio of CO to CO₂ once again governed by the Boudouard reaction (Eqn. 1.7) [12]. As the converter scrap is melted and vessel temperature intensifies, CO fraction will increase in relation to the decrease in CO₂. When carbon oxidation eventually decreases, so does temperature within the converter and the carbonaceous gas fractions again begin to converge [20]. The hood lowered onto the converter is maintained under negative pressure, leading to entrainment of atmospheric N₂ in the collection flow. Furthermore, diminutive quantities of H₂ can also be collected within the gas. This can result from atmospheric H₂O and its further influence on stored fluxes and scrap, with an example being the hydration of lime to form calcium hydroxide (Ca(OH)₂) [25]. However, such fractions are small, and a representative average BOS gas composition is shown in Fig. 1.8.

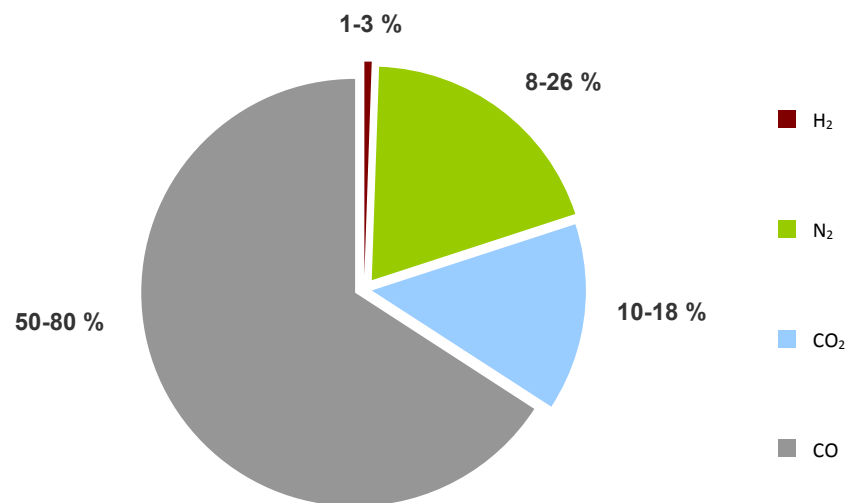


Fig. 1.8 – Volumetric breakdown of typical BOS Gas composition [12, 17].

With a higher proportion of CO compared to BFG, BOS gas has a resultant calorific value of approximately 6-7 MJ·kg⁻¹ [12, 17]. However, BOS gas does require extensive cleaning as a result of the significant amount of particulate matter generated during production. Venturi scrubbers or electrostatic precipitators will typically be employed to reduce the amount of particulate matter to around 5-10 mg, per kilogram of gas produced [12].

1.4 Aim of this Work

To facilitate the flexible use of synthesised fuels with increasingly complex and efficient technologies such as gas turbines, extensive research is being performed in connection with fundamental fuel combustion properties, and the development of numerical models to aid in design processes. Such work enables engineers to develop flexible combustors capable of utilising a wide range of fuel mixtures, with high conversion efficiencies, whilst maintaining low emission levels [26]. This research dissertation aims to perform an investigation concerning the production of indigenous steelworks gases, characterising dynamic combustion performance in relation to fuel compositional change, representative of any variation experienced in generation and distribution.

One of the most important fundamental physicochemical properties of any fuel is the laminar burning velocity, and has been chosen as the focus of concentration for this study. This characteristic typifies combustive behaviour, influencing premixed operational instabilities such as blowoff or flashback, and can be employed to validate chemical reaction mechanisms used in numerically simulating combustion processes [27, 28, 29]. The following chapter details a review of prior work undertaken with steelworks gases, following a case study at the Tata Port Talbot steelworks. Further specification of investigative objectives could be made as opportunities were identified from the relevant research literature.

Chapter 2. Background Research and Literature Review

This chapter outlines the background research performed as a foundation for the work presented in this dissertation. A case study is employed to analyse the practical generation and usage of indigenous steelworks gases, before an outline of relevant research is provided. With potential opportunities identified, the objectives of this work are then defined.

2.1 Case Study- Tata Steel Strip Products UK Port Talbot Works

2.1.1 - Historical Works Overview

Production of steel in the Port Talbot area began early in the twentieth century, however the modern day *Abbey* works located in Margam, was first opened in 1951 as part of the *Steel Company of Wales* [30]. Following the 1967 Iron and Steel Act of Nationalisation, where Britain's fourteen largest steelmaking companies were combined to form the *British Steel Corporation* (BSC), the Steel Company of Wales became the South Wales group of BSC. The company was reorganised on a product basis, with Port Talbot linked to the Llanwern and Ravenscraig works for the production of steel strip. 1988 saw the privatisation of BSC, and a merger in 1999 with the Dutch Manufacturer *Koninklijke Hoogovens* led to the formation of *Corus Group* [30].

Today the *Tata Steel Strip Products UK Port Talbot Works* is owned by the Indian manufacturer *Tata Steel*, following acquisition of the Corus Group in 2007. The modern day works is a large integrated site, employing the process operations outlined in Chapter 1. for the production of hot and cold rolled annealed steel coils. The works is capable of producing up to four million tonnes of steel per year, thereby accounting

for over one-third of steel production in the UK [31]. The site currently operates in partnership with the Llanwern works, employing around five thousand members of staff to provide steel for various industry sectors including automotive and construction [30]. The following section outlines the current production of indigenous by-product gases at the Port Talbot site*.

2.1.2 – Generation of Coke Oven Gas at the Port Talbot Works

Commissioned in 1981, and refitted in 2005, the Port Talbot works currently employs the *Morfa* coke ovens to partially meet the coking requirements of two on-site blast furnaces, with any surplus demand met through import. Cokemaking within the *Morfa* ovens is a batch process, whereby two batteries of 42 *Otto Simon Carves* ovens are sequentially charged with blended coal, and heated to over 1,300°C for approximately seventeen hours [16]. Each oven converts around 33,500 kg of coal to 22,000 kg of coke, and at full capacity an oven is *pushed* (emptied) every 12-13 minutes to produce around 18,000,000 kg of coke per week (based on 2007 figures [32]). The volatilised mass released from the process is collected and cleaned of contaminant condensates (such as tar, Benzole and Naphthalene), and the remaining gaseous by-product is distributed as COG. On-site production figures suggest over 15,000 kg of COG are produced every hour [33].

Gas composition is analysed twice a week by chromatograph, with samples obtained from the last stage in the by-product cleaning process, after the output of the Naphthalene washer. Each of these analyses has a report certificate (example provided in Appendix A.1), provided by chemical technologists from Tata Steel Central Labs (*Carl Greenslade* and *Andrew Jones*). Fig. 2.1 shows an area chart for the gaseous COG composition of 122 chromatograph analyses performed between February 2009 and July 2010, with the numerical average and standard deviation provided in Table 2.1.

** Many of the values presented in this section were obtained from the OSIsoft PI Historian data storage system employed on site, where the accuracy and precision of values could not be quantified. Consequently, some values herein should be analysed only for broad trends, and references have been provided where possible that vindicate any observations made.*

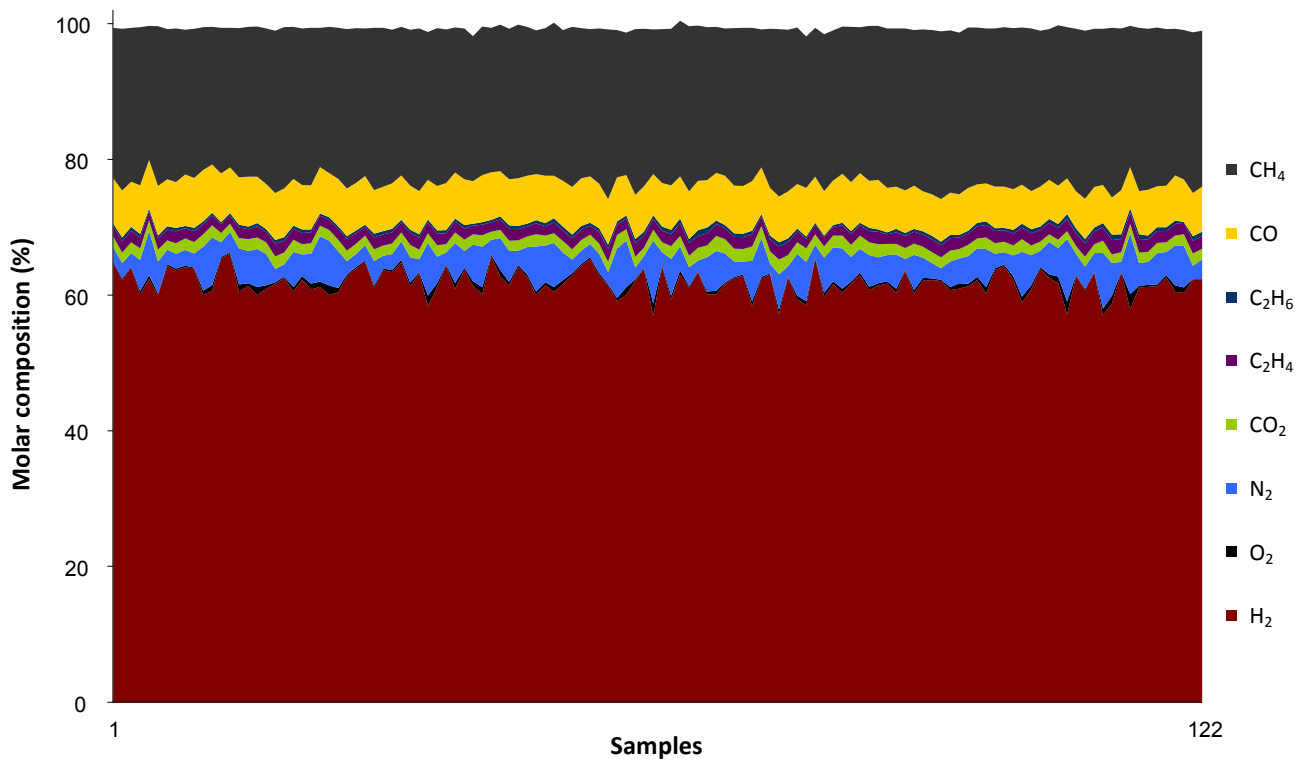


Fig. 2.1 – COG compositions attained from analyses performed by Tata Steel central laboratories

Table. 2.1 – Average and Standard deviation of analysed COG composition

	H ₂	O ₂	N ₂	CO ₂	C ₂ H ₄	C ₂ H ₆	CO	CH ₄
Average (% Mol):	62.12	0.49	3.95	1.63	1.7	0.5	6.67	22.94
Standard Deviation (%):	2.07	0.36	1.87	0.21	0.18	0.12	0.47	1.09

The gross calorific value of this average composition is approximately $45 \text{ MJ}\cdot\text{kg}^{-1}$, or $19 \text{ MJ}\cdot\text{Nm}^{-3}$, if conditions are normalised to STP (273.15 K and 100 kPa, with reference energy density values in appendix A.2). The portions of N₂ and O₂ demonstrate the most significant relative fluctuation of all the constituent fractions, and upon consultation with Tata Steel engineers, the suggested mechanism responsible is infusion of air when the ovens are emptied. This means that sample time is significant with respect to the last oven push, when analysing a representative composition. An additional parameter that will influence gas composition is the quality of coal used in the process [12], and is likely to be responsible for some of the other minor fluctuation in evidence.

2.1.3 – Generation of Blast Furnace Gas on the Port Talbot Site

The Port Talbot works employs two blast furnaces, referred to as numbers 4 and 5, with the former undergoing a 6-month £185m recommission in the second half of 2012, and the latter rebuilt in 2003 following a catastrophic explosion [34, 35]. At full capacity, operation of the two furnaces should allow for steel production to increase towards five million tonnes per year. Furthermore, each furnace, when fully operational, is capable of producing over 400,000 Nm³·hr⁻¹ of BFG as a by-product of the process. Three of the main constituents of BFG composition are quantified at the furnace top using duplicate sensors for each gas. The measured gases are CO, CO₂ and H₂, with the remaining dry molar fraction assumed to be N₂. The top gas analysis data from furnace number 4 was sampled every five minutes for several months (whenever the system was online) in 2010, and averaged to give dry composition as shown in Table 2.2.

Table. 2.2 – Average and Standard Deviation of BFG composition

	H ₂	CO	CO ₂	Calculated N ₂
Average (% Mol):	2.57	23.16	22.77	51.51
Standard Deviation (%):	1.12	1.47	1.37	2.80

The H₂ fraction gives the most significant amount of relative fluctuation, influenced by the use of additional reductants within the furnace (see section 1.3.1) [12, 21]. In the case of blast furnace number 4 at Port Talbot, *Granulated Coal Injection* (GCI) is frequently employed to reduce coke demand, whilst simultaneously increasing the required amount of injected steam for the management of burden porosity and temperature [21]. Fig 2.2 shows an example of H₂ fluctuation within the measured gas composition, plotted against the GCI injection rate over a 10-hour period on 11/04/2011 (data points sampled every minute).

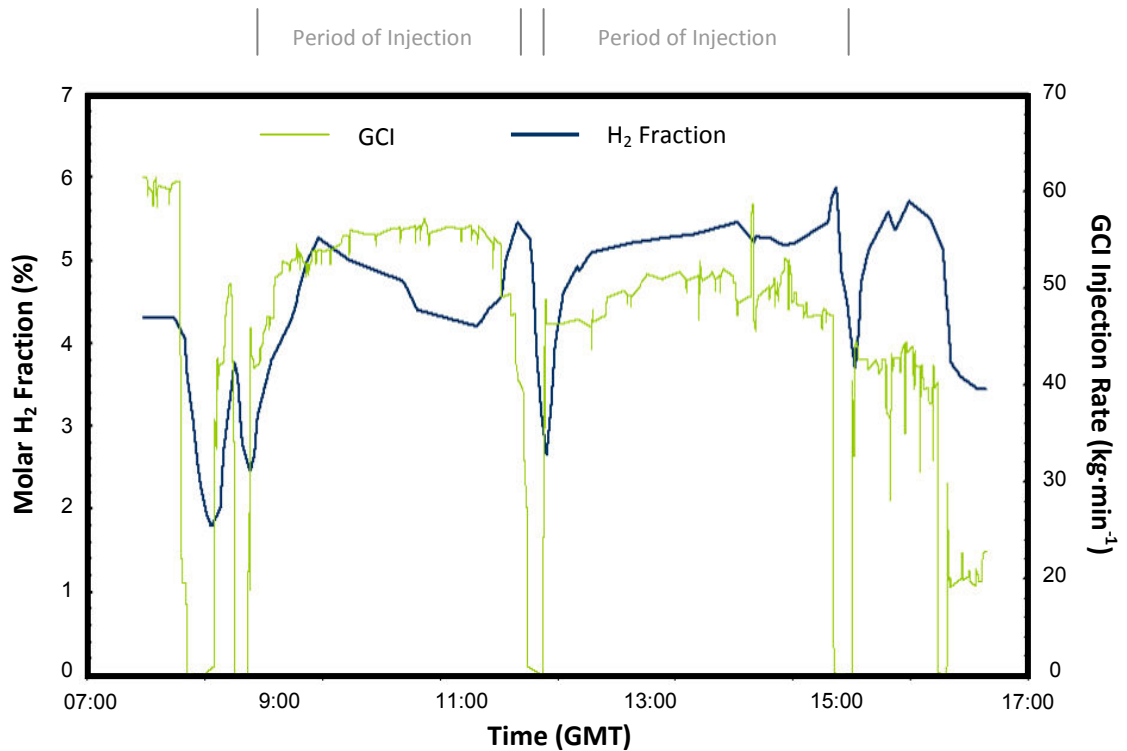


Fig. 2.2 – BFG H₂ fraction and GCI injection rate from furnace 4 at the Port Talbot works
(taken 11/04/2011)

A correlation is evident between the reduction in GCI injection rate and H₂ fraction of the gas (note how quickly the stoppage in GCI results in a change in gas composition). As the remainder of BFG composition contains predominantly inert diluents, this H₂ fluctuation is significant in characterising the behaviour of BFG as a fuel. If influence of BFG composition was to be investigated further, it was important to ensure the remaining unmeasured fraction of the gas comprised N₂, as assumed [12].

A simple sampling circuit was connected to an access point in the BFG pipeline approximately 1.5 km from where the gas is generated in the furnaces. BFG was drawn through a vacuum pump, and exhausted out of the system by manually loading bespoke cylinders using a Gresham portable gas sampling kit. Fig. 2.3 gives a simple schematic of some significant components in the gas sampling system [36]. Each 100 ml cylinder was connected at both ends, purged with BFG by opening flow from the sampling circuit, then sealed and pumped up to 20 bar. Five sampling cylinders were available for each day of testing, with analyses performed in the university laboratories using a Varian CP-3800 gas chromatograph. Linear response factors were calculated using a calibration gas standard made to the equivalent representative composition as

provided in Table 2.2. The dry molar compositions chromatographically attained from three days of testing are showing in Table 2.3. The results show good agreement with theoretical BFG compositions, and also changes in the level of fluctuation on different days. For instance, the results on 16/02/2011 show significantly more variation than tests performed on either of the first two days.

Table. 2.3 – BFG composition obtained by chromatographic analysis [36].

Date – Time	Composition (% Mol)			
	N ₂	H ₂	CO	CO ₂
01/02/11 – 11:45	48.3	2.7	25.6	23.3
01/02/11 – 12:25	46.7	2.6	26.7	23.9
01/02/11 – 13:35	48.3	2.7	25.4	23.4
01/02/11 – 14:14	48.6	2.6	25.5	23.2
01/02/11 – 14:16	48.3	2.7	25.4	23.5
10/02/11 – 11:00	49.6	2.8	25	22.4
10/02/11 – 11:40	49.3	2.8	25.2	22.5
10/02/11 – 13:00	49.3	2.8	25.5	22.3
10/02/11 – 13:50	50	2.7	25	22.2
10/02/11 – 14:45	49.3	2.9	25.5	22.2
16/02/11 – 11:00	53.1	2.2	23.4	21.2
16/02/11 – 12:00	52.9	2.5	26.2	18.2
16/02/11 – 13:25	49.4	2.8	27	20.7
16/02/11 – 14:50	53.2	2.3	24.4	19.9

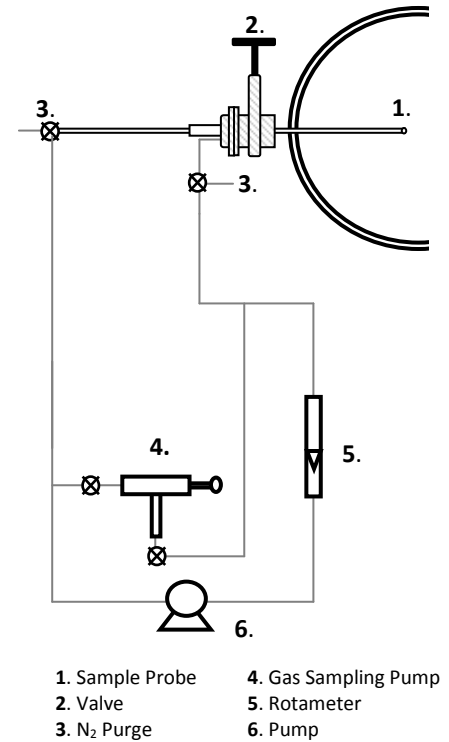


Fig. 2.3 – Components of BFG sampling system

A final consideration for practical BFG composition is the effect of humidity. Plant sensors suggest that as gas is processed through wet scrubbers in the cleaning system, it cools from over 140°C, to around 35-40°C [24]. This process saturates the vapour pressure of BFG at these conditions, and consequently condensate forms as the gas is distributed and cooled around the works. Therefore unless it has been heated after initially cooling, BFG composition will have a vaporised H₂O fraction equivalent to the maximum relative humidity. This implies the possibility for characteristics of BFG to be altered by location and change in ambient condition [36]. Taking fluctuation of composition into account, BFG on the Port Talbot site has a typical gross calorific value in the range of 2-3 MJ·kg⁻¹, or 3-4 MJ·Nm⁻³.

2.1.4 – Generation of BOS Gas on the Port Talbot Site

In 2010 the Port Talbot works completed a ~£60m project for the collection and utilisation of BOS gas, from the two 300 tonne LD converters employed on site [37]. Steelmaking in each vessel is a batch decarburisation process whereby O_2 is propelled into molten blast furnace iron at a flow rate of over $17 \text{ Nm}^3 \cdot \text{s}^{-1}$ for approximately 20 minutes. The composition of the produced BOS gas is monitored, and collected from hoods lowered over the converters when the following criteria are met [38]:

- The molar CO fraction of the gas must be above 35% vol.
- O_2 concentration is required to drop to below 2% vol.

Gas is typically collected for around 14 minutes, with Fig. 2.4 showing an example of the relative change in constituent molar fractions throughout a blow cycle.

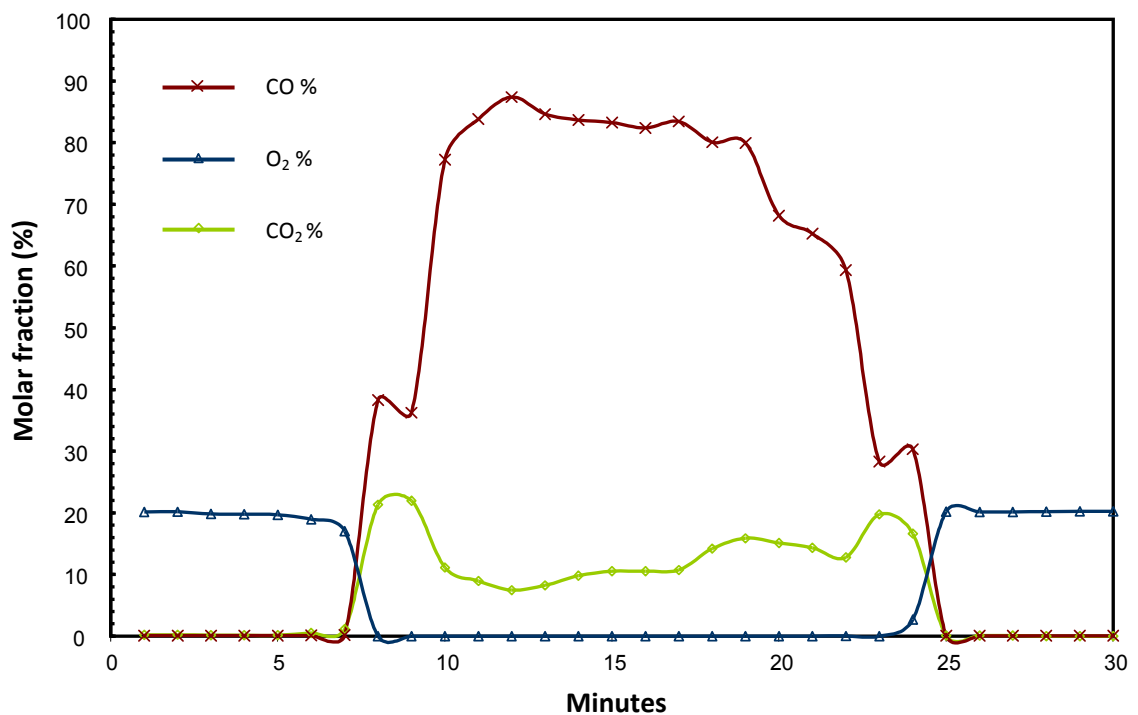


Fig. 2.4 – Change in composition of BOS gas throughout blow cycle
(Data obtained from Vessel 1, commencing 23:39 22/08/2010)

These example data shown in Fig. 2.4 were obtained from the six gas analysers employed on vessel 1 (H_2 , CO_2 , and duplicate CO and O_2 sensors that were averaged), with the negligible H_2 data omitted. It is evident from Fig. 2.4 that CO and CO_2 are

simultaneously generated throughout the blow, with atmospheric O₂ concentration decreasing with commencement of the highly exothermic process. Again the surplus fraction of the gas is assumed to be N₂ entrained in the system, (together with the small amounts of H₂) [12, 38]. Data for over 300 blow cycles were collected from a combination of these sensors, and the analogous set employed on vessel 2, between 9/8/2010, and 22/8/2010. These data were filtered according to the conditions for gas collection, and averaged to give the composition provided in Table 2.4.

Table. 2.4 – Average collected BOS gas composition from two vessels (9/8/2010 - 22/8/2010)

	H ₂	CO	CO ₂	O ₂	Calculated N ₂
Vessel 1 (% Mol)	0.47	66.41	14.02	0.10	19.00
Vessel 2 (% Mol)	0.80	64.85	14.39	0.06	19.91

The composition shown in table 2.4 gives BOS gas at the Port Talbot works an average gross calorific value of ~6.5 MJ·kg⁻¹, or ~8 MJ·Nm⁻³, with the system typically collecting around 30,000 Nm³ per cycle [38]. The BOS gas collection system had recently been commissioned when this research began, and therefore the steelworks did not have the opportunity to commit staff and designate a safe point in the system for separate penetration and chromatographic analysis. This meant initially BOS gas composition could only be studied through the recently employed gas sensors, and research literature [38].

2.1.5 – Gas Usage at the Port Talbot Works

BFG and COG pipelines distributed across the Port Talbot works allow for flexibility in the employed usage strategy, with an overall approach change following the introduction of BOS gas collection in 2010. Typically, the coke ovens and blast furnace stoves are powered by a combination of BFG, COG and natural gas, with ratios dictated by calorific value of the mixed fuel. Any surplus gas was traditionally used in power plant boilers for the generation of electricity and steam, which is also piped around the site to feed various individual work area processes. With the introduction of BOS gas to the system, atmospheric boilers in the power plant run more predominantly on an

amalgamation of BFG and BOS gas. The excess COG is distributed to reheat furnaces used in the rolling mill, thereby reducing the site's demand for natural gas. Additional ways in which fuel gases are consumed include the BOS plant, service boilers (used to supplement pressure in the steam circuit) and flaring when the system produces more gas than can be used or stored. Monthly site consumption data was averaged for one year after BOS gas collection was introduced in 2010, with Fig. 2.5 – Fig. 2.8 showing the respective areas in which COG, BFG, BOS gas and natural gas were consumed (the plots show the distribution of energy within the gases, see note below for more information).

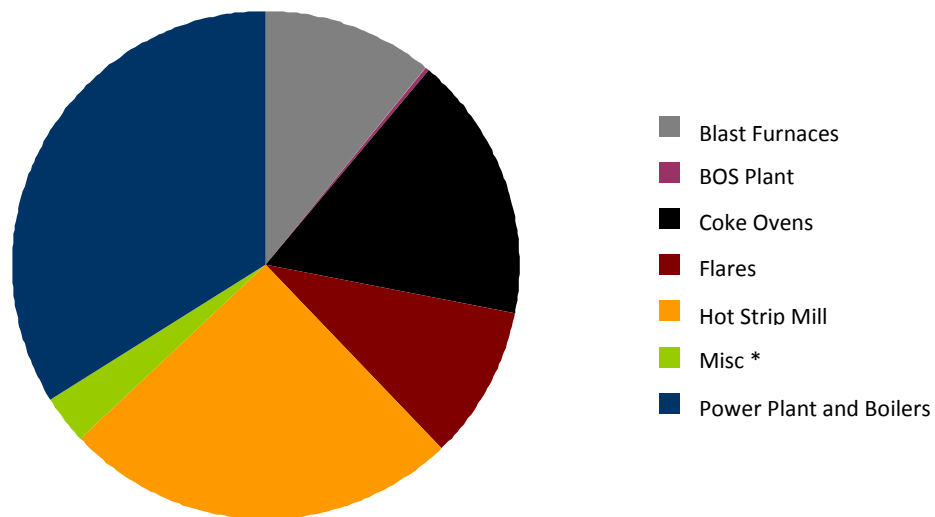


Fig. 2.5 – Average monthly COG distribution at Port Talbot works.

*Note - Data in Fig. 2.5 – Fig. 2.8 represent energy consumption figures, taken from April 2010 – March 2011. The energy in each gas been normalised using a calculated calorific value (for example $\sim 3.4 \text{ MJ}\cdot\text{Nm}^3$ for BFG), based on live composition measurements, or chromatographic analysis. This energy content was summated for each of the twelve sampled months. * Misc denotes additional operations unnecessary for the direct steelmaking process such office heating.*

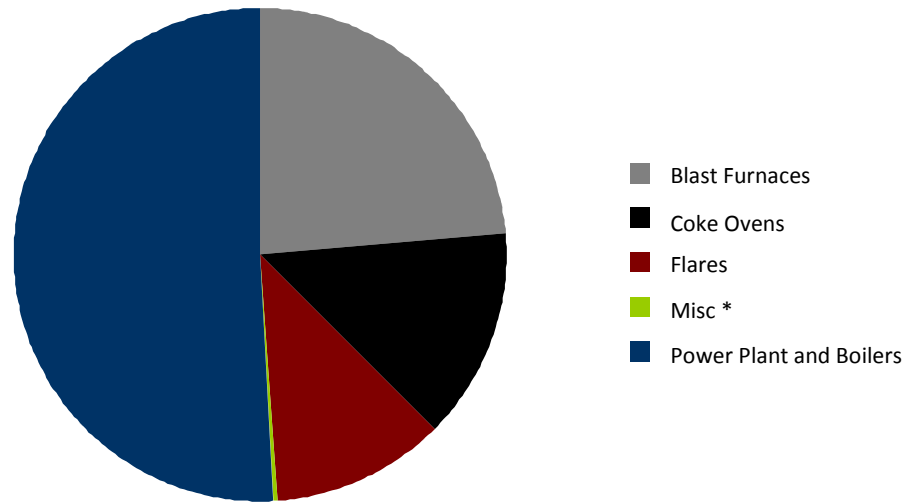


Fig. 2.6 – Average monthly BFG energy distribution at Port Talbot works.

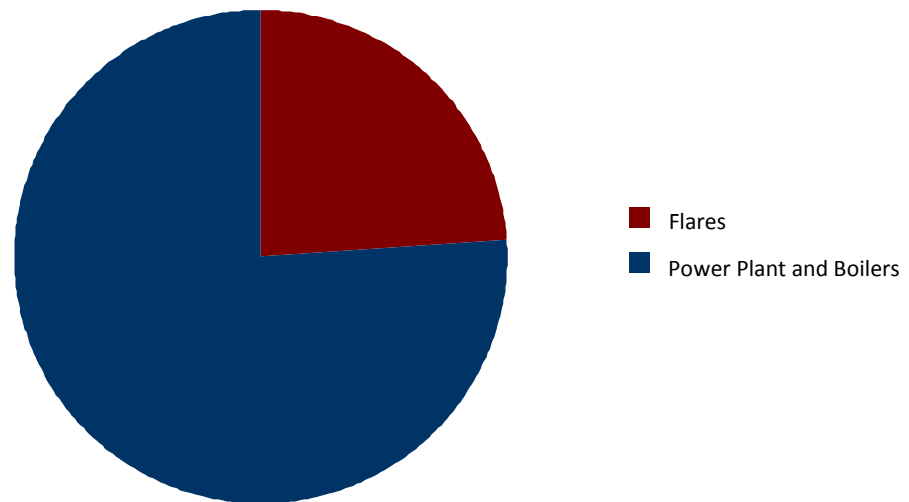


Fig. 2.7 – Average monthly BOS gas energy distribution at Port Talbot works.

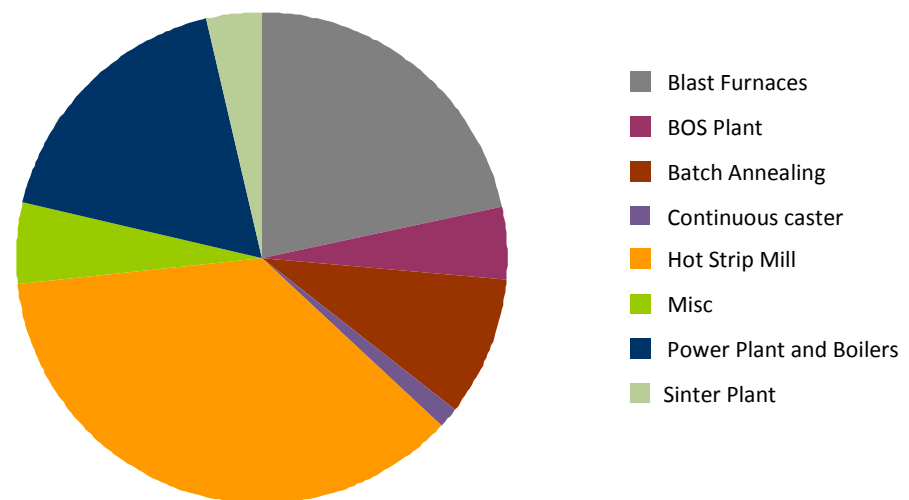


Fig. 2.8 – Average monthly natural gas energy distribution at Port Talbot works.

It is apparent from Fig. 2.5 – Fig. 2.8 that significant amounts of gaseous by-product are flared, whilst natural gas is still consumed for many additional process operations. It was observable from conversations with plant operational engineers, that work areas requiring consistent performance preferred using clean, stable, and relatively energetic natural gas, opposed to the indigenous process gases generated on site. However, if the quantity of available energy in each of the four gases is compared from the amounts consumed (as shown in Fig. 2.8, for the same period), it is possible that more efficient and complete usage of by-product gases could drastically reduce the requirement for natural gas consumption [1, 12, 15].

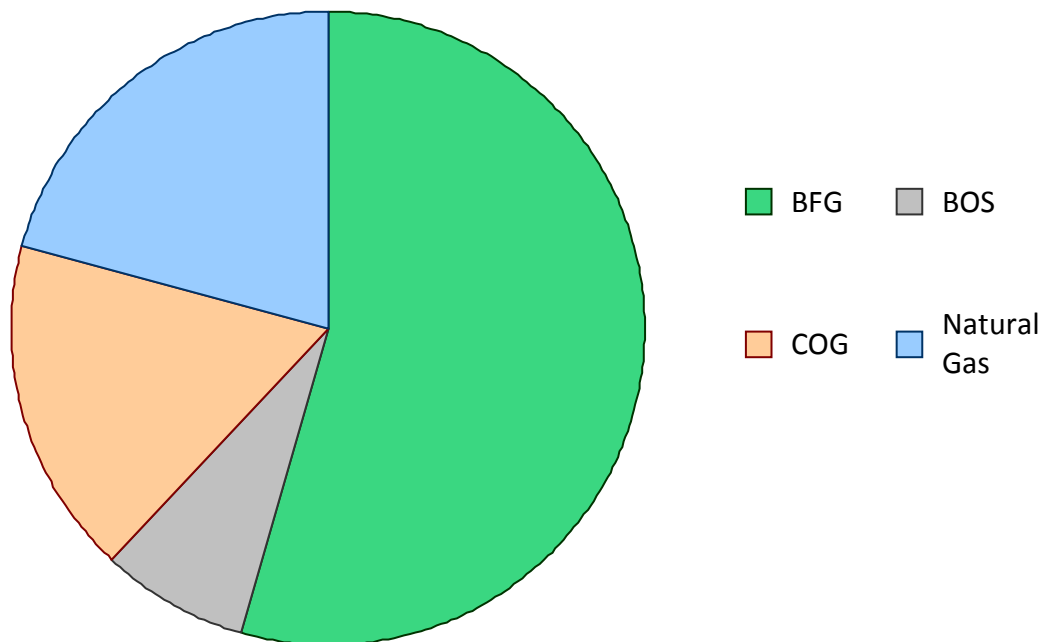


Fig. 2.9 – Average monthly quantities of gaseous energy consumed at the Port Talbot works.
(From same data as Fig. 2.5 – Fig. 2.8)

It is also evident from Fig. 2.8 that more energy is consumed in the form of BFG than the other three fuel gases combined, with proportionately vaster quantities wasted in flares. The weak and compositionally dynamic nature of BFG also necessitates the need for natural gas consumption in operationally unnecessary by-product functions (like operation of the power plant), to supplement the energy available and stabilise combustion performance [1, 12, 15].

2.2 Overview of Steelworks Gases in Research Literature

2.2.1 – Steelworks Gas Distribution and Usage Optimisation

Researchers have been interminably investigating ways to improve efficiency in the steelmaking process through enhanced utilisation and distribution of steelworks gases. One way of approaching this is to adapt usage strategies to try and minimise the amounts of by-products flared. The comparatively older work of Markland [39] analysed how improvements in fuel usage efficiency could be achieved using traditional methods of linear programming, with the field advancing through the use of computational modelling. Mixed Integer Linear Programming (MILP) has been used by several authors [40, 41] to develop optimisation techniques for improved gas holder control, thereby minimising temporal excesses or shortages in gas supply. An example of more contemporary work in this field is that of Zhang *et al.* [42] where a distribution model has been employed to investigate the optimal relationship between blast furnaces, power plant and gas holder, whilst also accounting for cost of supplementary fuels. Furthermore, an alternative linear Petri net technique has also been employed by Zhu *et al.* [43] to simulate gas energy flows, again aiming to optimise fuel distribution. This approach to improvement is limited and works operation often dynamic, therefore more potential may result from specifically how the by-products are utilised, particularly from the perspective of minimising supplementary fuels.

2.2.2 – Steelworks Gas Usage in Boilers and Furnaces

With regard to traditional steelworks gas utilisation, there is work investigating usage in boilers and furnaces without the need for supplementary materials. Numerous manufacturers such as Babcock and Wilcox, ANDRITZ, and Western Power [44, 45, 46] all provide boiler solutions capable of utilising steelworks gases, with flexibility in the fuels employed. Contemporary research by Shieh *et al.* [47] detailed an optimisation control model for gas blends, aiming for improvements in thermal efficiency of large scale multi-fuel boilers, based on residual oxygen in the system flue gas. The work

highlights problems with efficiently controlling boilers due to fluctuations in supply and composition of the gases, and employs multiple systems from a Taiwanese steelworks as the case study for model validation. The work presented by Hou *et al.* [48] enhanced this area, demonstrating theoretical and stable experimental combustion of BFG, with variable rates of supplementary COG, and lower flame temperatures shown to decrease NO_x production. However, some parts of this study are vague, and few details are provided regarding absolute change in fuel gas composition, giving only two stable operational case studies.

Although not desirable, traditionally steelworks gases are blended with alternative fuels for more stabilised combustion [1, 12, 15]. The detail presented by Green *et al.* [44] delivers practical insight to the designed versatility in boilers for the combustion of mixed steelworks fuels, including potential addition of natural gas and heavy fuel oil. The work of Bojic and Mourdoukoutas [49] and earlier Bojic and Tomic [50] investigated the relationship between combustion of a constant BFG composition, with supplementary natural gas and oxygen, quantifying how fluctuations in blended ratios influence CO₂ production. This study emphasised absolute change in CO₂ output from the system, opposed to analysing the influence of oxygen on fundamental combustion performance. Alternatively, case studies have been undertaken by various institutions [51] investigating boilers employing two-phase combustion of BFG and coal. Ma and Wu [52] presented more specified research analysing the burnout problems experienced when blending coal with BFG, and validated simulations of change in furnace parameters, such as residence time and temperature.

2.2.3 – Steelworks Gas Usage in Alternative Technologies

A different possibility for improving the efficiency of steelworks gas usage is the application of alternative technologies. Internal combustion (*IC*) engines offer potential improvements when used with combined cycles [53, 54]. Research investigating the use of BFG in IC engines dates back over a century [55], and more contemporary work by Lawton [56] reviews the historic use of steelworks gases in this manner. The traditional problem for IC engines related the large volumes of low quality gas

available, to the relatively small capacity of systems to date. Application in this way is becoming more financially viable to engineer by employing larger numbers of cylinders, with manufacturers providing potentially applicable solutions [57]. However, technical limitations are stipulated for stable operation, and restrict parameters such as change in fuel composition, resultant energy density fluctuation, moisture content, and contaminant matter [58]. Thus, more specified papers are being released, such as the work of Lieu *et al.* [59] where the combustion of BFG in IC engines has been modelled using GT-POWER, developed by Gamma technologies. Operational characteristics, such as ignition timing angle have been optimised for change in modelled flame speed, but this depends highly on the hydrogen content of the fuel. This topic also arises in the work of Ando *et al.* [60], who utilised low energy gases in an IC engine, and found that variability in combustion characteristics was far more influential to stable operation, compared with power output. Work has also been done utilising COG, for example Roy *et al.* [61] presented the output optimised operation of a dual-fuel supercharged IC engine, employing diesel as a pilot. This differed from other analogous work [62] by increasing the hydrogen fraction to be representative of COG (~60%), with exhaust gas recirculation simulated for thermal efficiency and NO_x improvements. However, the system was shown to experience problems with two stage combustion under certain conditions, leading to engine knocking.

The viability of using steelworks gases in combined cycle-gas turbines is also a good possibility, and although proven as a concept, is not currently employed as a widespread option in Europe due to issues arising from fuel operability and contamination [12]. However, turbine manufacturers are increasingly offering solutions capable of working with steelworks gases, with GE having provided 47 low energy units currently in operation worldwide [63], and others offering similar solutions (Siemens [64], Alstom [65], Mitsubishi [66]). Most of these turbines operate predominantly using BFG, blended with additional fuels, typically natural gas or COG, and burnt using highly resilient and flexible combustors. However, use of these fuels, particularly COG, requires significant pre-processing and cleaning, with manufacturers again stipulating limitations on the quality of fuel necessary for stable operation [26]. Bonzani *et al.* [67], present a case study where performance of an Alstom V94.2

turbine was evaluated for operation with a mixture of BFG, COG, and natural gas. Although stable operation was achieved, natural gas was mixed in significant proportions (~50%), together with being used for start-up. The study initially presented Lee *et al.* [68, 69], investigated the use of syngases containing the same combustible components as BFG, with performance shown to depend heavily on ratio of H₂ to CO. Pulsation instability experienced in the combustor was shown to compare favourably with diluted CH₄, though NO_x production was shown to be highly variable. Additional work by the authors then expanded on this with the addition of CO₂, N₂ and H₂O as diluents, demonstrating a detrimental influence on CO emission. Analogous work with different fuels blends by Chacartegui *et al.* [70] showed that compositional change between syngases led to increased problems with stability, particularly blow-off. Where as the work of Khalil *et al.* [71] attempted to relate diluted CH₄ to equivalent low calorific fuels from the perspective of laminar burning velocity and adiabatic temperature.

2.2.4 – Steelworks Gas Combustion

It appears one of the more significant contributory factors limiting the use of steelworks gases is the variable and potentially weak nature of combustion, particularly as operational instabilities are experienced. The numerical study performed by Gicquel *et al.* [72] varied the ratios of BFG, COG and oxidiser in simulations performed by EQUIL and PREMIX codes. The authors also vary the oxidiser, from standard air to a vitiated composition representative of the output exhausted from a gas turbine, and determine temperature and flame speed profiles, together with variation in extinction strain rate. The extinction limits of COG are shown to be much larger than the slow burning BFG, before the paper presents some Reynolds Averaged Navier Stokes (RANS) diffusion flamelet models. Covering a large area, the work appears to suffer from several weaknesses. Firstly, a constant composition of COG and BFG are assumed, and only one chemical reaction mechanism (referencing Lindstedt *et al.* [73], the performance of which has not been benchmarked for these types of fuels) is tested. The investigation also presents significant amounts of modelled work, with only the RANS simulation compared to an experimental burner.

The study presented by Abdulsada *et al.* [74] investigates the flashback and blowoff performance of several fuels, including a representative COG composition. Different swirl configurations are used with open and confined flames to characterise the practical combustion of COG on a burner, with greater instabilities experienced for lower mass flow rates. Furthermore, the work of Lewis *et al.* [75] demonstrated a correlation between a change in H₂ content of a representative syngas, the consequential change in burning velocity, and blowoff from swirl stabilised combustion. Paubel *et al.* [76] attempted to characterise BFG oxy-flame stability using a quadricoaxial burner, with CH₄ as a pilot. The work suffers from a similar weakness to others in that a constant BFG composition is assumed, and the burner requires the CH₄ pilot for stable operation.

2.2.5 – Summarising Steelworks Gas Background Research

Several conclusions are observable from the preliminary review of steelworks gas research and case study undertaken at the Tata Steel Port Talbot works, thus;

- Of the three steelworks gases, typically the most abundant is BFG, both in terms of volume produced and available thermal energy. However, it is also the most variable, least calorific and consequently the most unstable to burn, often requiring the addition of supplementary material. The most widespread application of BFG appears to be either in furnaces fuelling process operations, or in boilers used for the auxiliary generation of electricity and steam.

- There is contemporary research analysing the usage of blended steelworks gases in increasingly efficient technologies, such as IC engines and gas turbines. A frequent weakness in these works is the assumption of one representative fuel composition for each gas, which often varies between studies.

- Several practical analyses attempt to characterise operational instabilities resulting from the application of steelworks gases, however do this under specified conditions without necessarily quantifying variation in the fundamental properties of combustion. Furthermore, when computational models are applied to potentially optimise performance, there is little or no validation regarding the applicability of the technique.

There is a need for a more elementary understanding of inherent variation in the combustive properties of steelworks gases, and relating these characteristics to the validation of applicable chemical models. Such work would also relate directly to the combustion of analogous heavily diluted syngases, giving the investigation a wider field of interest. The property employed for characterising fuel behaviour in this investigation is the laminar burning velocity.

2.3 Fuel Combustion Properties

2.3.1 – Definition of Laminar Burning Velocity and Flame stretch

Under given ambient conditions of temperature and pressure, a one-dimensional planar adiabatic flame will propagate through a premixed combustible mixture at a constant rate, as a result of the thermal and mass diffusion of reactants. This is a fundamental physiochemical property of a fuel called the laminar burning velocity (sometimes termed laminar flame speed, or laminar burning rate), designated herein as u_L . It is one of the most significant parameters for defining fuel behaviour, relating to premixed operational instabilities such as extinction, flashback and blow off (section 2.3.3), whilst also used for characterising turbulent flame propagation [27-29]. In practise u_L is seen as idealistic, due to difficulties achieving an upstream quiescent mixture necessary for planar propagation, together with potential for heat loss.

Initial experimental investigation of flame speeds began with the early work of Bunsen and Roscoe [77] using a cylindrical burner (configuration detailed in section 2.3.2a), eventually enhanced with the propagation theory of Mallard and Le Chatelier [78].

Further advancements were made in measurement techniques, including the transparent observation of optical flame growth by Chamberlin and Clarke [79], and the *soap-bubble* method introduced by Stevens [80]. In the latter technique the combustible mixture is ignited within a bubble film, which is optically measured and experiences negligible external pressure increase. However, much of the early work with constant volume chambers used internal pressure rise to evaluate propagation rate. Wheeler [81] observed that values obtained using this technique with CH₄ were dependent on the chamber shape, the intensity and point of ignition, and ambient condition of the combustible mixture. Payman [82] attempted to correlate the propagation of many different fuels, and also noted the potential for change in obtained speeds from different conditions.

At the second international symposium on combustion in 1937, Payman presented continued work with Coward [83], and qualified the experimental influences on flame propagation further, namely motion of combustible mixture and flame speed relative to it, and size of the flame in relation to the confining area. Consequently, an attempt was made at a unified definition of linear flame speed normal to the surface of propagation. The initial theoretical work of Mallard and Le Chatelier was then also advanced by Lewis and Von Elbe [84], who achieved good correlations between experimental and calculated flame speed, after accounting for the combined effects of heat flow and diffusion. At the same symposium Fiock and Marvin [85] reviewed the various employed experimental methodologies, and presented a combination of the soap bubble and confined chamber methods, where optical measurements could be directly correlated against pressure rise. The work also highlighted a significant limitation of the soap bubble technique, namely water vapour from the bubble interacting with confined reactants. Von Elbe and Lewis [86] advanced the field further by introducing particle tracking to flame measurement. Later Powling [87] developed a burner that employed glass beads, wire mesh and small diameter tubes to enable combustion of a quasi-laminar flat flame. This technique was eventually adapted with water cooling [88], to become the flat flame heat flux method (section 2.3.2b).

In practise flame propagation is ordinarily influenced by aerodynamic strain, reactant motion or surface curvature, several influences encompassed by the term stretching. The origins of this concept relate back to the work of Karlovitz *et al.* [89], who first presented the comprehension that changes in surface velocity gradients influence flame propagation, inasmuch that local speed relates to the change of surface area (**A**) production. This concept introduces a parameter identified as the stretch rate (**α**), and is defined in relation to temporal change in A:

$$\alpha = \frac{1}{A} \cdot \frac{dA}{dt} \quad (2.1)$$

At a similar time, initial work undertaken by Markstein [90] also matched flame speed to the influence of curvature, and linearly characterised this relationship. The work was eventually expanded by Markstein [91] to account for diffusive effects, as characterised by an important parameter called the Lewis number (**Le**), or ratio of thermal to mass diffusivity:

$$Le = \frac{\lambda}{\rho \cdot c_p \cdot D} = \frac{k}{D} \quad (2.2)$$

where **λ** represents thermal conductivity, **ρ** the density, **c_p** specific heat (combined to define the thermal diffusivity **k**), and **D** ; the mass diffusivity. If an outwardly propagating flame is taken as an example, it is termed positively stretched. This means when $Le > 1$, thermal diffusion is more dominant and the flame loses heat in proportion to the surrounding reactant, and consequently accelerates as it expands. This is because stretch effects are more influential when the flame is small, and in relation curvature is large. This also means that flames become weakened, and burn slower in highly turbulent stretched environments. Conversely the opposite holds for flames with $Le < 1$. The parameter used by Markstein to characterise this effect of flame stretch is the burned gas Markstein Length (**L_b**), with further detail provided in chapter 3. When experimentally attaining values for u_L , the change in α must be obtained and accounted for in the observed propagation rate. This was suggested by Wu and Law [92] as a reason for the observed scatter in experimental data, and summarised by Andrews and Bradley [93].

2.3.2 – Importance of u_L in Characterising Operational Fuel Stability

Of the issues involved with premixed burner operability, the most significant relate to flame positioning and constancy, together with instabilities that arise from oscillations in pressure [94]. u_L directly characterises these parameters, and is therefore of significant importance for the prediction of flame behaviour (hence why there are extensive continued research activities surrounding this topic [95-97]). Simplistically, any operability issues that relate to flame position are a result of an imbalance between the velocities of premixed reactants reaching the burner, and the flame. Fig 2.10 helps explain this further (adapted from [29]), with a simplified example of a generic flame configuration positioned on a rim.

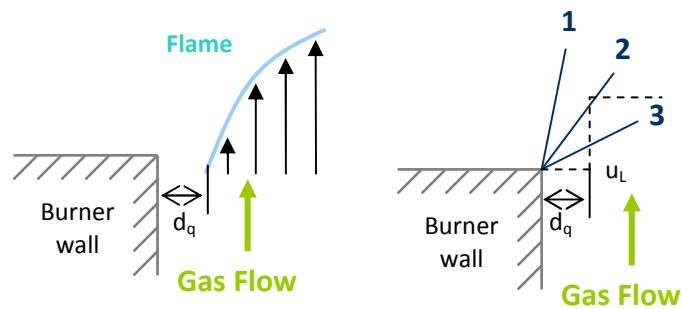


Fig. 2.10 – Diagrammatic representation of fuel velocity gradients for a simple rim burner (from [29]).

The left side of the image in Fig 2.10 shows flame position together with the fuel velocity profile as it reaches the burner (note - extinction due to heat loss at the edge, equivalent to the quenching distance (d_q)), with flow velocity increasing from zero at the wall. The three lines labelled **1**, **2**, and **3** on the right represent flow velocity gradients from the boundary, with the dotted step change equivalent u_L . Gradient **1** signifies a sharp rise in speed, for a large flow rate. At this condition the fuel velocity is entirely larger than u_L , and the flame is physically *blown* from the burner (blowoff). For gradient **3**, the fuel velocity is slower than u_L , leading to upstream propagation of the flame into the reactant flow, and potential *flashback*. Gradient **2** represents a stabilised flame, where flow is balanced with burning velocity. This is a simplified ideal representation of a premixed combustion system, and in practise stabilising mechanisms exist (for instance change in wall quenching effects with axial position,

and swirl) to enable a region of stable flow between flashback and blowoff. In addition these characteristics will be further influenced with how the burning velocity is affected by flame stretch. This concept of a stable burning region is depicted graphically for the combustion of natural gas in Fig. 2.11 (from [28] and [29]).

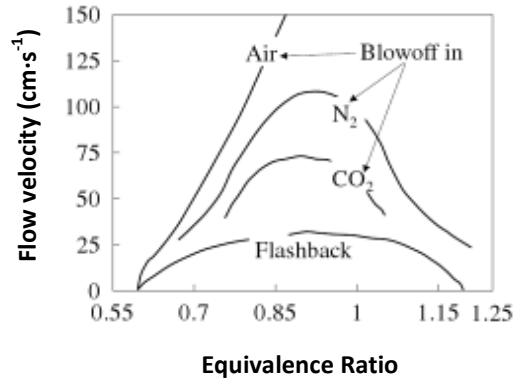


Fig. 2.11 – Flashback and blowoff profiles for the combustion of natural gas (from [28, 29]).

A critical velocity gradient (g_f) resulting in boundary layer flashback can be approximated directly from knowledge of u_L , the quenching distance, and thermal diffusivity of the flame (k) thus [94];

$$g_f = c \cdot \frac{u_L}{d_q} = c \cdot \frac{u_L^2}{k} \quad (2.3)$$

where c is a constant of the employed burner. Whilst this classical relationship provides a good approximation for boundary layer velocity gradients, complete flashback behaviour is fully characterised by further effects from stretch, pressure pulsation or vortex breakdown in a swirling flow [94]. Similarly lean blowoff behaviour can be characterised by k and u_L , with a Damköhler number relating thermo-chemical reaction time (k/u_L^2), to residence time [94]. This association is also simplified, with the additional influences such as turbulent flow and stretch influential in characterising burner velocity gradients and critical Karlovitz numbers [29]. Nevertheless accurate knowledge of u_L for a given fuel type is a necessary requirement for engineers to model and predict system behaviour, in addition to influences such as flame stretch. Consequently, whilst fluctuation in parameters such as equivalence ratio and u_L are inevitable in practical combustion systems, it is desirable to minimise any inherent variation to improve system stability.

There are typically four flame configurations that are applicable for experimental determination of u_L , and the influence of stretch is dependent on which is employed. The configurations have been presented in the following section, with the operation, merits, and limitations of each discussed before one is detailed for specified use in this investigation.

2.3.3 – Selecting an Experimental Flame Configuration

Fig. 2.12 provides representative schematics of four flame configurations that can be employed for determination of u_L .

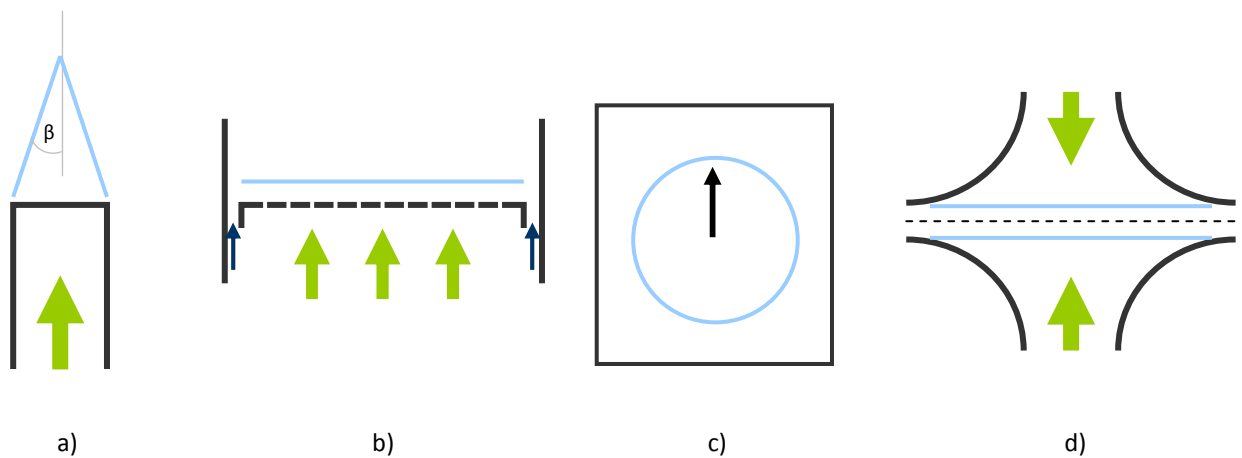


Fig. 2.12 – Schematic representation of four experimental flame configurations for determination of u_L : a) Bunsen burner flame. b) Flat flame. c) Outwardly propagating spherical flame. d) Counterflow flame.

2.3.3a – Stabilised Bunsen Flame

This simple method uses a negatively stretched conical flame fixed on the rim of a cylindrical (or typically Bunsen) burner, as represented in Fig. 2.12a. If the gas exit velocity profile is taken to be uniform, then the localised laminar burning velocity can be related to the half cone angle (denoted β in Fig. 2.12a) of the flame, the gaseous mass flow, and dimensions of the burner. The flame surface is identified using either Schlieren or chemiluminescent visualisation techniques, or even seeded for velocimetric determination of local speeds [86]. Issues arise from a combination of heat loss, change in flame intensity at the tip of the cone, and defining the exact location of the flame front [93].

2.3.3b – Flat Flame with Heat Flux Correction

This technique is similar to the stabilised Bunsen flame, and is depicted schematically in Fig. 2.12b. The flame is fixed onto a porous plug, and the flow rate of the gas adjusted until a flat combustion front is achieved, with burning velocity attained from the geometry of the system. The flame stabilises due to heat loss in the porous plug, so the measurement is inherently non-adiabatic, and not representative of the desired value. An adaptation suggested by Bootha and Spalding [88] involved measuring different values of heat loss to the plug by cooling to distinct temperatures. If the attained flow values are plotted and extrapolated to adiabatic conditions, the laminar burning velocity can be attained. One characteristic of using this method is that the flame is subjected to minimal stretch, so a quasi-direct measurement can be made. However, the technique does require a relatively complex experimental setup, and a steady accurate gas supply flow rate. Further adaptations have been presented for more precise measurement of heat loss [98].

2.3.3c – Spherically Expanding Flame with Stretch Correlation

This is the most direct of the employed measurement techniques, and requires extensive numerical processing of the attained data. The method involves filling a constant volume chamber with a quiescent mixture which is centrally ignited, and the rate of outward, positively stretched, flame propagation measured (as shown schematically in Fig. 2.12c) [27]. Expansion of the combusted gases must be accounted for, and the influence of flame stretch on burning velocity can be quantified as a property of the mixture with determination of L_b , with extrapolation required for representative unstretched conditions. Another significant advantage of using the technique is that ambient conditions of pressure and temperature can be easily varied and controlled, with a comparable burning velocity also attainable using the pressure rise technique. Disadvantages include the influence of heat loss to ignition electrodes, and the buoyancy of combustion products distorting the flame [27].

2.3.3d – Counterflow Flame with Stagnation Zone

This method was developed by Wu and Law [92], and requires the creation of a divergent stagnation field, by directing two combustible flows symmetrically into each other. Following measurement of the flow velocity profile through the flame toward the stagnation plane (represented by the dashed line in Fig 2.12d), numerical processing of a specified reference velocity is required [96]. Like the spherical method, extrapolation of plotted velocities against stretch rate (generated through the non uniform flow, and varied through change in mass flow rate or separation distance) yields the desired value of u_L . Position of the flames relative to the burner head mean conditions can be assumed to be quasi-adiabatic, with the method well suited to laser based velocimetry. Similar to the first two methods, this technique requires a constant gas and tracing seed supply, and is also comparatively complex [27].

For the purposes of this work, the spherically expanding flame configuration was chosen, with a methodology developed for quantifying outward rates of flame propagation. This technique was selected as a result of several factors; firstly due to the accuracy, simplicity, and resultant flexibility of the approach. An investigation of this nature requires the mixture of several gases in different ratios, with all other techniques requiring continuous gas streams, hence potentially necessitating several mass flow controllers. Consequently, it would be more difficult and expensive to attain high accuracy in blending, together with larger amounts of wasted gas [96]. The technique is also more adaptable for defining ambient condition of the reactants, and particularly more suited to pressure variation. In addition, a constant volume chamber is apposite to the use of simultaneous analytical techniques, with u_L measurable from internal pressure rise, together with the quantified optical propagation of the flame. There is also flexibility for future use, with ancillary studies also possible for systematic investigation of parameters such as ignition energy [99] and turbulence intensity [100].

Prior to outlining the objectives of this research dissertation further, it was first necessary to investigate relevant fuel characteristics already published in literature, and how these relate to the steelworks gases under investigation.

2.4 Analogous Research with Alternative Fuels

2.4.1 – Flame Speed Research with Methane

Early studies in the area of laminar flame speeds were largely performed for the combustion of CH₄-air, (section 2.3.1), with the fuel widely-applied in literature for benchmarking methodologies and critical review [92, 93, 101]. With regard to spherical CH₄ flames and the extrapolation technique employed in this study, Bradley *et al.* [99] presented a computational investigation for combustion of CH₄ with air at atmospheric ambient conditions. The impact of variation in ignition energy was investigated (Fig. 2.13a), with stretch influence also separated to individual parameters of flow field strain and curvature. Further work by Gu *et al.* [102] expanded upon this by changing ambient conditions of temperature and pressure with equivalence ratio, and presenting power law correlations for the data (example given in Fig 2.13b).

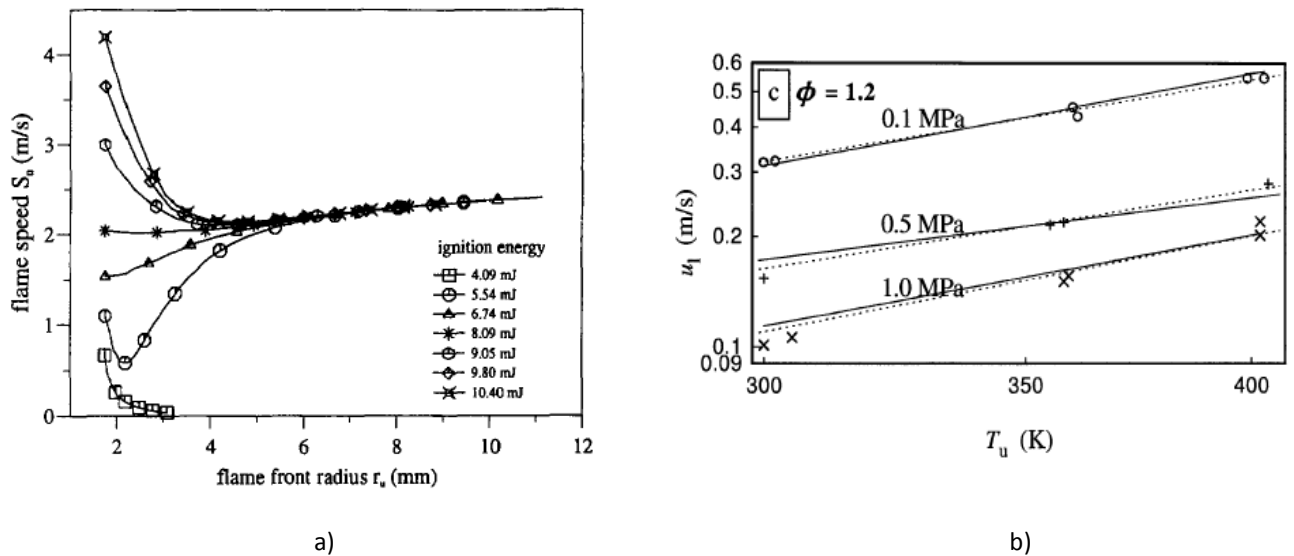


Fig. 2.13 – Examples of the variation in work undertaken by a) Bradley *et al.* [99] and b) Gu *et al.* [102]

With vast quantities of information available on CH₄ flame speeds, it is frequently employed whenever modifications or adaptations to analytical techniques are presented. Examples of this include the more contemporary works of Tahtouh *et al.* [103], Kelley and Law [104], Halter *et al.* [105] and Varea *et al.* [106], with these respective works discussed further in section 3.1. Furthermore, there are also

significant quantities of CH₄ data available from the application of alternative techniques, often demonstrating good agreement between comparative works [92, 107, 108]. It was therefore deemed appropriate that CH₄ be used for benchmarking performance of the experimental technique developed for this study.

As alternative fuel blends have become more prevalent, the broad direction of research has shifted to investigate the flame speed characterisation of CH₄ when blended with different gases. Ilbas *et al.* [109] investigated the change in observed flame speed for the addition of H₂, with further instances of analogous works by Halter *et al.* [110] and Hu *et al.* [111]. H₂ is shown to increase u_L for CH₄ combustion, whilst simultaneously lowering L_b . Fig. 2.14 demonstrates these trends at different H₂ fractions, for u_L (a) and L_b (b) with equivalence ratio - ϕ (taken from Hu *et al.* [111]).

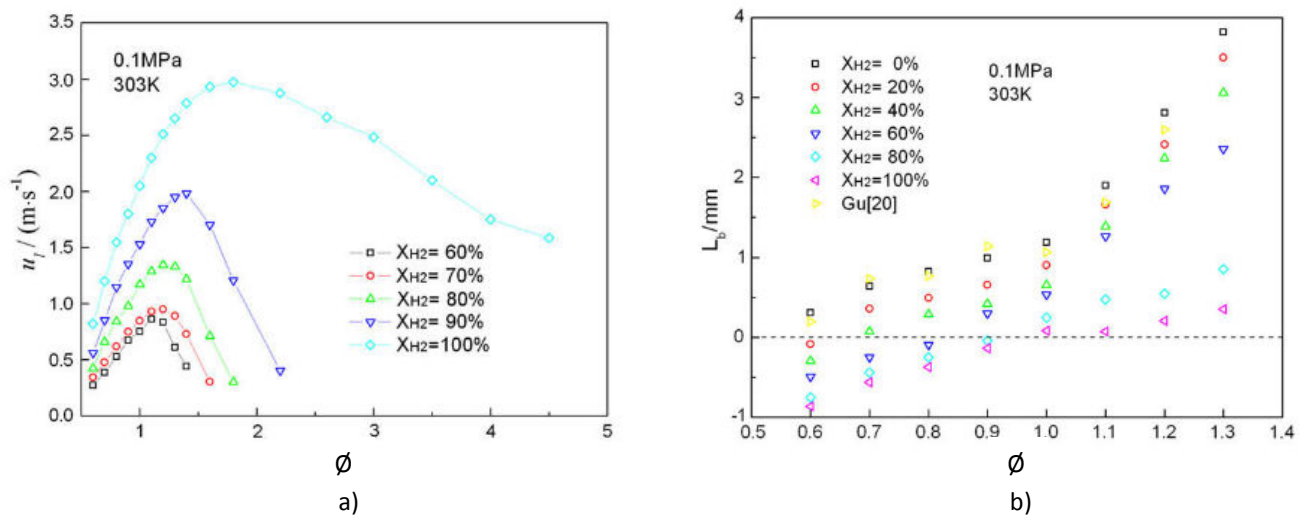


Fig. 2.14 – Variation in u_L (a) and L_b (b) with equivalence ratio (ϕ) for CH₄ with increasing H₂ fraction (X), taken from Hu *et al.*[111]

There is further work by numerous authors investigating the addition of diluents. Boushaki *et al.* [112] investigated the change in u_L characteristics of CH₄-H₂ blends with steam addition, and an alternative slot burner technique. Taylor [113], Tahtouh *et al.* [114] and later Miao *et al.* [115] similarly investigated the influence of N₂ dilution and change in ambient pressure, together with CO₂ dilution in different work [116]. All of these diluents are shown to suppress CH₄ combustion and slow u_L by differing amounts. Whilst there are several tested compositions that comprise diluted CH₄ and H₂ combustion, there are no published works analysing of an approximate COG composition.

2.4.2 – Research with Hydrogen and Carbon Monoxide Syngases

As interest in the use of alternative fuels increase, significant amounts of data are now being published for diluted syngases and biomass derived fuels containing H_2 and CO . These fuels are pertinent as they comprise the same constituents as BFG and BOS gas. Independent H_2 combustion with air was characterised using spherical flames by Dowdy *et al.* [117]. However, the use of expanding flames in this way for independent H_2 characterisation is troublesome due to the onset of instabilities with pressure rise, that increase flame surface area and consequently influence flame speed. This vast research area has been investigated by several authors, including; Bradley *et al.* [118], and Law *et al.* [119], and applicable for spherical flames by obtaining data up to a defined critical radius (related to Péclet number) from which the flame becomes unstable. Alternatively, Helium can be employed as a diluent to minimise diffusive instabilities [120], or a different measurement technique can be used. Egolfopoulos and Law [121] investigated H_2 flames on a counterflow burner, with changing oxidiser N_2/O_2 ratio, and effectively demonstrated how positive stretching decreased the inception of cellular instabilities. Similarly Vagelopoulos and Egolfopoulos [107] employed the same counterflow technique to investigate how flame speed of CO is increased with the addition of H_2 and CH_4 . Fig. 2.15 highlights the trend of change in u_L for CO blended with increasing quantities of H_2 , taken from the work of Bouvet *et al.* [122].

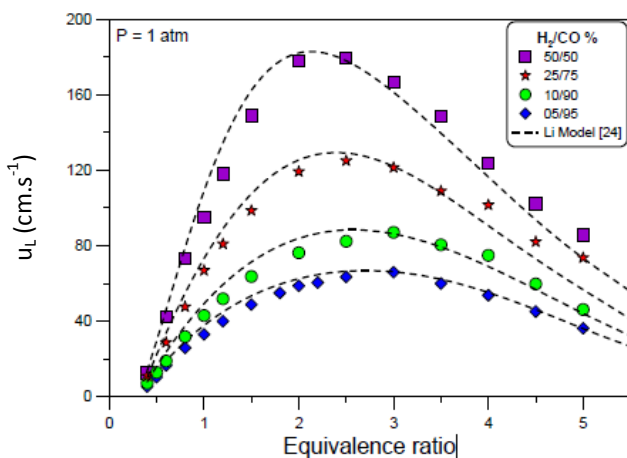


Fig. 2.15 – Variation in u_L with equivalence ratio for CO with increasing H_2 fraction. (Bouvet *et al.*[122])

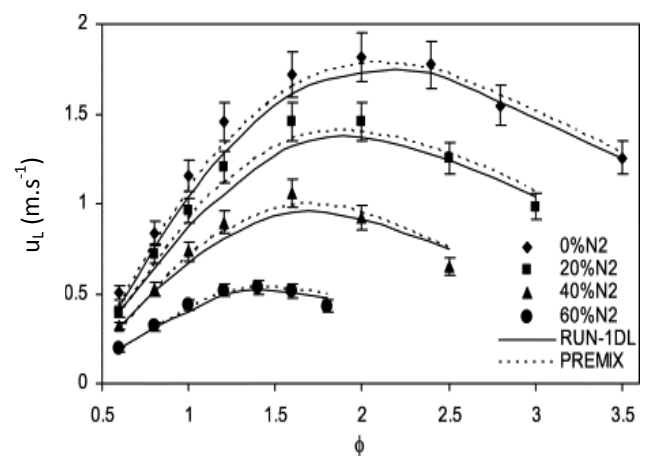


Fig. 2.16 – Variation in u_L with equivalence ratio for an equal H_2 - CO blend with N_2 addition. (Prathap *et al.*[123])

The disparate effects of CO₂ and N₂ (Fig. 2.16) dilution on an equal volumetric H₂-CO mixture was detailed by Prathap *et al.* [123] and [124] for atmospheric ambient conditions using spherically expanding flames. Diluent addition was shown to shift the peak u_L toward stoichiometric conditions, together with negative L_b experienced with leaner mixtures. CO₂ was also shown to be more influential to suppression of u_L compared with N₂, with potential for increased involvement with intermediate chemical reactions highlighted as a potential cause. Das *et al.* [125] analysed the change in u_L resulting from addition of water vapour to syngas blends of different H₂-CO ratios, with the result shown to be dependent on a complex relationship between chemical effect in the generation of intermediate species, and heat loss. This work highlights a pertinent area of investigation for humid steelworks gas combustion, without quantifying the influence of diluents.

Other syngas mixtures have been analysed by various authors for a range of ambient conditions, for instance the work of Monteiro *et al.* [126] employed three compositions representative of producer fuel from wood gasification. Characteristics of the three tested compositions were shown to be most sensitive to fluctuation in H₂ fraction, with peak burning velocities experienced at near stoichiometric air-fuel ratios. The study presented by Burbano *et al.* [127] gave details of a syngas mixture tested for variation in diluent content using a slot burner at atmospheric ambient conditions. Data were generated and compared to numerical models. Further work by Burbano *et al.* [128], and Liu *et al.* [129] looked at similar syngas compositions, but varied ambient pressure away from atmospheric conditions.

2.5 Investigation Objectives

After undertaking the research presented in this chapter several objectives were identified to fulfil the aim of this research dissertation. These are as follows;

- Firstly, an experimental rig is required to facilitate the accurate determination of flame speeds and the inherent influence of stretch effects, by quantifying the outward propagation of spherical flames. Furthermore, a computational analytical technique needs to be subsequently developed that allows for rapid and precise measurement of temporal changes in flame radius. The developed solution needs to be benchmarked against analogous studies in literature to ensure experimental performance is accurate and repeatable with respect to other works.

- Steelworks gases then must be tested to attain representative burning velocities, however opposed to attaining values for a single gaseous composition, attention will be given to the inherent variability in flame speed that results from compositional change. Being both the most abundant, and difficult to utilise, considerable focus will be on the combustion of BFG with air. This part of the study will investigate the sensitivity to changes in hydrogen fraction, as this is the most significant contributory factors to fuel performance, and offers the largest amount of relative variation as the gas is produced.

- Together with variation in composition, the influence of changes in ambient condition will also be quantified. The aim of this is to investigate the extent to which fluctuation in u_L from hydrogen fraction can be dampened by altering the physical characteristics of the gas. This will include independent changes in temperature and pressure to limits specified by the mechanical properties of the equipment.

- A further area of interest is change in relative humidity of the fuel, again with particular attention paid to BFG. The moisture content of BFG is potentially variable depending on the cleaning methods employed, and a function of the gas temperature. However, even if BFG is assumed to be dry there can still be changes in the relative humidity of atmospheric air used for combustion. It is estimated that due to the high levels of diluents in BFG composition, the tested characteristics will be particularly sensitive to changes in relative humidity. Again BFG composition will have to be varied to attain data representative of fluctuation experienced in practise.
- Having investigated the performance of individual steelworks gases, the fuels will then be blended in different ratios to fundamentally characterise dynamic combustive properties relating to fuel flexibility. In this regard some fuel properties will be benchmarked with respect to combustion of widely utilised natural gas. Attention will primarily be given to analysing the effectiveness of blending gases to minimise inherent fluctuation in BFG combustion.
- Whilst attaining experimental data for the combustion of various steelworks gases and blends, significant attention will be given to computational chemical kinetics modelling. The performance of several reaction mechanisms will be evaluated with respect to accuracy of modelling steelworks gas combustion. If models are shown to be capable of accurately predicting fuel behaviours, then simulated data can be applied to reduce the number of points in the experimental testing matrices, and subsequently accommodate further parameters of study in the time available.

Chapter 3. Theory and Experimental Method

3.1 Theory

3.1.1 - Flame Configuration and Analysis

The technique presented herein is an adaptation of the contemporary method developed by Dowdy *et al.* [117] and Taylor [113] for an outwardly propagating spherical flame. In order to quantify flame speeds in this way, a constant volume is filled with combustible mixture at a specified air-fuel ratio, under defined ambient conditions of temperature and pressure. The mixture is then centrally ignited, and the size of the spherical flame measured as it propagates outward toward the chamber walls.

When employing this method several factors must be taken into consideration: The expansion of combusted products leads to an increase in the observed flame propagation rate, and also raises pressure within the chamber. This reactant compression can inhibit the flame, whilst simultaneously increasing the temperature of the unburned mixture. In addition, early flame development can be influenced by the stored energy discharge from spark ignition, and buoyancy affects observed if propagation is slow. Therefore, detailed care must be taken when selecting and analysing appropriate measured data [27].

These factors are discussed further in this chapter, where the design of an operational experimental rig is considered, but first follows a derivative analysis for measuring u_L in this way. Fig. 3.1 gives a diagrammatic representation of the employed flame configuration.

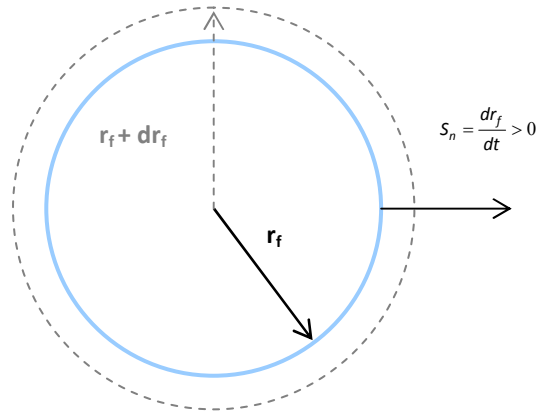


Fig. 3.1 – Outwardly propagating spherical flame configuration [27].

The observed flame speed (S_n) is measured as the first order derivative of radius (r_f) with respect to time, and for an outwardly propagating flame is always greater than zero, as follows:

$$S_n = \frac{dr_f}{dt} \quad (3.1)$$

It is important to emphasise the discrepancy in the used definition between the desired value of laminar burning velocity (u_L), and this observed speed, which has been accelerated by the expansion of hot combustion products. S_n is also influenced by flame stretch (as discussed in section 2.3.2), and therefore shall be recognised in text as the *stretched flame speed*. In order to attain experimental values of u_L , both expansion and the effects of stretch must be negated.

3.1.2 - Defining Stretch Rate for Spherical Flames

The stretch rate (α) was earlier expressed in relation to the change in area gradient of the flame (Eqn. 2.1 in section 2.3.1, and for the employed configuration is defined as follows [113, 117, 27, 99].

Firstly, the surface area (A) of a spherical flame is given by:

$$A = 4 \cdot \pi \cdot r_f^2 \quad (3.2)$$

and substituting Eqn. (3.2) into (2.1) for stretch rate, expands to give:

$$\begin{aligned}
 \alpha &= \frac{1}{A} \cdot \frac{dA}{dt} = \frac{1}{4 \cdot \pi \cdot r_f^2} \cdot \frac{dA}{dt} \\
 &= \frac{1}{4 \cdot \pi \cdot r_f^2} \cdot \frac{dA}{dr_f} \cdot \frac{dr_f}{dt} \\
 &= \frac{1}{4 \cdot \pi \cdot r_f^2} \cdot 8 \cdot \pi \cdot r_f \cdot \frac{dr_f}{dt} \\
 &= \frac{2}{r_f} \cdot \frac{dr_f}{dt} \tag{3.3}
 \end{aligned}$$

substituting Eqn. (3.1) therefore gives:

$$\alpha = \frac{2}{r_f} \cdot S_n \tag{3.4}$$

Bradley *et al.* [99] derived expressions to show total stretch rate defined for this flame configuration encompasses the cumulated influences of flow-field strain (α_s), and flame curvature (α_c), or:

$$\alpha = \alpha_s + \alpha_c \tag{3.5}$$

Calculated values of α can therefore be applied with measured S_n to negate the effects of stretch and attain the unstretched flame speed (S_u). In this thesis, two methods of optically obtaining S_u from changes in S_n and α have been employed.

3.1.3 - Linear Extrapolation Methodology

The aforementioned work of Wu and Law [92] with the counter-flow stagnation burner was the first methodology presented that extrapolated different attained flame speeds with α to representative unstretched conditions. The method employed by Dowdy *et al.* [117] and Taylor [113] developed based on the work of Markstein [90, 91], utilised this rationale, suggesting a linear relationship between α and flame speed as follows:

$$S_u - S_n = L_b \cdot \alpha \tag{3.6}$$

where L_b (the burned gas Markstein Length) is the parameter used to characterise the influence of stretch of flame speed. L_b is directly related to the earlier defined Lewis number (Le), with this diffusivity ratio influencing both sign and magnitude of the influence of stretch. This relationship was derived to be sufficiently accurate when the stretch effects, and any subsequent losses, are small. It follows from Eqn. (3.6) that having experimentally measured S_n , and calculated the corresponding values of α , the two can be plotted with a gradient of L_b . That data can then be used to extrapolate the relationship to a corresponding intercept value, equivalent to a rate of zero stretch, thereby attaining S_u for a theoretical spherical flame with infinite radius.

Eqn. (3.6) can also be expressed in the following form [27]:

$$\frac{S_n}{S_u} = 1 - Ma \cdot Ka \quad (3.7)$$

where Ma and Ka are the respective Markstein and Karlovitz numbers defined thus:

$$Ma = \frac{L_b}{d_t} \quad (3.8)$$

$$Ka = \frac{d_t}{S_u} \cdot \alpha \quad (3.9)$$

with d_t representing the unstretched flame thickness, defined as the quotient of thermal diffusivity (k) to the laminar burning velocity.

The linear methodology has been widely applied in literature for combustion characterisation (for example [99], [102], and [115]). Alternative ways of applying this linear methodology have been proposed by different institutions, for instance, utilising Lambert's W -function to avoid the use of regression in obtaining S_n , by Tahtouh *et al.* [103], or combining and integrating equations (3.1) and (3.6) [120]. These methodologies however, do not account for the observable nonlinearity of S_n against α when propagation is heavily influenced by stretch [104, 105].

3.1.4 - Nonlinear Extrapolation Methodology

A methodology was presented by Kelley and Law [104] that utilises a separate nonlinear relationship between S_n and α , developed from the work of Ronney and Sivashinsky [130] and Clavin [131]. This nonlinear relationship is derived to account for deviation from adiabatic and planar assumptions that are more prominent when the flame experiences losses from the heavy influence of stretch, and is expressed:

$$\left(\frac{S_n}{S_u}\right)^2 \cdot \ln\left(\frac{S_n}{S_u}\right) = -\frac{2 \cdot L_b \cdot \alpha}{S_u} \quad (3.10)$$

Relationships of the same form have been derived to express other similar parameters, such as the upstream flame speed of a counterflow flame, and can be generalised in the form [104]:

$$\bar{S}^2 \cdot \ln \bar{S}^2 = \sigma \quad (3.11)$$

with \bar{S} representing stretch normalised flame speed (S_n/S_u), and σ a separate loss parameter. It has been shown [105] from simplifying the detailed model given by Chen *et al.* [132], that for weakly stretched flames ($\bar{S} \rightarrow 1$), Eqn. (3.10) tends towards the linear relationship given in Eqn. (3.6).

Contemporary literature [104, 105] proposes improvements in accuracy that can be achieved by using this relationship. However, the numerical processing of experimental data necessary to obtain values for S_u and L_b is more complex. Detailed examples of the procedures undertaken to obtain values from both optical methodologies are provided in the next chapter, where experimental performance is benchmarked against other research. Regardless of which methodology is employed, the attained values of unstretched flame speed are still influenced by the expansion of combusted gas, which must be numerically accounted for in the derivation.

3.1.5 – Accounting for Expansion of Combustion Products

At constant pressure, the adiabatic expansion can be expressed as the ratio between the burned (ρ_b) and unburned (ρ_u) densities of the products and reactants [99]. S_u is therefore related to u_L as follows:

$$u_L = S_u \cdot \left(\frac{\rho_b}{\rho_u} \right) \quad (3.12)$$

This relationship is widely utilised in the relevant literature (e.g. [99] [102] [115]), and whilst ρ_u can be calculated with relative ease, the method still requires precise knowledge of ρ_b . For the purposes of this work, it was established computationally using chemical kinetics modelling. The package chosen to determine these parameters was CHEMKIN-PRO, with section 3.4 providing further detail regarding numerical use of this software.

3.1.6 – Dynamic Pressure Measurement Approach

The need to computationally determine the burned gas density is the most significant limitation of employing the specified configuration. However, a direct comparison can be made between the calculated expansion ratio and pressure rise within the chamber. These values cannot be used directly due to heat loss in measurement, but variation from change in equivalence ratio and ambient condition can be used for a comparison in trends. Furthermore, it is also possible to observe a direct relationship for the determination of u_L from analysing the temporal pressure transients resulting from combustion. Dahoe *et al.* [133] [134] recently presented work using this relationship, with the equation derived from the work of O'Donovan and Rallis [135] as follows:

$$\frac{dP}{dt} = \frac{3}{R_c} \cdot \left(\frac{dx_m}{dP} \right)^{-1} \cdot \left[1 - \frac{P_i}{P} \cdot \frac{1}{\nu_u} \cdot (1 - x_m) \right]^{\frac{2}{3}} \cdot \left(\frac{P}{P_i} \right)^{\frac{1}{\nu_u}} \cdot u_L \quad (3.13)$$

where P_i represents the initial pressure prior to combustion, R the chamber radius, and γ_u isentropic exponent of the unburned gas, otherwise defined as the ratio between isobaric and isochoric specific heats:

$$\gamma_u = \left(\frac{C_p}{C_v} \right) \quad (3.14)$$

x_m corresponds to the burned mass fraction, originally proposed by Lewis and Von Elbe [28] to be linearly related to the final or end pressure (P_e) as follows:

$$x_m = \left(\frac{P - P_i}{P_e - P_i} \right) \quad (3.15)$$

There have been several other models proposed by Dahoe *et al.* [133] for the determination of x_m to be used in this way [134].

The accuracy of the pressure method relies on several significant assumptions; firstly a uniform pressure within the vessel, together with negligible heat loss or gain (from ignition), isentropic compression of the unburned reactants, and finally a buoyancy-free, infinitely thin spherical flame front.

The experimental rig was developed to allow data acquisition for both the optical and pressure analytical techniques. A direct comparison of each method is made in the following chapter where the experimental performance is benchmarked against analogous results from literature. First follows the design setup, and operational methodology of the system employed.

3.2 Experimental Apparatus

3.2.1 - Components of the Experimental Rig

A constant-volume combustion bomb (herein referred to as *CVCB*) was built and developed into an experimental rig for the determination of u_L for this study. A simplified schematic layout of the *CVCB* rig is shown with labelled additional components in Fig. 3.2, with a photograph of the assembled system is provided in appendix A.3. The first section of this work describes the individual specification of these major rig components to provide an overview of system design, functionality and operation, before moving on to discuss the employed experimental procedure.

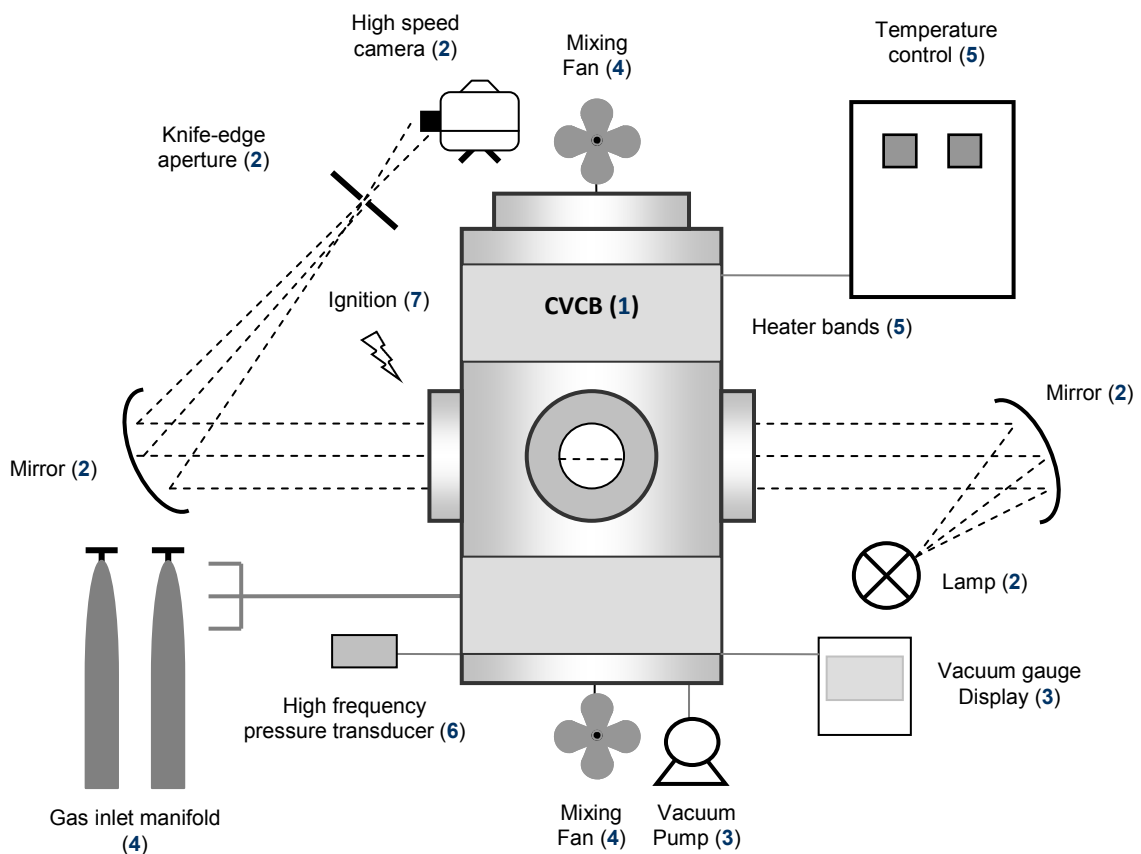


Fig. 3.2 – Experimental rig schematic.

3.2.2 - CVCB Design Overview

The CVCB was constructed from grade 316 stainless steel, and designed to allow for a sufficiently long experimental time window in the pressure unaffected region of flame expansion. As introduced in section 3.1.1, the observed flame speed is increasingly influenced by reactant pressure building as the flame propagates, with Burke *et al.* [136] recommending that for a cylindrical bomb, the maximum usable flame radius is approximately 30 percent of the overall chamber dimension. The CVCB developed in this study has a cylindrical volume of approximately 36 L with an internal diameter of 260 mm, thereby giving a maximum usable flame radius of 39 mm. Four diametrically-opposed ports were added to allow perpendicular line of sight through the centre of the chamber. These ports house quartz windows, 100 mm in diameter, thereby allowing optical access to the maximum usable flame radius. The significant chamber dimensions are outlined in Fig. 3.3.

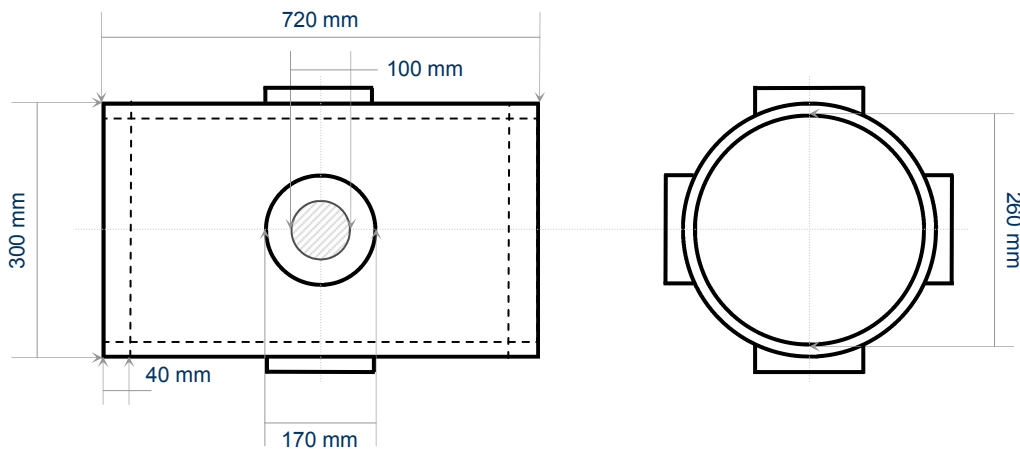


Fig. 3.3 – CVCB dimensions.

The chamber was designed to withstand an internal pressure rise of 14 bar, and was hydrostatically tested prior to fitting an over-pressure valve in the exhaust line, thereby fixing the overall limit to a maximum of 9 bar (60% of the design pressure). This value was specified to be in the order of the maximum pressure increase anticipated from the preliminary test specification. However, the system was designed with a large safety factor of seven, and by modifying the size or number of bolts used

(calculated to be the most significant limiting factor, with welds and quartz windows much stronger); this value could be significantly increased for further testing.

A total of twelve ports were included in the CVCB wall to allow access for the various sensors and pipes necessary for system operation. Four ports were used by k-type thermocouples, two by ignition electrodes, and two had pressure transducers attached; one vacuum gauge readout, and the other a high frequency sensor (sections 3.2.4 and 3.2.7 respectively). The remaining four lines were independently connected to the vacuum pump, exhaust, fuel supply manifold, and oxidant feed, with isolation valves used to separate the ports from the chamber when necessary.

3.2.3 - Schlieren Imaging Setup

High-speed capture of flame propagation was achieved through use of Schlieren cinematography, widely employed in the relevant literature (e.g. [99] [104] [122]). The technique utilises the change in refractive index resulting from variation in gas density [137], with Fig. 3.4 showing a schematic of the employed principle.

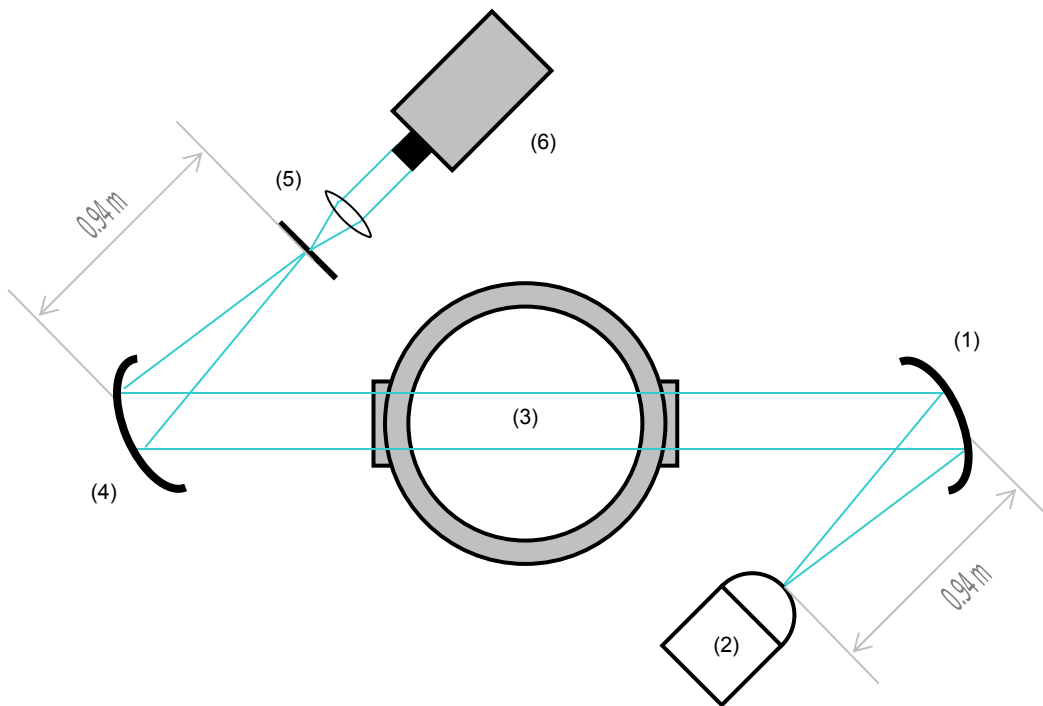


Fig. 3.4 – Outline of the Schlieren imaging principle used in this study.

A converging mirror (Fig. 3.4 – (1)) is initially used to collimate a filament light source (Fig. 3.4 – (2)) through two of the diametrically opposed viewing windows. The region in the path of the light beam is the working area under study, which passes through the centre of the chamber and gases contained within (Fig. 3.4 – (3)). A secondary reflection (Fig. 3.4 – (4)) is then used to focus the light beam onto an aperture (Fig. 3.4 – (5)), where the refracted portion of the beam, unblocked by the knife-edge, focuses imperfectly prior capture by a high-speed camera (Fig. 3.4 – (6)).

This process creates light intensity gradients influenced by variation in refractive index that result from changes in working gas density. Consequently, any shadowed or brightened edges resulting from combustion are isotherms indicative of a significant change in density, and therefore taken to be representative of the flame front boundary [99]. Fig. 3.5 gives some examples of Schlieren images. Firstly refracting light through the gases of a small butane torch, with (a), and without (b) the fuel burning (visible through the disparity in fluid densities between the fuel, and air it is released into), and secondly a typical spherical flame ignited from electrodes within the CVCB.

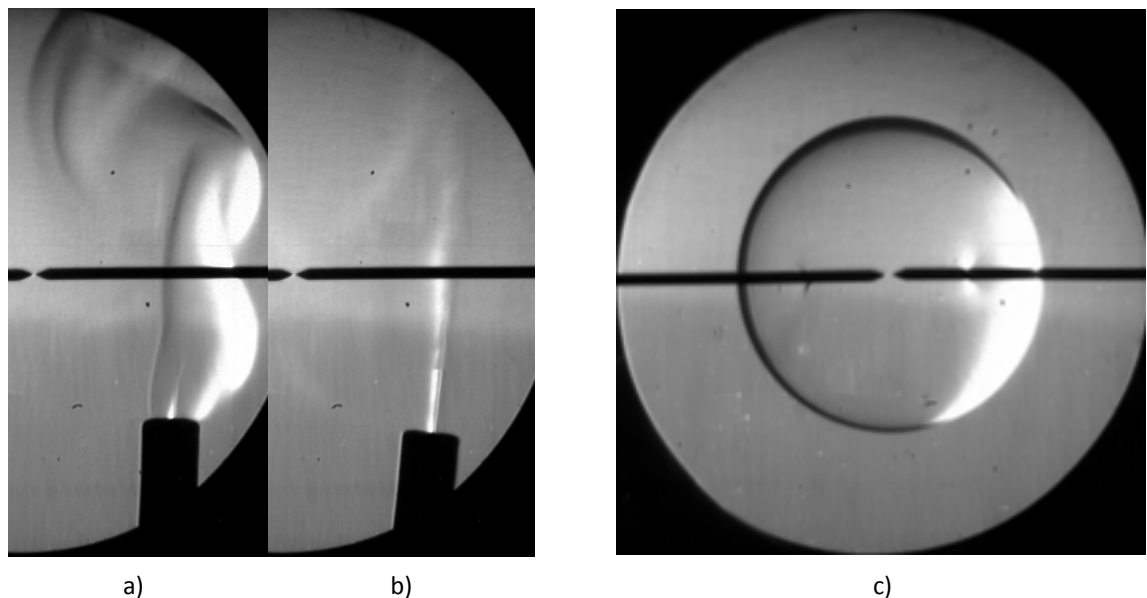


Fig. 3.5 – Schlieren images of: a) Burning butane. b) Butane release. c) Spherically propagating flame

The light is focussed through a lens and captured by a charge-coupled device used in a Photron FASTCAM APX-RS high-speed camera. The specified filming rate was dependent on the fuel under investigation, and altered to pragmatically capture as many usable frames (effective data points) as possible. For slower flames the filming rate was adjusted to avoid excessively large video files. The increase in frame-rate is also limited by the image size, shutter speed, and in turn, the power and intensity of the light in the system [138]. Independent camera specifications are therefore discussed for the different results presented. The output from each test was a series of frames recorded in the form of a video file which were computationally scaled and processed, (described further in section 3.3.3 and 3.3.4). The timing of frame capture rate is controlled from the internal processor within the camera, and has a specified full scale accuracy of 0.005 percent.

3.2.4 - Vacuum System

A SCROLLVAC SC15D dry-scroll vacuum pump was used to evacuate the contents of the CVCB between each test at a nominal rate of $15 \text{ m}^3 \cdot \text{h}^{-1}$. The use of a dry scroll pumping mechanism was specified to avoid potential contamination resulting from the migration of oil vapour into the evacuated chamber, which can be experienced when using high-performance rotary vane alternatives [139]. The pump was sized to allow maximum pumping rate for available expenditure. A real-time value of the internal chamber pressure was given by an Edwards D35727000 ASG 0-2000 mbar sensor with a resolution of 0.1 mbar, and a full scale accuracy of ± 0.2 percent. The pressure was read from a real-time Edwards D39700000 TIC instrument controller 3 head readout. This allowed use of internal partial pressure for control of fuel composition and air-fuel ratio, which is discussed further in section 3.3.2. The vacuum output and exhaust line were both connected to the laboratory extract ventilation system, mitigating risk of exposure to gaseous products or reactants.

3.2.5 - Gas Delivery and Mixing System

Fuel and oxidiser were independently introduced to the chamber by means of needle valve control, allowing for fine adjustment of the internal partial pressures to the resolution of the gauge readout (0.1 mbar). Fuel valves were connected into a manifold using 1/4 inch stainless steel tubing, and attached to all specified cylinders. This meant multiple feeds could be used in a test, whilst occupying a single chamber port. The fuel manifold was also connected to a nitrogen supply that was employed to purge the system when necessary. Cylinder and gas quality specifications are described for each of the results presented.

Adjacent internal fans were employed to blend the gases after filling to the required partial pressure mixture ratio. Fans were actuated by high temperature Portescap 426SP 102 W motors installed externally to the chamber, and connected to a variable voltage supply. Rotary *Viton* fluoroelastomer o-ring seals were employed to maintain the vacuum seal on the motor shafts. These seals remain functional up to ~500 K; however require frequent replacement to ensure vacuum integrity is maintained as they deteriorate, particularly as chamber temperature is increased. Prior to each test, vacuum integrity was ensured by observing the sealed internal pressure readout for one minute, with any rise indicative of a leak, hence requiring necessary maintenance. Advent A2108 optical tachometers were installed and connected to the data acquisition system (section 3.2.7), so shaft rotational velocity could be monitored and controlled.

3.2.6 - Temperature control system

Reactant temperature was regulated by dual control through the utilisation of two monitoring systems. Firstly, eight external band-heaters and two k-type thermocouples were employed in a hardware PID control system, and enabled approximate regulation of the chamber temperature up to 400 K. Four larger bands were used to heat the bulk of the CVCB, with localised smaller heaters employed to avoid cold-spot formation on the viewing windows. The control system hardware employed two separate operating

circuits for each heater band size. A Watlow EC12RG controller is used to specify the set point, with a Watlow HTLV-1LV used as an over-temperature alarm to cease heat provision in the event of failure. The alarm temperature was maintained at a set point of the system maximum: 400 K. The temperature readout from this primary system offers a resolution of ± 1 K, and was not calibrated with sufficient accuracy. Therefore a second more accurate temperature monitoring system was developed, directly feeding two further thermocouples into the data acquisition system discussed in section 3.2.7. This system was calibrated using a combination of a high precision thermocouple with a Hart Scientific 9100 HDRC Dry Block Calibrator. The system software was developed to allow for precise live readout of chamber temperature, and was used to highlight when small manual adjustments to the primary system were necessary. The software also allowed real-time plotting of trends, and data to be logged for each test. Analyses were performed to quantify any convective differential in temperature from the top and bottom of the viewing window, and were shown to be negligible. Considering the precision of the equipment used, an overall conservative estimate of the system accuracy was taken to be ± 2 K.

3.2.7 - Data Logging System

The data logging system used on the CVCB rig is a National Instruments (NI) cRIO-9012, employing multiple series modules for several types of data input. The NI 9213 is a 16-channel thermocouple module with built in cold-junction compensation. The two calibrated thermocouples of the secondary monitoring system discussed in section 3.2.6 were connected here. A program was written in NI LabVIEW, to give real-time numerical and plotted data from the system. The program was specified to run using *scan-interface* architecture. This meant the software could be updated and asked to run without having to compile on the cRIO. The downside of employing this type of programming is that data capture rates are slower (specified at 10 Hz) than the alternative, but still sufficient for this application. Fig. 3.6 shows a snippet of the graphical programming code, and *front panel*; the output screen for control and data display. Full details of written programs are provided in Appendix A.4.1.

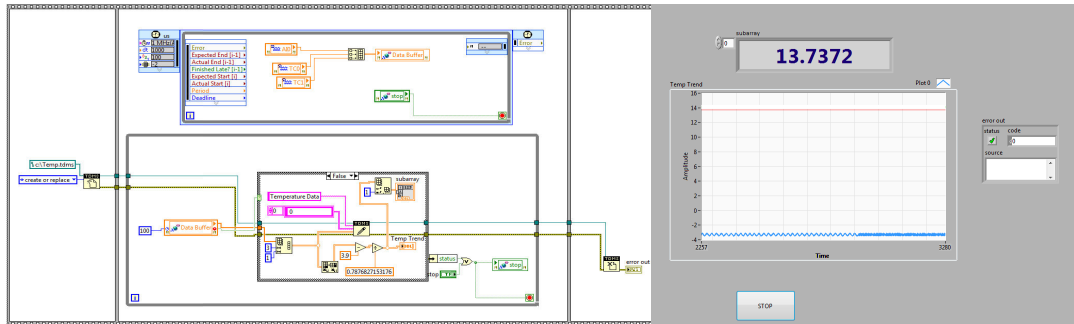


Fig. 3.6 – Code from temperature data capture system, with live readout expressed on the front panel.

The second module used in the data acquisition system is a NI 9205 32 channel, ± 10 V, analogue input block. Four channels were used by this unit; one for a high frequency pressure transducer, two for optical tachometers, and finally one from the output of a TTL pulse generator used for ignition timing. High-frequency data capture was required from this module and therefore a separate alternative piece of code was written. This time NI LabVIEW was programmed to access the Field-Programmable Gate Array or 'FPGA'. This system interrogates desired channels at specified higher frequencies, but requires compiling before operation, taking approximately 20 minutes. The program was written so data capture rates could be modified as required without the need for recompiling, however for the purposes of this work, capture rates were maintained at 2 kHz. The use of the two different programming methodologies (scan-interface and FPGA) in this way meant the cRIO could instantaneously switch between programs as required. Fig. 3.7 provides a snippet of graphical programming code and front-panel readout, this time for the FPGA code with full details provided in Appendix A.4.2.

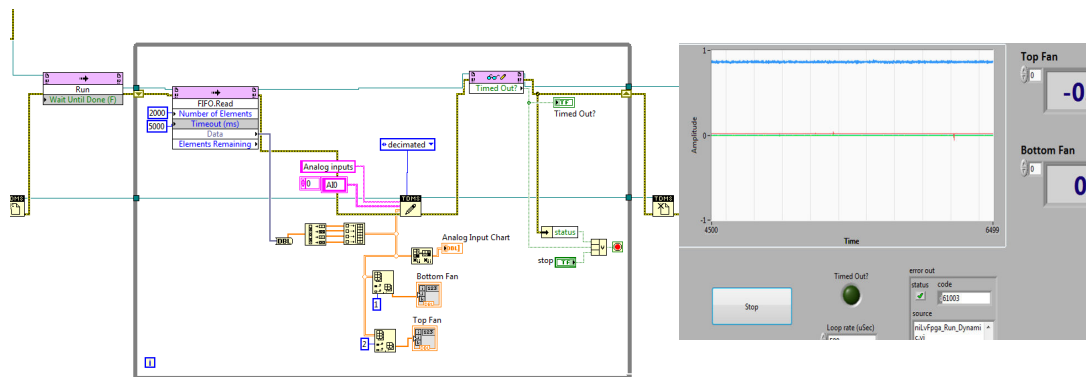


Fig. 3.7 – Code from temperature data capture system, with live readout expressed on the front panel.

The employed pressure transducer was a 0-12 bar GE Unik-5000 0-10 V voltage output unit, integrated within the system to capture the pressure transients resulting from combustion. The transducer was calibrated using a DRUCK DPI 610 unit (details in Appendix A.7), and has a full scale accuracy of ± 0.04 percent. The 0-6000rpm A2108 optical tachometers were 0-6 V output, with a full scale accuracy of 0.5%. The real-time display of fan speed was used when mixing the reactants prior to combustion. Finally the output from the 5 V TTL pulse generator, used to trigger a test, (see section 3.2.8) was captured. This was to ensure the ignition point could be specified when analysing data streams.

3.2.8 - Ignition system

Capacitor discharge ignition was achieved through use of a variable voltage supply and auto-ignition coil. The system was developed from a similar process previously employed by Crayford [140] and Cameron [141], and is depicted schematically in Fig. 3.8.

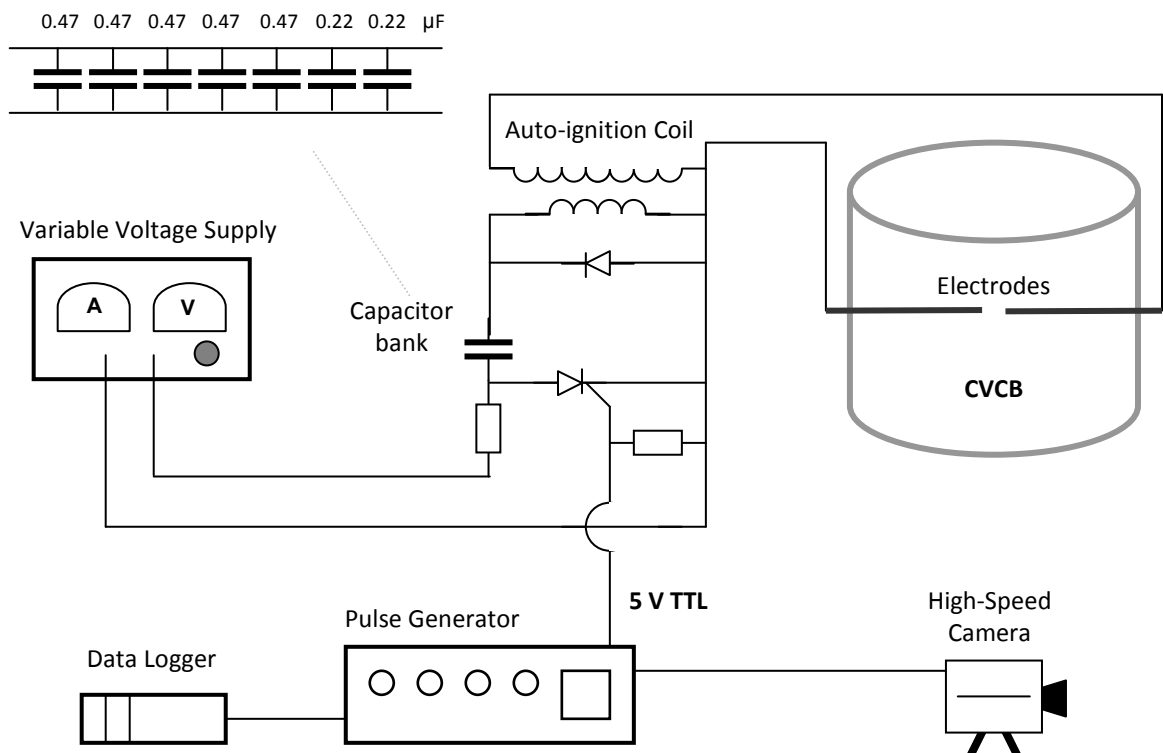


Fig. 3.8 – Schematic of the ignition system employed on the CVCB rig.

A total of seven capacitors were connected in parallel to give a summated theoretical capacitance of 2.79 μF , with the variable (0-350 V) supply held primarily at 250 V. Applying the equation shown in 3.16 gives an employed ignition energy of approximately 87 mJ. Use of a variable supply however, meant this value could be reduced for bespoke applications, or increased to a theoretical maximum of over 170 mJ.

$$e = \frac{C \cdot V^2}{2} \quad (3.16)$$

Ignition was triggered by a 5 V pulse from a Farnell PG102 TTL generator facilitating conduction of the system Thyristor, with voltage stepped up using an auto-ignition coil (ratio of 100:1) and ensuring the supply is large enough to break down the 2 mm spark gap. Energy stored in the system is rapidly discharged from the capacitors to the primary side of the coil, where it is stepped-up to a theoretical maximum of 35,000 V. This breakdown voltage is large enough to ionise the reactant gas contained within the gap, allowing for a spark to generate between the two electrodes.

Fine, 1.5 mm diameter stainless steel electrodes were designed to have minimal influence on flame propagation, and were installed in the chamber at 45° to the plane of Schlieren image measurement. Electrode tips were ground to points in order to try and achieve more repeatable spark formation, with specially designed PEEK (Polyether ether ketone) shrouds included to insulate the electrodes from chamber walls, and allow for a compression vacuum seal to be maintained.

The pulse generator was also connected to the high-speed camera and logging systems so video and data capture were also sequenced to the point of ignition.

3.3 Experimental Procedure and Data Acquisition

3.3.1 - Step-by-step test methodology

The initial detail in this section describes the employed experimental procedure, with further information regarding specific aspects of the methodology provided thereafter.

1. Firstly, the CVCB rig and laboratory had to be set up according to the health and safety requirements as specified in the risk assessment and method statement.
2. Once all necessary checks had been performed, the equipment was ready to establish the ambient condition of temperature required for the test. The primary heating control system was used to warm the CVCB to the approximate desired temperature. The secondary calibrated system was then employed to make any minor necessary adjustments to chamber temperature, and log the values recorded. At the start of a new testing regime the equipment was left on condition at the desired temperature for at least 30 minutes to ensure uniformity by overcoming the significant thermal inertia of the CVCB mass.
3. Meanwhile the Schlieren optical system was initialised, with the camera set to the required specification of image size, frame capture rate, and shutter speed. The effective image darkness would be standardised against these specifications and light supply. A set of Vernier calipers were then used to scale the image generated by the camera, with section 3.3.4 providing more detail.
4. At this time all other ancillary components of the rig were activated and tested, such as the ignition and mixing systems.
5. The contents of the CVCB were then displaced by opening the isolation valve to the vacuum pump. Between each test, the CVCB was evacuated twice to remove the products of combustion from the previous experiment. The aim of

this was to minimise errors arising from an imperfect vacuum. The evacuation rate of the pump underwent exponential decay as chamber pressure decreased, meaning it took increasingly longer to reach lower values of pressure. Consequently, a compromise was reached whereby the chamber was evacuated to a minimum pressure of 15 mbar, which still allowed for at least 15 tests to be performed per day. After removing the combustion products down to this value, the chamber would be filled to atmospheric pressure with compressed air, and then evacuated again. This meant that, assuming perfect mixing, the residual pressure remaining after the second evacuation could be added to the air fraction of the partial pressure calculation, with a resultant contamination error in the order of 0.225 mbar (or 0.02 percent for a 1 bar test).

6. Once at the appropriate starting evacuated pressure, the chamber was ready to be filled with reactants and the gas cylinders were opened. The amount of fuel required for the corresponding equivalence ratio and starting conditions were controlled by filling to the appropriate values of partial pressure, with more detail of these calculations provided in section 3.3.2. Firstly the required amount of Fuel was slowly introduced by fine needle valve control, allowing time for the vacuum gauge to settle out at a given value as the gas responded to chamber temperature. After the appropriate fuel pressure was achieved, oxidiser would be infused (again with fine needle valve control) into the chamber, to the total value required for the specified ambient condition.
7. The reactants in the chamber were now mixed. The rotational speed of both fans was increased to approximately 1000 rpm, and operated at the speed for one minute. The faster and longer the fans were used, the sooner the rotational seals needed replacing. It was assumed that one minute of this intense operation combined with the high diffusive coefficients of the gases, would leave the reactants suitably well mixed. After the fans were stopped the reactants were left for a further 30 seconds to allow any residual turbulence to dissipate. When benchmarking the chamber, simple efforts were made to

determine the influence of mixing and settlement time by analysing the sphericity of an ignited flame. While it appeared that at 303 K approximately 15 seconds of mixing appeared to suitably blend the reactants, this was increased to add in a large compensation factor.

8. Prior to ignition, the FPGA data logging module would be engaged to capture the pressure transients from combustion and the camera primed to record. The chosen trigger mechanism in the camera software was specified as *Random-Centre*; whereby the system would continuously record in a loop, and the eventual trigger point used to designate the centre frame. The initial rationale for this choice was to ensure none of the first frames in the video were missed from the point of ignition, however it transpired that this was an unnecessary precaution.
9. With one final check that adequate safety regulations were being adhered to, and all isolation valves and gas cylinders closed, the pulse generator was triggered and the reactants ignited. Ensuring combustion had taken place (from live temperature readout), the exhaust valve would be initially opened to relieve any residual pressure, and then the vacuum pump activated to begin removing the hot gaseous products.
10. With the contents of the chamber now evacuating in preparation for the next test, results in the form of the video file, temperature and pressure data were stored and replicated. The processing of results is covered in further detail in section 3.3.3.

Minor modifications to the overall methodology were necessary as different tests were performed. These variations are detailed in the appropriate results chambers.

3.3.2 - Equivalence Ratio Calculation

The employed method of controlling fuel to oxidiser ratio was by filling to equivalent values of partial pressure. The following is a simple derivation of the undertaken numerical process. The overall aim is to calculate the necessary values of partial pressure in terms of a specified total pressure (P_T) and air-fuel ratio (AFR_{act}), defined as the fraction of air (or oxidiser- o) to fuel (f - mixture of all components within representative blend, including diluents) mass [27]:

$$AFR_{act} = \frac{m_o}{m_f} \quad (3.17)$$

Dalton's Law of partial pressure states that the total pressure exerted by a mixture of constituent non-reactive gases is equal to the sum of the partial pressure exerted by each individual gas [143], or

$$P_T = P_i + P_j + P_k \dots \quad (3.18)$$

Gases in this derivation are treated as ideal, and therefore the partial pressure fraction for a gas mixture is the equivalent of the mole fraction (x_i), viz:

$$x_i = \frac{P_i}{P_T} = \frac{n_i}{n_T} \quad (3.19)$$

Rearranging Eqn. 3.19 gives:

$$P_i = P_T x_i = P_T \frac{n_i}{n_T} \quad (3.20)$$

The mixture for the consideration of air-fuel ratio comprises fractions of fuel and oxidiser, so the total pressure equates to:

$$P_T = P_f + P_o \quad (3.21)$$

Therefore, applying the relationship shown in Eqn. 3.20 gives Eqns. 3.22 and 3.23 for the respective fuel and oxidiser partial pressures.

$$P_f = P_T \cdot \left(\frac{n_f}{n_o + n_f} \right) \quad (3.22)$$

$$P_o = P_T \cdot \left(\frac{n_o}{n_o + n_f} \right) \quad (3.23)$$

The number of moles of fuel is equivalent to the fraction of fuel over molar mass (M), or:

$$n_i = \frac{m_i}{M_i} \quad (3.24)$$

So therefore, taking the example of fuel partial pressure and applying Eqn. 3.24, 3.22 becomes:

$$P_f = P_T \cdot \left(\frac{\frac{m_f}{M_f}}{\frac{m_f}{M_f} + \frac{m_o}{M_o}} \right) \Rightarrow P_f = P_T \cdot \left(\frac{\frac{1}{M_f}}{\frac{1}{M_f} + \frac{m_o}{m_f M_o}} \right)$$

substituting Eqn 3.17 gives:

$$P_f = P_T \cdot \left(\frac{\frac{1}{M_f}}{\frac{1}{M_f} + \frac{AFR_{act}}{M_o}} \right) \Rightarrow P_f = P_T \cdot \left(\frac{\frac{M_o}{AFR_{act}}}{M_f + \frac{M_o}{AFR_{act}}} \right)$$

which simplifies to give:

$$P_f = P_T \cdot \left(\frac{M_o}{M_o + M_f \cdot AFR_{act}} \right) \quad (3.25)$$

Similarly, applying the same derivation for the partial pressure of the oxidiser gives:

$$P_o = P_T \cdot \left(\frac{M_f \cdot AFR_{act}}{M_o + M_f \cdot AFR_{act}} \right) \quad (3.26)$$

The solutions provided above are given in terms of a total required pressure, and perhaps counter-intuitively, do not require specification of the internal volume of the CVCB or gas temperature. A comprehensive derivation of this process from first principles of the ideal gas law is provided in Appendix A.5 to mathematically demonstrate how these terms are negated.

For the purposes of presenting work in this thesis, air-fuel ratios are normalised to an equivalence ratio [27], as shown in Eqn. 3.27:

$$\phi = \frac{AFR_{stoich}}{AFR_{act}} \quad (3.27)$$

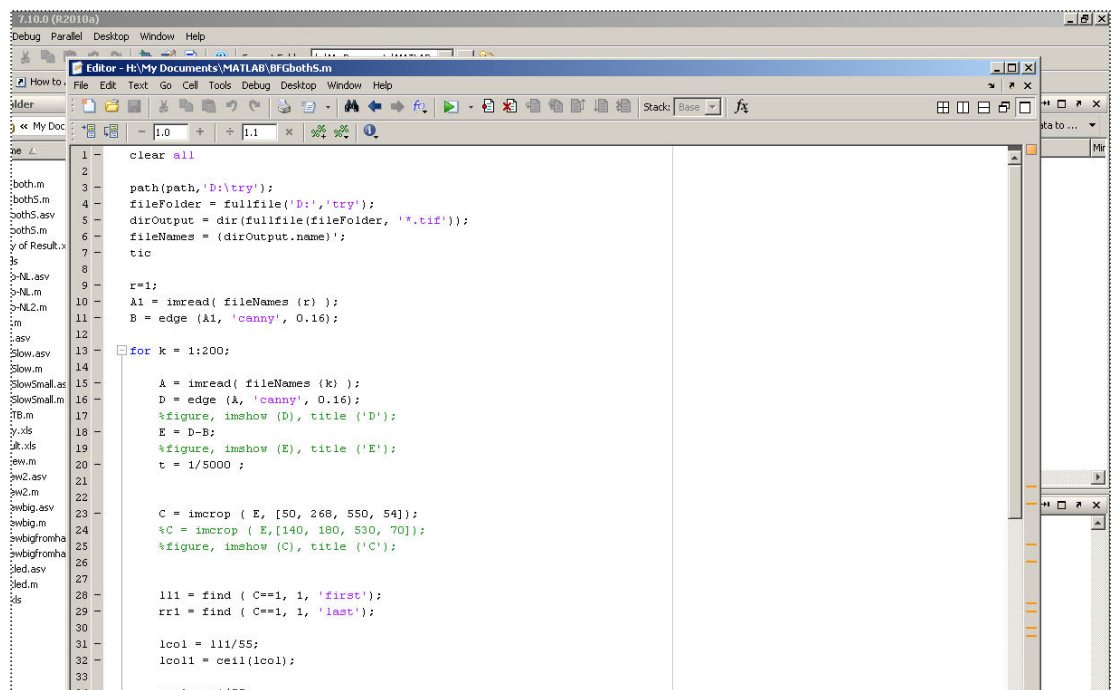
where AFR_{stoich} represents the air-fuel ratio required for stoichiometric combustion. A spreadsheet was created that calculated the required amount of oxidiser necessary for stoichiometric combustion of a given fuel mixture. With consideration to the investigated fuel mixtures, the sheet was initially designed for specification of blends comprising amounts of H_2 , CH_4 , CO , CO_2 , N_2 and O_2 . The constituent mole fractions of the fuel mixture are provided by the user; with AFR_{stoich} and the equivalent fuel molar mass calculated using Eqn. 3.28.

$$M_f = \sum_{i=1}^n x_i \cdot M_i \quad (3.28)$$

The average fuel and oxidiser molar masses (specific values will be provided with each data set) were used with Eqn.s 3.25 and 3.26 to give an output of partial pressures necessary to meet a series of equivalence ratios, for a user-defined total pressure. As the testing regimes changed to investigate different fuel blends or pressures, the sheet was adapted accordingly. A list of all the coefficients and constants used in these calculations is provided in appendix A.2.

3.3.3 - Video Processing

The high-speed video files recorded for each test were saved as a series of greyscale frames in .tif format. These frames were sequentially processed in order to measure the temporal rate of spherical flame growth. A code was written using MATLAB software to computationally analyse the video files, facilitating the rapid sequential processing of each large video file. Fig. 3.9 shows a screenshot example of the operational code.



```

1 clear all
2
3 path(path,'D:\try');
4 fileFolder = fullfile('D:', 'try');
5 dirOutput = dir(fullfile(fileFolder, '*.tif'));
6 fileNames = (dirOutput.name)';
7
8 tic
9
10 r=1;
11 A1 = imread( fileNames (r) );
12 B = edge (A1, 'canny', 0.16);
13
14 for k = 1:200;
15
16     A = imread( fileNames (k) );
17     D = edge (A, 'canny', 0.16);
18     %figure, imshow (D), title ('D');
19     E = D-B;
20     %figure, imshow (E), title ('E');
21     t = 1/5000 ;
22
23     C = imcrop ( E, [50, 268, 550, 54]);
24     %C = imcrop ( E,[140, 180, 530, 70]);
25     %figure, imshow (C), title ('C');
26
27
28     l11 = find ( C==1, 1, 'first');
29     r11 = find ( C==1, 1, 'last');
30
31     lcol = l11/55;
32     lcol1 = ceil(lcol);
33
34

```

Fig. 3.9 – Screenshot of the employed MATLAB code.

The script was continuously adjusted in accordance with several factors, including; slight adjustments in position, or the number of images being processed. However, the general operating algorithm remained the same. This algorithm has been illustrated on the following page in the form of a flow chart (Fig. 3.10), with a more comprehensive description of each step provided thereafter.

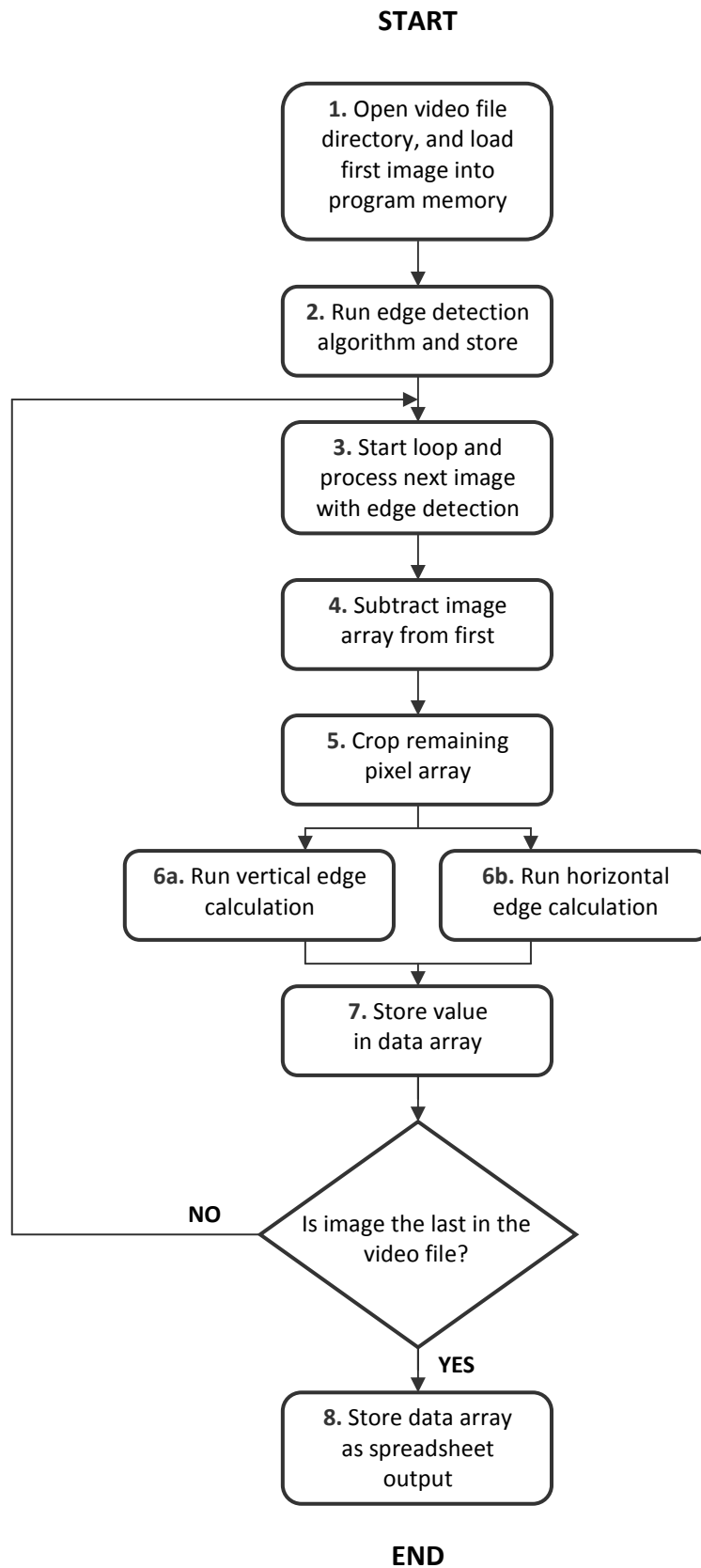
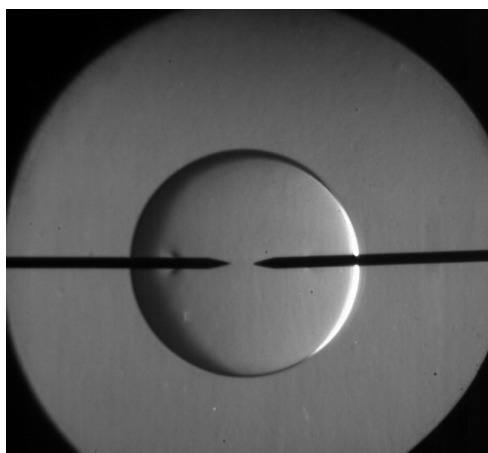


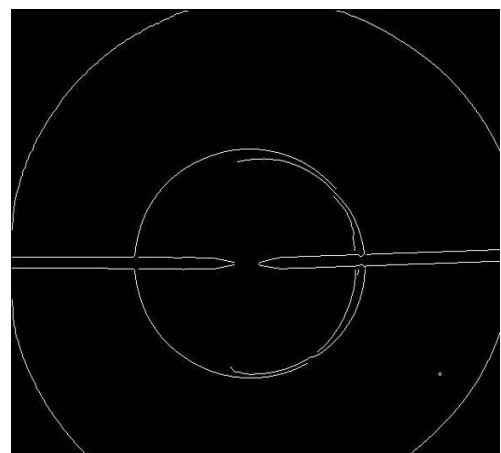
Fig. 3.10 – Flow chart of employed MATLAB algorithm.

1. All program memory was cleared prior to opening the image file directory; allowing the software to now consecutively read each frame in the video folder from the beginning. Image filenames were saved with ascending numbers by the camera software, facilitating the sequential processing performed by the MATLAB code. The first, flameless image was accessed by the program memory, and served as the effective blank for the remainder of the frames processed in the loop.

2. The system converted the greyscale intensity value of each pixel from the first image into a numerical array. Pixels were valued between zero (black) and one (white), and the *Canny* edge-detection algorithm was then employed by the software thus: Firstly, a Gaussian filter was passed over the image to remove any minor noise, represented by significant increases in pixel intensity over a small area. Practically this may materialise from dust settling on the camera lens or mirrors. The standard deviation of the Gaussian filter was kept at 1.4, although it was still possible for some noise to be retained in the image. The Canny algorithm then utilised the *Sobel* operator, whereby the horizontal, vertical and diagonal pixels are numerically compared. If the difference in pixel intensity exceeded a specified threshold value, an edge was assigned to that point. This threshold was typically in the range 0.08 - 0.15, depending on the image brightness and early strength of the flame front. Edges were assigned in the numerical array as one, with all other pixels set to zero, converting the collection into a binary image. Fig. 3.11 gives examples of actual (a) and binary (b) images of a spherical flame, and demonstrates the effectiveness of the canny algorithm in designating edges.



a)



b)

Fig. 3.11 – Schlieren and binary images of a spherical flame.

Although requiring more light, the advantage of employing rapid shutter speeds meant clearly defined edges were generated by the Schlieren system, and therefore any changes to the sensitivity threshold were shown to not adjust the position of a well defined flame edge. This was tested, with the only significant impact seen on the first frames where edges were more indistinct, and these data was not used for the measurement process regardless due to the influence of ignition energy (chapter 3). Once the first entire binary image had been generated, it was stored in a separate array in the program memory for further processing.

3. A loop was now started for the sequential processing of the remaining frames in the video file. The next frame in the sequence was loaded into a new memory array, and once again the edge detection algorithm applied.

4. The first binary image was now numerically subtracted from the newly processed array, and stored again in the program memory under a different name. At any point where two corresponding pixels read one, the value reverted to zero, effectively removing any common edges such as those of the electrodes, or remaining image noise. Assuming the flame was moving fast enough, this theoretically leaves only the spherical outline in the stored array.

5. The binary image of the spherical flame was now cropped to minimise the number of pixels to be subsequently processed by the program. The size of the cropped section was dependent on whether a horizontal or vertical diameter is processed.

6. Measuring the diameter of the flame: The code exploited the *find* operator in MATLAB to search for any nonzero elements within a specified array. In the binary images these elements were pixels identified as flame edges and set to one in the cropped array produced in step 5. The indices of the *first* and *last* pixels were found using this operator, by counting sequentially downwards through each pixel column of the cropped section. If analysing a vertical diameter, the attained values were subtracted to return the difference between the two, giving a representative equivalent number of pixels. The numerical processing of horizontal edges was more

numerically complex, with the entire upper hemisphere analysed. In this instance the first and last indices were divided into the number of pixels in each column, and rounded up, thereby giving integers equivalent to the column number they appear in. These column numbers were then subtracted from each other to attain the number of pixels equivalent to the horizontal diameter.

Both vertical and horizontal processing techniques were employed when analysing the data, with each having advantages. A minor limitation of using the vertical technique is that the cropped image has to be run through the flame centre, to ensure the maximum diameter was measured. This meant fine adjustments and checks were necessary between processing each file. The technique was more limited when propagation was slow and therefore influenced by buoyancy, meaning the flame could begin to rise as it propagated. It is in these circumstances, the upper-hemisphere horizontally attained data were preponderant [143, 144]. However, the immediate limitation of this technique is that the diametric flame centre needs to be monitored to ensure it has risen above the electrodes, together with being more computationally intensive, and therefore taking longer. This is specified with the employed technique detailed in the apt results chapters.

7. Whichever technique was used, the value attained for the number of diametric pixels in the flame was stored in a new dataset. As each new frame was processed, this dataset grew to give increasing values of diameter. This is in contrast to most of the other data stored in the program memory, which would be overwritten for each new frame.

8. Once the final frame in the video was processed, the loop ceased and the diametric data set was exported from the software and saved into a spreadsheet. A sample of the working MATLAB code is provided in Appendix A.6.

3.3.4 – Image Scaling

In order to accurately analyse the results of each high speed video file, a calibrated datum of scale had to be attained. This was achieved by capturing individual frames of a calibrated distance, and computationally measuring the number of pixels.

A digital set of Vernier callipers were used to prepare a range of distances, and photographed in the collimated beam of the Schlieren setup. Five different widths were prepared in the range of 5-25 mm, and five separate images captured at different positions in the viewing window. These positions were top, bottom, left, right and centre. This was completed for both horizontal and vertical scales, and repeated each time a new testing regime was started (any time equipment could have been moved or repositioned). The number of pixels per distance was attained by processing the individual images in the MATLAB program described in section 3.3.3. Photographs were transformed to binary images, following edge detection processing. This is demonstrated with an example image in Fig. 3.12.

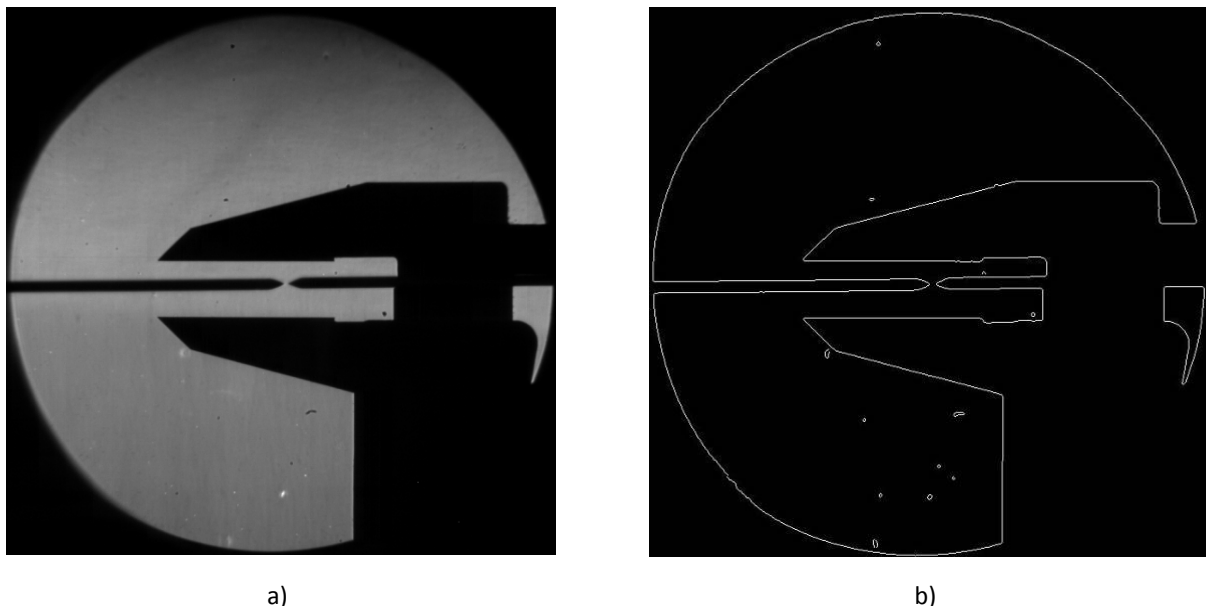


Fig. 3.12 – Schlieren and binary scaling images.

The configuration afforded a spatial resolution in the order of 0.14 mm per pixel. This meant the accuracy and resolution of the calibrated callipers was one order of magnitude greater than the pixel resolution of the camera, and therefore deemed to give a satisfactorily accurate measure of scale. The Schlieren equipment positioning was marked and always returned to the same approximate point, and consequently the measured scale, and order of variance in the values attained did not change at any point this calibration procedure was performed. Also, the callipers could be held at any spatial position within the collimated section of light and the recorded distance would not change. This provided an effective indicator that the light was suitably collimated in the Schlieren system. The exact scaling resolution is provided with apt results.

3.4 Chemical Kinetics Modelling

3.4.1 – Software Operation Overview

Computational models of chemical kinetics were employed to predict values of laminar burning velocity, and obtain the burned gas density necessary for the numerical processing described in section 3.1.5. The software package chosen to perform this task was CHEMKIN-PRO, developed by Sandia National Laboratories. This software is widely employed in analogous fields of research (e.g. [96] [102], [105]), and was programmed to perform one-dimensional premixed laminar calculations for the determination of flame speed. This employed configuration utilises PREMIX [145], a code for modelling the spatial profiles of temperature and chemical species throughout a steady-state laminar flame front.

The employed operational algorithm uses a combination of the modified Newton method, and time integration to converge finite difference approximations of a given set of continuity and boundary equations. If the Newton method fails to converge, the solution estimate is integrated in time to provide a new datum, potentially within the field of convergence for the algorithm [146]. The conservation and state equations solved using this configuration are summarised below [96, 146].

$$\text{Continuity:} \quad \dot{M} = \rho \cdot u \cdot A \quad (3.29)$$

Energy:

$$\dot{M} = \frac{dT}{dx_i} - \frac{1}{c_p} \cdot \frac{d}{dx_i} \left(\lambda A \frac{dT}{dx_i} \right) + \frac{A}{c_p} \sum_{k=1}^K \rho \cdot Y_k \cdot V_k \cdot C_{pk} \frac{dT}{dx} + \frac{A}{c_p} \sum_{k=1}^K \dot{\omega}_k \cdot h_k \cdot W_k = 0 \quad (3.30)$$

$$\text{Species:} \quad \dot{M} = \frac{dY_k}{dx} + \frac{d}{dx} (\rho \cdot A \cdot Y_k \cdot V_k) - A \cdot \dot{\omega}_k \cdot W_k = 0 \quad (3.31)$$

$$\text{Equation of State:} \quad \rho = \frac{P \cdot \bar{W}}{R \cdot T} \quad (3.32)$$

In the continuity equation, \dot{M} represents the mass flow rate, ρ and u the respective mixture density and velocity, and A the stream cross sectional area, which by default is equal to unity. The energy equation introduces x , the spatial co-ordinate of the flame, together with thermodynamic properties such as; thermal conductivity (λ), isobaric heat capacity (C_p), specific enthalpy (h), and the universal gas constant (R). Many properties are defined in relation to a specific chemical species ($k=1\dots K$), for instance the mass fraction (Y_k) or the diffusion velocity (V_k), with molecular weight defined for both individual constituents, and the mixture average (\bar{w}). $\dot{\omega}_k$ represents the net chemical production rate resulting from the competition of all chemical reactions involving that species. The law of mass action is followed, and forward rate coefficients are obtained in the following Arrhenius form:

$$k_f = A_\alpha \cdot T^\beta \exp\left(\frac{-E_a}{R \cdot T}\right) \quad (3.33)$$

where E_a is the activation energy. A_α and β are the respective pre-exponential, and temperature factors defined for each chemical reaction [146a]. The flow chart in Fig. 3.13 provides a graphic representation of the CHEMKIN PREMIX operational algorithm [146b].

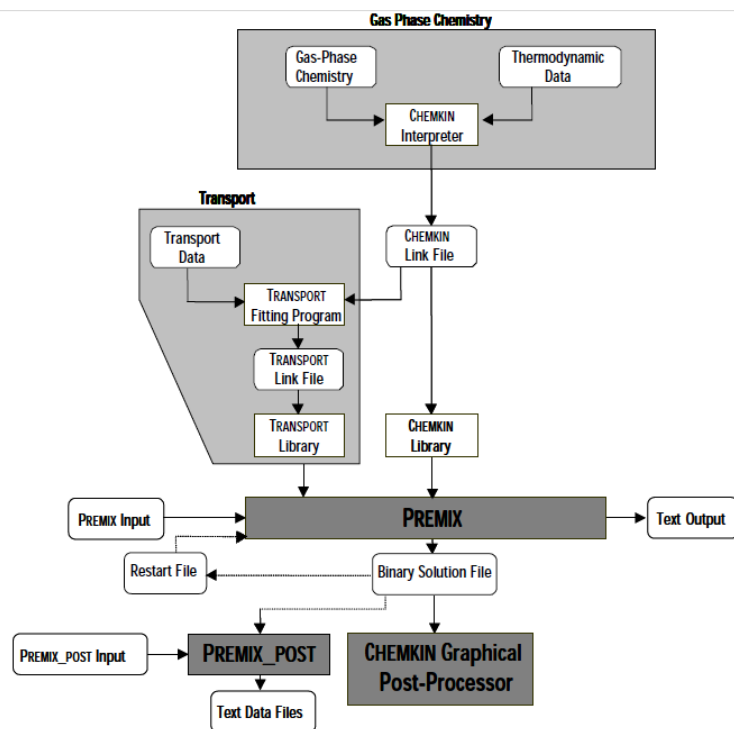


Fig. 3.13 – CHEMKIN PREMIX operational flow chart.

3.4.2 – Reaction Mechanisms Overview

PREMIX only provides the methodology to obtain a numerical solution, meaning all of the thermo-chemical properties described above have to be pre-processed by the software as a separate input. The data files used to do this typically list most of the known reactions leading to generation of intermediate species for the complete combustion of a given fuel. These reaction mechanisms are usually broken into three components; the first of which is the CHEMKIN interpreter input, which lists the elements and chemical species associated with all of the identified reactions [147]. More significantly, the file also provides the Arrhenius factors defined above (Eqn. 3.33) for each reaction. The second file can also form part of the interpreter, and contains the coefficients necessary to calculate most of the species' thermodynamic properties from the form of NASA polynomials [148]. The final part of the reaction mechanism provides data on chemical transport properties, which are used to calculate the thermal conductivities and diffusion velocities of each species. For the premixed freely propagating configuration, the flame is modelled in one direction with no heat loss. Therefore, by applying attained values of burned gas density to Eqn. 3.12, adiabatic conditions must be assumed for the data, with a total spatial distance of 10 cm maintained for designation of end point density for all models.

Each reaction mechanism will be typically optimised to model combustion of a given fuel under specified ambient conditions, where the parameters defined above have usually been determined experimentally by different research institutions. An example of this is the GRI Mech 3.0 mechanism developed for chemically modelling the combustion of natural gas [149]. Details of the reaction mechanisms utilised in this study are supplied alongside appropriate results. The software could also be modified to run different specifications in the calculation procedure, for example using mixture-averaged or multi-component transport properties, or numerically accounting for the Soret effect. Again, full details are provided with each model specification with the appropriate results.

Chapter 4. Benchmarking Experimental Performance

This chapter outlines the numerical process undertaken for analysing experimental results, employing CH₄ to benchmark the attained values against data from analogous research literature. Results are evaluated for both linear and nonlinear optical methodologies, together with a comparison of the dynamic pressure measurement approach. The purpose of this work was to ensure the experimental procedure was precise and repeatable with respect to published data. Experimental and statistical uncertainties are then more comprehensively explored.

4.1 Numerically Processing Experimental Data

For this section, the numerical processing of a single test is described in detail. This test was performed for the stoichiometric combustion of CH₄ with air at ambient conditions of 303 K, and 0.1 MPa. Having computationally processed the test video file (recorded at 5,000 fps), the returned output is a series of growing pixel counts, which are then scaled to give a propagating Schlieren flame radius (r_{sch}), as plotted in Fig. 4.1.

Data up to a radius of 8 mm are neglected to mitigate the influence of ignition energy discharge, during initial stages of propagation. This follows the addition of a further safety factor to the 6 mm minimum suggested by Bradley *et al.* [99] (see Fig. 2.11a). Similarly data are only obtained up to a maximum radius of 39 mm (see section 3.2.2), to minimise the influence of confined reactant pressure rise.

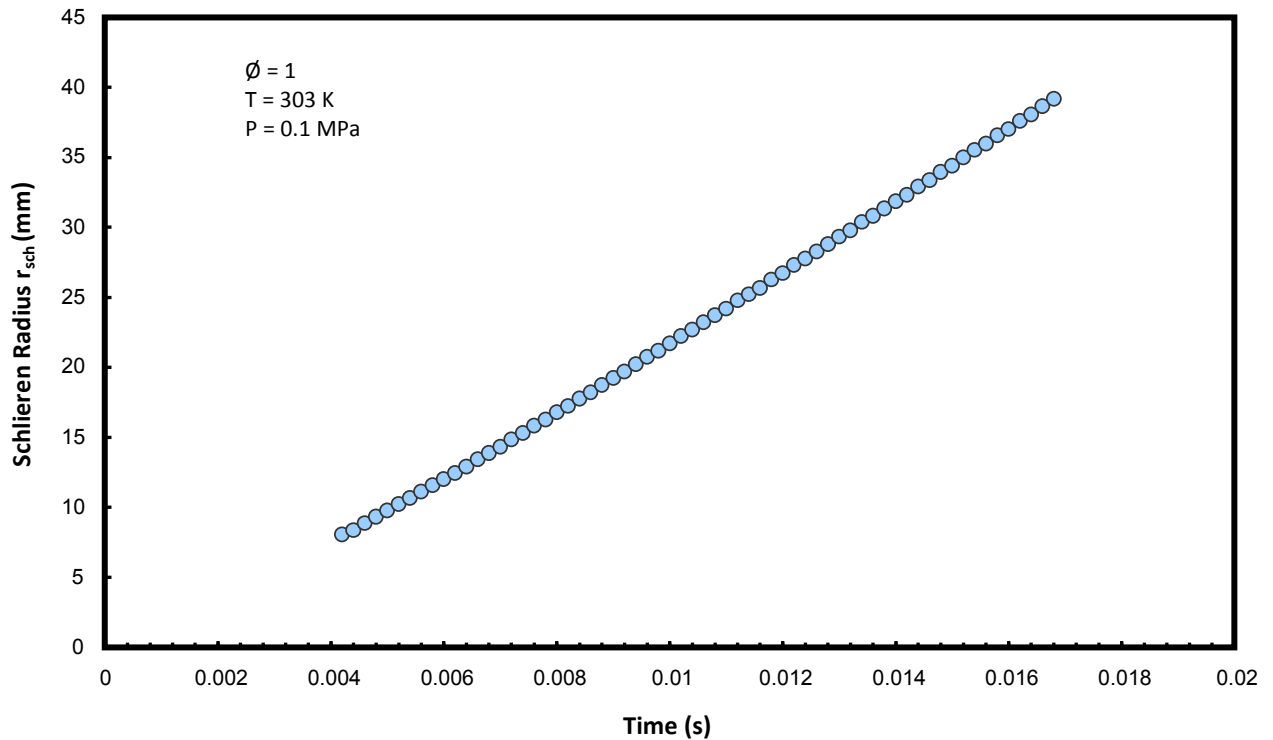


Fig. 4.1 – Plotted radii of CH₄/air spherical flame propagation.

Third order polynomial regression is then used to fit a relationship to this plotted curve. The accuracy of fitting an association in this way can be evaluated by quantifying the root-square error between the returned temporal polynomial (r_{poly}) value, and each corresponding flame radius;

$$r_{error} = \sqrt{(r_{sch} - r_{poly})^2} \quad (4.1)$$

If these error data are plotted (as shown in Fig. 4.2 for the example), then it is evident that most discrepancies are smaller than the spatial resolution of the optical system ($\sim 0.14 \text{ mm}$), and the larger errors occur near the end points of the curve. Tahtouh *et al.* [103] also showed how the accuracy of applying polynomial regression in this way diminishes near the end points of the relationship. It should be noted that in the example presented here, the polynomial coefficients are obtained up to a minimum of ten significant figures [150], which was maintained for all tests performed. The coefficient of determination (R^2 value) for this fit is 0.99998, and all corresponding values are provided with presented results.

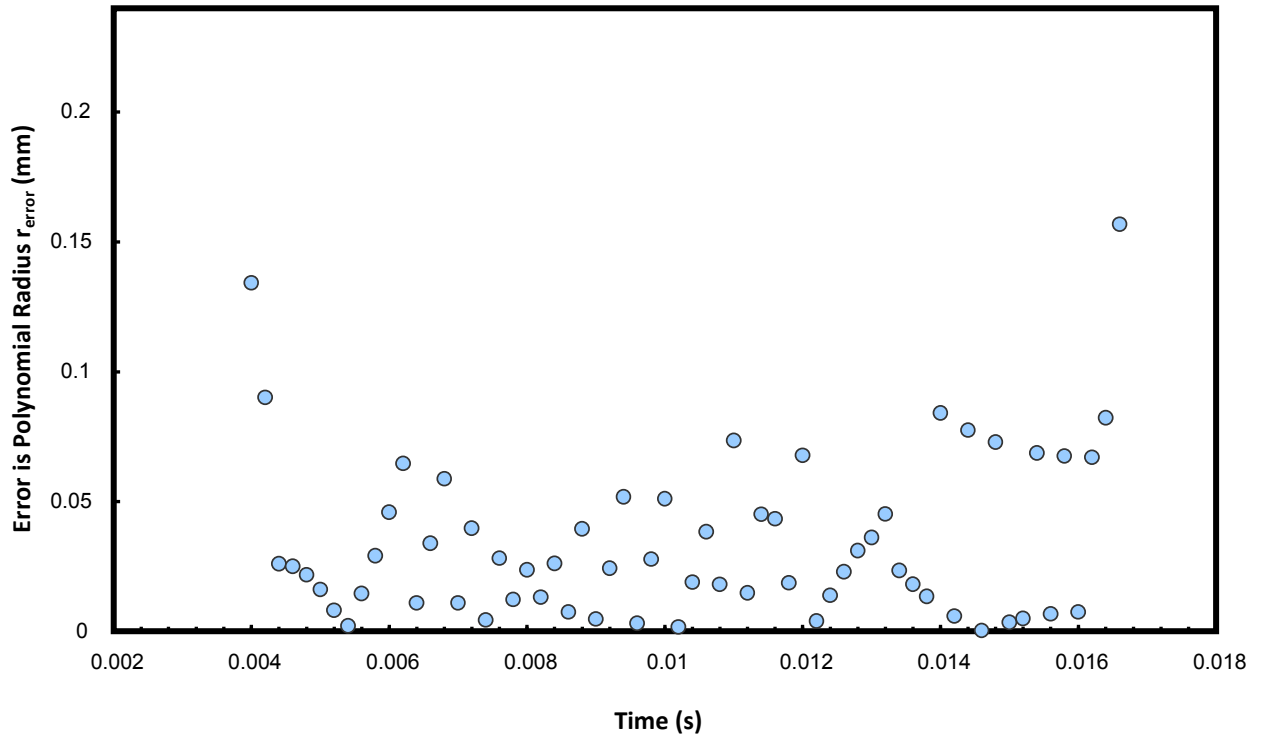


Fig. 4.2 – Plotted error in obtained polynomial radius.

As a consequence of the end point errors, the dataset is trimmed to encompass values only in the range 10 - 35 mm after the initial fit. For each flame radius a value of stretched flame speed (S_n) and corresponding stretch rate (α) are respectively obtained through differentiating the polynomial and applying Eqns. 3.1 and 3.4. The calculated changes in these parameters with flame growth are plotted in Fig. 4.3.

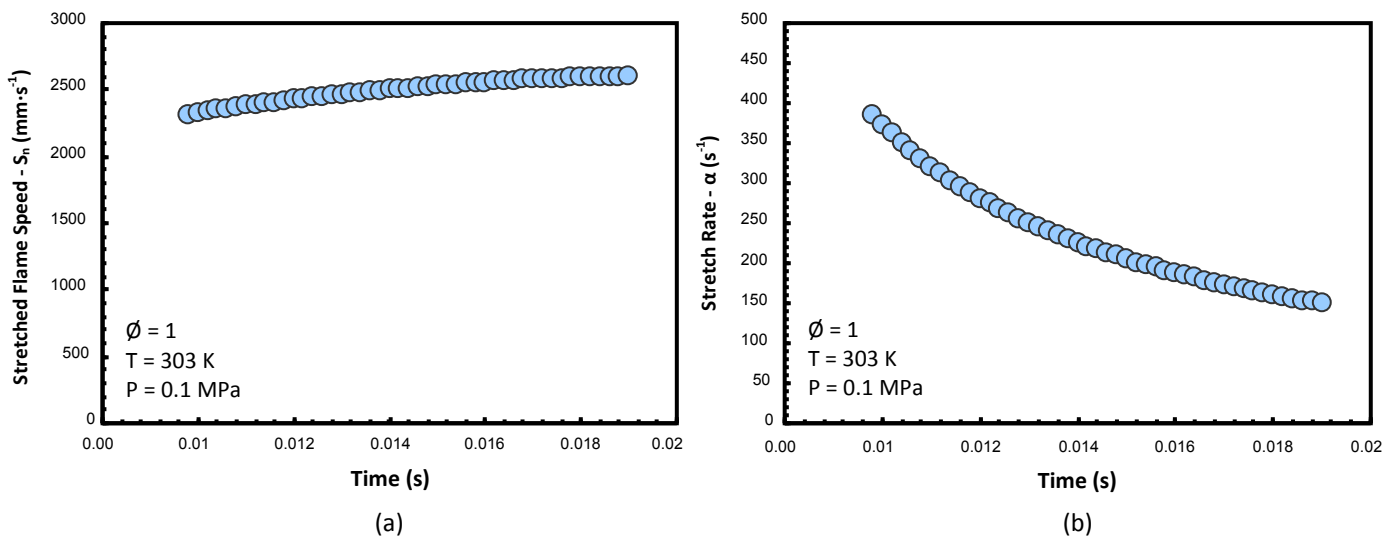


Fig. 4.3 – Plotted change in CH₄/air (a) S_n and (b) α with time as the flame propagates.

It is evident from the plots shown in Fig. 4.3 that the positively stretched CH_4 flame in this example accelerates as the flame grows, and the influence of stretch is reduced. In order to attain a representative unstretched flame speed, the relationship between S_n and α must be analysed further. Fig. 4.4 shows the two parameters plotted against each other.

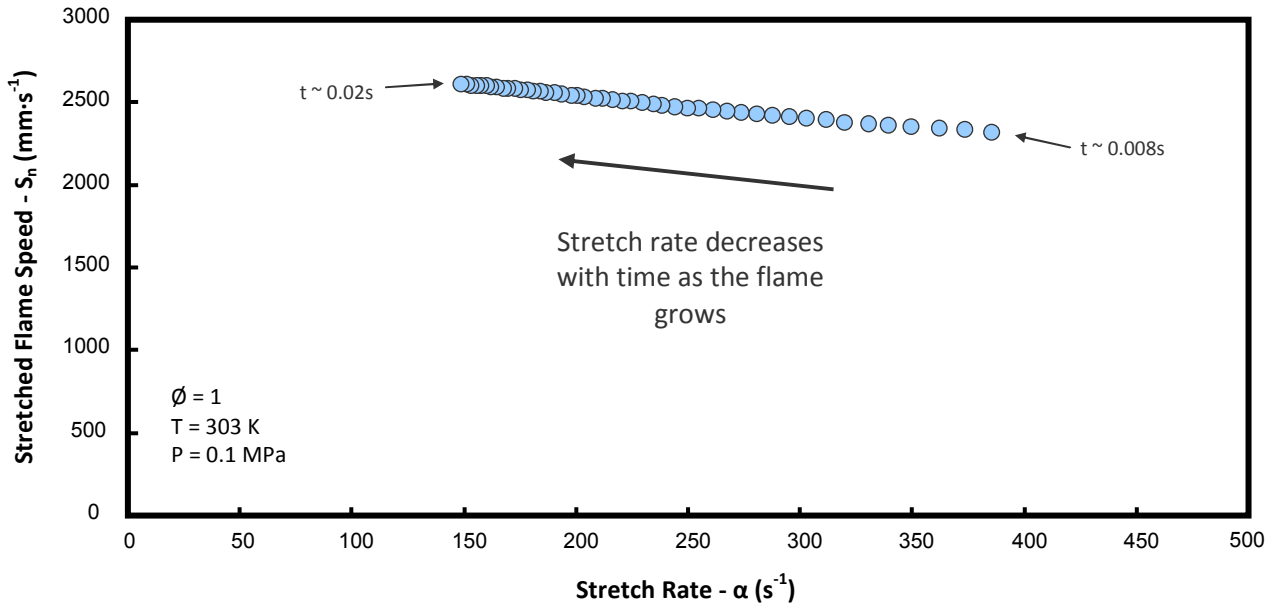


Fig. 4.4 – Plotted CH_4/air values of S_n against α .

The two proposed theoretical relationships discussed in sections 3.1.3 and 3.1.4 can now be used with this dataset, in order to attain a representative flame speed uninfluenced by stretch (S_u).

4.1.1 - Linear Extrapolation Technique

This technique uses the relationship presented in Eqn. 3.6 ($S_u - S_n = L_b \cdot \alpha$) in attributing a linear trend to the data, and extrapolating to conditions of zero stretch rate; inasmuch that the intercept corresponds to S_u , and the gradient of the data $-L_b$. Thus, the method is simple to employ, by regressing a linear fit to the plotted data, and obtaining the required coefficients. Fig 4.4 shows the data previously presented with this linear relationship superimposed, and forecast to conditions of zero stretch.

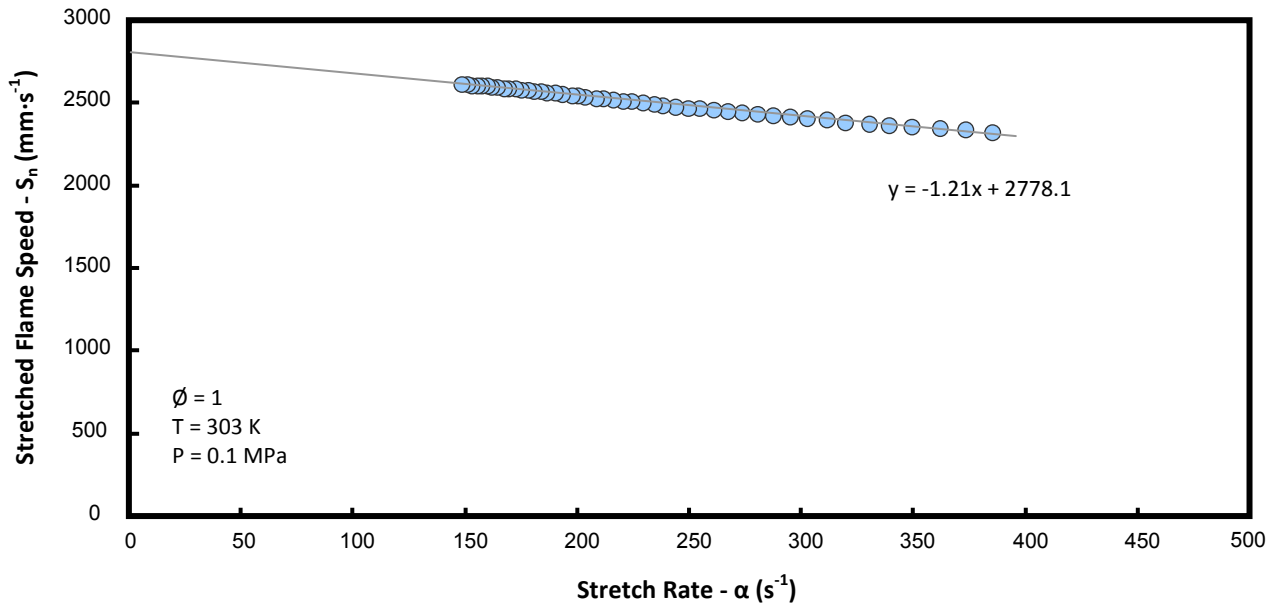


Fig. 4.5 – Stoichiometric CH_4/air values of S_n against α with linear relationship (Eq. 3.6) superimposed.

Therefore the result of this sample test would yield a stoichiometric unstretched flame speed of **2778.1** $\text{mm}\cdot\text{s}^{-1}$ and a Markstein Length of **1.21** mm. In order to attain a value for the laminar burning velocity (u_L) the adiabatic density ratio of products to reactants must be applied, as in Eqn. 3.12. For this test the reaction mechanism employed to calculate the respective densities was the GRI-Mech 3.0 dataset [149], designed to model the combustion of natural gas. Further details of the model specifications are provided in section 4.2.2.

The obtained density ratio is equal to: **0.13493**

thereby giving a resultant u_L of: **37.4** $\text{cm}\cdot\text{s}^{-1}$.

4.1.2 - Nonlinear Extrapolation Technique

The methodology for applying the nonlinear technique detailed in section 3.1.4 was more involved than the steps described above. Eqn. 3.10 had to be solved for S_u and L_b , from changes in each value of S_n and corresponding α . Least square nonlinear

regression was used to fit the association to the plotted points. Ergo, Eqn. 3.10 was rearranged thus;

$$\left(\frac{S_n}{S_u}\right)^2 \cdot \ln\left(\frac{S_n}{S_u}\right)^2 + \frac{2 \cdot L_b \cdot \alpha}{S_u} = 0 \quad (4.2)$$

with any divergence from zero, summated as the dependent error used for regression. Consequently, the relationship was fitted to the dataset for the resolution of S_u and L_b as variables, with the superimposed result shown in Fig. 4.6.

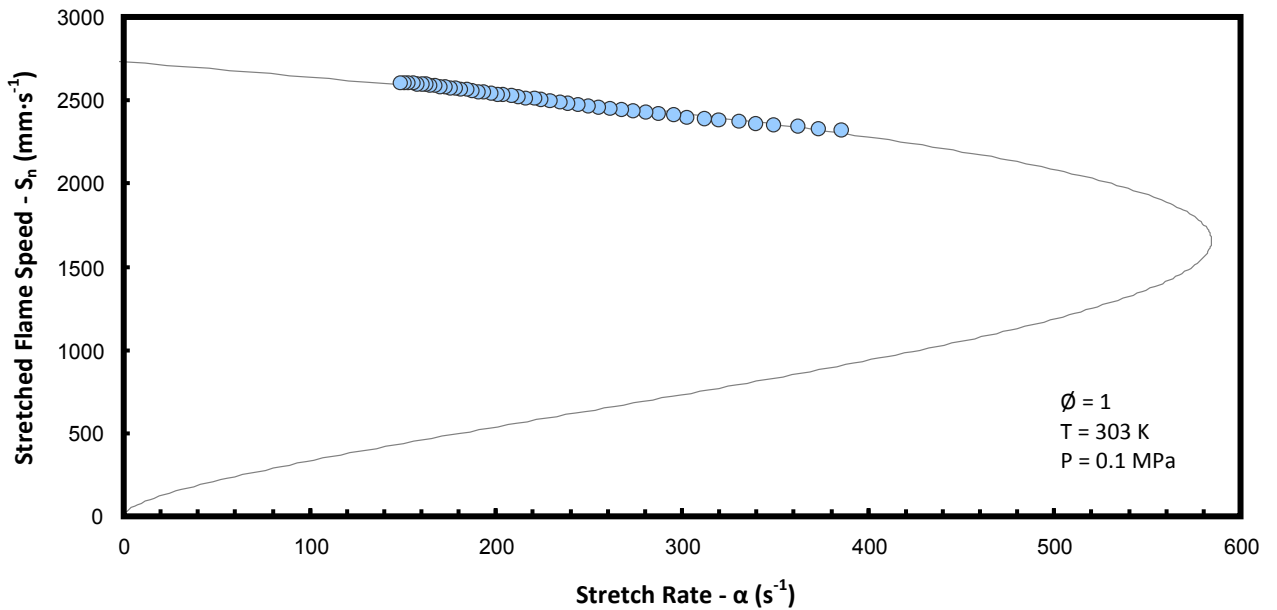


Fig. 4.6 – Stoichiometric CH_4/air values of S_n against α with nonlinear relationship (Eq. 3.10) superimposed.

This association yields an S_u equal to **2730.3** $\text{mm}\cdot\text{s}^{-1}$ and an L_b of **0.86** mm.

Applying the same density ratio as the linear method gives a resultant u_L of **36.8** $\text{cm}\cdot\text{s}^{-1}$.

The comparative results of each methodology are consistent with analogous works [104, 105], in that the linear technique is estimated to provide an increasing overestimation of u_L under conditions of heavier stretch. Nevertheless, the difference in attained results is in the order of two percent, and would be expected to increase with a rise in L_b . There is a more significant difference between the attained values of Markstein length. Again, this has been seen in relevant literature [105], and purportedly results from the overestimation of the influence of stretch in the linear method.

The improved accuracy of applying the nonlinear technique has been discussed by several authors for different fuels [104, 105], and its use has been ostensibly vindicated with obtained data that follows the curve of the suggested relationship. Fig. 4.7a below is adapted from Kelley and Law [104], and shows n-butane data exhibiting this behaviour. The two different plots are shown for the same fuel to emphasise the influence of ignition energy during early flame growth, and confinement from the chamber walls.

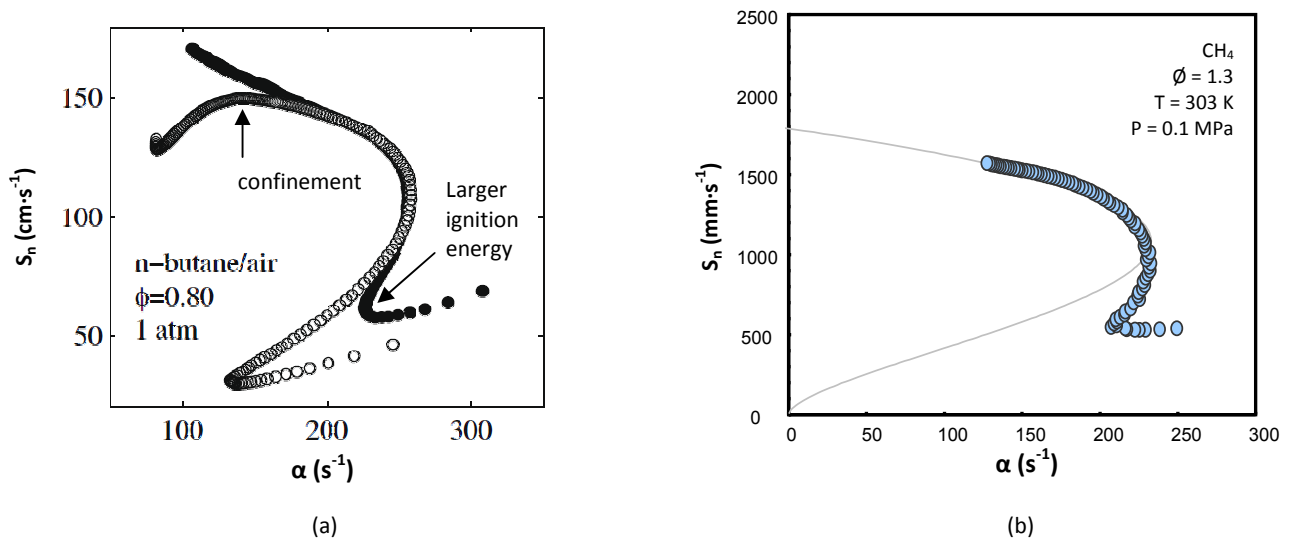


Fig. 4.7 – Plotted data to emphasise the curvature accounted for by the nonlinear relationship for both; (a) n-butane/air From Kelley and Law [104], and (b) CH₄/air experimental results obtained for the Cardiff CVCB.

In order for data to exhibit this trend, the flame must be heavily influenced by stretch (for greater curvature), with a low enough ignition energy to ensure the early stages of propagation are not overdriven by spark energy discharge. For the purposes of this work, the theory was tested with a rich CH₄ mixture, and approximate ignition energy of 60 mJ. The result is shown in Fig. 4.7b. with the fitted nonlinear relationship superimposed over the data. There appears to be a good correlation between the majority of values and the turning point, however a moderate discrepancy near the point of ignition influence. Nevertheless the curvature accounted for by the nonlinear relationship is evident. The remainder of the results presented for this thesis will provide data obtained from both relationships, with apt comparisons made.

4.1.3 - Pressure Measurement Technique

High frequency pressure data were also obtained for the specified test, facilitating employment of the technique theoretically described in section 3.1.6. A methodology utilising chamber pressure differential has been adapted based on the work published by Dahoe and de Goey [133]. An overview of the temporal change in pressure resulting from the specified CH₄/air test is plotted in Fig. 4.8.

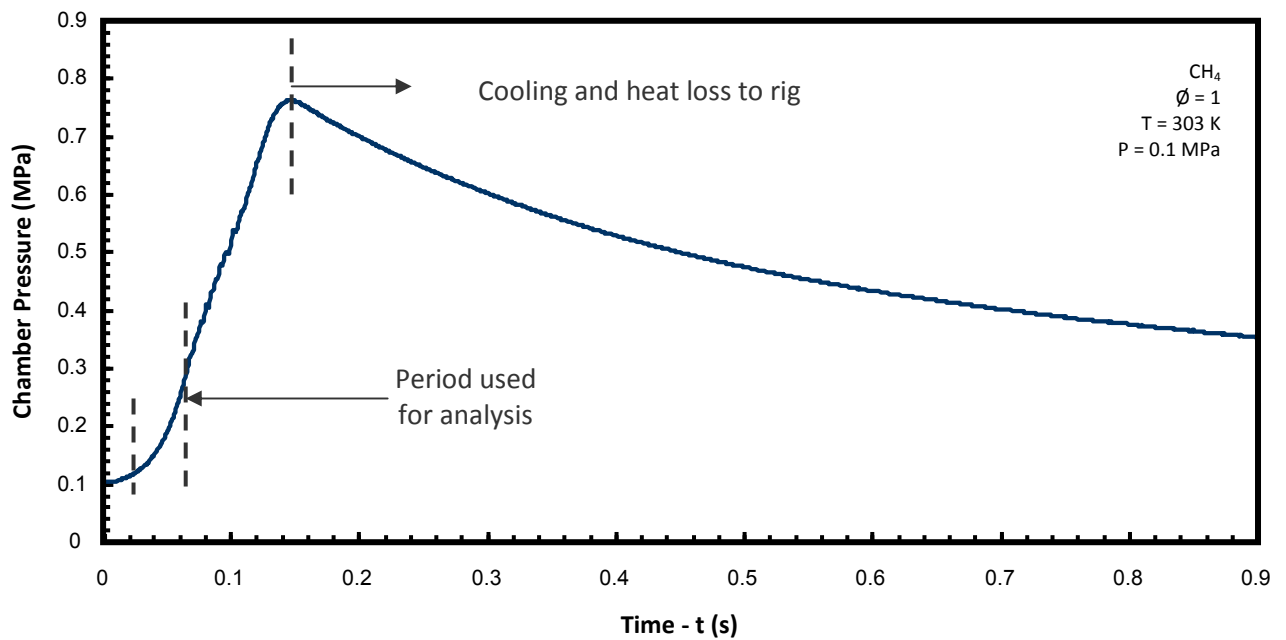


Fig. 4.8 – Internal chamber pressure trace for the specified test.

The employed methodology required trimming of this dataset to encompass values only in the range of 0.12 – 0.30 MPa, for initial change in pressure differential. This results from the estimated inapplicability of the governing equation outside this range, in addition to mitigating the influence of ignition energy and confinement effects. The trimmed dataset is plotted in Fig. 4.9.

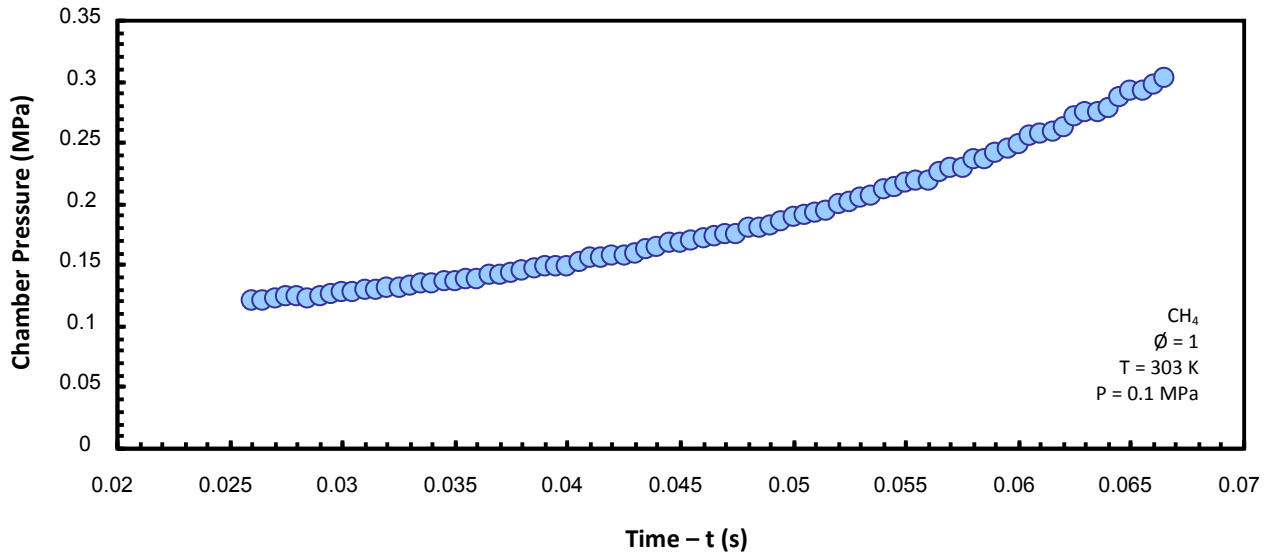


Fig. 4.9 – Internal chamber pressure rise in the range 0.12 to 0.3 MPa.

For this work Eqn. 3.13 was rearranged so the difference in both terms could be used to quantify an error variable;

$$\frac{dP}{dt} - \left[\frac{3}{R_c} \cdot \left(\frac{dx_m}{dP} \right)^{-1} \cdot \left[1 - \frac{P_i}{P} \gamma_u \cdot (1 - x_m) \right]^{\frac{2}{3}} \cdot \left(\frac{P}{P_i} \right)^{\frac{1}{\gamma_u}} \cdot u_L \right] = 0 \quad (4.3)$$

The first pressure differential term was again obtained from the regressed polynomial of a curve fitted to the dataset shown in Fig. 4.9. The second term (encompassed in the large brackets) was calculated for each plotted data point, with change in mass fraction (x_m) attained using Eqn. 3.15 and the maximum observed pressure reading (P_e). The ideal isentropic expansion factor (γ_u) was calculated using the molar fractions of the entire reactant mixture, with reference values obtained from polynomials available from the NIST database [151] (all reference values are available in Appendix A.2). A value for u_L was then attained through nonlinear regression, minimising the squared error between terms and summated for the entire dataset. This resulted in a regressed u_L of **34.99** $\text{cm}\cdot\text{s}^{-1}$. This value is lower than the corresponding figures obtained from the employed optical methodologies, with possible explanations resulting from heat loss in measurement, or the methodology not accounting for the influence of stretch on flame speed.

Table 4.1 summarises the values ($\phi = 1$) obtained from each methodology, and compares them to analogous published CH₄/air data obtained from a range of experimental configurations.

Table 4.1 – Stoichiometric laminar burning velocities from this work and published values ($cm \cdot s^{-1}$).

<i>L</i>	<i>NL</i>	<i>P</i>	1	2	3	4	5	6	7	8	9	10	11	12	13	14	<i>M</i>
37.4	36.8	34.9	37.8	36.8	35.0	35.0	36.2	36.3	38.8	36.0	36.3	36.7	34.5	41.1	37.6	40.0	37.7

Table Key

This work:

L – Linear optical method, NL – Nonlinear optical method, P – Pressure method.

Bomb measurements:

- 1 – Bradley *et al.* [99] 300 K, 0.1 MPa, linear optical technique.
- 2 – Gu *et al.* [102] 301 K, 0.1 MPa, linear optical technique.
- 3 – Halter *et al.* [105] 300 K, 0.1 MPa, nonlinear optical technique.
- 4 – Hassan *et al.* [152] 298 K, 0.1 MPa, linear optical technique.
- 5 – Hu [153] 303 K, 0.1 MPa, linear optical technique.
- 6 – Taylor [113] 298 K, 0.1 MPa

Counter flow flame technique:

- 7 – Vagelopoulos and Egolfopoulos [107] 300 K, 0.1 MPa.
- 8 – El-Sherif [155] 300 K, 1 atm.

Heat flux technique:

- 9 – Hermans [154] 298 K, 0.1 MPa.
- 10 – Coppens *et al.* [156] 298 K, 0.1 MPa.

Bunsen burner technique:

- 11 – Kurata *et al.* [108] 303 K, 0.1 MPa.

Flat flame technique:

- 12 – Haniff *et al.* [157] 298 K, 0.1 MPa.

Pressure measurement technique:

- 13 – Stone *et al.* [158] 298 K, 0.1MPa

- 14–Dahoe and de Goey [133] 298 K, 0.1 MPa.

Model:

M – CHMEKIN-PRO: GRI -Mech 3.0 reaction mechanism. 303K, 0.1 MPa (see section 4.2.2) [149]

Data from the three tested methodologies all sit within the range of published values shown in table 4.1. However, if the chamber performance was to be more comprehensively benchmarked, then experimental repeatability and variation in equivalence ratio needed to be analysed further.

4.2 Fully Benchmarking CH₄ Combustion

A detailed study was undertaken to further validate the performance and repeatability of the experimental method, and subsequent data processing techniques. Three repetitions of eleven equivalence ratios in the range 0.75 - 1.25 were tested for CH₄/air combustion, under initial ambient conditions of 303 K and 0.1 MPa, and frame capture rate of the optical system maintained at 5,000 fps. Fig. 4.10 provides an illustrative comparison of the difference in radial propagation rates for four samples of tested equivalence ratios.

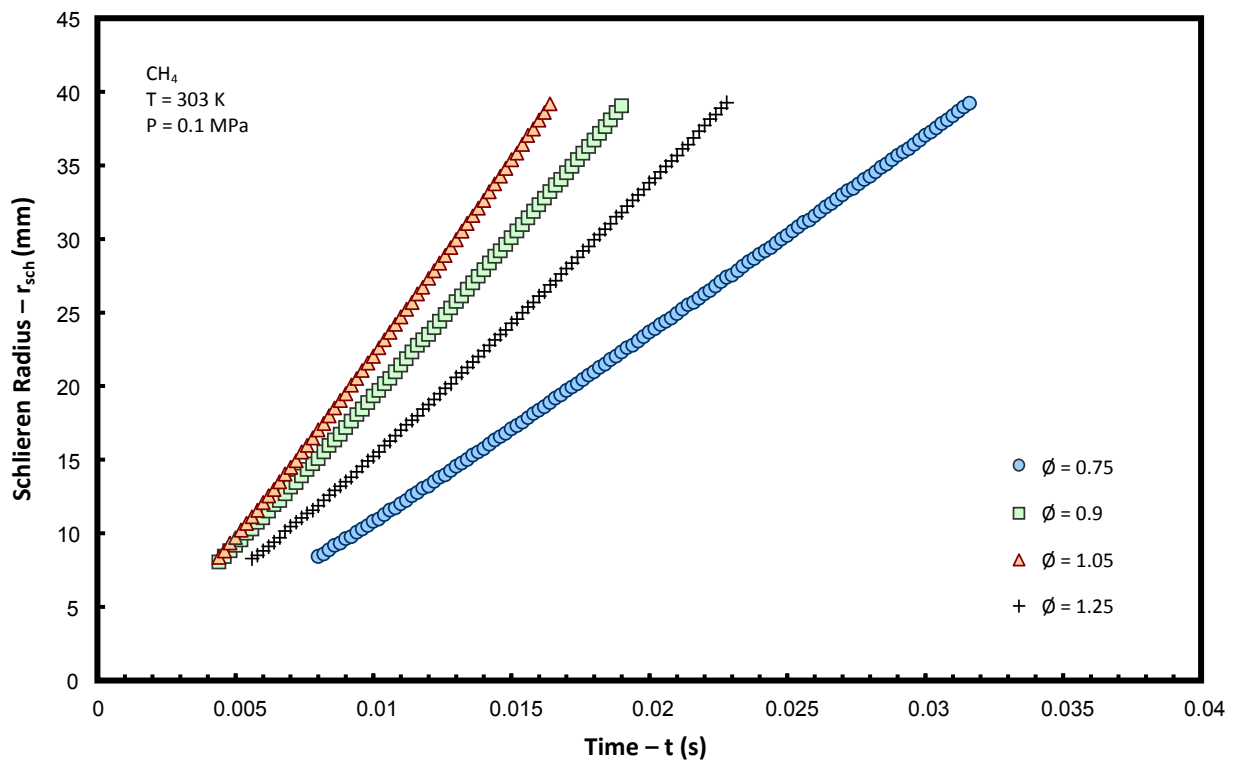


Fig. 4.10 – Comparison of radial propagation rates for different equivalence ratios.

Figs. 4.11 and 4.12 show typical plotted S_n against α data for respective lean to stoichiometric, and stoichiometric to rich conditions (separated for clarity). The linear and nonlinear optical relationships of sections 4.1.1 and 4.1.2 have been applied, and superimposed onto each curve.

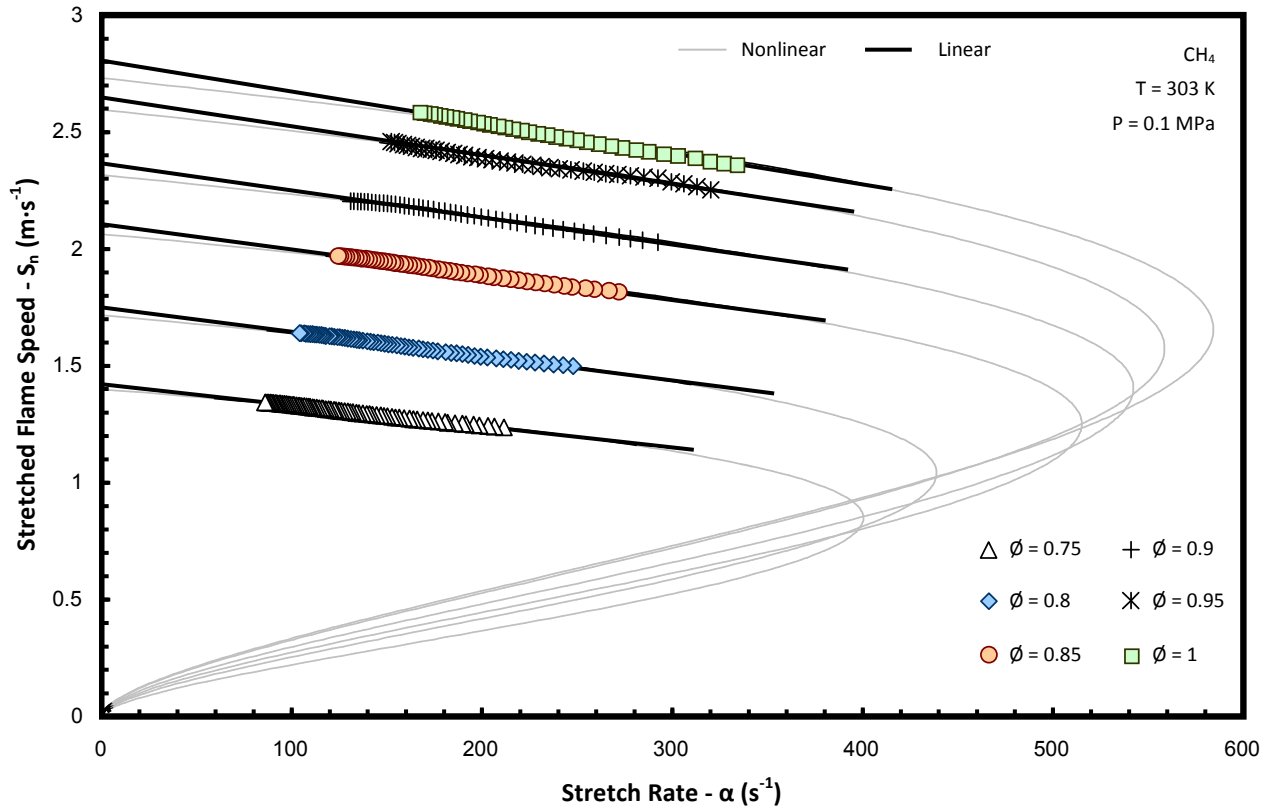


Fig. 4.11 – Samples of plotted CH₄/air S_n against α data, for lean to stoichiometric equivalence ratios.

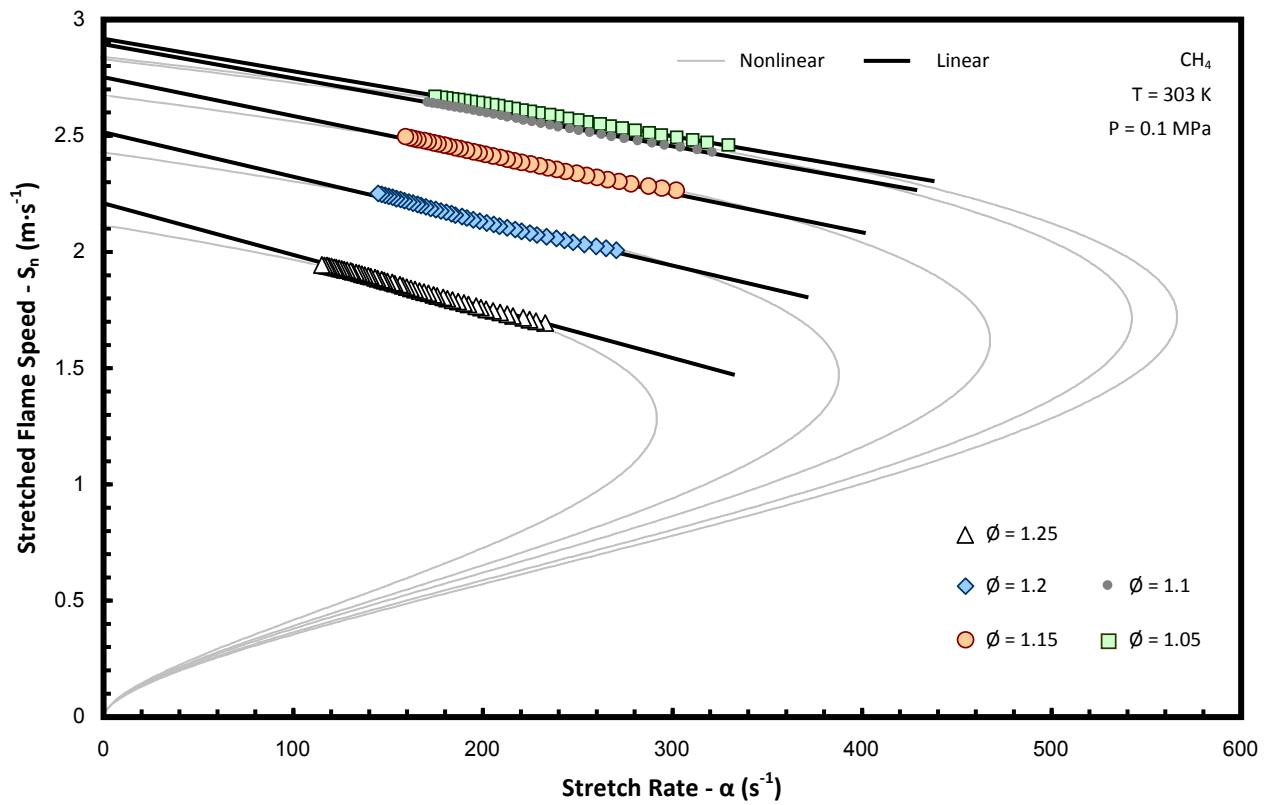


Fig. 4.12 – Samples of plotted CH₄/air S_n against α data, for rich equivalence ratios.

At lower equivalence ratios in Fig. 4.11 only a small difference in intercept points (or equivalent S_u) is evident using either the linear or nonlinear techniques. The propagation of richer flames becomes increasingly influenced by stretch (as highlighted by a steepening of the data gradient), and the difference in representative S_u between each methodology widens, as nonlinear effects become more influential. This is seen to continue in Fig. 4.12, and suggests a tendency of increasing L_b with equivalence ratio, consistent with previously observed trends (e.g. [99], [102], [105]). Fig. 4.13 shows the experimental scatter seen in obtained values of S_u (for both methodologies) for each of the three performed repetitions.

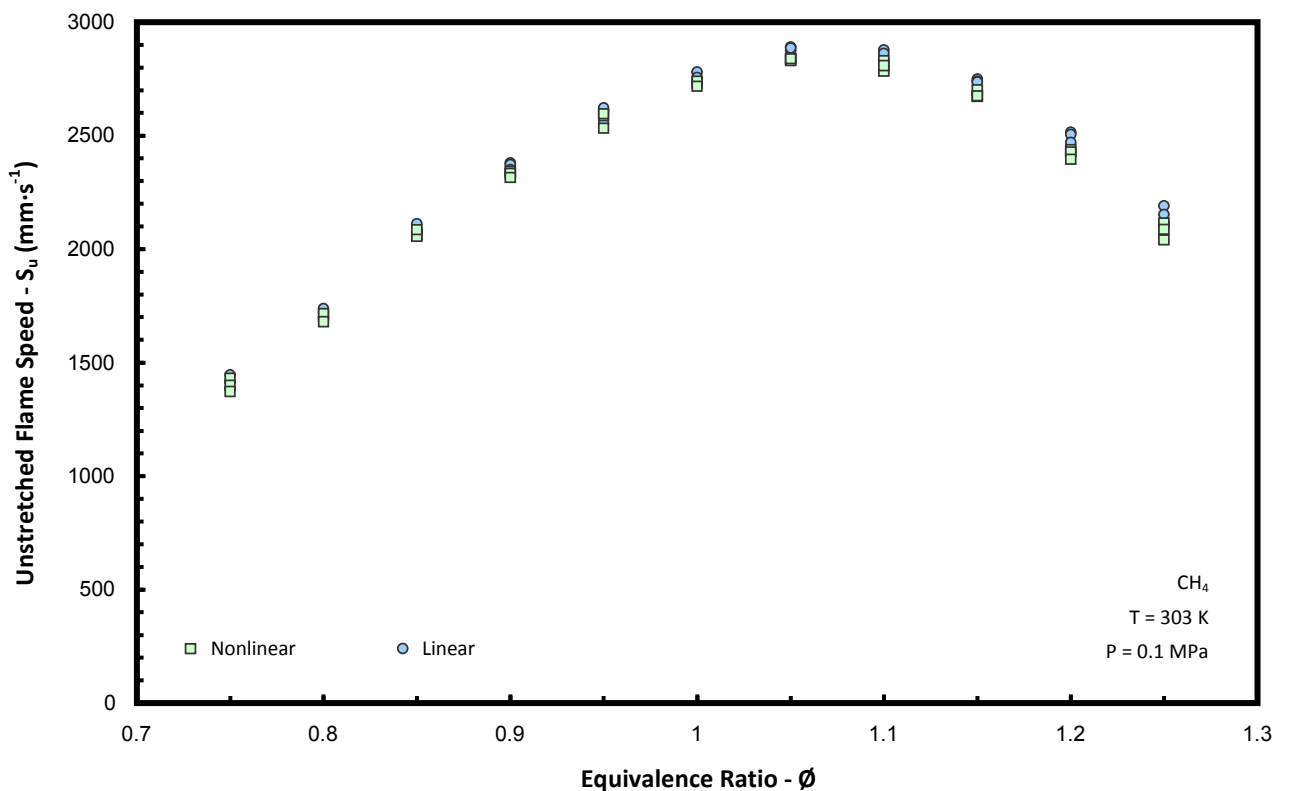


Fig. 4.13 – Experimental scatter seen in obtained values of S_u for each of the optical methodologies.

As was expected from the initial analyses of Figs. 4.11 and 4.12, the difference in S_u between each methodology grows with richness, as the flames become increasingly influenced by stretch. There also appears to be a widening of scatter in the obtained data, suggesting experimental repeatability is worsened with the increased uncertainty induced. Nevertheless, if the standard deviation of scatter in each equivalence ratio is

averaged, then the entire S_u dataset has dispersion in the order of one percent for either optical technique.

4.2.1 - CH₄/air Markstein Length

Fig. 4.14 shows the equivalent scatter observed for values of L_b attained from both optical methodologies.

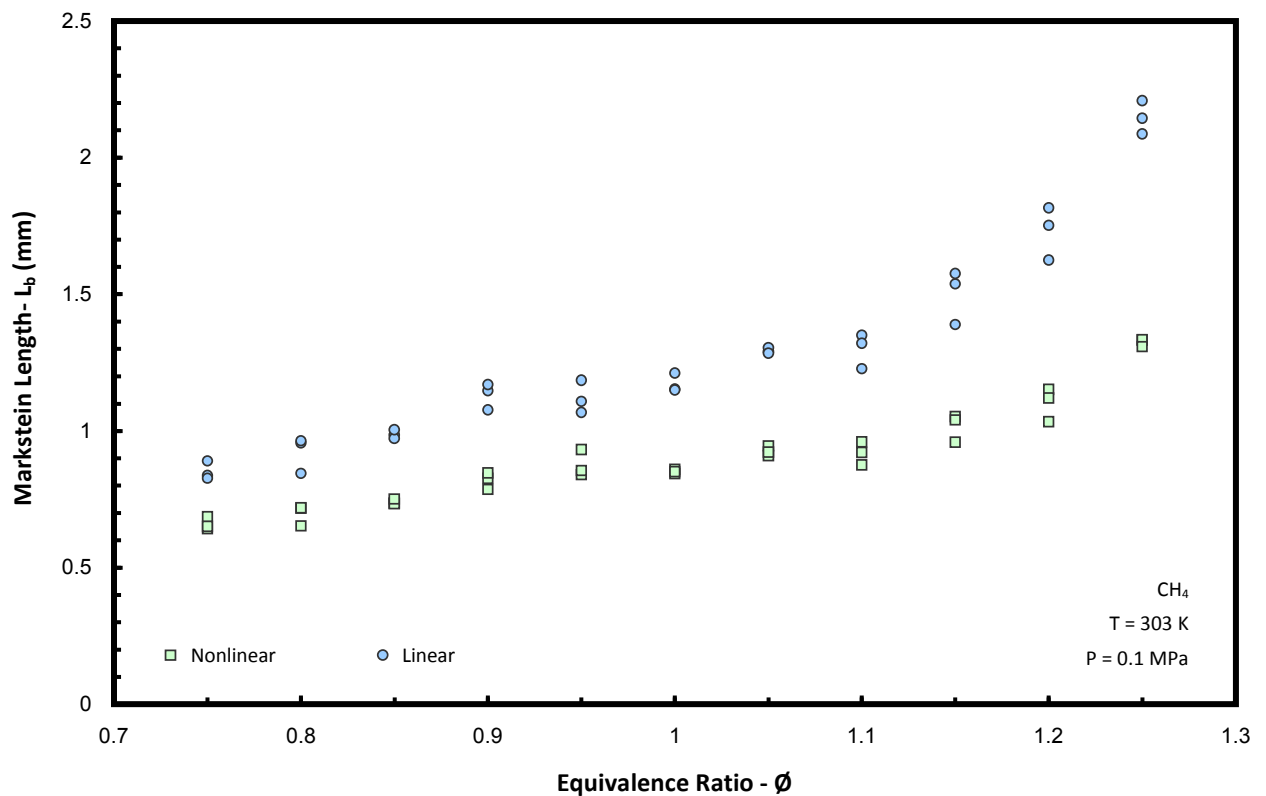


Fig. 4.14 – Experimental scatter seen in obtained values of L_b for each of the optical methodologies.

The aforementioned (section 4.1.2) difference in L_b measured between each methodology is shown to increase with richness, and is in agreement with previous work [105]. Again, this is attributed to overestimation of the stretch influence induced by the linear methodology. There also appears to be a higher relative dispersion in the L_b data, with a respective averaged standard deviation of four and five percent, for the linear and nonlinear techniques. Fig. 4.15 shows a comparison of averaged L_b data obtained from this work, with those published by other researchers. Details of the ambient temperature and specified technique are provided for each dataset.

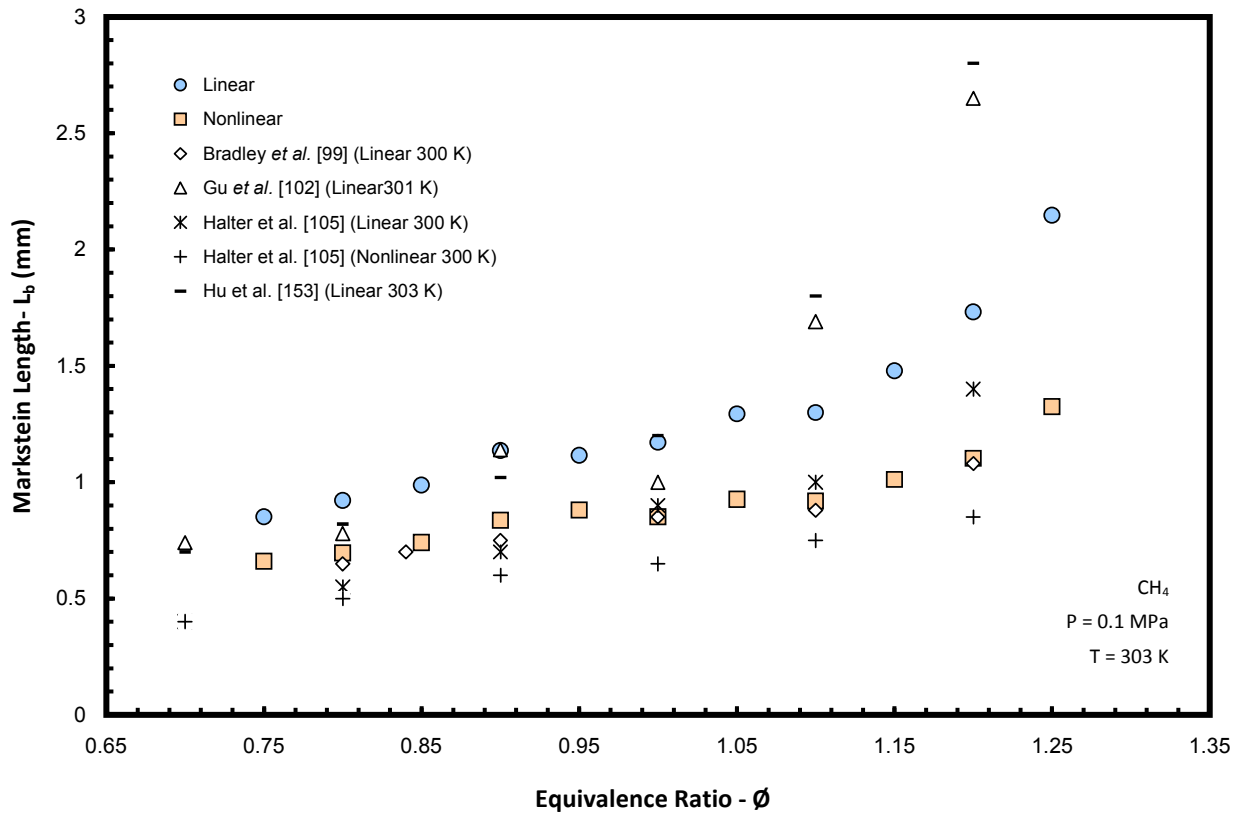


Fig. 4.15 – Comparison of average L_b values from each optical technique with data from literature.

There appears to be a relatively poor correlation between any of the published L_b data from different institutions, with the work conducted for this study enclosed within the scatter of the displayed values. Nevertheless, data attained using the nonlinear methodology display a closer correlation to equivalent tests.

All data exhibit the same trend for rising L_b with equivalence ratio, indicative of an increasing mixture Le [27]. This suggests thermal diffusivity becomes increasingly prominent, and the flame loses more heat to the surrounding reactant when highly stretched, thereby inhibiting the flame speed.

4.2.2 - CH₄/air Laminar Burning Velocity

In order to convert the optically measured unstretched flame speed to a corresponding value of u_L , it was first necessary to attain values of adiabatic density ratio for the entire dataset. As with the stoichiometric case (section 4.1.1 - 4.1.2), these were obtained by employing the GRI-Mech 3.0 [149] reaction mechanism in CHEMKIN-PRO. GRI-Mech 3.0 employs 53 chemical species with 325 reactions, and has been similarly used in many of the studies benchmarked for experimental comparison [102]. Solutions were based on an adaptive grid of 1000 points, with mixture averaged transport properties and trace series approximation. The oxidiser specified for the model was a simple 79/21-N₂/O₂ air composition. The obtained density ratios are plotted in Fig. 4.16.

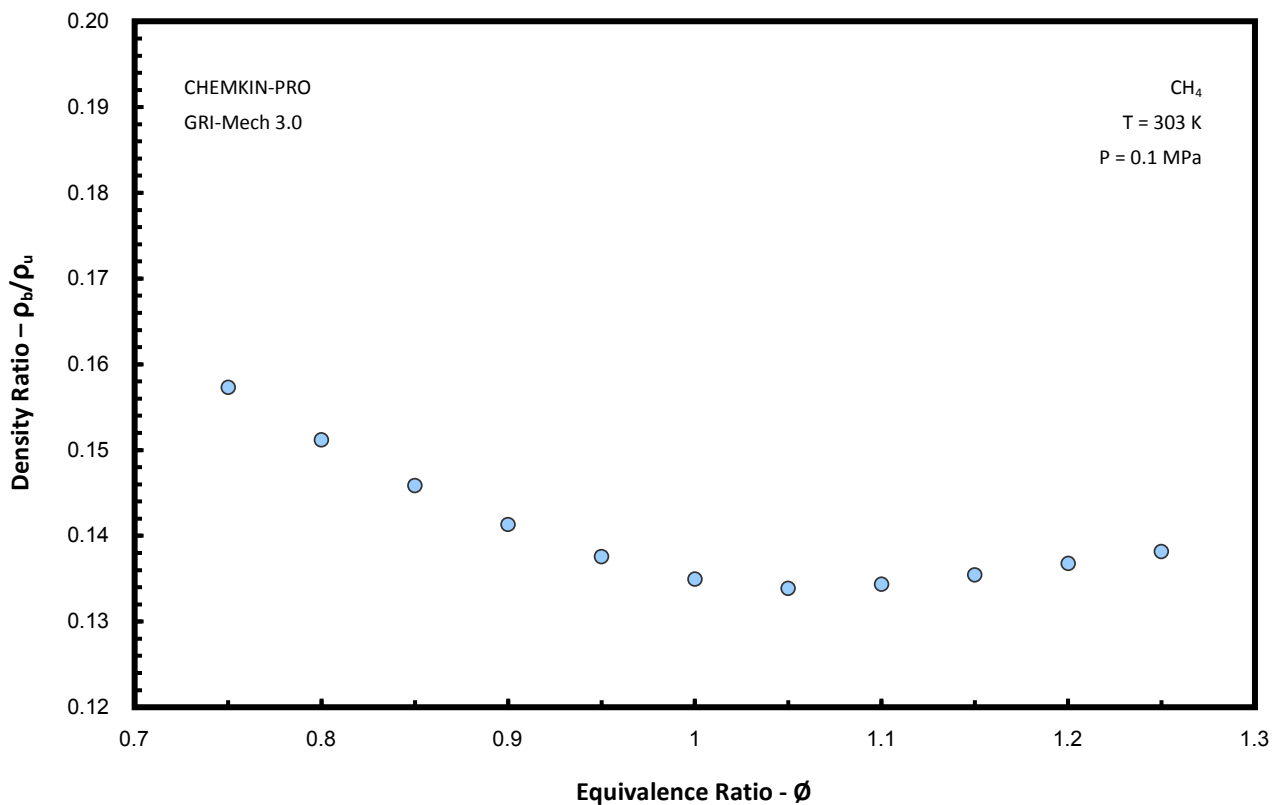


Fig. 4.16 – Values of adiabatic density ratio obtained from GRI-Mech 3.0 in CHEMKIN-PRO.

Where published data was available, a direct comparison was made between average measured S_u values from the Cardiff CVCB, shown in Fig. 4.17. A corresponding comparison of u_L values is given in Fig. 4.18.

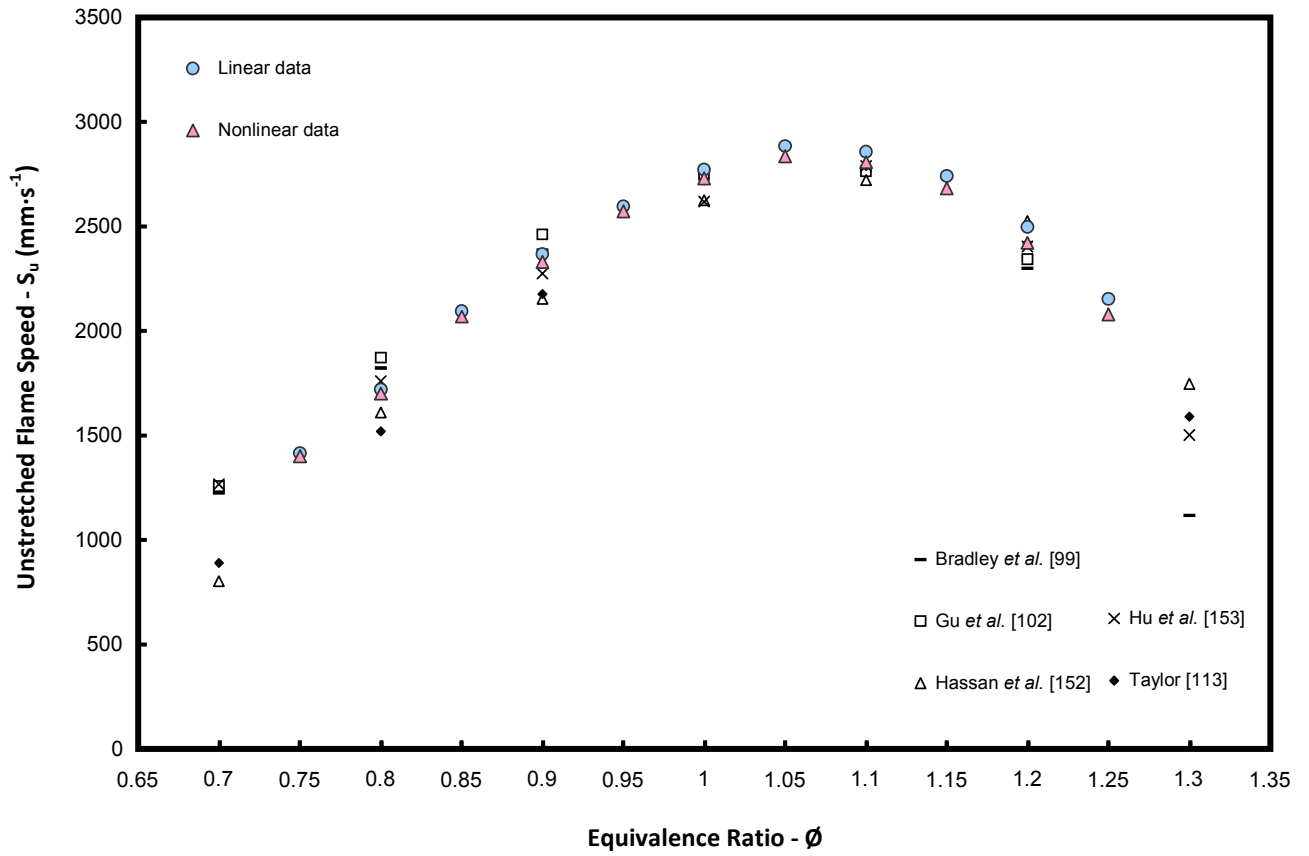


Fig. 4.17 – Comparison of attained S_u data with selected values published in literature.

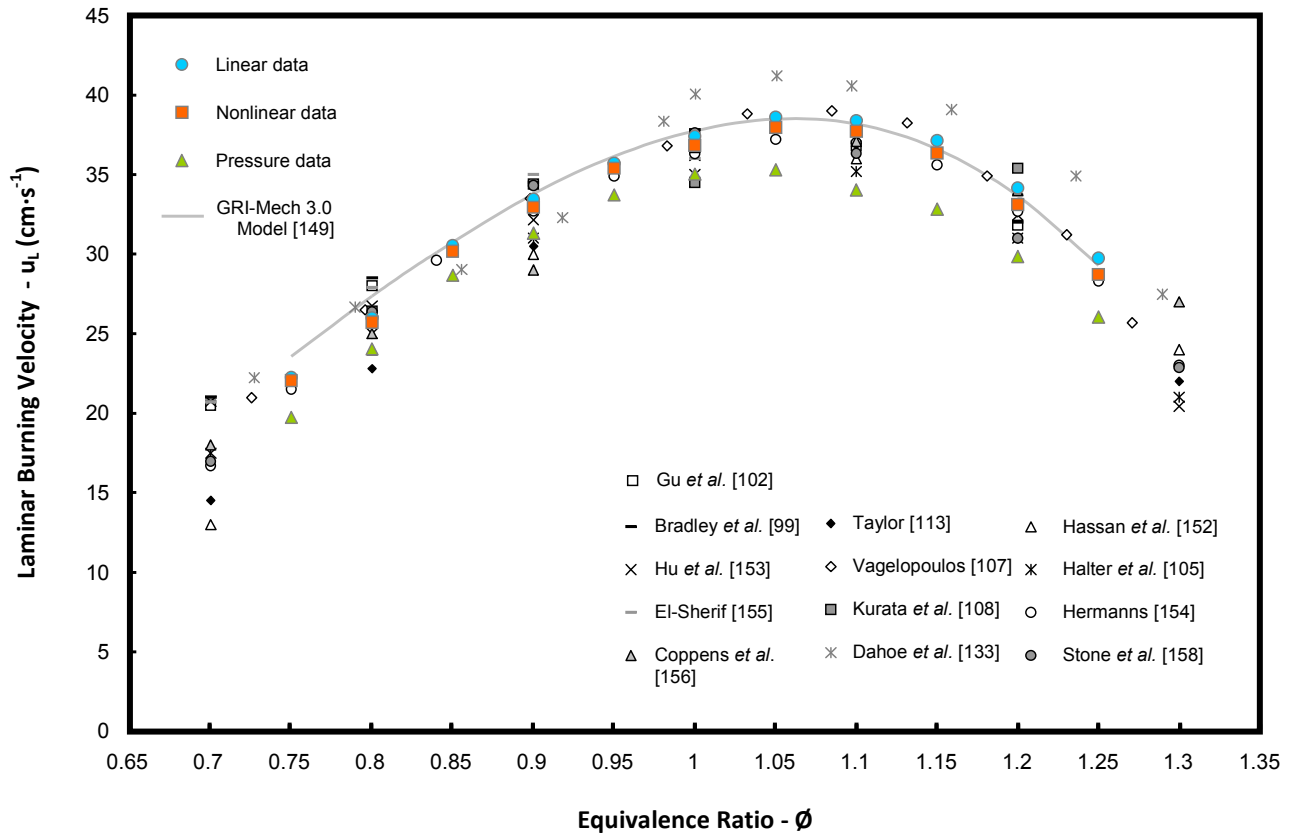


Fig. 4.18 – Comparison of attained u_L data with selected values published in literature.

Where necessary, some values displayed in Fig. 4.17 have been calculated using the u_L and density ratio data presented by the stated authors. There appears to be a good correlation between the data measured in the Cardiff CVCB and those previously published, particularly around peak flame speeds. This trend is continued in Fig. 4.18 where the spread of the faster published data is smaller than under the leanest and richest conditions. The values returned from the use of either optical methodology are in very good agreement with numerical results given by the chemical model, and show a peak u_L at an approximate equivalence ratio of 1.05. This is also in agreement with the majority of analogous data, some of which has been obtained using alternative flame configurations. For example, close correlation is shown with the heat flux (section 2.3.3b) work of Hermanns [154] and similarly data presented by Vagelopoulos and Egolfopoulos [107] who utilised a counterflow technique (section 2.3.3d).

The biggest disparities in the presented data result from the use of lesser employed techniques, such as the pressure method of Dahoe *et al.* [133], or the Bunsen flame used by Kurata *et al.* [108] where u_L is presented to peak under richer conditions. There is also a negative offset between the Cardiff optical data, and those obtained using the stated pressure method. Interestingly this appears to worsen under the richest conditions, and therefore could result from an underestimation induced by not accounting for the heavier influence of flame stretch. This argument is strengthened by the deceleration that results from increasing stretch rates for the presented data, however contrary to this, the work of Dahoe *et al.* [133] appears to provide an overestimation of the representative values. The authors suggest the stated methodology is useful for providing an approximate depiction of trends, opposed to exact quantification of desired values, particularly when use of the optical methodology is not possible (studying dust explosions for example). Consequently, data presented herein will only result from the vindicated use of either optical method.

4.2.3 - Change in Ambient Temperature

The benchmarking work undertaken thus far has demonstrated good overall agreement between published, modelled, and attained experimental data, potentially vindicating use of the employed methodology. However, a further significant contributory parameter in the determination of u_L is ambient temperature (T) of the unburned reactants. The author deemed it necessary to investigate change in initial T to ensure control of this parameter was accurate enough to be in comparable agreement with corresponding data. Three repetitions of five equivalence ratios were tested in the range 0.8 - 1.2, at ambient conditions of 358 K, and 0.1 MPa. Fig. 4.19a gives examples of the measured relationship between stretch rate and flame speed, with 4.19b providing average L_b plotted for the dataset. It should be noted that only the linear optical methodology is shown for this regime, as was the same in the small amount of comparable literature data.

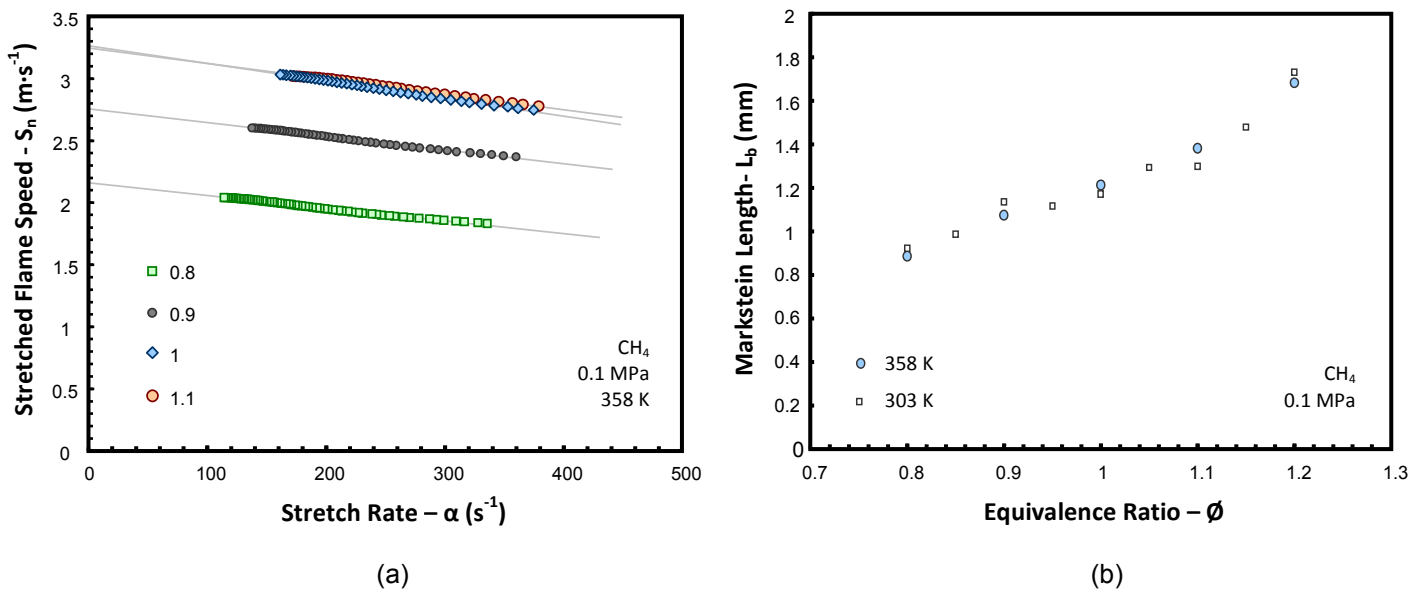


Fig. 4.19 - CH₄/air experimental parameters of S_n against α (a), and resultant change in L_b (b) at elevated temperature.

The observed change in L_b with equivalence ratio was minimal with the respect to the previously attained data at 303 K. Adiabatic density ratios were again obtained using the GRI-Mech 3.0 mechanism, and applied to the unstretched data to obtain values of

u_L . Fig. 4.20 shows the average experimental values plotted against comparable data from research literature, and the chemical model output.

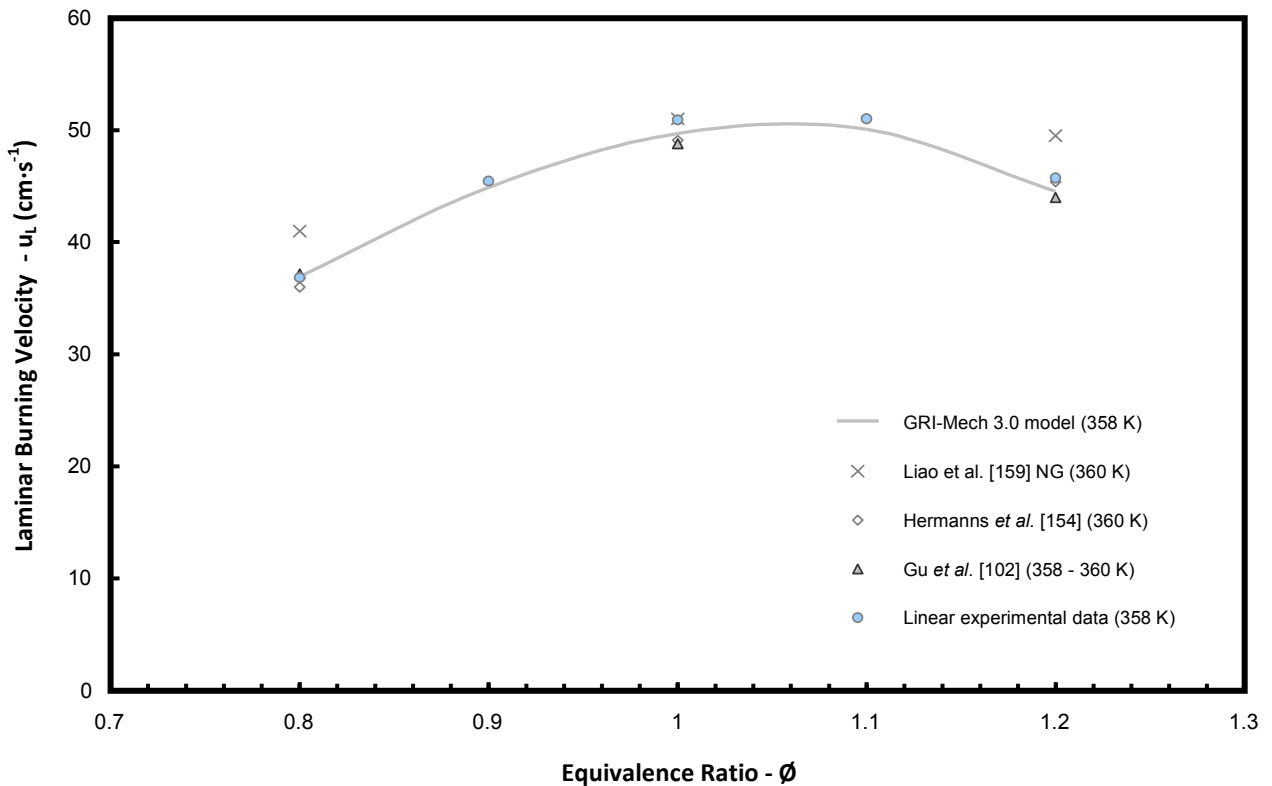


Fig. 4.20 – Comparison of average u_L values for CH₄/air experiments at elevated temperature.

There is once again favourable agreement between the attained experimental values, model and the limited dataset. The most significant difference is shown between the data and values presented by Liao et al. [159], however it should be noted that this work was performed for a natural gas composition comprising 97 percent CH₄ with a balance of higher hydrocarbons and nitrogen.

Consequently, the data obtained from the benchmarking study were deemed by the author to be in sufficient agreement with analogous research to vindicate accurate use of the specified methodologies with the Cardiff CVCB. Nevertheless, further investigation of possible experimental uncertainties was still necessary.

4.3 Exploring Experimental Uncertainties

The approach made to quantifying experimental uncertainty was developed from the method outlined by Moffat [160]. Parametric fluctuations are combined with statistical ambiguity to form a total uncertainty estimate for each unstretched flame speed (U_{Su}), as defined in Eqn. 4.4. Where B_{Su} represents the total bias uncertainty, $t_{M-1,95}$ Student's t value at a 95 percent confidence level [161] for $M-1$ degrees of freedom, and M the number of experimental repeats. This is combined with the corresponding experimental standard deviation (σ_{Su}).

$$U_{Su} = \sqrt{B_{Su}^2 + \left(\frac{t_{M-1,95} \sigma_{Su}}{\sqrt{M}} \right)^2} \quad (4.4)$$

Uncertainty has been quantified for S_u opposed to u_L , because this is the parameter that is experimentally measured. The uncertainty associated with computationally determining an applicable density ratio is discussed separately with apt results.

4.3.1 - Influences On Total Bias Uncertainty

B_{Su} quantifies systematic influences by combining the relationship between changes in S_u for an independent variable (v_i , for example temperature), and the fixed error in that variable (y_i), as shown in Eqn. 4.5:

$$B_{Su} = \sqrt{\sum_{i=1}^n \left(\frac{\partial S_u(v_i)}{\partial v_i} y_i \right)^2} \quad (4.5)$$

So if the influence of temperature on stoichiometric unstretched flame speed is taken for example: With a change of 1 K in ambient reactant temperature, obtained results suggest a difference in S_u of approximately $8.4 \text{ mm}\cdot\text{s}^{-1}$. The level of accuracy outlined for the temperature control system is $\pm 2 \text{ K}$ (see section 3.2.6), leading to a systematic uncertainty of approximately $\pm 16.8 \text{ mm}\cdot\text{s}^{-1}$. In this example the relationship between S_u and temperature was established from experimental data, however whenever this was not possible (for instance; change in ambient pressure), then estimations were made from apt chemical models.

The following systematic uncertainties were included for calculation of the total bias, with example values outlined for the case of stoichiometric CH₄/air combustion.

Ambient Temperature:

As stated above, experimental data were used where possible to obtain this value, and applied with the specified error in the thermal system (± 2 K). The stoichiometric CH₄ case has an estimated uncertainty in S_u of $\pm 16.8 \text{ mm}\cdot\text{s}^{-1}$.

Ambient Pressure:

Experimental (when available), or modelled data were used to give an estimated influence of ambient pressure. For the CH₄ case this was equivalent to $\sim 1 \text{ mm}\cdot\text{s}^{-1}$ per 0.1 kPa fluctuation. The accuracy of initial pressure measurement was also specified as ± 0.05 kPa. This value is conservative, with the system regulated to 0.01 kPa, but engrossed to compensate for the manual control of needle valves and applicability of the applied model. Nevertheless, the influence of pressure is small, introducing an example uncertainty of $\pm 0.5 \text{ mm}\cdot\text{s}^{-1}$.

Equivalence Ratio:

A relationship was fitted with the attained experimental data to numerically quantify the influence of uncertainty from specified equivalence ratio. As the mixing system was controlled by partial pressure, the same order of error was applied (± 0.05 kPa). For the case of stoichiometric CH₄, the required fuel partial pressure for a 0.1 MPa test was 9.5 kPa, and applying the error factor gives a resultant range in specified equivalence ratio of ~ 0.994 - 1.006 . This results in an S_u uncertainty of either ~ 2715 - $2746 \text{ mm}\cdot\text{s}^{-1}$, or ~ 2757 - $2788 \text{ mm}\cdot\text{s}^{-1}$, for respective use of nonlinear and linear optical methodologies. Because the order of difference is the same ($\sim 30.8 \text{ mm}\cdot\text{s}^{-1}$), only specification of one methodology was required with each equivalence ratio, giving an example resultant uncertainty of $\pm 15.4 \text{ mm}\cdot\text{s}^{-1}$. As this error has been significantly increased from the overcompensated pressure inaccuracy, it is also specified to encompass uncertainties resulting from the compressibility of gases used, and the

ideal assumption employed in the mixture calculation. The quantity of this uncertainty is heavily influenced by the specified equivalence ratio, with errors minimised at near peak conditions.

System Optics:

The spatial resolution of the produced digital image is ~ 0.14 mm per pixel, giving potential for fluctuation in the order of ± 0.07 mm for every time step. The error induced from polynomial fitting, was also of this order, so to introduce a compensative factor, the fluctuation was doubled back to 0.14 mm. Applying this value with the filming rate of the camera (5,000 fps for this study), gives an initial uncertainty of: $0.14/0.0002 = 700 \text{ mm}\cdot\text{s}^{-1}$. As this uncertainty is applied to the entire dataset, the value is averaged across the number frames used for measurement (in this instance 64, giving $\sim 11 \text{ mm}\cdot\text{s}^{-1}$).

This uncertainty is increased by twenty percent to account for any error induced through calliper calibration (to give $\pm 13.2 \text{ mm}\cdot\text{s}^{-1}$ for the CH_4 example). Although the callipers have a resolution and accuracy of better than an order of magnitude when compared with the system optics, this value was doubled to introduce a further factor of compensation. Taking the CH_4 test as an example, the inaccuracy in filming rate was specified as 5,000 ± 0.25 fps, and when applying this factor to the approximate measured flame speeds, there was a resultant error in the order of 0.01 percent. Consequently, this part of the optical error was deemed negligible enough to ignore for the purposes of uncertainty calculation. Optical uncertainty was derived to each test for individual specifications of filming rate, and number of frames obtained.

Gas Mixture Quality:

This uncertainty is specified to account for the errors resulting from imperfect vacuum, and purity of the employed fuel. An effective worst case flame speed of zero is assumed from the gaseous impurity, and applied in proportion with the corresponding fraction. So for example, the employed CH_4 purity was 99.9 percent [162], and therefore the resultant uncertainty in flame speed (approximate S_u rounded up from

the average of the linear and nonlinear methodologies) is approximately $\pm 2.8 \text{ mm}\cdot\text{s}^{-1}$. The error resulting from imperfect vacuum (0.02 percent, section 3.3.1) is added to this to give a mixture uncertainty of 0.12 percent: $\pm 3.3 \text{ mm}\cdot\text{s}^{-1}$. (Note: application of the error calculation in this way assumes an impurity that will not accelerate flame speed by a greater quantity than the opposing zero assumption).

4.3.2 - Example Uncertainty Calculation For Stoichiometric CH₄

Calculating the rms of all of the systematic uncertainties in section 4.3.1 gives an example total bias uncertainty, and is applied to data obtained from either methodology:

$$B_{Su} = \sqrt{16.8^2 + 0.5^2 + 15.4^2 + 13.2^2 + 3.32^2} = \pm \mathbf{26.5 \text{ mm}\cdot\text{s}^{-1}}$$

The standard deviation of the stoichiometric CH₄ data (M=3) was 13.8, and 11.3 $\text{mm}\cdot\text{s}^{-1}$ for the respective linear and nonlinear data. The t value at a 95 percent confidence level for M-1 repeats is 4.303 [161], giving stoichiometric U_{Su} values of:

$$\text{Linear } U_{Su} = \sqrt{26.5^2 + \left(\frac{4.303 \cdot 13.8}{\sqrt{3}}\right)^2} = \pm \mathbf{43.4 \text{ mm}\cdot\text{s}^{-1}}$$

$$\text{Nonlinear } U_{Su} = \sqrt{26.5^2 + \left(\frac{4.303 \cdot 11.3}{\sqrt{3}}\right)^2} = \pm \mathbf{38.6 \text{ mm}\cdot\text{s}^{-1}}$$

or the approximate equivalent of $\pm 1.5\%$.

4.3.3 - CH₄ Dataset Uncertainty

The calculative procedure undertaken in section 4.3.2 has been employed for the entire CH₄/air dataset, with resultant uncertainty shown with error bars in Fig. 4.21. The spread of data obtained using the linear technique is shown, with $\pm U_{Su}$ shown from the average value.

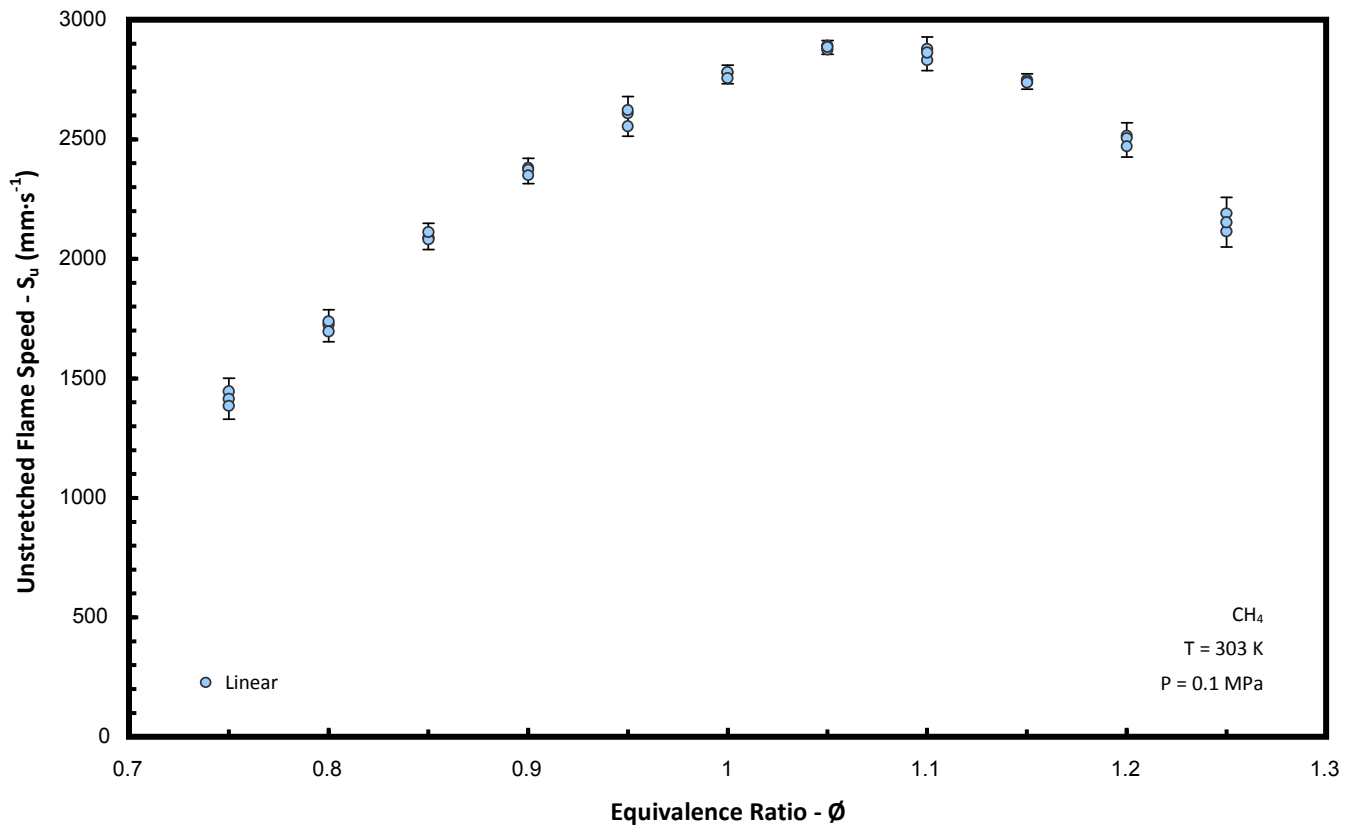


Fig. 4.21 – Linear unstretched flame speed of CH_4/air experiments with superimposed uncertainty.

It is evident from Fig 4.21, that as peak conditions are approached and the corresponding B_{S_u} values reduce, there is an overall trend for the U_{S_u} range to compress. This is approximately shown with the spread of data, and more variation present at leanest and richest conditions. Consequently, the order of uncertainty increases from 1-2 percent at peak conditions, to 5-6 percent of the corresponding S_u values at the extremities of the curve. There are exceptions to this overall trend shown, for example with data at $\phi = 0.95$, and 1.1, where some comparatively spurious points have increased the standard deviation of the data, and consequently the calculated values of U_{S_u} . It should be noted that whilst uncertainty values are presented for S_u , a corresponding value in L_b has not been determined. This was because the calculations required to determine the effect of the systematic influences on B_{S_u} were deemed potentially too inaccurate to give worthwhile values. As a consequence, L_b data presented in the rest of this research dissertation have superimposed error bars to represent only standard deviation of the data.

Fig. 4.22 shows the corresponding uncertainty values for the higher temperature CH₄ tests.

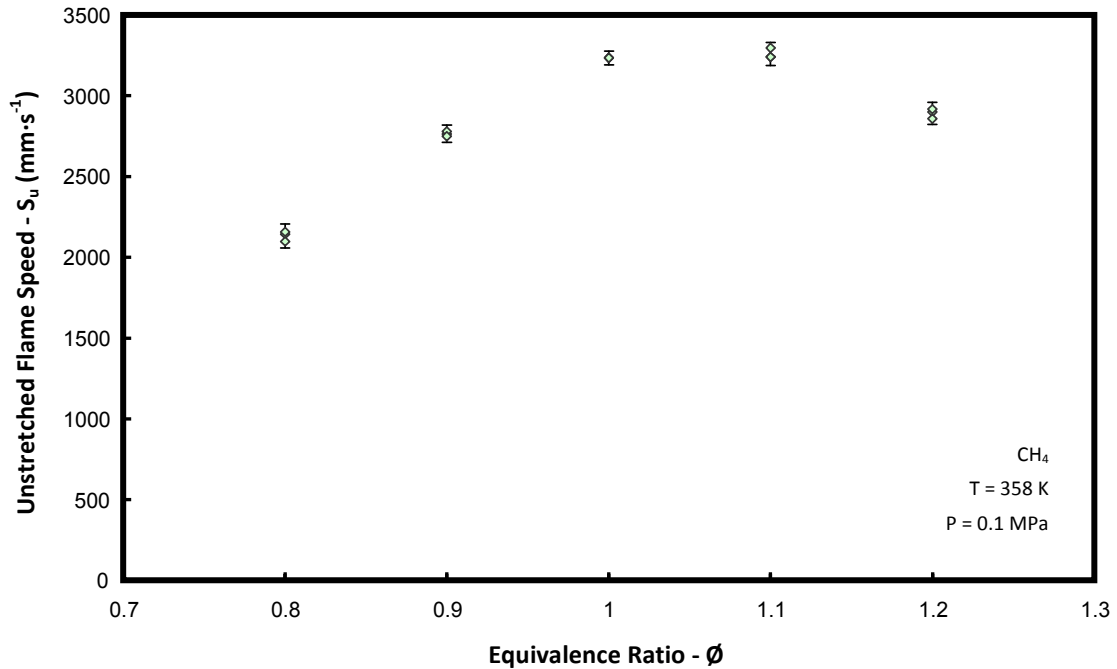


Fig. 4.22 – Linear unstretched flame speed of CH₄/air experiments with superimposed uncertainty at 358 K.

4.4 Summary

The benchmarking work presented in this chapter demonstrates that optical results obtained from the Cardiff CVCB are in sufficient agreement with corresponding data in the research literature, particularly with esteemed and well referenced works employing similar methodologies. Use of the system for the designated characterisation of steelworks gases was therefore deemed by the author to be satisfactorily vindicated on the basis of produced result quality.

Variation in the values obtained from either optical methodology was shown to be of the same order as quantified systematic and statistical uncertainties. Therefore, in order to avoid confusion, plotted results herein will be presented predominantly using the nonlinear technique, because of the perceived accuracy increase when employing this relationship with highly stretched flames. Full linear datasets will however; be

provided for all experimental tests. Furthermore, because of the spread in obtained L_b values between each methodology, and corresponding data presented in the relevant literature (section 4.2.1), results will be primarily analysed for overall trend of stretch influence, opposed to exact quantification of precise values.

Appendices B.1 and B.2 provide details of the experimental results obtained and described in this chapter. Full test specifications are provided, together with returned individual and averaged values. Furthermore, the employed fuel partial pressure is tabulated for each equivalence ratio, together with the coefficient of determination for each specified polynomial fit. Results from the three employed methodologies are distinguished, together with the modelled values, and coefficients obtained for quantifying the apt levels of uncertainty (total bias, and standard deviation). Therefore, with chamber use benchmarked in this way, one fundamental objective body of work was completed.

Chapter 5. BFG H₂ Variation - Atmospheric Conditions

Having benchmarked CVCB experimental performance with CH₄, work was now undertaken to characterise the specified steelworks gases. This chapter focuses on potential variability in the combustion of BFG resulting from compositional variation.

5.1 Chapter Introduction

As discussed in Chapter 2. BFG is the most abundant of the steelworks gases, with an inherently variable composition that is dependent on operational specifications employed by the furnace. The heavily dilute makeup of the fuel suggests the relative influence of changes in composition will be exaggerated depending on the fluctuation of specific constituents. For instance, a proportional decrease and increase of respective preponderant CO₂ and N₂ levels would potentially not influence performance as much as other constituents. Conversely, small changes in H₂ fraction could not only influence fuel calorific value, but potentially provide a higher relative fluctuation in combustive properties such as laminar burning velocity. The aim of this section of work was to investigate this fluctuation to values representative of those experienced in production.

Research literature suggests that the most influential of the relevant fuel components on flame speed is H₂ [94], and was therefore investigated to effective worst case conditions: Inasmuch that H₂ fraction of the fuel was increased, with the other constituents displaced in proportion. This is ostensibly representative of the behaviour between H₂ and diluent fractions when changes are made to GCI rates (see section 2.1.3 [163]). It was important to quantify the effect of this compositional fluctuation over a small range, as it has been shown by other works [109, 111] that the influence

on flame speed exponentially increases with H₂ addition (Fig. 2.12). Mixture laminar burning velocities, and Markstein lengths were characterised with changes in both composition and equivalence ratio, for combustion with air.

5.1.1 – Defining Experimental Parameters

A certified molar composition of CO-23.07%, CO₂-23.35%, and N₂-53.58% was used as the foundation BFG composition employed for this section of the study. H₂ was introduced in the range of 1-7 % to test four effective BFG mixtures, with the makeup of each individual blend detailed in table 5.1.

Table 5.1 – Dry BFG compositions employed in this part of the study.

FUEL BLEND (<i>Molar Fraction</i>)				
Blend	1	2	3	4
H ₂	0.01	0.03	0.05	0.07
CO	0.2284	0.2238	0.2192	0.2145
CO ₂	0.2312	0.2265	0.2218	0.2172
N ₂	0.5304	0.5197	0.5090	0.4983

Three repetitions of nine equivalence ratios in the range 0.7 – 1.5 were tested for ambient conditions of 303 K and 0.1 MPa. It was estimated from chemical models that this range should provide a characteristic peak in u_L for the given mixtures. The purity of the specified H₂ grade was >99.995%, and was employed with compressed air having a volumetric moisture content of <0.02 percent. Camera filming-rate was also reduced to 3,000 fps. This was a pragmatic decision taken to avoid the storage of excessively large video files (at 3,000 fps videos were up to 400 MB, with over 100 tests performed for this experimental phase alone). Even with this reduction in filming rate, the associated uncertainty is improved relative to the CH₄ work, with the number of usable frames processed increased by a factor of around four (see section 4.3.1 for further details).

5.1.2 – Adaptations to the Experimental Methodology

The methodology for filling the chamber with fuel had to be adapted to ensure that the specified mixture and equivalence ratio were both correct. For this, the previously employed partial pressure methodology was slightly adapted:

- Firstly, the necessary values of fuel and oxidiser partial pressure were calculated for each required equivalence ratio of the four compositions specified in Table 4.1. If stoichiometric combustion of the 1% H₂ mixture is taken as an example, the respective pressures for fuel and oxidiser are 63.8 and 36.2 kPa.
- The H₂ partial pressure was then calculated as a fraction of the full fuel value, so in the example this equates to 0.638 kPa. H₂ was subsequently released into the chamber until this value was met.
- The chamber was then filled with the foundation BFG mixture to the required fuel partial pressure (63.8 kPa in the example), with oxidiser subsequently charged to the specified ambient condition (100 kPa). This method introduced further experimental uncertainty, and is discussed further in Section 5.2.3, with specified partial pressure values provided with tabulated results in Appendix B.3

5.2 Results

Results were again obtained in the form of Schlieren greyscale video files, with a series of example frames shown for a stoichiometric 7% H₂ mixture in Fig. 5.1. In an attempt to minimise the influence of buoyancy on attained results, radial flame growth was quantified from only the rate of horizontal propagation [143, 144].

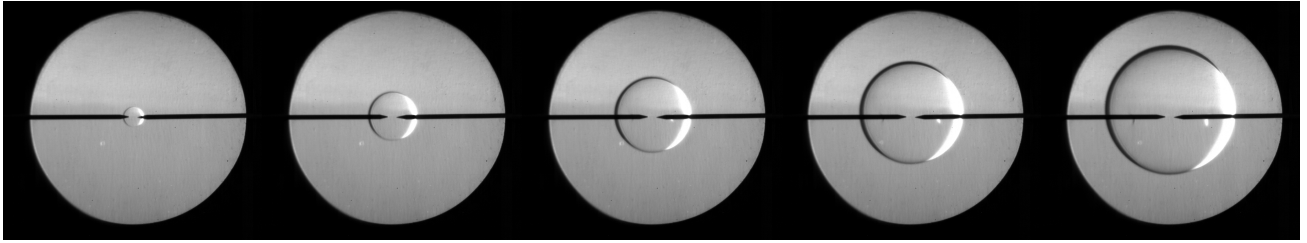


Fig. 5.1 – Example Schlieren images of BFG flame growth (time-step = 0.01333 s).

Fig. 5.2a shows examples of the difference between stoichiometric flame propagation rates for each of the tested BFG mixtures. The 7% H₂ composition has been used to provide a further illustrative comparison of radial growth between two equivalence ratios in Fig. 5.2b. This is shown with two mixtures of similar flame speeds to highlight the subtle influence of flame stretch on propagation, which is more prominent when flame radii are small. There are contrasting inflections near the base of each curve, suggesting Markstein lengths of opposing signs.

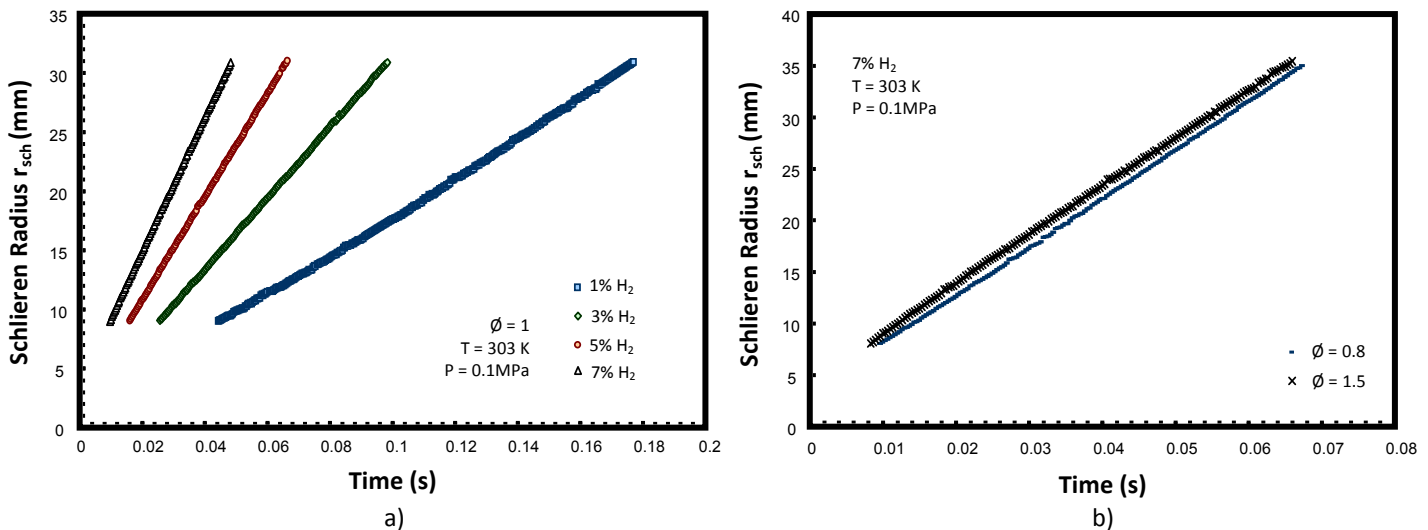


Fig. 5.2– Examples of BFG radial flame growth.

5.2.1 – Relationship between Flame Speeds, Stretch Rates and Markstein Lengths

Having fully processed the dataset, Fig. 5.3 – Fig. 5.10 show examples of the plotted relationships between S_n and α , with superimposed nonlinear associations for each equivalence ratio of the four tested compositions.

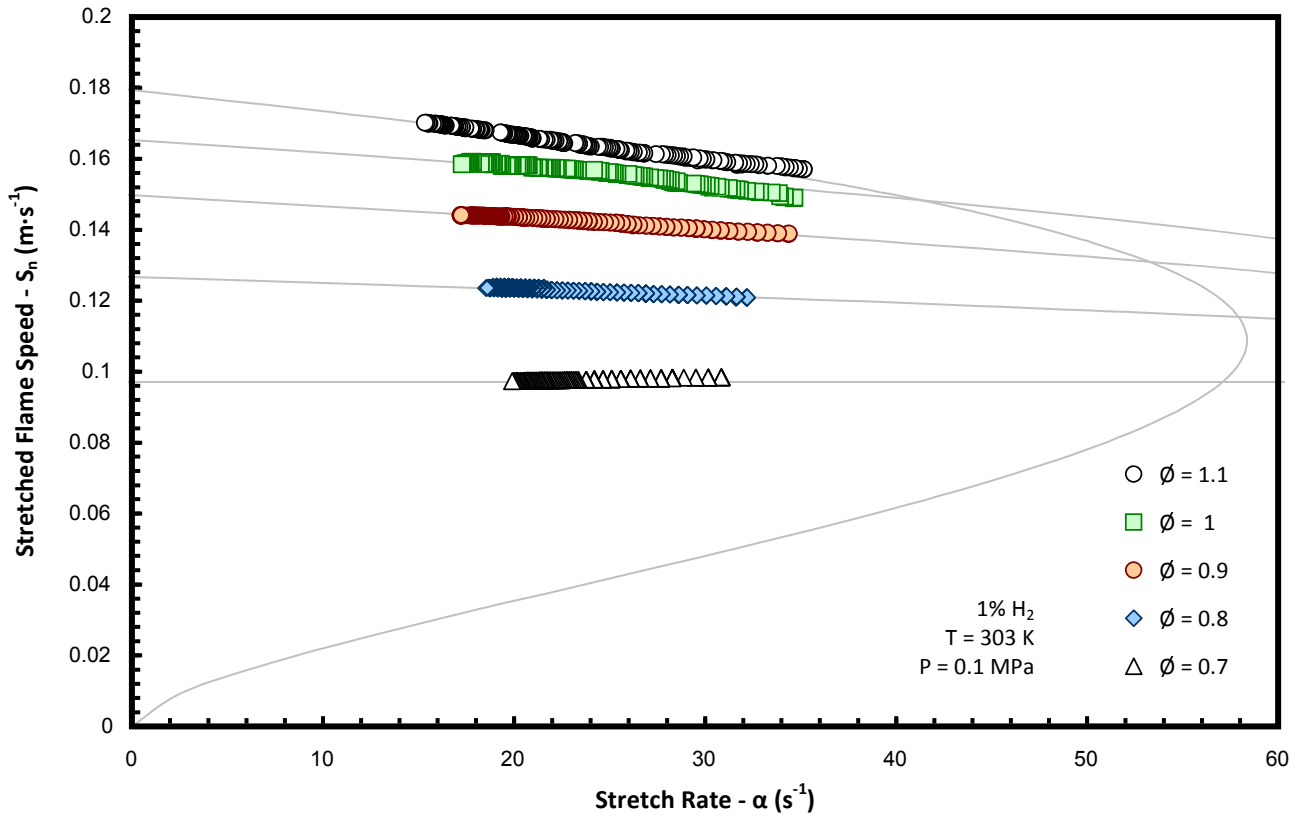


Fig. 5.3 – Samples of plotted 1% H₂ BFG/air S_n against α data, for $\phi = 0.7 - 1.1$.

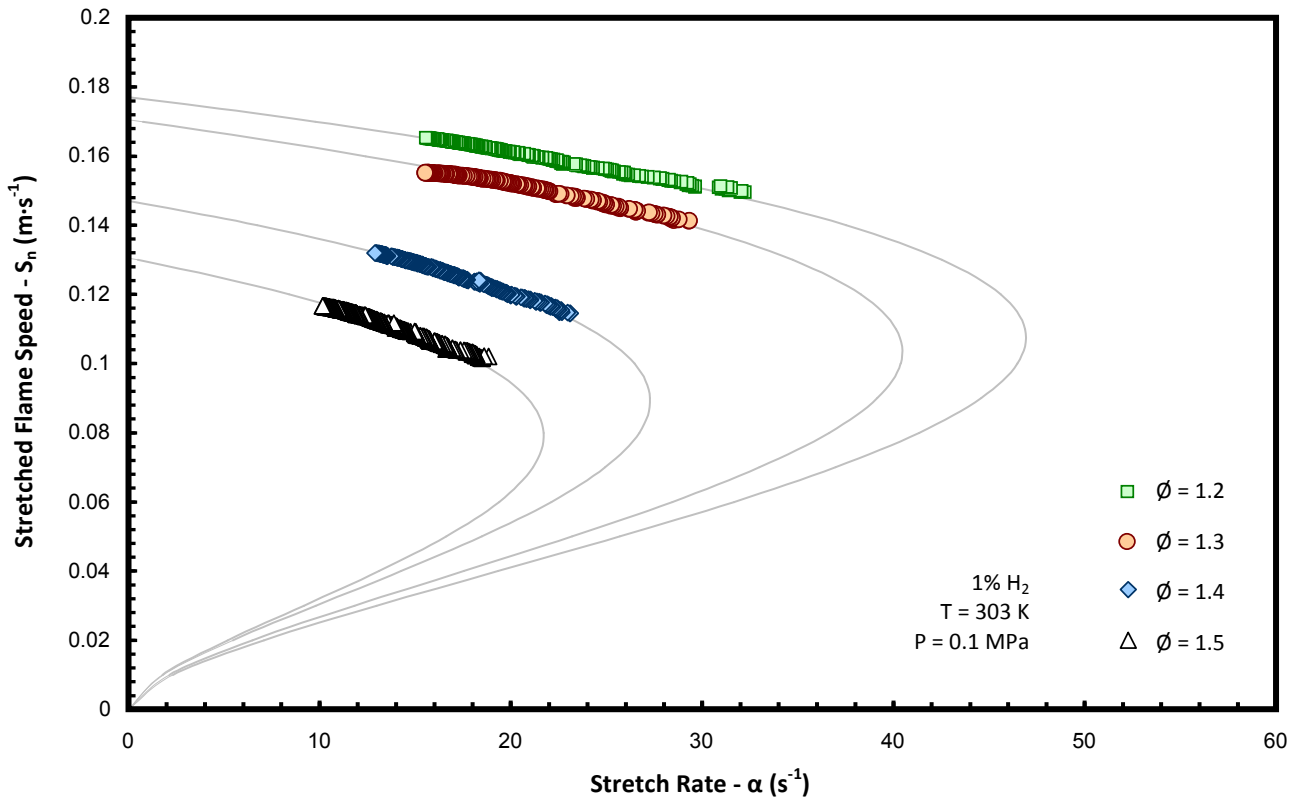


Fig. 5.4 – Samples of plotted 1% H₂ BFG/air S_n against α data, for $\phi = 1.2 - 1.5$.

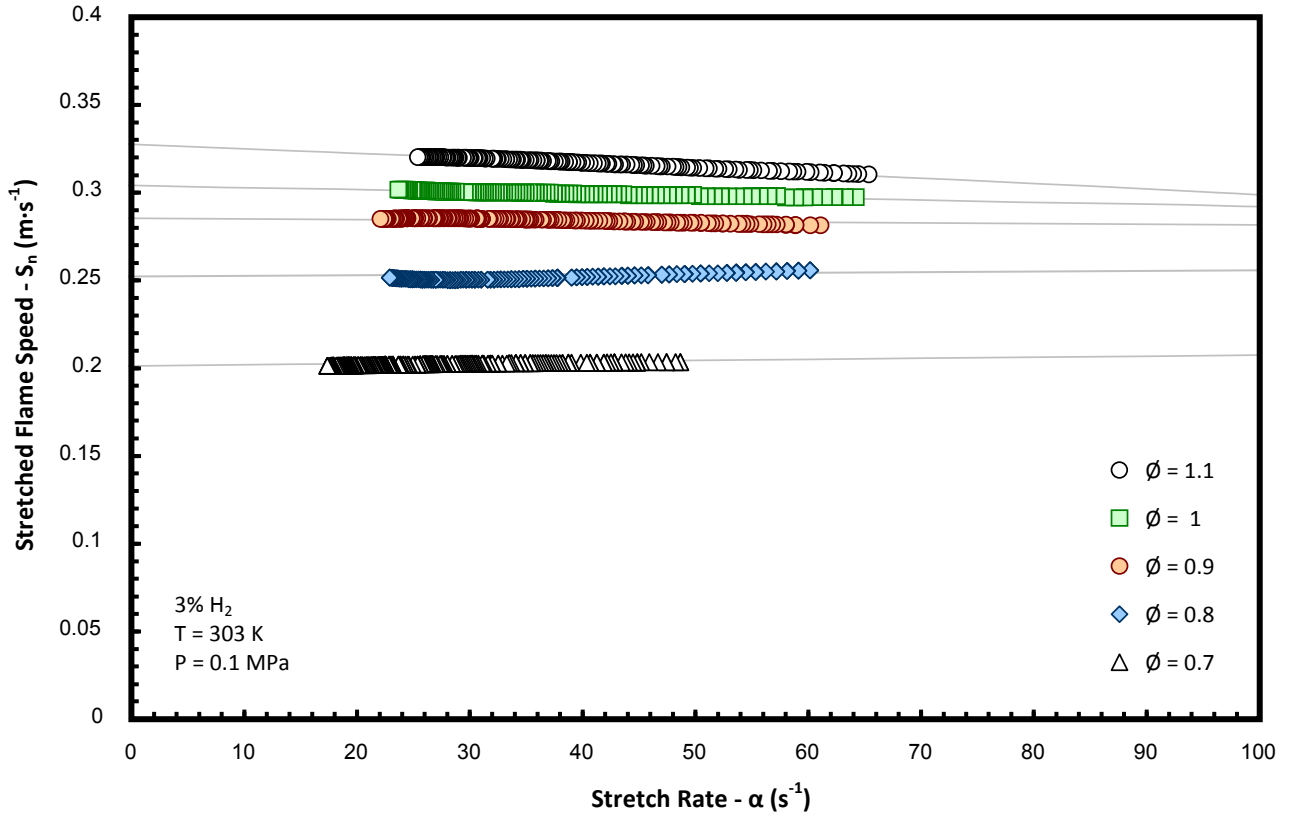


Fig. 5.5 – Samples of plotted 3% H₂ BFG/air S_n against α data, for $\phi = 0.7 - 1.1$.

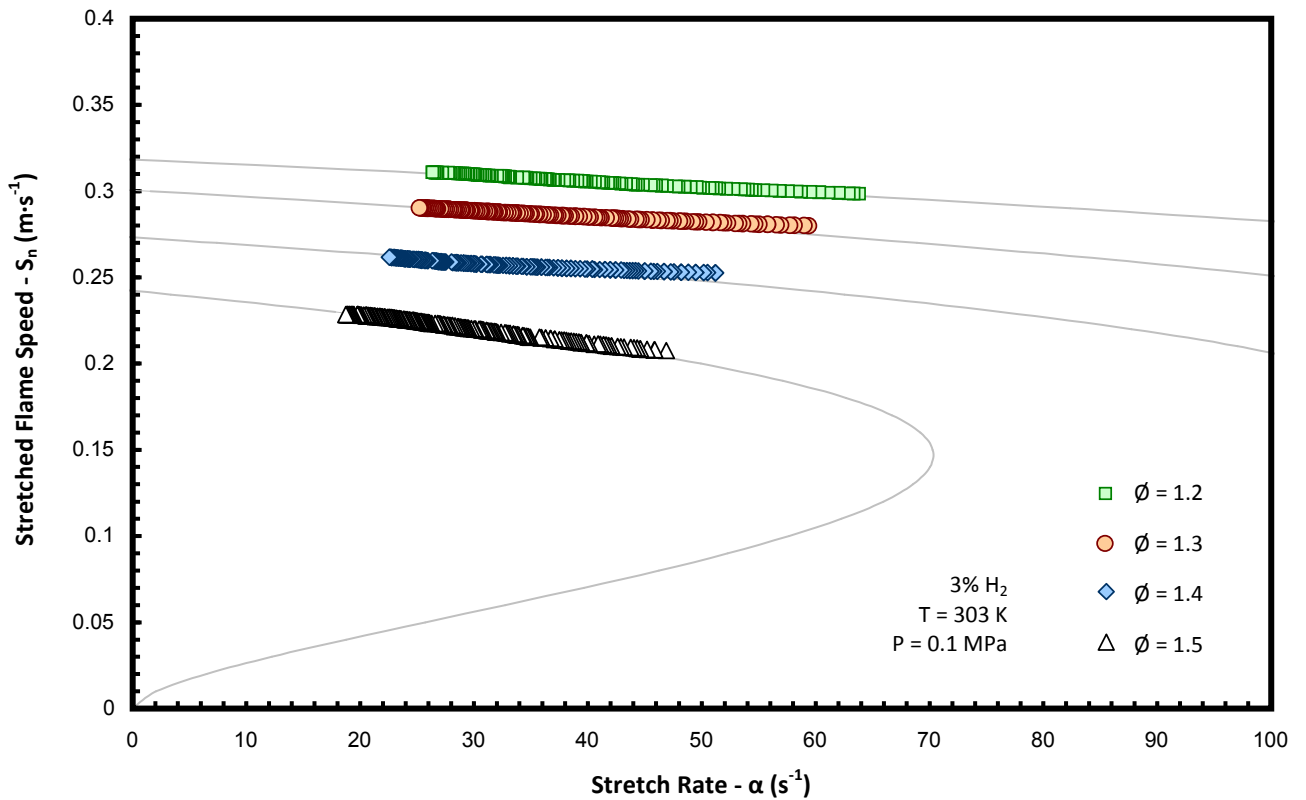


Fig. 5.6 – Samples of plotted 3% H₂ BFG/air S_n against α data, for $\phi = 1.2 - 1.5$.

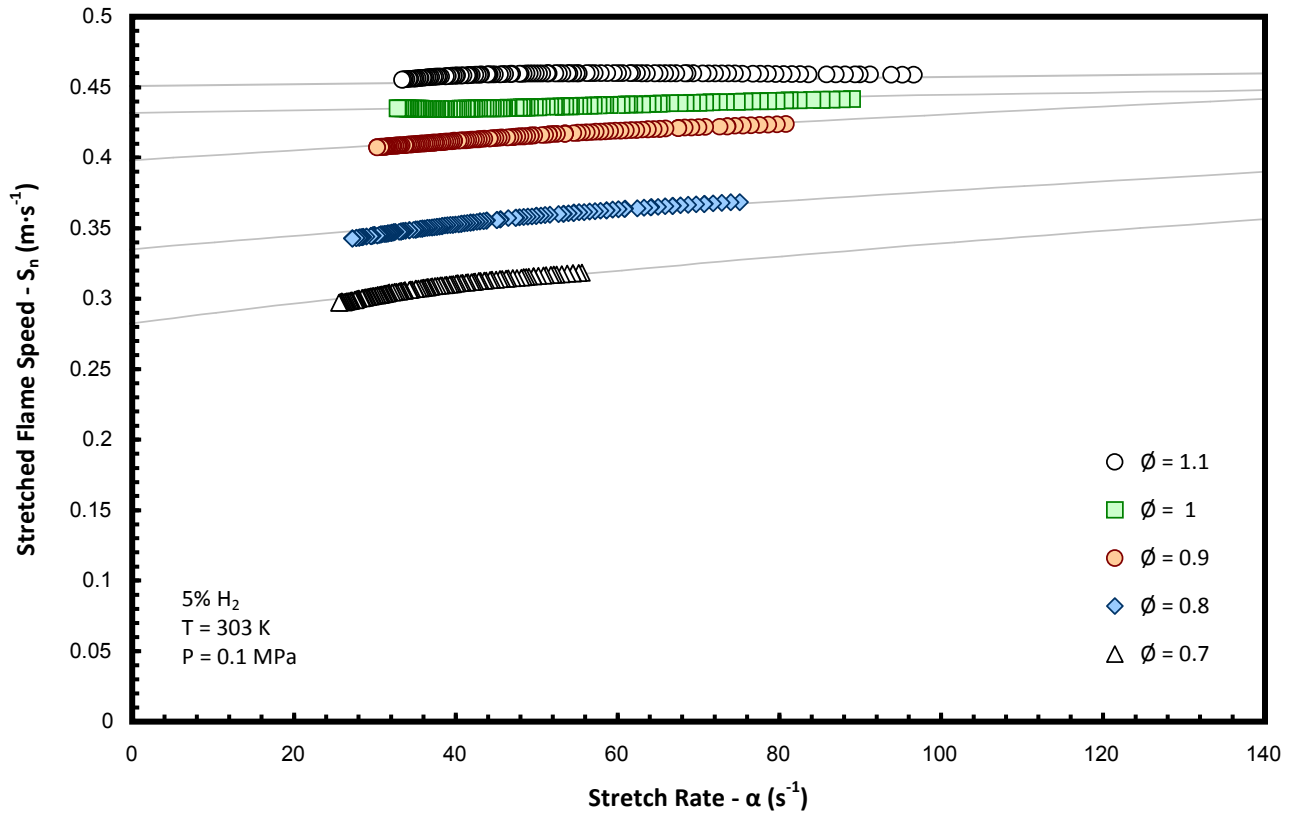


Fig. 5.7 – Samples of plotted 5% H₂ BFG/air S_n against α data, for $\phi = 0.7 - 1.1$.

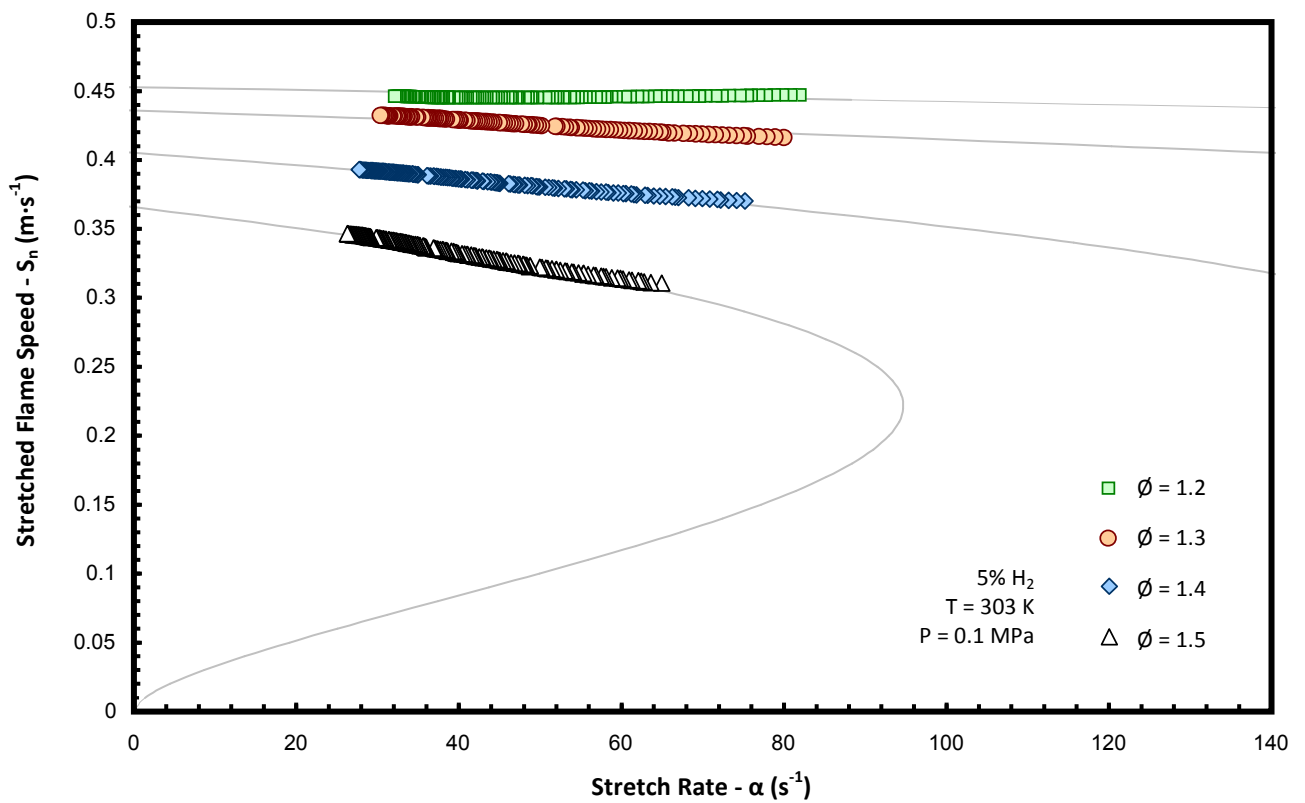


Fig. 5.8 – Samples of plotted 5% H₂ BFG/air S_n against α data, for $\phi = 1.2 - 1.5$.

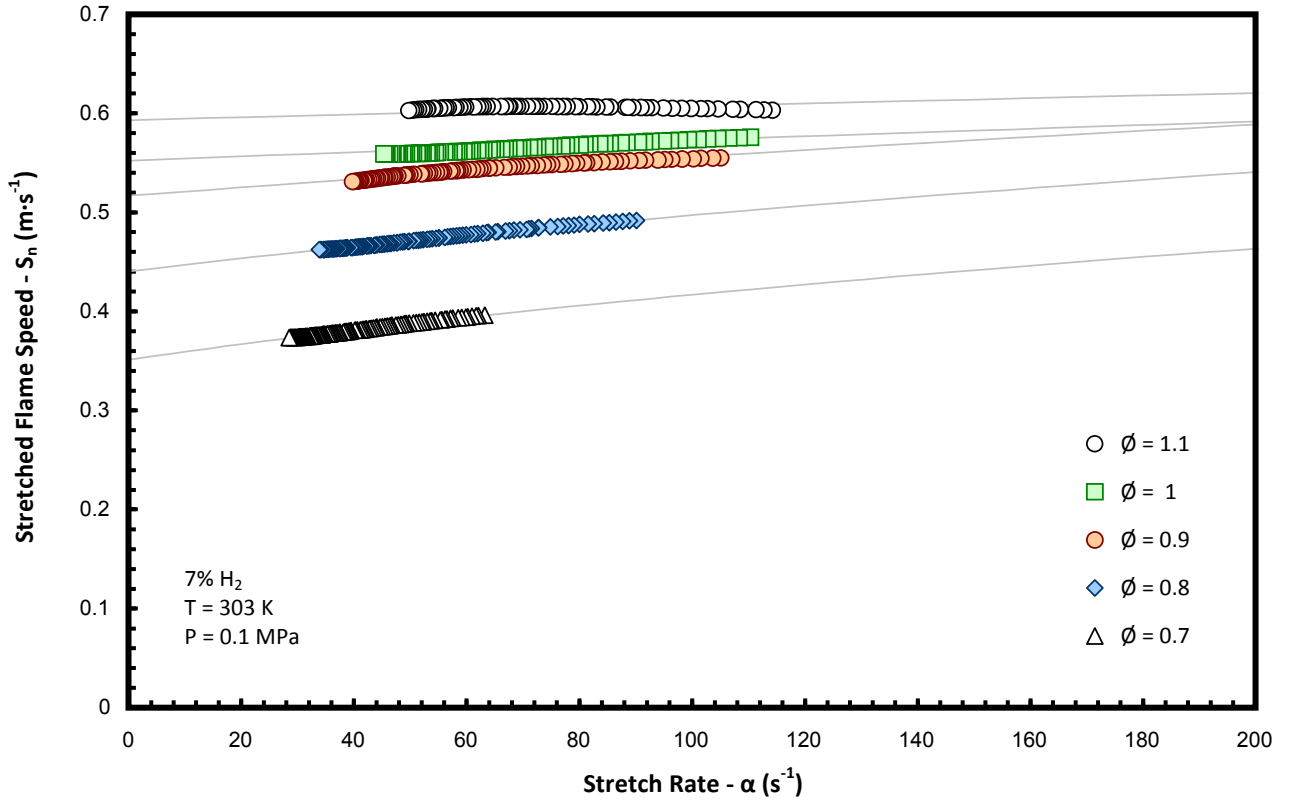


Fig. 5.9 – Samples of plotted 7% H₂ BFG/air S_n against α data, for $\phi = 0.7 - 1.1$.

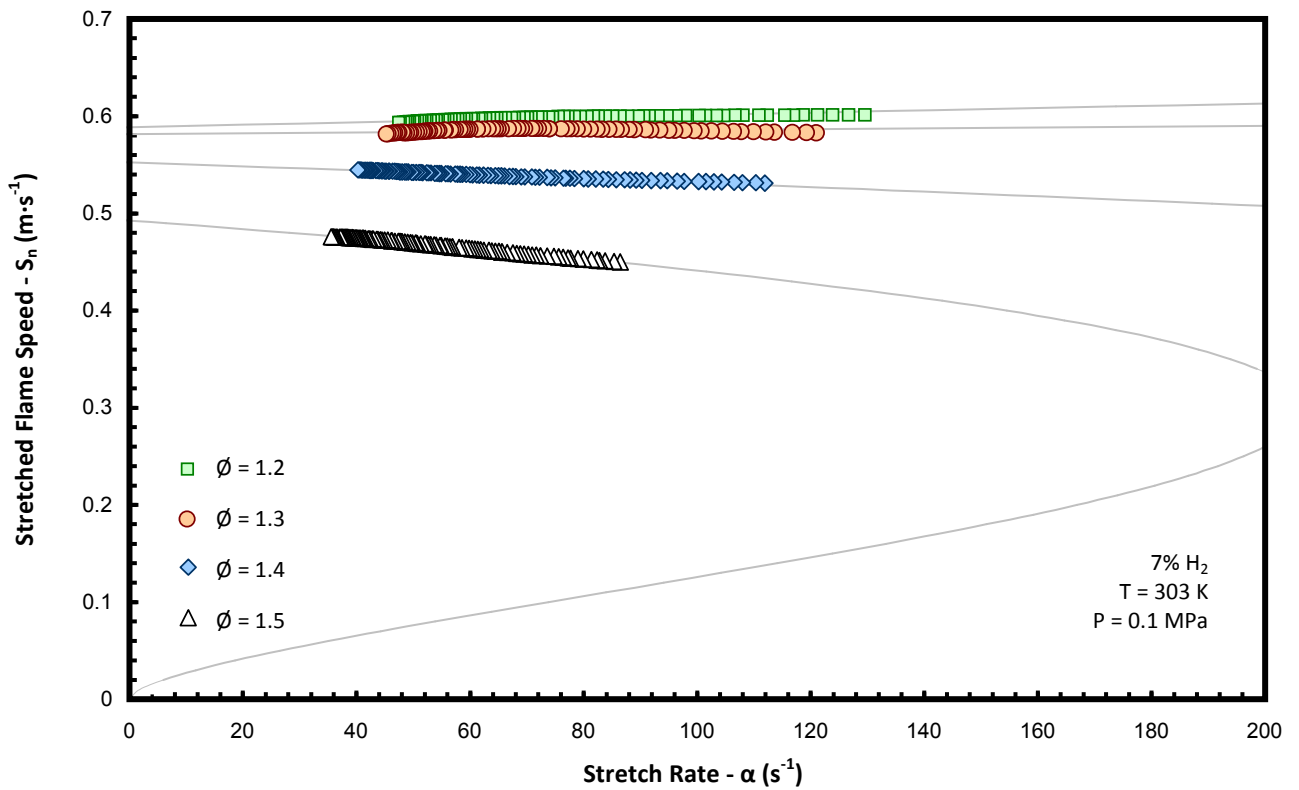


Fig. 5.10 – Samples of plotted 7% H₂ BFG/air S_n against α data, for $\phi = 1.2 - 1.5$.

Similar trends are evident across all of the presented datasets. A positive gradient demonstrates acceleration in flame speed with stretch rate and corresponds to a negative value of L_b ; it is apparent that as mixture equivalence ratios increase, gradients level out before eventually turning negative. This indicates that under richest conditions the most heavily stretched flames lose more heat to the surrounding reactants in proportion to mass diffusion, and corresponds to Lewis numbers greater than one [27]. This characteristic is evident in the plotted values of L_b , as shown in Fig. 5.11 (hollow grey points representing results of individual tests, with the averages larger and coloured).

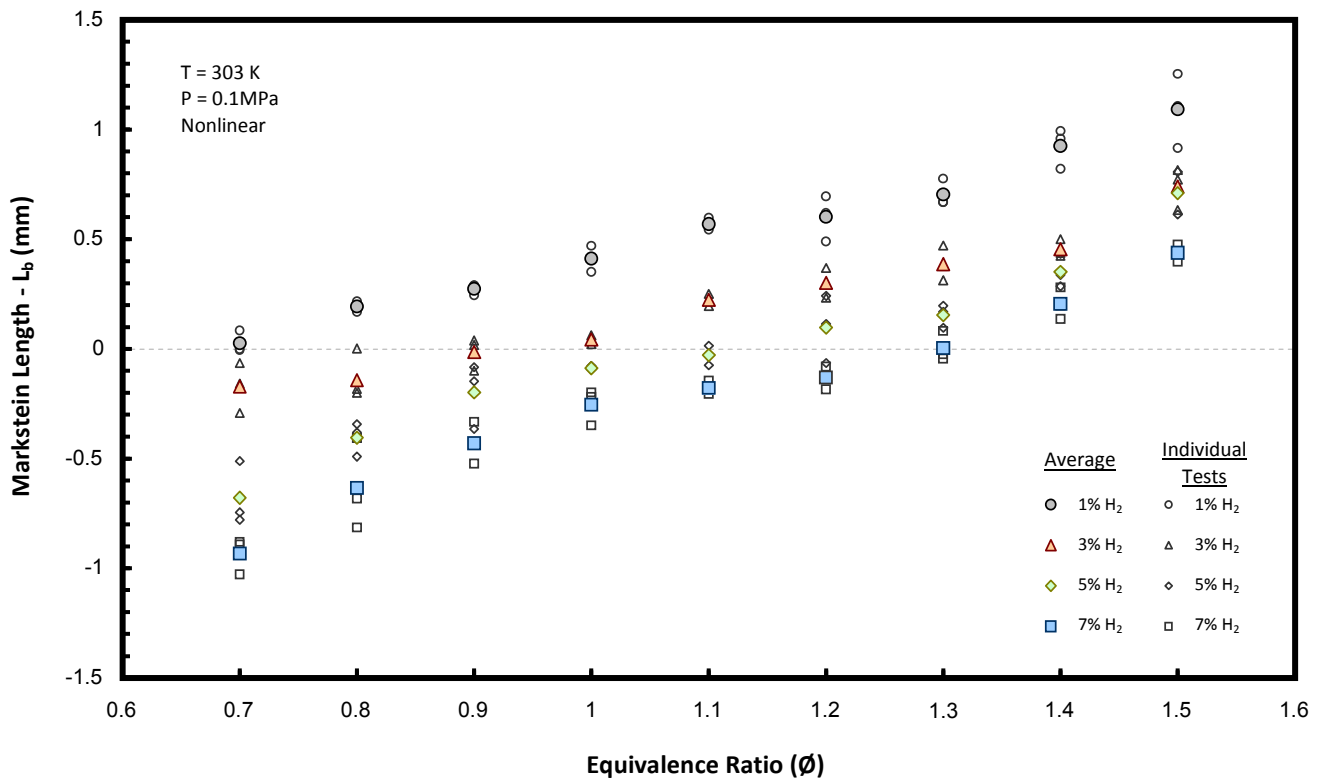


Fig. 5.11 – Changes in Markstein length with equivalence ratio for each of the tested BFG compositions.

It is also apparent in Fig. 5.11 that the trends for increasing L_b with equivalence ratio are negatively offset as H_2 fraction within the fuel mixture increases. This trend for values to become more negative with H_2 addition is consistent with similar observations [111], and results from the substantial difference in diffusive properties between the fuel and the other constituents. The result is for the mass diffusivity of leaner mixtures to potentially become more dominant in proportion to reactant heat

conduction, and Lewis numbers of less than one, particularly with heavy diluent addition [123]. Nevertheless, the influence of flame stretch on propagation is marginally less significant when compared with CH₄ (section 4.2.1), and more so, other hydrocarbons [104, 119], with BFG near equidiffusive around stoichiometric conditions for all tested compositions.

The average observed standard deviation of L_b in experimental data is of the same order for all compositions: $\sim 0.06\text{--}0.08$ mm for the nonlinear relationship. Whilst not presented in the figure, the difference in L_b between the linear and nonlinear relationship is smaller than with CH₄ (as stretch effects are weaker), but nevertheless still significant under leanest and richest conditions. It can be seen that whilst the magnitude of nonlinear L_b is always smaller for positive values, data become more negative for values < 0 , and the gradient effectively increased. This is the opposing effect evident for the increasingly positive values of L_b in section 4.2.1, and should be expected given the curvature of the data. To emphasise this, the two illustrative relationships are shown for example datasets in Fig. 5.12.

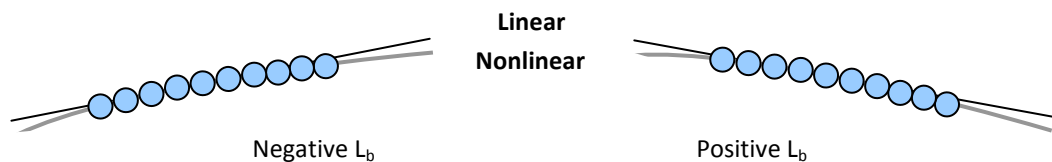


Fig. 5.12 – Illustrative example of the difference in slope between linear and nonlinear relationships with positive and negative L_b .

It should however be emphasised that the observed effect was minimal, as the influence of stretch on flame speed was small for the given mixtures, with all apt linear and nonlinear values provided in Appendix B.3. More significantly, change in fuel H₂ demonstrates the possibility for opposing influences on burning velocity (either acceleration, or deceleration resulting from flame stretch), depending on the equivalence ratio employed, and with increased propensity for thermo-diffusive instability under leanest conditions.

5.2.2 – Unstretched Flame Speeds, Laminar Burning Velocity and Other Properties

Fig. 5.13 shows the scatter in all attained values of nonlinear unstretched flame speed, again with hollow grey data corresponding to individual tests, and the average overlaid in colour.

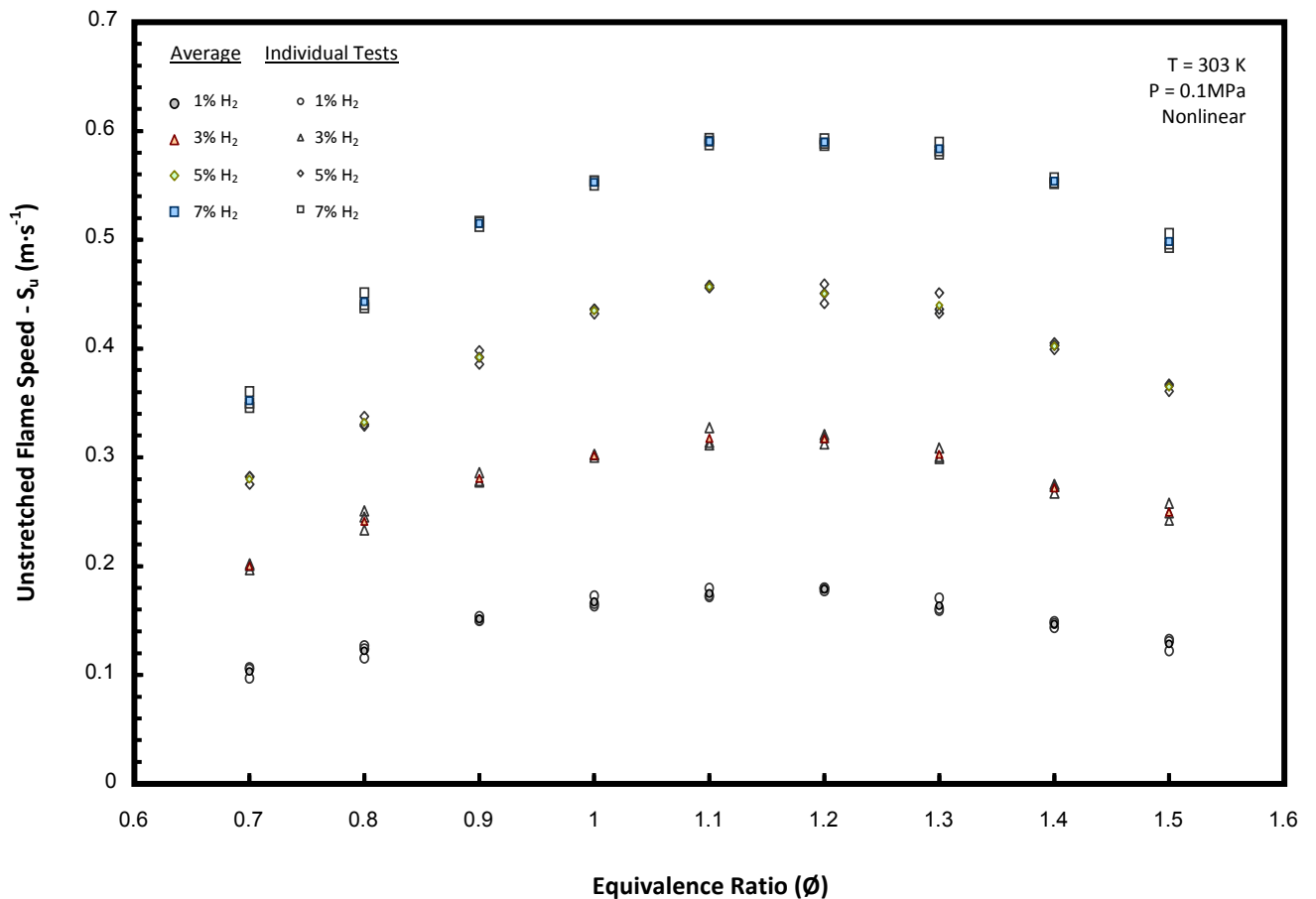


Fig. 5.13 – Changes in S_u with equivalence ratio for each of the tested BFG compositions.

The specified range of equivalence ratios provides a characteristic peak in S_u for all of the tested mixtures. There is a significant difference (greater than a factor of 3) between S_u values across the tested 1-7% H₂ range, highlighting the potential for variation in BFG combustion performance. The actual variability (effective curvature) in S_u with ϕ is shown to become more pronounced with an increase with H₂ fraction, whereas the relative difference between peak values and slowest remains of a similar order for each mixture (slowest values at $\phi = 0.7$ being around 60% of the peak). The measured scatter in S_u data is small, with mixture-averaged standard deviation

decreasing from approximately 3% for the lowest H₂ fraction, to <1% for the fastest burning fuel. This is discussed further with experimental uncertainties in section 5.2.3. Again, only data attained using the nonlinear relationship are presented to avoid confusion, however with the small stretch influence highlighted in section 5.2.1, the difference in average speeds attained using either methodology was less than one percent.

Adiabatic density ratios were required in order to convert the values of unstretched flame speed to a corresponding laminar burning velocity. However, a significant issue was the need to select the most suitable reaction mechanism to work with. Three mechanisms were initially tested; the previously employed (section 4.2.2), and potentially unsuited GRI-Mech 3.0 [149] (not designed for work with this type of fuel), the mechanism presented by Li *et al.* [164] for the oxidation of H₂/CO/CH₂O and other C1 species, and finally the interactions given by Davis *et al.* [165] optimised for H₂ and CO reaction paths. These three were initially chosen to assess the scope of variation in attained results from different reactions. Further details of model specifications are provided in section 5.3, with the resultant density ratios provided in Table 5.2.

Table 5.2 – Adiabatic density ratios obtained from three reaction mechanisms.

ϕ	1% H ₂ (ρ_b/ρ_u)			3% H ₂ (ρ_b/ρ_u)			5% H ₂ (ρ_b/ρ_u)			7% H ₂ (ρ_b/ρ_u)		
	Li <i>et al.</i> [164]	Davies <i>et al.</i> [165]	GRI- Mech 3.0 [149]	Li <i>et al.</i> [164]	Davies <i>et al.</i> [165]	GRI- Mech 3.0 [149]	Li <i>et al.</i> [164]	Davies <i>et al.</i> [165]	GRI- Mech 3.0 [149]	Li <i>et al.</i> [164]	Davies <i>et al.</i> [165]	GRI- Mech 3.0 [149]
0.7	0.23587	0.23586	0.23563	0.23156	0.23157	0.23159	0.22764	0.22767	0.22764	0.22407	0.22407	0.22409
0.8	0.22800	0.22803	0.22803	0.22356	0.22359	0.22357	0.21950	0.21965	0.21957	0.21578	0.21581	0.21579
0.9	0.22187	0.22191	0.22188	0.21727	0.21731	0.21727	0.21309	0.21313	0.21308	0.20925	0.20928	0.20923
1	0.21816	0.21827	0.21817	0.21343	0.21348	0.21344	0.20914	0.20917	0.20915	0.20520	0.20523	0.20523
1.1	0.22597	0.22594	0.22606	0.22092	0.22096	0.22097	0.21638	0.21642	0.21641	0.21215	0.21221	0.21222
1.2	0.23479	0.23481	0.23481	0.22957	0.22960	0.22960	0.22479	0.22483	0.22484	0.22035	0.22040	0.22038
1.3	0.24336	0.24349	0.24350	0.23800	0.23794	0.23801	0.23300	0.23304	0.23303	0.22836	0.22840	0.22839
1.4	0.25186	0.25202	0.25186	0.24621	0.24623	0.24623	0.24103	0.24105	0.24104	0.23620	0.23623	0.23621
1.5	0.26006	0.26005	0.26008	0.25423	0.25424	0.25423	0.24884	0.24886	0.24886	0.24384	0.24387	0.24385

It is apparent from the tabulated data that the difference in attained ratios was typically less than 0.05 percent (average $\sim 0.016\%$), and therefore the selection of a single mechanism was not critical with respect to the influence of other experimental uncertainties. Consequently, the density ratios given by the Li *et al.* [164] mechanism were arbitrarily chosen for the determination of u_L . The specified values are plotted in Fig. 5.14.

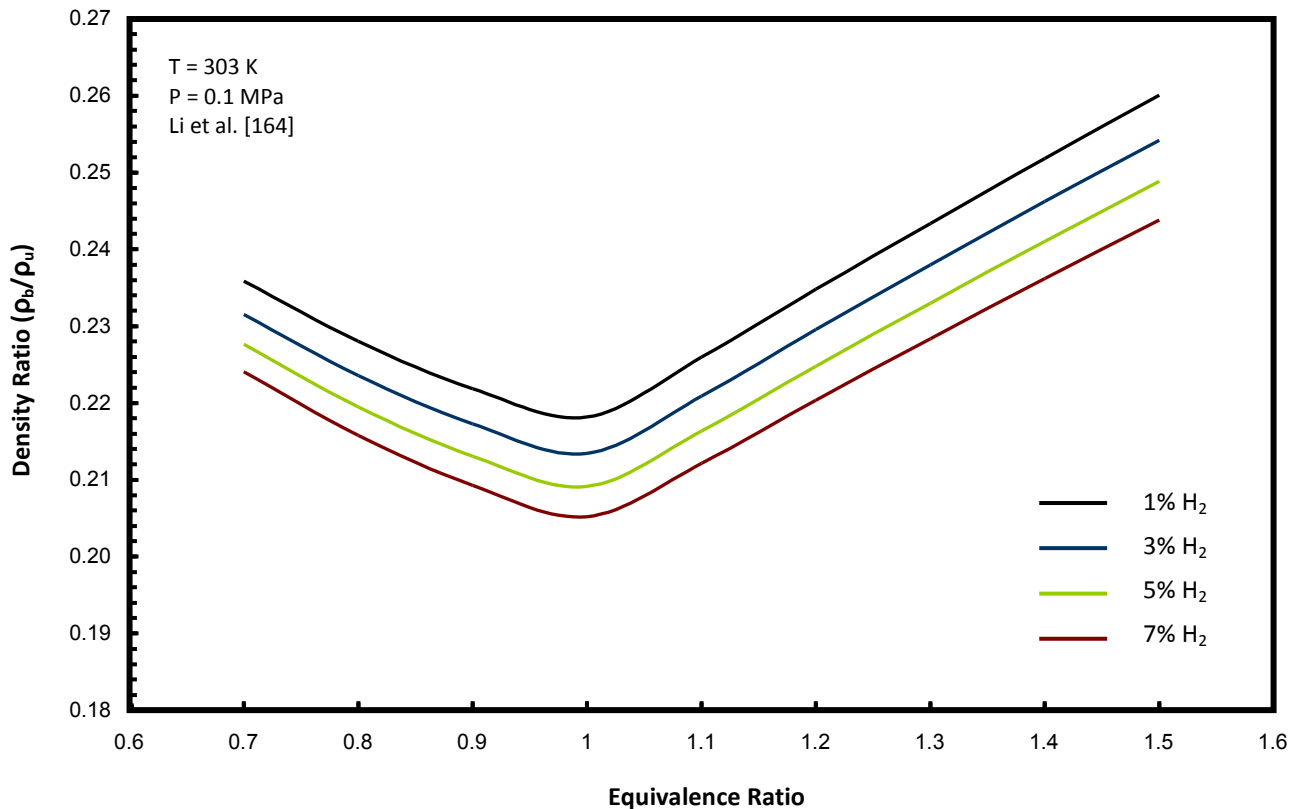


Fig. 5.14 – Adiabatic density ratios attained using the Li et al. [164] mechanism.

Laminar burning velocities were calculated using the average values attained for S_u and are presented in Fig. 5.15. Results demonstrate an absolute increase by more than a factor of three for all equivalence ratios in the tested H₂ range, highlighting the high sensitivity of BFG to small perturbations in H₂ fraction. As previously mentioned, H₂ addition also results in a significant change to thermal diffusivity, the square-root of which is proportional to u_L when combined with overall reaction rate, and increases with richness for H₂ flames [27]. Therefore, the peak value shifts towards richer equivalence ratios with compositions containing higher fractions of H₂. This trend is visualised in Fig. 5.15 with the peak of each representative curve becoming marginally

richer with H₂ addition, eventually resulting in a maximum at an equivalence ratio of approximately 1.3 for the 7% H₂ mixture. The trend would also continue if H₂ was increased to 100 percent, where the peak value of u_L is reached at an equivalence ratio of approximately 1.95 (Fig. 2.12 [111]).

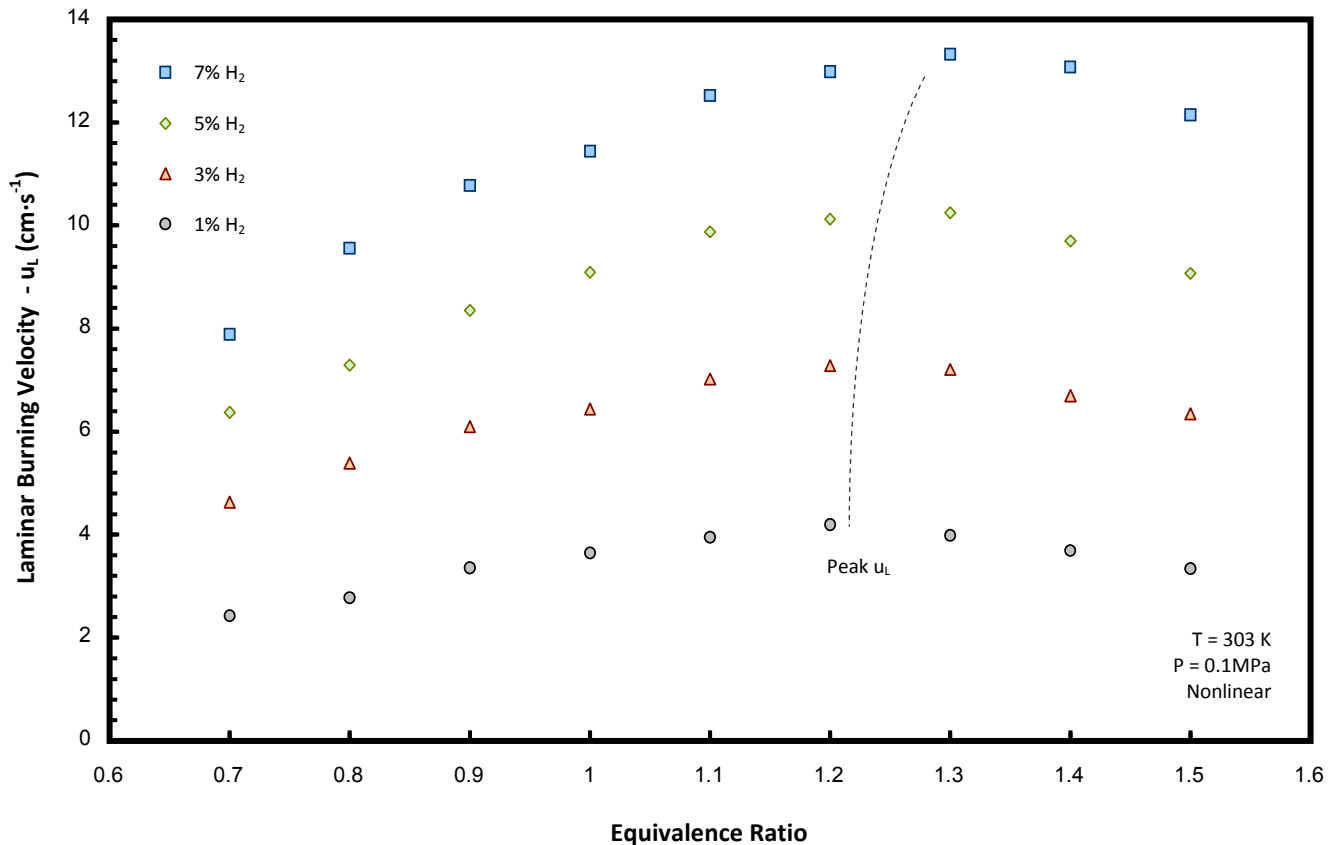


Fig. 5.15 – Variation in average u_L with equivalence ratio for each of the four tested compositions.

These tendencies have been further visualised with the data gradients in Fig. 5.16, where change in average u_L is plotted against increasing H₂ fraction. There is a divergence in speed increase between the $\phi=1$ and $\phi=1.2$ data, in approximate relative proportion to the difference in quantity (i.e. a steady offset of ~12 % between the $\phi=1$ and 1.2 values for every composition). However, when the richest data is compared, the difference in values between $\phi=1.2$ and 1.5 drops from approximately 20 to 6 % for the respective 1 to 7 percent compositions.

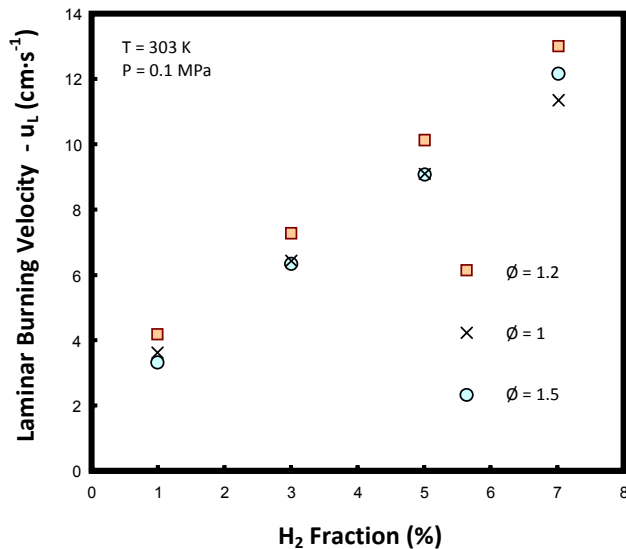


Fig. 5.16 – Growth in average BFG u_L with H₂ fraction for $\phi = 1, 1.2$ and 1.5 .

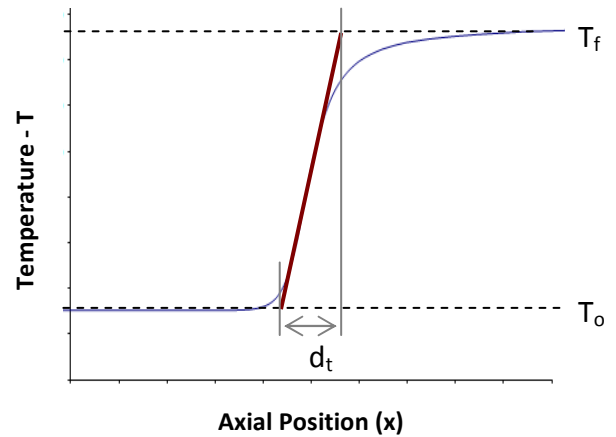


Fig. 5.17 – Theoretical use of temperature profile to obtain flame thickness [27, 97].

5.2.3 – Practical Implication of Obtained Results

The exaggerated difference between the characteristics of the 1 and 7% H₂ BFG mixtures can be analysed for from several practical perspectives. The sensitivity to change in flame speed and stretch characteristic underlines the propensity for potential premixed operational combustion instabilities. The level of relative fluctuation is exacerbated by the heavily dilute nature of the syngas, and slow burning velocities with lower levels of H₂. In addition there is potential for contrasting influence from flame stretch on propagation as Le decreases through unity with H₂ addition. The influence from variation in velocity has been emphasised further by attempting to further characterise flame behaviour.

An approximation of the effective thickness of the reaction zone, or laminar flame thickness (d_t) can be obtained from the temperature profile with axial distance through the flame [27]. A linear gradient is applied as the tangent of the inflection (corresponding to maximum dT/dx) in modelled temperature change from ambient (T_0) to burned (T_f) conditions, as depicted in Fig. 5.17 [27, 97]. The reaction mechanism created by Li et al. [164] (see section 5.3 for further details) was used to calculate the laminar flame thicknesses for the 1 and 7% H₂ BFG mixtures, and are plotted against equivalence ratio in Fig. 5.18.

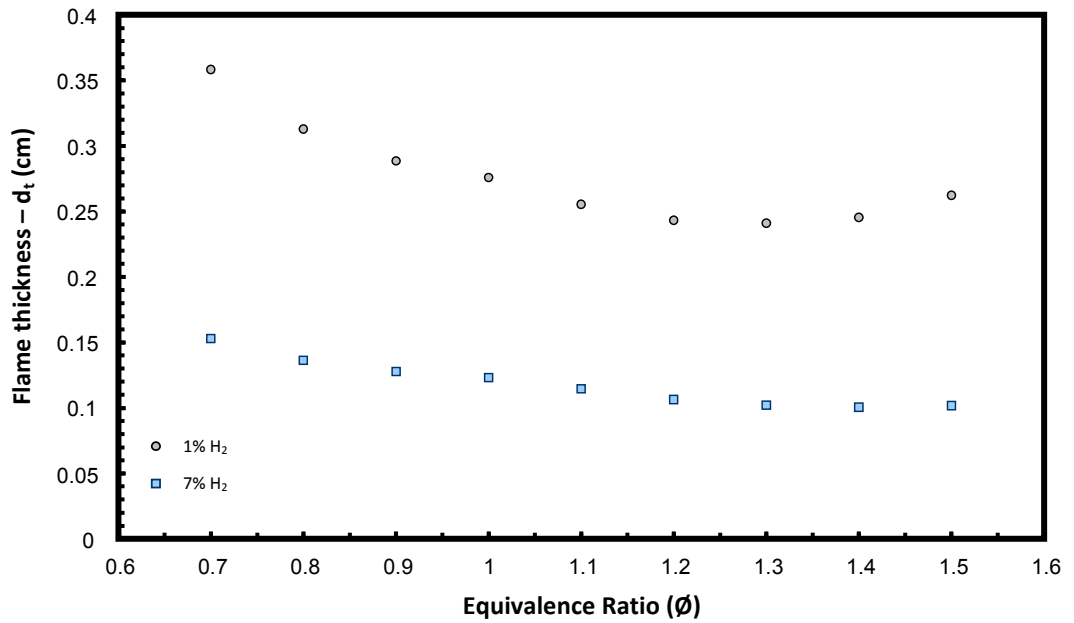


Fig. 5.18 – Calculated flame thicknesses of the 1 and 7% H₂ BFG mixtures.

If these modelled values of d_t are equated to the approximate magnitude of the quenching distance (d_q) [29, 94], then through the application of Eqn. (2.3), burner-independent critical velocity gradients (g_f/c) can be estimated to prevent flashback in the boundary layer. The profiles for change in these velocity gradients are plotted in Fig. 5.19, with almost an order of magnitude difference between the critical values calculated for each fuel mixture.

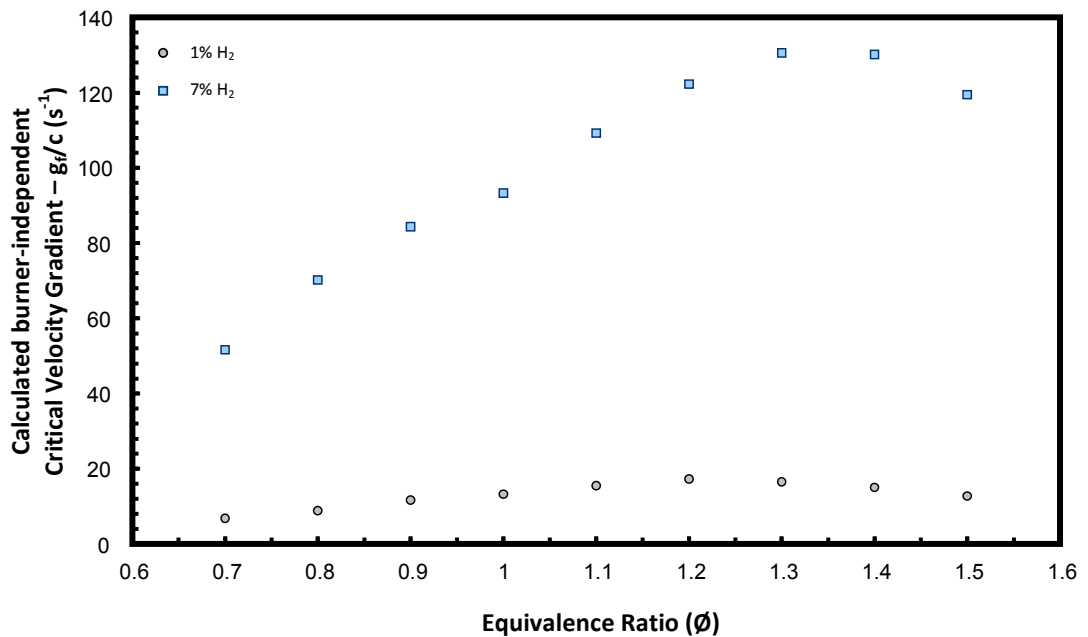


Fig. 5.19 – Calculated burner independent critical velocity gradients of the 1 and 7% H₂ BFG mixtures.

This simplistic approximation relates to only one aspect of operational flame behaviour, nevertheless the significant order of variation highlights a propensity for instability with the given mixtures. This is further exacerbated by a similar order of difference (by definition see section 2.3.3) in chemical residence time, thereby suggesting that whilst flashback issues are easily resolved by high flow rates, then blowoff could be a significant problem when gas is produced comprising low quantities of H₂. Furthermore the contrasting trends in u_L and L_b for compositional H₂ change mean that small fluctuations cannot be fully countered by simply a change in ϕ . For instance; lowering BFG H₂ reduces u_L but increases L_b , and if the mixture was made richer to burn faster, this could enhance the influence of stretch and hence flame stability. Work in the following chapters therefore investigates potential influences to reduce this variation in BFG u_L and L_b .

The inherent change in operational fuel characteristics can also be analysed from the perspective of energy delivery. Consequently the gross calorific value (CV_G) of each composition was calculated for ideal mass fractions, and normalised to the tested conditions of temperature and pressure (303 K, 0.1 MPa). This value was then used to calculate gross Wobbe Index (interchangeability indicator relating energy output to fuel density, and commonly employed by operational engineers - WI_G) for that composition [166]:

$$WI_G = \frac{CV_G}{\sqrt{SG_{air}}} \quad (5.1)$$

With SG_{air} , corresponding to the specific gravity of the mixture in relation to the density of air (ideally calculated [142] to be 1.1452 kg·Nm⁻³). The obtained values are provided in Table 5.3.

Table 5.3 – CV_G and WI_G values for each tested composition

FUEL BLEND				
H ₂ fraction (%)	1	3	5	7
CV_G	2.679	2.854	3.028	3.202
WI_G	2.566	2.759	2.957	3.158

The 1-7 % proportional rise in H₂ fraction yields respective increases of 19.5 and 23.1 % in gross fuel calorific value and Wobbe Index. This further highlights the weakness and potential inherent variability in the performance of BFG as a fuel, and further emphasises why it is frequently blended with other materials in practical operation.

Fig. 5.20 demonstrates the relative difference in initial measured pressure rise resulting from stoichiometric combustion of both mixtures. As would be expected, there is a factor in time difference of over three for pressure to increase to the same value. Together with the resultant change in flammability limits [28], this highlights the additional potential for variation in explosive characteristics from the perspective of operational health and safety [28], with there having been several industrial incidents involving accidental ignition of BFG mixtures [35].

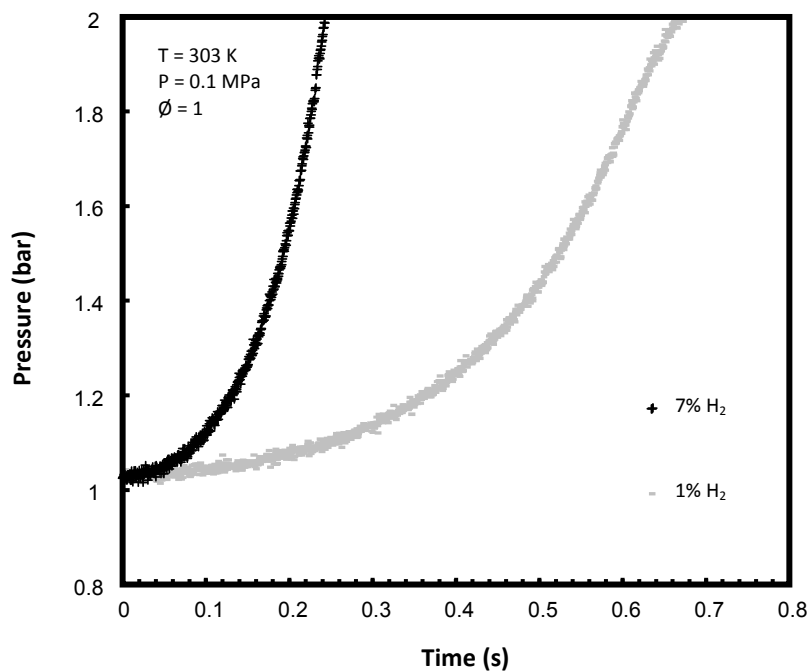


Fig. 5.20 – Example stoichiometric pressure/time curves for two of the tested BFG compositions.

5.2.4 – Quantifying Experimental Uncertainty

Experimental uncertainties were principally calculated using the same methodology as employed with the CH₄ benchmarking work, outlined in section 4.3. However, the need to blend in the H₂ fraction by partial pressure introduced a further possible area of

uncertainty. This was accounted for as an additional factor in the calculation of the total bias uncertainty (B_{Su}). Using the attained results, an approximate relationship was fitted to S_u against H₂ partial pressure for each equivalence ratio, and then possible fluctuation calculated in relation to the resolution of the readout (± 0.01 kPa). This value represented the third largest possible source of error behind the temperature and optical systems, and was proportionally more significant for the slower mixtures. This was balanced with the uncertainty of faster mixtures being more influenced by system optics (having processed fewer frames), and experiencing larger absolute variation in relation to temperature and equivalence ratio.

Having again performed three repetitions the specified t-value at a 95 % confidence level (for M-1) was 4.303, and used with values of standard deviation to calculate the total uncertainty. Fig. 5.21 shows plotted data with $\pm U_{Su}$, together with hollow grey individual data points.

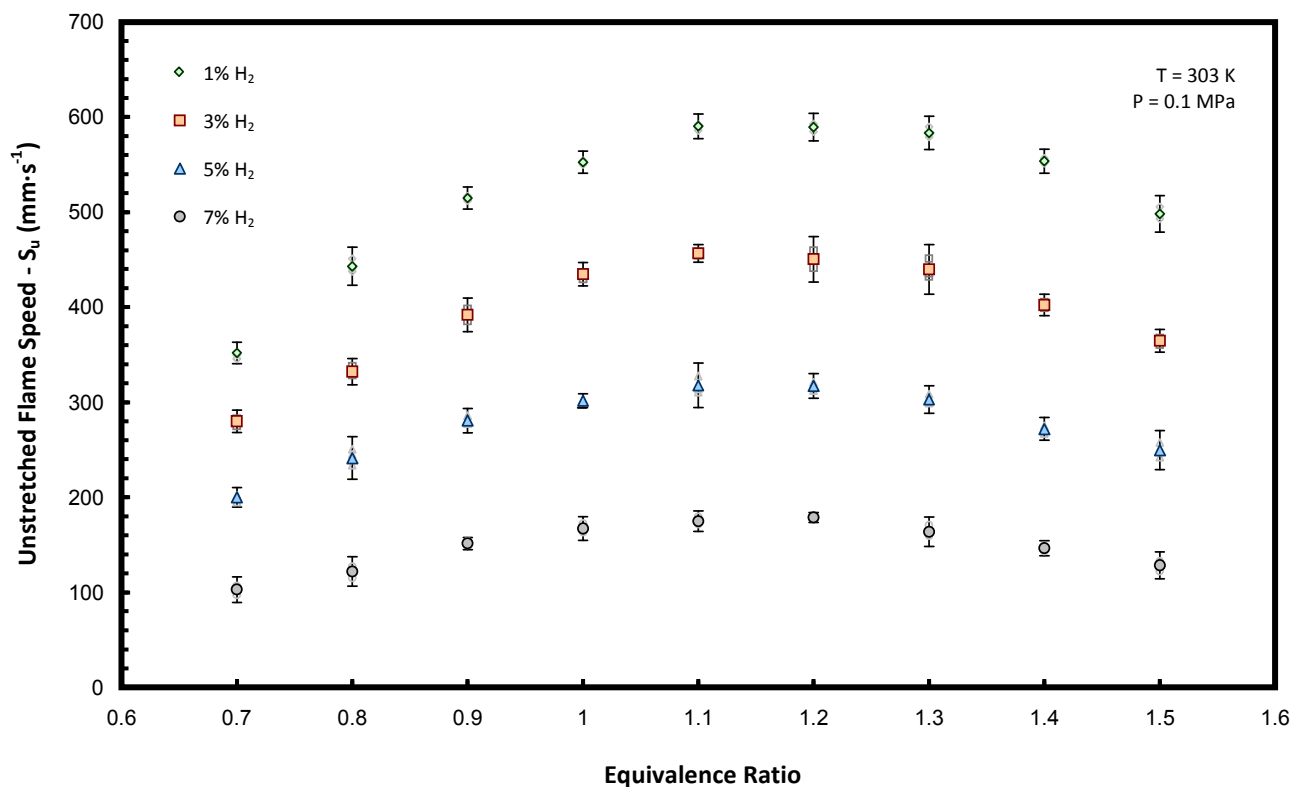


Fig. 5.21 – Plotted BFG S_u data with superimposed $\pm U_{Su}$ and individual data points

It is clear from Fig. 5.21 that calculated uncertainty values are heavily influenced by the standard deviation in each measured dataset. Furthermore, if uncertainties are averaged for each mixture, then as expected absolute values increase in parallel with flame speed. Nonetheless relative uncertainties are greater for slower mixtures, ranging from around 7-2 % of the average speeds for the respective 1-7 % H₂ compositions. Fig. 5.22 shows plotted values of L_b , with superimposed $\pm \sigma_{su}$ error bars.

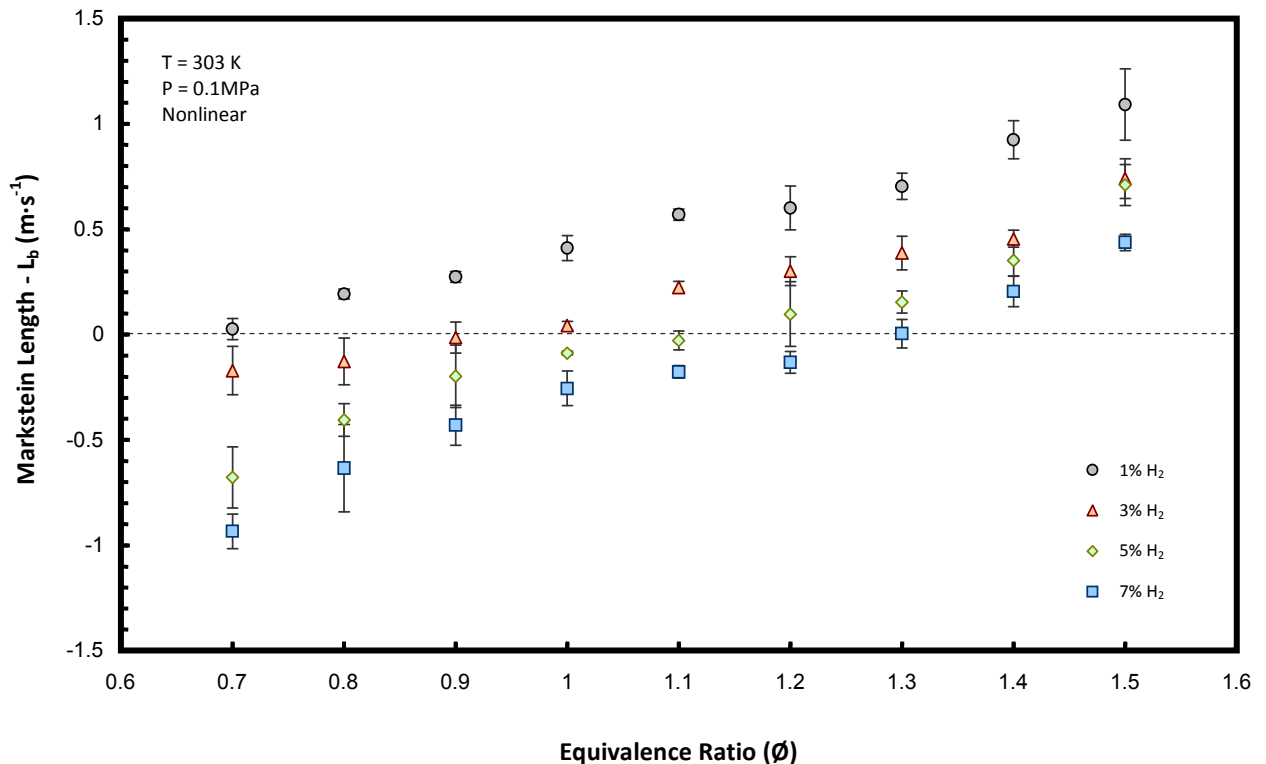


Fig. 5.22 – Plotted BFG L_b data with superimposed $\pm \sigma_{su}$

Similar to the benchmarking work undertaken with CH₄, the relative standard deviation in L_b is again larger than with the S_u dataset. There also appears to be higher amount of scatter for the data of a greater magnitude (either positive or negative) at the leanest and richest conditions.

5.3 Comparison with Chemical Models

In order for designers to accurately predict the behaviour of BFG combustion, it is important that chemical kinetic mechanisms provide the best representative detail in numerically modelling reaction kinetics and resultant fuel performance. Therefore the next stage of this work was to undertake a comparative study between modelled values and those attained experimentally. In doing so a preferential mechanism could be identified that best represents not only the combustion of BFG, but potentially other increasingly prominent dilute syngases containing H₂ and CO.

A freely propagating flame configuration was used in CHEMKIN-PRO to compare flame speeds predicted by various proposed reaction mechanisms against the new experimental data presented in this study. The utilised PREMIX code solves one-dimensional conservation equations based on an estimate of initial temperature profile, and the fuel conditions specified. The mechanisms evaluated were those developed by Li *et al.* [164] and Davis *et al.* [165] for combustion of H₂ and CO mixtures, and these were compared with the GRI-Mech 3.0 mechanism [149], considered likely to be unsuitable at the onset. The Li model employs 18 chemical species and 93 reactions, compared with 14 species and 43 reactions used in the Davis mechanism. GRI-Mech 3.0 employs 53 chemical species and 325 reactions; however the mechanism has been optimised for natural gas combustion, and hence was most usefully employed in the benchmarking work with CH₄ in Section 4. Solutions were based on an adaptive grid of 1000 points with mixture-averaged transport properties and trace series approximation. Fig. 5.23 provides a visual comparison between the experimental values, and numerically modelled datasets, with upper and lower bounds of 1% and 7% H₂ fuel fraction under conditions of 303 K and 0.1 MPa presented.

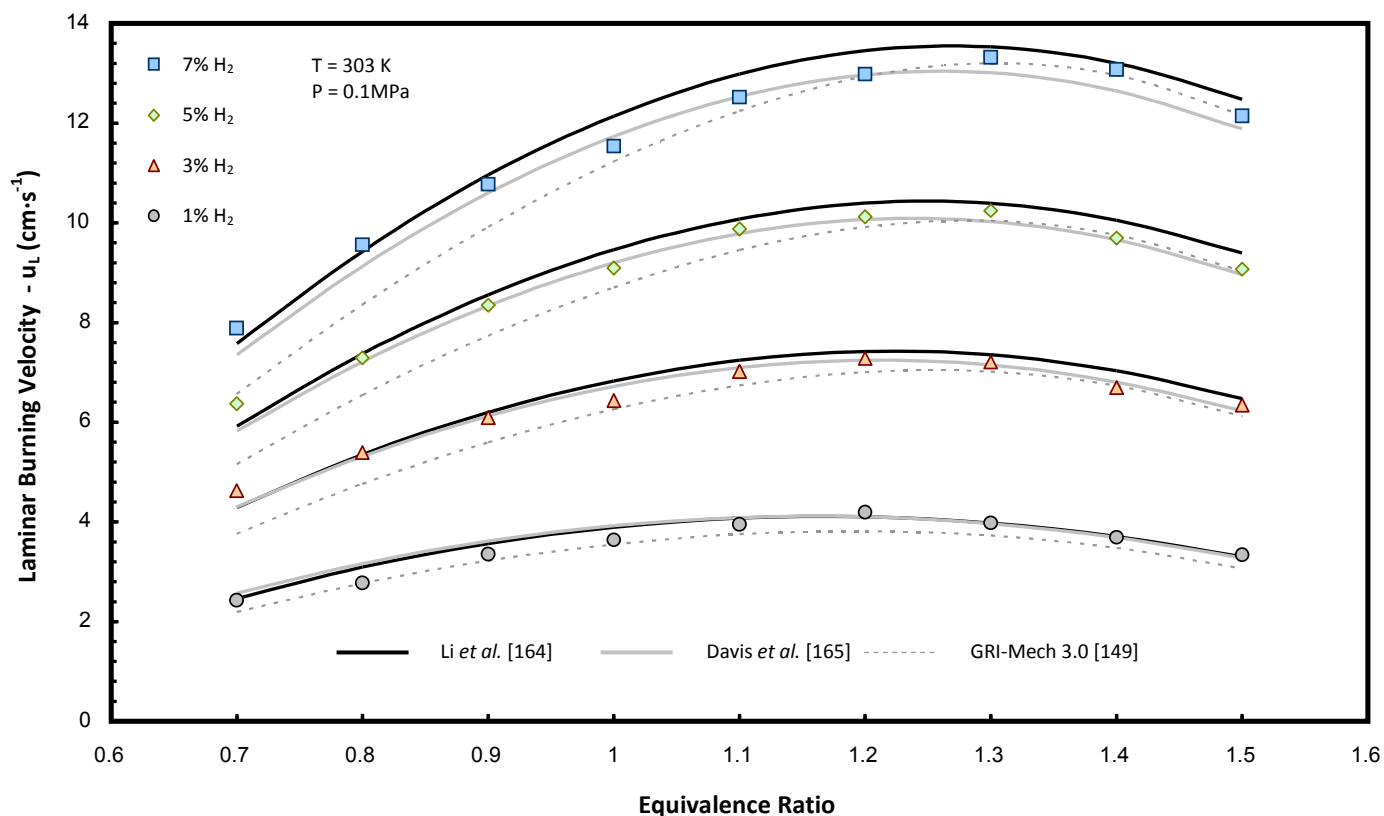


Fig. 5.23 – BFG u_L data with superimposed data from chemical models.

The difference in results obtained from the Li and Davis mechanisms for the 1% H₂ fraction appear negligible, with both reaction sets ostensibly providing good agreement with experimental data. As the BFG H₂ fraction increases, the modelled values from the Li and Davis mechanisms begin to diverge, with relative performance dependent on the equivalence ratio under consideration. Overall there is a tendency for the more contemporary Li mechanism to return marginally higher values, with revised parameters for the $\text{CO} + \text{OH} = \text{CO}_2 + \text{H}$ and $\text{HCO} + \text{M} = \text{H} + \text{CO} + \text{M}$ reactions [164]. The GRI-Mech 3.0 mechanism is notably different to the other two as anticipated, and generally under-predicts the data particularly at leaner conditions for the 7% case. However, the reason the mechanism has been included is for when it is used in a comparative analysis in subsequent chapters. The reason other apt mechanisms (such as Mueller *et al.* [167]) have not been included in the comparison is because two of the more contemporary and representative H₂/CO datasets have been employed. The others are mostly modifications or variations of these sets.

A standard error of the estimate (SEE) is introduced to quantify the variation in performance of the different mechanisms relative to experimental data. The SEE was calculated for averages of all equivalence ratios, for each fuel fraction as derived in Eqn. (5.2), where N is the number of tests.

$$SEE_{u_L} = \sqrt{\frac{\sum_{i=1}^n (u_L - u_{L\text{CHEMKIN}})^2}{N}} \quad (5.2)$$

The assumption made when evaluating the reaction mechanisms in this way is that the density ratio provided by the Li mechanism derives the most accurate values for experimental u_L , as it was used in the determination of the assessment criterion. However, as has been stated, the difference in density ratios obtained from all mechanisms was negligible, and inconsequential relative to the significant figures for the values of SEE provided. The calculated values are given in Table 5.4.

Table 5.4 – Calculated SEE values for each tested BFG mixture and three chemical reaction mechanisms.

SEE (cm·s ⁻¹) (italic - % of average u_L)								
BFG H ₂ Fraction (%)	1		3		5		7	
Li <i>et al.</i> [164]	0.162	4.65	0.236	3.72	0.290	3.26	0.394	3.42
Davis <i>et al.</i> [165]	0.196	5.62	0.158	2.49	0.209	2.35	0.333	2.89
GRI-Mech 3.0 [149]	0.225	6.45	0.431	6.79	0.561	6.30	0.671	5.83

It is clear from the values presented that the standard error increases with a rise in BFG H₂ fraction, and consequential change in burning velocity. However, if these errors are presented as percentages of average mixture burning velocity, then a proportional decrease is observed. For example the standard error of 0.162 cm·s⁻¹ for the 1% H₂ Li mechanism translates to a difference of 4.6% for the average mixture velocity, which in turn reduces down to 3.4% for the 7% H₂ blend. When compared this way the Davis mechanism provides marginally favourable results, with an average percentage error for all mixtures of 3.3% compared to the 3.7% for the Li dataset. Whereas the average error for the GRI-Mech 3.0 mechanism is almost doubled at 6.4%. The results therefore suggest that careful consideration should be given when selecting a mechanism to most accurately model BFG, concerning the preponderant composition and equivalence ratio of interest.

5.4 Summary and Conclusions

Variation in the combustive behaviour of BFG has been characterised for small changes in volumetric H₂ concentration, representative of fluctuation experienced during production. H₂ fraction within the BFG makeup was increased in the molar range of 1-7% for the equalised displacement of all other constituents. Results were obtained for unstretched flame speed and equivalent laminar burning velocity, with values shown to increase by more than a factor of three for each equivalence ratio across the tested range, thus highlighting the potential for significant variation in combustion performance. The influence of flame stretch was also quantified using measured values of Markstein length, with an increasing tendency evident for a rise in equivalence ratio. This was offset by a decrease in values as the H₂ fraction within the fuel rose, with both positive and negative quantities measured. Resultant changes in additional fuel properties were also considered, with an equivalent change in fuel calorific value of up to 20% in evidence across the tested range. Finally, experimental values of burning velocity were compared to those obtained using computational models, employing several chemical reaction mechanisms. The two suitable mechanisms demonstrated favourable correlation (<5%), with the Davis H₂/CO dataset providing marginally superior results, and careful consideration of fuel composition necessary when selecting the most suitable model.

Chapter 6. BFG H₂ Fluctuation - Variation in Ambient Conditions

Having initially demonstrated the fluctuation in laminar burning velocity that results from small changes in BFG H₂ concentration, work was undertaken to expand the testing matrix and investigate the influence of variation in ambient condition.

6.1 Chapter Introduction

The levels of u_L and L_b fluctuation quantified for BFG combustion in the previous chapter were large considering the small absolute changes in fuel composition, and represent a potential source of practical instability. Hence this study was expanded to investigate the impact of changes in ambient condition, quantifying any extent to which the relative fluctuation is mitigated. This is chiefly practical with regard to temperature as steelworks tend to have plenty of low grade waste heat [12]. Therefore, mixture laminar burning velocities and Markstein lengths were characterised for changes in composition and equivalence ratio, together with ambient temperature and pressure, for combustion with air. The accuracy of chemical models in predicting this behaviour could then also be evaluated to identify the optimal mechanism for modelling combustion at these conditions.

6.1.1 – Defining Experimental Parameters

The remaining certified molar composition of CO - 23.07 %, CO₂ - 23.35 %, and N₂ - 53.58 % employed in Chapter 5. was again used as the foundation BFG mixture. Similarly the same four levels of H₂ were introduced in the range of 1-7 %, (with the makeup of each individual blend detailed in table 4.1). The results produced thus far demonstrated favourable repeatability, hence only two repetitions of four equivalence ratios in the range 0.8-1.4 were tested. These values were selected following an estimation that the characteristic peak in the profile of u_L against ϕ would be in evidence.

The changes in ambient condition were specified in accordance with the limits of the CVCB rig design. The temperature control system facilitated operation up to 400 K, leading to the specification of four test points with step changes of 30 K in the range of 303-393 K. Control of ambient pressure was restricted by the specified upper limit of the vacuum pressure gauge and readout (0.2 MPa) used for partial pressure regulation. The maximum pressure rise recorded from testing undertaken in Chapter 5. was approximately 0.45 MPa, and this could be more than doubled safely with the current CVCB configuration. Consequently three test points were outlined, and encompassed by the initial pressure range of 0.1-0.2 MPa. The purity of the specified H₂ grade was again >99.995 %, and employed with compressed air having a volumetric moisture content of <0.02 %. The camera filming rate was also maintained at 3,000 fps, in order to maintain the same level of optical uncertainty as with the original BFG data (see section 5.1.1).

6.1.2 – Considerations for the Experimental Methodology

The same partial pressure methodology outlined in section 5.1.2 was again used for filling the chamber with the specified mixture at the required equivalence ratio. An increase in ambient pressure meant calculations were performed with a modified P_T value, leading a proportional rise in each required partial pressure. In addition, the system was always given at least 30 minutes to soak at the specified temperature, with reactants introduced slowly, thereby allowing partial pressure readings to stabilise as the gases were heated.

6.2 Results for Variation in Ambient Pressure

Schlieren video files were again obtained, with radial flame growth quantified from the rate of horizontal propagation analogous to previously processed results. Fig. 6.1 gives examples of the difference between obtained stoichiometric flame propagation rates for the 7% H₂ BFG mixture, with changes in initial ambient pressure. From preliminary observations of the raw data, it is apparent that an increase in pressure appears to slow the rate of flame propagation, with numerical processing required to quantify this change.

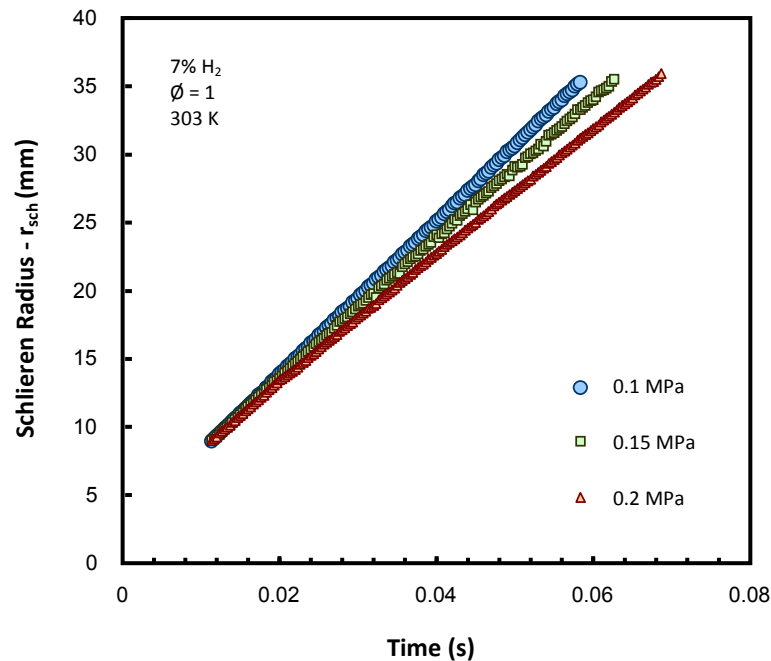


Fig. 6.1 – Examples of stoichiometric flame growth for the 7% H₂ BFG mixtures at different initial ambient pressures.

6.2.1 – Relationship between Flame Speeds, Stretch Rates and Markstein Lengths

Data was processed to examine the association between propagation rate, and flame stretch using the same numerical methods previously employed. Fig. 6.2 – Fig. 6.9 show examples of the plotted relationships between S_n and α , with the superimposed nonlinear association for each equivalence ratio of the four tested compositions, and data separated for each initial ambient pressure.

6. BFG H₂ Fluctuation – Variation in Ambient Conditions

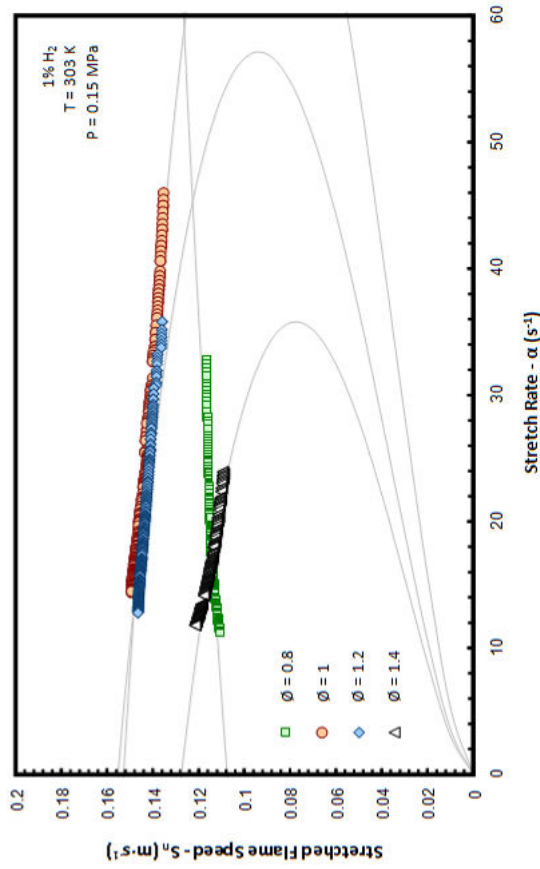


Fig 6.2 – Samples of plotted 0.15 MPa 1% H₂ BFG/air S_n against α data, for $\phi = 0.8 - 1.4$.

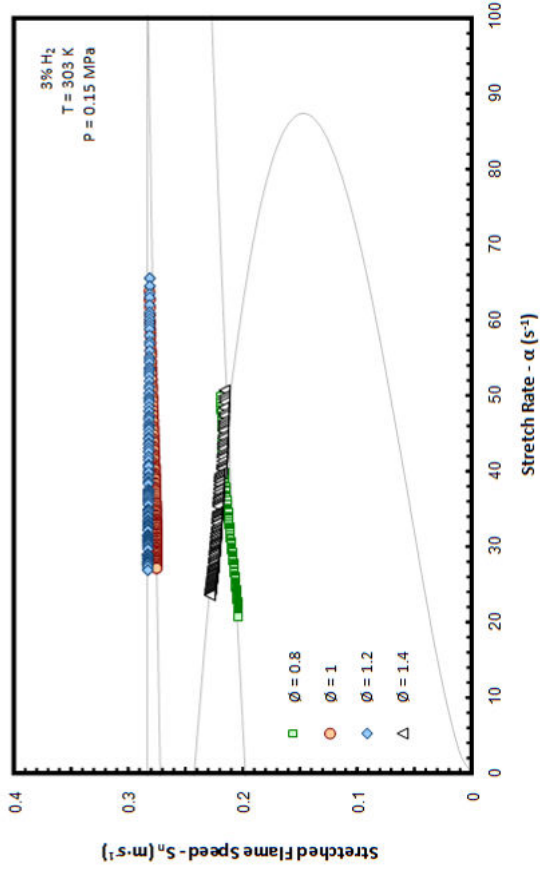


Fig 6.3 – Samples of plotted 0.15 MPa 3% H₂ BFG/air S_n against α data, for $\phi = 0.8 - 1.4$.

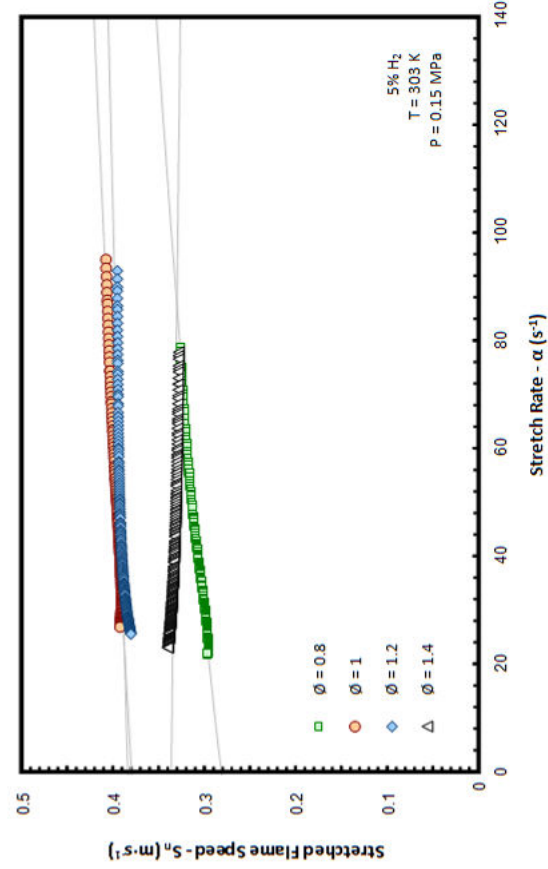


Fig 6.4 – Samples of plotted 0.15 MPa 5% H₂ BFG/air S_n against α data, for $\phi = 0.8 - 1.4$.

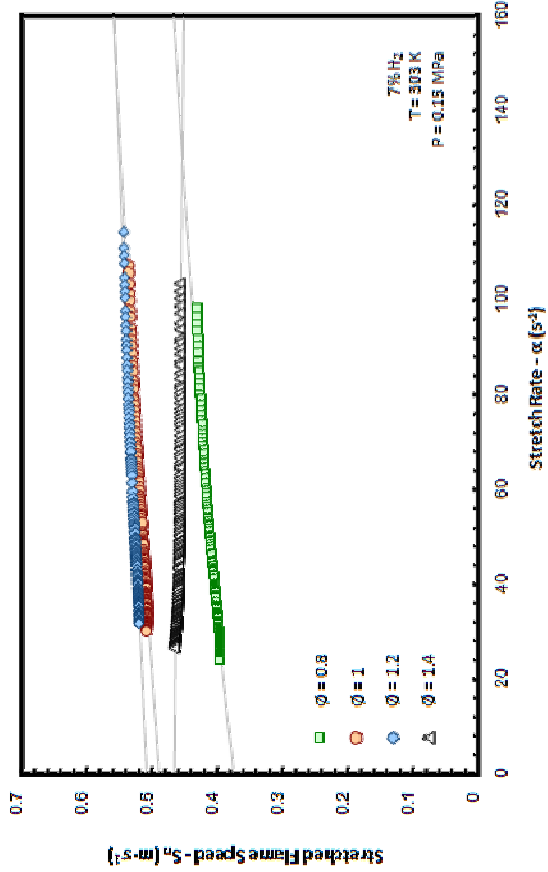


Fig 6.5 – Samples of plotted 0.15 MPa 7% H₂ BFG/air S_n against α data, for $\phi = 0.8 - 1.4$.

6. BFG H₂ Fluctuation – Variation in Ambient Conditions

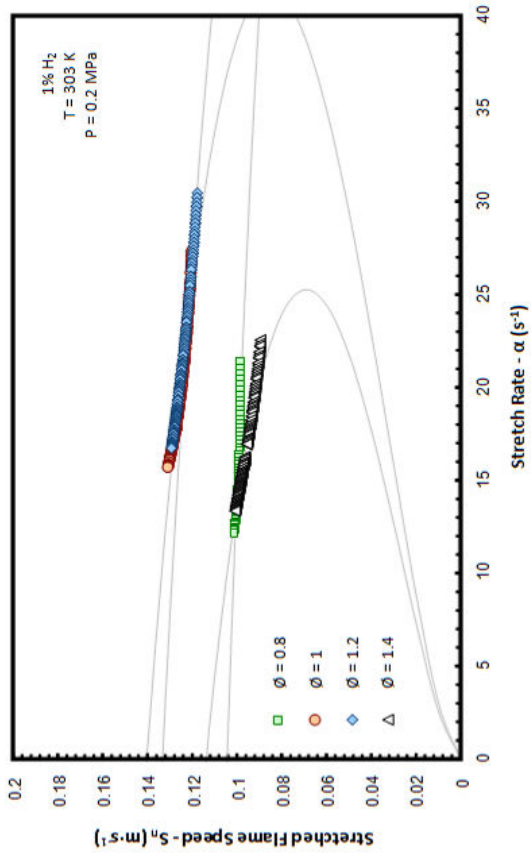


Fig 6.6 – Samples of plotted 0.2 MPa 1% H₂ BFG/air S_n against α data, for $\phi = 0.8 - 1.4$.

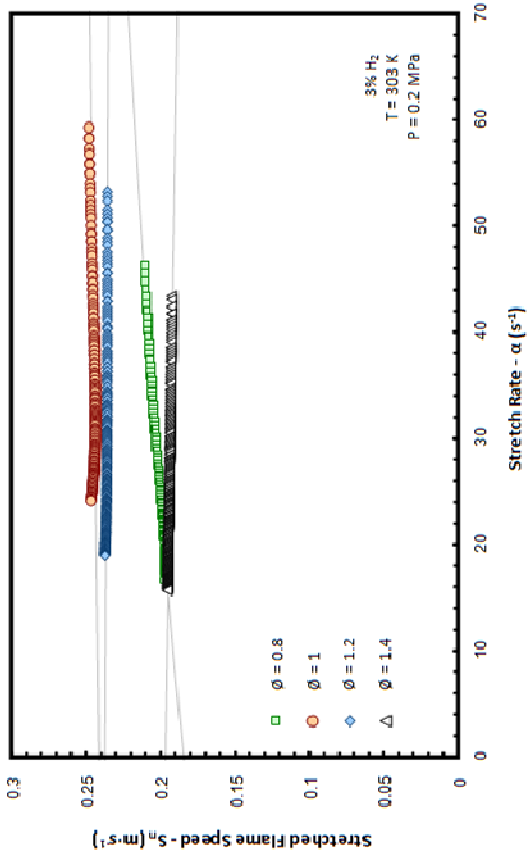


Fig 6.7 – Samples of plotted 0.2 MPa 3% H₂ BFG/air S_n against α data, for $\phi = 0.8 - 1.4$.

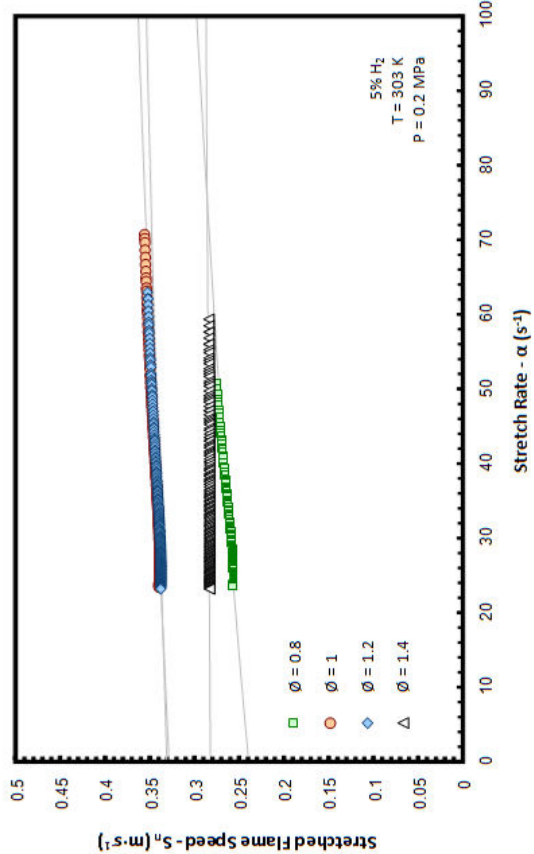


Fig 6.8 – Samples of plotted 0.2 MPa 5% H₂ BFG/air S_n against α data, for $\phi = 0.8 - 1.4$.

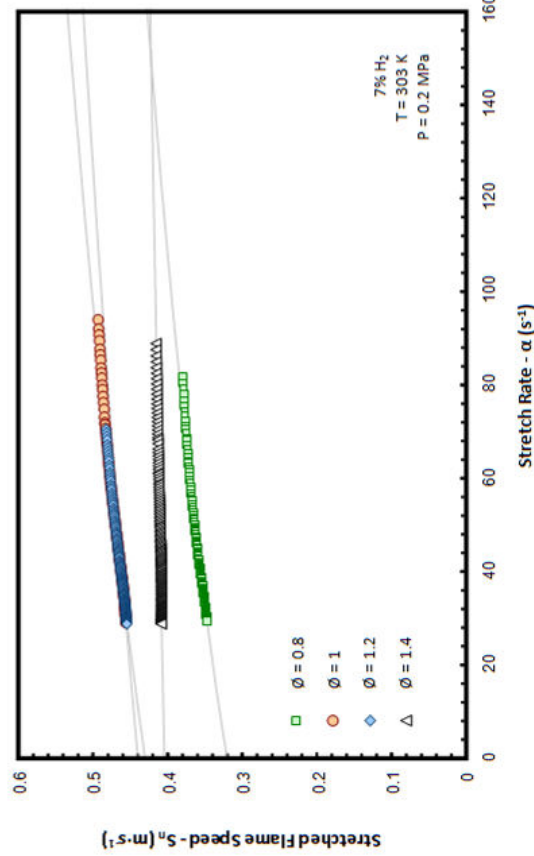


Fig 6.9 – Samples of plotted 0.2 MPa 7% H₂ BFG/air S_n against α data, for $\phi = 0.8 - 1.4$.

There appear to be similar trends for all analysed datasets, with gradients of lean associations becoming increasingly negative with richness subsequent to levelling out. These trends are analogous to those seen with other BFG data presented in the previous chapter. Furthermore, there also appears to be increasing negative tendency with a rise in H₂ fraction, suggesting an equivalent offset to associations previously observed. These trends can be visualised with plotted values of L_b , shown for all obtained and averaged data in Fig. 6.10 (0.15 MPa data), and Fig. 6.11 (0.2 MPa data).

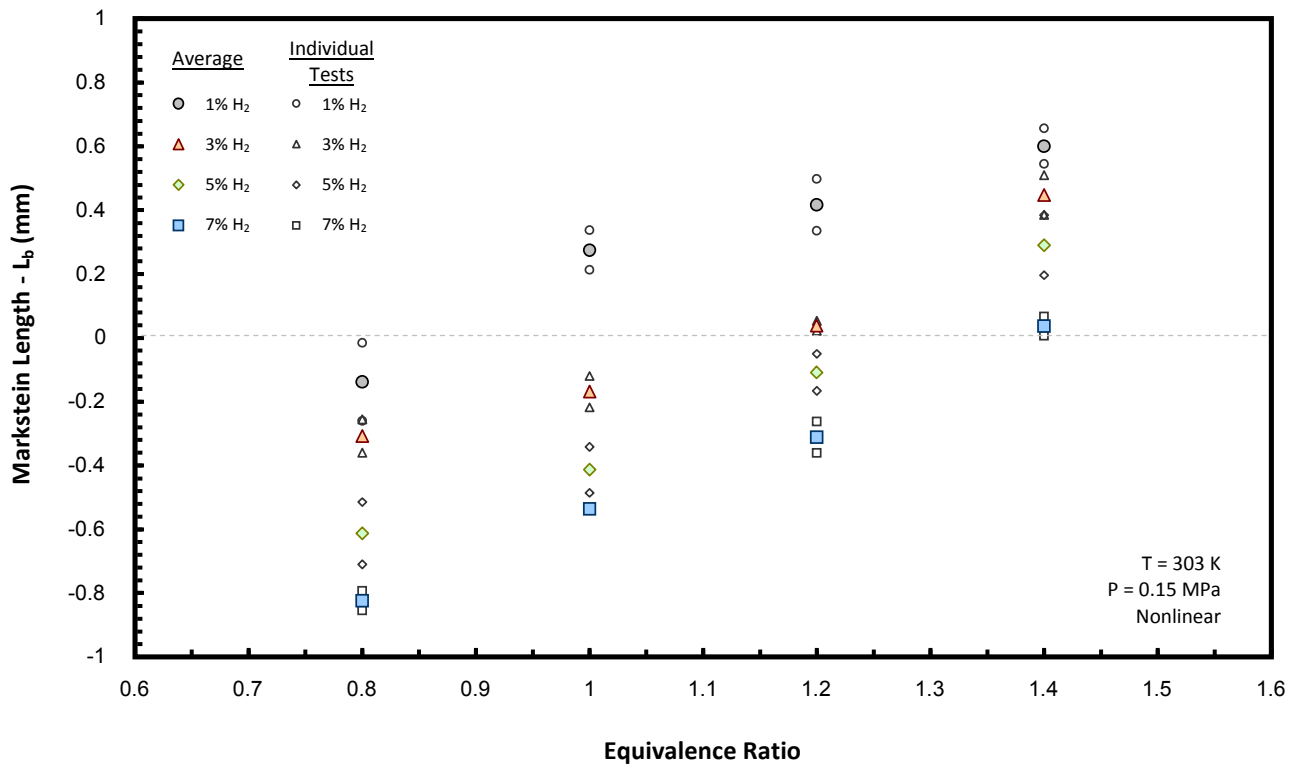


Fig. 6.10 – Plotted values of Markstein length against equivalence ratio for each of the tested BFG compositions at 0.15 MPa.

These plots suggest a tendency for thermal diffusivity to become more dominant with respect to mass diffusion for the observed increase in richness [27]. Similarly the increase in highly diffusive H₂ is again shown to negatively offset observed L_b , as propagation begins to accelerate under the influence of stretch, particularly at lean conditions. Ostensibly these behavioural trends are the same as those previously observed, however when the data are analysed with respect to pressure a distinct

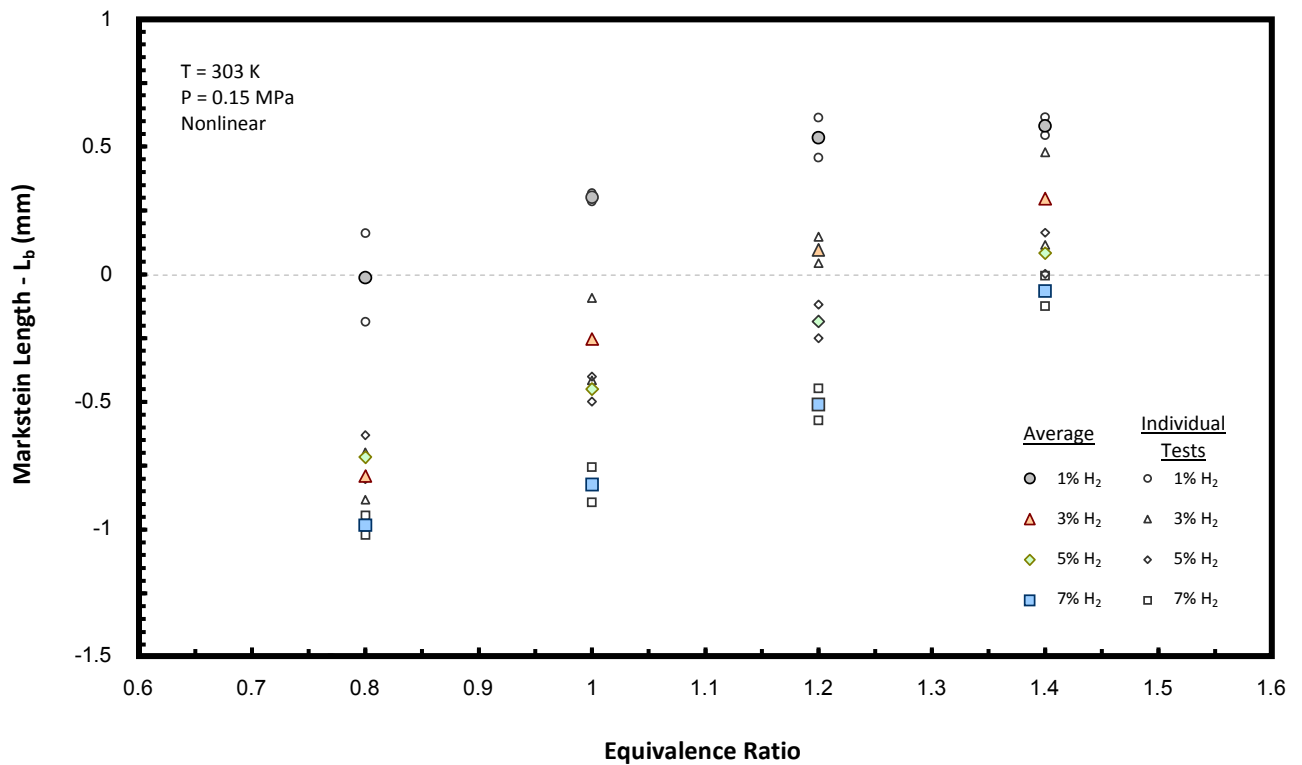


Fig. 6.11 – Plotted values of Markstein length against equivalence ratio for each of the tested BFG compositions at 0.2 MPa.

association is identified. The average L_b values have been rearranged in Fig. 6.12 for each representative BFG mixture, and plotted against initial ambient condition. There is an observable tendency for values to decrease with a rise in pressure (consistent with other works [102, 115]). This suggests that relative to thermal conduction, reactant diffusion becomes increasingly prominent with an increase in pressure, and consequently results in a decrease of mixture L_e . Ergo BFG flames will accelerate more when highly stretched at conditions of higher pressure, such as those experienced in a gas turbine combustion system [29]. This is particularly prominent when the mixtures containing higher fractions of H₂ are burned under leaner conditions.

Overall experimental repeatability was reasonably good with average standard deviation of ~ 0.1 mm for all mixtures and pressures, and therefore of a similar order to those previously observed, with more repetitions performed. The magnitude of

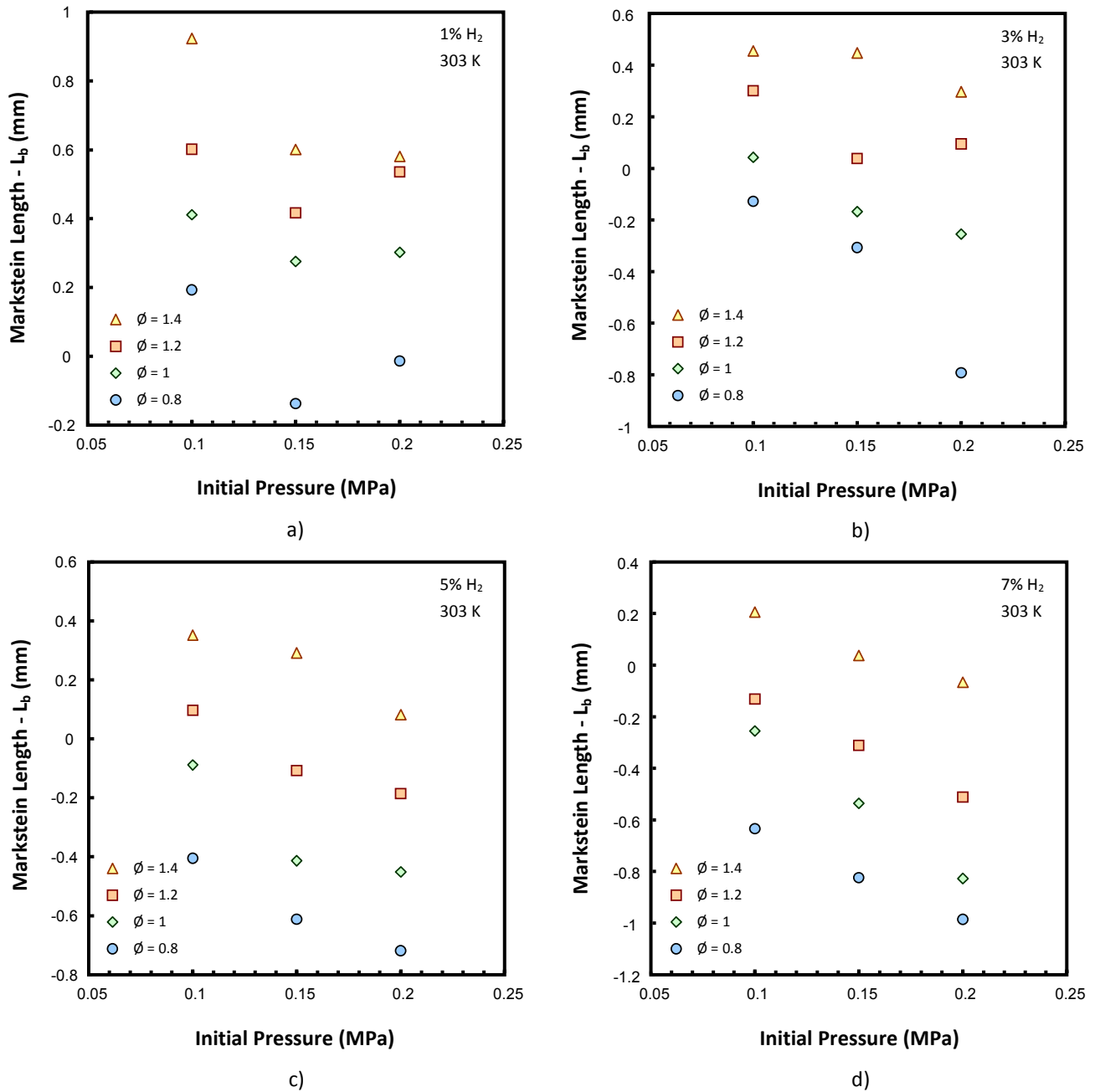


Fig. 6.12 – Plotted values of L_b against initial ambient pressure for each tested BFG composition. a) 1, b) 3, c) 5, d) 7 % H₂.

difference evident between nonlinear and linear derived L_b was again small (< 10%) for most values, and only increased as the mixtures became less equidiffusive and the influence of stretch enhanced. Again increased negativity (as discussed in section 5.2.1) was evident from values provided by the nonlinear method.

6.2.2 – Unstretched Flame Speeds, and Laminar Burning Velocity

The values attained for unstretched flame speed are plotted for respective 0.15 and 0.2 MPa ambient conditions in Fig. 6.13 and Fig. 6.14. Again hollow grey points represent the results from individual tests, with the average points coloured.

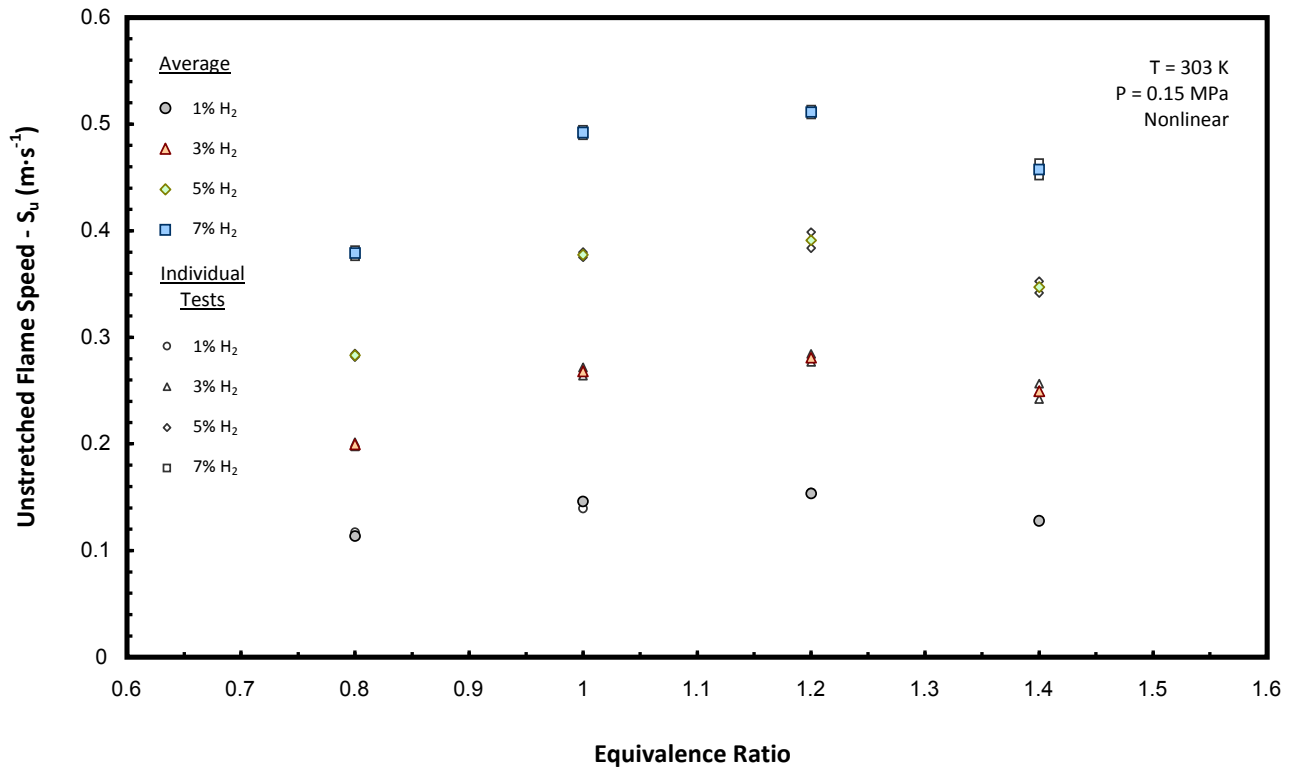


Fig. 6.13 – Experimental values of S_u against ϕ for each BFG composition at 0.15 MPa

It is evident from the Fig. 6.13 and Fig. 6.14 that the selected range of equivalence ratios provide rich characteristic peaks in S_u for the conditions tested. There also appears to be an increase in S_u by a factor of over three for each equivalence ratio and ambient pressure, equivalent to previous results. Furthermore the relative levels of experimental scatter in the plotted results are small when compared with the attained values of L_b , which is again similar to results presented in chapter 5. In order to obtain representative values of u_L from the measured S_u , again an apt reaction mechanism was required to attain values of the burned gas density ratio. The Li et al. [164]

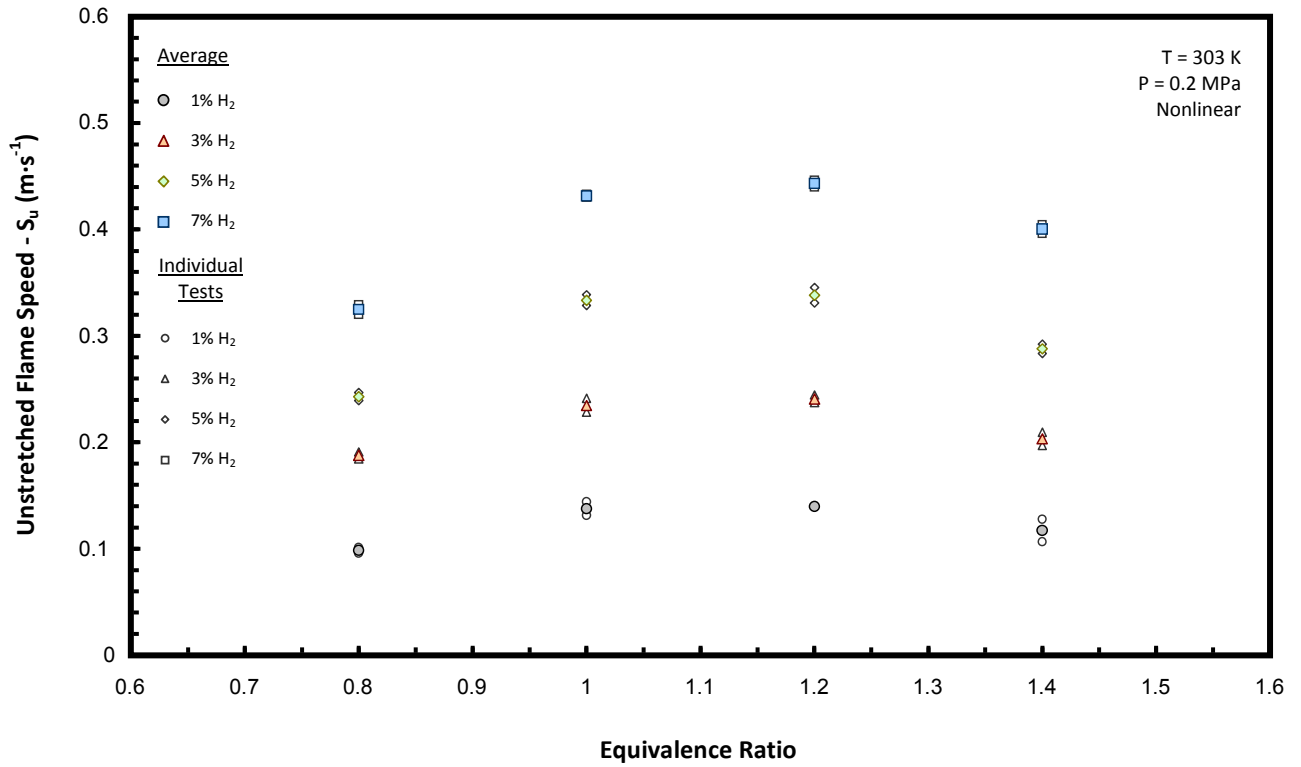


Fig. 6.14 – Experimental values of S_u against ϕ for each BFG composition at 0.2 MPa

mechanism was selected once more to maintain consistency with respect to previous results, although as previously demonstrated (Table 5.2) there is negligible difference to resultant values of u_L . As calculations are ideal, adiabatic and isobaric there is also negligible difference in the attained density ratio from change in ambient pressure as demonstrated in Table 6.1.

Table 6.1 – Calculated adiabatic density ratios for different conditions of ambient pressure

ϕ	1% H ₂			3% H ₂			5% H ₂			7% H ₂		
	ρ_u (g/cm ³)	ρ_b (g/cm ³)	(ρ_b/ρ_u)	ρ_u (g/cm ³)	ρ_b (g/cm ³)	(ρ_b/ρ_u)	ρ_u (g/cm ³)	ρ_b (g/cm ³)	(ρ_b/ρ_u)	ρ_u (g/cm ³)	ρ_b (g/cm ³)	(ρ_b/ρ_u)
0.15 MPa												
0.8	0.00181	0.00041	0.2280	0.00179	0.00040	0.2236	0.00176	0.00039	0.2195	0.00174	0.00038	0.2158
1	0.00182	0.00040	0.2180	0.00179	0.00038	0.2130	0.00177	0.00037	0.2087	0.00175	0.00036	0.2047
1.2	0.00182	0.00043	0.2348	0.00180	0.00041	0.2296	0.00177	0.00040	0.2248	0.00175	0.00039	0.2204
1.4	0.00183	0.00046	0.2519	0.00180	0.00044	0.2462	0.00178	0.00043	0.2411	0.00175	0.00041	0.2362
0.2 MPa												
0.8	0.00241	0.00055	0.2280	0.00238	0.00053	0.2236	0.00235	0.00052	0.2195	0.00233	0.00050	0.2158
1	0.00242	0.00053	0.2177	0.00239	0.00051	0.2127	0.00236	0.00049	0.2084	0.00233	0.00048	0.2045
1.2	0.00243	0.00057	0.2348	0.00240	0.00055	0.2296	0.00236	0.00053	0.2248	0.00233	0.00051	0.2204
1.4	0.00244	0.00061	0.2519	0.00240	0.00059	0.2462	0.00237	0.00057	0.2411	0.00233	0.00055	0.2362

The ratios provided in Table 6.1 were used with the measured values of S_u to give average laminar burning velocities as plotted in Fig. 6.15.

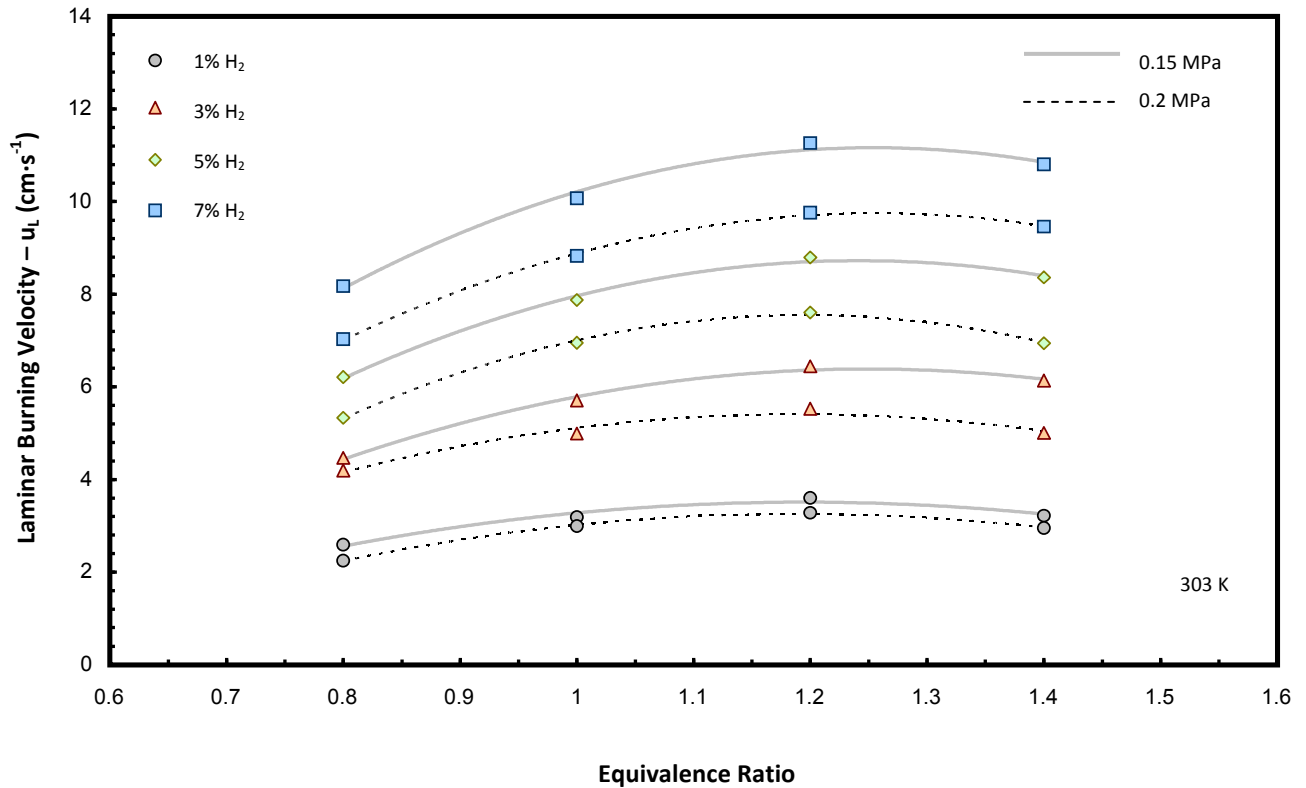


Fig. 6.15 – Experimental values of u_L against ϕ for each BFG composition at 0.15 and 0.2 MPa

It is clear from the Fig. 6.15 that an increase in pressure leads to a corresponding decrease in u_L , resulting from a change in the combination of chemical kinetics and reactant density; with an increase in pressure leading to a corresponding rise in chain terminating reactions, working to slow the rate of propagation [28, 102]. From the perspective of BFG combustion, it was important to quantify if this change reduces the relative fluctuation experienced as a result of compositional H₂ variation. If the percentage change in u_L for peak values is calculated for the 1-7% compositional H₂ change, an increase in the order of 211 % is seen. This value respectively increases and decreases by small amounts for initial ambient pressures of 0.15 and 0.2 MPa, suggesting the quantity of any relative change is encompassed by experimental scatter. Interestingly, chemical models predict a small increase in this sensitivity, as is evidenced in the following section.

6.2.3 – Experimental and Modelled values of Laminar Burning Velocity

Experimental u_L values have been re-plotted for change in ambient pressure, with equivalent modelled values from three chemical reaction mechanisms (Li et al. [164], Davis et al. [165], and GRI-Mech 3.0 [149]) superimposed in Fig. 6.16. The mechanism and model specifications are the same as those detailed in section 5.3.

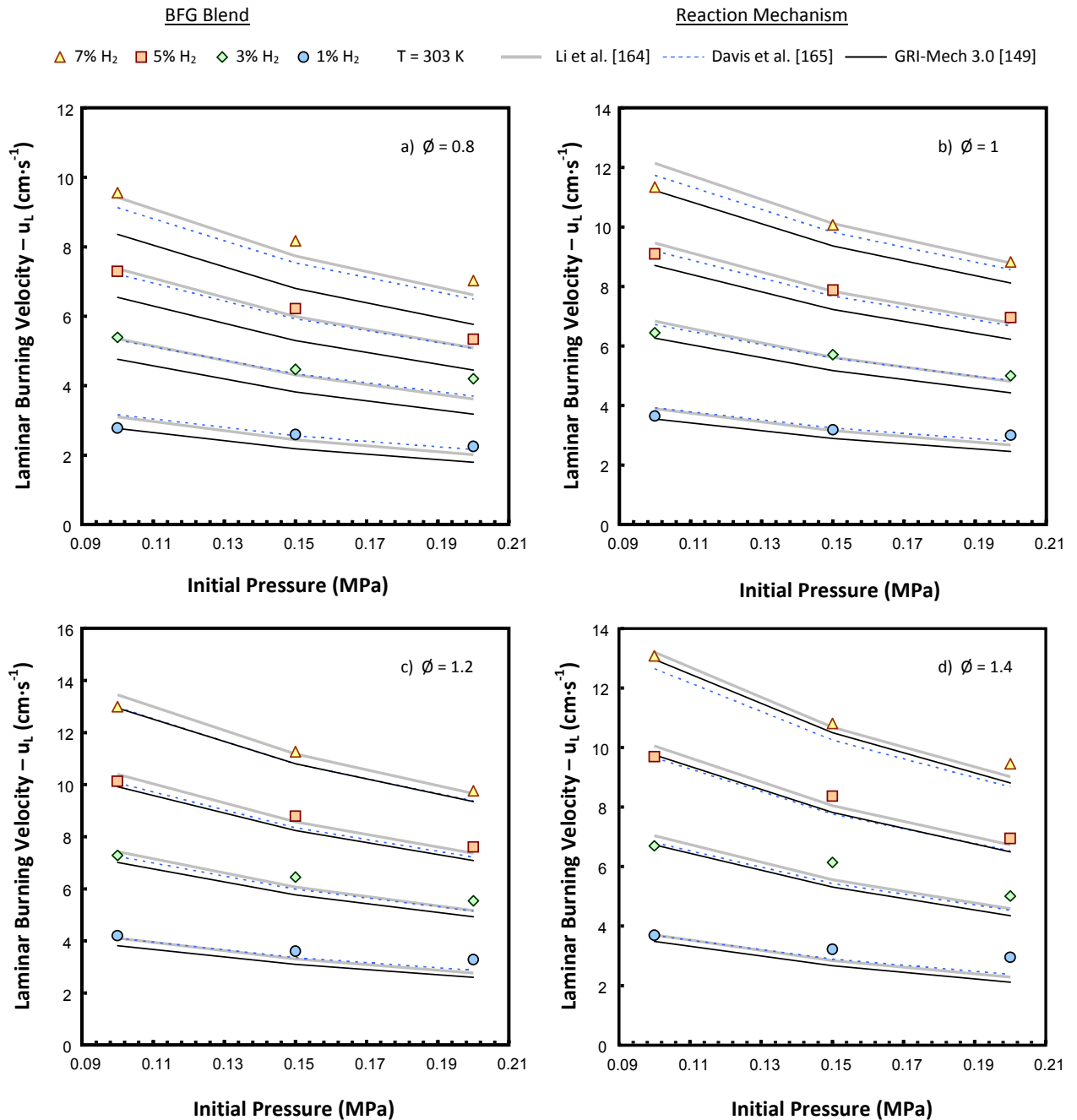


Fig. 6.16 – Plotted values of u_L against initial ambient pressure for each tested BFG composition, at $\phi = 0.8$ (a), $\phi = 1$ (b), $\phi = 1.2$ (c), $\phi = 1.4$ (d), with modelled values superimposed

The plots are separated on the basis of equivalence ratio in order to improve clarity and avoid data overlap. Several trends can be outlined from the plotted results; firstly the values modelled by the Li and Davis mechanisms are in closer agreement than the unsuited GRI-Mech 3.0 dataset, particularly at low concentrations of H₂ and lean equivalence ratios. As the mixtures begin to burn faster with more H₂ the results from the two aforementioned models then begin to diverge, and there is variation in which mechanism provides the best representative results. The GRI-Mech 3.0 mechanism also begins to perform better as equivalence ratios increase. With a rise in pressure there is an observable tendency for modelled values to under-predict the measured speed for all conditions of BFG H₂, and relative performance begins to drop. The accuracy of each set of results has been numerically quantified in the same way as section 5.3, with a calculation of standard error in the estimate (SEE - Eqn. 5.2). The calculated values of SEE are provided in Table 6.2, with values averaged for all equivalence ratios of each data set (for corresponding ϕ at 0.1 MPa).

Table 6.2 – Calculated model SEE values with increasing pressure

Ambient Pressure SEE - ($\text{cm}\cdot\text{s}^{-1}$)									
BFG H ₂ (%)	Li et al. [164]			Davis et al. [165]			GRI-Mech 3.0 [149]		
	0.1 MPa	0.15 MPa	0.2 MPa	0.1 MPa	0.15 MPa	0.2 MPa	0.1 MPa	0.15 MPa	0.2 MPa
1	0.21	0.26	0.47	0.24	0.21	0.37	0.22	0.45	0.64
3	0.27	0.36	0.41	0.16	0.43	0.40	0.36	0.68	0.73
5	0.29	0.23	0.22	0.07	0.42	0.34	0.43	0.69	0.67
7	0.47	0.24	0.31	0.36	0.50	0.53	0.61	0.82	0.82

The values shown in the table vindicate the observations in trends made above, and the Li mechanism provides marginally lower overall SEE values compared with the Davis set. However, if the correlated values of SEE are expressed as a percentage of overall burning velocity then the Davis mechanism performs better: With an increase in the Li percentage difference from 8 to 12 % with pressure rise, compared with 4 to 12 % for the Davis set. In this regard GRI-Mech 3.0 is inferior with a relative SEE variation of 8 to 18 %. All experimental and modelled values are tabulated in Appendix B.4.

6.3 Results for Change in Temperature

Fig. 6.17 demonstrates the difference in measured propagation rates resulting from change in ambient temperature, for sample 7% H₂ BFG mixtures. There is a clear increase in gradient resulting from temperature rise, and hence an acceleration in flame speed. The following sections provide detail of analyses performed using the nonlinear optical technique to numerically characterise this behaviour.

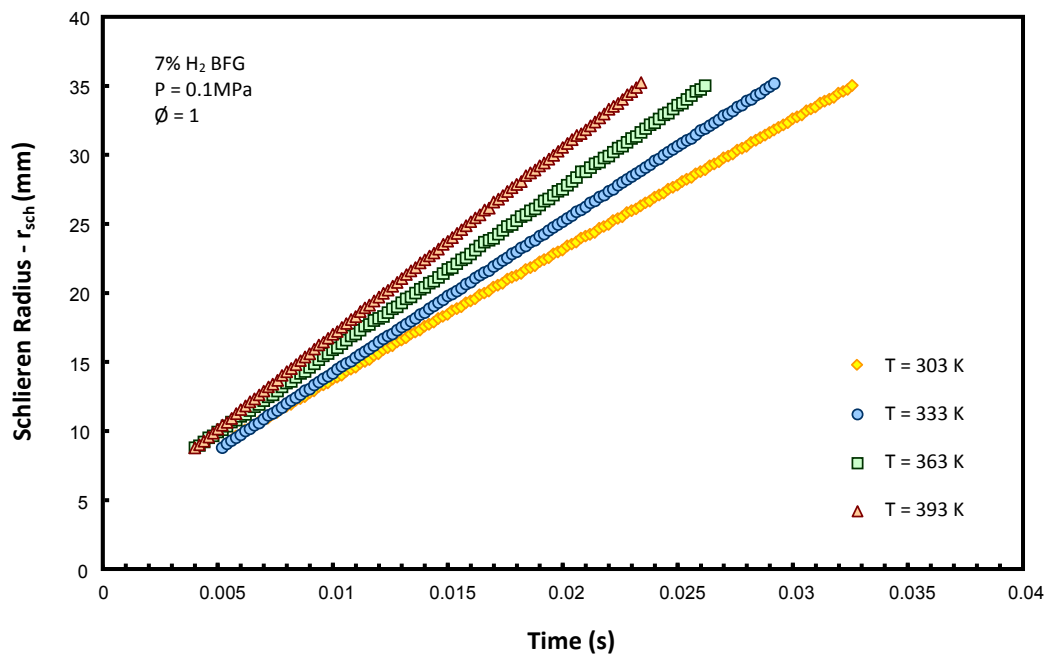


Fig. 6.17 – Examples of stoichiometric flame growth for 7% H₂ BFG at different initial ambient temperatures.

6.3.1 – Relationship between Flame Speeds, Stretch Rates and Markstein Lengths

Plots of S_n against α were produced for each performed test, with analyses suggesting that reactant temperature rise provides little difference in the measured stretch influence in relation to the observed experimental scatter. This is shown in Fig. 6.18 where a comparison in the stretched propagation relationship is provided for the same fuel blend at two disparate temperatures; 333 K (a), and 393 K (b). The plotted flame speeds are larger for the higher temperature plot, however there is little difference in the apparent gradients. The observation is emphasised further in Fig. 6.19, where two

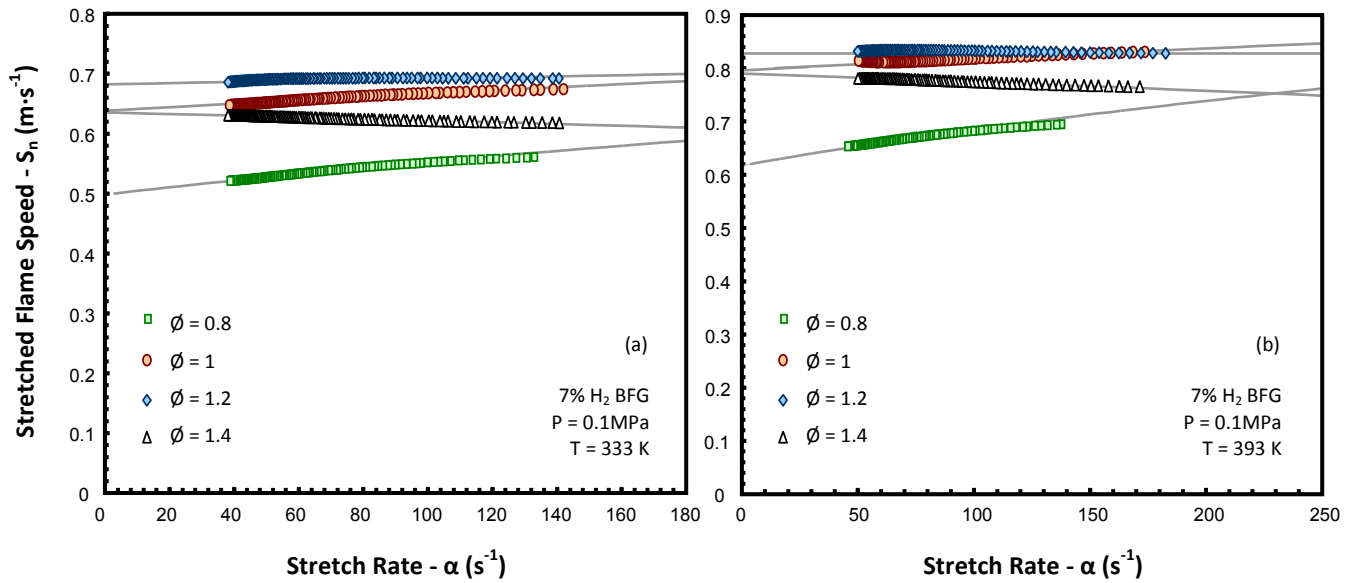


Fig. 6.18 – Examples of plotted 7% H₂ BFG /air S_n against α , for $\phi = 0.8-1.4$, a) T = 333 K and b) T = 393 K (b).

heavily stretched rich mixtures (3 % H₂(a), and 5 % H₂(b) BFG) are plotted with increasing temperature, and the nonlinear association superimposed. There are parallel offsets between each plot equivalent to a change in flame speed; however the gradients of each relationship are ostensibly similar. The trend is once again more easily visualised with plotted values of L_b, shown for the average values of all tested conditions in Fig. 6.20 on the following page.

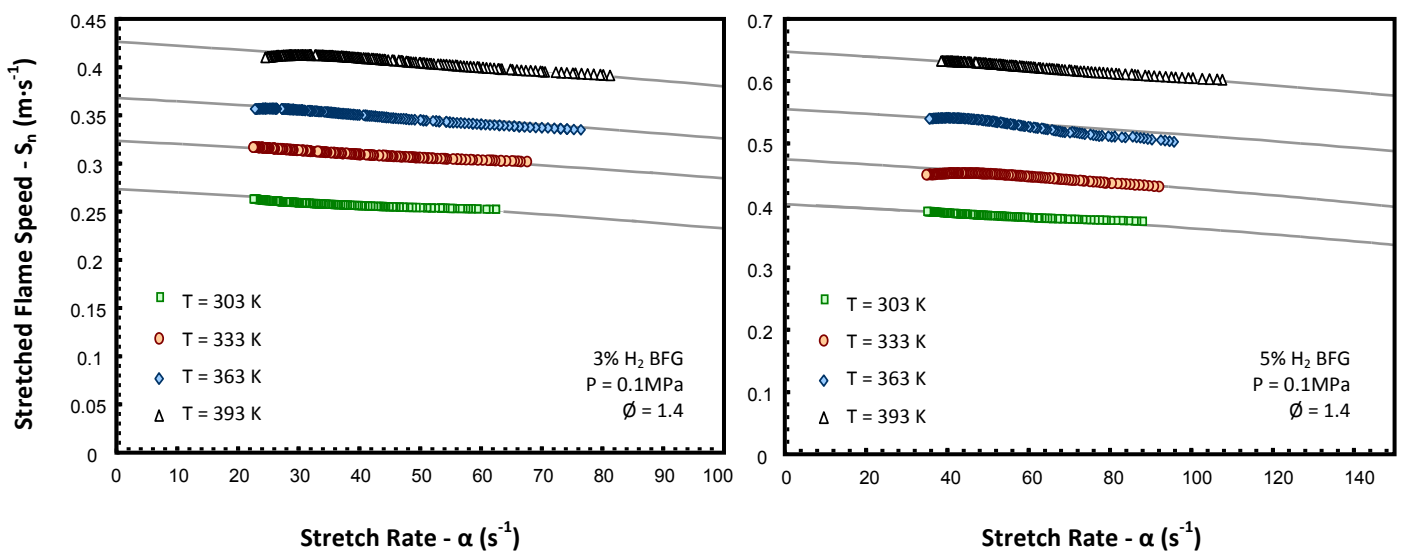


Fig. 6.19 – Examples of plotted BFG /air S_n against α , for a) 3%, and b) 5% H₂BFG and variation in Temperature.

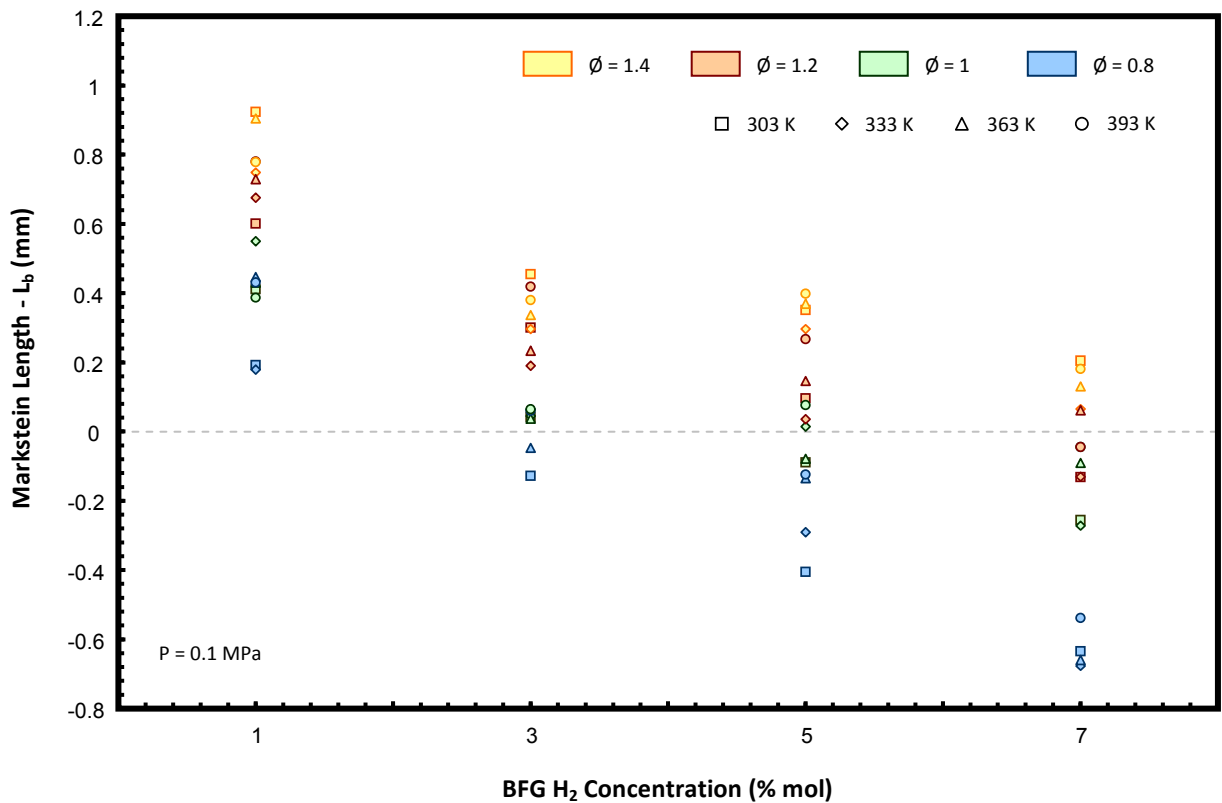


Fig. 6.20 – Examples of plotted BFG /air S_n against α , for 3% (a), and 5% (b) H₂ and variation in T.

It is clear from the plot that experimental repeatability is too poor (from two tests per condition) to discern any apparent trend in relation to initial temperature. Inasmuch that there is moderate grouping for each equivalence ratio (colour), but no repeatable change in the height of each marker. This has been seen with other similar works [102], where temperature increase hasn't provided significant change in measured L_b , and consistent with the high temperature benchmarking study in Chapter 4. This suggests mixture Le is not heavily influenced by temperature (across the tested range), with any change is mass diffusivity balanced by a proportional adjustment in thermal conduction.

6.3.2 – Change in Unstretched flame speed

Fig. 6.21 on the following page gives separate plots for change in unstretched flame speed for each tested temperature, again with the average values coloured.

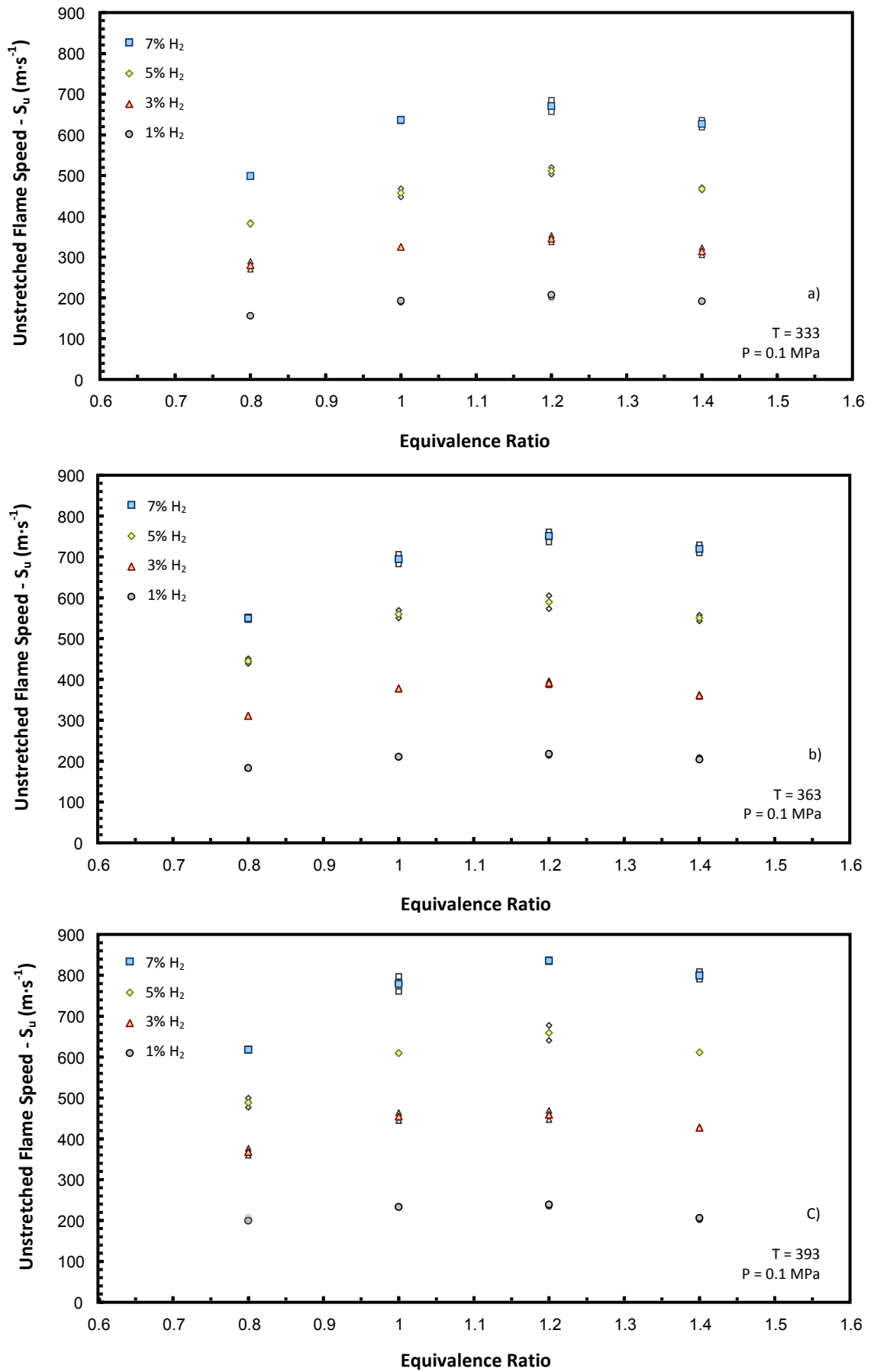


Fig. 6.21 – BFG /air S_u against ϕ , for a) 333 K, b) 363 K, and c) 393 K.

The plots demonstrate analogous profiles for change in ϕ to those seen for atmospheric conditions, and changes in elevated pressure. Furthermore, there are also anticipated proportional increases in S_u for each level of temperature rise. This acceleration results from a combination of influences; firstly an increase in adiabatic flame temperature, and the resultant rise in reaction rates of the intermediate chemistry. In addition, changes to reactant temperature will also modify the mixture transport properties, and overall gas density; both of which will further influence a fluctuation in observed flame speed [27]. The result for BFG is for respective peak S_u to increase by $\sim 60 \text{ mm}\cdot\text{s}^{-1}$ ($\sim 34\%$) and $245 \text{ mm}\cdot\text{s}^{-1}$ ($\sim 42\%$) for the 1 and 7 % H₂ mixtures across the tested 120 K range. The order of scatter in S_u measurements was similar to those previously seen, with only two repetitions performed, and standard deviations scaling with overall rise in speed. This is discussed further in Section 6.4

6.3.3 – Experimental and modelled values of Laminar Burning velocity

The Li et al. [164] mechanism was used once more to obtain values of adiabatic density ratio for application in Eqn. 3.12. Fig. 6.22 shows the shift in stoichiometric ratio resulting from a change in initial temperature, with the full set of applied values given in Appendix B.5.

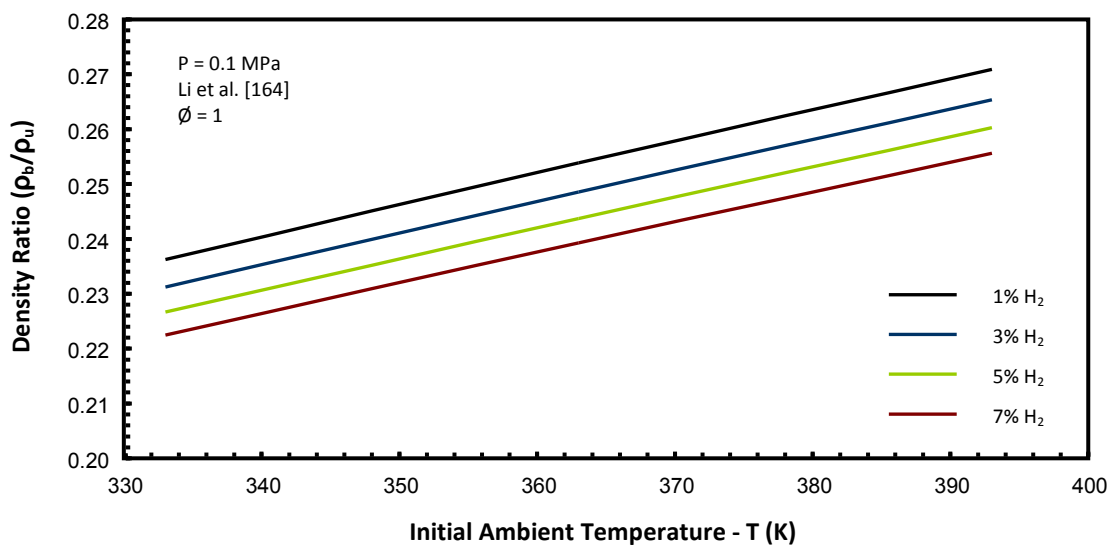


Fig. 6.22 – Change in density ratio with initial ambient temperature for each BFG mixture.

The increase in initial temperature lowers the density of the reactant mixture, and consequently causes the rise of plotted ratios observed in Fig. 6.22. Average experimental u_L values are plotted against corresponding modelled data in Fig. 6.23, with plots separated for each equivalence ratio in order to improve clarity. The three reaction mechanisms applied with the pressure dataset in 6.2.3 were employed with identical specifications.

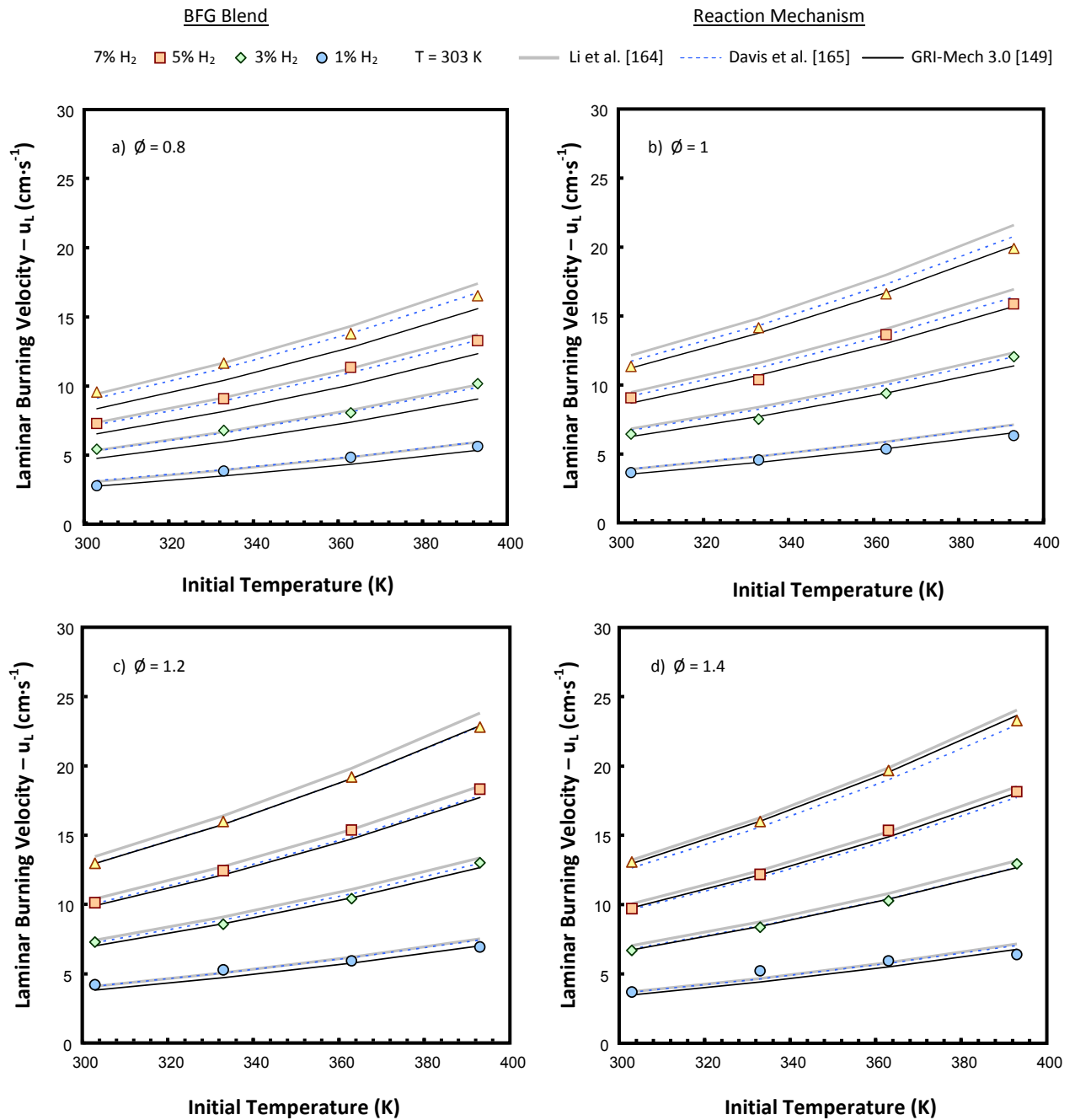


Fig. 6.23 – Plotted values of u_L against initial ambient temperature for each tested BFG composition, at a) $\phi = 0.8$, b) $\phi = 1$, c) $\phi = 1.2$, d) $\phi = 1.4$, with modelled values superimposed.

A rise in temperature appears to yield a corresponding proportional increase in u_L for all compositions and equivalence ratios. The plots also suggest that relative mechanism performance changes with equivalence ratio. If the $\phi=1.4$ dataset is taken as an example (Fig. 6.23d), there appears to be closer a correlation between the values returned from each chemistry set, and the experimental data. Furthermore this agreement seems to hold with an increase in reactant temperature. Conversely, if the leanest (Fig. 6.23a) equivalence ratio is considered, there is a significant offset between GRI-Mech 3.0, and the other two mechanisms, which themselves begin to diverge with an increase in BFG H₂. The Li mechanism appears to provide an overestimation at these conditions, compared to the small values given by GRI-Mech 3.0. The Davis mechanism was optimised for performance at higher temperatures, and it therefore fits that this dataset is in closest agreement with measured values. This relative model performance has again been indexed using a SEE, with values averaged for all equivalence ratios in Table 6.3.

Table 6.3 – Calculated model SEE values with increasing temperature.

Ambient Temperature SEE - ($\text{cm}\cdot\text{s}^{-1}$)									
BFG H ₂ (%)	Li et al. [164]			Davis et al. [165]			GRI-Mech 3.0 [149]		
	333 K	363 K	393 K	333 K	363 K	393 K	333 K	363 K	393 K
1	0.31	0.31	0.65	0.34	0.30	0.59	0.53	0.34	0.26
3	0.55	0.59	0.26	0.40	0.36	0.19	0.42	0.34	0.69
5	0.64	0.22	0.62	0.46	0.47	0.41	0.51	0.81	0.57
7	0.42	0.80	1.15	0.30	0.49	0.47	0.67	0.51	0.51

The performance of the Li mechanism is shown to deteriorate with a rise in H₂ fraction, or elevation in temperature. GRI-Mech 3.0 performance is reasonably consistent, and better at low H₂ concentrations. However, as expected the values calculated for the Davis dataset are superior, particularly relative to the highest tested temperature.

6.3.4 – Practical significance of temperature change

With regard to dampening fluctuation resulting from H₂ variation, temperature does not provide an overall solution if applied to all tested BFG blends. Firstly, there is

negligible influence demonstrated in altering the influence of stretch on propagation. Furthermore, a proportional rise in u_L is experienced relative to the initial values, together with effective divergence seen with each plot in Fig. 6.23. If step changes were achieved, the relative fluctuation in u_L would decrease, however the percentage change for 1-7 % H₂ at 393 K is around 16.3 cm·s⁻¹, or 236 % increase from the lowest value, and this compares with a corresponding value of 211 % for the atmospheric dataset.

Some fuel preheating control could be employed to increase flame speeds of the lower H₂ BFG mixtures by a small amount, and raise the speeds towards equivalent higher H₂ blends. In order to more accurately quantify and characterise this, a power law association can be fitted for each fuel, and used to model flame speed change with ambient condition. This has been undertaken in the following section (6.4.2).

6.4 Quantifying Uncertainty and Power Law Correlation

6.4.1 – Experimental Uncertainty

Experimental uncertainties were quantified using the same method as previously employed in Chapter 5. Adjustments were made in the calculation of total bias, adjusted on the basis of changed ambient condition. Errors in the calculated influence of equivalence ratio, H₂ fraction, and variation in optical properties, were all scaled with change in condition for each specified test case. However, with only two repetitions per condition performed, resultant uncertainty values were larger than those previously calculated due to a rise in the standard deviation of each test, and corresponding t-value (see Eqn. 4.4). The latter parameter increased from 4.303 for three repetitions at a 95 % confidence level, to 12.71 [161]. As a consequence of this, uncertainty increased to values above ten percent, regardless of the reasonable repeatability of observed for S_u data (Fig. 6.13, Fig. 6.14, and Fig. 6.21). All calculated estimations of experimental uncertainty in S_u , B_{Su} , and σ_{Su} are provided with the full numerical dataset given in Appendices B.4 and B.5.

6.4.2 – Power Law Association

Independent power law correlations have been made to characterise change in u_L with ambient condition, employing an empirically derived association similar to that utilised by analogous research [102, 154].

$$u_L = u_{L0} \left(\frac{T}{T_0} \right)^{\alpha T} \quad (6.1)$$

An example of this relationship is shown above in Eqn. (6.1), with u_L expressed relative to the datum burning velocity (u_{L0}) for an initial temperature of 303 K (T_0) and a condition dependent exponent (αT). The same relationship was applied for change in pressure, with a datum value (P_0) of 0.1 Mpa and an alternative constant (αP). The magnitude of each exponent is indicative of the sensitivity to change in burning velocity for that condition, and has been calculated across the entire tested range for each independent composition and equivalence ratio. These exponents are provided in Table 6.4, together with comparative values for CH₄ and H₂ obtained from the literature [102, 154].

Table 6.4 – Calculated conditional BFG exponents, benchmarked against CH₄ and H₂ values from literature.

ϕ	Temperature exponent (αT)				Pressure exponent (αP)			
	BFG							
	1% H ₂	3% H ₂	5% H ₂	7% H ₂	1% H ₂	3% H ₂	5% H ₂	7% H ₂
0.8	2.60	2.53	2.21	2.11	-0.398	-0.333	-0.451	-0.452
1	2.08	2.04	2.09	1.92	-0.270	-0.348	-0.410	-0.383
1.2	1.95	2.09	2.19	2.00	-0.354	-0.377	-0.393	-0.407
1.4	2.38	2.29	2.35	2.13	-0.470	-0.422	-0.477	-0.479
Literature Values								
ϕ	Gu et al [102] 300 K CH ₄ (αT)	Han et al. [168] 298 K CH ₄ (αT)	(αT) Liao et al. [159] 300 K CH ₄ (αP)		Gu et al [102] 300 K CH ₄ (αP)		Heimel et al. [169] H ₂ (αT)	
0.8	2.105	-	1.98		-0.465	-0.504	-	
1	1.612	1.653	1.58		-0.398	-0.374	1.712	
1.2	2.000	-	1.68		-0.405	-0.438	-	

There is limited accuracy in fitting associated relationships to plots consisting of 3 (α_P) or 4 (α_T) points, and consequently the obtained values should only be regarded for approximate analysis in overall trends. In doing so several tendencies can be observed in the tabulated points, firstly that the α_T values are mostly larger than the corresponding data supplied for CH₄ and H₂, suggesting BFG is more sensitive to a relative change in temperature, compared with the other benchmarked fuels. Furthermore, the temperature exponents are shown to decrease with an overall elevation in BFG H₂ concentration, as values tend towards other corresponding data. These benchmarked datasets also suggest a decrease in exponent magnitude near the peak stoichiometric values. For BFG, the lowest values appear to potentially shift from equivalence ratios of 1 towards 1.2, nearer the position where peak u_L was measured. From a practical perspective these associations allow for the prediction of fuel behaviour based on experimental data. For example, using the fitted exponents with a stoichiometric case, the temperature of 1% H₂ BFG would need to be increased to ~520 K in order to reach an equivalent burning velocity measured for the 7% mixture (It is however difficult from the results obtained, to predict any change in the influence in stretch).

Characterising trends in the obtained pressure exponents is more difficult, with smaller changes observed overall. It can be seen that there is a general tendency for exponent magnitude to further decrease as H₂ concentration is elevated in the BFG mixtures. This suggests that elevated pressure influences mixtures containing larger H₂ fraction more, however the quantified change is small, and not conspicuous with a comparison of plotted u_L data. The fitted pressure exponents are also closer to values observed for the benchmarked fuels, and agree with the increased influence observed with leaner and richer conditions.

Fig. 6.24 gives example power law correlations made for mixtures with the most extreme exponents. The fitted relationships are plotted against the normalised experimental data, with a reasonable fit observed. All coefficients of determination (R^2) values attained from this analysis were above 0.99, and are given with the full dataset in Appendices B.4 and B.5.

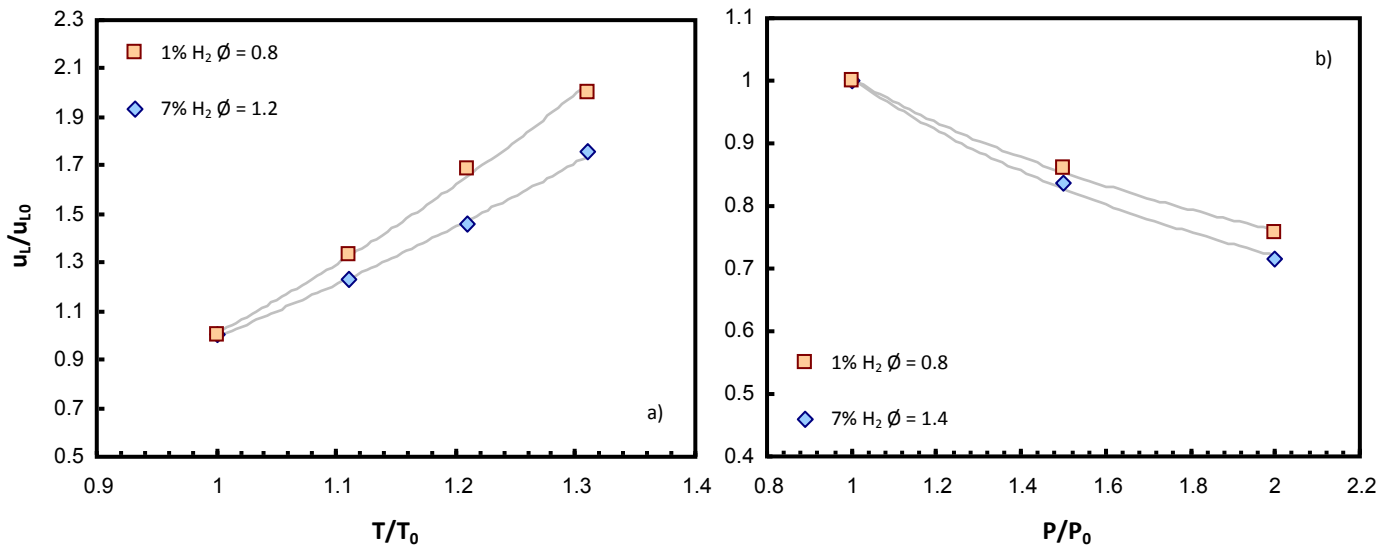


Fig. 6.24 – Power law correlations for sample mixtures of αT (a) and αP (b).

6.5 Summary and Conclusions

The changes observed in laminar burning velocity and Markstein length for fluctuation in concentration of BFG H₂ (Chapter 4.) were investigated further to quantify the influence of variation in ambient condition. Relative change in values were analysed for three disparate pressures and four temperatures across the respective ranges of 303-393 K and 0.1-0.2 MPa, as specified by the designed physical characteristics of the experimental setup. Change in mixture equivalence ratio was also investigated for each parameter with four specified points in the range 0.8-1.4.

Increase in ambient pressure demonstrated a drop in measured values of laminar burning velocity for each tested BFG composition. The change in pressure also demonstrated a tendency for decrease in observed values of Markstein length, suggesting a drop in mixture Lewis number and therefore a proportional rise in the influence of mass diffusion on propagation. This change was quantified as a proportional offset for all tested mixtures and equivalence ratios, and was observed alongside the increase induced by a rise in equivalence ratio or drop in H₂ concentration. Obtained values of laminar burning velocity were then compared

against data obtained from chemical models employing three kinetic reaction mechanisms. The Li and Davis datasets offer equivalent correlations for experimental data, with superior performance dependent on the mixture and equivalence ratio employed. This performance was again quantified using a measurement in standard error.

An increase in ambient temperature was shown to induce a rise in laminar burning velocity, observed for all mixtures and equivalence ratios. However, variation in the specified condition provided little demonstrable change in the analysed influence of flame stretch, with relative levels of experimental scatter too high. Nevertheless the same tendencies for change in L_b with equivalence ratio and composition were observed, compared to atmospheric tests. The same three reaction mechanisms employed with the pressure dataset were used to computationally model values of laminar burning velocity for comparison with measured data. The Davis mechanism was shown to provide superior performance, with lower overall values of standard error in the estimate. However, performance was shown to depend on composition and equivalence ratio, together with the ambient condition, and therefore due consideration should be given when selecting a mechanism to best model combustion of BFG in this way.

Power law correlations were made with the experimental data to quantify the relative change in each condition, with exponent magnitude benchmarked against analogous values from research literature. BFG was shown to be more heavily influenced by change in temperature compared to CH₄ and H₂, with similar magnitudes observed in the exponents fitted for pressure. The results suggest some form of preheating control (based on the fitted correlations) could be used to raise the burning velocity of low H₂ BFG, however influence of temperature was small across the tested range when compared with Hydrogen, and a typical temperature differential of over 200 K would be required for the slowest mixtures to approximate the 7% H₂ velocities. Furthermore this increase in temperature would have little effect in reducing variation in the influence of flame stretch.

Chapter 7. BFG H₂ Fluctuation - Variation in H₂O Concentration

7.1 Chapter Introduction

With characterisation studies undertaken to evaluate the potential for inherent variability in BFG combustion, further work was outlined to investigate the change in relative humidity of the fuel. It was hypothesised by the author that the slow and variable nature of the results obtained thus far would be significantly influenced by small increases in gaseous water fraction, ostensibly representative of those experienced during production. As introduced in section 1.3.2, and demonstrated with the case study in section 2.1.3, there is potential for BFG that has been *wet-scrubbed* to have a variable water fraction, fluctuating as a function of temperature. Furthermore change in the relative humidity of atmospheric air could also lead to a variation in combustive properties of the reactant mixture.

Again laminar burning velocities were characterised for changes in composition, this time with variation in the H₂ and H₂O fraction of the fuel, together with equivalence ratio. Markstein lengths were also used to characterise the effect water has on flame stretch, and the corresponding influence on propagation. It is important to characterise this behaviour as water can be used as an additive in practical combustion systems, for example in gas turbine operation [29]. The accuracy of models in predicting this behaviour was again evaluated to identify optimal reaction mechanism performance, and further investigate chemical kinetics of combustion at these conditions.

7.1.1 – Defining Experimental Parameters

As a result of the number of tests performed with the old mixture, a new foundation BFG blend was required for this study, comprised of a marginally different certified molar composition; CO - 23 %, CO₂ - 23.5 %, and N₂ - 53.5 %. This change necessitated new baseline tests to be undertaken with no variation in H₂O content. Similar to previous work, four concentrations of H₂ were introduced in the range of 1-7 %, with four disparate quantities of water vapour added to the overall reactant mixture (exact blending details are outlined in section 7.1.2). The tests were conducted at quasi-atmospheric (303 K and 0.1 MPa) ambient conditions and thus calculations were required to determine the vapour pressure, and corresponding mass of water to be introduced to the system. The Antoine equation (as given in Eqn. 7.1) was employed to calculate the H₂O vapour pressure (P_v) utilising the following coefficients; $A_A = 5.40221$, $B_A = 1838.675$, and $C_A = -31.737$ (NIST database [151]), for conditions of 303 K [170].

$$P_v = 10^{A_A - \frac{B_A}{C_A + T}} \quad (7.1)$$

This gives a resultant vapour pressure equal to 4.207 kPa. In order to calculate a corresponding mass to be introduced to the system, an accurate measure of the CVCB internal volume was required. This could not be obtained from simple engineering drawings of the rig, due to the introduction of additional pipe work and internal objects such as mixing fans and thermocouple probes. Instead a method was outlined based on mass displacement: Pipes were isolated at the chamber, with all other internal objects left in place, and the CVCB then filled with water. The mass was measured as water was introduced to the system, and when the chamber was full the temperature was recorded. A corresponding water density was obtained (from NIST database [151]), and used to give an internal volume measurement of the rig. This was repeated four times (giving a standard deviation of < 0.1 %), with the average taken as the representative rig volume. The obtained values are given in Table. 7.1.

Table. 7.1 – Calculated values of CVCB internal volume.

Introduced Mass of water (g)	Volume (m ³)
34817.06	0.03486
34832.47	0.034875
34800.85	0.034856
34804.14	0.03486
Average:	<u>0.034863</u>
Standard Deviation:	1.437 x 10 ⁻⁵ (~0.04%)

This average chamber volume was used with the ideal gas equation [142] and calculated vapour pressure to give a maximum mass of gaseous water equal to **1.0488** g at 303 K. The designated increments of water addition were therefore specified at 0.25 g, in the range 0 - 0.75 g, and hence reaching a relative humidity in the reactant mixture of approximately 72 %. Full vapour pressure was not realised to mitigate any inaccuracies in the employed calculations, or reduce the chance of condensate formation from any potential cold spots. It was reasoned that the specified range should provide characteristic trends for water addition, with potential for extrapolation to fully saturated conditions.

In order to reduce potential uncertainty, the number of experimental repetitions was increased to five for the initial experiments performed at stoichiometric conditions. Further testing was completed at leaner ($\phi = 0.8$) and richer ($\phi = 1.4$) air-fuel ratios, with the number of repeats reduced to three to save fuel for additional testing with other steelworks gas blends. These equivalence ratios were selected as any increased influence in the addition of H₂O for leaner or richer conditions could be more easily quantified.

The purity of the specified H₂ grade was again >99.995 %, and employed with dry zero-grade compressed air. The camera filming rate was maintained at 3,000 fps, to remain consistent with the previously undertaken BFG testing in Chapters 5 and 6.

7.1.2 – Considerations for the Experimental Methodology

Liquid water was introduced to the gas for this testing, and was vaporised prior to the addition of further reactants. This was to allow for finer control of the small masses required for infusion within the chamber. The CVCB was modified with the addition of a self-sealing septa, and a fine-needle syringe was required to facilitate injection of water to the system. The employed deionised water was obtained from a Millipore synergy 185 system, with the required mass measured on a Mettler Toledo AE50 high-precision balance. The experimental methodology was modified thus:

- Firstly the system was evacuated twice to the required residual pressure (1.5 kPa), and the specified mass of water (0.25 - 0.75 g) measured on the equalised balance. The designated precision of the measurement was to within ± 0.0005 g, with water then injected through the septa.

- The system was then monitored to ascertain when the injected water had fully evaporated. This was identified by a combination of visual checks through the chamber windows, and a monitored increase of internal pressure rise, approximately equivalent to the anticipated vapour pressure.

- This measured vapour pressure within the chamber would then be negated from the desired P_T value of 0.1 MPa, for the necessary partial pressure calculations. Having established each new pressure fraction, the individual reactants were introduced to the system, as before beginning with H₂.

- With each gas fraction added, the reactants were then mixed in preparation for ignition and testing.

7.2 Stoichiometric BFG/H₂O Mixtures

As with studies provided in previous chapters, results will be presented from use of the nonlinear method of numerical processing, which was performed subsequent to the computational evaluation of growing flame radii. Corresponding results obtained using the linear technique are provided with all tabulated data in Appendix B.6. Fig. 7.1 shows examples of the plotted change in radial growth for each of the four tested BFG mixtures with the addition of H₂O.

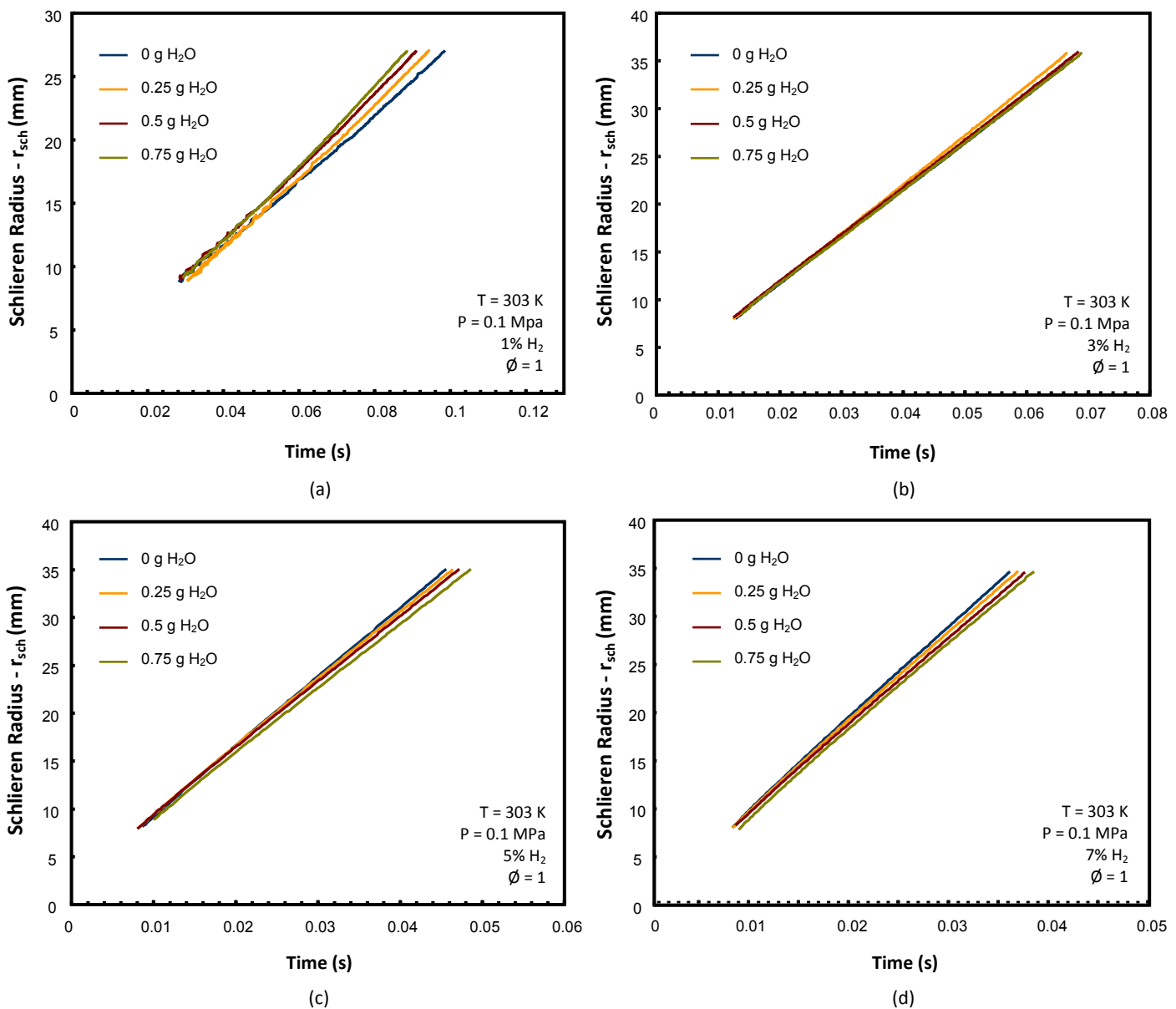


Fig. 7.1 – Plotted growth of flame radii for the 1 % (a), 3 % (b), 5 % (c), and 7 % (d) H₂ BFG mixtures, with the four injected masses of H₂O.

Initial trends evident in Fig. 7.1 suggest contrasting behaviour exhibited by the flame resulting from addition of H₂O, as the H₂ fraction within the fuel is increased: Inasmuch that propagation rate is perceived to increase with water content for the 1 % H₂ mixture, and conversely the flame inhibited for the corresponding 7% H₂ tests.

7.2.1 – Relationship between Stretch and Flame Speed

These trends can be analysed further when evaluating the relationship between stretch rate and flame speed. Fig. 7.2 – Fig. 7.5 give examples of the association of S_n plotted against α for each of the tested BFG mixtures, and increasing masses of injected water (with evaluated nonlinear relationships superimposed).

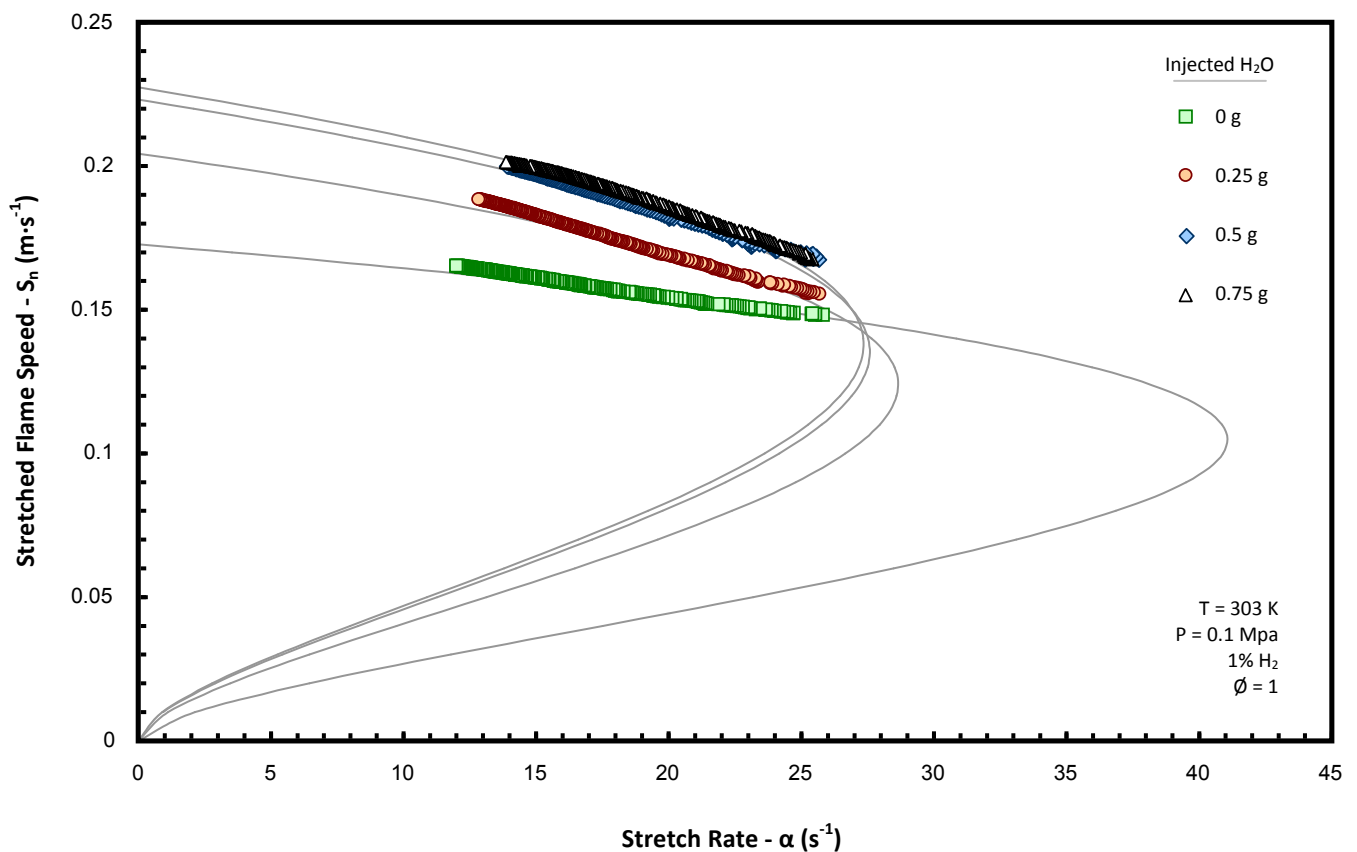


Fig. 7.2 – Samples of stoichiometric 1% H₂ BFG/air S_n against α data with increasing water fraction.

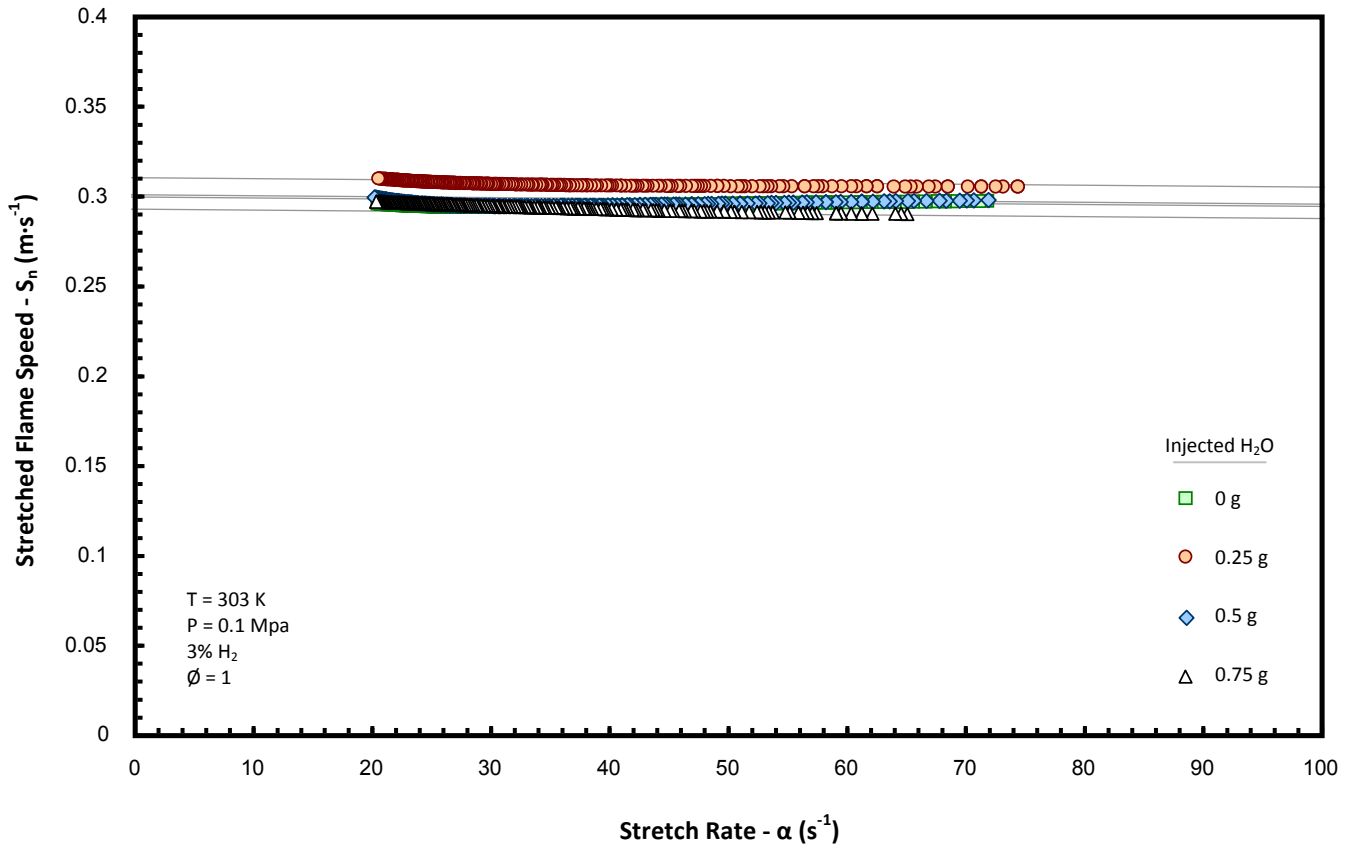


Fig. 7.3 – Samples of stoichiometric 3% H₂ BFG/air S_n against α data with increasing water fraction.

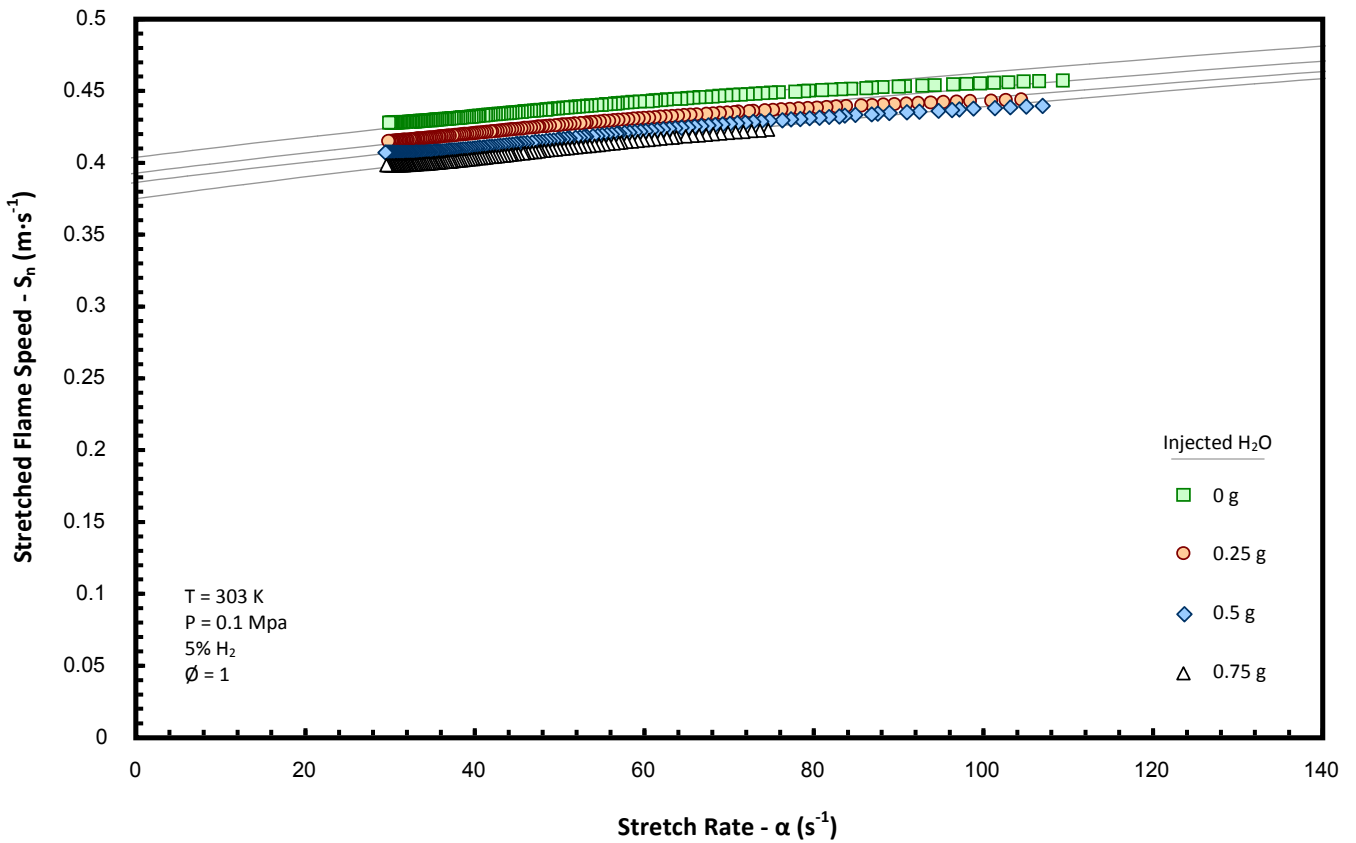


Fig. 7.4 – Samples of stoichiometric 5% H₂ BFG/air S_n against α data with increasing water fraction.

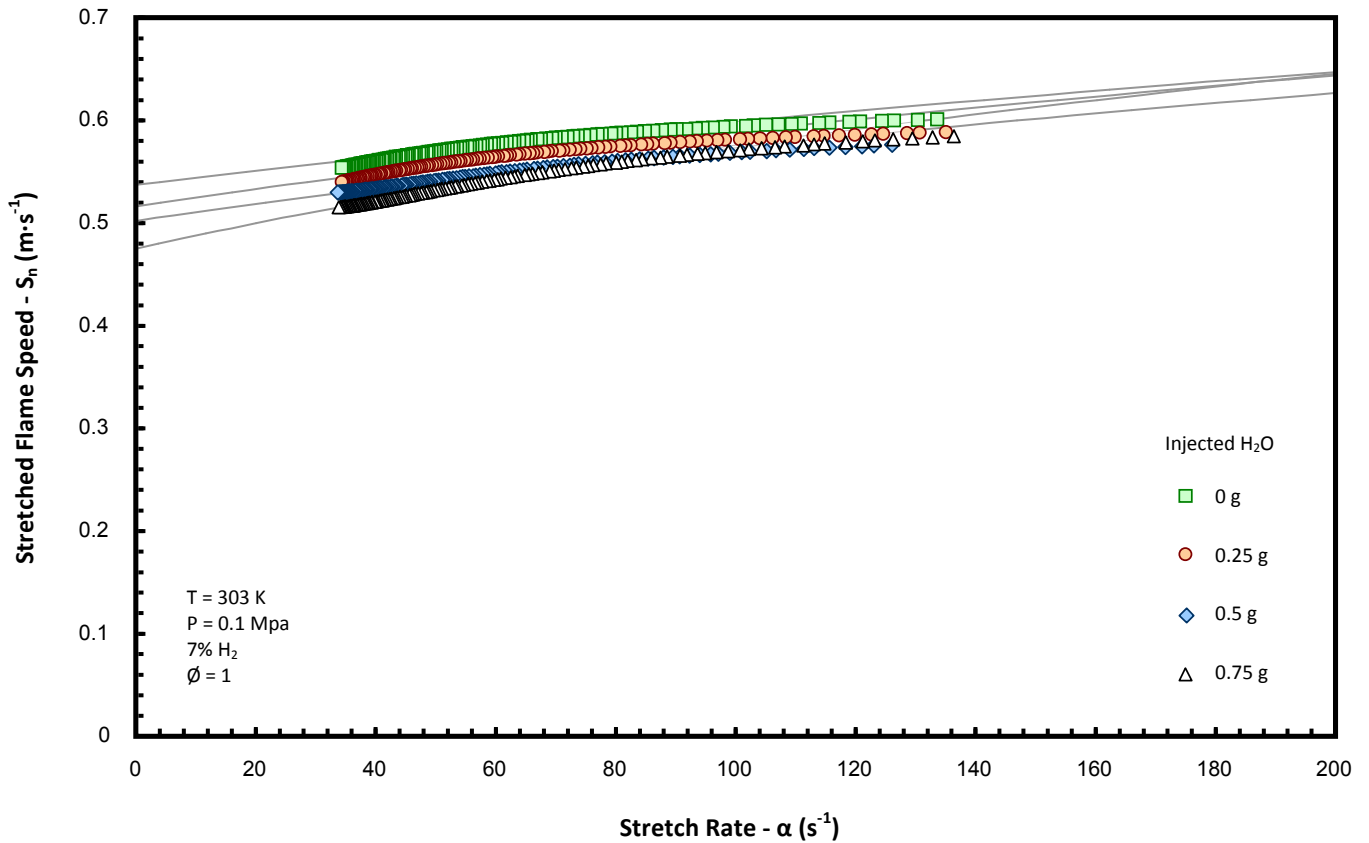


Fig. 7.5 – Samples of stoichiometric 7% H₂ BFG/air S_n against α data with increasing water fraction.

It is evident from Fig. 7.2 – Fig. 7.5 that the employed BFG mixtures exhibit non-monotonic behaviour between stretched propagation and an increase in H₂O fraction. The influence of stretch rate on flame growth appears to be exaggerated with the addition of water, as gradients of plotted data become increasingly steep in either the positive or negative direction. This trend is further visualised in Fig. 7.6 where the obtained values of L_b are plotted for all mixtures against increasing H₂O fraction. Ostensibly the plotted values of L_b for the 1 and 7% H₂ mixtures diverge with an increase in water fraction, however if the positive values are examined further (for the 1 and 3% mixtures), the influence of stretch appears to peak before beginning to fall. Plotted values of measured S_u , suggest a trend of initial convergence as shown in Fig. 7.7. Inasmuch that the 1% H₂ mixture is shown to initially accelerate with water addition, compared to the 7% flame which is only quelled.

7. BFG H₂ Fluctuation - Variation in H₂O Concentration

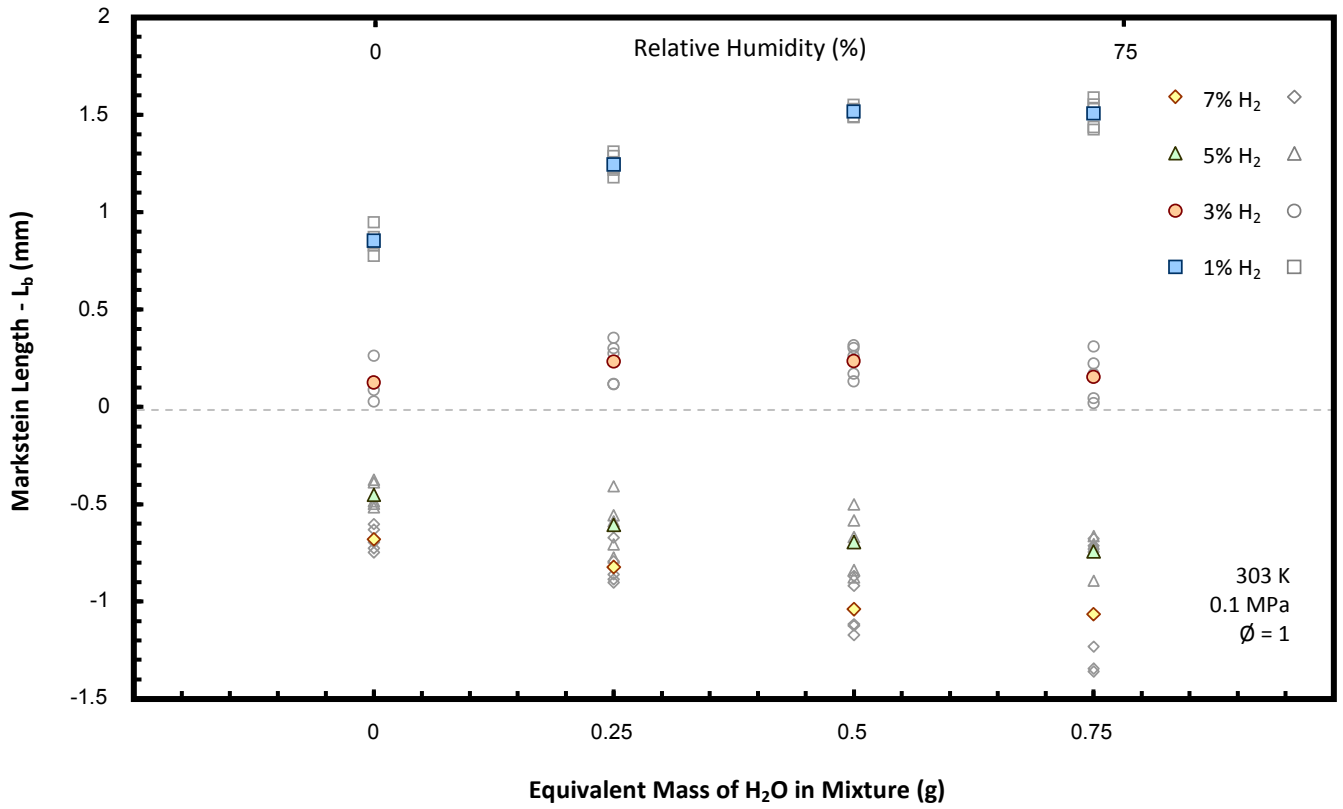


Fig. 7.6 – Measured individual (grey), and averaged (coloured) values of L_b for all BFG mixtures with increasing H₂O.

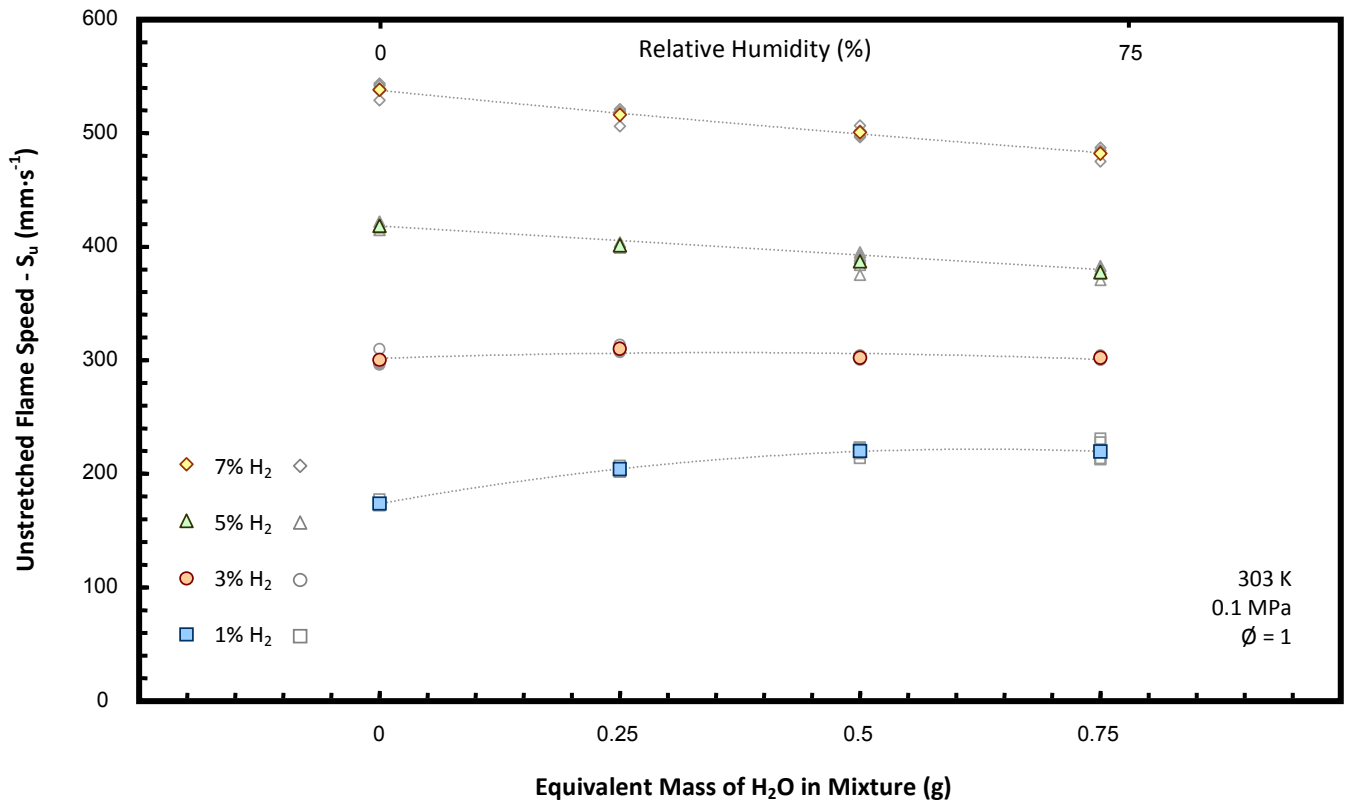


Fig. 7.7 – Measured individual (grey), and averaged (coloured) values of S_u for all BFG mixtures with increasing H₂O.

The non-monotonic behaviour exhibited by the tested BFG blends for change in H₂O fraction suggests two competing influences on propagation: Firstly a predictable suppressive effect whereby water acts as a diluent, and speed is slowed by a reduction in flame temperature. The second proposed influence is more subtle, and results from changes in flame thermochemistry and an increase in the overall reaction rate, due to changes in production of intermediate chemical species. For BFG blends containing low concentrations of H₂, the addition, and subsequent disassociation of H₂O results in the production of more reactive intermediate radicals such as H, OH, and HCO, and subsequent reaction pathways, for instance; $\text{H}_2\text{O} + \text{O} \leftrightarrow 2\text{OH}$, $\text{H}_2\text{O} + \text{H} \leftrightarrow \text{H}_2 + \text{OH}$, $\text{CO} + \text{H}_2\text{O} \leftrightarrow \text{HCO} + \text{OH}$, and $\text{CO} + \text{OH} \leftrightarrow \text{CO}_2 + \text{H}$ [125]. Furthermore the catalysing effect of these radicals on CO consumption reactions have been shown to reduce the slow terminating reaction $\text{CO} + \text{O} = \text{CO}_2$ [125]. The suppressive effect of H₂O as a diluent is counteracting this, and appears to become more dominant as the water fraction increases, flame temperature decreases, and subsequently propagation begins to slow. Furthermore, if the fuel blend contains higher fractions of H₂, larger quantities of intermediate radicals are inherently produced from a proportionate increase in reactions such as $\text{CO} + \text{H}_2 \leftrightarrow \text{H} + \text{HCO}$ anyway, hence the catalytic influence of H₂O is lost, and the flame suppression effect is consistently dominant.

Chemical kinetic computations have been performed to try and vindicate this explanation. CHEMKIN-PRO was utilised together with the reaction mechanism developed by Li *et al.* [164] to model combustion of the tested BFG blends, with Fig. 7.8a and Fig. 7.8b showing the respective maximum modelled molar fractions of H and OH radicals for each test. The plots demonstrate similar trends to the values obtained for unstretched flame speed, whereby the influence of H₂O increase is more substantial for BFG blends containing 1% H₂. Although not shown, the modelled data suggest analogous trends for other intermediate species such as HCO. The maximum H fraction is also shown to decrease for the 7% H₂ mixture as the production rate drops with heat release.

7. BFG H₂ Fluctuation - Variation in H₂O Concentration

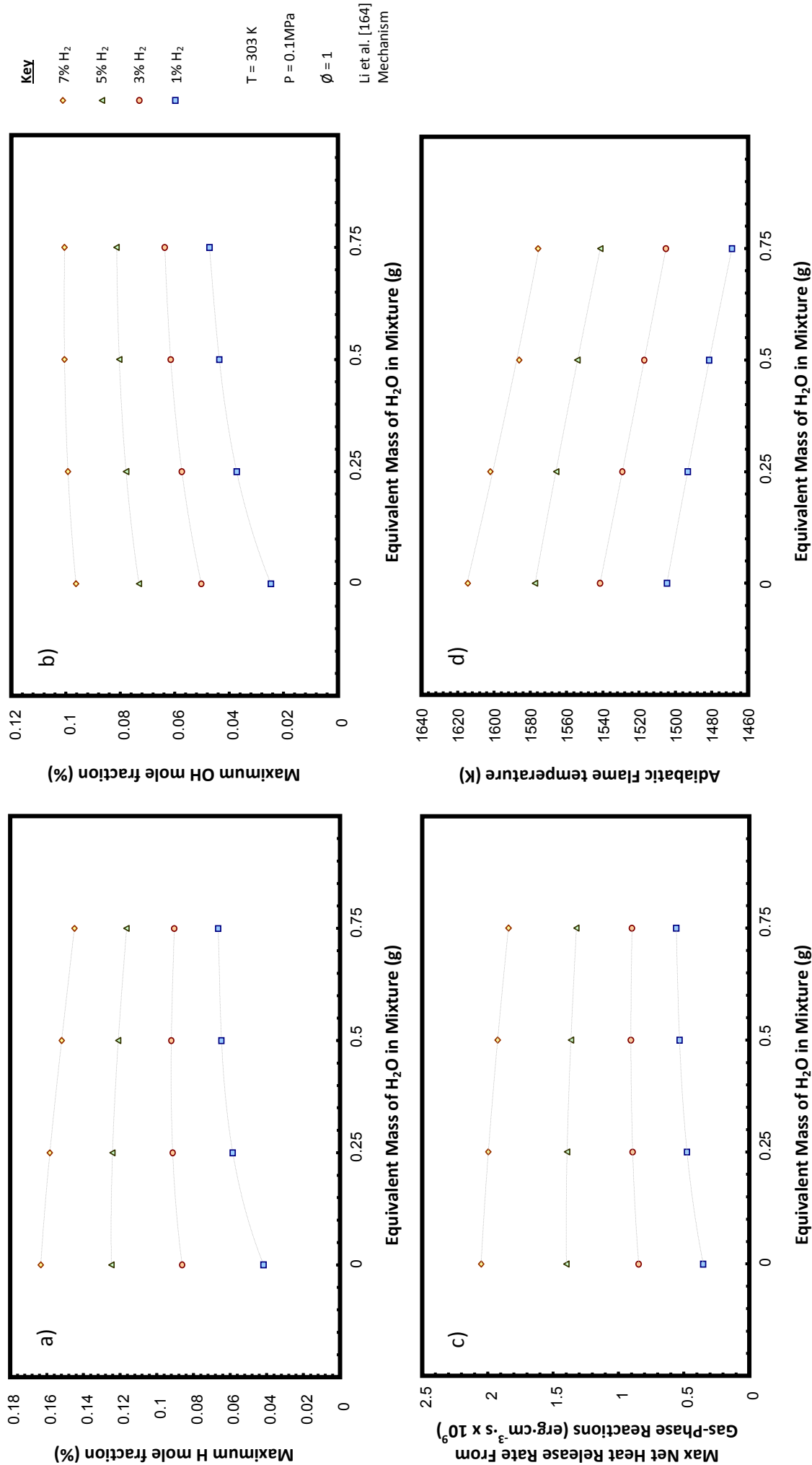


Fig. 7.8 – Computationally modelled values of: a) Maximum H fraction, b) maximum OH fraction, c) maximum net heat release, and d) adiabatic flame temperature for each tested stoichiometric BFG blend, with rise in injected water fraction.

Fig. 7.8c shows a plot of the modelled maximum net heat release rate from the gas phase reactions, with results again following analogous trends to those previously observed. This plot is distinctive however, as it ties directly to observed changes in the behaviour of flame stretch influence. For the 1% H₂ mixture, the maximum heat release rate is shown to rise to a plateau in the same way as observed values of L_b . This suggests maximum net heat release rate increases together with thermal diffusivity in the reaction zone in relation to mass diffusion, resulting in an overall increase in L_e . However, the parallel lowering of adiabatic flame temperature (Fig. 7.8d) and suppression of the flame induced by an increase in H₂O fraction will apparently become more dominant eventually leading to acceleration of the flame with stretch rate. This is significant because the non-monotonic behaviour in evidence could lead to operational instability of highly stretched flames not only as a result of compositional fuel variation, but also mixture moisture content.

7.2.2 – Measured and Computational Values of Laminar Burning Velocity

Analogous chemical models performed using the Li et al. [164] mechanism were used to obtain values for the burned/unburned gas density ratio, as necessary for the conversion of S_u to u_L . Fig. 7.9 shows the plotted values obtained for each mixture (further details in 7.3.2).

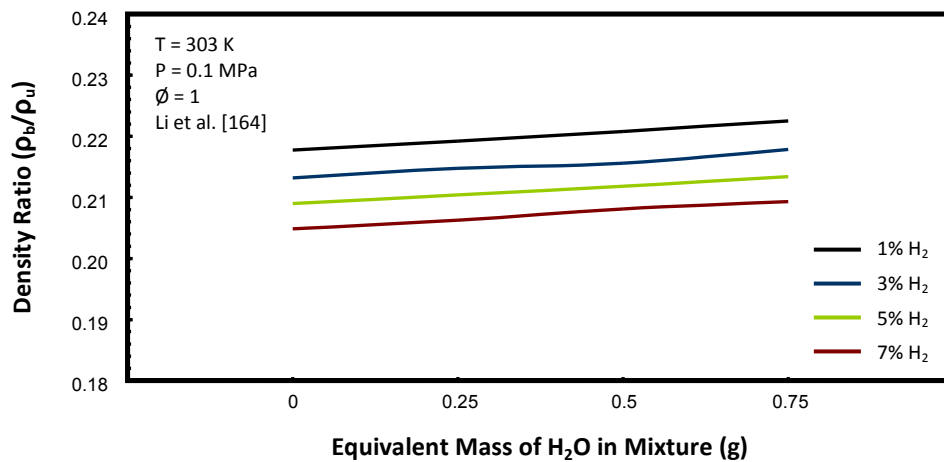


Fig. 7.9 – Modelled values of adiabatic density ratio for each stoichiometric mixture.

The average values of S_u were combined with the obtained density ratios to give equivalent values of u_L , as plotted in Fig. 7.10, together with speeds modelled by the Li *et al.* [164] and Davis *et al.* [165] reaction mechanisms in CHEMKIN-PRO. The apparent trends are similar to those evident with S_u and L_b data, where change in burning velocity for each mixture is non-monotonic with respect to water addition. The addition of 0.75 g of water to the 1 % H₂ blend (equivalent to an overall mole fraction change of 0 to ~5 percent), can be seen to increase u_L by 1.1 cm·s⁻¹ or ~30 %. In comparison, introducing the equivalent quantity of water to the 7 % H₂ mixture results in a reduction in flame speed of 0.86 cm·s⁻¹ or ~8 %.

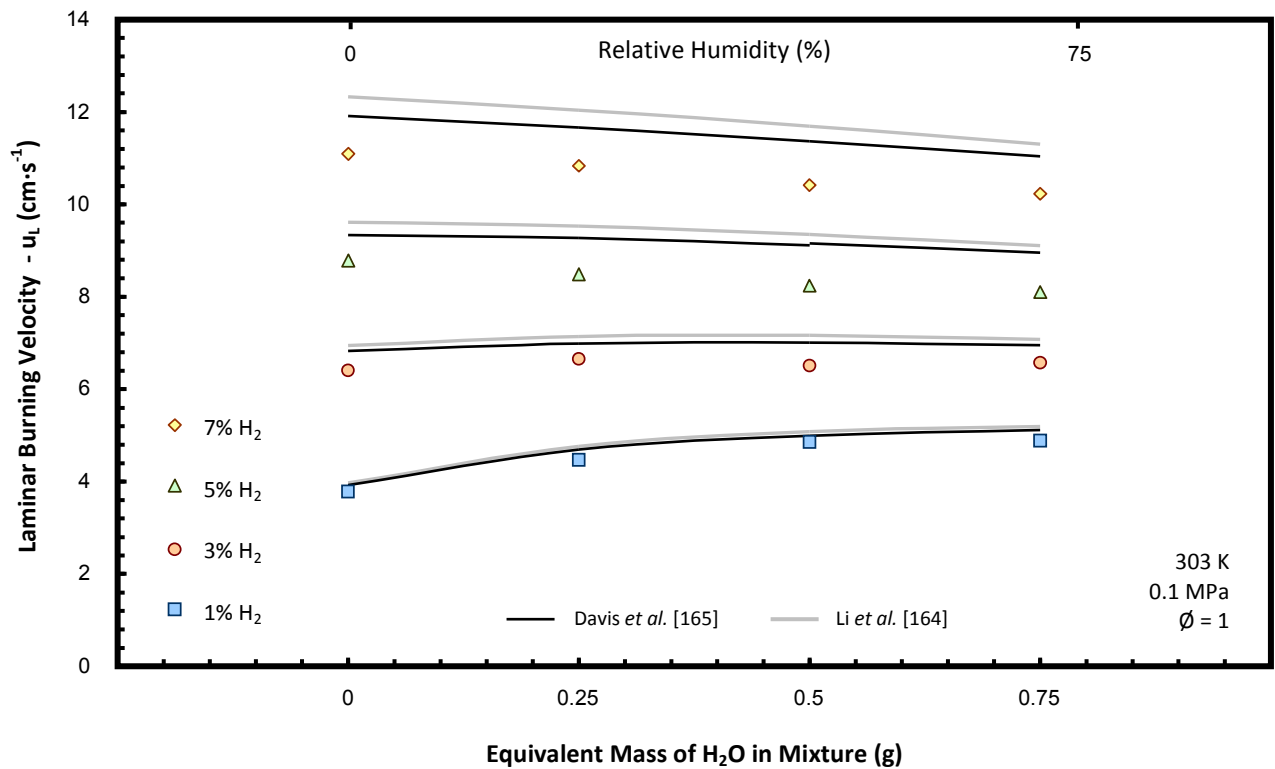


Fig. 7.10 – Experimental and modelled values of u_L for each stoichiometric BFG mixture against water addition.

As discussed in the previous section, there is apparent positive change in thermal diffusivity with the lowest H₂ BFG mixture, which is proportional to u_L when combined with overall reaction rate [27]. It is therefore understandable that there is a parallel relationship in the acceleration in u_L for water addition, and the change in influence of stretch as characterised by the obtained values of L_b .

Analogous trends of respective acceleration and deceleration for the 1 and 7 % H₂ mixtures are also seen for the modelled values of u_L with water addition, plotted in fig 7.10. An increased overestimation in modelled flame speed is evident as the H₂ percentage increases, as was the case with stoichiometric data presented in section 5.3. The Davis et al. mechanism [165] appears to provide closer representative values to experimental results. However, a better standard error of the estimate could be made once further data at different equivalent ratios were obtained.

7.3 Variation in Equivalence Ratio of BFG/H₂O Mixtures

Further testing was undertaken at lean and rich conditions to investigate the change in relative influence of moisture addition to variable BFG mixtures. Fig. 7.11 demonstrates the change in spherical propagation rates at the extreme tested conditions: 1 and 7% H₂, with 0 and 0.75 g of H₂O addition. Water is again shown to have opposing influences on each mixture.

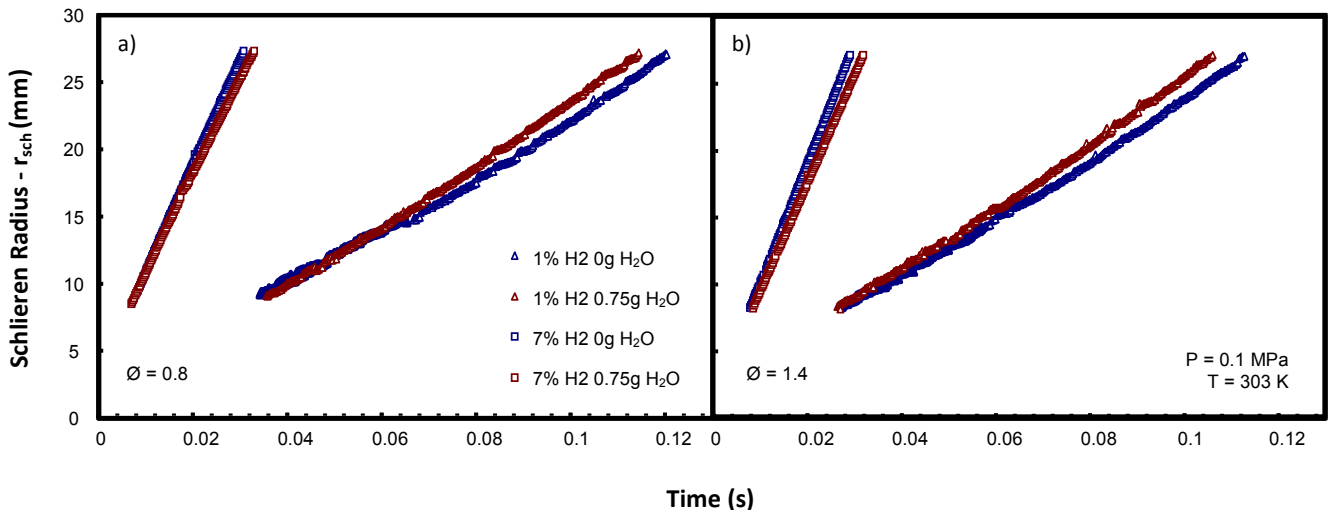


Fig. 7.11 – Examples of propagating flame radii for 1 and 7 % H₂ BFG mixtures, for a) $\phi = 0.8$, b) $\phi = 1.4$.

7.3.1 – Relationship between Stretch and Flame Speed

The analysed flame radii were again processed using the nonlinear methodology, with Fig. 7.12 and Fig. 7.13 giving examples of the obtained relationships between S_n and α , for each tested mixture.

7. BFG H₂ Fluctuation - Variation in H₂O Concentration

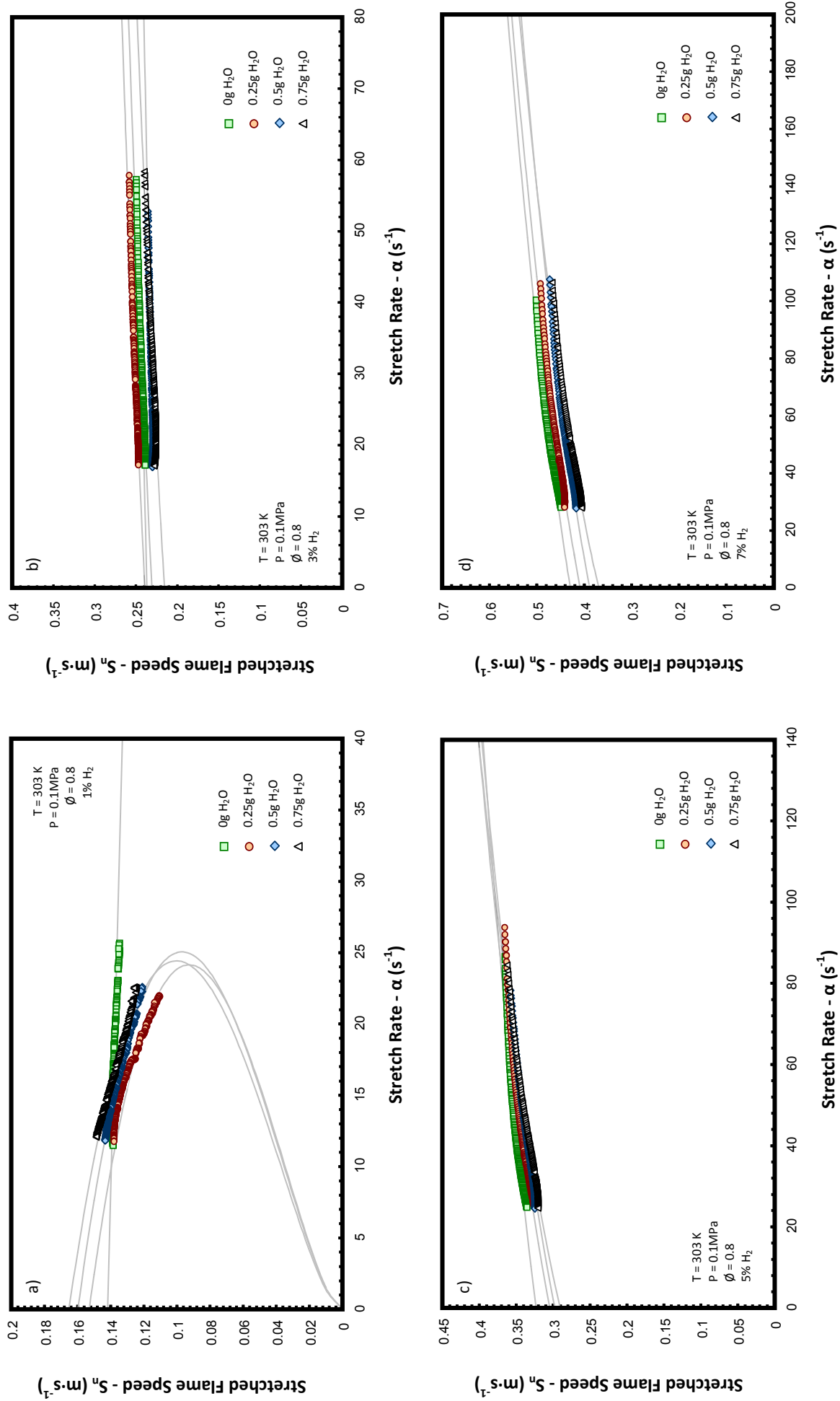


Fig. 7.12 – Samples of a) 1 %, b) 3 %, c) 5 %, d) 7% H₂ BFG/air S_n against α with increasing water fraction, for $\phi = 0.8$.

7. BFG H₂ Fluctuation - Variation in H₂O Concentration

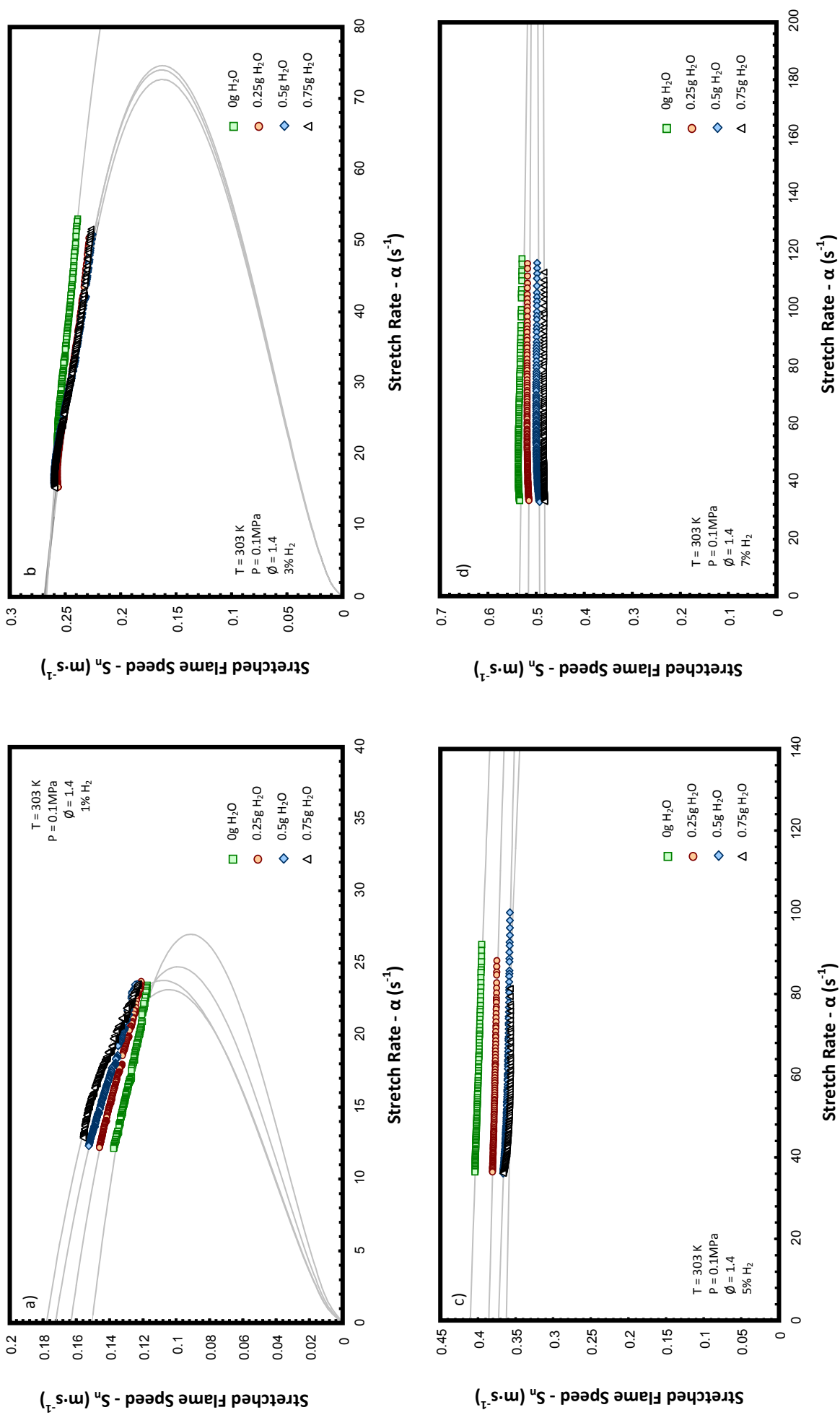


Fig. 7.13 – Samples of a) 1 %, b) 3 %, c) 5 %, d) 7% H₂ BFG/air S_n against α data with increasing water fraction, for $\phi = 1.4$.

Trends similar to the stoichiometric dataset are observed, with water addition shown to increase gradients in the 1% H₂ plot, and the inverse tendency demonstrated to a lesser extent with the 7 % H₂ mixture. However H₂O addition does appear to have a more significant influence on the leaner mixture with respect to flame stretch, a tendency more easily visualised in Fig. 7.14 and Fig. 7.15 where the obtained values of L_b are plotted (grey points representing individual tests).

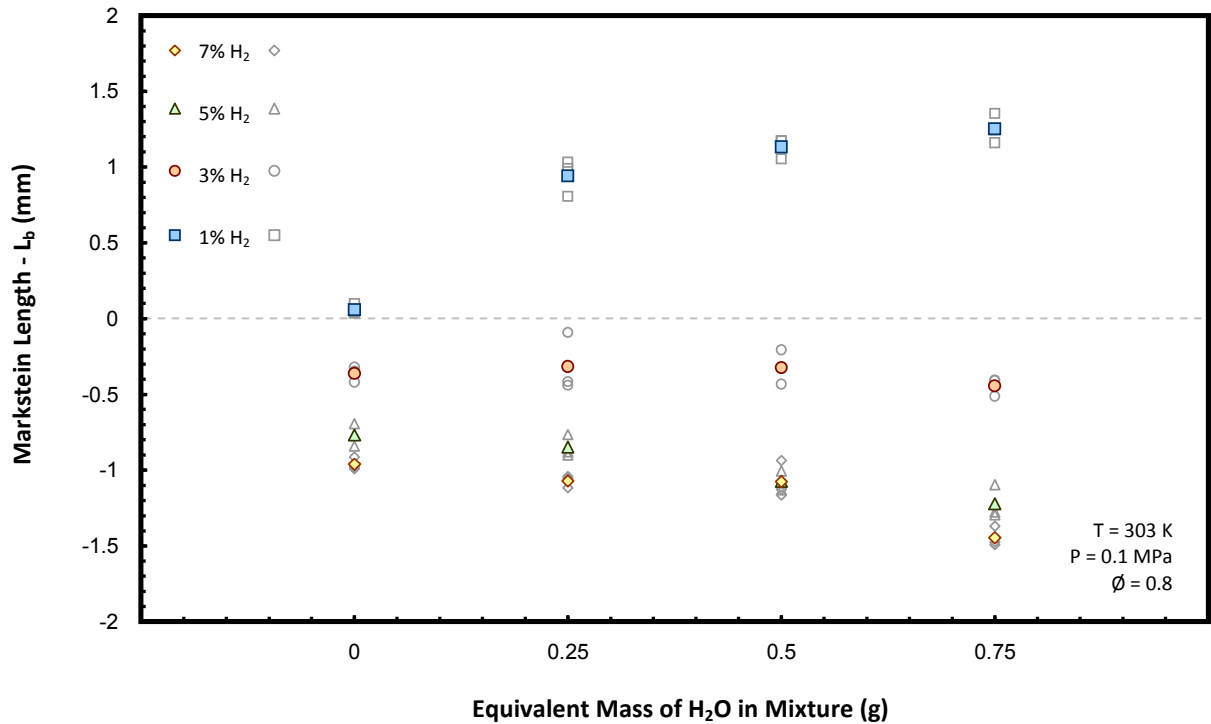


Fig. 7.14 – Values of L_b for BFG mixtures with increasing H₂O addition, for $\phi = 0.8$.

The positive values of L_b for the 1 % H₂ $\phi = 0.8$ mixture are shown to increase appreciably with water addition compared to data for the other BFG mixtures. In comparison, the richer data (in Fig. 7.15) for the 1% H₂ mixture, does not demonstrate such a significant increase. This suggests that the enhanced thermal diffusivity induced by chemical heat release (discussed in section 7.2.1) is lessened for rich conditions. Furthermore, all initial values of L_b for the rich mixture are initially positive, with the higher H₂ fuel L_b decreasing by a smaller magnitude than the corresponding lean blends. This leads to a difference in the 1 and 7% H₂ L_b values that is approximately doubled for the $\phi = 0.8$ mixture at 0.75 g H₂O when compared with the rich, and therefore suggests wet lean mixtures are more heavily influenced when highly

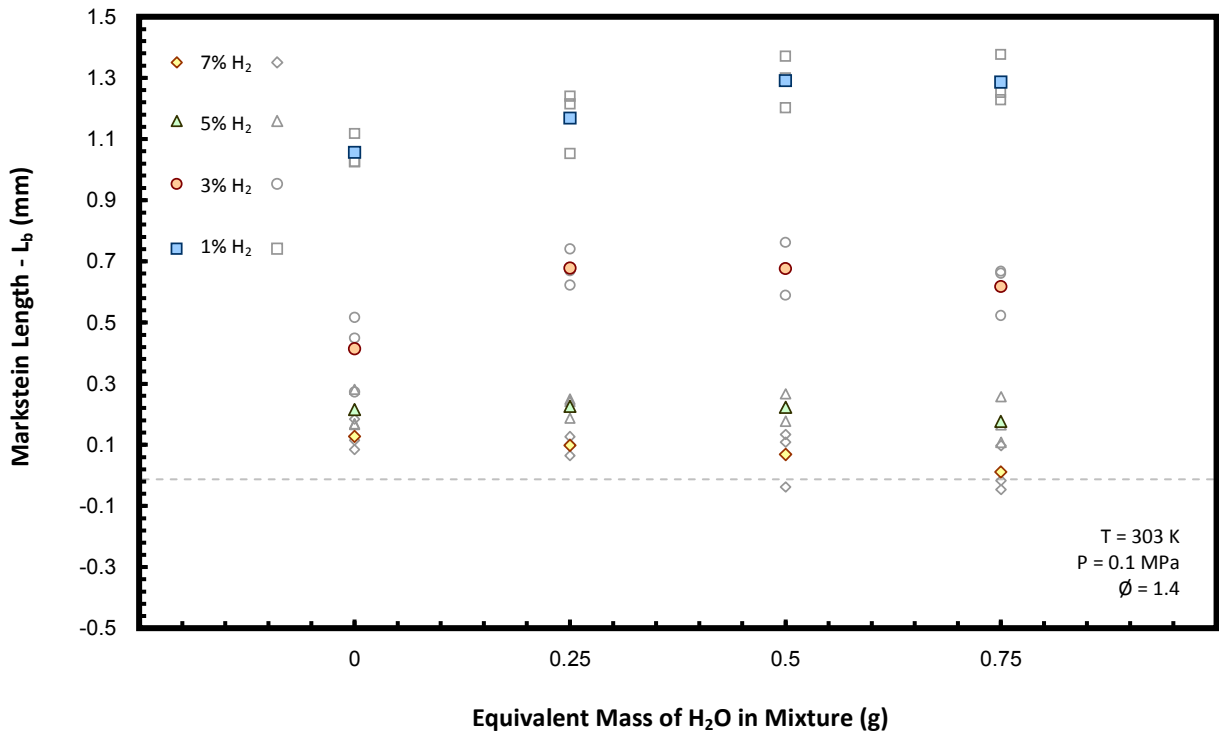


Fig. 7.15 – Values of L_b for BFG mixtures with increasing H₂O addition, for $\phi = 1.4$.

stretched in turbulent operational combustion systems [29]. The 3% H₂ mixture appears to be least influenced by the change in moisture addition, with an apparent balance in the induced chemical and diluent effects across the tested range.

The obtained values of unstretched flame speed have been plotted in Fig. 7.16 ($\phi = 0.8$) and Fig. 7.17 ($\phi = 1.4$) with grey individual tests, and the average coloured. The results demonstrate similar tendencies to the stoichiometric dataset, with opposing influences on the 1 and 7% H₂ mixtures. The effective compression of values resulting from water addition means the factor of increase in S_u between the 1 and 7% blends decreases from ~ 3.1 to 2.2 for the lean mixtures, and from ~ 3.6 to 2.6 for the rich. There is a greater difference between the rich mixtures as a result of the shift in peak flame speed, caused by the increase in H₂ (as discussed in section 5.2.2) in the BFG fuel fraction.

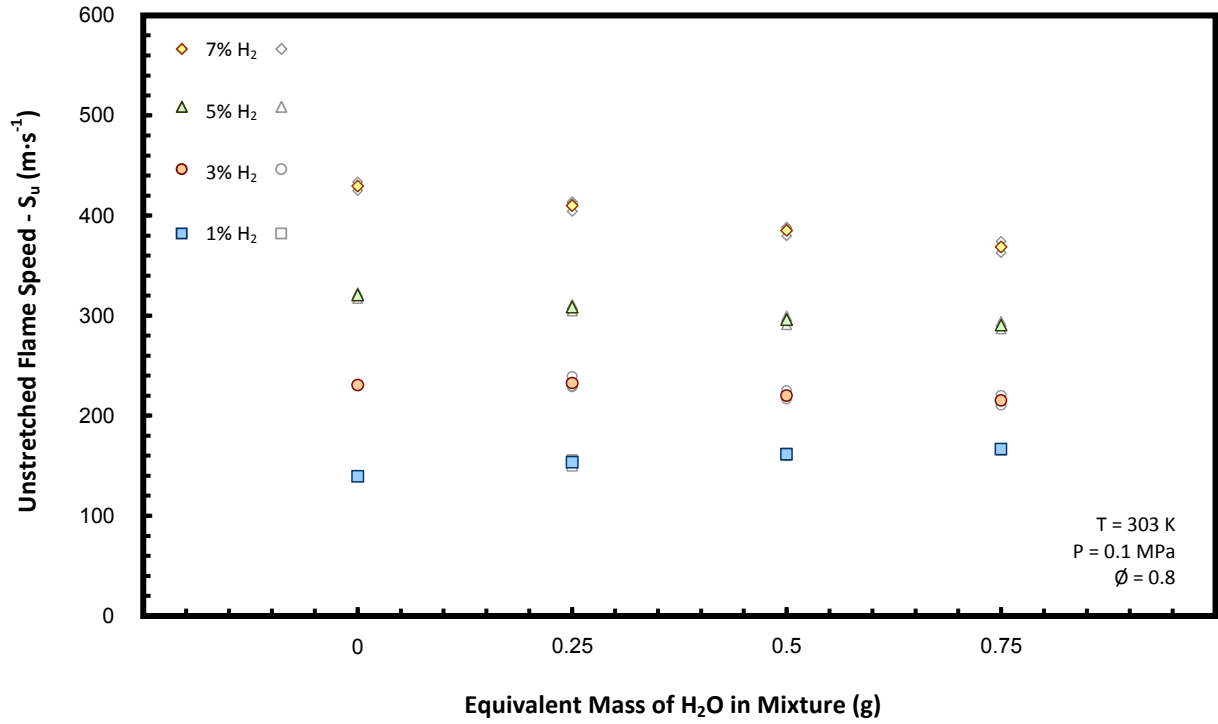


Fig. 7.16 – Plotted values of S_u for BFG mixtures with increasing H₂O addition, for $\phi = 0.8$.

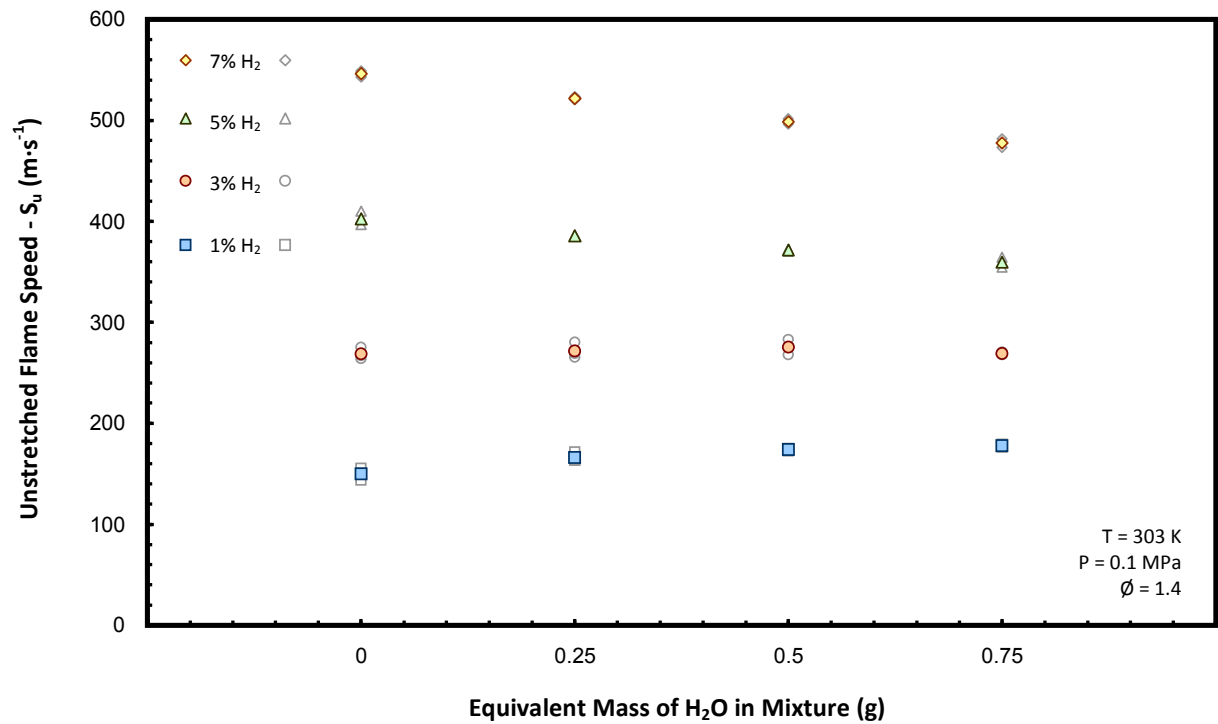


Fig. 7.17 – Plotted values of S_u for BFG mixtures with increasing H₂O addition, for $\phi = 1.4$.

7.3.2 – Measured and Computational Values of Laminar Burning Velocity

Density ratios were again obtained with CHEMKIN-PRO using the Li *et al.* [164] reaction mechanism, and are plotted in Fig. 7.18. A comparative analysis was again performed to check the difference in returned density values from multiple reaction mechanisms, with a disparity of <0.1%. Consequently the Li *et al.* [164] reaction mechanism was arbitrarily chosen to be consistent with previous chapters. The decrease in reactant density, drop in adiabatic flame temperature, and increase in burned product density leads to ratios rising as H₂O is added to each mixture.

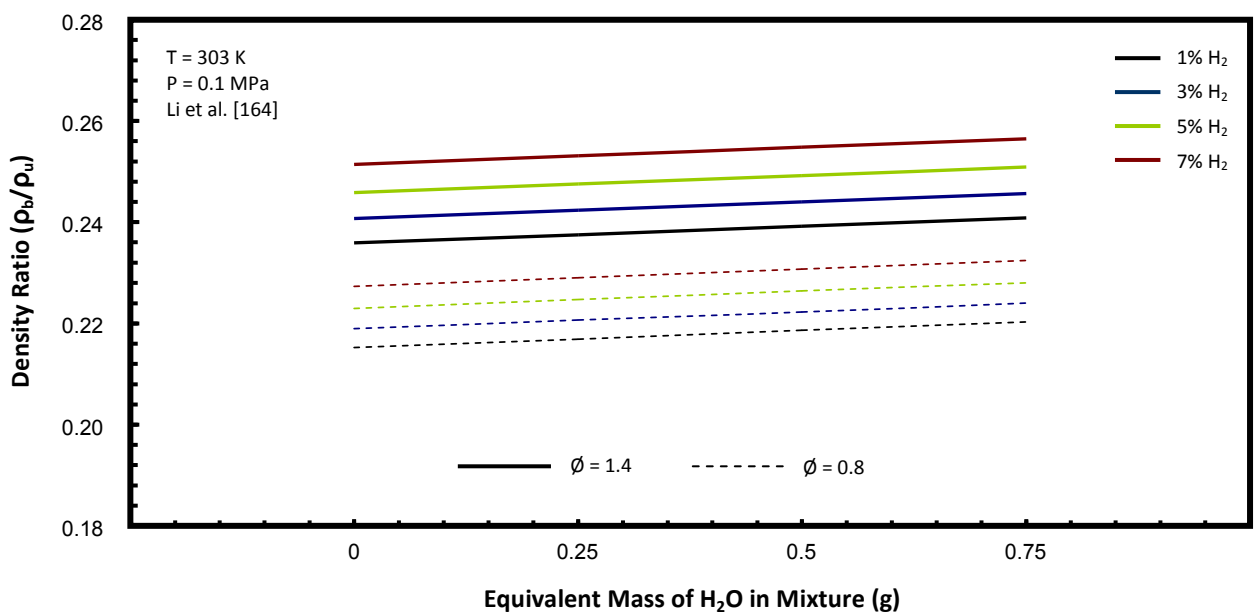


Fig. 7.18 – Plotted values of density ratio with increasing H₂O addition, for $\phi = 1.4$, and $\phi = 0.8$.

The obtained values of density ratio were combined with the average unstretched flame speed for each tested condition to give equivalent values of u_L , and are plotted in Fig. 7.19 ($\phi = 0.8$), and Fig. 7.20 ($\phi = 1.4$). Parallel trends are evident between the two presented datasets, and the ones shown for the stoichiometric case; with speeds increasing for the 1% H₂ mixture, and the trend inverting for the 7% H₂ case. The 1% H₂ mixture u_L increases by $0.7 \text{ cm}\cdot\text{s}^{-1}$, (22.1 %) for the lean mixture, and by $0.79 \text{ cm}\cdot\text{s}^{-1}$ (21.1 %) for the rich. In comparison respective drops of 1.16 (13%) and $1.3 \text{ cm}\cdot\text{s}^{-1}$ (10%) are seen for 7% H₂ BFG, suggesting a higher relative influence on the lean mix.

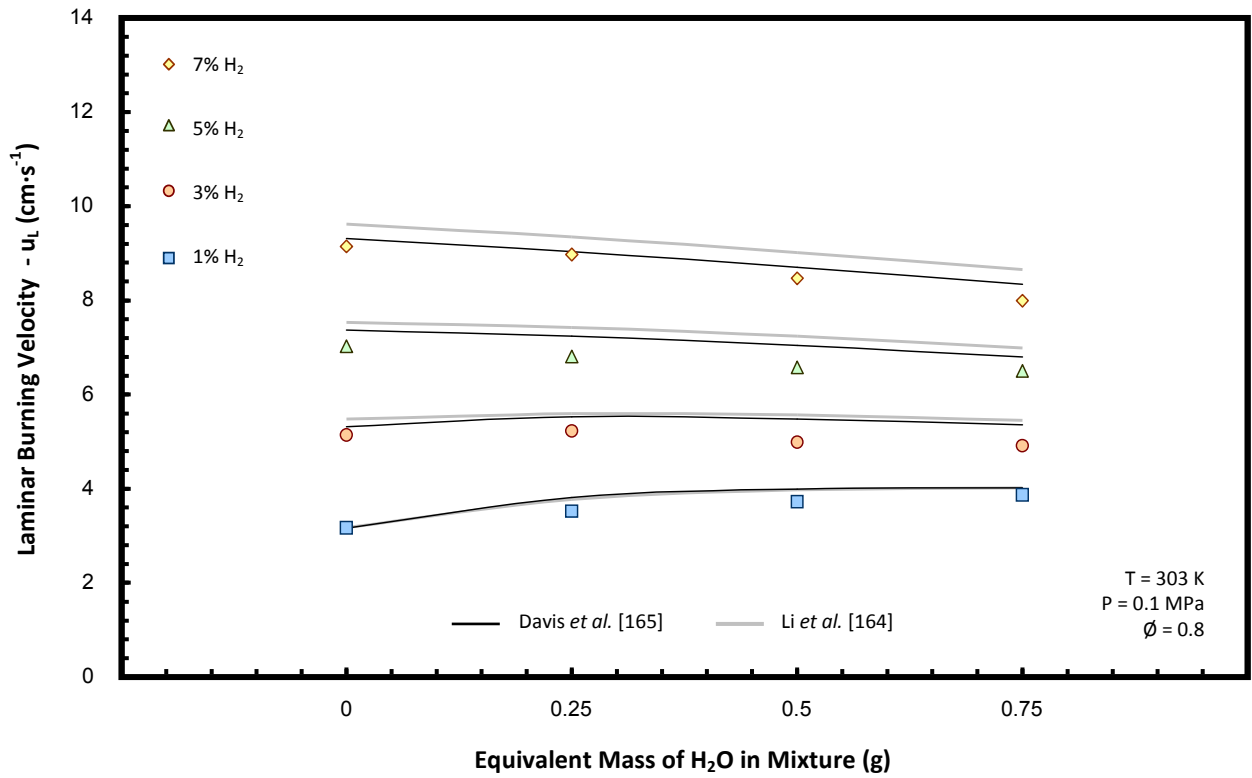


Fig. 7.19 – Average experimental and modelled BFG u_L with increasing H_2O addition for $\phi = 0.8$.

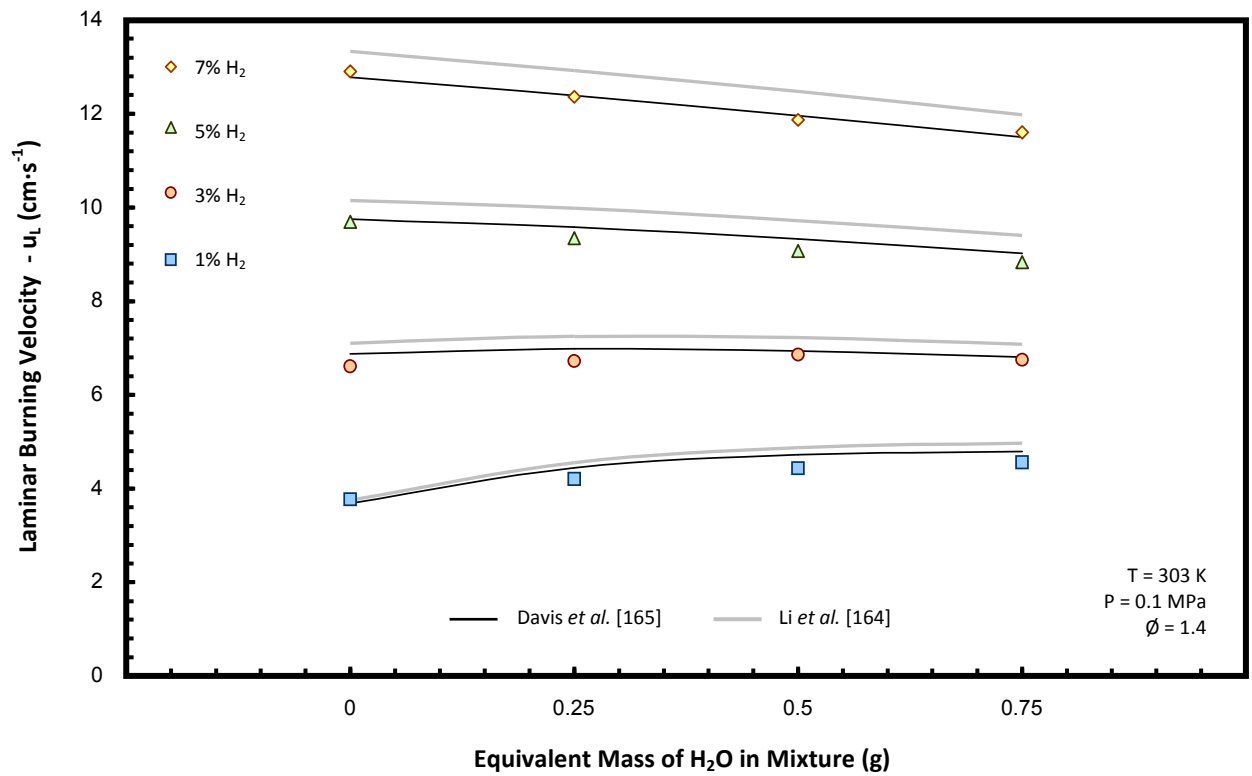


Fig. 7.20 – Average experimental and modelled BFG u_L with increasing H_2O addition for $\phi = 1.4$.

Superimposed onto each plot are relationships modelled using the freely propagating flame configuration in CHEMKIN-PRO, and the Li *et al.* [164] and Davis *et al.* [165] reaction mechanisms. A full specification of the employed kinetic mechanisms is provided in section 5.3. Closer associations between the experimental data and modelled values are evident when compared with the stoichiometric values, particularly at rich conditions. The Davis *et al.* mechanism especially demonstrates favourable performance when modelling BFG combustion with small quantities of water vapour. A standard error of the estimate (SEE - Eqn. (5.2)) was again used to quantify the respective performance of the two employed reaction mechanisms, with comparative results provided in table 7.2 for all tested equivalence ratios.

Table. 7.2 – SEE values averaged for each H₂ mixture with change in H₂O fraction.

SEE (cm·s ⁻¹)				
H ₂ O mass (g)	0	0.25	0.5	0.75
Ø = 0.8				
Li <i>et al.</i> [164]	0.38	0.42	0.53	0.50
Davis <i>et al.</i> [165]	0.21	0.30	0.38	0.32
Ø = 1				
Li <i>et al.</i> [164]	0.84	0.89	0.95	0.84
Davis <i>et al.</i> [165]	0.59	0.65	0.74	0.66
Ø = 1.4				
Li <i>et al.</i> [164]	0.40	0.53	0.53	0.43
Davis <i>et al.</i> [165]	0.16	0.21	0.20	0.16

The calculated values of SEE have been averaged for all tested H₂ percentages in each BFG mixture, to evaluate which is numerically superior for modelling overall water addition. There is a repeatable trend for models to initially decrease in accuracy as water fraction is increased, before improving for all 0.75 g H₂O mixtures, and this evident for both tested reaction mechanisms. It is clear from the figures in table 7.2 and Fig. 7.19 and Fig. 7.20 that the Davis *et al.* [165] mechanism suggests better numerical agreement with the attained experimental data for H₂O addition.

7.3.3 – Practical Implication of Obtained Results

For each of the tested BFG mixtures and equivalence ratios, there is an apparent convergence in u_L as a consequence of H₂O increase. This suggests that water addition is influential from the perspective of reducing premixed combustion instabilities that result from variation in BFG H₂ fraction. As was performed in chapter 5, this can be emphasised by analysing theoretical critical velocity gradients that prevent boundary layer flashback as an example. Again flame thickness was calculated from modelled temperature profiles and approximated to d_q , with application of Eqn. (2.3), to give the values plotted in Fig. 7.21 (the figure shows worst case conditions only; 0 and 0.75 g H₂O, with 1 and 7 % BFG H₂ for clarity).

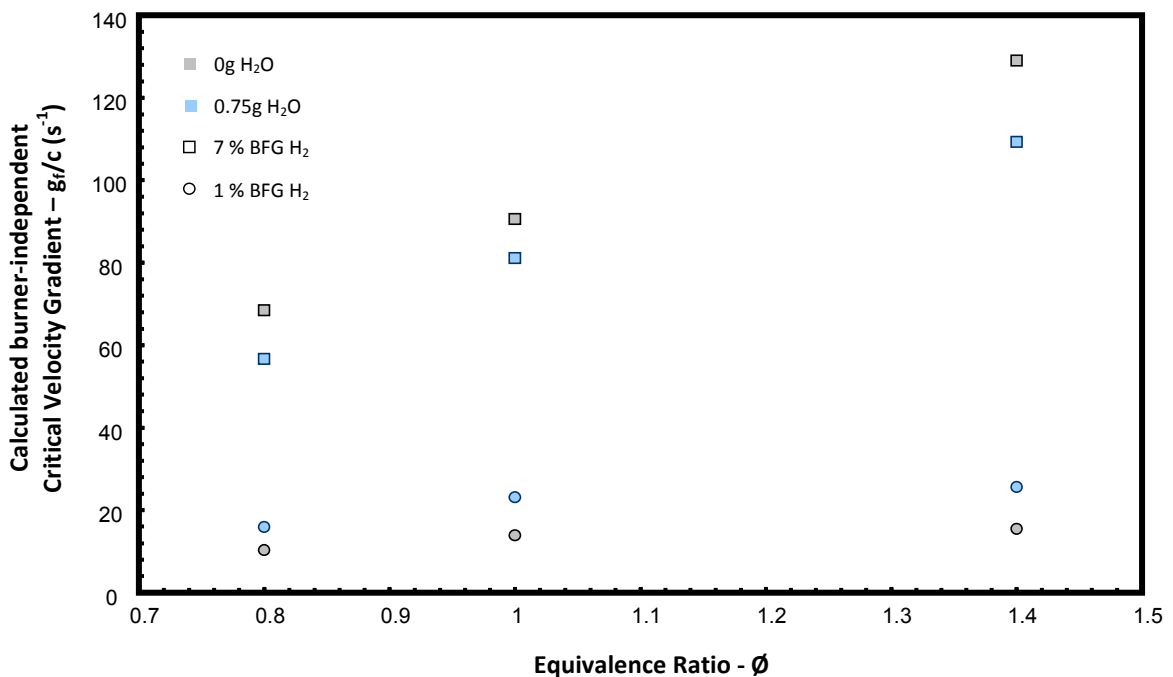


Fig. 7.21 – Theoretical g_i/c values that prevent boundary layer flashback, for selected BFG compositions.

Taking the stoichiometric case as an example, the factor of difference between the calculated gradients for the 1 and 7% H₂ mixtures is almost halved by the addition of 0.75g H₂O (all calculated values of flame thickness and velocity gradients are provided for each plotted mixture in Appendix B.6). However, the exaggerated change in the influence of flame stretch (and any subsequent impact on combustive behaviour) is not accounted for in this example, with operational testing required to fully characterise this effect.

7.4 Quantifying Experimental Uncertainty

The observed changes in flame speed presented in this chapter were relatively small, increasing the importance of quantifying, and trying to reduce, the measured uncertainty. The same method was used as has been employed previously (detailed in section 4.3), with slight adjustments required for the calculation of the total bias (B_{Su}).

An additional uncertainty factor was introduced to account for the addition of water to the reactant mixture. The relationship between each obtained value of S_u , and the amount of injected water was used to estimate the influence of uncertainty in the measured water mass. This was achieved by fitting a third order polynomial relationship to each data set, and calculating the resultant change from the measured uncertainty in water mass. A conservative value of ± 0.01 g was used for this calculation, two orders of magnitude higher than the precision of the employed balance, but exaggerated to account for the human element of repeatability in measurement and any error in the polynomial fit.

The number of experimental repetitions was increased to five for the stoichiometric case in an attempt to reduce the σ_{su} for each condition. For five tests the employed t (95 % confidence) value also reduces to 2.776 from 4.303 for three repetitions [161], thereby lowering the overall calculated values of total uncertainty (U_{su}). Fig. 7.22 plots the measured stoichiometric S_u values, with $\pm U_{su}$ shown superimposed in error bars. It is evident from the figure that the estimated uncertainty in each measurement was considerably smaller than the changes observed from H₂O addition for the most variable (1 and 7% H₂) mixtures. If the calculated uncertainty had not been smaller than the observed changes in u_L for H₂O addition, then the number of repetitions would need to have been increased further (for example increasing the performed repeats to 10 would have reduced the t value by a further ~20 % to 2.262).

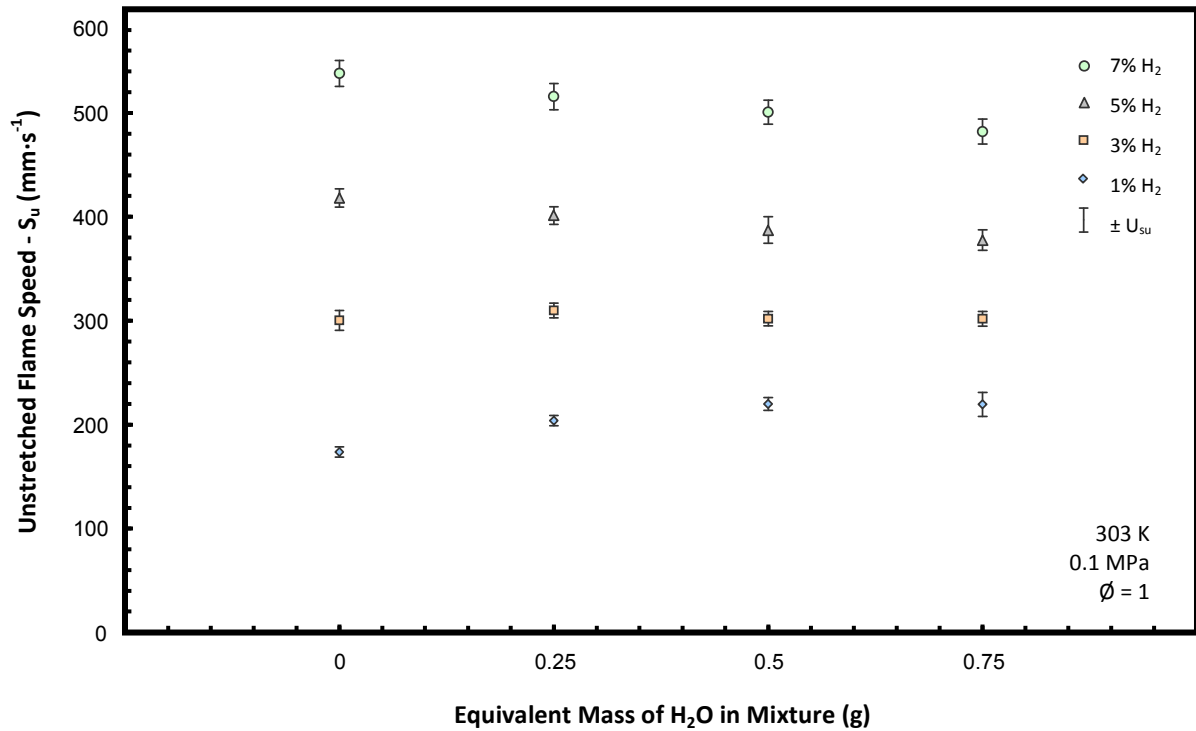


Fig. 7.22 – Values of average stoichiometric BFG S_u with increasing H₂O addition and calculated U_{su} .

For testing with variation in equivalence ratio there were limitations with the amount of remaining BFG, and therefore the number of experimental repeats was reduced to three. Consequently the t values and calculated $\pm U_{su}$ were larger, and have been seen superimposed on each dataset in Fig. 7.23 and Fig. 7.24, with all presented data available in Appendix B.6.

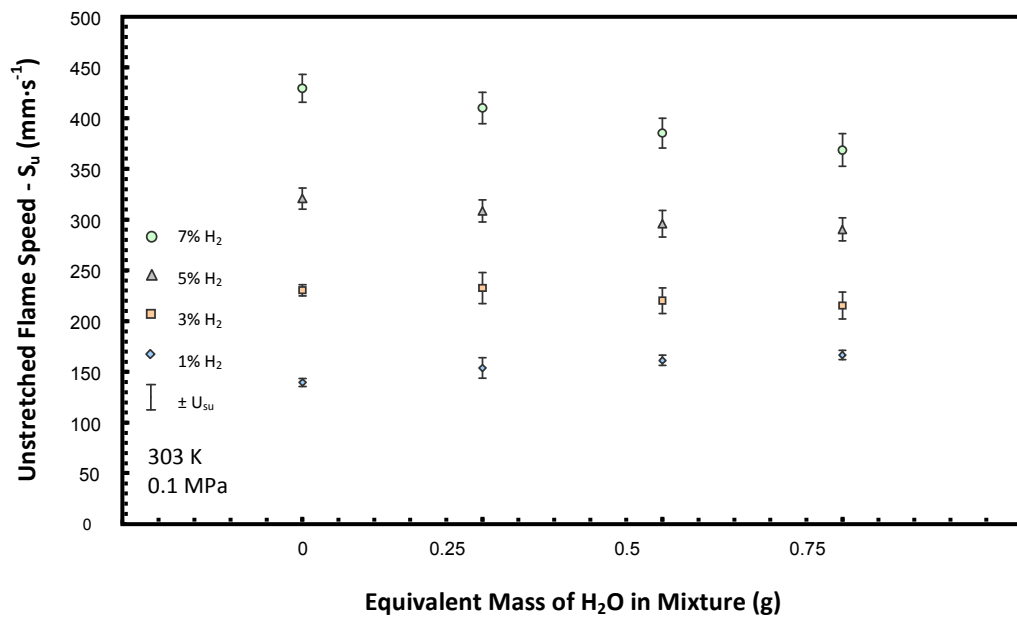


Fig. 7.23 – Average BFG S_u with increasing H₂O addition and calculated U_{su} for $\phi = 0.8$.

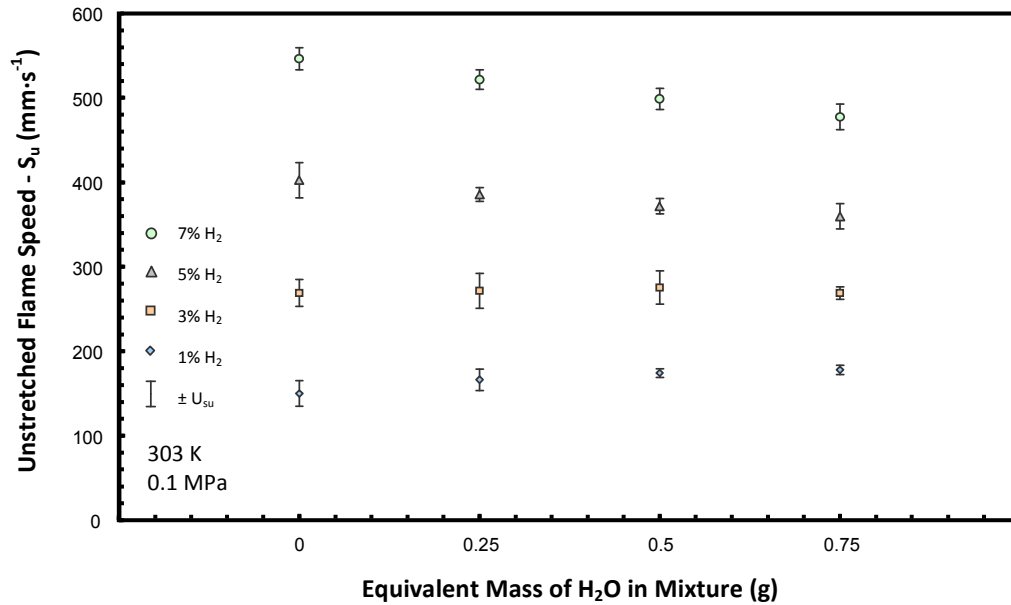


Fig. 7.24 – Average BFG S_u with increasing H₂O addition and calculated U_{su} for $\phi = 1.4$.

7.5 Summary and Conclusions

In this chapter the influence of variation in H₂ fraction of BFG was investigated further for change in relative humidity of the fuel. Masses of water up to 0.75 g were introduced to the reactant mixture, thereby increasing the water fraction to ~72% of the vapour pressure.

The introduction of a water component to the fuel fraction was shown to have a potentially non-monotonic divergent influence on the attained results, as a function of the amount of original H₂ in the fuel blend. For mixtures comprising low fractions of H₂, the addition of water was shown to have a catalysing effect, with measured flame speeds, and resultant laminar burning velocities shown to increase. Conversely, the corresponding values for BFG blends containing larger H₂ fractions decreased as more water was added. This suggests water addition has a potentially beneficial influence in reducing the amount of fluctuation in u_L , and subsequent operational instabilities, resulting from fluctuation in BFG H₂ fraction. Two opposing mechanisms of diluent suppression and gas thermochemistry enhancement have been discussed in comparison with modelled data of flame reaction kinetics.

A similarly opposing influence on flame stretch was also in evidence, with rates of propagation of low H₂ mixtures shown to be increasingly decelerated for addition of water with stretch rate increase, and the opposite in evidence for the higher H₂ mixtures. The influence of water on Markstein Length was shown to be increased for leaner conditions, with propagation therefore more susceptible to thermo-diffusive instability from the influence of flame stretch. Nevertheless the significant impact on burning velocity suggests that burning BFG mixtures with high relative humidity lowers the potential for instability resulting from H₂ variation.

The results demonstrate reasonable overall agreement with chemical models, and the performance of two reaction mechanisms numerically evaluated. Simulations performed using the Davis et al. [165] reaction mechanism were shown to be in better agreement with the experimental data, as water fraction within the fuel blend increased.

Chapter 8. Further Steelworks Gas Testing

Thus far, research presented in this dissertation has predominantly focussed on the potential for variability in the combustive properties of compositionally dynamic BFG. The work comprised within this chapter concerns the combustion of COG and BOS gas, both independently, and when blended with BFG.

8.1 Coke Oven Gas

As described in section 1.3.1, and 2.1.2, COG is a fuel that results from the high temperature carbonisation of coal, and as a consequence predominantly comprises large quantities of H₂, CH₄ and CO. Therefore, not only does it have a much higher calorific value than BFG, but also a faster flame speed. In order to characterise how effectively COG can be used to enhance and stabilise BFG combustion, first representative properties of laminar burning velocity and Markstein length had to be benchmarked for standalone combustion of the fuel.

8.1.1 – Defining Experimental Parameters

In order to test a representative COG mixture, firstly a suitable fuel composition had to be defined. The basis of this definition were the chromatographic measurements detailed in section 2.1.2, which predominantly agreed with values given by other references [12]. The average molar composition given from the specified analyses contained small fractions of higher hydrocarbons, notably Ethane (C₂H₆ - 0.5 %mol) and Ethylene (C₂H₄ - 1.7 %mol). These constituents were combined as part of the CH₄ fraction, as it was estimated that any resultant change in flame speed would be minimal. This follows from the work of Liao et al. [159] who investigated the laminar burning velocity of natural gas containing higher hydrocarbons in relation to CH₄, and found minimal difference. Chemical models were also performed (GRI-Mech 3.0

reaction mechanism, section 4.2.2 for further details) which suggested a change in measured flame speed of <1 %. The resultant molar composition of the representative COG mixture is provided in Table 8.1.

Table 8.1 – Representative COG composition acquired for COG testing.

Fuel component	Mole Fraction (%)
CO ₂	1.5
N ₂	4.0
CO	7.1
CH ₄	25.6
H ₂	61.8

Combustion of this COG mixture was characterised for three repetitions of nine equivalence ratios in the range 0.7–1.5, undertaken at representative atmospheric ambient conditions of 303 K and 0.1 MPa. The required filming rate of the camera was adjusted to account for the increase in anticipated flame speed, specified at 7,000 fps. This value was maximised to allow for fastest capture of the entire flame, and whilst filming rate could be increased, this would necessitate a lowering of the camera resolution. This resulted in a decrease in the relative accuracy of the COG tests, as fewer frames could be employed compared to the CH₄ and BFG data. This is accounted for in the calculated experimental uncertainty (see section 4.3.1 for further detail). Partial pressure calculations were performed to determine the necessary values for each specified equivalence ratio, with the employed oxidiser again a dry zero-grade air.

8.1.2 – Relationship between Stretch and Flame speed

The Schlieren files were computationally processed to give propagating values of the flame radius, with both linear and nonlinear numerical techniques employed to evaluate the behaviour of stretch. Fig. 8.1 and Fig. 8.2 show examples of the processed data for all equivalence ratios with the fitted nonlinear association superimposed onto each dataset.

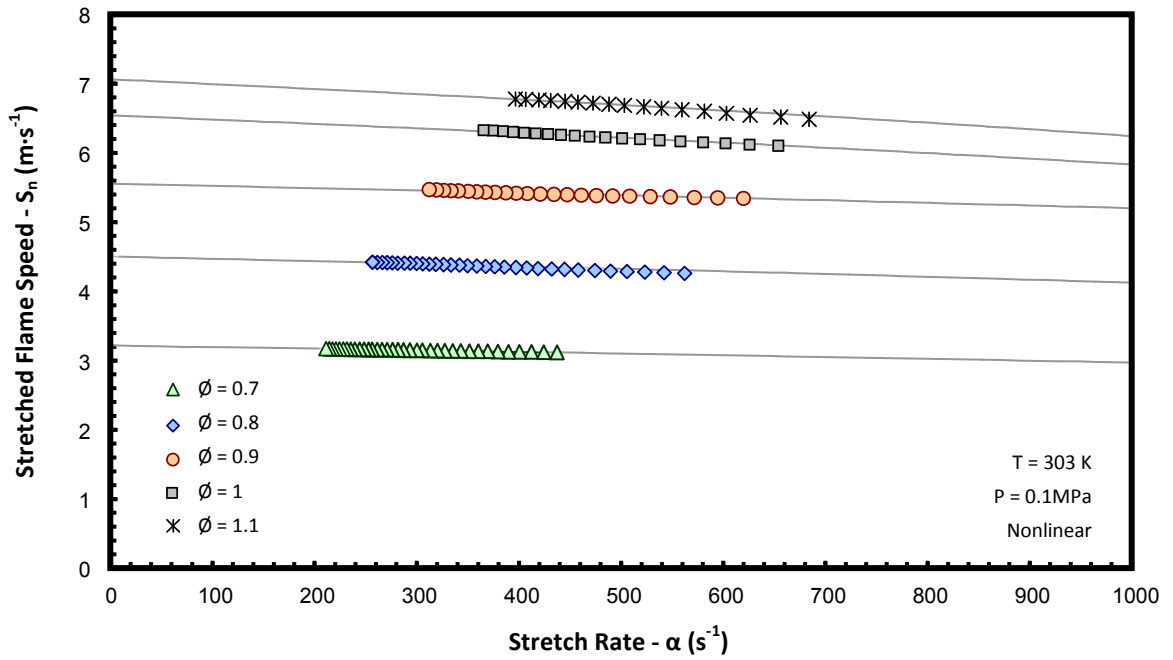


Fig. 8.1 – Samples of COG/air S_n against α relationships, for $\phi = 0.7 - 1.1$.

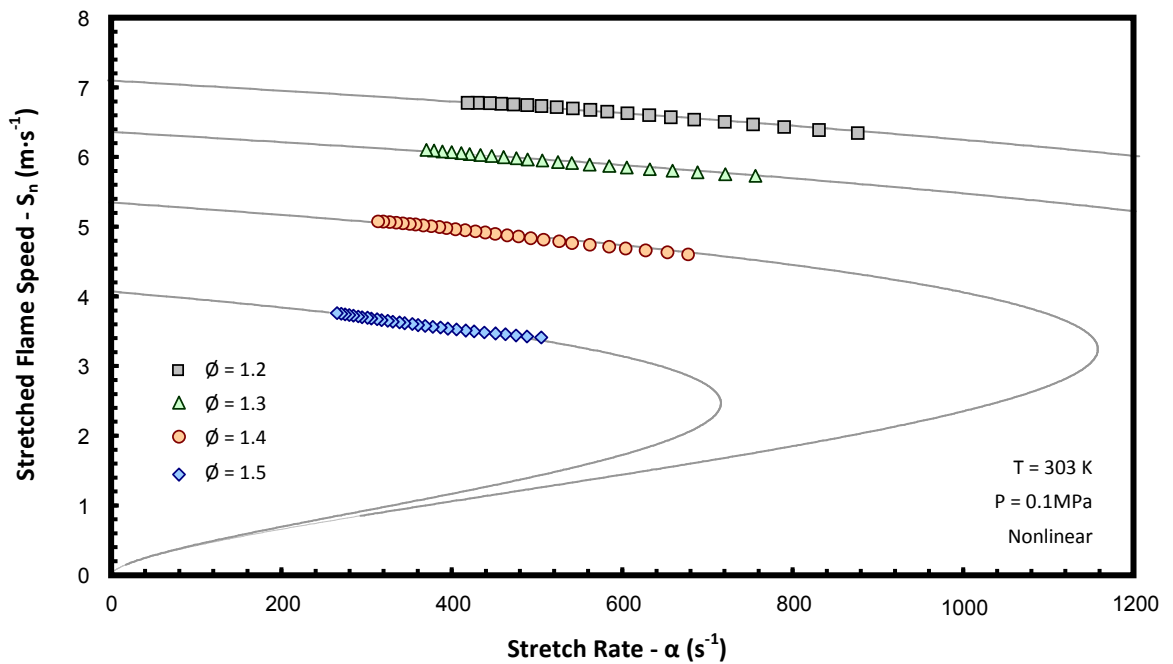


Fig. 8.2 – Samples of COG/air S_n against α relationships, for $\phi = 1.2 - 1.5$.

The plots have been separated to avoid overlapping data and improve clarity. It is evident from the gradients of the plotted values that propagation becomes more heavily influenced by flame stretch as equivalence ratio increases. All observed gradients in the specified range are also negative, implying a positive value of L_b and a corresponding decrease in flame speed as stretch rate increases. These trends are

more easily visualised in the plotted values of L_b as given in Fig. 8.3, with the results of individual tests (grey) shown alongside averaged data (coloured).

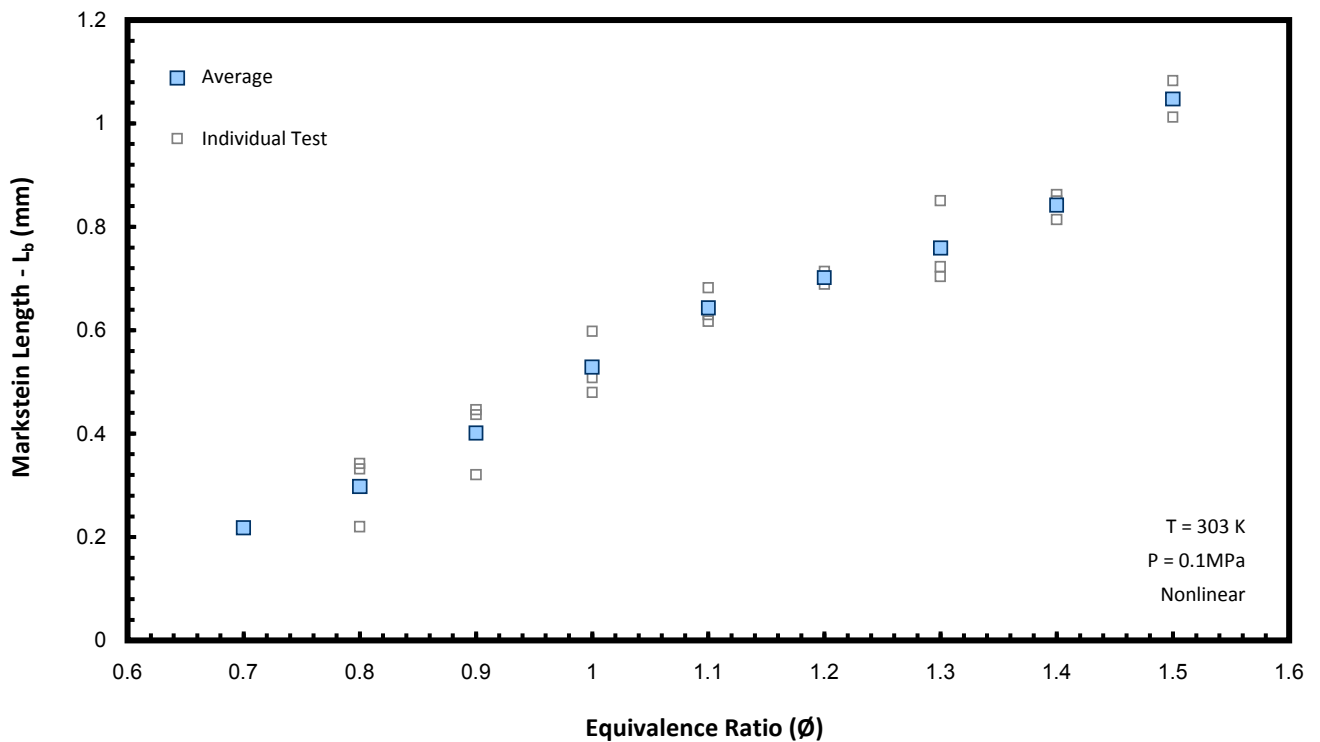


Fig. 8.3 – Individual and average values of COG/air L_b against equivalence ratio.

The plotted tendency presents a notable similarity to the CH_4 benchmarking data presented in Chapter 4. All values being positive indicates preferential thermal diffusion in relation to mass and Lewis numbers greater than one. This is interesting as the most significant fuel fraction is H_2 , which is more than double the nearest constituent CH_4 fraction; and an increase in H_2 tends to provide a decrease in the measured L_b , as was seen with the BFG results and data from other institutions [111]. However, the negative offset in L_b resulting from H_2 addition is increased by the presence of heavier inert diluents in the fuel fraction [123], which is minimal for COG (respective molar CO_2 and N_2 fractions of 1.5 and 4 %). This tendency is continued in Fig. 8.4 where all experimental S_u data are plotted, together with the averages, against equivalence ratio. Data is shown to peak at marginally rich conditions, again similar to the methane dataset. The plotted values of S_u are however, much faster than those

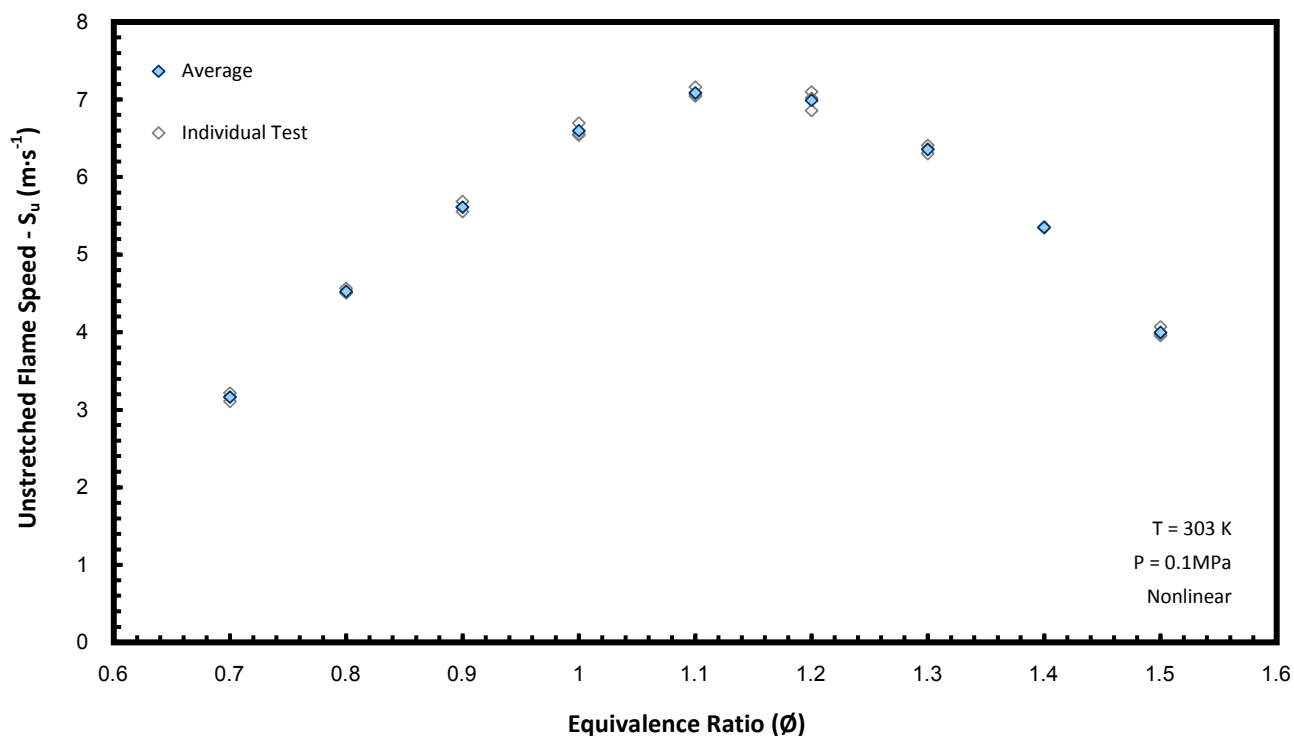


Fig. 8.4 – Plotted values of COG/air S_u against equivalence ratio.

observed for methane; a result of the preponderant H_2 component of the fuel fraction. The results also demonstrate significant variation between the peak measured flame speeds, and the extreme values of each tested equivalence ratio. These increasing gradients of the profile indicate that when burning the fuel at heavily lean or rich conditions, there will be potentially more variation induced by a change in equivalence ratio, and hence increased chance of instability. The repeatability of the COG dataset is good, and of a similar order to tests previously performed, with typical standard deviations in measured S_u of around two percent. This will be discussed further with experimental uncertainty in section 8.1.3.

8.1.3 – Measured and Computational Laminar Burning Velocity

As the performances of reaction mechanisms are optimised for combustion of certain fuels, the options for modelling COG were more limited, with only the Li et al. [164] and GRI-Mech 3.0 reaction mechanisms employed (the Davis et al. [165] mechanism does not contain the requisite species for modelling CH_4 combustion). However the differences in calculated burned gas density ratios were again minimal (<0.1 %), with presented values attained through use of the GRI-Mech 3.0 [149] reaction mechanism,

employing 53 chemical species in 325 reactions. Figure 8.5 gives the consequential values of u_L attained from S_u , together with results modelled using the freely propagating flame configuration of CHEMKIN-PRO, and the two aforementioned mechanisms (together with 7% H_2 BFG for comparison). All measured and modelled data is provided in Appendix B.7.

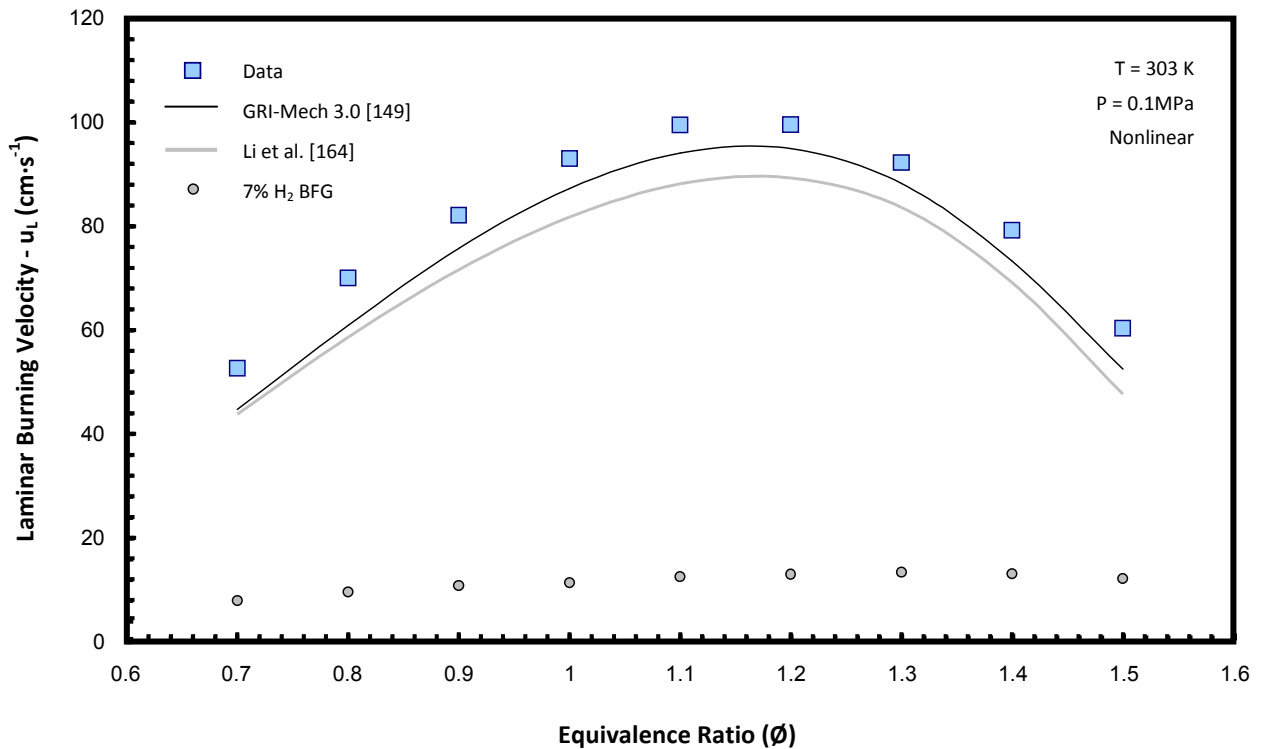


Fig. 8.5 – Plotted values of COG/air u_L against equivalence ratio.

The results demonstrate the same tendency as the measured unstretched flame speed, with a peak burning velocity achieved at marginally rich conditions. The reason the flame speed does not peak at richer air-fuel ratios (as would be expected with a high H_2 mixture [27]), results from the dominant thermal diffusivity of the flame, proportional to u_L when combined with overall reaction rate. The plotted burning velocities are more than double the equivalent values for methane, and around an order of magnitude higher than those of BFG. It is also clear from the plot that there is poor correlation between either of the tested reaction mechanisms and the COG dataset, with the GRI-Mech 3.0 model offering the more favourable results. To quantify this, the standard error of the estimate (Eqn. 5.1) has been calculated for the results modelled by each mechanism, with the Li et al. [164] data achieving an average

value of $10.6 \text{ cm}\cdot\text{s}^{-1}$ compared to $6.3 \text{ cm}\cdot\text{s}^{-1}$ from GRI-Mech 3.0 [149]. Results therefore suggest that when employing a given reaction mechanism to model COG combustion, GRI-Mech 3.0 is the favourable selection.

8.1.4 – Experimental Uncertainties for the COG dataset

Total uncertainty in unstretched flame speed (U_{Su}) was quantified in the same way as had previously been employed in Chapters 4-7, by first calculating the total bias (B_{Su}), and combining the observed standard deviation (further details in section 4.3). Several considerations had to be given to the calculation of B_{Su} ; firstly the influences of temperature and pressure were estimated from chemical models performed using the GRI-Mech 3.0 mechanism. Secondly the error in the optical system had to be recalculated in accordance with the camera filming rate and number of frames used per file (see section 4.3.1). The calculated values of U_{Su} are shown superimposed as error bars on the plotted S_u data in Fig. 8.6.

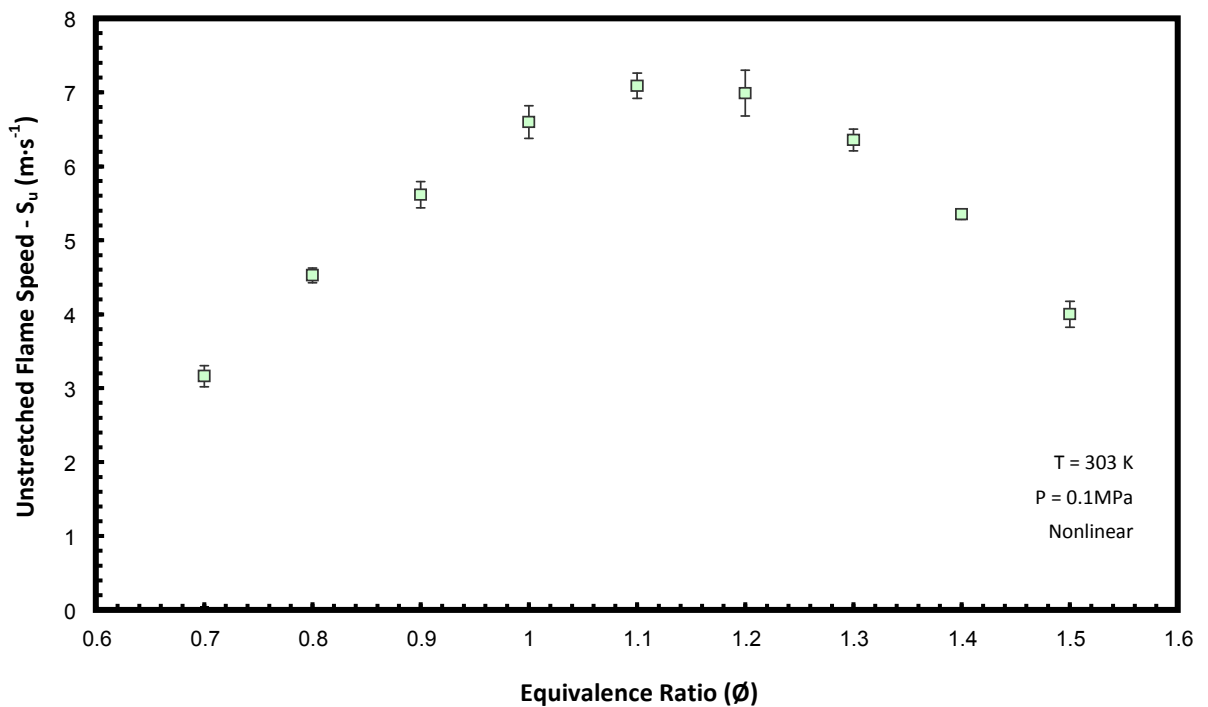


Fig. 8.6 – Plotted values of COG/air S_u against equivalence ratio with superimposed $\pm U_{Su}$

As has been seen with previous data, there is a strong dependency on σ_{Su} in the calculated uncertainty, and hence why some values have significantly larger error bars

than others. The typical average uncertainty was in the order of three percent for the dataset, with larger relative uncertainty at the curve extremities, where the speeds are slowest. The uncertainty in the obtained values of L_b have again been expressed using the standard deviation of the dataset. Fig. 8.7 shows the plotted COG L_b data with $\pm\sigma_{L_b}$ superimposed. All experimental data, including details of uncertainty can be found in Appendix B.7.

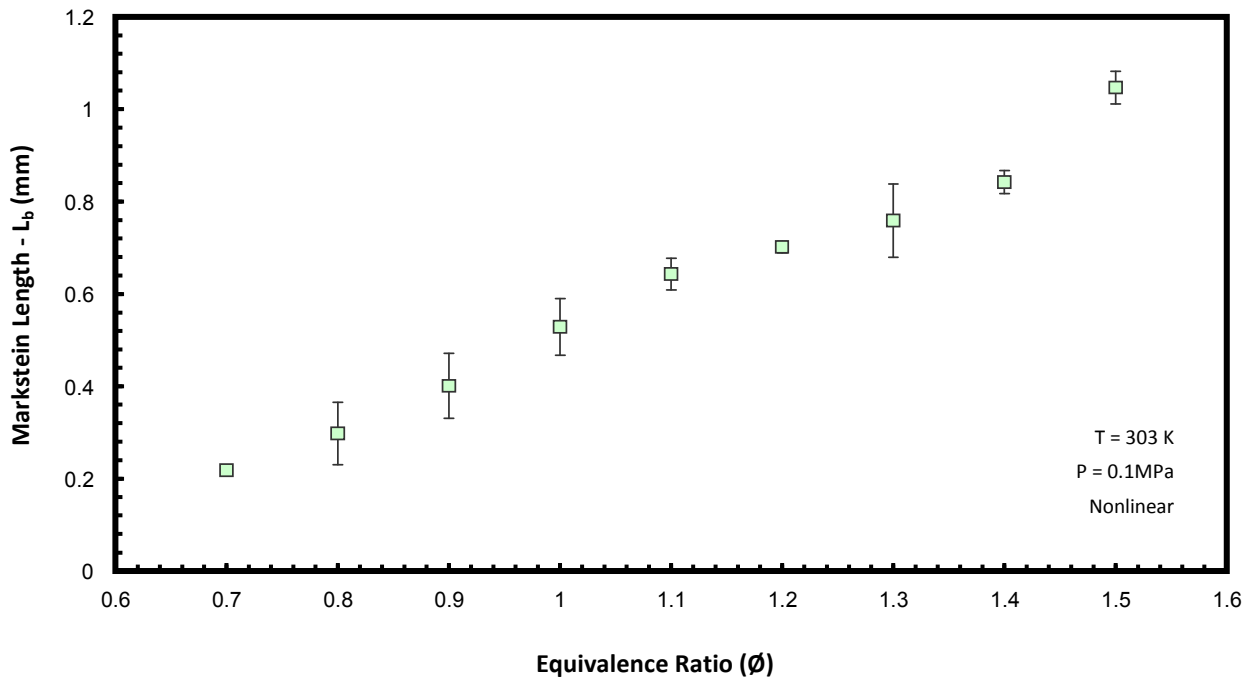


Fig. 8.7 – Plotted values of COG/air L_b against equivalence ratio with superimposed $\pm\sigma_{L_b}$

8.2 BFG blended with COG

Results presented in previous chapters quantified the potential variation in combustive properties resulting from small changes in BFG H_2 fraction, with further investigations analysing the influence of change in ambient condition and water content on the observed effects. The aim of the next section of work was to quantify the effectiveness of blending small amounts of COG to dampen out this fluctuation for the same level of compositional variation, as is commonly done in practise [12, 26]. This is analysed from the perspectives of both laminar burning velocity and fuel energy content.

8.2.1 – Defining Experimental Parameters

Results are presented for sixteen blends of COG and BFG in different fractions, for variation in four equivalence ratios. The four BFG H₂ fractions remained unchanged from the previous chapters, with COG added in the range of 0 - 15 % of total fuel fraction. The representative COG composition benchmarked in section 8.1 was employed for this study. The resultant molar fractions of all tested fuel compositions (including the specified COG values) shown in Table 8.2.

Table 8.2 - Molar compositions of fuels tested in the blended BFG/COG study.

BFG H ₂ %		1				3				5				7			
COG %	100	0	5	10	15	0	5	10	15	0	5	10	15	0	5	10	15
CO ₂	0.015	0.232	0.222	0.211	0.200	0.228	0.217	0.207	0.196	0.223	0.213	0.202	0.192	0.219	0.208	0.198	0.188
N ₂	0.040	0.530	0.505	0.481	0.456	0.519	0.495	0.471	0.447	0.508	0.485	0.461	0.438	0.497	0.475	0.452	0.429
CO	0.071	0.228	0.220	0.212	0.204	0.223	0.216	0.208	0.200	0.219	0.211	0.204	0.196	0.214	0.207	0.200	0.193
CH ₄	0.256	0.000	0.013	0.025	0.039	0.000	0.013	0.025	0.039	0.000	0.013	0.026	0.039	0.000	0.013	0.025	0.038
H ₂	0.618	0.010	0.040	0.071	0.101	0.030	0.059	0.089	0.118	0.050	0.078	0.107	0.135	0.070	0.097	0.125	0.152

It was necessary to reduce the number of experimental repetitions to two, as a result of the large number of compositions outlined in the testing matrix. The four specified equivalence ratios were in the range 0.8 - 1.4 as it was estimated that this would provide characteristic peaks in maximum u_L. Ambient conditions were maintained at quasi-atmospheric values previously employed; 303 K and 0.1 MPa. For this work the camera filming rate was reduced to 3,000 fps (to remain consistent with previous BFG work – section 5.1.1), with dry zero-grade air again employed as the oxidiser.

8.2.2 – Changes to the Experimental Methodology

The original design of the fuel manifold had to be updated to facilitate the delivery of three independent gases (BFG, COG, H₂), and N₂ required for purging. The methodology for calculation of required partial pressure also had to be updated thus:

- The specified blend (from Table 8.2) was fed into a spreadsheet to calculate the overall partial pressures of fuel and oxidiser.
- The fuel pressure was then broken down into constituent COG, BFG, and subsequent H₂ fractions, in accordance with volumetric ratio.
- Filling of the chamber commenced with H₂, then COG, BFG, and finally oxidiser before preparation for ignition.

All calculated values of each component partial pressure are detailed in Appendix B.8.

8.2.2 – Relationship between Stretch and Flame speed

Experiments were performed as outlined in section 8.2.1. with each optical file processed using both the linear and nonlinear analytical techniques. Samples of each plotted dataset are provided in Fig. 8.8 – Fig. 8.11, with plots separated on the basis of equivalence ratio and BFG H₂ fraction. Several observations can be made; firstly for lean air fuel ratios the addition of COG appears to increase the positive gradient of each plot, causing mixtures to accelerate more under stretched conditions. The BFG mixtures already displaying this tendency (blends containing higher H₂) show little change, with plots appearing offset only by the difference in measured speeds. This overall trend begins to even out as equivalence ratios of the mixtures increase, until under richest conditions the addition of COG causes the inverse effect, and plots to become more negative, and hence decelerate with a rise in stretch rate. These tendencies are clarified in Fig. 8.12 where the measured values of L_b are plotted for each mixture. The overriding trend is for values of L_b to converge as COG fraction increases, particularly for equivalence ratios of 1 and 1.2, where the mixtures exhibit near equidiffusive characteristics, and influences of stretch are minimised. The only tested fuel blends not to follow this tendency are the lowest H₂ BFG mixtures at the leanest and richest conditions. The overall convergence of L_b values with COG addition demonstrates the propensity for the difference in diffusive properties of each blend,

8. Further Steelworks Gas Testing

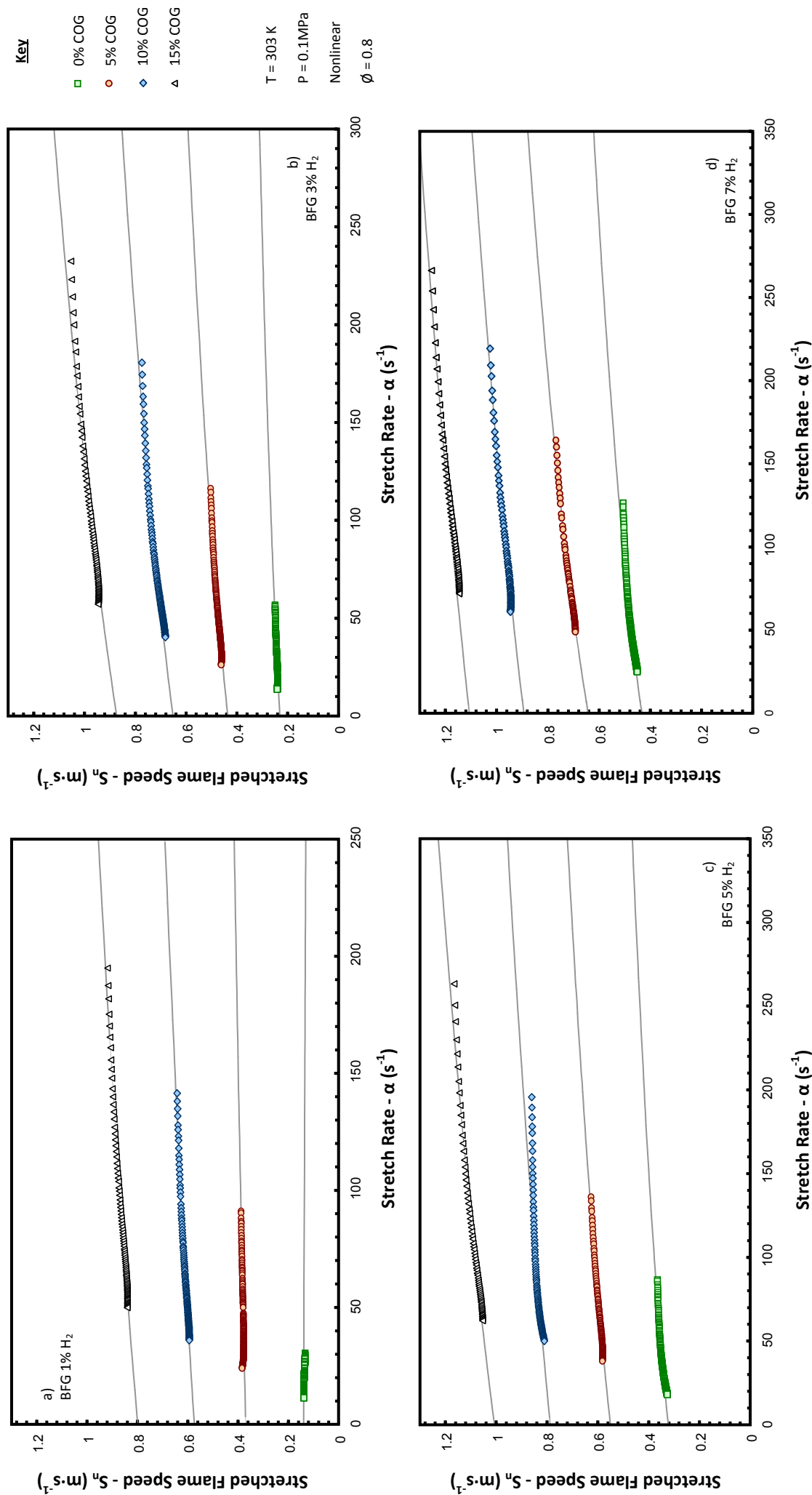


Fig. 8.8 – Samples of plotted BFG/COG/air S_n against α relationships, for a) 1, b) 3, c) 5, d) 7 % BFG H₂ Fraction, $\phi = 0.8$.

8. Further Steelworks Gas Testing

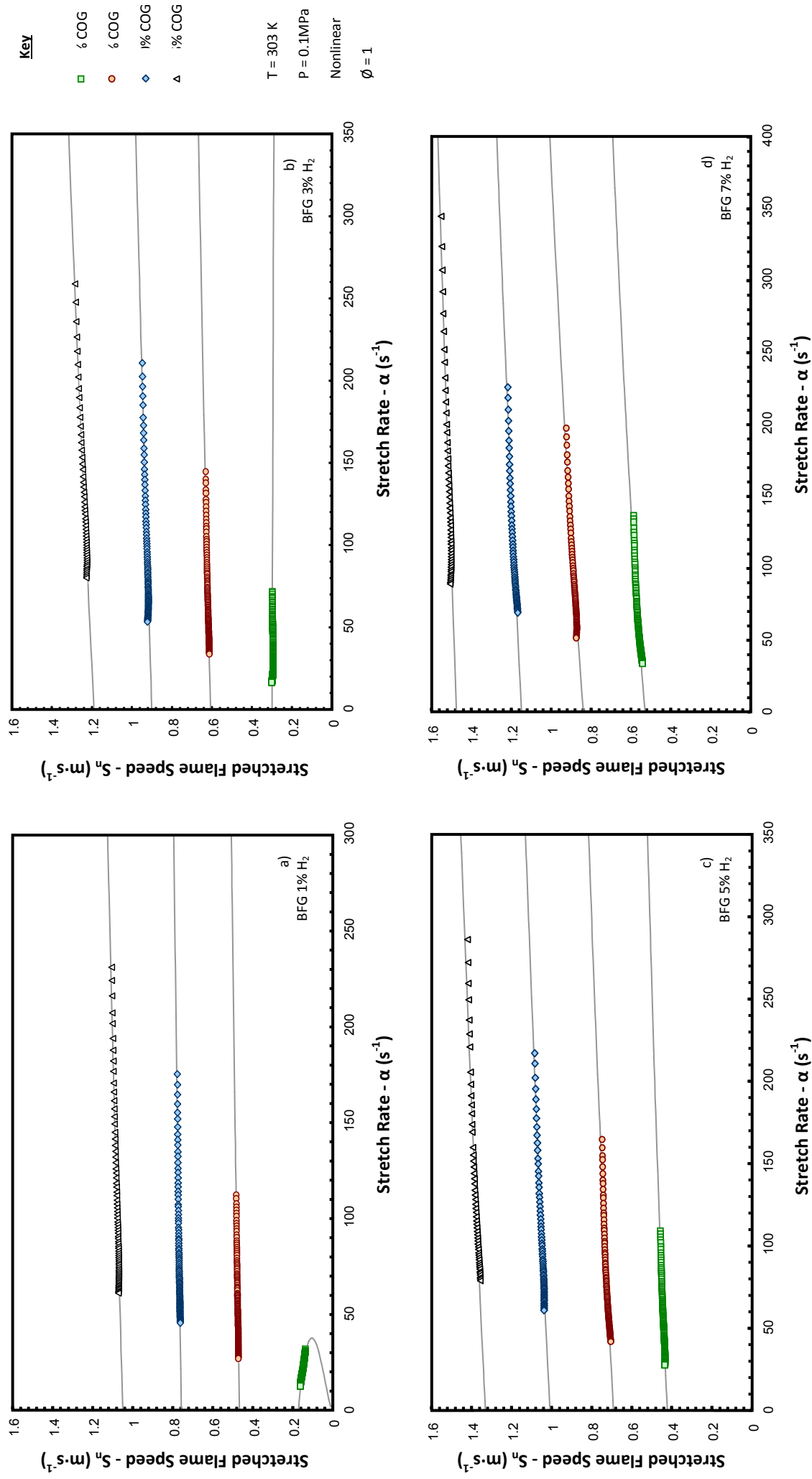


Fig. 8.9 – Samples of plotted BFG/COG/air S_n against α relationships, for a) 1, b) 3, c) 5, d) 7 % BFG H₂ Fraction, $\phi = 1$.

8. Further Steelworks Gas Testing

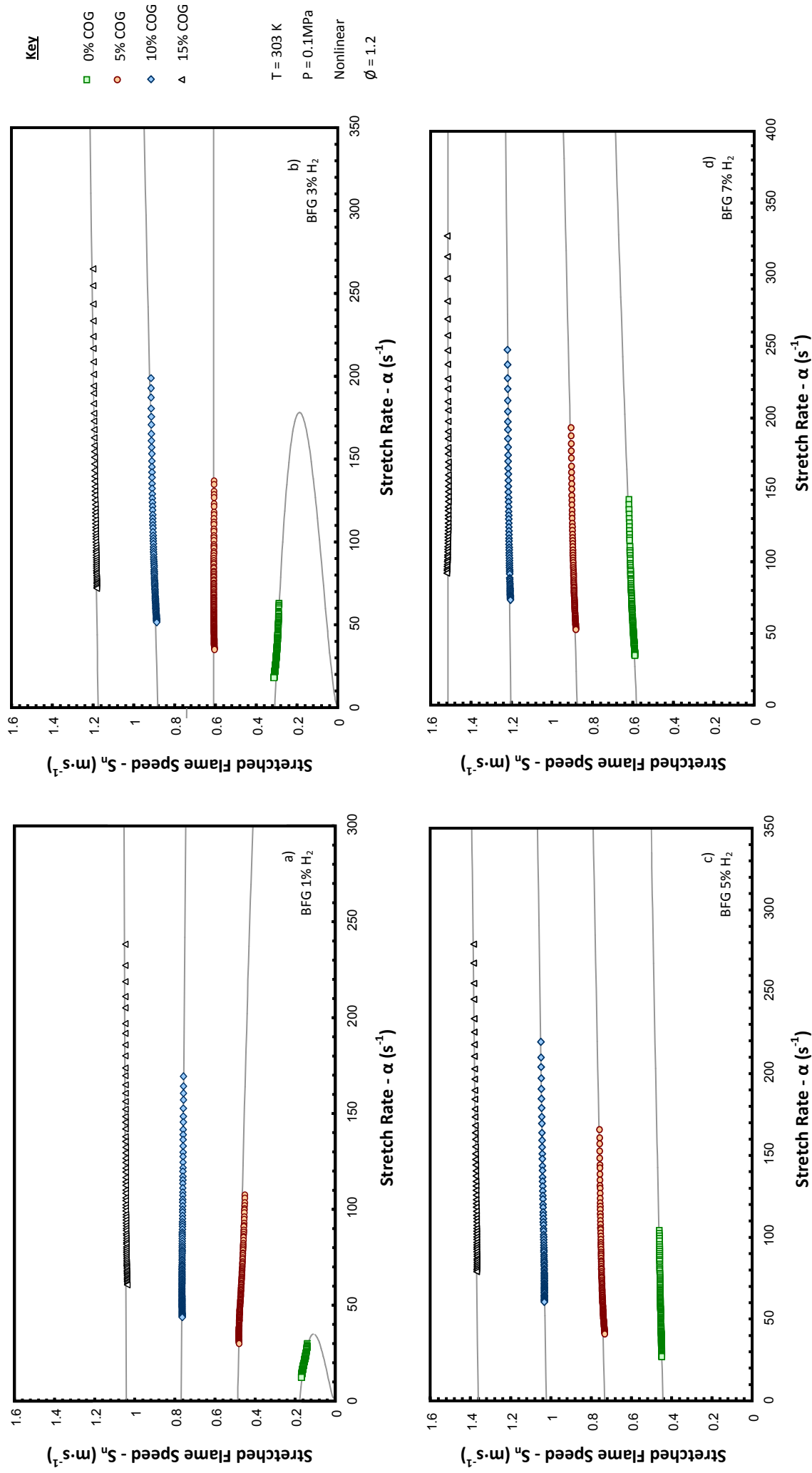


Fig. 8.10 – Samples of plotted BFG/COG/air S_n against α relationships, for a) 1, b) 3, c) 5, d) 7 % BFG H₂ Fraction, $\phi = 1.2$.

8. Further Steelworks Gas Testing

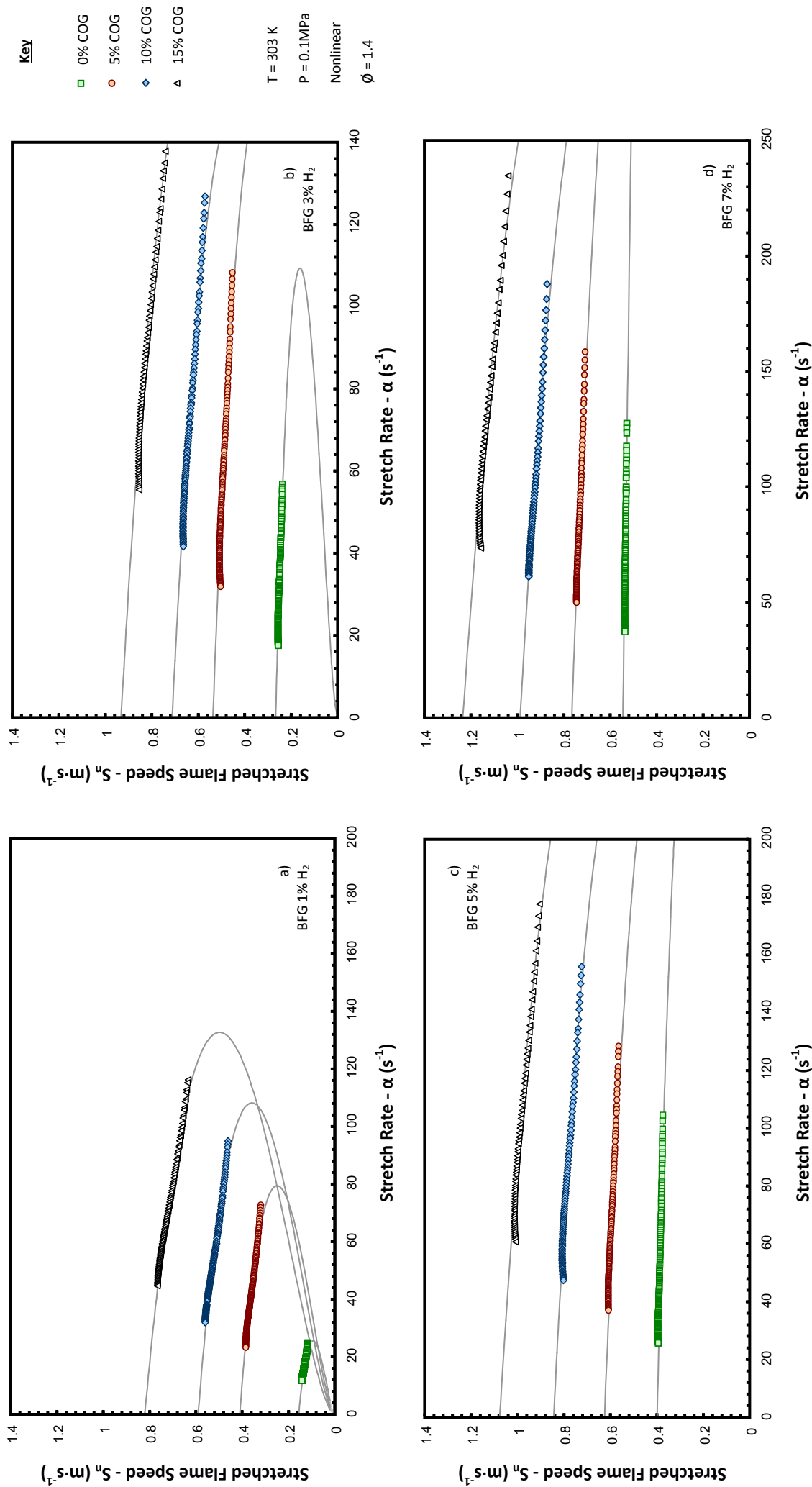


Fig. 8.11 – Samples of plotted BFG/COG/air S_n against α relationships, for a) 1, b) 3, c) 5, d) 7 % BFG H₂ Fraction, $\phi = 1.4$.

8. Further Steelworks Gas Testing

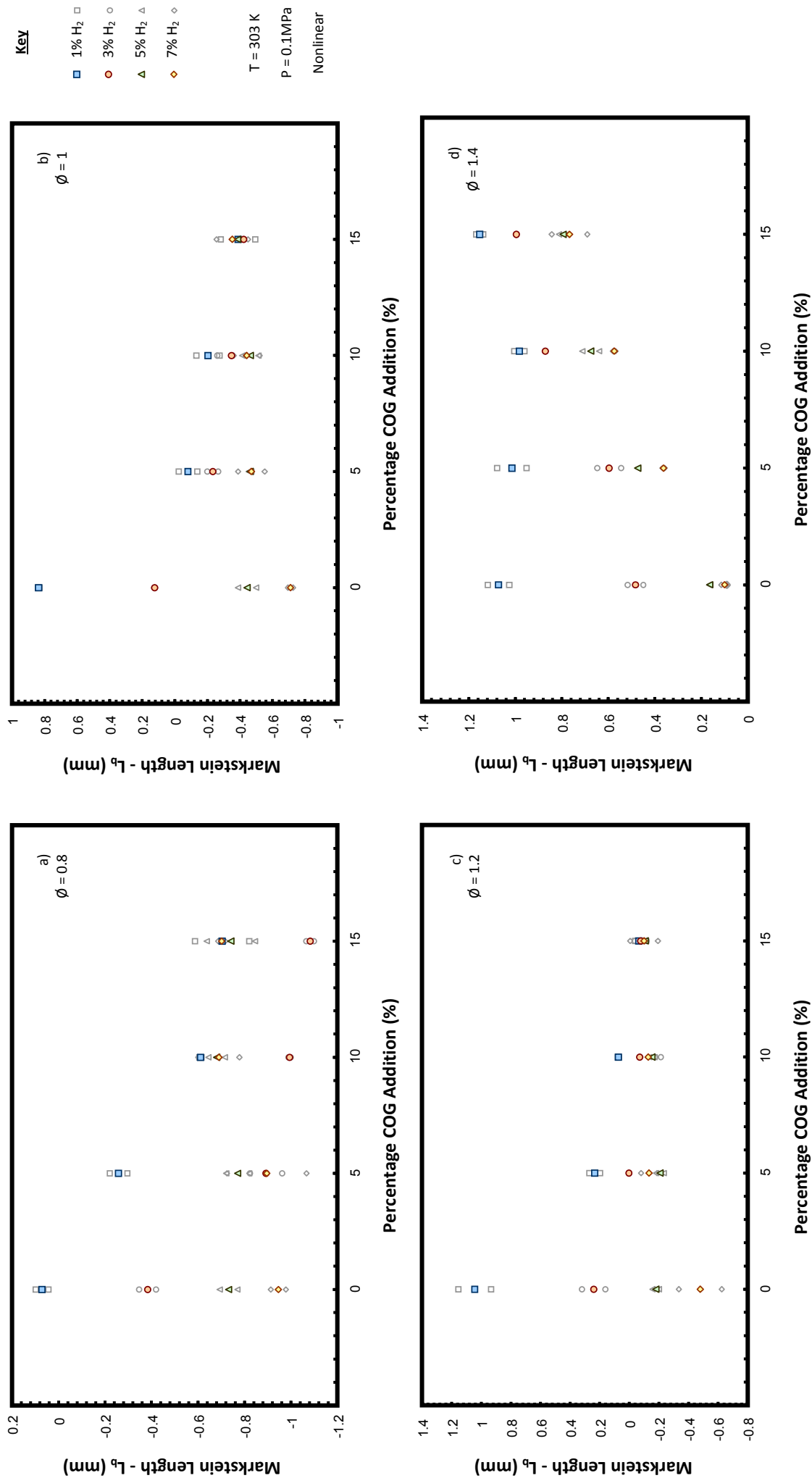


Fig. 8.12 – Each plotted BFG/air mixture L_p against COG addition, for a) $\phi = 0.8$, b) $\phi = 1$, c) $\phi = 1.2$, d) $\phi = 1.4$.

resulting from variable BFG H_2 , to be minimised. Furthermore, the negative values of L_b for the $\phi = 0.8$ and $\phi = 1$ mixtures suggest a dominance of mass diffusion compared to thermal conduction in the reaction zone. An explanation for this results from the diffusive properties of reactant H_2 fraction compared with the heat absorbed by diluents, which are increasingly preponderant at lean conditions. This also offers an explanation for the tendency of L_b readings to converge towards lower values than those measured for baseline COG. Analogous research from other institutions also demonstrates similar tendencies, with a negative decrease in mixture L_b observed for H_2 blended with increasing quantities of N_2 [111, 123]. The data therefore suggests the influence of BFG H_2 fraction on stretched flame behaviour is significantly lessened with the addition of COG.

The obtained values of unstretched flame speed have been plotted for the increasing COG fraction of each tested mixture in Fig. 8.13, with individual values again represented by hollow grey points and the average coloured. There are similar trends observed for all blends and equivalence ratios, with a near linear increase in flame speed for the addition of COG. Whilst the offset between each BFG mixture appears near parallel, there is some expected minor convergence as values tend towards those measured for baseline COG results presented in section 8.1. Nevertheless the increase in S_u with COG addition is significant, particularly for low H_2 BFG, as speeds rise by over a factor of five across the tested 0 – 15 % range. Experimental repeatability and uncertainty are explored in section 8.2.5.

8. Further Steelworks Gas Testing

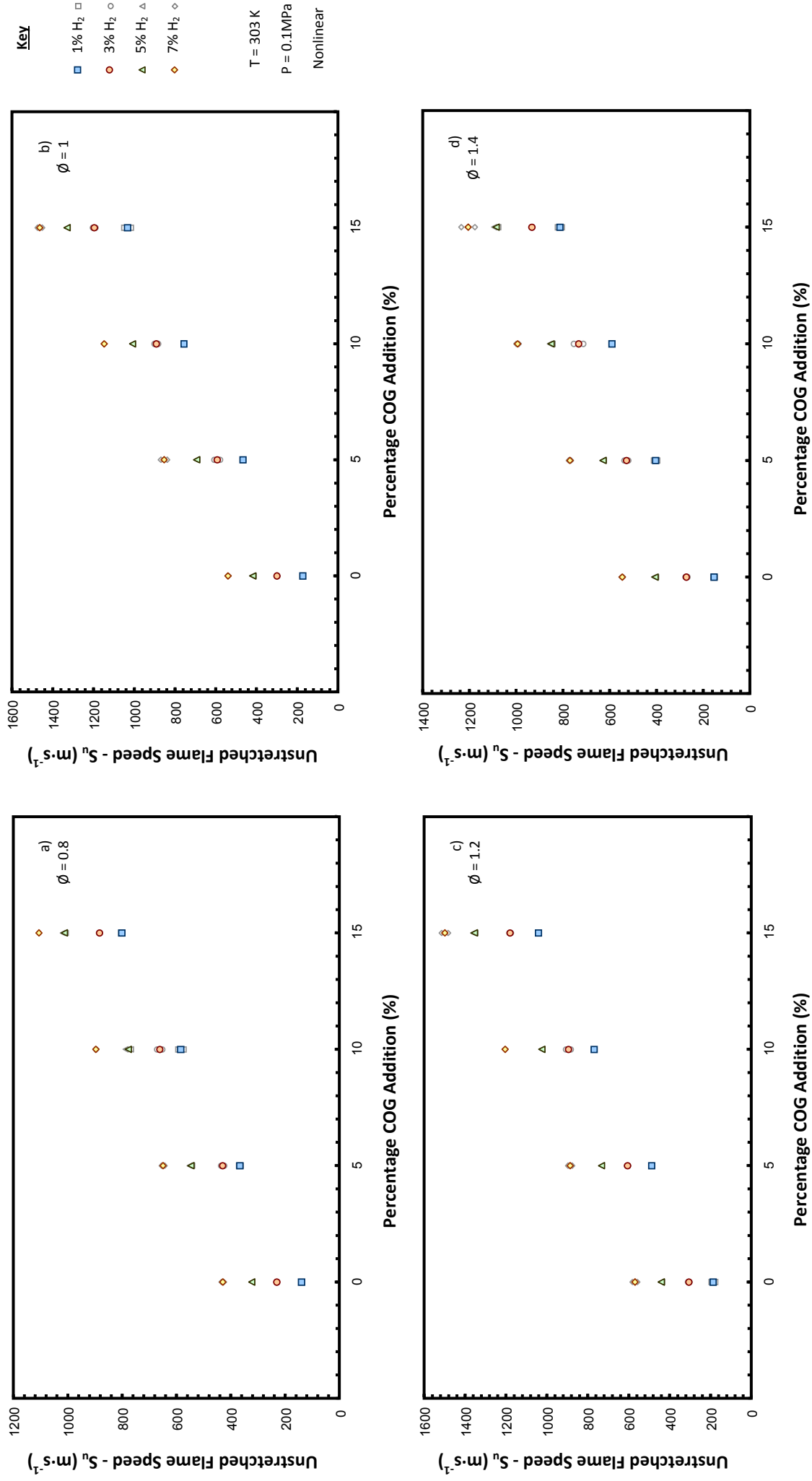


Fig. 8.13 – Each plotted BFG/air mixture S_u against COG addition, for a) $\phi = 0.8$, b) $\phi = 1$, c) $\phi = 1.2$, d) $\phi = 1.4$.

8.2.3 – Change in Experimental and Modelled Laminar Burning Velocity

The Li et al. [164] reaction mechanism was chosen to model the required adiabatic density ratio, to remain consistent with other BFG data. However the difference between values returned from other thermochemistry sets was again $<0.1\%$, with these data provided with the full experiment set in Appendix B.8. Modelled values were used to convert each S_u value to a corresponding u_L , with the averages in plotted in Fig. 8.14.

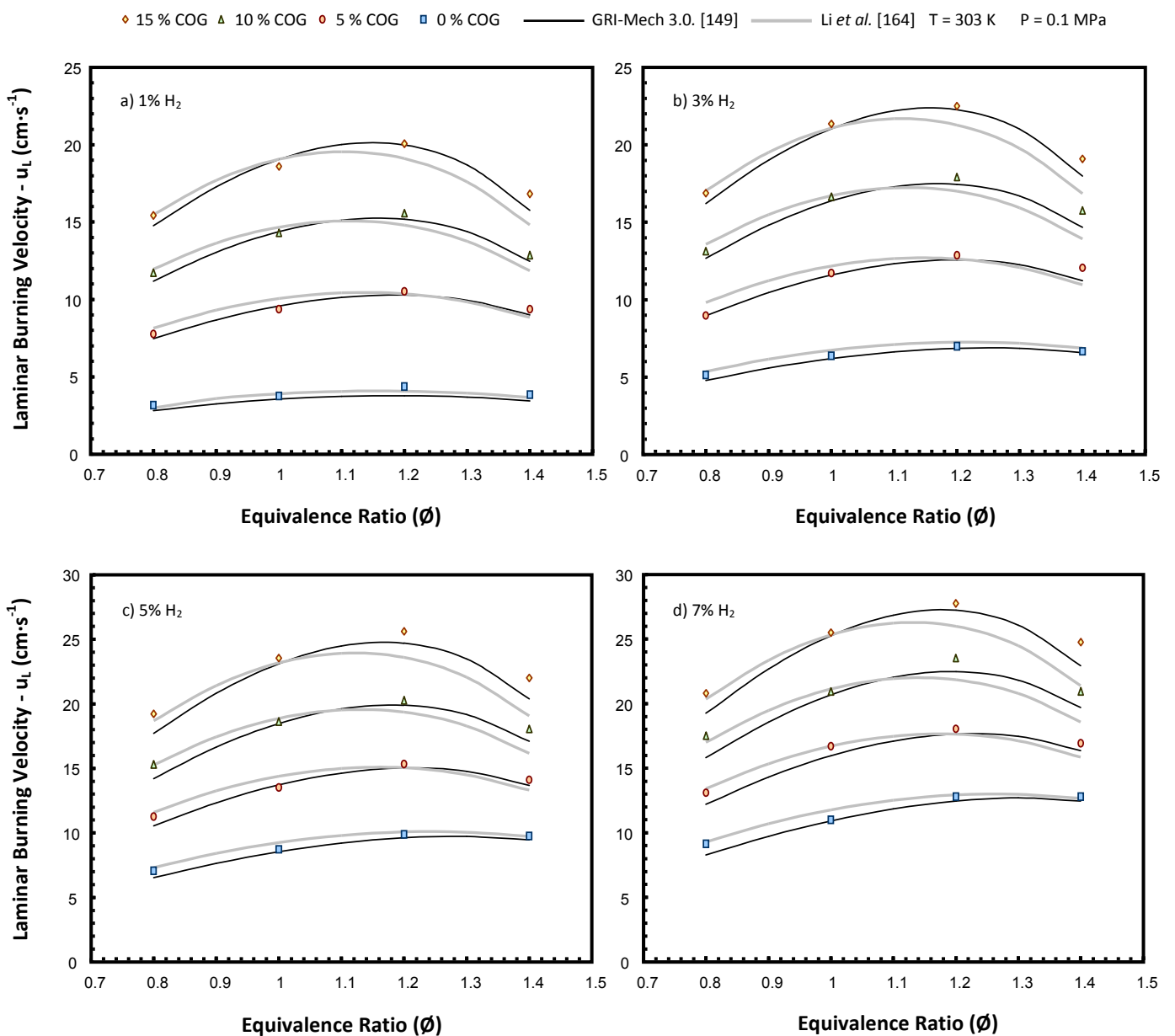


Fig. 8.14 – Each plotted BFG/COG/air mixture u_L against ϕ , for 1 (a), 3 (b), 5 (c), 7 (d) % BFG H_2 , with equivalent modelled velocities superimposed.

The introduction of COG appears to not only increase the u_L of each tested mixture but also cause an apparent shift in the peak velocity of each equivalence ratio profile. As has been shown with pure BFG mixtures, the maximum values is reached at equivalence ratios near 1.3, however this appears to shift towards stoichiometric conditions with the addition of COG, and the baseline results presented in section 8.1 are approached. The effect of this is for the mixture burning velocity to be increasingly changed by variation in richness as the profile becomes more pronounced.

In Fig. 8.14 comparisons are also made with the Li and GRI-Mech chemically modelled velocities using the PREMIX coded flamespeed calculator in CHEMKIN-PRO [149] (reaction mechanism specifications are provided in sections 5.3 and 4.2.2 respectively). The Li mechanism is shown to provide the most representative results for BFG, but as COG levels increase the performance significantly diminishes and GRI-Mech 3.0 offers better correlation in values. This suggests that as fuel mixtures, and resultant reaction chemistry, become more complex, careful consideration should be given to which mechanism is selected to most accurately model each fuel. The GRI-Mech 3.0 data offers particularly better correlation at rich conditions, with the crossover in modelled results tending towards leaner ratios with COG addition. However, the results presented in section 8.1.3 suggest that this relative performance would only diminish with further COG addition.

8.2.4 – Practical Implications of Fuel Property Change

The effectiveness of COG in dampening out the fluctuation in u_L , experienced as BFG H_2 increases, was analysed by calculating the relative percentage change in values attained across the tested range. This was performed for every fuel blend at each specified equivalence ratio. For example, an increase of 1-7 % in stoichiometric BFG H_2 , causes a rise in u_L from $3.75 \text{ cm}\cdot\text{s}^{-1}$ to $11.05 \text{ cm}\cdot\text{s}^{-1}$, or an increase of $\sim 195\%$. All values are plotted in Fig. 8.15.

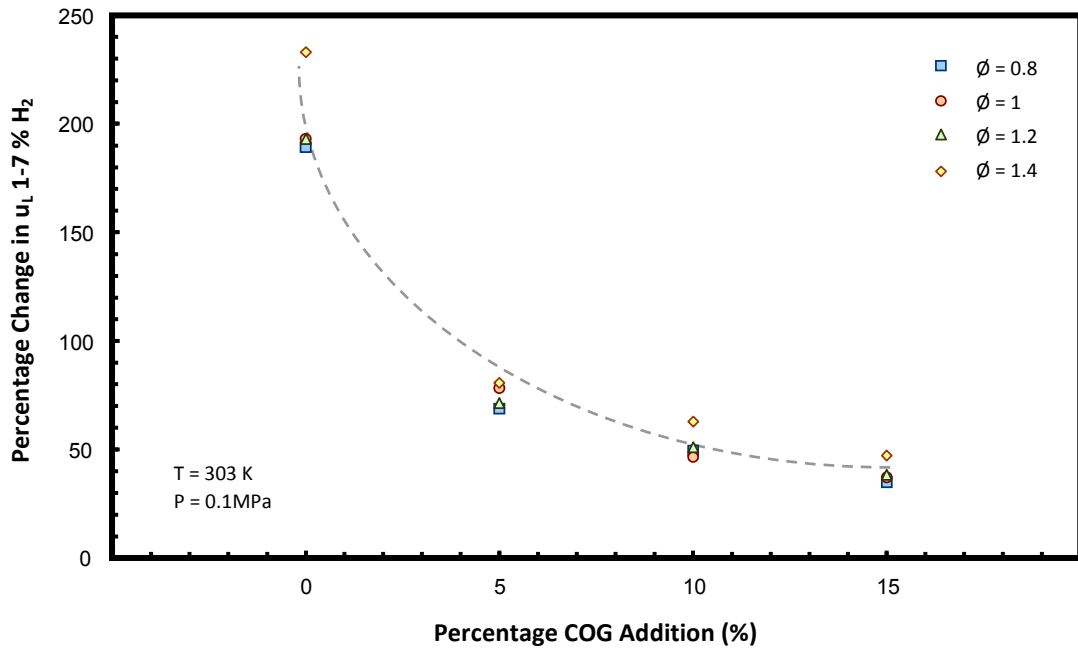


Fig. 8.15 – Percentage change in u_L resulting from 1-7% BFG H_2 increase with COG addition.

The plot emphasises the significant reduction achieved in the relative change of BFG u_L by the addition of COG: Mixing BFG with 5% COG reduces the calculated sensitivity to H_2 variation by over 100 %, dropping to a maximum of ~ 40 % for the tested range. Variation in critical boundary velocity gradient (g_f - as employed in previous chapters) for the extreme tested cases is plotted in Fig. 8.16 (with d_t ($\sim d_q$) calculated using temperature profiles from GRI-Mech 3.0, and all data provided in Appendix B.8).

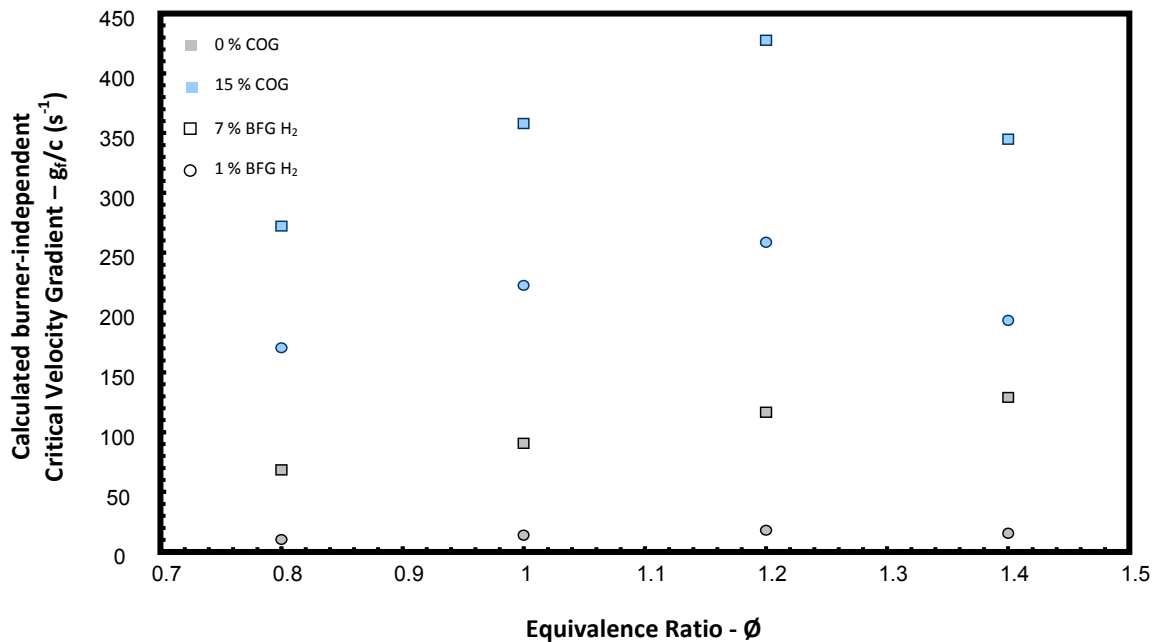


Fig. 8.16 – g_f/c values that prevent boundary layer flashback, for selected BFG/COG compositions.

A change in equivalence ratio profile is seen for the addition of COG, together with a widening of the gap between the 1 and 7 % H₂ BFG cases. However, the factor of difference decreases from almost an order of magnitude in some cases, to ~1.6 (Again this is only a theoretical example employed to emphasise the significant change resulting from variation in u_L). Additionally supplementary COG also dampens changes in stretch influence by causing values of L_b to converge, and thereby offers an advantage that both water addition and temperature increase do not.

The corresponding reduction in additional fuel characteristics of gross calorific value (CV_G) and equivalent Wobbe Index have also been considered for all tested fuels. Properties were calculated for ideal mass fractions, and normalised to STP (273.15 K and 100 kPa, with reference energy density values in appendix A.2). This value was then used to calculate the WI_G for that mix using Eqn. (5.1), Where the specific gravity of the mixture in relation to the density of air was calculated to be $1.276 \text{ kg}\cdot\text{m}^{-3}$. Fig. 8.17 shows the plotted change in fuel CV_G (a), and the equivalent percentage fluctuation (b) resulting from 1 - 7 % BFG H₂ variation, together with WI_G . The CV_G and WI_G of the specified mixtures is as much as an order of magnitude lower than values typical for natural gas [159], however are almost doubled with the addition of 15% COG. Furthermore, the addition of COG is shown to halve the BFG H₂% percentage fluctuation in both plotted properties. Therefore, COG not only has the potential to dampen relative fluctuation in flame speed and stability, but also the heating power output from combustion.

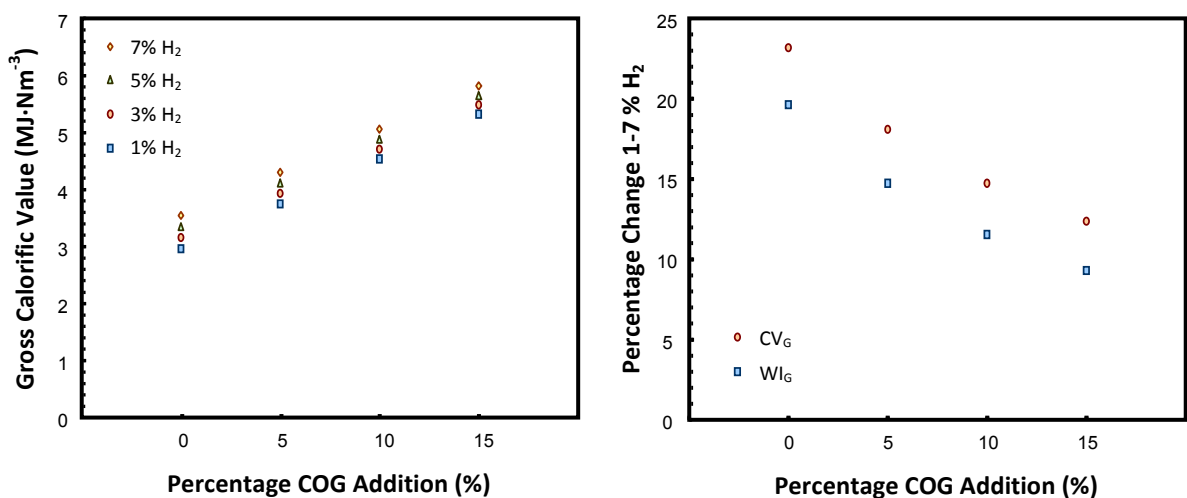


Fig. 8.17 – Actual values and percentage change in CV_G/WI_G resulting from 1-7% BFG H₂ increase with COG addition.

8.2.5 – Experimental Uncertainty

Calculated values of experimental uncertainty were increased significantly for this testing, with only two experimental repetitions performed per condition. Consequently the employed t-value rose to 12.71 (from 4.303) for the 95% confidence limit [161]. In addition to this a further factor of uncertainty resulted from error in the control of COG input. Linear changes in S_u from the obtained results were used to estimate fluctuations in flame speed resulting from over/under filling of COG equivalent to ± 0.01 kPa. These changes were included in the calculation of total bias for each test. Furthermore, errors resulting from temperature and pressure change were estimated from scaled chemical models, and a drop in the number of frames per video led to a rise in optical uncertainty. The combination of these factors meant overall uncertainty values of over 10 % for the measured speeds. However, this is regarded as an overestimation, with smaller levels of scatter shown for most of the plotted data (Fig. 8.13), and results largely from statistical influence (t-value) on calculation. To highlight the additional uncertainty primarily from COG addition, calculated values of B_{Su} have been averaged for all equivalence ratios, and presented in Table 8.4 (full U_{Su} dataset presented in appendix B.8).

Table 8.4 – Calculated uncertainty values for the COG/BFG blend study ($\text{mm}\cdot\text{s}^{-1}$).

COG %	5				10				15			
BFG H ₂ %	1	3	3	7	1	3	3	7	1	3	3	7
B_{Su}	12.7	14.2	15.6	18.1	16.7	19.0	20.6	23.0	20.2	22.4	27.0	28.8

8.3 BOS Gas Modelling

The collection and utilisation of BOS gas is becoming inerasably widespread as steelworks strive for site-wide efficiency improvements [12], and the purpose of this section is to characterise the fuel performance in relation to analyses already performed. Due to financial and time restrictions this study has been limited to chemical kinetic modelling as a foundation for potential future work, however analogous work with similar fuels in this thesis demonstrated reasonable agreement with experimental data, vindicating use of these simulations for an initial analysis.

8.3.1 – Fuel Specification

In order to simulate a representative BOS gas mixture, an approximate baseline composition had to be specified. This was formulated on the basis of the data collected and summarised for the case study presented in section 2.1.4, with average molar fractions given in Table 8.5.

Table 8.5 – Specified baseline BOS gas composition used for modelling.

Fuel component	Mole Fraction (%)
CO ₂	0.1420
N ₂	0.1945
CO	0.6563
O ₂	0.0008
H ₂	0.0064

Ambient conditions were kept at the same quasi-atmospheric values (303 K 0.1MPa) to provide a direct comparison between results presented for the other steelworks gases. Furthermore, the specified range of modelled equivalence ratios was also maintained at 0.7 - 1.5 for the same reason. The reaction mechanism chosen to perform the required chemical modelling was the set developed by Davis *et al.* [165]. Results obtained from this mechanism had thus far provided the best overall agreement for fuels containing mixtures of H₂ and CO. Simulations were performed using the freely propagating flame speed calculator (utilising PREMIX) of CHEMKIN-PRO, with the mechanism employing 14 chemical species in 43 reactions. As before, modelled solutions were based on an adaptive grid of 1,000 points, with mixture-averaged transport properties and trace series approximation. Modelled baseline values of u_L for the specified mixture are shown in Fig. 8.18, with those, and all other modelled result presented in this in section tabulated in Appendix B.9.

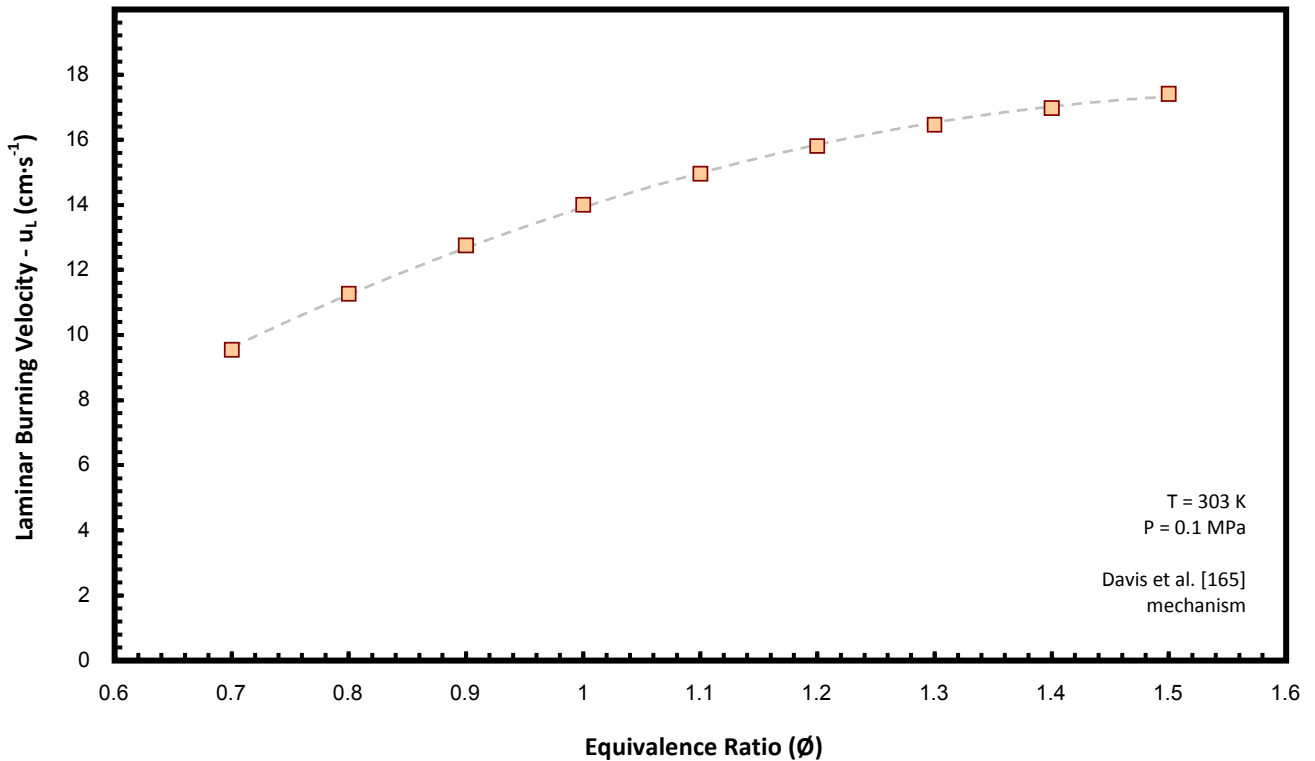


Fig. 8.18 – Modelled values of u_L for specified BOS/air mixtures against ϕ .

The returned values are of a similar order to BFG results containing the largest quantities of H_2 , even though diluent concentration is more than halved for the BOS gas mixture. The modelled peak burning velocity is also reached at apparently richer equivalence ratio compared with BFG. This suggests the suppression resulting from a drop in adiabatic flame temperature is being exacerbated by the rate of chemical heat release. This is a result of the preponderant CO in the BOS gas mixture, and the heavy influence of the terminating reaction $\text{CO} + \text{O}_2 \rightarrow \text{CO}_2 + \text{O}$. This process has relatively high activation energy, and is slow even at high temperatures [125]. It was therefore important to model the kinetics of BOS gas combustion for mixtures containing more H_2 and H_2O as potential catalysts for CO oxidation.

8.3.2 – Variable moisture in BOS gas mixtures

Following from the observed chemically enhancing influence of water addition reported in chapter 7, larger CO and smaller H_2 fractions suggested BOS gas could be influenced more by H_2O addition, relative to the changes observed with BFG. A direct

comparison between the two fuels was made by adding the same amounts of moisture to the modelled fuel blend, with all modelled mass fractions available in Table 8.6. Fig. 8.19 demonstrates the simulated increase in modelled burning velocity experienced by the baseline BOS gas mixture for the equivalent addition of up to 0.75 g of water (molar compositional increase of $\sim 5\%$), with the 1% H₂ BFG data from Chapter 7 shown for comparison.

Table 8.6 – Specified BOS gas composition with increasing water fraction.

Fuel Composition (mass fraction)						
Water Mass (g)	H ₂	CO	CO ₂	N ₂	H ₂ O	O ₂
0	0.00042	0.61027	0.20753	0.18093	0.00000	0.00085
0.25	0.00042	0.60434	0.20552	0.17917	0.00971	0.00084
0.5	0.00042	0.59852	0.20354	0.17744	0.01924	0.00083
0.75	0.00041	0.59282	0.20160	0.17575	0.02858	0.00083

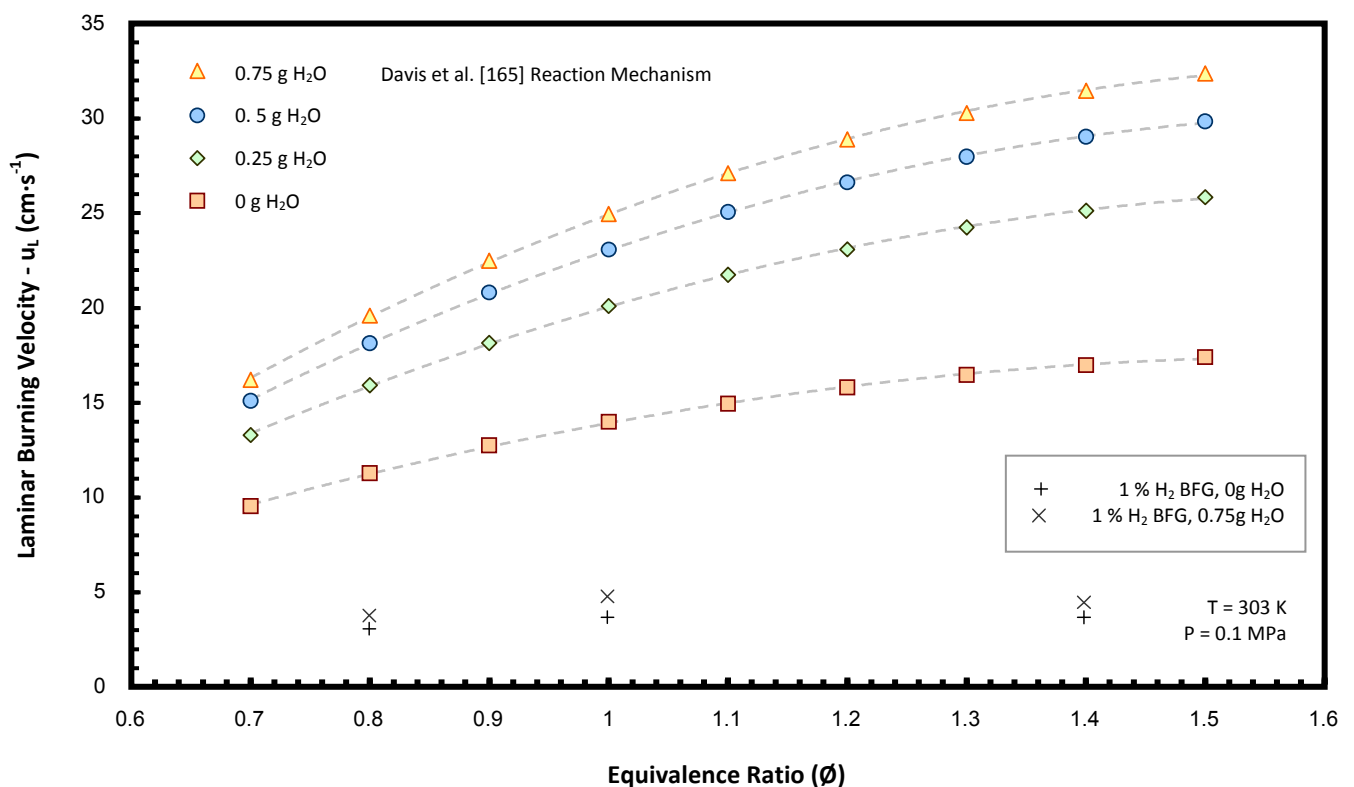


Fig. 8.19 – Modelled values of u_L for BOS/air mixtures against ϕ , with increasing water fraction.

There is clear enhancement to the modelled BOS gas burning velocity experienced as a result of H₂O addition, with values increasing for each equivalence ratio. The enhancement also appears to follow the same tendency as the 1% H₂ BFG mixture, with the level of acceleration decreasing with as more H₂O is added. This again suggests the chemically catalysing influence is counterbalanced, and eventually surpassed, by the suppressive and cooling effect of H₂O as a diluent [125]. The relative influence of water addition is also simulated to rise with ϕ , inasmuch that there are respective full range increases from ~70, to ~86 percent for equivalence ratios of 0.7, and 1.5. These points are emphasised in Fig. 8.20, which plots the change in u_L against water addition for three values of ϕ . BOS gas is more heavily accelerated by the addition of water compared to BFG, suggesting a propensity for stronger variation with smaller changes in H₂O concentration, and potential for atmospheric humidity to have a significant effect on combustion characteristics.

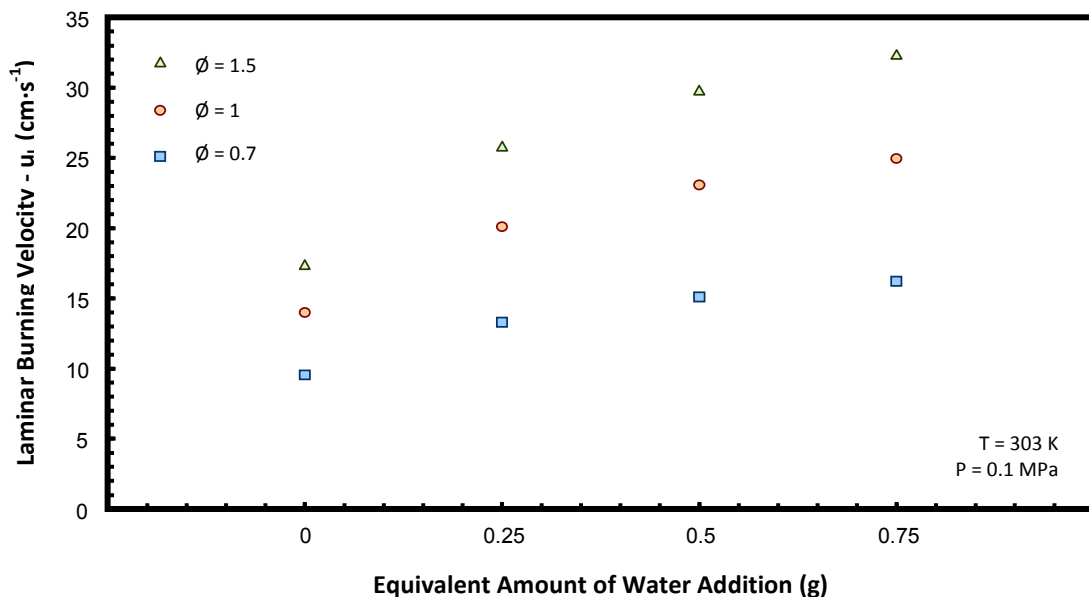


Fig. 8.20 – Modelled values of u_L for BOS/air mixtures against water fraction, for three equivalence ratios.

8.3.3 – Blended BFG and BOS gas mixtures

Following from the work presented in section 8.2 with COG, an equivalent modelling study was performed to assess the effectiveness of BOS gas in dampening out BFG H₂ u_L fluctuation. The level of BOS gas dilution was increased in the equivalent range of 0 - 15 % for each tested BFG composition, with molar fractions provided in Table 8.7. The

BOS gas mixture was the same as previously employed (section 8.3.1) with results shown for ϕ variation in Fig. 8.21.

Table 8.7 - Molar compositions of fuels modelled in the blended BFG/BOS study.

BFG H ₂ % →		1				3				5				7			
BOS %	100	0	5	10	15	0	5	10	15	0	5	10	15	0	5	10	15
CO ₂	0.142	0.2327	0.2281	0.2236	0.2191	0.2280	0.2237	0.2194	0.2151	0.2233	0.2192	0.2151	0.2111	0.2186	0.2147	0.2109	0.2071
CO	0.656	0.2277	0.2491	0.2706	0.2920	0.2231	0.2448	0.2664	0.2881	0.2185	0.2404	0.2623	0.2842	0.2139	0.2360	0.2581	0.2803
N ₂	0.195	0.5297	0.5129	0.4961	0.4794	0.5190	0.5027	0.4865	0.4703	0.5083	0.4926	0.4769	0.4612	0.4976	0.4824	0.4673	0.4521
H ₂	0.006	0.0100	0.0098	0.0096	0.0095	0.0300	0.0288	0.0276	0.0265	0.0500	0.0478	0.0456	0.0435	0.0700	0.0668	0.0636	0.0605
O ₂	0.001	0.0000	0.0000	0.0001	0.0001	0.0000	0.0000	0.0001	0.0001	0.0000	0.0000	0.0001	0.0001	0.0000	0.0000	0.0001	0.0001

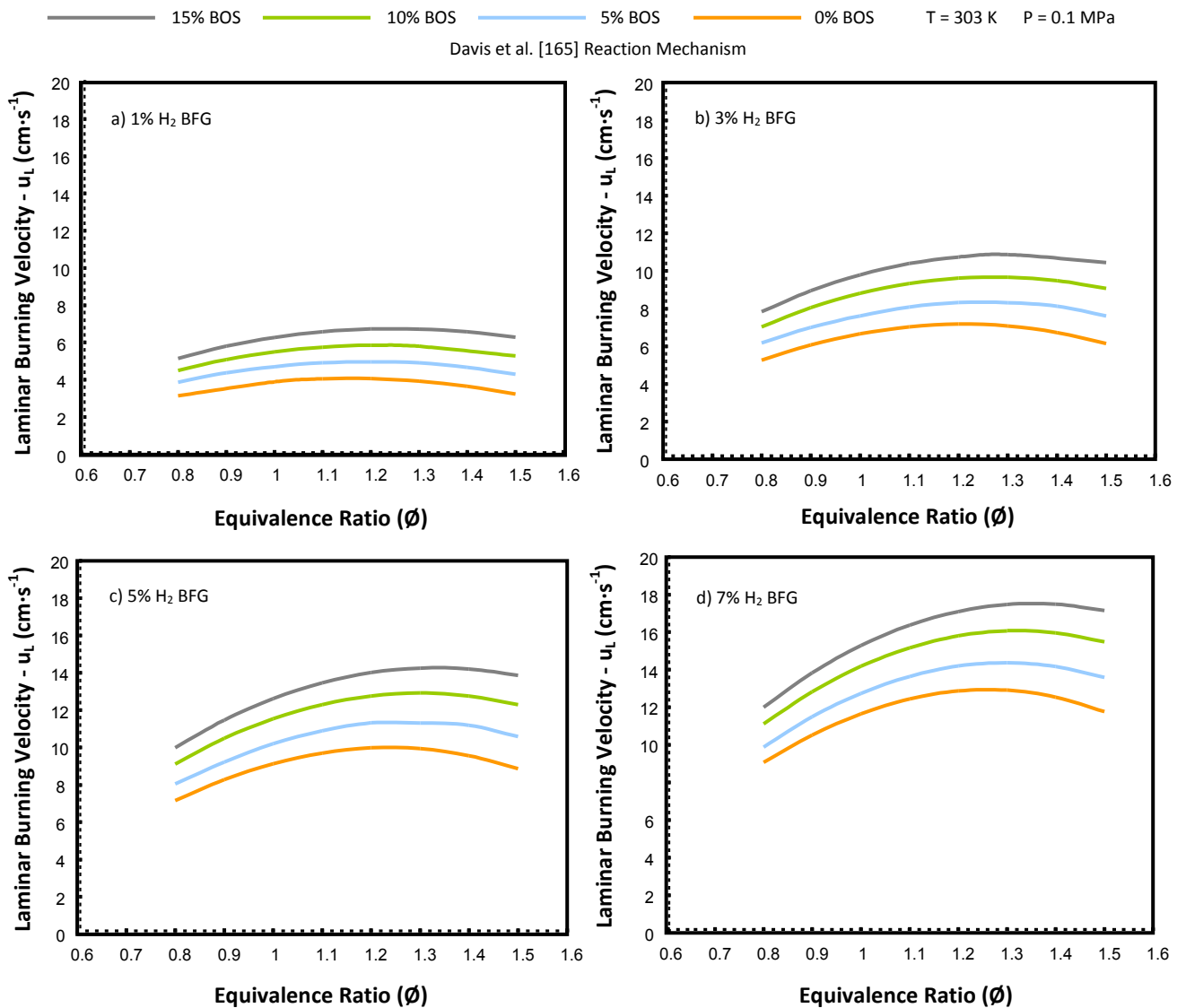


Fig. 8.21 – Modelled BFG/air/BOS gas u_L against ϕ , for 1(a), 3(b), 5(c), 7(d) % BFG H₂ and increasing BOS fraction.

The modelled results suggest analogous trends for each BFG mixture, and an apparent increase in u_L with BOS gas addition. Furthermore, the models simulate a tendency for peak values of u_L to become richer with increased dilution, leading toward the baseline profile presented in Fig. 8.18. If the effectiveness of BOS gas in dampening BFG variation is quantified in a similar way as COG (section 8.2.3), the percentage difference in *peak* u_L from 1 - 7 % H_2 reduces from ~218, to ~160 % across the tested range. This is compared to approximately 40 % for COG blends (note, with COG values were calculated for each corresponding ϕ). To quantify this further for 15 % BOS gas addition, the modelled peak u_L for the 1% H_2 BFG mixture increases to $6.7 \text{ cm}\cdot\text{s}^{-1}$, compared with a corresponding rise to $20.1 \text{ cm}\cdot\text{s}^{-1}$ for COG. This therefore suggests BOS gas is inferior to COG as a u_L stabilising additive, unsurprising considering the significant difference between the baseline fuel values. However, the change in u_L with BOS gas addition does show an interesting non-monotonic effect over the tested range, due to the reaction chemistry: The addition of 15 % BOS gas to the 7 % H_2 BFG mixture appears to raise peak u_L to a value marginally larger than the dry baseline for either fuel. Therefore, as the mixture tends towards 100 % dry BOS gas, there would be a relative deceleration in the observed speeds. Again this is due to the catalysing effect of H_2 addition to the preponderant CO in the BOS gas mixture. Therefore the complex behaviours exhibited between CO, H_2 , and H_2O , and subsequent reaction chemistry could lead to significant variation in blended fuel burning velocity, and propensity for operational instability.

8.4 Summary and Conclusions

Laminar burning velocities were obtained for nine equivalence ratios of a representative COG mixture at atmospheric ambient conditions. The significant H_2 fraction of the fuel led to high speeds, more than double the equivalent for methane and around an order of magnitude faster than BFG. Observed propagation was also shown to be more heavily suppressed by flame stretch with an increase in mixture richness. The relative performance of two chemical reaction mechanisms used with CHEMKIN-PRO were analysed with respect to experimental data, and GRI-Mech 3.0

shown to model values most representative of the tested mixture. A detailed attempt was made to quantify possible experimental error, with an average uncertainty of around three percent at a 95% confidence level.

The same COG mixture was then blended with BFG to quantify the effectiveness of dampening out the previously studied variation in burning velocities, that result from compositional H₂ variation. COG was introduced to each of the four representative BFG mixtures, at ambient conditions and four disparate equivalence ratios, specified to provide the approximate peak for that blend. COG was shown to have a significant impact on obtained burning velocities across the tested range, increasing values for the low H₂ BFG mixture by as a much as a factor of five. The addition of COG was also shown to dramatically reduce variation in the influence of flame stretch on propagation, as values of Markstein length converged across the tested range. Furthermore, relative u_L fluctuation resulting from the addition of BFG H₂ was shown to decrease from over two hundred percent to less than forty with the highest COG mixture. This effect demonstrated an inverse exponential tendency, with the lowest level of COG addition still reducing fluctuation by over one hundred percent. Equivalent variation in the fuel Gross calorific value and Wobbe index was also halved with blending across specified range. It is therefore suggested that COG addition is the most effective mechanism for reducing inherent fluctuation in BFG combustive properties, dampening change in not only u_L , but also stretch influence, and energy delivery.

Again a comparison of values simulated by chemical reaction mechanisms was undertaken with respect to predicting this behaviour, with optimal performance shown to shift between chemistry sets as the fuel blends change. Therefore careful consideration should be given when selecting a mechanism to model the reaction kinetics of these mixtures. Detailed calculations were once more performed to quantify experimental uncertainty, with higher returned values due to a necessary reduction in the number of experimental repeats.

The final section of this chapter employed the Davis reaction mechanism to model behaviour of a representative BOS gas mixture, after the set was shown to provide favourable results for fuels containing H₂ and CO. An equivalent laminar burning velocity profile was generated for the same equivalence ratios and ambient conditions as tested with previous fuels. The magnitude of modelled speeds was of a similar order to the fastest BFG mixtures, with values shown to peak under richer conditions than previously observed. Models were then adapted, firstly for the introduction of increasing gaseous H₂O fractions, equivalent to those tested with BFG in chapter 7. The catalysing influence of H₂O in opening further CO reaction paths was shown to have a dramatic influence on modelled flame speed, with values almost doubling across the tested range. The suppressive effect of H₂O as a diluent slowed the rate of acceleration between each step change in water fraction, however not enough to provide an overall reduction in values. Finally, models of blended BFG and BOS gas were performed, with fractions of the latter increased to the equivalent fifteen percent as COG. The dampening influence of BOS gas on BFG H₂ variation was small in comparison with COG. However, the catalysing influence of H₂ within the BFG fraction led to a blended peak burning velocity higher than any modelled for the independent combustion of either fuel. Therefore the complex behaviours exhibited between blended constituent fractions, could lead to significant variation in burning velocity, and propensity for operational instability.

Conclusions and Outcomes of Work

Given the remit of initial objectives, several conclusions can be drawn from the work undertaken in this thesis:

The initial objective of designing and developing an experimental setup capable of obtaining the desired results was achieved. Results were presented to demonstrate that optical measurements obtained from the Cardiff CVCB were in agreement with corresponding CH₄ data from research literature, thereby vindicating use of the outlined experimental system for this, and future studies.

Variation in the combustive behaviour of atmospheric BFG was subsequently characterised for small changes in H₂ concentration, representative of fluctuation (1-7 %mol) experienced during production. S_u and u_L values were shown to increase by more than a factor of three for each equivalence ratio across the tested range (0.7-1.5), thus highlighting the significant potential for premixed operational instabilities such as blowoff and flashback. The influence of flame stretch was also investigated with measured values of L_b rising with equivalence ratio. This was offset by a decrease in values as fuel H₂ fraction rose, with both positive and negative quantities measured. The opposing tendencies in u_L and L_b resulting from H₂ addition suggest that any minor flame behavioural change resulting from compositional variation can not be fully negated with an alteration in equivalence ratio.

BFG combustion was investigated further to quantify the influence of change in ambient condition, and to what extent waste heat can be used to mitigate the variation in atmospheric u_L and L_b . Increase in ambient pressure resulted in a decrease of u_L for each BFG composition, together with a tendency for lowering measured L_b . This change was quantified as a proportional offset for all tested mixtures, and was observed alongside the increase induced by a rise in equivalence ratio or drop in H₂ concentration. An increase in ambient temperature was shown to induce a rise in u_L , however variation in the specified condition provided little demonstrable change in the analysed influence of flame stretch. The rise in u_L with temperature was proportional to the initial value, and therefore consistent fuel preheating would not dampen the impact of the fluctuations initially measured. However, BFG u_L could be maintained within a given range with controlled preheating (based on the fuel H₂

content) however this may not fully negate instability due to stretch influence. Consequently power law correlations were made for variation in ambient condition, applicable for modelling BFG burning velocities with a change in temperature and pressure, with exponents compared to analogous values for different fuels.

Variation in BFG u_L and L_b was investigated further with H_2 fraction, and change in relative humidity. Masses of water were introduced to the reactant mixture, thereby increasing the relative humidity to 72 %. This was shown to have a potentially non-monotonic divergent influence on the attained u_L , as a function of the ratio of CO to H_2 in the fuel blend. For mixtures comprising low H_2 the addition of water demonstrated a catalysing influence, with resultant u_L shown to increase. Conversely, the corresponding values for blends containing larger H_2 fractions decreased with more water and a drop in flame temperature. A similarly opposing influence on flame stretch was also in evidence, with rates of propagation of low H_2 mixtures shown to decelerate with stretch rate increase for water addition, and the opposite in evidence for the higher H_2 mixtures. Results therefore suggest that water addition works to potentially stabilise BFG u_L , decreasing the magnitude of the range measured from H_2 increase.

A representative COG blend was tested with resultant atmospheric u_L shown to be significantly faster than any BFG composition, in addition to natural gas. Consequently small fractions of COG were added to the previously tested BFG blends to again quantify the dampening influence for change in u_L . COG addition was shown to be beneficial in reducing not only the magnitude of relative fluctuation in u_L , but also the quantified influence of flame stretch and energy density, and therefore possibly the best mechanism for reducing the inherent variation initially quantified. BOS gas blends were then modelled based on the accuracy of previous results, and suggested the potential for influential relationships with both moisture content, and BFG blending.

Experimental values of burning velocity were compared to those obtained using computational models, employing multiple chemical reaction mechanisms. The Li and Davis mechanisms demonstrated the most accurate results for modelling BFG u_L , with the preferable selection based on a function of composition, equivalence ratio and ambient condition. None of the mechanisms employed in this study modelled COG combustion in close agreement with experimental data, and is unsurprisingly complex given the number of constituent species, and resultant intermediate reactions.

Recommendations for further Work

Several recommendations for further investigation can be made as a result of the work presented in this thesis:

Firstly the experimental setup could be modified with larger, or an increased number of bolts. This would facilitate the performance of tests at higher values of initial ambient pressure. This would also allow for further development and validation of chemical reaction mechanisms at non atmospheric-conditions, such as those experienced in gas turbine combustors.

The work presented in the final chapter highlighted the potential for BOS gas combustion to be significantly influenced by H₂O addition, and more than the presented work with BFG. These results were only modelled, and it would be interesting to experimentally quantify this influence with BOS gas becoming a more widely utilised fuel, particularly from the perspective of blended BOS and BFG. The results would also allow the quantification of the influence of flame stretch, and potentially have wider ramifications concerning the use of other synthesised fuels.

The mechanisms presented in this thesis suggest ways of improving practical BFG combustion by reducing operational instabilities and dampening u_L fluctuation. This work is presented from a perspective of fundamental fuel characterisation, and it would be beneficial to see the presented suggestions applied on a practical burner. This would also facilitate the further characterisation of flame stretch influence, and determination of critical Karlovitz numbers, together with providing an opportunity to correlate some of the values attained for u_L with equivalent turbulent flame speeds.

References

- [1] Contribution of Working Groups I, II and III to the Fourth Assessment Report of the Intergovernmental Panel on Climate Change. Core Writing Team, Pachauri, R.K. and Reisinger, A. (Eds.). IPCC, Geneva, Switzerland. pp 104
- [2] D.M. Etheridge, L.P. Steele, R.L. Langenfelds, R.J. Francey, J.-M. Barnola and V.I. Morgan. 1998. Historical CO₂ records from the Law Dome DE08, DE08-2, and DSS ice cores. In Trends: A Compendium of Data on Global Change. Carbon Dioxide Information Analysis Center, Oak Ridge National Laboratory, U.S. Department of Energy, Oak Ridge, Tenn., U.S.A.
- [3] Keeling, C. D. "The concentration and isotopic abundances of atmospheric carbon dioxide in rural areas" *Geochimica et Cosmochimica Acta*, Volume 13, Issue 4, 1958, pp 322–33.
- [4] NOAA/ESRL data servers. <<ftp://ftp.cmdl.noaa.gov/ccg/co2/in-situ/>> Accessed 17/01/2013
- [5] Caldeira, K.; Wickett, M. E. (2003). "Anthropogenic carbon and ocean pH". *Nature* 425 (6956): 365–365.
- [6] WEO 2012 – World Energy Outlook. (2012). International Energy Agency, IEA publications.
- [7] Kim, Y., Worrell, E. "International comparison of CO₂ emission trends in the iron and steel industry", *Energy Policy*, Volume 30, Issue (10), 2002, pp 827-838.
- [8] World Steel Association–climate change. "<http://www.worldsteel.org/steel-by-topic/climate-change.html>". Accessed 17/01/2013.
- [9] Hidalgo, I. Szabo, L. Ciscar, J. Soria, A. "Technological prospects and CO₂ emission trading analyses in the iron and steel industry: A global model". *Energy*, Volume 30, Issue 5, 2005, pp 583–610
- [10] World Steel Association – Statistics Archive. "<http://www.worldsteel.org/statistics/statistics-archive.html>". Accessed 18/01/2013.
- [11] Tanaka, K., K. Sasaki, and H. Kudoh, 2005: Estimation of CO₂ reduction potentials through energy efficient technologies. *Journal of Institute for Energy Economics in Japan*, 31, pp. 61-81.
- [12] IPPC, European Commission, (2001). "Best Available Techniques Reference Document on the Production of Iron and Steel".
- [13] Steel University. "<http://www.steeluniversity.org>". Accessed 19/01/2013.
- [14] Biswas, A.K. 1981. "Principles of blast furnace Ironmaking: Theory and Practice" Cootha.
- [15] The State-of-the-Art Clean Technologies (SOACT) for Steelmaking Handbook. 2010.
- [16] Razzaq, R. Li, C. Zhang, S. "Coke oven gas: Availability, properties, purification, and utilization in China Fuel, Volume 113, November 2013, pp 287–299.
- [17] Ghosh, Chatterjee. 2008. "Iron maing and Steelmaking: Theory and Practise". Prentice-Hall of India
- [18] Stolte, G. 2002. "Secondary Metallurgy: Fundamentals, Processes, Applications". Stahleisen.
- [19] Nicholson, G, Stafford, M. Process for dissolving coke oven deposits comprising atomizing a composition containing N-methyl-2-pyrrolidone into the gas lines. US 5225002 A

- [20] Higman, C and van der Burgt. 2008. M. "Gasification" Gulf Professional Publishing.
- [21] Ziebek, A. and W. Stanek, 2001: Forecasting of the energy effects of injecting plastic wastes into the blast furnace in comparison with other auxiliary fuels. *Energy*, 26, pp. 1159-1173.
- [22] US department of Energy. "Blast Furnace Granulated Coal Injection System Demonstration Project": A DOE Assessment. DOE/NETL-2000/1122. 2000
- [24] Lajtonyi, A. 2006. "Blast Furnace Gas Cleaning Systems" Danieli Corus.
- [24] Industriail efficiency technology database. <<http://www.ietd.iipnetwork.org/content/bof-heat-and-gas-recovery>>. Accessed 21/01/2013
- [25] Macheimer SD. Characterization of airborne and bulk particulate from iron and steel manufacturing facilities. *Environ Sci Technol*. 2004 Jan 15;38(2):381-9.
- [26] Ge energy. "Addressing Gas Turbine Fuel Flexibility". GER4601 2011.
- [27] Law, C, K. "Combustion Physics", 2006. Cambridge University Press.
- [28] Bernard Lewis, Guenther von Elbe. 1987. "Combustion, Flames and Explosions of Gases", Third Edition.
- [29] Lieuwen, T. "Unsteady Combustor Physics", 2012, Cambridge University Press.
- [30] Parry, S. 2011. "History of the Steel Industry in the Port Talbot Area 1900-1988". Ph.D thesis. University of Leeds.
- [31] Tata Steel, "Visitor Guide - Port Talbot Works". www.tatasteeleurope.com. Accessed 18/01/2013
- [32] EEF UK Steel. 2012. "UK Steel Key Statistics 2012". <http://www.eef.org.uk/uksteel/Publications/UK-Steel-Key-Statistics-2012.htm> Accessed 18/01/2013
- [33] Duffy, G. Hoffrock, W. Lines, G. Stirling, C. 2008. "Energy Optimisation at Morfa Coke Ovens". COMA meeting 2008, Scunthorpe.
- [34] BBC news. <<http://www.bbc.co.uk/news/uk-wales-south-west-wales-21427441>> Accessed 18/01/2013.
- [35] BBC news. <<http://news.bbc.co.uk/1/hi/wales/1763883.stm>> Accessed 18/01/2013.
- [36] Daniel Pugh, Anthony Giles, Andrew Hopkins, Tim O'Doherty, Anthony Griffiths, Richard Marsh, "Thermal distributive blast furnace gas characterisation, a steelworks case study", *Applied Thermal Engineering*, Volume 53, Issue 2, 2 May 2013, Pages 358-365.
- [37] BBC news. <http://news.bbc.co.uk/1/hi/wales/south_west/8677820.stm> Accessed 18/01/2013.
- [38] Steve dye presentation "BOS Gas - Toxic, Flammable and Explosive". Accessed 23/01/2013.
- [39] Robert E. Markland, "Improving fuel utilization in steel mill operations using linear programming". *Journal of Operations Management*, Volume 1, Issue 2, November 1980, Pages 95-102.
- [40] J.H. Kim, H. Yi, C. Han, C. Park, Y. Kim, "Plant-wide multiperiod optimal energy resource distribution and byproduct gas holder level control in the iron and steel making process under varying energy demands". *Computer Aided Chemical Engineering*, Elsevier, 2003, Volume 15, Pages 882-887.

- [41] Haining Kong, Ershi Qi, Hui Li, Gang Li, Xing Zhang, "An MILP model for optimization of by-product gases in the integrated iron and steel plant", *Applied Energy*, Volume 87, Issue 7, July 2010, Pages 2156-2163.
- [42] Zhang, Q. Cai, J.-J Pang, X.-L. Jiang, W.-H. "Analysis for gas energy flow network of steel enterprises based on hybrid Petri net"
- [43] Zhu, J. Qiao, F., Zhao, F., Li, L., Li, G.-Q. *Coal International Communications in Heat and Mass Transfer*, Volume 19, Issue 3, May–June 1992, Pages 409-421 H.K Ma, F.S Wu.
- [44] Green, J, Strickland, A, E. Kimsesiz, I. Temuçin "Blast Furnace Gas-Fired Boiler for Ereğli Iron &Steel Works (Erdemir), Turkey". American Power Conference April 9-11, 1996 Chicago, Illinois, U.S.A.
- [45] Andritz power <<http://www.andritz.com/products-and-services/pf-detail.htm?productid=13623>> Accessed 23/01/2013.
- [46] Mitsubishi Power ,<http://english.cwpc.com.cn/business.aspx?cate=2>> Accessed 23/01/2013.
- [47] Shyan-Shu Shieh, Yi-Hsin Chang, Shi-Shang Jang, Ming-Da Ma, Ta-Sung Huang "Improving fuel utilization in steel mill operations using linear programming" *Journal of Operations Management*, Volume 1, Issue 2, November 1980, Pages 95-102.
- [48] S.S. Hou, C.H. Chen, C.Y. Chang, C.W. Wu, J.J. Ou, T.H. Lin, "Firing blast furnace gas without support fuel in steel mill boilers", *Energy Conversion and Management*, Volume 52, Issue 7, July 2011, Pages 2758-2767.
- [49] Milorad Bojic, Panos Mourdoukoutas, "Energy saving does not yield CO2 emissions reductions: the case of waste fuel use in a steel mill", *Applied Thermal Engineering*, Volume 20, Issue 11, 1 August 2000, Pages 963-975.
- [50] M. Bojić, M. Tomić, "Effect of refuse-gas fuel use on energy consumption in an industrial pusher furnace", *Energy*, Volume 23, Issue 9, September 1998, Pages 767-775,
- [51] Takashi Kiga, Takehiko Ito, Motoya Nakamura, Shinji Watanabe "Development of Blast-Furnace Gas Firing Burner for Cofiring Boilers with Pulverized Coal" *Impact of Mineral Impurities in Solid Fuel Combustion*. 2002, pp 285-295.
- [52] H.K Ma, F.S Wu, "Effect of BFG cofiring on unburned carbon formation in a coal-fired boiler", *International Communications in Heat and Mass Transfer*, Volume 19, Issue 3, May–June 1992, Pages 409-421.
- [53] Clarke Energy <<http://www.clarke-energy.com/gas-type/steel-production-gas/>> Accessed 24/01/2013.
- [54] GE energy <<http://www.genewscenter.com/Press-Releases/Yonggang-Group-to-Install-GE-Cogeneration-Systems-Fueled-with-Blast-Furnace-Gas-to-Provide-Cleaner-E-40ed.aspx>> Accessed 23/01/2013.
- [55] Richards, J. W. 1900. "The use of blast furnace gases in gas engines". *Journal of the Franklin Institute* 150(6), pp. 406-415.
- [56] Lawton, B. 2011. "A Short History of Large Gas Engines". *International Journal for the History of Engineering & Technology*, Volume 81, Number 1, January 2011 , pp. 79-107(29)

- [57] Jenbacher steelworks gases. <http://www.ge-energy.com/solutions/steel_gas.jsp> accessed 02/03/2011.
- [58] GE Technical Instruction No.: 1000-0302 Fuel gas quality Special gases
- [59] Liu, Y., Wang X., Zhu G, Liu R, Gao Z. 2011. "Simulation on the Combustion Property of Blast-Furnace Gas Engine by GT-POWER. Advanced Materials Research". Volumes 156 – 157, AMT . pp. 965-968.
- [60] Y. Ando, K. Yoshikawa, M. Beck, H. Endo, "Research and development of a low-BTU gas-driven engine for waste gasification and power generation", Energy, Volume 30, Issues 11–12, August–September 2005, Pages 2206-2218
- [61] Murari Mohon Roy, Eiji Tomita, Nobuyuki Kawahara, Yuji Harada, Atsushi Sakane, "Comparison of performance and emissions of a supercharged dual-fuel engine fueled by hydrogen and hydrogen-containing gaseous fuels", International Journal of Hydrogen Energy, Volume 36, Issue 12, June 2011, Pages 7339-7352.
- [62] D.B. Lata, Ashok Misra, S. Medhekar, "Investigations on the combustion parameters of a dual fuel diesel engine with hydrogen and LPG as secondary fuels", International Journal of Hydrogen Energy, Volume 36, Issue 21, October 2011, Pages 13808-13819.
- [63] GE news <<http://www.genewscenter.com/Press-Releases/Industry-Milestone-GE-s-Heavy-Duty-Gas-Turbines-Surpass-2-Million-Fired-Hours-on-Low-Carbon-Intensity-Fuels-3753.aspx>>. Accessed 01/03/2013.
- [64] Mcmillan R, Marriot D, "Fuel flexible gas turbine co generation". Power gen Asia 2008, Kuala Lumpur, Malaysia.
- [65] Alstom Power <<http://www.alstom.com/power/gas-power/turnkey-power-plants/combined-cycle/ka11n2/>>. Accessed 02/03/2013
- [66] Komori T., Yamagami N., Hara H. Design for blast furnace gas firing gas turbine. Available at: <http://www.mnes-usa.com/power/news/sec1/pdf/2004_nov_04b.pdf> accessed 04/03/2013
- [67] Bonzani, F. Pollarolo, G. Rocca, F. 2002. "Operating Experience of Ansaldo V94.2 K Gas Turbine Fed by Steelworks Gas". ASME Conference Proceedings 2002(36061), pp. 203-208.
- [68] Min Chul Lee, Seok Bin Seo, Jae Hwa Chung, Si Moon Kim, Yong Jin Joo, Dal Hong Ahn, "Gas turbine combustion performance test of hydrogen and carbon monoxide synthetic gas", Fuel, Volume 89, Issue 7, July 2010, Pages 1485-1491.
- [69] Min Chul Lee, Seok Bin Seo, Jisu Yoon, Minki Kim, Youngbin Yoon, "Experimental study on the effect of N₂, CO₂, and steam dilution on the combustion performance of H₂ and CO synthetic gas in an industrial gas turbine". Fuel, Volume 102, December 2012, Pages 431-438.
- [70] R. Chacartegui, D. Sánchez, J.M. Muñoz de Escalona, A. Muñoz, T. Sánchez, "Gas and steam combined cycles for low calorific syngas fuels utilisation", Applied Energy, Volume 101, January 2013, Pages 81-92.
- [71] Ahmed E.E. Khalil, Vaibhav K. Arghode, Ashwani K. Gupta, Sang Chun Lee, "Low calorific value fuelled distributed combustion with swirl for gas turbine applications", Applied Energy, Volume 98, October 2012, Pages 69-7.
- [72] Olivier Gicquel, Luc Vervisch, Guillaume Joncquet, Bernard Labegorre, Nasser Darabiha, "Combustion of residual steel gases: laminar flame analysis and turbulent flamelet modelling", Fuel, Volume 82, Issue 8, May 2003, Pages 983-991.

- [73] Peter Lindstedt, "Modeling of the chemical complexities of flames", Symposium (International) on Combustion, Volume 27, Issue 1, 1998, Pages 269-285.
- [74] Mohammed Abdulsada, Nicholas Syred, Philip Bowen, Tim O'Doherty, Anthony Griffiths, Richard Marsh, Andrew Crayford, "Effect of exhaust confinement and fuel type upon the blowoff limits and fuel switching ability of swirl combustors", Applied Thermal Engineering, Volume 48, 15 December 2012, Pages 426-435.
- [75] Jonathan Lewis, Richard Marsh, Yura Sevcenco, Steven Morris, Anthony Griffiths, Philip Bowen, "The effect of variable fuel composition on a swirl-stabilised producer gas combustor", Energy Conversion and Management, Volume 64, December 2012, Pages 52-61.
- [76] X. Paubel, A. Cessou, D. Honore, L. Vervisch, R. Tsiava, "A flame stability diagram for piloted non-premixed oxycombustion of low calorific residual gases", Proceedings of the Combustion Institute, Volume 31, Issue 2, January 2007, Pages 3385-3392
- [77] Bunsen, R. & Roscoe, H.E. 1857 "Photochemische Untersuchungen". Poggendorffs Ann. Physik 100, 43-88.
- [78] Mallard, E. & Le Chatelier, H.L. 1883 Recherches Experimentelles et Théoriques sur la Combustion des Mélanges Gaseux Explosifs. Ann. Mines 8, 274.
- [79] Chamberlin, D.S. & Clarke, D.R. 1928 "Flame Speed of Hydrogen Sulfide". Proc. Combust. Inst. 1, 33-35.
- [80] Stevens, F.W. 1923 Natl. Advisory Comm. Aeronaut., Rept. No. 176.
- [81] Wheeler, R.V. 1918 J. Chem. Soc. (London) 113, 840.
- [82] Payman, W. 1928 The "Normal" Propagation of Flame in Gaseous mixtures. Proc. Combust. Inst. 1, 51-60.
- [83] Coward, H.F. & Payman, W. 1937 Problems in Flame Propagation. Proc. Combust. Inst. 2, 189-193.
- [84] Lewis, B. & Von Elbe, G. 1937 Theory of Flame Propagation. Proc. Combust. Inst. 2, 183-188.
- [85] Fiock, E.F. & Marvin Jr., C.F. 1937 The Measurement of Flame Speeds. Proc. Combust. Inst. 2, 194-205.
- [86] Von Elbe, G. and Lewis, B. Stability and structure of burner flames, J. Chem. Phys. 11, 75-97 (1943).
- [87] Powling, J. 1949 "A New Burner Method for the Determination of Low Burning Velocities and Limits of Inflammability". Fuel 28, 25-28.
- [88] Botha, J.P. and Spalding, D.B. (1954) "The Laminar Flame Speed of Propane/Air Mixtures with Heat Extraction from the Flame. Proceedings of the Royal Society of London". Series A, Mathematical and Physical Sciences, 225, 71-96.
- [89] Karlovitz, B., Denniston, D.W., Knapschafer, D.H. & Wells, F.E. 1952 "Studies on Turbulent Flames". Proc. Combust. Inst. 4, 613-620.
- [90] Markstein, G.H. 1951 "Experimental and Theoretical Studies of Flame-Front Stability". J. Aero. Sci. 18, 199.
- [91] Markstein, G.H. (ed.) 1964 "Nonsteady Flame Propagation". The Macmillan Co., New York.

- [92] Wu, C.K. & Law, C.K. 1984 "On the Determination of Laminar Flame Speeds from Stretched Flames". Proc. Combust. Inst. 20, 1941-1949.
- [93] Andrews, G.E. & Bradley, D. 1972 "Determination of Burning Velocities: A Critical Review". Combust. Flame 18, 133-153.
- [94] T. Lieuwen, V. McDonell, D. Santavicca, T. Sattelmayer, "Burner development and operability issues associated with steady flowing syngas fired combustors" Combust Sci Tech, 180 (2008), pp. 1169–1192
- [95] Hermanns. Phd Thesis. 2007. "Laminar Burning Velocities of Methane-Hydrogen-Air Mixtures"
- [96] Bouvet. Phd Thesis. 2009. "Experimental and Numerical Studies of the Fundamental Flame Speeds of Methane/Air and Syngas (H₂/CO)/Air Mixtures".
- [97] Eichler. Phd Thesis. 2011. "Flame flashback in wall boundary layers in premixed combustion systems".
- [98] Van Maaren, A., Thung, D.S. and De Goey, L.R.H. (1994) "Measurement of Flame Temperature and Adiabatic Burning Velocity of Methane/Air Mixtures". Combustion Science and Technology, 96, 327-344.
- [99] Bradley, D., Gaskell, PH, Gu, X,J. 1996. "Burning Velocities, Markstein Lengths, and Flame Quenching for Spherical Methane-Air Flames: A Computational Study" Combustion and Flame, 104, (1-2): pp 176-198.
- [100] Derek Bradley, "How fast can we burn?", Symposium (International) on Combustion, Volume 24, Issue 1, 1992, Pages 247-262.
- [101] C.J. Rallis, A.M. Garforth, "The determination of laminar burning velocity", Progress in Energy and Combustion Science, Volume 6, Issue 4, 1980, Pages 303-32.
- [102] Gu, X., Haq, M., Lawes, M., Wooley, R. 2000. "Laminar burning velocity and Markstein lengths of methane-air mixtures" Combustion and Flame, 2000. 121(1-2): pp. 41-58.
- [103] Toni Tahtouh, Fabien Halter, Christine Mounaïm-Rousselle, "Measurement of laminar burning speeds and Markstein lengths using a novel methodology, Combustion and Flame", Volume 156, Issue 9, September 2009, Pages 1735-1743.
- [104] Kelley, A.P. and C.K. Law. 2009. "Nonlinear effects in the extraction of laminar flame speeds from expanding spherical flames". Combustion and Flame. 156(9): pp. 1844-1851.
- [105] Halter, F., Tahtouh, T., and Mounaïm-Rousselle, C., 2010 "Nonlinear effects of stretch on the flame front propagation. Combustion and Flame". 157(10): pp. 1825-1832.
- [106] E. Varea, V. Modica, A. Vandiel, and B. Renou. "Measurement of laminar burning velocity and markstein length relative to fresh gases using a new postprocessing procedure: Application to laminar spherical flames for methane, ethanol and isooctane/air mixtures". Combustion and Flame, 159:577–590, 2012.
- [107] Vagelopoulos, C.M. and Egolfopoulos, F.N. (1994) "Laminar flame speeds and extinction strains rates of mixtures of carbon monoxide with hydrogen, methane, and air". Symposium (International) on Combustion, 25, 1317-1323.
- [108] O. Kurata, S. Takahashi, and Y. Uchiyama. "Influence of preheat temperature on the laminar burning velocity of methane-air mixtures". SAE Technical Paper, 1994.

- [109] Ilbas M, Crayford AP, Yilmaz I, Bowen PJ, Syred N. 2006 "Laminar burning velocities of hydrogen–air and hydrogen–methane–air mixtures: an experimental study". *International Journal of Hydrogen Energy*; 31: pp.1768–79.
- [110] Fabien Halter, Christian Chauveau, Iskender Gökalp, "Characterization of the effects of hydrogen addition in premixed methane/air flames", *International Journal of Hydrogen Energy*, Volume 32, Issue 13, September 2007, Pages 2585-2592.
- [111] Erjiang Hu, Zuohua Huang, Jiajia He, Chun Jin, Jianjun Zheng, "Experimental and numerical study on laminar burning characteristics of premixed methane–hydrogen–air flames", *International Journal of Hydrogen Energy*, Volume 34, Issue 11, June 2009, Pages 4876-4888.
- [112] T. Boushaki, Y. Dhué, L. Selle, B. Ferret, T. Poinso, "Effects of hydrogen and steam addition on laminar burning velocity of methane–air premixed flame: Experimental and numerical analysis", *International Journal of Hydrogen Energy*, Volume 37, Issue 11, June 2012, Pages 9412-9422.
- [113] Taylor. PhD Thesis. 1991. "Burning velocity and the influence of flame stretch".
- [114] T. Tahtouh, F. Halter, E. Samson, C. Mounaïm-Rousselle, "Effects of hydrogen addition and nitrogen dilution on the laminar flame characteristics of premixed methane–air flames", *International Journal of Hydrogen Energy*, Volume 34, Issue 19, October 2009, Pages 8329-8338.
- [115] Haiyan Miao, Min Ji, Qi Jiao, Qian Huang, Zuohua Huang, "Laminar burning velocity and Markstein length of nitrogen diluted natural gas/hydrogen/air mixtures at normal, reduced and elevated pressures". *International Journal of Hydrogen Energy*, Volume 34, Issue 7, April 2009, Pages 3145-3155.
- [116] Ji, M.a , Miao, H.ab, Jiao, Q.a, Huang, Q.a, Huang, Z.a. "Flame propagation speed of CO₂ diluted hydrogen-enriched natural gas and air mixtures". *Energy and Fuels* Volume 23, Issue 10, 15 October 2009, Pages 4957-4965
- [117] Dowdy, D.R., Smith, D.B., Taylor, S.C. & Williams, A. 1990 "The Use of Expanding Spherical Flames to Determine Burning Velocities and Stretch Effects in Hydrogen/Air Mixtures". *Proc. Combust. Inst.* 23, 325-332.
- [118] D. Bradley, M. Lawes, Kexin Liu, S. Verhelst, R. Woolley, "Laminar burning velocities of lean hydrogen–air mixtures at pressures up to 1.0 MPa", *Combustion and Flame*, Volume 149, Issues 1–2, April 2007, Pages 162-172.
- [119] C.K. Law, G. Jomaas, J.K. Bechtold, "Cellular instabilities of expanding hydrogen/propane spherical flames at elevated pressures: theory and experiment". *Proceedings of the Combustion Institute*, Volume 30, Issue 1, January 2005, Pages 159-167.
- [120] Lowry, W. de Vries, J. Krejci, M. Petersen, E. Serinyel, Z. Metcalfe, W. Curran, H. Bourque, G. 2011. "Laminar Flame Speed Measurements and Modeling of Pure Alkanes and Alkane Blends at Elevated Pressures" *J. Eng. Gas Turbines Power* 133.
- [121] Egolfopoulos, F.N. & Law, C.K. 1990 "An Experimental and Computational Study of the Burning Rates of Ultra-Lean to Moderately-Rich H₂/O₂/N₂ Laminar Flames with Pressure Variations". *Proc. Combust. Inst.* 23, 333-340.
- [122] Bouvet N., Chauveau C., Gokalp I., Halter F. 2011. "Experimental studies of the fundamental flame speeds of syngas (H₂/CO)/air mixtures" *Proceedings of the Combustion Institute*; 33: pp.913–920.
- [123] C. Prathap, Anjan Ray, M.R. Ravi, "Investigation of nitrogen dilution effects on the laminar burning velocity and flame stability of syngas fuel at atmospheric condition", *Combustion and Flame*, Volume 155, Issues 1–2, October 2008, Pages 145-160.

- [124] C. Prathap, Anjan Ray, M.R. Ravi, "Effects of dilution with carbon dioxide on the laminar burning velocity and flame stability of H₂-CO mixtures at atmospheric condition", *Combustion and Flame*, Volume 159, Issue 2, February 2012, Pages 482-492.
- [125] Apurba K. Das, Kamal Kumar, Chih-Jen Sung, "Laminar flame speeds of moist syngas mixtures", *Combustion and Flame*, Volume 158, Issue 2, February 2011, Pages 345-353.
- [126] Eliseu Monteiro, Abel Rouboa, "Multi-zone modeling and simulation of syngas combustion under laminar conditions", *Applied Energy*, Available online 18 September 2012.
- [127] Hugo J. Burbano, Jhon Pareja, Andrés A. Amell, "Laminar burning velocities and flame stability analysis of H₂/CO/air mixtures with dilution of N₂ and CO₂", *International Journal of Hydrogen Energy*, Volume 36, Issue 4, February 2011, Pages 3232-3242.
- [128] Hugo J. Burbano, Jhon Pareja, Andrés A. Amell, "Laminar burning velocities and flame stability analysis of syngas mixtures at sub-atmospheric pressures", *International Journal of Hydrogen Energy*, Volume 36, Issue 4, February 2011, Pages 3243-3252.
- [129] C.C. Liu, S.S. Shy, C.W. Chiu, M.W. Peng, H.J. Chung, "Hydrogen/carbon monoxide syngas burning rates measurements in high-pressure quiescent and turbulent environment", *International Journal of Hydrogen Energy*, Volume 36, Issue 14, July 2011, Pages 8595-8603.
- [130] Ronney, P.D. and Sivashinsky, G.I. (1989) "A Theoretical Study of Propagation and Extinction of Non-steady Spherical Flame Fronts". *SIAM Journal on Applied Mathematics*, 49, 1029-1046.
- [131] Clavin, P. (1985) "Dynamic behaviour of premixed flame fronts in laminar and turbulent flows". *Progress in Energy and Combustion Science*, 11, 1-59.
- [132] Z. Chen, Y. Ju, *Combust. Theor. Model.* 11 (2007) 427-453.
- [133] A.E. Dahoe, L.P.H. de Goey, "On the determination of the laminar burning velocity from closed vessel gas explosions", *Journal of Loss Prevention in the Process Industries*, Volume 16, Issue 6, November 2003, Pages 457-478
- [134] C.C.M. Luijten, E. Doosje, J.A. van Oijen, L.P.H. de Goey, "Impact of dissociation and end pressure on determination of laminar burning velocities in constant volume combustion", *International Journal of Thermal Sciences*, Volume 48, Issue 6, June 2009, Pages 1206-1212.
- [135] K. O'Donovan, C. Rallis, *Combust. Flame* 3 (1959) 201-214.
- [136] Burke, M., Chen, Z., Ju, Y., Dryer, F., 2009. "Effect of cylindrical confinement on the determination of laminar flame speeds using outwardly propagating flames". *Combustion and Flame*, 156(4): pp. 771-779.
- [137] Holder, D. North, R. Schlieren methods. 1963 National Physical Laboratory.
- [138] Photron fastcam APX-RS manual. Available from <www.downloads.techimaging.com>
- [139] Considerations for Primary Vacuum Pumping in Mass Spectrometry Systems. Edwards. Accessed 01/12/2010 <<http://www.edwardsvacuum.com/>>
- [140] Crayford. PhD Thesis. 2004 "Suppression of Methane-Air Explosions with Water in the form of 'Fine' Mists".
- [141] Cameron. PhD Thesis. 1999. "Aerosol explosion hazard quantification".
- [142] Daniel L. Reger, Scott R. Goode, David Warren Ball "Chemistry: Principles and Practice":

- [143] Ross. PhD thesis. 1997. "Lean combustion characteristics of Hydrogen-Nitrous Oxide-Ammonia mixtures in air".
- [144] U.J Pfahl, M.C Ross, J.E Shepherd, K.O Pasamehmetoglu, C Unal, "Flammability limits, ignition energy, and flame speeds in H₂-CH₄-NH₃-N₂O-O₂-N₂ mixtures", *Combustion and Flame*, Volume 123, Issues 1-2, October 2000, Pages 140-158.
- [145] R. J. Kee, J. F. Grcar, M. D. Smooke, J. A. Miller, and E. Meeks PREMIX: "AFORTRAN Program for Modeling Steady Laminar One- dimensional Premixed Flames" 1998.
- [146a] Reaction Design, CHEMKIN-PRO Theory manual.
- [146b] Reaction Design, CHEMKIN-PRO PREMIX manual.
- [147] Reaction Design, CHEMKIN-PRO manual (for interpreter input).
- [148] Nasa polynomials available at <http://www.me.berkeley.edu/gri_mech/data/nasa_plnm.html> Accessed 03/04/2011
- [149] Bowman CT, Frenklach M, Gardiner WC, Smith GP.1999 The "GRIMech 3.0" chemical kinetic mechanism"; www.me.berkeley.edu/grimech.
- [150] Bruce R. Hargreaves, Thomas P. McWilliams, "Polynomial Trendline function flaws in Microsoft Excel, *Computational Statistics & Data Analysis*", Volume 54, Issue 4, 1 April 2010, Pages 1190-1196.
- [151] NIST Chemistry WebBook <<http://webbook.nist.gov/chemistry/>>
- [152] M.I Hassan, K.T Aung, G.M Faeth, "Measured and predicted properties of laminar premixed methane/air flames at various pressures", *Combustion and Flame*, Volume 115, Issue 4, December 1998, Pages 539-550.
- [153] Erjiang Hu, Zuohua Huang, Jiajia He, Chun Jin, Jianjun Zheng, "Experimental and numerical study on laminar burning characteristics of premixed methane-hydrogen-air flames", *International Journal of Hydrogen Energy*, Volume 34, Issue 11, June 2009, Pages 4876-4888.
- [154] R.T.E. Hermanns, A.A. Konnov, R.J.M. Bastiaans, L.P.H. de Goey, K. Lucka, H. Köhne, "Effects of temperature and composition on the laminar burning velocity of CH₄ + H₂ + O₂ + N₂ flames", *Fuel*, Volume 89, Issue 1, January 2010, Pages 114-121.
- [155] El-Sherif SA. "Control of emissions by gaseous additives in methane-air and carbon monoxide-air flames". *Fuel* 2000;79(5):567-75.
- [156] Coppens FHV, De Ruyck J, Konnov AA. "Effects of hydrogen enrichment on adiabatic burning velocity and NO formation in methane + air flames". *Exp Therm Fluid Sci* 2007;31(5):437-44.
- [157] Haniff MS, Melvin A, Smith DB, Williams A. "The burning velocities of methane and SNG mixtures with air". *J I Energy* 1989;62:229-36.
- [158] Stone R, Clarke A, Beckwith P. "Correlations for the laminar burning velocity of methane/diluent/air mixtures obtained in free fall experiments". *Combust Flame* 1998;114:546-55.
- [159] S.Y. Liao, D.M. Jiang, Q. Cheng, "Determination of laminar burning velocities for natural gas", *Fuel*, Volume 83, Issue 9, June 2004, Pages 1247-1250.
- [160] Moffat RJ. "Describing uncertainties in experimental results". *Exp Therm Flu Sci* 1988;1:3-17.

- [161] Student t-values. <www.sjsu.edu/faculty/gerstman/StatPrimer/t-table.pdf> accessed 09/03/2011.
- [162] BOC Product Code and Product Listings available from <<http://www.boconline.co.uk/en/products-and-supply/speciality-gas/pure-gases/pure-gases.html>>.
- [163] Ziebig A, Stanek W. "Identification of the influence of blast-furnace working parameters upon the supply and net calorific value of blast furnace gas". *Acta Montan Slovaca* 2003;4.
- [164] Li J., Zhao Z., Kazakov A., Chaos M., Dryer F.L., 2007 "A comprehensive kinetic mechanism for CO, CH₂O, and CH₃OH combustion". *Int. J. Chem. Kinet.* 39: pp.109–136.
- [165] Davis, S. G., Joshi, A. V., Wang, H., and Egolfopoulos, F. 2005. "An optimized kinetic model of H₂/CO combustion." *Proceedings of the Combustion Institute*, 30, pp. 1283- 1292.
- [166] Derek Dunn-Rankin, *Lean combustion: technology and control* Amsterdam; Boston: Academic Press, 2008.
- [167] Mueller, M.A., Yetter, R.A., and Dryer, F.L., *Int. J. Chem. Kinet.* 1999, 31, 113.
- [168] Han P, Checkel MD, Fleck BA, Nowicki NL. "Burning velocity of methane/diluent mixture with reformer gas addition". *Fuel* 2007;86(4):585–96.
- [169] S. Heibel, "Effect of Initial Mixture Temperature on Burning Velocity of Hydrogen-Air Mixtures with preheating and simulated preburning", NASA TN- 3833, 1956.
- [170] R K Sinnott. "Chemical Engineering Design", Volume 6. 2005.

Appendices

Appendix A – Ancillary Information

A.1 - Example Tata Gas Chromatograph Analysis



Central Laboratory
BOS Administration
Block
Corus Strip Products
Port Talbot Works
Port Talbot
West Glamorgan
SA13 2NG



PDG
Corus Strip Products
Port Talbot Works
Port Talbot
West Glamorgan
SA13 2NG

Component	Hydrogen	Oxygen	Nitrogen	Carbon	Ethylene	Ethane	Carbon	Methane	Total	Total
	H2	O2	N2	Dioxide			Monoxide			
Analysis Method	GC	GC	GC	GC	GC	GC	GC	GC	Permanent Gases	Including Aromatics
Sample Identity										
CO Gas 22/03/10 (% composition)	61.50	0.60	4.27	1.56	1.65	0.37	5.96	23.49	99.40	
CO Gas 22/03/10 Gross CV (MJ/m ³)	7.87	0.00	0.00	0.00	1.03	0.26	0.76	9.34	19.25	19.43
CO Gas 22/03/10 Net CV (MJ/m ³)	6.64	0.00	0.00	0.00	0.96	0.23	0.76	8.40	16.99	17.16
Aromatics	Benzole (g/m ³)	Gross (MJ/m ³)	Net (MJ/m ³)			Naph (g/m ³)	Gross (MJ/m ³)	Net (MJ/m ³)		
	4.20	0.18	0.17			0.011	0.00	0.00		

Key: CA=Combustion Analysis, OES=Optical Emission Spectroscopy, XRF=X-Ray Fluorescence, ICP= Inductively Coiled Plasma, AA=Atomic Absorption, GC= Gas Chromatography.

Certificate No. Port Talbot Job No:-0129 Page 1 of 1 Date of Issue 22/03/2010 Customer Specification--	Description of Test Sample Morfa Coke Ovens Gas
---	--

All work is carried out in accordance with our Terms and Conditions, a copy of which is available on request. This report shall not be reproduced except in full, without written approval of Corus Central Laboratory.

Sampled at Naphth Washer Outlet on 22/03/10 Barometric Pressure = 1012mb Gas Pressure = 31 psig Gas Temp = 23.97°C N.E. C.V. calculated as sampled. No Normalisation or correction for pressure, temperature or water content.	These results are certified by Corus Central Laboratory Signed: CARC GREGG/CLADE - Senior Chemist Countersigned: Andrew Jones - Technologist
--	--

A.2 - Reference Properties, Constants and Coefficients

Universal Gas Constant – $R = 8.314472 \text{ J}\cdot(\text{K}\cdot\text{mol}^{-1})$

The values of any molar masses were calculated using the following atomic weights, with examples of some example calculated values (shown to 4 significant figures)

Atomic weight (u)	
C	12.0107
H	1.00794
O	15.9994
N	14.00674
Ar	39.948

Molar Mass ($\text{g}\cdot\text{mol}^{-1}$) - M_i	
H ₂	2.0159
CO	28.0101
CH ₄	16.0425
N ₂	28.0135
C ₂ H ₄	28.0532
C ₂ H ₆	30.0690
CO ₂	44.0095
O ₂	31.9988
H ₂ O	18.0153

Average molar masses of gaseous mixtures were calculated using the values above and Eqn. (3.28). So for example, the equivalent molar mass of air comprising 79 percent nitrogen and 21 percent oxygen had an equivalent molar mass thus:

$$M_{\text{air}} = [(0.79 \times 28.0135) + (0.21 \times 31.9988)] = \underline{28.8503 \text{ g}\cdot\text{mol}^{-1}}$$

This value was used for the partial pressure calculations performed to control equivalence ratio.

The table below lists the gross energy densities used for calculation of approximate calorific values:

Gross Energy Densities ($\text{MJ}\cdot\text{kg}^{-1}$)	
H ₂	141.51
CO	10.10
CH ₄	55.51
C ₂ H ₄	50.30
C ₂ H ₆	51.08

Tables below give coefficients used in NASA polynomials used for determination of γ_u

N₂

Coefficient	Temperature Range		
	100 - 500	500 - 2000	2000 - 6000
A	28.98641	19.50583	35.51872
B	1.853978	19.88705	1.128728
C	-9.647459	-8.598535	-0.196103
D	16.63537	1.369784	0.014662
E	0.000117	0.527601	-4.55376

O₂

Coefficient	Temperature Range		
	100-700	700 - 2000	2000 - 6000
A	31.32234	30.03235	20.91111
B	-20.23531	8.772972	10.72071
C	57.86644	-3.988133	-2.020498
D	-36.50624	0.788313	0.146449
E	-0.007374	-0.741599	9.245722

CH₄

Coefficient	Temperature Range	
	298 - 1300	1300 - 6000
A	-0.703029	85.81217
B	108.4773	11.26467
C	-42.52157	-2.114146
D	5.862788	0.13819
E	0.678565	-26.42221

A.3 - Experimental Rig



Fig. A.2 – Photograph of experimental rig.

A.4 - LabVIEW programs created for data acquisition

A.4.1 Temperature Data Logging

The program written for temperature acquisition used the scan-interface programming model, running the cRIO in scan mode. The system real-time processor periodically scans the input/output, and places the returned values in a memory map ready for access as requested. The overall graphical program structure is presented in Fig. A.3, annotated with numbers to help describe the sequence of program operation.

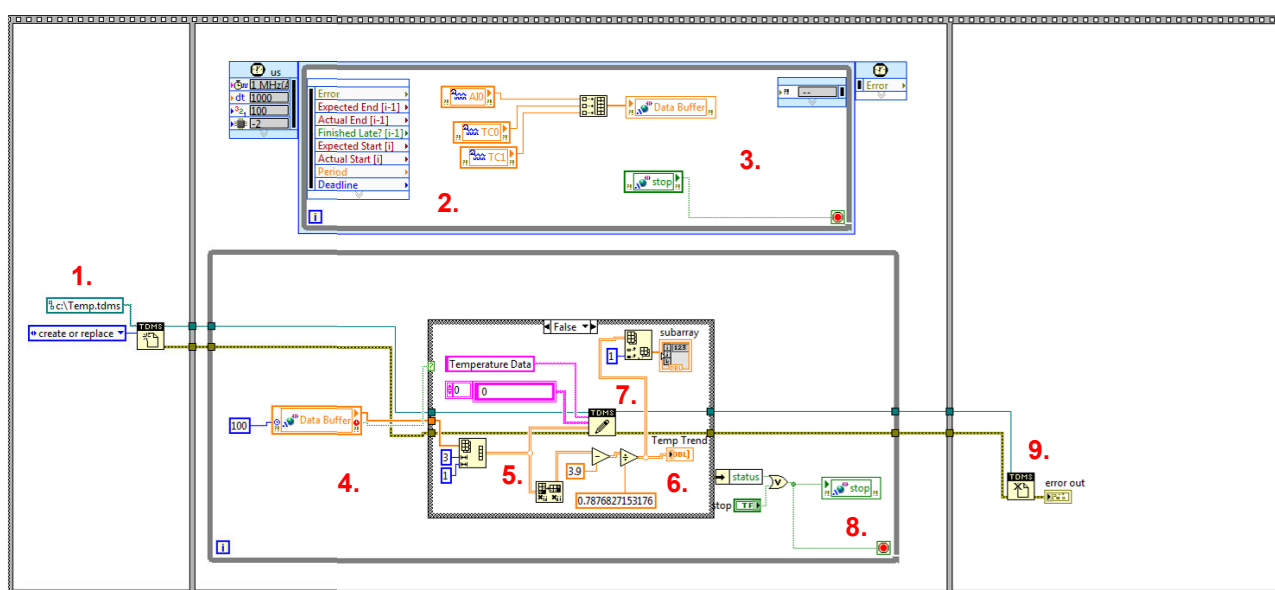


Fig. A.3 – Overview of the temperature control code.

1. This program is designed to run a *Flat Sequence Structure* (the boxes surrounding the operational components), with the three frames accessed and executed in sequence. The first part of the structure creates a *.tdms* (the designated data storage format) file in the cRIO host memory, to store the real-time data. The program then moves onto the next frame, where a timed-loop is employed (2.) to access the desired channel inputs (primarily *TC0* and *TC1*), and arrange this data into an array. This data is then streamed into a buffer (3.), to ensure a consistent sampling rate, and avoid the system timing out under heavy loading.

4. A while-loop runs simultaneously, extracting the data array from the buffer and rearranging to the separate channel components once more. The stream is written to the .tdms file created in the first part of the program (5.), and also replicated (6.) to give a live display of the data being read on the *front panel* of the executed program. Sample calibration factors are shown as mathematical operators, with one numerical and one plotted output (7.).

8. A universal stop input is included in the program so the user can specify when all the necessary data has been logged. Use of this one operator ceases execution of both simultaneous loops and moves the program to the final frame of the sequence structure. Here the .tdms file is saved and closed (9.), ready for the user to access in the cRIO memory. An error stream and indicator have been included should the system become unstable and time-out.

The front panel used in program operation is shown in Fig. A.4

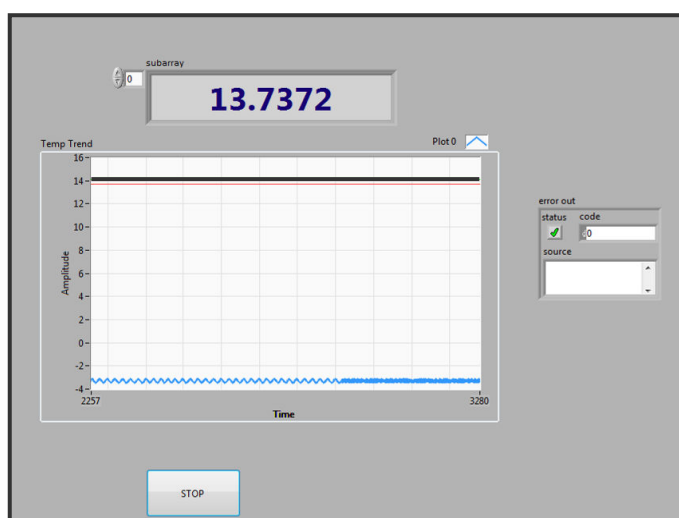


Fig. A.4 – Front panel of the temperature control program.

The numerical output of the desired channel (in this case 0) is given above the plotted trend of the previous 1000 data points. The error indicator has been included on the right of the panel to display any standard error codes that could lead to system failure. The stop button at the bottom is the control used to cease operation of the program loops.

A.4.2 Analogue Data input

The program written for analogue data acquisition utilised the *Field Programmable Gate Array* (FPGA) to achieve high frequency data capture (up to 5 kHz – the limit of the pressure transducer). The system for data acquisition comprised two parts, one compiled directly on the FPGA, and the other compiled and installed in the memory of the cRIO. The first of the two parts of the program is presented in Fig. A.5, again annotated with numbers to help describe the sequence of program operation.

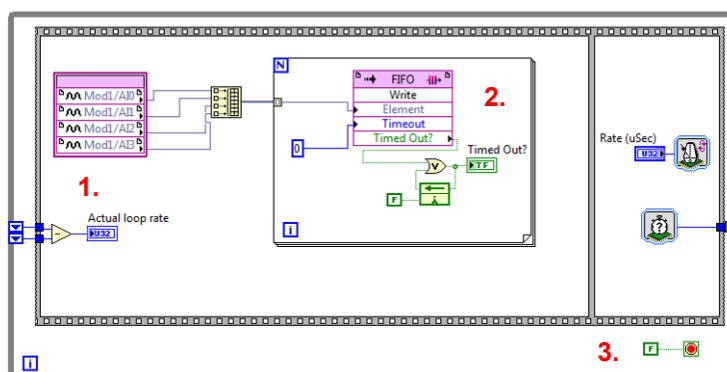


Fig. A.5 – Overview of FPGA compiled control code

This part of the program again uses a Flat Sequence Structure, housed within an encompassing while-loop. 1. The first frame of the sequence collects data from the four specified channels of the analogue input module (AI0-3), and collates the data into an array. This data is then streamed into a *First-In-First-Out* (FIFO) data buffer, with a time-out check included in a for-loop (2.). The second frame of the flat sequence structure cross references a user specified sampling rate, allowing the sequence to repeat (or the channels to be sampled) at the user specified frequency (3.). This part of the program is housed within the FPGA to automatically run as required, when the secondary program is functioning. This second part is shown in Fig. A.6 again annotated with numbers to help describe the sequence of operation.

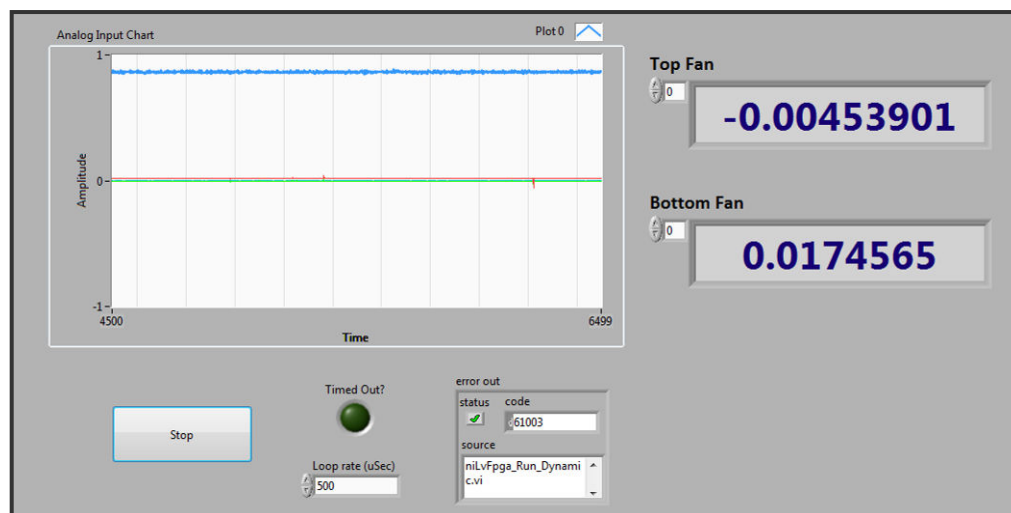


Fig. A.7 – Front panel of the secondary analogue input program.

The plot shows data from 3 of the channels; the blue line showing the current pressure transient, together with the red and green voltage output from the two tachometers. There are also two numerical outputs from these fans (both showing the slight noise in the system), to allow for precise control of fan rotational speed. Again, a stop control button is included to allow the user to cease program operation, together with the writable loop rate of the program, or how quickly the data is sampled (currently set to 500 μ Secs). As with the previous program, an error output is included to specify a standard code should a problem occur, together with a time-out indicator.

A.5 - derivation of partial pressure from first principles

Section 3.3.2 gives a simple derivation for the calculation of partial pressure, however what follows is comprehensive analysis, employing the ideal gas equation from first principles to express values of partial pressure as a function of air fuel ratio. Firstly the ideal gas equation describes the state of a gas relative to its pressure, volume and temperature:

$$P \cdot V = n \cdot R \cdot T \quad (\text{A.1})$$

The number of moles can be substituted for the mass, and molar mass using Eqn. 3.24 to give:

$$P = \frac{m \cdot R \cdot T}{M \cdot V} \quad (\text{A.2})$$

Section 3.3.2 describes how the total pressure of a gas mixture is comprised of partial pressures of each mixture, in this case fuel and oxidiser:

$$P_T = P_f + P_o \quad (\text{A.3})$$

Substituting Eqn. A.2 into A.3 gives:

$$P_T = \left[\left(\frac{m_f \cdot T \cdot R}{M_f \cdot V} \right) + \left(\frac{m_o \cdot T \cdot R}{M_o \cdot V} \right) \right] \quad (\text{A.4})$$

R is the universal gas constant, and the volume and temperature do not change inside the CVCB allowing the equation to be rearranged thus:

$$\frac{P_T \cdot V}{R \cdot T} = \left[\left(\frac{m_f}{M_f} \right) + \left(\frac{m_o}{M_o} \right) \right] \quad (\text{A.5})$$

Rearranging Eqn. 3.17 gives

$$m_o = m_f AFR_{act} \quad (\text{A.6})$$

Substituting Eqn. A.6 into A.5 gives:

$$\frac{P_T \cdot V}{R \cdot T} = \left[\left(\frac{m_f}{M_f} \right) + \left(\frac{m_f \cdot AFR_{act}}{M_o} \right) \right] \Rightarrow$$

$$\frac{P_T \cdot V}{R \cdot T} = m_f \cdot \left[\left(\frac{1}{M_f} \right) + \left(\frac{AFR_{act}}{M_o} \right) \right]$$

which can be rearranged in terms of mass, giving Eqn. A.7

$$m_f = \frac{\left(\frac{P_T \cdot V}{R \cdot T} \right)}{\left[\left(\frac{1}{M_f} \right) + \left(\frac{AFR_{act}}{M_o} \right) \right]} \quad (A.7)$$

Substituting Eqn. 3.24 into A.7 gives

$$n_f = \frac{\left(\frac{P_T \cdot V}{R \cdot T} \right)}{M_f \left[\left(\frac{1}{M_f} \right) + \left(\frac{AFR_{act}}{M_o} \right) \right]}$$

$$\Rightarrow n_f = \frac{\left(\frac{P_T \cdot V}{R \cdot T} \right)}{\left(1 + \frac{M_f \cdot AFR_{act}}{M_o} \right)} \quad (A.8)$$

And similarly the number of oxidiser moles can be derived to give:

$$n_o = \frac{\left(\frac{P_T \cdot V}{R \cdot T} \right)}{\left(1 + \frac{M_o}{AFR_{act} \cdot M_f} \right)} \quad (A.9)$$

Rearranging and substituting Eqns. A.8 and A.9 into Eqn. A.4 yields:

$$P_f = P_T \cdot \frac{\left[\frac{\left(\frac{P_T \cdot V}{R \cdot T} \right)}{\left(1 + \frac{M_f \cdot AFR_{act}}{M_o} \right)} \right]}{\left[\frac{\left(\frac{P_T \cdot V}{R \cdot T} \right)}{\left(1 + \frac{M_o}{AFR_{act} \cdot M_f} \right)} \right] + \left[\frac{\left(\frac{P_T \cdot V}{R \cdot T} \right)}{\left(1 + \frac{M_f \cdot AFR_{act}}{M_o} \right)} \right]} \quad (A.10)$$

Allowing the $\left(\frac{P_T \cdot V}{R \cdot T}\right)$ term to drop out to give:

$$\begin{aligned}
 P_f &= P_T \cdot \left[\frac{\frac{1}{\left(1 + \frac{M_f \cdot AFR_{act}}{M_o}\right)}}{\frac{1}{\left(1 + \frac{M_o}{AFR_{act} \cdot M_f}\right)} + \frac{1}{\left(1 + \frac{M_f \cdot AFR_{act}}{M_o}\right)}} \right] \\
 \Rightarrow P_f &= P_T \cdot \left[\frac{\left(1 + \frac{M_o}{AFR_{act} \cdot M_f}\right)}{\left(1 + \frac{M_o}{AFR_{act} \cdot M_f}\right) + \left(1 + \frac{M_f \cdot AFR_{act}}{M_o}\right)} \right] \\
 \Rightarrow P_f &= P_T \cdot \left(\frac{M_o}{M_o + M_f \cdot AFR_{act}} \right) \tag{A.11}
 \end{aligned}$$

with a similar process applicable to the partial pressure of the oxidiser.

A.6 - Sample MATLAB code

```

clear all

path(path,'D:\try');
fileFolder = fullfile('D:','try');
dirOutput = dir(fullfile(fileFolder, '*.tif'));
fileNames = {dirOutput.name};
tic

r=1;
A1 = imread( fileNames {r} );
B = edge (A1, 'canny', 0.16);

for k = 1:200;

    A = imread( fileNames {k} );
    D = edge (A, 'canny', 0.16);
    %figure, imshow (D), title ('D');
    E = D-B;
    %figure, imshow (E), title ('E');

    C = imcrop ( E, [50, 268, 550, 54]);
    %figure, imshow (C), title ('C');

    l11 = find ( C==1, 1, 'first');
    r11 = find ( C==1, 1, 'last');

    lcol = l11/55;
    lcol1 = ceil(lcol);

    rcol= r11/55;
    rcol1= ceil(rcol);

    if (isempty(l11))
        Ledge(k) = 0;
    else
        Ledge(k)= 460-lcol1;
    end;

    if (isempty(r11))
        Redge(k) = 0;
    else
        Redge(k)= rcol1-460;
    end;

    if ((isempty(l11))||isempty(r11))
        fd(k) = 0;
        P(k) = 0;
    else
        fd(k) = rcol1-lcol1;
        P(k) = (55-((lcol1*55)-l11));
    end;

end

Tre = transpose (Redge);
Tle = transpose (Ledge);
Tfd = transpose (fd);
TP = transpose (P);

xlswrite('Result.xls',Tfd,1,'A1');
xlswrite('Result.xls',TP,1,'B1');
xlswrite('Result.xls',Tre,1,'C1');
xlswrite('Result.xls',Tle,1,'D1');

```

A.7- Calibration plots

A.7.1 Thermocouples

Thermocouple one

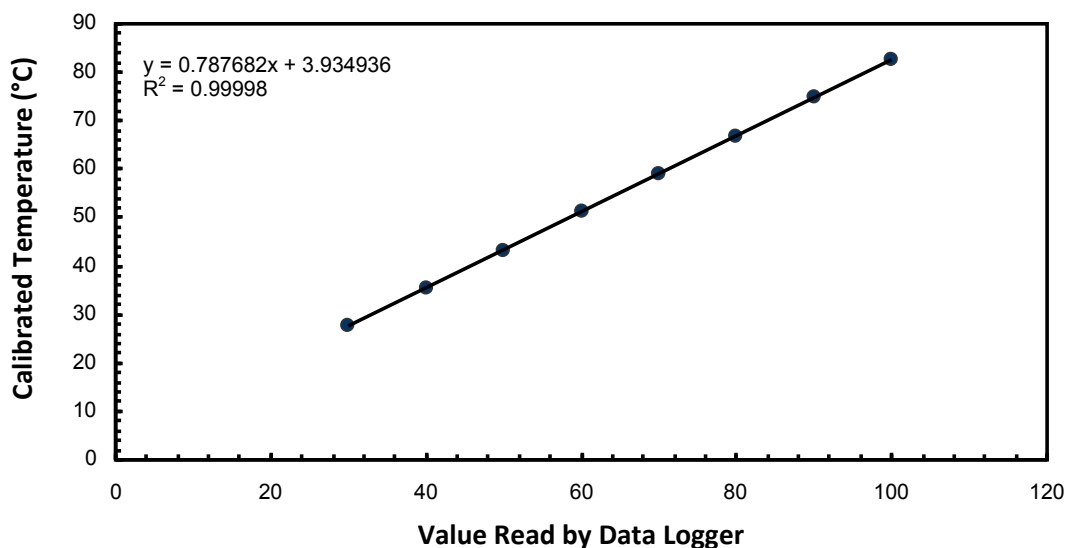


Fig. A.8 – Calibration plot of thermocouple one with 9100 HDRC dry block system

Thermocouple two

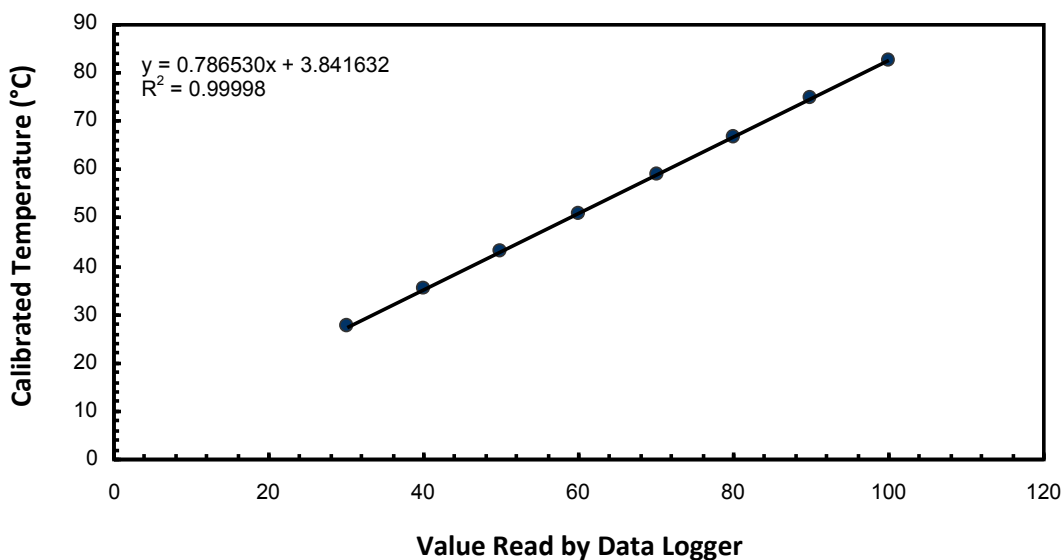


Fig. A.9 – Calibration plot of thermocouple two with 9100 HDRC dry block system

A.7.2 Pressure transducers

High-frequency pressure transducer calibration plot

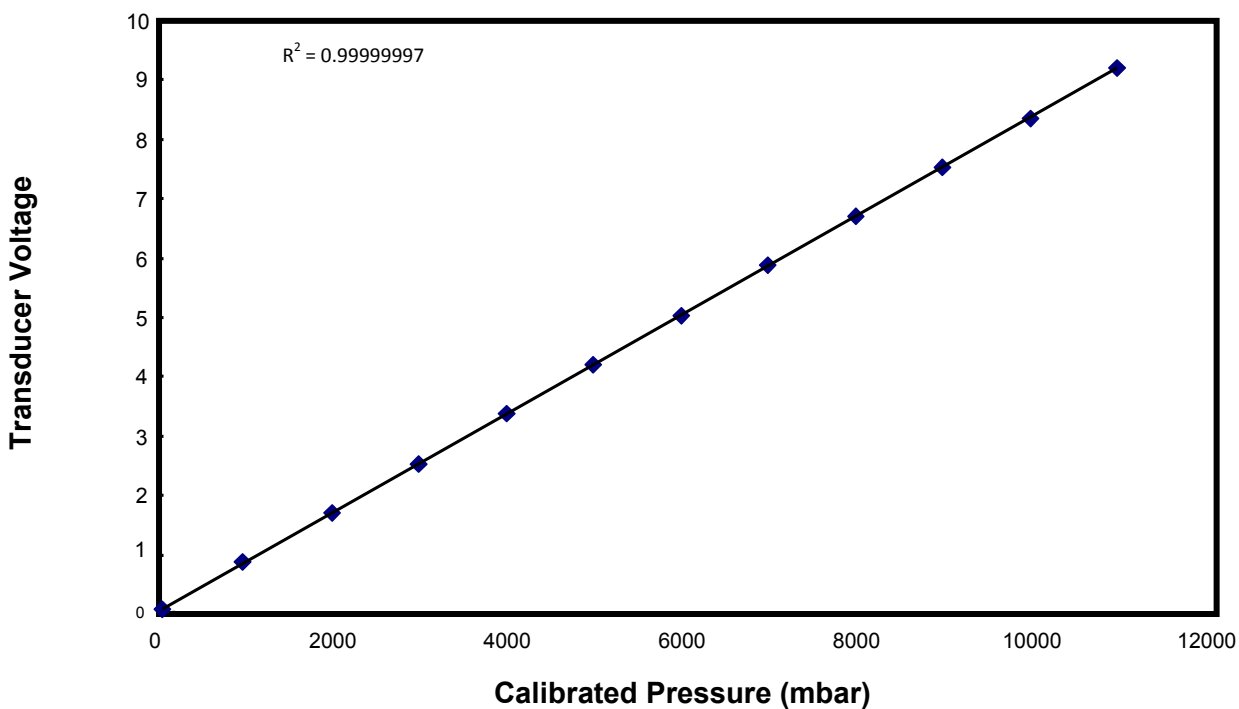


Fig. A.10 – Calibration plot of high frequency pressure transducer with Druck DPI 610

Vacuum gauge pressure transducer calibration plot

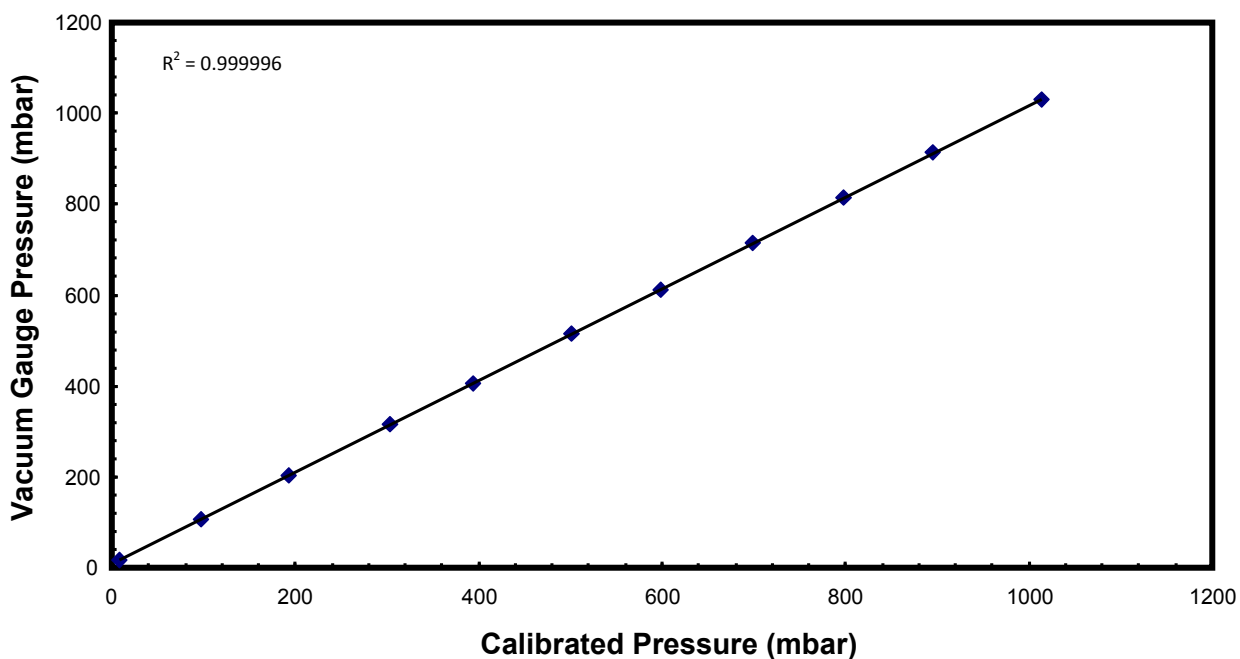


Fig. A.11 – Calibration plot of vacuum transducer with Druck DPI 610

Appendix B - Results Tables

B.1 - Benchmarking Atmospheric CH₄ Results Dataset

Test Conditions

Fuel:	CH ₄	<i>purity:</i>	99.9%
Temperature:	303 K		
Pressure:	0.1 MPa		
Camera Speed	5,000 fps		

Dynamic Pressure Measurement Results

ϕ	γ_u	u_L	u_L	u_L	Ave
		Test 1 (cm·s ⁻¹)	Test 2 (cm·s ⁻¹)	Test 3 (cm·s ⁻¹)	u_L (cm·s ⁻¹)
0.75	1.3893	20.1	19.6	19.5	19.7
0.8	1.3887	24.2	24.2	23.7	24.0
0.85	1.3882	29.0	27.9	29.2	28.7
0.9	1.3877	31.1	31.3	31.5	31.3
0.95	1.3872	34.0	33.8	33.4	33.7
1	1.3866	35.0	35.1	35.0	35.0
1.05	1.3862	35.5	34.9	35.5	35.3
1.1	1.3856	34.0	34.2	33.9	34.0
1.15	1.3852	33.6	32.3	32.6	32.8
1.2	1.3846	30.0	30.1	29.5	29.8
1.25	1.3842	25.5	26.4	26.2	26.1

Individual Tests – Optical Results

ϕ	P_{fuel} (kPa)	ρ_b/ρ_u	GRI-Mech 3.0 ($\text{cm}\cdot\text{s}^{-1}$)	Linear Technique			Nonlinear Technique		
				S_u ($\text{mm}\cdot\text{s}^{-1}$)	u_L ($\text{cm}\cdot\text{s}^{-1}$)	L_b (mm)	S_u ($\text{mm}\cdot\text{s}^{-1}$)	u_L ($\text{cm}\cdot\text{s}^{-1}$)	L_b (mm)
0.75	7.30	0.15729	23.58	1445.84	22.74	0.890	1431.30	22.51	0.686
				1414.24	22.24	0.837	1399.98	22.02	0.643
				1384.98	21.78	0.827	1373.12	21.60	0.651
0.8	7.75	0.15117	27.36	1725.09	26.08	0.956	1704.56	25.77	0.717
				1737.93	26.27	0.964	1716.47	25.95	0.719
				1696.56	25.65	0.845	1680.30	25.40	0.653
0.85	8.19	0.14584	30.80	2088.91	30.47	0.986	2063.10	30.09	0.737
				2081.85	30.36	0.972	2057.66	30.01	0.733
				2111.39	30.79	1.004	2085.24	30.41	0.751
0.9	8.63	0.14129	33.78	2380.13	33.63	1.147	2342.81	33.10	0.826
				2372.72	33.52	1.184	2333.58	32.97	0.846
				2350.06	33.20	1.076	2315.99	32.72	0.786
0.95	9.07	0.13757	36.15	2555.35	35.15	1.193	2533.31	34.85	0.946
				2608.80	35.89	1.046	2588.53	35.61	0.840
				2622.36	36.08	1.109	2595.47	35.71	0.855
1	9.50	0.13493	37.74	2778.15	37.49	1.212	2730.30	36.84	0.860
				2780.91	37.52	1.153	2740.56	36.98	0.844
				2755.73	37.18	1.150	2717.98	36.67	0.851
1.05	9.93	0.13386	38.48	2890.85	38.70	1.291	2838.46	37.99	0.910
				2875.30	38.49	1.304	2830.71	37.89	0.946
				2886.68	38.64	1.285	2838.77	38.00	0.922
1.1	10.35	0.13433	38.18	2831.55	38.04	1.227	2784.54	37.40	0.876
				2877.76	38.66	1.350	2829.14	38.00	0.960
				2863.60	38.47	1.320	2808.93	37.73	0.921
1.15	10.77	0.13543	36.61	2748.23	37.22	1.323	2700.90	36.58	0.944
				2740.31	37.11	1.576	2673.73	36.21	1.052
				2736.94	37.07	1.538	2674.52	36.22	1.040
1.2	11.19	0.13674	33.66	2515.04	34.39	1.624	2438.45	33.34	1.034
				2505.70	34.26	1.816	2428.44	33.21	1.152
				2470.27	33.78	1.752	2396.20	32.77	1.120
1.25	11.60	0.13817	29.29	2114.53	29.22	2.208	2032.38	28.08	1.332
				2191.01	30.27	2.144	2115.43	29.23	1.334
				2152.63	29.74	2.087	2087.57	28.84	1.308

Summary and Error – Linear Optical Results

ϕ	B_{Su} (mm·s ⁻¹)	Ave S_u (mm·s ⁻¹)	Ave u_L (cm·s ⁻¹)	Ave L_b (mm)	σ_{Su} (mm·s ⁻¹)	U_{Su} (mm·s ⁻¹)
0.75	40.93	1415.02	22.26	0.851	30.4	85.901
0.8	41.48	1719.86	26.00	0.921	21.1	66.845
0.85	39.35	2094.05	30.54	0.987	15.4	54.885
0.9	35.49	2367.64	33.45	1.136	15.6	52.547
0.95	31.43	2595.51	35.71	1.116	30.7	82.490
1	26.56	2771.60	37.40	1.172	11.3	43.370
1.05	20.53	2884.28	38.61	1.293	8.1	28.659
1.1	21.82	2857.64	38.39	1.299	27.0	70.537
1.15	28.28	2741.83	37.13	1.479	5.8	31.743
1.2	40.78	2497.00	34.14	1.731	23.6	71.416
1.25	57.85	2152.72	29.74	2.146	38.2	111.146

Summary and Error – Nonlinear Optical Results

ϕ	B_{Su} (mm·s ⁻¹)	Ave S_u (mm·s ⁻¹)	Ave u_L (cm·s ⁻¹)	Ave L_b (mm)	σ_{Su} (mm·s ⁻¹)	U_{Su} (mm·s ⁻¹)
0.75	40.93	1401.47	22.04	0.660	29.1	83.123
0.8	41.48	1700.44	25.71	0.696	18.4	61.792
0.85	39.35	2068.67	30.17	0.740	14.6	53.532
0.9	35.49	2330.79	32.93	0.836	13.6	49.035
0.95	31.43	2572.44	35.39	0.880	34.1	90.267
1	26.56	2729.61	36.83	0.852	11.3	38.655
1.05	20.53	2835.98	37.96	0.926	4.6	23.454
1.1	21.82	2807.54	37.71	0.919	22.3	59.619
1.15	28.28	2683.05	36.34	1.012	15.5	47.709
1.2	40.78	2421.03	33.11	1.102	22.1	68.345
1.25	57.85	2078.46	28.72	1.324	42.3	111.146

B.2 - Benchmarking High Temperature CH₄ Results Dataset

Test Conditions

Fuel:	CH ₄	<i>purity:</i>	99.9%
Temperature:	358 K		
Pressure:	0.1 MP		
Camera Speed	5,000 fps		

Individual Tests – Optical Results

ϕ	P_{fuel} (kPa)	ρ_b/ρ_u	GRI-Mech 3.0 ($\text{cm}\cdot\text{s}^{-1}$)	Linear Technique		
				S_u ($\text{mm}\cdot\text{s}^{-1}$)	u_L ($\text{cm}\cdot\text{s}^{-1}$)	L_b (mm)
0.8	7.75	0.175	36.93	2143.74	37.59	0.95
				2158.22	37.84	1.01
				2098.64	36.79	0.98
0.9	8.63	0.164	44.89	2763.27	45.44	1.13
				2780.00	45.71	1.02
				2749.77	45.22	1.07
1	9.50	0.157	49.71	3235.24	50.94	1.17
				3234.40	50.93	1.28
				3234.38	50.93	1.19
1.1	10.35	0.156	50.07	3239.37	50.62	1.30
				3296.23	51.51	1.40
				3240.29	50.64	1.31
1.2	11.19	0.159	44.54	2898.82	46.02	1.57
				2857.82	45.37	1.71
				2916.84	46.30	1.77

Summary and Error – Linear Optical Results

ϕ	B_{S_u} ($\text{mm}\cdot\text{s}^{-1}$)	Ave S_u ($\text{mm}\cdot\text{s}^{-1}$)	Ave u_L ($\text{cm}\cdot\text{s}^{-1}$)	Ave L_b (mm)	σ_{S_u} ($\text{mm}\cdot\text{s}^{-1}$)	U_{S_u} ($\text{mm}\cdot\text{s}^{-1}$)
0.8	52.42	2133.32	37.40	0.98	31.43	74.13
0.9	37.62	2764.35	45.46	1.07	15.15	54.01
1	26.30	3234.67	50.93	1.21	0.49	43.21
1.1	23.08	3258.63	50.93	1.34	32.56	70.94
1.2	36.15	2891.16	45.90	1.68	30.25	68.88

B.3 - BFG Atmospheric Ambient Condition Dataset

Test Conditions

Fuel: BFG (CO-23.07%, CO₂-23.35%, and N₂-53.58%)
 Temperature: 303 K
 Pressure: 0.1 MPa
 Camera Speed 3,000 fps

Individual Tests – Optical BFG Results 1 % H₂ Addition

ϕ	P_{fuel} (kPa)	ρ_b/ρ_u	Linear Technique			Nonlinear Technique		
			S_u (mm·s ⁻¹)	u_L (cm·s ⁻¹)	L_b (mm)	S_u (mm·s ⁻¹)	u_L (cm·s ⁻¹)	L_b (mm)
0.7	55.22	0.23587	105.58	2.49	0.11	105.20	2.48	0.08
			96.98	2.29	0.00	96.95	2.29	0.00
			106.58	2.51	-0.10	106.71	2.52	-0.01
0.8	58.50	0.22800	114.87	2.62	0.23	115.16	2.63	0.22
			127.09	2.90	0.19	126.82	2.89	0.17
			124.50	2.84	0.23	123.73	2.82	0.19
0.9	61.32	0.22186	151.51	3.36	0.30	150.38	3.34	0.24
			154.15	3.42	0.33	153.80	3.41	0.29
			149.33	3.31	0.30	149.72	3.32	0.29
1	63.79	0.21816	166.03	3.62	0.41	165.37	3.61	0.35
			166.74	3.64	0.66	163.44	3.57	0.47
			172.83	3.77	0.46	172.44	3.76	0.41
1.1	65.96	0.22597	173.23	3.91	0.63	173.23	3.91	0.54
			181.43	4.10	0.74	179.42	4.05	0.57
			170.45	3.85	0.63	171.74	3.88	0.60
1.2	67.89	0.23478	179.40	4.21	0.59	179.40	4.21	0.49
			179.69	4.22	0.67	179.77	4.22	0.62
			180.59	4.24	0.98	177.23	4.16	0.69
1.3	69.61	0.24336	163.09	3.97	0.85	160.95	3.92	0.67
			160.98	3.92	0.85	159.40	3.88	0.67
			175.78	4.28	1.18	170.60	4.15	0.78
1.4	71.15	0.25186	148.37	3.74	1.29	143.49	3.61	0.82
			155.60	3.92	1.77	147.21	3.71	0.99
			156.74	3.95	1.68	148.95	3.75	0.96
1.5	72.55	0.26005	127.88	3.33	2.11	122.18	3.18	1.25
			133.29	3.47	1.21	132.53	3.45	0.92
			138.56	3.60	2.00	130.55	3.40	1.11

Individual Tests – Optical BFG Results 3 % H₂ Addition

ϕ	P_{fuel} (kPa)	ρ_b/ρ_u	Linear Technique			Nonlinear Technique		
			S_u (mm·s ⁻¹)	u_L (cm·s ⁻¹)	L_b (mm)	S_u (mm·s ⁻¹)	u_L (cm·s ⁻¹)	L_b (mm)
0.7	53.67	0.23156	202.08	4.68	-0.27	202.05	4.68	-0.29
			196.00	4.54	-0.21	195.08	4.52	-0.16
			200.00	4.63	-0.08	200.62	4.65	-0.06
0.8	56.97	0.21727	245.47	5.49	-0.17	245.12	5.48	-0.18
			250.65	5.60	-0.20	250.67	5.60	-0.20
			237.57	5.31	0.08	233.53	5.22	0.00
0.9	59.83	0.22355	277.52	6.03	0.02	277.52	6.03	0.02
			280.31	6.09	-0.03	278.56	6.05	-0.10
			285.66	6.21	0.04	285.73	6.21	0.04
1	62.33	0.21343	302.25	6.45	0.04	302.17	6.45	0.04
			302.65	6.46	0.07	302.44	6.46	0.06
			300.17	6.41	0.04	300.17	6.41	0.02
1.1	64.55	0.22957	311.53	6.88	0.17	310.54	6.86	0.19
			313.67	6.93	0.22	313.99	6.94	0.23
			327.65	7.24	0.27	327.55	7.24	0.25
1.2	66.51	0.22092	319.38	7.33	0.34	318.37	7.31	0.30
			312.13	7.17	0.24	312.28	7.17	0.23
			322.27	7.40	0.44	320.84	7.37	0.37
1.3	68.27	0.23799	299.41	7.13	0.34	299.01	7.12	0.31
			300.55	7.15	0.40	300.60	7.15	0.38
			310.16	7.38	0.56	308.59	7.34	0.47
1.4	69.85	0.25422	268.85	6.62	0.51	267.26	6.58	0.43
			276.02	6.80	0.57	275.23	6.78	0.50
			273.53	6.73	0.48	273.31	6.73	0.44
1.5	71.28	0.24621	254.64	6.47	1.12	248.84	6.33	0.77
			262.89	6.68	1.17	257.82	6.55	0.81
			245.20	6.23	0.81	242.18	6.16	0.63

Individual Tests – Optical BFG Results 5 % H₂ Addition

ϕ	P_{fuel} (kPa)	ρ_b/ρ_u	Linear Technique			Nonlinear Technique		
			S_u (mm·s ⁻¹)	u_L (cm·s ⁻¹)	L_b (mm)	S_u (mm·s ⁻¹)	u_L (cm·s ⁻¹)	L_b (mm)
0.7	52.20	0.22764	285.37	6.50	-0.58	282.59	6.43	-0.74
			277.41	6.32	-0.62	275.22	6.27	-0.78
			281.48	6.41	-0.48	282.00	6.42	-0.51
0.8	55.52	0.21950	335.09	7.36	-0.49	330.22	7.25	-0.49
			339.38	7.45	-0.29	337.65	7.41	-0.34
			334.87	7.35	-0.43	328.75	7.22	-0.38
0.9	58.41	0.21309	398.23	8.49	-0.11	392.01	8.35	-0.08
			385.47	8.21	-0.14	385.46	8.21	-0.15
			398.98	8.50	-0.32	398.16	8.48	-0.36
1	60.94	0.20914	436.08	9.12	-0.09	436.05	9.12	-0.09
			436.35	9.13	-0.08	436.36	9.13	-0.08
			431.09	9.02	-0.14	429.79	8.99	-0.09
1.1	63.19	0.21638	457.57	9.90	-0.03	457.96	9.91	-0.02
			456.92	9.89	-0.08	455.03	9.85	-0.07
			455.14	9.85	-0.02	454.91	9.84	0.01
1.2	65.19	0.22479	460.43	10.35	-0.07	459.21	10.32	-0.06
			450.57	10.13	0.12	450.51	10.13	0.11
			441.88	9.93	0.26	441.36	9.92	0.24
1.3	66.98	0.23300	442.98	10.32	0.35	435.95	10.16	0.20
			450.29	10.49	0.08	451.13	10.51	0.10
			432.51	10.08	0.18	432.20	10.07	0.17
1.4	68.60	0.24103	399.62	9.63	0.31	399.07	9.62	0.28
			406.87	9.81	0.51	405.19	9.77	0.43
			403.88	9.73	0.38	402.79	9.71	0.34
1.5	70.07	0.24884	380.15	9.46	1.26	367.35	9.14	0.81
			367.97	9.16	0.86	360.79	8.98	0.61
			373.60	9.30	1.02	365.74	9.10	0.71

Individual Tests – Optical BFG Results 7 % H₂ Addition

ϕ	P_{fuel} (kPa)	ρ_b/ρ_u	Linear Technique			Nonlinear Technique		
			S_u (mm·s ⁻¹)	u_L (cm·s ⁻¹)	L_b (mm)	S_u (mm·s ⁻¹)	u_L (cm·s ⁻¹)	L_b (mm)
0.7	50.82	0.22407	348.77	7.82	-0.79	349.73	7.84	-0.88
			350.06	7.84	-0.67	345.76	7.75	-0.89
			354.70	7.95	-0.86	352.42	7.90	-1.03
0.8	54.15	0.21578	443.63	9.57	-0.55	440.36	9.50	-0.68
			441.94	9.54	-0.62	437.38	9.44	-0.81
			451.51	9.74	-0.37	451.23	9.74	-0.41
0.9	57.05	0.20925	517.66	10.83	-0.40	511.98	10.71	-0.52
			518.10	10.84	-0.39	516.72	10.81	-0.44
			517.19	10.82	-0.29	515.93	10.80	-0.33
1	59.61	0.20520	550.32	11.29	-0.21	550.09	11.29	-0.22
			555.39	11.40	-0.31	554.05	11.37	-0.35
			553.41	11.36	-0.20	553.72	11.36	-0.20
1.1	61.88	0.21215	590.64	12.53	-0.16	588.98	12.50	-0.18
			593.08	12.58	-0.16	591.87	12.56	-0.15
			587.13	12.46	-0.22	585.86	12.43	-0.20
1.2	63.91	0.22035	592.22	13.05	-0.09	592.82	13.06	-0.08
			585.72	12.91	-0.19	584.74	12.88	-0.18
			588.89	12.98	-0.12	588.64	12.97	-0.13
1.3	65.74	0.22836	590.17	13.48	0.09	589.62	13.46	0.08
			587.05	13.41	0.01	581.54	13.28	-0.04
			581.01	13.27	-0.02	578.94	13.22	-0.02
1.4	67.39	0.23620	557.67	13.17	0.40	556.87	13.15	0.28
			551.02	13.01	0.13	551.42	13.02	0.14
			552.97	13.06	0.21	552.53	13.05	0.20
1.5	68.89	0.24384	496.19	12.10	0.54	492.86	12.02	0.44
			499.51	12.18	0.59	496.16	12.10	0.48
			505.36	12.32	0.41	505.56	12.33	0.40

Optical BFG Results 1 % H₂ Addition

Summary – Linear Optical and Modelled Results

ϕ	Ave S_u (mm·s ⁻¹)	Ave u_L (cm·s ⁻¹)	Ave L_b (mm)	GRI-Mech 3.0 (cm·s ⁻¹)	Li et al. (cm·s ⁻¹)	Davis et al. (cm·s ⁻¹)
0.7	103.05	2.43	0.00	2.19	2.46	2.57
0.8	122.15	2.79	0.22	2.77	3.10	3.16
0.9	151.66	3.36	0.31	3.22	3.57	3.62
1.0	168.53	3.68	0.51	3.55	3.90	3.92
1.1	175.04	3.96	0.66	3.75	4.08	4.09
1.2	179.89	4.22	0.75	3.82	4.10	4.10
1.3	166.62	4.05	0.96	3.73	3.98	3.97
1.4	153.57	3.87	1.58	3.48	3.70	3.68
1.5	133.24	3.46	1.77	3.07	3.30	3.27

Summary and Error – Nonlinear Optical Results

ϕ	B_{Su} (mm·s ⁻¹)	Ave S_u (mm·s ⁻¹)	Ave u_L (cm·s ⁻¹)	Ave L_b (mm)	σ_{Su} (mm·s ⁻¹)	U_{Su} (mm·s ⁻¹)
0.7	3.04	102.96	2.43	0.03	5.25	13.4
0.8	3.38	121.90	2.78	0.19	6.04	15.4
0.9	3.67	151.30	3.36	0.27	2.19	6.6
1.0	3.88	167.08	3.65	0.41	4.74	12.4
1.1	3.94	174.80	3.95	0.57	4.07	10.9
1.2	3.91	178.80	4.20	0.60	1.37	5.2
1.3	3.87	163.65	3.98	0.70	6.06	15.6
1.4	3.78	146.55	3.69	0.92	2.79	7.9
1.5	3.72	128.42	3.34	1.09	5.49	14.2

Optical BFG Results 3 % H₂ Addition

Summary – Linear Optical and Modelled Results

ϕ	Ave S_u (mm·s ⁻¹)	Ave u_L (cm·s ⁻¹)	Ave L_b (mm)	GRI-Mech 3.0 (cm·s ⁻¹)	Li et al. (cm·s ⁻¹)	Davis et al. (cm·s ⁻¹)
0.7	199.36	4.62	-0.17	3.76	4.29	4.31
0.8	244.56	5.47	-0.09	4.76	5.35	5.32
0.9	281.16	6.11	0.01	5.60	6.20	6.12
1.0	301.69	6.44	0.05	6.26	6.83	6.72
1.1	317.61	7.02	0.22	6.74	7.24	7.10
1.2	317.93	7.30	0.34	7.01	7.42	7.25
1.3	303.37	7.22	0.43	7.02	7.35	7.15
1.4	272.80	6.72	0.52	6.73	7.03	6.80
1.5	254.24	6.46	1.03	6.12	6.47	6.23

Summary and Error – Nonlinear Optical Results

ϕ	B_{Su} (mm·s ⁻¹)	Ave S_u (mm·s ⁻¹)	Ave u_L (cm·s ⁻¹)	Ave L_b (mm)	σ_{Su} (mm·s ⁻¹)	U_{Su} (mm·s ⁻¹)
0.7	4.67	199.92	4.63	-0.19	3.68	10.3
0.8	5.36	241.21	5.39	-0.13	8.74	22.4
0.9	5.99	280.60	6.10	-0.01	4.47	12.6
1.0	6.53	301.66	6.44	0.04	1.24	7.2
1.1	6.73	317.69	7.02	0.22	8.99	23.3
1.2	6.72	317.16	7.28	0.30	4.41	12.8
1.3	6.61	302.73	7.20	0.39	5.13	14.4
1.4	6.33	271.94	6.70	0.45	4.16	12.1
1.5	6.12	249.61	6.35	0.74	7.85	20.4

Optical BFG Results 5 % H₂ Addition

Summary – Linear Optical and Modelled Results

ϕ	Ave S_u (mm·s ⁻¹)	Ave u_L (cm·s ⁻¹)	Ave L_b (mm)	GRI-Mech 3.0 (cm·s ⁻¹)	Li et al. (cm·s ⁻¹)	Davis et al. (cm·s ⁻¹)
0.7	281.42	6.41	-0.56	5.16	5.92	5.83
0.8	336.45	7.39	-0.40	6.54	7.37	7.21
0.9	394.23	8.40	-0.19	7.73	8.56	8.34
1.0	434.51	9.09	-0.10	8.71	9.46	9.20
1.1	456.54	9.88	-0.04	9.45	10.08	9.78
1.2	450.96	10.14	0.10	9.91	10.40	10.07
1.3	441.93	10.30	0.21	10.04	10.39	10.03
1.4	403.45	9.72	0.40	9.76	10.06	9.66
1.5	373.91	9.30	1.05	9.03	9.40	8.97

Summary and Error – Nonlinear Optical Results

ϕ	B_{Su} (mm·s ⁻¹)	Ave S_u (mm·s ⁻¹)	Ave u_L (cm·s ⁻¹)	Ave L_b (mm)	σ_{Su} (mm·s ⁻¹)	U_{Su} (mm·s ⁻¹)
0.7	6.01	279.94	6.37	-0.68	4.10	11.8
0.8	6.88	332.21	7.29	-0.40	4.77	13.7
0.9	7.77	391.88	8.35	-0.20	6.35	17.6
1.0	8.14	434.73	9.09	-0.09	3.71	12.3
1.1	8.25	456.63	9.88	-0.03	1.73	9.3
1.2	8.27	450.36	10.12	0.10	8.92	23.7
1.3	8.25	439.76	10.25	0.15	10.02	26.2
1.4	8.24	402.35	9.70	0.35	3.08	11.3
1.5	8.14	364.63	9.07	0.71	3.42	11.8

Optical BFG Results 7 % H₂ Addition

Summary – Linear Optical and Modelled Results

ϕ	Ave S_u (mm·s ⁻¹)	Ave u_L (cm·s ⁻¹)	Ave L_b (mm)	GRI-Mech 3.0 (cm·s ⁻¹)	Li et al. (cm·s ⁻¹)	Davis et al. (cm·s ⁻¹)
0.7	351.18	7.87	-0.77	6.57	7.58	7.36
0.8	445.69	9.62	-0.51	8.35	9.42	9.13
0.9	517.65	10.83	-0.36	9.91	10.96	10.60
1.0	553.04	11.35	-0.24	11.23	12.14	11.73
1.1	590.28	12.52	-0.18	12.24	12.99	12.53
1.2	588.94	12.98	-0.13	12.94	13.45	12.97
1.3	586.07	13.38	0.03	13.20	13.53	13.01
1.4	553.89	13.08	0.25	12.97	13.21	12.65
1.5	500.35	12.20	0.51	12.16	12.48	11.88

Summary and Error – Nonlinear Optical Results

ϕ	B_{Su} (mm·s ⁻¹)	Ave S_u (mm·s ⁻¹)	Ave u_L (cm·s ⁻¹)	Ave L_b (mm)	σ_{Su} (mm·s ⁻¹)	U_{Su} (mm·s ⁻¹)
0.7	7.57	351.97	7.89	-0.93	3.35	11.3
0.8	8.56	442.99	9.56	-0.63	7.29	20.0
0.9	9.60	514.88	10.77	-0.43	2.54	11.5
1.0	10.25	552.62	11.34	-0.26	2.20	11.6
1.1	10.53	590.28	12.52	-0.18	3.01	12.9
1.2	10.58	589.40	12.99	-0.13	4.04	14.6
1.3	10.53	583.37	13.32	0.00	5.57	17.4
1.4	10.47	553.61	13.08	0.20	2.88	12.7
1.5	10.24	498.19	12.15	0.44	6.59	19.3

Calculated BFG flame thicknesses, and critical boundary velocity gradients

ϕ	d_t (mm)	g_i/c (s ⁻¹)	d_t (mm)	g_i/c (s ⁻¹)
BFG	1% H₂		7% H₂	
0.7	3.58	6.78	1.53	51.62
0.8	3.13	8.89	1.36	70.18
0.9	2.88	11.64	1.28	84.36
1.0	2.76	13.22	1.23	92.19
1.1	2.55	15.48	1.15	109.27
1.2	2.43	17.27	1.06	122.24
1.3	2.41	16.53	1.02	130.54
1.4	2.45	15.04	1.00	130.15
1.5	2.62	12.73	1.02	119.47

B.4 - BFG Elevated Pressure Dataset

Test Conditions

Fuel: BFG (CO-23.07%, CO₂-23.35%, and N₂-53.58%)
 Temperature: 303 K
 Pressure: 0.15, 0.2 MPa
 Camera Speed 3,000 fps

Individual Tests – Optical BFG Results 1 % H₂ Addition – 0.15 MPa

ϕ	P_{fuel} (kPa)	ρ_b/ρ_u	Linear Technique			Nonlinear Technique		
			S_u (mm·s ⁻¹)	u_L (cm·s ⁻¹)	L_b (mm)	S_u (mm·s ⁻¹)	u_L (cm·s ⁻¹)	L_b (mm)
0.8	87.75	0.22800	110.19	2.51	-0.23	109.95	2.51	-0.26
			117.34	2.67	-0.02	117.27	2.67	-0.02
1	95.69	0.21816	155.55	3.39	0.47	152.79	3.33	0.34
			139.89	3.04	0.13	139.54	3.04	0.21
1.2	101.84	0.23478	154.11	3.62	0.47	152.24	3.57	0.34
			155.23	3.63	0.43	154.57	3.63	0.50
1.4	106.73	0.25186	130.62	3.29	0.95	127.74	3.22	0.66
			128.44	3.23	0.63	128.03	3.22	0.54

Individual Tests – Optical BFG Results 3 % H₂ Addition – 0.15 MPa

ϕ	P_{fuel} (kPa)	ρ_b/ρ_u	Linear Technique			Nonlinear Technique		
			S_u (mm·s ⁻¹)	u_L (cm·s ⁻¹)	L_b (mm)	S_u (mm·s ⁻¹)	u_L (cm·s ⁻¹)	L_b (mm)
0.8	85.46	0.21727	200.65	4.36	-0.28	201.63	4.38	-0.25
			197.28	4.29	-0.36	197.75	4.30	-0.36
1	93.50	0.21343	264.05	5.64	-0.12	264.30	5.64	-0.12
			276.19	5.89	-0.22	271.77	5.80	-0.22
1.2	99.77	0.22092	284.43	6.28	0.05	284.41	6.28	0.05
			277.01	6.12	0.02	277.23	6.12	0.02
1.4	104.78	0.25422	243.84	6.20	0.63	242.26	6.16	0.51
			256.06	6.51	0.39	256.52	6.52	0.39

Individual Tests – Optical BFG Results 5 % H₂ Addition – 0.15 MPa

ϕ	P_{fuel} (kPa)	ρ_b/ρ_u	Linear Technique			Nonlinear Technique		
			S_u (mm·s ⁻¹)	u_L (cm·s ⁻¹)	L_b (mm)	S_u (mm·s ⁻¹)	u_L (cm·s ⁻¹)	L_b (mm)
0.8	83.28	0.21950	282.62	6.20	-0.59	281.48	6.18	-0.71
			284.05	6.23	-0.48	284.74	6.25	-0.51
1	91.41	0.20914	380.44	7.96	-0.30	379.61	7.94	-0.34
			376.46	7.87	-0.42	375.10	7.84	-0.48
1.2	97.785	0.22479	398.56	8.96	-0.05	398.58	8.96	-0.05
			383.68	8.62	-0.16	383.66	8.62	-0.17
1.4	102.9	0.24103	342.02	8.24	0.21	341.71	8.24	0.20
			354.49	8.54	0.46	352.54	8.50	0.39

Individual Tests – Optical BFG Results 7 % H₂ Addition – 0.15 MPa

ϕ	P_{fuel} (kPa)	ρ_b/ρ_u	Linear Technique			Nonlinear Technique		
			S_u (mm·s ⁻¹)	u_L (cm·s ⁻¹)	L_b (mm)	S_u (mm·s ⁻¹)	u_L (cm·s ⁻¹)	L_b (mm)
0.8	81.23	0.21578	379.66	8.19	-0.62	376.03	8.11	-0.79
			385.52	8.32	-0.66	381.51	8.23	-0.85
1	89.42	0.20520	491.73	10.09	-0.45	489.40	10.04	-0.54
			492.06	10.10	-0.52	494.32	10.14	-0.53
1.2	95.87	0.22035	510.13	11.24	-0.32	508.96	11.21	-0.36
			515.82	11.37	-0.20	513.49	11.31	-0.26
1.4	101.09	0.23620	463.11	10.94	0.07	463.11	10.94	0.07
			454.83	10.74	0.01	451.52	10.66	0.01

0.2 MPa

Individual Tests – Optical BFG Results 1 % H₂ Addition – 0.2 MPa

ϕ	P_{fuel} (kPa)	ρ_b/ρ_u	Linear Technique			Nonlinear Technique		
			S_u (mm·s ⁻¹)	u_L (cm·s ⁻¹)	L_b (mm)	S_u (mm·s ⁻¹)	u_L (cm·s ⁻¹)	L_b (mm)
0.8	117.00	0.22800	101.26	2.31	0.17	101.29	2.31	0.16
			95.94	2.19	-0.17	95.81	2.18	-0.19
1	127.59	0.21816	132.23	2.88	0.39	131.24	2.86	0.32
			143.80	3.14	0.28	144.11	3.14	0.29
1.2	135.79	0.23478	140.27	3.29	0.54	139.71	3.28	0.46
			143.30	3.36	0.90	139.73	3.28	0.61
1.4	142.31	0.25186	108.25	2.73	0.85	106.50	2.68	0.62
			108.75	2.74	0.77	108.03	2.72	0.54

Individual Tests – Optical BFG Results 3 % H₂ Addition – 0.2 MPa

ϕ	P_{fuel} (kPa)	ρ_b/ρ_u	Linear Technique			Nonlinear Technique		
			S_u (mm·s ⁻¹)	u_L (cm·s ⁻¹)	L_b (mm)	S_u (mm·s ⁻¹)	u_L (cm·s ⁻¹)	L_b (mm)
0.8	113.95	0.21727	193.15	4.20	-0.67	190.90	4.15	-0.89
			186.78	4.06	-0.53	184.66	4.01	-0.70
1	124.67	0.21343	241.37	5.15	-0.09	241.23	5.15	-0.09
			229.87	4.91	-0.37	228.24	4.87	-0.42
1.2	133.03	0.22092	237.42	5.25	0.04	237.43	5.25	0.04
			238.97	5.28	-0.03	244.38	5.40	0.15
1.4	139.71	0.25422	197.17	5.01	0.12	197.11	5.01	0.11
			210.91	5.36	0.59	209.47	5.33	0.48

Individual Tests – Optical BFG Results 5 % H₂ Addition – 0.2 MPa

ϕ	P_{fuel} (kPa)	ρ_b/ρ_u	Linear Technique			Nonlinear Technique		
			S_u (mm·s ⁻¹)	u_L (cm·s ⁻¹)	L_b (mm)	S_u (mm·s ⁻¹)	u_L (cm·s ⁻¹)	L_b (mm)
0.8	111.04	0.21950	241.40	5.30	-0.63	239.32	5.25	-0.81
			247.25	5.43	-0.55	246.63	5.41	-0.63
1	121.88	0.20914	339.92	7.11	-0.40	338.64	7.08	-0.50
			328.35	6.87	-0.41	327.02	6.84	-0.40
1.2	130.38	0.22479	345.54	7.77	-0.12	345.51	7.77	-0.12
			330.60	7.43	-0.26	330.01	7.43	-0.25
1.4	137.20	0.24103	283.33	6.83	0.00	283.39	6.83	0.00
			292.52	7.05	0.17	292.34	7.05	0.16

Individual Tests – Optical BFG Results 7 % H₂ Addition – 0.2 MPa

ϕ	P_{fuel} (kPa)	ρ_b/ρ_u	Linear Technique			Nonlinear Technique		
			S_u (mm·s ⁻¹)	u_L (cm·s ⁻¹)	L_b (mm)	S_u (mm·s ⁻¹)	u_L (cm·s ⁻¹)	L_b (mm)
0.8	108.31	0.21578	332.33	7.17	-0.74	329.08	7.10	-0.95
			325.96	7.03	-0.73	320.48	6.92	-1.02
1	119.23	0.20520	432.50	8.87	-0.70	432.91	8.88	-0.76
			434.37	8.91	-0.70	430.35	8.83	-0.90
1.2	127.83	0.22035	440.59	9.71	-0.52	439.88	9.69	-0.57
			444.84	9.80	-0.46	444.32	9.80	-0.45
1.4	134.79	0.23620	404.55	9.56	-0.12	404.52	9.55	-0.13
			396.30	9.36	-0.01	396.33	9.36	-0.01

Summary – Optical BFG Results 1 % H₂ Addition 0.15 MPa

Summary – Linear Optical and Modelled Results

ϕ	Ave S_u (mm·s ⁻¹)	Ave u_L (cm·s ⁻¹)	Ave L_b (mm)	GRI-Mech 3.0 (cm·s ⁻¹)	Li et al. (cm·s ⁻¹)	Davis et al. (cm·s ⁻¹)
0.8	113.67	2.59	-0.13	2.18	2.44	2.56
1	146.72	3.20	0.30	2.89	3.16	3.24
1.2	153.17	3.60	0.45	3.09	3.30	3.36
1.4	129.53	3.26	0.79	2.66	2.84	2.89

Summary and Error – Nonlinear Optical Results

ϕ	B_{Su} (mm·s ⁻¹)	Ave S_u (mm·s ⁻¹)	Ave u_L (cm·s ⁻¹)	Ave L_b (mm)	σ_{Su} (mm·s ⁻¹)	U_{Su} (mm·s ⁻¹)
0.8	1.74	113.61	2.59	-0.14	5.18	46.55
1	1.98	146.17	3.19	0.28	9.37	84.23
1.2	1.97	153.41	3.60	0.42	1.65	14.94
1.4	1.95	127.89	3.22	0.60	0.21	2.69

Summary – Optical BFG Results 3 % H₂ Addition 0.15 MPa

Summary – Linear Optical and Modelled Results

ϕ	Ave S_u (mm·s ⁻¹)	Ave u_L (cm·s ⁻¹)	Ave L_b (mm)	GRI-Mech 3.0 (cm·s ⁻¹)	Li et al. (cm·s ⁻¹)	Davis et al. (cm·s ⁻¹)
0.8	198.97	4.33	-0.32	3.82	4.31	4.34
1	270.12	5.77	-0.17	5.17	5.62	5.59
1.2	280.72	6.20	0.04	5.77	6.07	5.98
1.4	249.95	6.36	0.51	5.31	5.56	5.43

Summary and Error – Nonlinear Optical Results

ϕ	B_{Su} (mm·s ⁻¹)	Ave S_u (mm·s ⁻¹)	Ave u_L (cm·s ⁻¹)	Ave L_b (mm)	σ_{Su} (mm·s ⁻¹)	U_{Su} (mm·s ⁻¹)
0.8	2.84	199.69	4.34	-0.31	2.74	20.33
1	3.30	268.04	5.72	-0.17	5.28	38.90
1.2	3.35	280.82	6.20	0.04	5.08	37.41
1.4	3.37	249.39	6.34	0.45	10.08	74.07

Summary – Optical BFG Results 5 % H₂ Addition 0.15 MPa

Summary – Linear Optical and Modelled Results

ϕ	Ave S_u (mm·s ⁻¹)	Ave u_L (cm·s ⁻¹)	Ave L_b (mm)	GRI-Mech 3.0 (cm·s ⁻¹)	Li et al. (cm·s ⁻¹)	Davis et al. (cm·s ⁻¹)
0.8	283.34	6.22	-0.54	5.29	5.99	5.92
1	378.45	7.92	-0.36	7.23	7.83	7.67
1.2	391.12	8.79	-0.11	8.23	8.57	8.34
1.4	348.26	8.39	0.34	7.82	8.05	7.76

Summary and Error – Nonlinear Optical Results

ϕ	B_{Su} (mm·s ⁻¹)	Ave S_u (mm·s ⁻¹)	Ave u_L (cm·s ⁻¹)	Ave L_b (mm)	σ_{Su} (mm·s ⁻¹)	U_{Su} (mm·s ⁻¹)
0.8	3.82	283.11	6.22	-0.61	2.31	17.34
1	4.46	377.36	7.89	-0.41	3.19	23.82
1.2	4.58	391.12	8.79	-0.11	10.55	77.55
1.4	4.64	347.13	8.37	0.30	7.66	56.39

Summary – Optical BFG Results 7 % H₂ Addition 0.15 MPa

Summary – Linear Optical and Modelled Results

ϕ	Ave S_u (mm·s ⁻¹)	Ave u_L (cm·s ⁻¹)	Ave L_b (mm)	GRI-Mech 3.0 (cm·s ⁻¹)	Li et al. (cm·s ⁻¹)	Davis et al. (cm·s ⁻¹)
0.8	438.63	9.21	-0.56	6.80	7.73	7.53
1	501.10	10.67	-0.42	9.36	10.12	9.82
1.2	489.47	11.16	-0.07	10.80	11.17	10.79
1.4	454.83	10.74	0.01	10.50	10.68	10.25

Summary and Error – Nonlinear Optical Results

ϕ	B_{Su} (mm·s ⁻¹)	Ave S_u (mm·s ⁻¹)	Ave u_L (cm·s ⁻¹)	Ave L_b (mm)	σ_{Su} (mm·s ⁻¹)	U_{Su} (mm·s ⁻¹)
0.8	4.87	435.46	9.14	-0.70	3.87	28.85
1	5.78	501.64	10.68	-0.45	3.48	26.17
1.2	5.96	488.30	11.13	-0.10	3.20	24.25
1.4	6.03	451.52	10.66	0.01	8.20	60.44

Summary – Optical BFG Results 1 % H₂ Addition 0.2 MPa

Summary – Linear Optical and Modelled Results

ϕ	Ave S_u (mm·s ⁻¹)	Ave u_L (cm·s ⁻¹)	Ave L_b (mm)	GRI-Mech 3.0 (cm·s ⁻¹)	Li et al. (cm·s ⁻¹)	Davis et al. (cm·s ⁻¹)
0.8	98.60	2.25	0.00	1.79	2.01	2.16
1	138.02	3.01	0.34	2.46	2.67	2.80
1.2	141.79	3.33	0.72	2.60	2.77	2.87
1.4	108.50	2.74	0.81	2.12	2.28	2.38

Summary and Error – Nonlinear Optical Results

ϕ	B_{Su} (mm·s ⁻¹)	Ave S_u (mm·s ⁻¹)	Ave u_L (cm·s ⁻¹)	Ave L_b (mm)	σ_{Su} (mm·s ⁻¹)	U_{Su} (mm·s ⁻¹)
0.8	1.74	98.55	2.25	-0.02	3.87	28.49
1	1.98	137.68	3.00	0.31	9.10	66.81
1.2	1.97	139.72	3.28	0.54	0.01	1.98
1.4	1.95	107.27	2.70	0.58	1.08	8.18

Summary – Optical BFG Results 3 % H₂ Addition 0.2 MPa

Summary – Linear Optical and Modelled Results

ϕ	Ave S_u (mm·s ⁻¹)	Ave u_L (cm·s ⁻¹)	Ave L_b (mm)	GRI-Mech 3.0 (cm·s ⁻¹)	Li et al. (cm·s ⁻¹)	Davis et al. (cm·s ⁻¹)
0.8	189.97	4.13	-0.60	3.18	3.61	3.70
1	235.62	5.03	-0.23	4.42	4.81	4.84
1.2	238.20	5.27	0.01	4.93	5.17	5.14
1.4	204.04	5.19	0.36	4.35	4.59	4.53

Summary and Error – Nonlinear Optical Results

ϕ	B_{Su} (mm·s ⁻¹)	Ave S_u (mm·s ⁻¹)	Ave u_L (cm·s ⁻¹)	Ave L_b (mm)	σ_{Su} (mm·s ⁻¹)	U_{Su} (mm·s ⁻¹)
0.8	2.84	187.78	4.08	-0.80	4.41	32.50
1	3.30	234.74	5.01	-0.26	9.19	67.48
1.2	3.35	240.91	5.33	0.10	4.91	36.22
1.4	3.37	203.29	5.17	0.30	8.74	64.22

Summary – Optical BFG Results 5 % H₂ Addition 0.2 MPa

Summary – Linear Optical and Modelled Results

ϕ	Ave S_u (mm·s ⁻¹)	Ave u_L (cm·s ⁻¹)	Ave L_b (mm)	GRI-Mech 3.0 (cm·s ⁻¹)	Li et al. (cm·s ⁻¹)	Davis et al. (cm·s ⁻¹)
0.8	244.33	5.37	-0.59	4.45	5.08	5.07
1	334.14	6.99	-0.41	6.23	6.77	6.68
1.2	338.07	7.60	-0.19	7.08	7.37	7.21
1.4	287.93	6.94	0.09	6.50	6.73	6.53

Summary and Error – Nonlinear Optical Results

ϕ	B_{Su} (mm·s ⁻¹)	Ave S_u (mm·s ⁻¹)	Ave u_L (cm·s ⁻¹)	Ave L_b (mm)	σ_{Su} (mm·s ⁻¹)	U_{Su} (mm·s ⁻¹)
0.8	3.82	242.98	5.33	-0.72	5.17	38.12
1	4.46	332.83	6.96	-0.45	8.22	60.46
1.2	4.58	337.76	7.60	-0.19	10.96	80.56
1.4	4.64	287.87	6.94	0.08	6.33	46.67

Summary – Optical BFG Results 7 % H₂ Addition 0.2 MPa

Summary – Linear Optical and Modelled Results

ϕ	Ave S_u (mm·s ⁻¹)	Ave u_L (cm·s ⁻¹)	Ave L_b (mm)	GRI-Mech 3.0 (cm·s ⁻¹)	Li et al. (cm·s ⁻¹)	Davis et al. (cm·s ⁻¹)
0.8	379.23	7.95	-0.72	5.76	6.61	6.49
1	437.48	9.31	-0.61	8.11	8.79	8.57
1.2	424.70	9.68	-0.29	9.34	9.66	9.38
1.4	396.30	9.36	-0.01	8.81	9.02	8.68

Summary and Error – Nonlinear Optical Results

ϕ	B_{Su} (mm·s ⁻¹)	Ave S_u (mm·s ⁻¹)	Ave u_L (cm·s ⁻¹)	Ave L_b (mm)	σ_{Su} (mm·s ⁻¹)	U_{Su} (mm·s ⁻¹)
0.8	4.87	376.70	7.90	-0.89	6.08	44.89
1	5.78	435.12	9.26	-0.74	1.81	14.48
1.2	5.96	424.42	9.68	-0.29	3.14	23.80
1.4	6.03	396.33	9.36	-0.01	5.79	42.92

B.5 - BFG Elevated Temperature Dataset

Test Conditions

Fuel: BFG (CO-23.07%, CO₂-23.35%, and N₂-53.58%)

Temperature: 333, 363, 393 K

Pressure: 0.1 MPa

Camera Speed 3,000 fps

Individual Tests – Optical BFG Results 1 % H₂ Addition – 333 K

ϕ	P_{fuel} (kPa)	ρ_b/ρ_u	Linear Technique			Nonlinear Technique		
			S_u (mm·s ⁻¹)	u_L (cm·s ⁻¹)	L_b (mm)	S_u (mm·s ⁻¹)	u_L (cm·s ⁻¹)	L_b (mm)
0.8	58.5	0.2465	156.70	3.86	0.22	156.64	3.86	0.21
			155.69	3.84	0.15	155.68	3.84	0.15
1	63.79	0.2363	201.52	4.76	0.98	196.64	4.65	0.67
			190.50	4.50	0.68	189.24	4.47	0.55
1.2	67.89	0.2537	216.46	5.49	0.79	214.02	5.43	0.61
			217.66	5.52	1.47	201.57	5.11	0.75
1.4	71.15	0.2717	193.10	5.25	0.86	191.72	5.21	0.69
			195.08	5.30	0.85	191.74	5.21	0.62

Individual Tests – Optical BFG Results 3 % H₂ Addition – 333 K

ϕ	P_{fuel} (kPa)	ρ_b/ρ_u	Linear Technique			Nonlinear Technique		
			S_u (mm·s ⁻¹)	u_L (cm·s ⁻¹)	L_b (mm)	S_u (mm·s ⁻¹)	u_L (cm·s ⁻¹)	L_b (mm)
0.8	56.97	0.2418	271.42	6.55	0.08	270.69	6.55	0.07
			291.61	7.01	0.22	290.10	7.01	0.06
1	62.33	0.2312	327.47	7.53	0.15	325.15	7.52	0.04
			326.50	7.53	0.15	325.68	7.53	0.04
1.2	66.51	0.2482	340.23	8.44	0.36	337.33	8.37	0.31
			353.23	8.77	0.06	353.12	8.77	0.07
1.4	69.85	0.2658	325.19	8.64	0.38	323.55	8.60	0.32
			306.49	8.15	0.30	306.10	8.14	0.27

Individual Tests – Optical BFG Results 5 % H₂ Addition – 333 K

ϕ	P_{fuel} (kPa)	ρ_b/ρ_u	Linear Technique			Nonlinear Technique		
			S_u (mm·s ⁻¹)	u_L (cm·s ⁻¹)	L_b (mm)	S_u (mm·s ⁻¹)	u_L (cm·s ⁻¹)	L_b (mm)
0.8	55.52	0.2375	381.27	9.03	-0.46	380.41	9.03	-0.49
			384.99	9.14	-0.31	384.96	9.14	-0.31
1	60.94	0.2267	447.72	10.15	-0.11	447.58	10.15	-0.12
			468.89	10.61	-0.10	467.88	10.61	-0.09
1.2	65.19	0.2431	520.55	12.65	0.19	520.27	12.65	0.18
			503.24	12.23	-0.10	503.15	12.23	-0.11
1.4	68.6	0.2603	472.82	12.31	0.44	470.83	12.26	0.38
			465.23	12.10	0.49	464.35	12.09	0.50

Individual Tests – Optical BFG Results 7 % H₂ Addition – 333 K

ϕ	P_{fuel} (kPa)	ρ_b/ρ_u	Linear Technique			Nonlinear Technique		
			S_u (mm·s ⁻¹)	u_L (cm·s ⁻¹)	L_b (mm)	S_u (mm·s ⁻¹)	u_L (cm·s ⁻¹)	L_b (mm)
0.8	54.15	0.2335	504.36	11.78	-0.56	499.56	11.66	-0.72
			501.79	11.72	-0.52	498.33	11.64	-0.64
1	59.61	0.2225	639.32	14.22	-0.28	638.29	14.20	-0.31
			635.05	14.13	-0.22	634.46	14.12	-0.24
1.2	63.91	0.2384	685.16	16.33	-0.10	685.16	16.33	-0.10
			656.69	15.66	-0.16	656.32	15.65	-0.16
1.4	67.39	0.2552	620.86	15.84	0.03	618.63	15.79	0.00
			636.88	16.25	0.15	635.58	16.22	0.13

363 K

Individual Tests – Optical BFG Results 1 % H₂ Addition – 363 K

ϕ	P_{fuel} (kPa)	ρ_b/ρ_u	Linear Technique			Nonlinear Technique		
			S_u (mm·s ⁻¹)	u_L (cm·s ⁻¹)	L_b (mm)	S_u (mm·s ⁻¹)	u_L (cm·s ⁻¹)	L_b (mm)
0.8	58.5	0.2644	185.28	4.90	0.43	183.17	4.84	0.45
			185.28	4.90	0.43	183.17	4.84	0.45
1	63.79	0.2538	218.85	5.56	0.60	211.31	5.36	0.65
			210.23	5.34	0.22	210.02	5.33	0.21
1.2	67.89	0.2720	225.10	6.12	0.70	221.88	6.03	0.73
			223.80	6.09	0.57	213.65	5.81	0.73
1.4	71.15	0.2908	200.21	5.82	1.13	199.79	5.81	0.90
			219.21	6.38	1.51	208.59	6.07	0.91

Individual Tests – Optical BFG Results 3 % H₂ Addition – 363 K

ϕ	P_{fuel} (kPa)	ρ_b/ρ_u	Linear Technique			Nonlinear Technique		
			S_u (mm·s ⁻¹)	u_L (cm·s ⁻¹)	L_b (mm)	S_u (mm·s ⁻¹)	u_L (cm·s ⁻¹)	L_b (mm)
0.8	56.97	0.2594	310.99	8.07	0.08	310.94	8.07	0.09
			310.99	8.07	-0.25	310.94	8.07	-0.18
1	62.33	0.2485	377.18	9.37	0.13	377.03	9.37	0.12
			378.68	9.41	-0.05	378.60	9.41	-0.05
1.2	66.51	0.2662	386.97	10.30	0.14	386.72	10.29	0.13
			396.11	10.54	0.33	396.97	10.57	0.34
1.4	69.85	0.2846	365.66	10.41	0.50	363.52	10.35	0.41
			358.74	10.21	0.31	358.58	10.21	0.29

 Individual Tests – Optical BFG Results 5 % H₂ Addition – 363 K

ϕ	P_{fuel} (kPa)	ρ_b/ρ_u	Linear Technique			Nonlinear Technique		
			S_u (mm·s ⁻¹)	u_L (cm·s ⁻¹)	L_b (mm)	S_u (mm·s ⁻¹)	u_L (cm·s ⁻¹)	L_b (mm)
0.8	55.52	0.2549	450.96	11.49	-0.02	450.91	11.49	-0.02
			439.72	11.21	-0.23	439.10	11.19	-0.25
1	60.94	0.2437	569.49	13.88	-0.08	569.36	13.88	-0.08
			566.83	13.81	-0.18	550.33	13.41	-0.43
1.2	65.19	0.2608	606.19	15.81	0.31	605.20	15.78	0.28
			573.09	14.95	0.01	573.09	14.95	0.01
1.4	68.6	0.2789	543.18	15.15	0.32	543.06	15.14	0.31
			559.97	15.62	0.52	557.58	15.55	0.43

 Individual Tests – Optical BFG Results 7 % H₂ Addition – 363 K

ϕ	P_{fuel} (kPa)	ρ_b/ρ_u	Linear Technique			Nonlinear Technique		
			S_u (mm·s ⁻¹)	u_L (cm·s ⁻¹)	L_b (mm)	S_u (mm·s ⁻¹)	u_L (cm·s ⁻¹)	L_b (mm)
0.8	54.15	0.2507	552.34	13.85	-0.49	546.48	13.70	-0.64
			553.09	13.87	-0.31	552.92	13.86	-0.33
1	59.61	0.2393	706.67	16.91	-0.01	706.27	16.90	-0.01
			682.92	16.34	-0.16	682.59	16.33	-0.17
1.2	63.91	0.2558	735.35	18.81	0.07	733.00	18.75	0.11
			769.35	19.68	0.00	768.62	19.66	0.01
1.4	67.39	0.2735	709.87	19.41	0.22	709.74	19.41	0.21
			729.66	19.96	0.35	729.58	19.95	0.35

393 K

 Individual Tests – Optical BFG Results 1 % H₂ Addition – 393 K

ϕ	P_{fuel} (kPa)	ρ_b/ρ_u	Linear Technique			Nonlinear Technique		
			S_u (mm·s ⁻¹)	u_L (cm·s ⁻¹)	L_b (mm)	S_u (mm·s ⁻¹)	u_L (cm·s ⁻¹)	L_b (mm)
0.8	58.5	0.2817	192.85	5.43	0.00	192.02	5.41	0.01
			207.86	5.86	1.59	207.61	5.85	0.01
1	63.79	0.2709	233.93	6.34	0.49	233.62	6.33	0.39
			233.93	6.34	0.49	233.62	6.33	0.39
1.2	67.89	0.2896	247.75	7.17	1.04	244.32	7.08	0.78
			236.68	6.85	1.58	234.21	6.78	1.19
1.4	71.15	0.3093	211.38	6.54	1.06	211.32	6.54	0.78
			202.34	6.26	1.03	201.58	6.23	0.78

 Individual Tests – Optical BFG Results 3 % H₂ Addition – 393 K

ϕ	P_{fuel} (kPa)	ρ_b/ρ_u	Linear Technique			Nonlinear Technique		
			S_u (mm·s ⁻¹)	u_L (cm·s ⁻¹)	L_b (mm)	S_u (mm·s ⁻¹)	u_L (cm·s ⁻¹)	L_b (mm)
0.8	56.97	0.2765	361.14	9.99	0.11	359.64	9.94	0.11
			377.08	10.43	-0.01	376.44	10.41	0.01
1	62.33	0.2654	444.93	11.81	0.01	444.77	11.80	0.01
			464.18	12.32	0.12	464.06	12.31	0.12
1.2	66.51	0.2835	470.86	13.35	0.35	469.75	13.32	0.31
			449.44	12.74	0.62	447.27	12.68	0.53
1.4	69.85	0.3028	428.51	12.97	0.47	426.31	12.91	0.40
			431.50	13.07	0.40	428.44	12.97	0.36

 Individual Tests – Optical BFG Results 5 % H₂ Addition – 393 K

ϕ	P_{fuel} (kPa)	ρ_b/ρ_u	Linear Technique			Nonlinear Technique		
			S_u (mm·s ⁻¹)	u_L (cm·s ⁻¹)	L_b (mm)	S_u (mm·s ⁻¹)	u_L (cm·s ⁻¹)	L_b (mm)
0.8	55.52	0.2718	477.23	12.97	-0.18	476.79	12.96	-0.19
			499.99	13.59	-0.06	499.94	13.59	-0.06
1	60.94	0.2603	611.09	15.91	-0.06	609.64	15.87	-0.08
			614.09	15.98	0.24	611.63	15.92	0.23
1.2	65.19	0.2779	679.12	18.88	0.30	677.58	18.83	0.27
			640.86	17.81	0.61	640.70	17.81	0.57
1.4	68.6	0.2968	650.55	19.31	0.47	615.14	18.26	0.40
			630.34	18.71	0.46	611.13	18.14	0.36

Individual Tests – Optical BFG Results 7 % H₂ Addition – 393 K

ϕ	P_{fuel} (kPa)	ρ_b/ρ_u	Linear Technique			Nonlinear Technique		
			S_u (mm·s ⁻¹)	u_L (cm·s ⁻¹)	L_b (mm)	S_u (mm·s ⁻¹)	u_L (cm·s ⁻¹)	L_b (mm)
0.8	54.15	0.2674	620.83	16.60	-0.49	617.14	16.50	-0.60
			621.17	16.61	-0.40	618.81	16.55	-0.47
1	59.61	0.2556	761.09	19.45	-0.25	760.18	19.43	-0.29
			797.89	20.40	-0.20	797.02	20.37	-0.22
1.2	63.91	0.2727	833.90	22.74	-0.14	833.66	22.73	-0.14
			838.01	22.85	0.05	837.96	22.85	0.05
1.4	67.39	0.2911	790.87	23.03	0.16	790.47	23.01	0.15
			811.78	23.63	0.21	809.03	23.55	0.18

Summary – Optical BFG Results 1 % H₂ Addition 333 K

Summary – Linear Optical and Modelled Results

ϕ	Ave S_u (mm·s ⁻¹)	Ave u_L (cm·s ⁻¹)	Ave L_b (mm)	GRI-Mech 3.0 (cm·s ⁻¹)	Li et al. (cm·s ⁻¹)	Davis et al. (cm·s ⁻¹)
0.8	156.20	3.85	0.19	3.49	3.89	3.95
1	196.01	4.63	0.83	4.39	4.82	4.83
1.2	217.06	5.51	1.13	4.72	5.07	5.05
1.4	194.09	5.27	0.86	3.49	4.68	4.64

Summary and Error – Nonlinear Optical Results

ϕ	B_{S_u} (mm·s ⁻¹)	Ave S_u (mm·s ⁻¹)	Ave u_L (cm·s ⁻¹)	Ave L_b (mm)	σ_{S_u} (mm·s ⁻¹)	U_{S_u} (mm·s ⁻¹)
0.8	1.74	156.16	3.85	0.18	0.68	5.28
1	1.98	192.94	4.56	0.61	5.23	38.45
1.2	1.97	207.80	5.27	0.68	8.80	64.63
1.4	1.95	191.73	5.21	0.66	0.01	1.96

Summary – Optical BFG Results 3 % H₂ Addition 333 K

Summary – Linear Optical and Modelled Results

ϕ	Ave S_u (mm·s ⁻¹)	Ave u_L (cm·s ⁻¹)	Ave L_b (mm)	GRI-Mech 3.0 (cm·s ⁻¹)	Li et al. (cm·s ⁻¹)	Davis et al. (cm·s ⁻¹)
0.8	281.52	6.78	0.15	5.97	6.68	6.61
1	326.99	7.53	0.15	7.71	8.40	8.23
1.2	346.73	8.61	0.21	8.61	9.11	8.88
1.4	315.84	8.40	0.34	8.42	8.77	8.47

Summary and Error – Nonlinear Optical Results

ϕ	B_{Su} (mm·s ⁻¹)	Ave S_u (mm·s ⁻¹)	Ave u_L (cm·s ⁻¹)	Ave L_b (mm)	σ_{Su} (mm·s ⁻¹)	U_{Su} (mm·s ⁻¹)
0.8	2.84	280.40	6.78	0.07	13.72	100.76
1	3.30	325.42	7.53	0.04	0.37	4.29
1.2	3.35	345.23	8.57	0.19	11.17	82.00
1.4	3.37	314.83	8.37	0.30	12.34	90.61

Summary – Optical BFG Results 5 % H₂ Addition 333 K

Summary – Linear Optical and Modelled Results

ϕ	Ave S_u (mm·s ⁻¹)	Ave u_L (cm·s ⁻¹)	Ave L_b (mm)	GRI-Mech 3.0 (cm·s ⁻¹)	Li et al. (cm·s ⁻¹)	Davis et al. (cm·s ⁻¹)
0.8	383.13	9.09	-0.39	8.17	9.16	8.93
1	458.31	10.38	-0.11	10.70	11.59	11.25
1.2	511.90	12.44	0.05	12.14	12.73	12.30
1.4	469.03	12.21	0.47	12.13	12.46	11.96

Summary and Error – Nonlinear Optical Results

ϕ	B_{Su} (mm·s ⁻¹)	Ave S_u (mm·s ⁻¹)	Ave u_L (cm·s ⁻¹)	Ave L_b (mm)	σ_{Su} (mm·s ⁻¹)	U_{Su} (mm·s ⁻¹)
0.8	3.82	382.69	9.09	-0.40	3.22	23.92
1	4.46	457.73	10.38	-0.11	14.35	105.43
1.2	4.58	511.71	12.44	0.04	12.11	88.95
1.4	4.64	467.59	12.18	0.44	4.58	33.94

Summary – Optical BFG Results 7 % H₂ Addition 333K

Summary – Linear Optical and Modelled Results

ϕ	Ave S_u (mm·s ⁻¹)	Ave u_L (cm·s ⁻¹)	Ave L_b (mm)	GRI-Mech 3.0 (cm·s ⁻¹)	Li et al. (cm·s ⁻¹)	Davis et al. (cm·s ⁻¹)
0.8	503.08	11.75	-0.54	10.40	11.68	11.29
1	637.19	14.18	-0.25	13.75	14.84	14.31
1.2	670.93	16.00	-0.13	15.78	16.40	15.79
1.4	628.87	16.05	0.09	16.03	16.28	15.59

Summary and Error – Nonlinear Optical Results

ϕ	B_{Su} (mm·s ⁻¹)	Ave S_u (mm·s ⁻¹)	Ave u_L (cm·s ⁻¹)	Ave L_b (mm)	σ_{Su} (mm·s ⁻¹)	U_{Su} (mm·s ⁻¹)
0.8	4.87	498.95	11.65	-0.68	0.87	8.03
1	5.78	636.38	14.16	-0.28	2.71	20.70
1.2	5.96	670.74	15.99	-0.13	20.39	149.76
1.4	6.03	627.11	16.01	0.07	11.99	88.16

Summary – Optical BFG Results 1 % H₂ Addition 363 K

Summary – Linear Optical and Modelled Results

ϕ	Ave S_u (mm·s ⁻¹)	Ave u_L (cm·s ⁻¹)	Ave L_b (mm)	GRI-Mech 3.0 (cm·s ⁻¹)	Li et al. (cm·s ⁻¹)	Davis et al. (cm·s ⁻¹)
0.8	185.28	4.90	0.43	4.34	4.84	4.88
1	214.54	5.45	0.41	5.38	5.89	5.87
1.2	224.45	6.10	0.64	5.78	6.20	6.16
1.4	209.71	6.10	1.32	5.50	5.82	5.76

Summary and Error – Nonlinear Optical Results

ϕ	B_{Su} (mm·s ⁻¹)	Ave S_u (mm·s ⁻¹)	Ave u_L (cm·s ⁻¹)	Ave L_b (mm)	σ_{Su} (mm·s ⁻¹)	U_{Su} (mm·s ⁻¹)
0.8	1.74	183.17	4.84	0.45	0.00	1.74
1	1.98	210.67	5.35	0.43	0.91	6.98
1.2	1.97	217.77	5.92	0.73	5.82	42.75
1.4	1.95	204.19	5.94	0.91	6.22	45.70

Summary – Optical BFG Results 3 % H₂ Addition 363 K

Summary – Linear Optical and Modelled Results

ϕ	Ave S _u (mm·s ⁻¹)	Ave u _L (cm·s ⁻¹)	Ave L _b (mm)	GRI-Mech 3.0 (cm·s ⁻¹)	Li et al. (cm·s ⁻¹)	Davis et al. (cm·s ⁻¹)
0.8	310.99	8.07	-0.09	7.39	8.25	8.12
1	377.93	9.39	0.04	9.42	10.23	10.00
1.2	391.54	10.42	0.24	10.47	11.07	10.77
1.4	362.20	10.31	0.41	10.39	10.79	10.42

Summary and Error – Nonlinear Optical Results

ϕ	B _{Su} (mm·s ⁻¹)	Ave S _u (mm·s ⁻¹)	Ave u _L (cm·s ⁻¹)	Ave L _b (mm)	σ_{Su} (mm·s ⁻¹)	U _{Su} (mm·s ⁻¹)
0.8	2.84	310.94	8.07	-0.05	0.00	2.84
1	3.30	377.82	9.39	0.04	1.11	8.79
1.2	3.35	391.85	10.43	0.24	7.25	53.29
1.4	3.37	361.05	10.28	0.35	3.49	25.85

Summary – Optical BFG Results 5 % H₂ Addition 363 K

Summary – Linear Optical and Modelled Results

ϕ	Ave S _u (mm·s ⁻¹)	Ave u _L (cm·s ⁻¹)	Ave L _b (mm)	GRI-Mech 3.0 (cm·s ⁻¹)	Li et al. (cm·s ⁻¹)	Davis et al. (cm·s ⁻¹)
0.8	445.34	11.35	-0.13	10.08	11.28	10.96
1	568.16	13.85	-0.13	13.01	14.06	13.62
1.2	589.64	15.38	0.16	14.72	15.41	14.87
1.4	551.58	15.39	0.42	14.89	15.26	14.63

Summary and Error – Nonlinear Optical Results

ϕ	B _{Su} (mm·s ⁻¹)	Ave S _u (mm·s ⁻¹)	Ave u _L (cm·s ⁻¹)	Ave L _b (mm)	σ_{Su} (mm·s ⁻¹)	U _{Su} (mm·s ⁻¹)
0.8	3.82	445.01	11.34	-0.14	8.35	61.40
1	4.46	559.85	13.65	-0.26	13.46	98.84
1.2	4.58	589.15	15.37	0.15	22.71	166.68
1.4	4.64	550.32	15.35	0.37	10.27	75.48

Summary – Optical BFG Results 7 % H₂ Addition 363 K

Summary – Linear Optical and Modelled Results

ϕ	Ave S _u (mm·s ⁻¹)	Ave u _L (cm·s ⁻¹)	Ave L _b (mm)	GRI-Mech 3.0 (cm·s ⁻¹)	Li et al. (cm·s ⁻¹)	Davis et al. (cm·s ⁻¹)
0.8	552.72	13.86	-0.40	12.79	14.32	13.80
1	694.80	16.62	-0.09	16.69	17.97	17.30
1.2	752.35	19.25	0.04	19.08	19.83	19.06
1.4	719.77	19.69	0.29	19.56	19.86	19.00

Summary and Error – Nonlinear Optical Results

ϕ	B _{Su} (mm·s ⁻¹)	Ave S _u (mm·s ⁻¹)	Ave u _L (cm·s ⁻¹)	Ave L _b (mm)	σ_{Su} (mm·s ⁻¹)	U _{Su} (mm·s ⁻¹)
0.8	4.87	549.70	13.78	-0.49	4.55	33.77
1	5.78	694.43	16.62	-0.09	16.74	123.01
1.2	5.96	750.81	19.21	0.06	25.19	184.92
1.4	6.03	719.66	19.68	0.28	14.03	103.12

Summary – Optical BFG Results 1 % H₂ Addition 393 K

Summary – Linear Optical and Modelled Results

ϕ	Ave S _u (mm·s ⁻¹)	Ave u _L (cm·s ⁻¹)	Ave L _b (mm)	GRI-Mech 3.0 (cm·s ⁻¹)	Li et al. (cm·s ⁻¹)	Davis et al. (cm·s ⁻¹)
0.8	200.36	5.64	0.80	5.34	5.94	5.96
1	233.93	6.34	0.49	6.53	7.13	7.09
1.2	242.22	7.01	1.31	7.00	7.51	7.44
1.4	206.86	6.40	0.55	6.76	7.15	7.05

Summary and Error – Nonlinear Optical Results

ϕ	B _{Su} (mm·s ⁻¹)	Ave S _u (mm·s ⁻¹)	Ave u _L (cm·s ⁻¹)	Ave L _b (mm)	σ_{Su} (mm·s ⁻¹)	U _{Su} (mm·s ⁻¹)
0.8	1.74	199.82	5.63	0.01	11.02	80.91
1	1.98	233.62	6.33	0.39	0.00	1.98
1.2	1.97	239.26	6.93	0.99	7.15	52.50
1.4	1.95	206.45	6.38	0.78	6.89	50.58

Summary – Optical BFG Results 3 % H₂ Addition 393 K

Summary – Linear Optical and Modelled Results

ϕ	Ave S_u (mm·s ⁻¹)	Ave u_L (cm·s ⁻¹)	Ave L_b (mm)	GRI-Mech 3.0 (cm·s ⁻¹)	Li et al. (cm·s ⁻¹)	Davis et al. (cm·s ⁻¹)
0.8	369.11	10.21	0.05	9.06	10.09	9.90
1	454.56	12.06	0.07	11.39	12.35	12.04
1.2	460.15	13.05	0.49	12.64	13.36	12.97
1.4	430.01	13.02	0.44	12.68	13.17	12.69

Summary and Error – Nonlinear Optical Results

ϕ	B_{Su} (mm·s ⁻¹)	Ave S_u (mm·s ⁻¹)	Ave u_L (cm·s ⁻¹)	Ave L_b (mm)	σ_{Su} (mm·s ⁻¹)	U_{Su} (mm·s ⁻¹)
0.8	2.84	368.04	10.18	0.06	11.88	87.22
1	3.30	454.42	12.06	0.07	13.64	100.15
1.2	3.35	458.51	13.00	0.42	15.90	116.69
1.4	3.37	427.38	12.94	0.38	1.51	11.56

Summary – Optical BFG Results 5 % H₂ Addition 393 K

Summary – Linear Optical and Modelled Results

ϕ	Ave S_u (mm·s ⁻¹)	Ave u_L (cm·s ⁻¹)	Ave L_b (mm)	GRI-Mech 3.0 (cm·s ⁻¹)	Li et al. (cm·s ⁻¹)	Davis et al. (cm·s ⁻¹)
0.8	488.61	13.28	-0.12	12.33	13.74	13.32
1	612.59	15.94	0.09	15.71	16.94	16.38
1.2	659.99	18.34	0.46	17.70	18.53	17.85
1.4	640.45	19.01	0.47	18.07	18.51	17.73

Summary and Error – Nonlinear Optical Results

ϕ	B_{Su} (mm·s ⁻¹)	Ave S_u (mm·s ⁻¹)	Ave u_L (cm·s ⁻¹)	Ave L_b (mm)	σ_{Su} (mm·s ⁻¹)	U_{Su} (mm·s ⁻¹)
0.8	3.82	488.36	13.27	-0.13	16.37	120.18
1	4.46	609.64	15.89	0.08	1.41	11.25
1.2	4.58	659.14	18.32	0.42	26.08	191.42
1.4	4.64	613.14	18.20	0.38	2.84	21.32

Summary – Optical BFG Results 7 % H₂ Addition 393 K

Summary – Linear Optical and Modelled Results

ϕ	Ave S_u (mm·s ⁻¹)	Ave u_L (cm·s ⁻¹)	Ave L_b (mm)	GRI-Mech 3.0 (cm·s ⁻¹)	Li et al. (cm·s ⁻¹)	Davis et al. (cm·s ⁻¹)
0.8	621.00	16.60	-0.45	15.59	17.40	16.73
1	779.49	19.93	-0.23	20.10	21.61	20.76
1.2	835.96	22.80	-0.05	22.90	23.81	22.83
1.4	801.33	23.33	0.19	23.65	24.04	22.96

Summary and Error – Nonlinear Optical Results

ϕ	B_{Su} (mm·s ⁻¹)	Ave S_u (mm·s ⁻¹)	Ave u_L (cm·s ⁻¹)	Ave L_b (mm)	σ_{Su} (mm·s ⁻¹)	U_{Su} (mm·s ⁻¹)
0.8	4.87	617.98	16.52	-0.54	1.18	9.94
1	5.78	778.60	19.90	-0.26	26.05	191.24
1.2	5.96	835.81	22.79	-0.05	3.04	23.09
1.4	6.03	799.75	23.28	0.17	13.12	96.49

B.6 - BFG Variable H₂O Dataset

Test Conditions

Fuel: BFG (CO-23.00 %, CO₂-23.50 %, and N₂-53.50 %)
 Temperature: 303 K
 Pressure: 0.1 MPa
 Camera Speed 3,000 fps

Individual Tests – Optical BFG Results 1 % H₂ Addition $\phi=1$

H ₂ O (g)	ρ_b/ρ_u	Linear Technique			Nonlinear Technique		
		S_u (mm·s ⁻¹)	u_L (cm·s ⁻¹)	L_b (mm)	S_u (mm·s ⁻¹)	u_L (cm·s ⁻¹)	L_b (mm)
0	0.2177	181.95	3.96	1.30	177.27	3.86	0.87
		180.17	3.92	1.42	172.00	3.74	0.84
		180.44	3.93	1.31	172.80	3.76	0.77
		180.73	3.93	1.54	173.71	3.78	0.95
		177.08	3.86	1.22	172.73	3.76	0.83
0.25	0.2192	219.09	4.80	2.32	206.81	4.53	1.29
		210.71	4.62	1.99	201.41	4.41	1.18
		223.75	4.90	2.73	204.31	4.48	1.31
		223.11	4.89	2.56	203.05	4.45	1.22
		217.36	4.76	2.27	203.95	4.47	1.23
0.5	0.2208	240.59	5.31	2.90	223.16	4.93	1.49
		232.84	5.14	3.07	218.12	4.82	1.53
		228.10	5.04	2.81	214.05	4.73	1.53
		237.05	5.23	2.90	221.95	4.90	1.55
		240.41	5.31	2.93	222.61	4.92	1.49
0.75	0.2225	250.37	5.57	3.11	230.70	5.13	1.55
		246.22	5.48	3.03	227.47	5.06	1.53
		228.76	5.09	3.04	212.69	4.73	1.59
		227.14	5.05	2.63	213.20	4.74	1.42
		237.11	5.28	3.13	213.54	4.75	1.44

Individual Tests – Optical BFG Results 3 % H₂ Addition $\phi=1$

H ₂ O (g)	ρ_b/ρ_u	Linear Technique			Nonlinear Technique		
		S_u (mm·s ⁻¹)	u_L (cm·s ⁻¹)	L_b (mm)	S_u (mm·s ⁻¹)	u_L (cm·s ⁻¹)	L_b (mm)
0	0.2132	297.88	6.35	0.08	297.79	6.35	0.09
		300.84	6.41	0.11	300.80	6.41	0.13
		296.60	6.32	0.11	297.34	6.34	0.12
		295.97	6.31	0.03	295.80	6.31	0.03
		309.99	6.62	0.27	309.87	6.61	0.26
0.25	0.2147	308.91	6.61	0.38	308.03	6.61	0.36
		313.77	6.74	0.29	313.58	6.73	0.27
		311.00	6.68	0.12	310.96	6.68	0.12
		310.62	6.67	0.33	310.13	6.66	0.30
		307.79	6.59	0.11	307.01	6.59	0.12
0.5	0.2156	300.39	6.47	0.13	300.25	6.47	0.13
		302.08	6.51	0.15	301.61	6.50	0.26
		302.58	6.50	0.10	301.28	6.50	0.17
		302.93	6.53	0.34	302.38	6.52	0.30
		304.72	6.57	0.35	304.37	6.56	0.32
0.75	0.2178	302.08	6.58	0.04	301.30	6.56	0.02
		300.46	6.54	0.18	300.15	6.54	0.17
		304.49	6.63	0.25	303.74	6.62	0.22
		301.93	6.58	0.37	300.46	6.54	0.31
		304.13	6.62	0.05	304.06	6.62	0.04

Individual Tests – Optical BFG Results 5 % H₂ Addition $\phi=1$

H ₂ O (g)	ρ_b/ρ_u	Linear Technique			Nonlinear Technique		
		S_u (mm·s ⁻¹)	u_L (cm·s ⁻¹)	L_b (mm)	S_u (mm·s ⁻¹)	u_L (cm·s ⁻¹)	L_b (mm)
0	0.2090	421.99	8.82	-0.36	421.96	8.82	-0.39
		419.91	8.75	-0.49	418.41	8.74	-0.49
		419.48	8.77	-0.29	417.03	8.72	-0.37
		422.64	8.83	-0.47	419.33	8.76	-0.52
		412.75	8.63	-0.49	414.64	8.67	-0.50
0.25	0.2104	400.93	8.44	-0.50	399.30	8.40	-0.59
		400.46	8.43	-0.64	400.83	8.43	-0.71
		406.59	8.55	-0.62	404.04	8.50	-0.77
		402.15	8.46	-0.36	401.30	8.44	-0.41
		403.04	8.48	-0.47	401.34	8.44	-0.56
0.5	0.2118	387.87	8.22	-0.65	384.04	8.13	-0.84
		378.67	8.02	-0.68	375.11	7.95	-0.88
		391.52	8.29	-0.49	389.81	8.26	-0.58
		393.51	8.34	-0.43	392.24	8.31	-0.50
		399.24	8.46	-0.52	395.10	8.37	-0.67
0.75	0.2133	378.69	8.08	-0.56	376.19	8.03	-0.70
		382.47	8.16	-0.54	377.64	8.06	-0.72
		375.80	8.02	-0.49	370.84	7.91	-0.74
		381.24	8.14	-0.58	380.35	8.12	-0.66
		386.53	8.25	-0.70	382.75	8.17	-0.89

Individual Tests – Optical BFG Results 7 % H₂ Addition $\phi=1$

H ₂ O (g)	ρ_b/ρ_u	Linear Technique			Nonlinear Technique		
		S_u (mm·s ⁻¹)	u_L (cm·s ⁻¹)	L_b (mm)	S_u (mm·s ⁻¹)	u_L (cm·s ⁻¹)	L_b (mm)
0	0.2048	537.93	11.02	-0.66	537.10	11.00	-0.73
		539.84	11.06	-0.60	539.42	11.05	-0.63
		529.06	10.84	-0.52	529.00	10.83	-0.60
		544.32	11.15	-0.79	543.57	11.13	-0.75
		543.78	11.14	-0.63	541.80	11.10	-0.69
0.25	0.2062	525.06	10.83	-0.64	521.09	10.74	-0.79
		510.53	10.53	-0.68	505.95	10.43	-0.86
		522.04	10.76	-0.55	519.06	10.70	-0.67
		520.43	10.73	-0.71	516.30	10.65	-0.89
		521.60	10.76	-0.71	517.09	10.66	-0.90
0.5	0.2081	501.49	10.44	-0.71	496.36	10.33	-0.92
		506.58	10.54	-0.68	502.13	10.45	-0.87
		516.25	10.74	-1.08	506.78	10.55	-1.12
		509.86	10.61	-0.83	500.93	10.42	-1.17
		508.38	10.58	-0.98	497.76	10.36	-1.12
0.75	0.2093	497.34	10.41	-0.79	484.53	10.14	-1.23
		490.45	10.27	-0.96	481.50	10.08	-1.36
		484.01	10.13	-0.95	475.01	9.94	-1.34
		487.37	10.20	-0.55	482.33	10.10	-0.71
		490.70	10.27	-0.55	487.35	10.20	-0.68

Individual Tests – Optical BFG Results 1 % H₂ Addition $\phi = 0.8, \phi = 1.4$

ϕ	H ₂ O (g)	ρ_b/ρ_u	Linear Technique			Nonlinear Technique		
			S_u (mm·s ⁻¹)	u_L (cm·s ⁻¹)	L_b (mm)	S_u (mm·s ⁻¹)	u_L (cm·s ⁻¹)	L_b (mm)
0.8	0	0.2273	138.89	3.16	0.10	138.84	3.16	0.10
			139.56	3.17	0.05	139.50	3.17	0.04
			140.33	3.19	0.04	140.33	3.19	0.04
	0.25	0.2290	166.32	3.81	1.93	155.60	3.56	1.03
			158.60	3.63	1.62	149.33	3.42	0.81
			163.66	3.75	1.68	156.25	3.58	0.99
	0.5	0.2307	173.48	4.00	2.35	159.84	3.69	1.17
			172.49	3.98	1.97	161.55	3.73	1.06
			178.81	4.13	2.47	162.74	3.75	1.17
	0.75	0.2325	176.63	4.11	2.05	167.32	3.89	1.16
			183.12	4.26	2.81	167.26	3.89	1.35
			177.68	4.13	2.40	165.19	3.84	1.24
1.4	0	0.2514	153.13	3.85	1.90	143.67	3.61	1.02
			157.81	3.97	1.82	150.57	3.79	1.03
			166.00	4.17	2.16	155.47	3.91	1.12
	0.25	0.2531	189.89	4.81	2.71	171.72	4.35	1.24
			172.32	4.36	2.18	163.30	4.13	1.21
			176.10	4.46	2.06	163.32	4.13	1.05
	0.5	0.2548	190.67	4.86	2.70	174.69	4.45	1.30
			185.70	4.73	2.68	172.46	4.39	1.37
			188.02	4.79	2.32	175.23	4.46	1.20
	0.75	0.2565	202.73	5.20	3.35	178.05	4.57	1.38
			196.40	5.04	2.62	179.40	4.60	1.23
			188.96	4.85	2.42	176.11	4.52	1.25

Individual Tests – Optical BFG Results 3 % H₂ Addition $\phi = 0.8, \phi = 1.4$

ϕ	H ₂ O (g)	ρ_b/ρ_u	Linear Technique			Nonlinear Technique		
			S_u (mm·s ⁻¹)	u_L (cm·s ⁻¹)	L_b (mm)	S_u (mm·s ⁻¹)	u_L (cm·s ⁻¹)	L_b (mm)
0.8	0	0.2230	231.56	5.16	-0.37	230.85	5.15	-0.42
			231.99	5.17	-0.26	230.07	5.13	-0.35
			230.98	5.15	-0.29	230.66	5.14	-0.32
	0.25	0.2247	240.13	5.40	-0.36	239.25	5.38	-0.42
			229.56	5.16	-0.09	229.61	5.16	-0.09
			229.73	5.16	-0.38	228.85	5.14	-0.44
	0.5	0.2264	225.29	5.10	-0.20	225.24	5.10	-0.21
			217.05	4.91	-0.37	216.39	4.90	-0.43
			219.47	4.97	-0.29	219.01	4.96	-0.33
	0.75	0.2280	211.77	4.83	-0.34	210.48	4.80	-0.41
			215.97	4.92	-0.45	215.48	4.91	-0.51
			221.45	5.05	-0.34	220.30	5.02	-0.41
1.4	0	0.2459	264.65	6.51	0.31	264.05	6.49	0.27
			268.32	6.60	0.54	267.00	6.57	0.45
			275.24	6.77	0.58	275.44	6.77	0.52
	0.25	0.2476	284.49	7.04	1.01	280.43	6.94	0.74
			274.01	6.78	0.94	269.01	6.66	0.67
			268.95	6.66	0.84	265.37	6.57	0.62
	0.5	0.2492	290.86	7.25	0.60	283.09	7.05	0.59
			274.96	6.85	1.01	267.93	6.68	0.68
			284.30	7.08	1.18	275.27	6.86	0.76
	0.75	0.2509	277.27	6.96	0.75	270.56	6.79	0.52
			275.63	6.92	0.98	268.32	6.73	0.67
			274.72	6.89	0.96	268.00	6.72	0.66

Individual Tests – Optical BFG Results 5 % H₂ Addition $\phi = 0.8, \phi = 1.4$

ϕ	H ₂ O (g)	ρ_b/ρ_u	Linear Technique			Nonlinear Technique		
			S_u (mm·s ⁻¹)	u_L (cm·s ⁻¹)	L_b (mm)	S_u (mm·s ⁻¹)	u_L (cm·s ⁻¹)	L_b (mm)
0.8	0	0.2190	322.11	7.05	-0.65	323.09	7.08	-0.69
			322.15	7.05	-0.68	322.12	7.05	-0.77
			318.08	6.97	-0.72	317.23	6.95	-0.84
	0.25	0.2207	307.11	6.78	-0.80	309.60	6.83	-0.90
			304.22	6.71	-0.67	304.75	6.72	-0.77
			318.38	7.03	-0.60	311.45	6.87	-0.88
	0.5	0.2222	295.37	6.56	-0.82	290.87	6.46	-1.13
			304.86	6.78	-0.73	297.72	6.62	-1.08
			305.14	6.78	-0.71	299.53	6.66	-1.01
	0.75	0.2240	291.49	6.53	-0.79	286.82	6.43	-1.10
			296.63	6.64	-0.88	290.44	6.51	-1.28
			300.48	6.73	-0.89	294.01	6.59	-1.29
1.4	0	0.2407	405.46	9.76	0.35	402.98	9.70	0.28
			410.36	9.88	0.18	410.07	9.87	0.17
			394.65	9.50	0.05	394.64	9.50	0.05
	0.25	0.2423	385.65	9.35	0.14	385.49	9.34	0.13
			385.91	9.35	0.20	385.60	9.35	0.19
			386.13	9.36	0.22	385.68	9.35	0.19
	0.5	0.2440	373.59	9.12	0.31	372.18	9.08	0.27
			372.70	9.09	0.19	372.58	9.09	0.18
			370.87	9.05	0.25	370.34	9.04	0.22
	0.75	0.2457	363.11	8.92	0.33	359.72	8.84	0.26
			364.54	8.96	0.11	364.57	8.96	0.11
			354.84	8.72	0.22	354.54	8.71	0.17

Individual Tests – Optical BFG Results 7 % H₂ Addition $\phi = 0.8, \phi = 1.4$

ϕ	H ₂ O (g)	ρ_b/ρ_u	Linear Technique			Nonlinear Technique		
			S_u (mm·s ⁻¹)	u_L (cm·s ⁻¹)	L_b (mm)	S_u (mm·s ⁻¹)	u_L (cm·s ⁻¹)	L_b (mm)
0.8	0	0.2152	430.76	9.27	-0.73	425.05	9.15	-0.98
			439.16	9.45	-0.68	433.70	9.33	-0.91
			435.12	9.36	-0.73	429.10	9.24	-0.99
	0.25	0.2169	414.58	8.99	-0.89	413.89	8.98	-1.04
			418.82	9.08	-0.76	412.02	8.94	-1.06
			408.42	8.86	-0.83	404.25	8.77	-1.11
	0.5	0.2186	390.89	8.55	-0.68	387.44	8.47	-0.94
			396.55	8.67	-0.81	388.41	8.49	-1.17
			387.25	8.47	-0.79	379.73	8.30	-1.13
	0.75	0.2203	370.18	8.16	-0.90	362.81	7.99	-1.37
			384.55	8.47	-0.97	373.87	8.24	-1.49
			380.10	8.37	-0.95	368.91	8.13	-1.48
1.4	0	0.2359	549.85	12.97	0.24	547.06	12.91	0.18
			543.13	12.81	0.12	542.91	12.81	0.11
			549.08	12.95	0.09	549.09	12.95	0.08
	0.25	0.2375	520.47	12.36	0.05	520.50	12.36	0.05
			523.60	12.44	0.07	523.55	12.44	0.07
			520.54	12.36	0.01	520.92	12.37	0.01
	0.5	0.2392	496.33	11.87	-0.04	496.44	11.87	-0.04
			498.40	11.92	0.14	498.18	11.91	0.13
			501.72	12.00	0.11	501.67	12.00	0.11
	0.75	0.2408	481.78	11.60	-0.05	481.81	11.60	-0.05
			477.17	11.49	-0.02	477.43	11.50	-0.02
			474.30	11.42	0.12	473.27	11.40	0.10

Summary H₂O Results

Summary – Linear Optical and Modelled Results 1 % H₂

ϕ	H ₂ O (g)	Ave S _u (mm·s ⁻¹)	Ave u _L (cm·s ⁻¹)	Ave L _b (mm)	Li et al. (cm·s ⁻¹)	Davis et al. (cm·s ⁻¹)
0.8	0	139.59	3.17	0.06	3.18	3.16
	0.25	162.86	3.73	1.74	3.77	3.81
	0.5	174.93	4.04	2.26	3.97	3.99
	0.75	179.14	4.17	2.42	4.01	4.01
1	0	180.07	3.92	1.36	3.97	3.92
	0.25	218.80	4.79	2.37	4.76	4.70
	0.5	235.80	5.21	2.92	5.08	4.99
	0.75	237.92	5.29	2.99	5.20	5.11
1.4	0	158.98	4.00	1.96	3.75	3.68
	0.25	179.44	4.54	2.32	4.56	4.45
	0.5	188.13	4.79	2.57	4.87	4.72
	0.75	196.03	5.03	2.80	4.97	4.79

Summary – Nonlinear Optical Results and Uncertainty 1 % H₂

ϕ	H ₂ O (g)	B _{Su} (mm·s ⁻¹)	Ave S _u (mm·s ⁻¹)	Ave u _L (cm·s ⁻¹)	Ave L _b (mm)	σ_{Su} (mm·s ⁻¹)	U _{Su} (mm·s ⁻¹)
0.8	0	3.46	139.56	3.17	0.06	0.74	3.92
	0.25	3.48	153.73	3.52	0.94	3.82	10.11
	0.5	3.41	161.38	3.72	1.13	1.45	4.97
	0.75	3.41	166.59	3.87	1.25	1.22	4.55
1	0	4.14	173.70	3.78	0.85	2.09	4.88
	0.25	4.31	203.91	4.47	1.25	1.97	4.96
	0.5	3.93	219.98	4.86	1.52	3.86	6.19
	0.75	3.95	219.52	4.88	1.51	8.81	11.63
1.4	0	3.88	149.90	3.77	1.06	5.93	15.24
	0.25	3.89	166.11	4.20	1.17	4.86	12.68
	0.5	3.80	174.13	4.43	1.29	1.47	5.28
	0.75	3.79	177.85	4.56	1.29	1.65	5.59

Summary – Linear Optical and Modelled Results 3 % H₂

ϕ	H ₂ O (g)	Ave S _u (mm·s ⁻¹)	Ave u _L (cm·s ⁻¹)	Ave L _b (mm)	Li et al. (cm·s ⁻¹)	Davis et al. (cm·s ⁻¹)
0.8	0	231.51	5.16	-0.31	5.47	5.32
	0.25	233.14	5.24	-0.28	5.59	5.53
	0.5	220.60	4.99	-0.29	5.57	5.48
	0.75	216.40	4.93	-0.38	5.45	5.36
1	0	300.26	6.40	0.12	6.94	6.83
	0.25	310.42	6.66	0.25	7.14	6.99
	0.5	302.54	6.52	0.21	7.16	7.01
	0.75	302.62	6.59	0.18	7.08	6.95
1.4	0	269.40	6.63	0.48	7.10	6.87
	0.25	275.82	6.83	0.93	7.25	6.99
	0.5	283.37	7.06	0.93	7.22	6.93
	0.75	275.87	6.92	0.90	7.09	6.81

Summary – Nonlinear Optical Results and Uncertainty 3 % H₂

ϕ	H ₂ O (g)	B _{Su} (mm·s ⁻¹)	Ave S _u (mm·s ⁻¹)	Ave u _L (cm·s ⁻¹)	Ave L _b (mm)	σ_{Su} (mm·s ⁻¹)	U _{Su} (mm·s ⁻¹)
0.8	0	5.40	230.53	5.14	-0.36	0.40	5.49
	0.25	5.40	232.57	5.23	-0.32	5.80	15.38
	0.5	5.45	220.21	4.99	-0.32	4.55	12.54
	0.75	5.38	215.42	4.91	-0.44	4.91	13.34
1	0	6.61	300.32	6.40	0.13	5.64	9.63
	0.25	6.53	309.94	6.65	0.23	2.58	7.27
	0.5	6.56	301.98	6.51	0.24	1.54	6.83
	0.75	6.60	301.94	6.58	0.15	1.84	6.98
1.4	0	6.33	268.83	6.61	0.41	5.91	16.00
	0.25	6.34	271.60	6.72	0.68	7.86	20.52
	0.5	6.33	275.43	6.86	0.68	7.59	19.88
	0.75	6.45	268.96	6.75	0.62	1.40	7.32

Summary – Linear Optical and Modelled Results 5 % H₂

ϕ	H ₂ O (g)	Ave S _u (mm·s ⁻¹)	Ave u _L (cm·s ⁻¹)	Ave L _b (mm)	Li et al. (cm·s ⁻¹)	Davis et al. (cm·s ⁻¹)
0.8	0	320.78	7.02	-0.68	7.53	7.36
	0.25	309.90	6.84	-0.69	7.42	7.24
	0.5	301.79	6.71	-0.75	7.24	7.04
	0.75	296.20	6.63	-0.85	6.99	6.79
1	0	419.35	8.76	-0.42	9.61	9.34
	0.25	402.63	8.47	-0.52	9.53	9.27
	0.5	390.16	8.27	-0.55	9.35	9.11
	0.75	380.95	8.13	-0.57	9.10	8.91
1.4	0	403.49	9.71	0.19	10.15	9.75
	0.25	385.90	9.35	0.19	9.98	9.58
	0.5	372.39	9.09	0.25	9.72	9.33
	0.75	360.83	8.87	0.22	9.41	9.02

Summary – Nonlinear Optical Results and Uncertainty 5 % H₂

ϕ	H ₂ O (g)	B _{Su} (mm·s ⁻¹)	Ave S _u (mm·s ⁻¹)	Ave u _L (cm·s ⁻¹)	Ave L _b (mm)	σ_{Su} (mm·s ⁻¹)	U _{Su} (mm·s ⁻¹)
0.8	0	6.90	320.81	7.03	-0.77	3.14	10.41
	0.25	6.97	308.60	6.81	-0.85	3.46	11.06
	0.5	6.93	296.04	6.58	-1.07	4.57	13.30
	0.75	6.88	290.42	6.51	-1.22	3.59	11.27
1	0	8.17	418.27	8.74	-0.45	2.72	8.84
	0.25	8.23	401.36	8.44	-0.61	1.71	8.50
	0.5	8.19	387.26	8.20	-0.69	7.92	12.79
	0.75	8.15	377.55	8.06	-0.74	4.52	9.90
1.4	0	8.27	402.56	9.69	0.17	7.73	20.90
	0.25	8.33	385.59	9.35	0.17	0.10	8.33
	0.5	8.30	371.70	9.07	0.22	1.20	8.82
	0.75	8.29	359.61	8.84	0.18	5.01	14.96

Summary – Linear Optical and Modelled Results 7 % H₂

ϕ	H ₂ O (g)	Ave S _u (mm·s ⁻¹)	Ave u _L (cm·s ⁻¹)	Ave L _b (mm)	Li et al. (cm·s ⁻¹)	Davis et al. (cm·s ⁻¹)
0.8	0	435.01	9.36	-0.71	9.62	9.32
	0.25	413.94	8.98	-0.83	9.35	9.03
	0.5	391.56	8.56	-0.76	9.02	8.70
	0.75	378.28	8.33	-0.94	8.66	8.34
1	0	538.99	11.04	-0.64	12.33	11.91
	0.25	519.93	10.72	-0.66	12.04	11.66
	0.5	508.51	10.58	-0.86	11.69	11.37
	0.75	489.97	10.26	-0.76	11.30	11.04
1.4	0	547.35	12.91	0.15	13.33	12.78
	0.25	521.54	12.39	0.04	12.92	12.39
	0.5	498.82	11.93	0.07	12.47	11.96
	0.75	477.75	11.50	0.02	11.98	11.50

 Summary – Nonlinear Optical Results and Uncertainty 7 % H₂

ϕ	H ₂ O (g)	B _{Su} (mm·s ⁻¹)	Ave S _u (mm·s ⁻¹)	Ave u _L (cm·s ⁻¹)	Ave L _b (mm)	σ_{Su} (mm·s ⁻¹)	U _{Su} (mm·s ⁻¹)
0.8	0	8.57	429.28	9.24	-0.96	4.33	13.75
	0.25	8.78	410.05	8.90	-1.07	5.11	15.44
	0.5	8.76	385.19	8.42	-1.08	4.75	14.70
	0.75	8.58	368.53	8.12	-1.45	5.54	16.22
1	0	10.32	538.18	11.02	-0.68	5.68	12.50
	0.25	10.34	515.90	10.64	-0.82	5.86	12.64
	0.5	10.32	500.79	10.42	-1.04	4.08	11.50
	0.75	10.43	482.14	10.09	-1.06	4.59	11.88
1.4	0	10.52	546.35	12.89	0.12	3.15	13.11
	0.25	10.64	521.66	12.39	0.04	1.65	11.40
	0.5	10.61	498.76	11.93	0.07	2.66	12.50
	0.75	10.59	477.50	11.50	0.01	4.27	15.00

Calculated BFG flame thicknesses, and critical boundary velocity gradients

H ₂ O (g)	ϕ	d _t (mm)	g _r /c (s ⁻¹)	d _t (mm)	g _r /c (s ⁻¹)
		1% H ₂		7% H ₂	
0	0.8	3.08	10.31	1.34	68.48
	1.0	2.72	13.89	1.21	90.59
	1.4	2.44	15.47	1.00	129.04
0.75	0.8	2.43	15.93	1.41	56.70
	1.0	2.11	23.15	1.25	81.11
	1.4	1.88	24.20	1.06	109.33

B.7 - COG Dataset

Test Conditions

Fuel: COG (H₂-61.8 %, CH₄-25.6%, CO-7.1 %, CO₂-1.5 %, and N₂-4 %)
 Temperature: 303 K
 Pressure: 0.1 MPa
 Camera Speed 7,000 fps

ϕ	P_{fuel} (kPa)	ρ_b/ρ_u	Linear Technique			Nonlinear Technique		
			S_u (mm·s ⁻¹)	u_L (cm·s ⁻¹)	L_b (mm)	S_u (mm·s ⁻¹)	u_L (cm·s ⁻¹)	L_b (mm)
0.7	14.65	0.1664	3165.19	52.66	0.23	3164.70	52.65	0.22
			3219.15	53.56	0.24	3215.31	53.50	0.22
			3109.38	51.73	0.21	3108.78	51.72	0.22
0.8	16.40	0.1548	4515.05	69.88	0.23	4512.01	69.83	0.22
			4515.53	69.89	0.39	4502.66	69.69	0.33
			4552.39	70.46	0.32	4564.61	70.65	0.34
0.9	18.08	0.1463	5559.43	81.33	0.35	5553.58	81.25	0.32
			5686.69	83.20	0.46	5685.63	83.18	0.44
			5675.80	83.04	0.43	5607.45	82.04	0.45
1.0	19.69	0.1411	6705.84	94.60	0.56	6696.36	94.47	0.51
			6572.54	92.72	0.71	6541.01	92.28	0.60
			6601.20	93.13	0.61	6554.90	92.47	0.48
1.1	21.24	0.1404	7125.52	100.01	0.87	7062.58	99.12	0.68
			7103.54	99.70	0.80	7040.14	98.81	0.63
			7235.47	101.55	0.81	7160.59	100.50	0.62
1.2	22.73	0.1425	6899.13	98.28	0.84	6857.22	97.69	0.69
			7072.19	100.75	0.90	7017.55	99.97	0.71
			7137.81	101.68	0.85	7097.33	101.11	0.70
1.3	24.17	0.1452	6471.10	93.94	1.09	6408.67	93.03	0.85
			6352.80	92.22	0.92	6299.00	91.44	0.72
			6433.24	93.39	0.93	6359.80	92.32	0.70
1.4	25.55	0.1481	5451.27	80.71	1.22	5348.11	79.18	0.85
			5446.80	80.64	1.15	5351.72	79.24	0.81
			5453.26	80.74	1.23	5352.81	79.25	0.86
1.5	26.89	0.1510	4117.13	62.18	1.91	3971.45	59.98	1.08
			4160.76	62.84	1.53	4069.74	61.47	1.05
			4019.41	60.71	1.41	3953.91	59.72	1.01

Summary – COG Linear Optical and Modelled Results

ϕ	Ave S_u ($\text{mm}\cdot\text{s}^{-1}$)	Ave u_L ($\text{cm}\cdot\text{s}^{-1}$)	Ave L_b (mm)	GRI-Mech 3.0 ($\text{cm}\cdot\text{s}^{-1}$)	Li et al. ($\text{cm}\cdot\text{s}^{-1}$)
0.7	3163.24	52.63	0.23	44.67	43.74
0.8	4527.66	70.08	0.31	60.95	58.60
0.9	5607.31	82.04	0.41	75.75	71.63
1.0	6626.53	93.48	0.63	87.27	81.79
1.1	7154.84	100.42	0.83	94.12	88.13
1.2	7036.38	100.24	0.86	94.97	89.32
1.3	6419.05	93.18	0.98	88.27	83.58
1.4	5450.44	80.70	1.20	73.31	69.16
1.5	4099.10	61.91	1.62	52.53	47.69

Summary and Error – COG Nonlinear Optical Results

ϕ	B_{Su} ($\text{mm}\cdot\text{s}^{-1}$)	Ave S_u ($\text{mm}\cdot\text{s}^{-1}$)	Ave u_L ($\text{cm}\cdot\text{s}^{-1}$)	Ave L_b (mm)	σ_{Su} ($\text{mm}\cdot\text{s}^{-1}$)	U_{Su} ($\text{mm}\cdot\text{s}^{-1}$)
0.7	54.94	3162.93	52.62	0.22	53.29	143.33
0.8	55.73	4526.43	70.06	0.30	33.40	99.95
0.9	55.81	5615.55	82.16	0.40	66.40	174.14
1.0	57.57	6597.42	93.07	0.53	85.97	221.19
1.1	56.01	7087.77	99.48	0.64	64.06	168.70
1.2	54.57	6990.70	99.59	0.70	122.29	308.66
1.3	59.79	6355.82	92.27	0.76	54.95	149.02
1.4	68.47	5350.88	79.22	0.84	2.46	68.74
1.5	81.28	3998.37	60.39	1.05	62.43	175.11

B.8 – BFG/COG Dataset

Test Conditions

Fuel: COG (H₂-61.8 %, CH₄-25.6%, CO-7.1 %, CO₂-1.5 %, and N₂-4 %)
 BFG (CO-23.00 %, CO₂-23.50 %, and N₂-53.50 %)

Temperature: 303 K
 Pressure: 0.1 MPa
 Camera Speed 3,000 fps

Individual Tests – Optical BFG/COG Results 1 % H₂ Addition

COG (%)	ϕ	P _{BFG} (kPa)	P _{COG} (kPa)	ρ_b/ρ_u	Linear Technique			Nonlinear Technique		
					S _u (mm·s ⁻¹)	u _L (cm·s ⁻¹)	L _b (mm)	S _u (mm·s ⁻¹)	u _L (cm·s ⁻¹)	L _b (mm)
5	0.8	49.30	2.59	0.2119	364.28	7.72	-0.26	363.50	7.70	-0.30
					369.72	7.83	-0.20	369.28	7.82	-0.22
	1.0	54.55	2.74	0.2012	466.13	9.38	-0.15	467.24	9.40	-0.14
					457.63	9.21	-0.17	464.50	9.35	-0.02
	1.2	58.71	2.87	0.2162	489.20	10.58	0.31	487.66	10.54	0.27
					495.36	10.71	0.41	486.42	10.52	0.20
	1.4	62.10	2.99	0.2324	424.79	9.87	1.52	410.68	9.54	0.95
					407.25	9.46	1.65	395.94	9.20	1.08
10	0.8	41.93	4.66	0.2010	596.29	11.99	-0.50	593.26	11.92	-0.61
					577.18	11.60	-0.50	573.69	11.53	-0.62
	1.0	46.94	4.95	0.1894	754.74	14.29	-0.25	753.76	14.28	-0.27
					757.32	14.34	-0.13	757.09	14.34	-0.13
	1.2	51.01	5.22	0.2030	766.81	15.57	0.07	766.73	15.56	0.07
					769.20	15.61	0.08	769.11	15.61	0.08
	1.4	54.38	5.45	0.2181	606.06	13.22	1.47	589.79	12.86	0.96
					614.11	13.39	1.67	590.56	12.88	1.00
15	0.8	35.92	6.34	0.1928	807.55	15.57	-0.48	802.99	15.48	-0.59
					806.36	15.55	-0.63	798.27	15.39	-0.82
	1.0	40.61	6.77	0.1802	1020.39	18.39	-0.42	1016.14	18.31	-0.49
					1050.35	18.93	-0.26	1048.85	18.90	-0.28
	1.2	44.49	7.17	0.1929	1039.83	20.06	-0.04	1039.83	20.06	-0.04
					1041.58	20.09	-0.09	1041.40	20.09	-0.09
	1.4	47.74	7.52	0.2070	861.81	17.84	1.99	820.83	16.99	1.14
					828.83	17.16	1.80	804.47	16.65	1.17

Individual Tests – Optical BFG/COG Results 3 % H₂ Addition

COG (%)	ϕ	P _{BFG} (kPa)	P _{COG} (kPa)	ρ_b/ρ_u	Linear Technique			Nonlinear Technique		
					S _u (mm·s ⁻¹)	u _L (cm·s ⁻¹)	L _b (mm)	S _u (mm·s ⁻¹)	u _L (cm·s ⁻¹)	L _b (mm)
5	0.8	48.21	2.54	0.2090	429.09	8.97	-0.72	423.61	8.85	-0.96
					439.82	9.19	-0.64	435.62	9.10	-0.82
	1.0	53.48	2.68	0.1978	578.37	11.44	-0.25	578.39	11.44	-0.27
					607.30	12.01	-0.19	606.88	12.00	-0.20
	1.2	57.68	2.81	0.2127	607.11	12.91	0.00	607.53	12.92	0.00
					602.49	12.81	0.00	602.50	12.82	0.00
	1.4	61.11	2.93	0.2284	543.54	12.41	0.86	536.69	12.26	0.65
					524.09	11.97	0.69	519.61	11.87	0.55
10	0.8	41.14	4.57	0.1989	656.14	13.05	-0.80	651.64	12.96	-1.00
					671.66	13.36	-0.75	670.80	13.34	-0.99
	1.0	46.15	4.86	0.1868	874.71	16.34	-0.46	881.65	16.47	-0.44
					901.61	16.84	-0.24	900.54	16.82	-0.26
	1.2	50.23	5.13	0.2004	882.78	17.69	-0.20	882.20	17.68	-0.21
					906.21	18.16	0.08	905.96	18.16	0.07
	1.4	53.61	5.37	0.2152	731.54	15.74	1.32	712.35	15.33	0.87
					775.15	16.68	1.35	752.92	16.20	0.87
15	0.8	35.34	6.24	0.1912	903.20	17.27	-0.71	880.84	16.84	-1.10
					914.85	17.49	-0.65	884.55	16.91	-1.07
	1.0	40.02	6.67	0.1786	1192.54	21.30	-0.37	1188.98	21.24	-0.42
					1206.71	21.55	-0.37	1202.98	21.49	-0.42
	1.2	43.89	7.06	0.1909	1192.54	22.77	0.03	1183.34	22.59	-0.04
					1175.09	22.43	-0.11	1174.81	22.43	-0.12
	1.4	47.15	7.42	0.2048	968.05	19.83	1.63	932.01	19.09	1.00
					960.41	19.67	0.92	931.00	19.07	1.00

Individual Tests – Optical BFG/COG Results 5 % H₂ Addition

COG (%)	ϕ	P _{BFG} (kPa)	P _{COG} (kPa)	ρ_b/ρ_u	Linear Technique			Nonlinear Technique		
					S _u (mm·s ⁻¹)	u _L (cm·s ⁻¹)	L _b (mm)	S _u (mm·s ⁻¹)	u _L (cm·s ⁻¹)	L _b (mm)
5	0.8	47.17	2.48	0.2062	555.24	11.45	-0.57	550.67	11.35	-0.72
					548.84	11.32	-0.62	542.46	11.19	-0.82
	1.0	52.45	2.63	0.1949	695.11	13.55	-0.37	691.18	13.47	-0.45
					694.92	13.54	-0.45	695.84	13.56	-0.47
	1.2	56.68	2.76	0.2093	729.58	15.27	-0.22	733.14	15.34	-0.18
					725.39	15.18	-0.30	732.34	15.33	-0.23
	1.4	60.15	2.88	0.2247	629.98	14.16	0.60	625.03	14.04	0.47
					635.21	14.27	0.58	631.18	14.18	0.47
10	0.8	40.38	4.49	0.1969	789.26	15.54	-0.56	787.11	15.50	-0.64
					779.00	15.34	-0.79	767.50	15.11	-0.72
	1.0	45.38	4.78	0.1847	1012.25	18.70	-0.43	1007.85	18.61	-0.51
					1011.59	18.68	-0.36	1008.74	18.63	-0.41
	1.2	49.47	5.04	0.1979	1027.18	20.33	-0.16	1026.62	20.32	-0.17
					1023.45	20.25	-0.13	1023.10	20.25	-0.13
	1.4	52.87	5.28	0.2124	873.63	18.56	1.02	855.93	18.18	0.71
					864.16	18.35	0.94	844.69	17.94	0.64
15	0.8	34.78	6.14	0.1898	1031.09	19.57	-0.48	1018.30	19.33	-0.64
					1017.52	19.31	-0.65	1007.27	19.12	-0.84
	1.0	39.44	6.57	0.1771	1326.03	23.48	-0.28	1328.02	23.52	-0.37
					1335.82	23.66	-0.29	1330.74	23.57	-0.40
	1.2	43.31	6.96	0.1890	1360.53	25.71	-0.09	1359.62	25.70	-0.10
					1350.41	25.52	-0.11	1350.14	25.52	-0.11
	1.4	46.57	7.32	0.2027	1112.91	22.56	1.14	1094.29	22.18	0.81
					1094.66	22.19	1.08	1077.09	21.83	0.78

Individual Tests – Optical BFG/COG Results 7 % H₂ Addition

COG (%)	ϕ	P _{BFG} (kPa)	P _{COG} (kPa)	ρ_b/ρ_u	Linear Technique			Nonlinear Technique		
					S _u (mm·s ⁻¹)	u _L (cm·s ⁻¹)	L _b (mm)	S _u (mm·s ⁻¹)	u _L (cm·s ⁻¹)	L _b (mm)
5	0.8	46.17	2.43	0.2037	654.15	13.32	-0.76	643.29	13.10	-1.07
					658.43	13.41	-0.60	654.81	13.34	-0.72
	1.0	51.46	2.58	0.1922	871.18	16.74	-0.34	869.06	16.70	-0.39
					842.34	16.19	-0.46	838.32	16.11	-0.55
	1.2	55.72	2.71	0.2062	876.10	18.07	-0.18	875.61	18.06	-0.19
					896.72	18.49	-0.07	895.89	18.47	-0.08
	1.4	59.21	2.83	0.2212	767.88	16.99	0.41	765.69	16.94	0.36
					776.66	17.18	0.42	774.63	17.13	0.37
10	0.8	39.64	4.40	0.1950	903.49	17.62	-0.50	898.81	17.53	-0.60
					902.96	17.61	-0.60	894.22	17.44	-0.78
	1.0	44.64	4.70	0.1828	1151.47	21.05	-0.44	1146.41	20.96	-0.52
					1156.35	21.14	-0.29	1148.24	20.99	-0.36
	1.2	48.73	4.96	0.1956	1202.29	23.52	-0.08	1203.28	23.54	-0.07
					1201.41	23.50	-0.19	1203.62	23.54	-0.18
	1.4	52.15	5.20	0.2097	1008.60	21.15	0.74	999.61	20.96	0.58
					996.56	20.90	0.72	988.28	20.72	0.57
15	0.8	34.23	6.04	0.1884	1110.80	20.93	-0.56	1105.20	20.82	-0.69
					1111.75	20.95	-0.59	1106.04	20.84	-0.72
	1.0	38.88	6.47	0.1757	1457.08	25.60	-0.39	1452.18	25.51	-0.45
					1476.17	25.94	-0.23	1474.35	25.90	-0.26
	1.2	42.74	6.86	0.1872	1487.57	27.85	-0.12	1483.11	27.76	-0.19
					1513.75	28.34	-0.01	1513.80	28.34	-0.01
	1.4	46.01	7.22	0.2006	1252.56	25.13	0.94	1234.75	24.77	0.69
					1200.96	24.09	1.21	1176.63	23.60	0.84

Summary Results – BFG/COG 1 % H₂ Addition

COG (%)	ϕ	B_{Su} (mm·s ⁻¹)	σ_{Su} (mm·s ⁻¹)	U_{Su} (mm·s ⁻¹)	GRI-Mech 3.0 (cm·s ⁻¹)	Li et al. (cm·s ⁻¹)	Linear Technique			Nonlinear Technique		
							S_u (mm·s ⁻¹)	u_L (cm·s ⁻¹)	L_b (mm)	S_u (mm·s ⁻¹)	u_L (cm·s ⁻¹)	L_b (mm)
5	0.8	11.72	4.08	38.53	7.46	8.14	367.00	7.78	-0.23	366.39	7.76	-0.26
	1.0	13.67	1.94	22.15	9.58	10.06	461.88	9.30	-0.16	465.87	9.38	-0.08
	1.2	13.67	0.88	15.78	10.29	10.36	492.28	10.65	0.36	487.04	10.53	0.24
	1.4	11.73	10.42	94.39	9.01	8.84	416.02	9.67	1.59	403.31	9.37	1.02
10	0.8	15.88	13.84	125.40	11.19	11.96	586.74	11.80	-0.50	583.48	11.73	-0.62
	1.0	18.41	2.35	28.03	14.38	14.68	756.03	14.32	-0.19	755.43	14.31	-0.20
	1.2	17.35	1.68	23.01	15.18	14.79	768.01	15.59	0.08	767.92	15.59	0.08
	1.4	15.29	0.55	16.07	12.47	11.86	610.09	13.31	1.57	590.18	12.87	0.98
15	0.8	19.13	3.33	35.54	14.77	15.48	806.96	15.56	-0.56	800.63	15.44	-0.71
	1.0	22.22	23.13	209.03	19.06	19.06	1035.37	18.66	-0.34	1032.50	18.61	-0.39
	1.2	20.73	1.11	23.01	19.98	19.11	1040.71	20.08	-0.07	1040.62	20.08	-0.07
	1.4	18.87	11.57	105.68	15.76	14.82	845.32	17.50	1.90	812.65	16.82	1.16

Summary Results – BFG/COG 3 % H₂ Addition

COG (%)	ϕ	B_{Su} (mm·s ⁻¹)	σ_{Su} (mm·s ⁻¹)	U_{Su} (mm·s ⁻¹)	GRI-Mech 3.0 (cm·s ⁻¹)	Li et al. (cm·s ⁻¹)	Linear Technique			Nonlinear Technique		
							S_u (mm·s ⁻¹)	u_L (cm·s ⁻¹)	L_b (mm)	S_u (mm·s ⁻¹)	u_L (cm·s ⁻¹)	L_b (mm)
5	0.8	15.84	8.15	74.91	8.97	9.83	434.46	9.08	-0.68	429.62	8.98	-0.89
	1.0	20.12	21.74	196.41	11.60	12.18	592.84	11.73	-0.22	592.64	11.72	-0.24
	1.2	19.80	14.34	130.41	12.58	12.63	604.80	12.86	0.00	605.02	12.87	0.00
	1.4	16.47	6.33	59.18	11.24	10.97	533.82	12.19	0.78	528.15	12.07	0.60
10	0.8	15.88	13.84	125.40	12.67	13.57	663.90	13.21	-0.78	661.22	13.15	-1.00
	1.0	18.41	2.35	28.03	16.37	16.71	888.16	16.59	-0.35	891.10	16.65	-0.35
	1.2	17.35	1.68	23.01	17.45	17.01	894.50	17.93	-0.06	894.08	17.92	-0.07
	1.4	15.29	0.55	16.07	14.69	13.92	753.35	16.21	1.34	732.64	15.77	0.87
15	0.8	20.61	2.62	31.29	16.22	17.05	909.03	17.38	-0.68	882.70	16.88	-1.09
	1.0	24.38	9.90	92.26	21.04	21.07	1199.63	21.43	-0.37	1195.98	21.37	-0.42
	1.2	23.78	6.03	59.17	22.27	21.29	1183.82	22.60	-0.04	1179.08	22.51	-0.08
	1.4	20.87	0.72	21.84	17.99	16.87	964.23	19.75	1.28	931.51	19.08	1.00

Summary Results – BFG/COG 5 % H₂ Addition

COG (%)	ϕ	B_{Su} (mm·s ⁻¹)	σ_{Su} (mm·s ⁻¹)	U_{Su} (mm·s ⁻¹)	GRI-Mech 3.0 (cm·s ⁻¹)	Li et al. (cm·s ⁻¹)	Linear Technique			Nonlinear Technique		
							S_u (mm·s ⁻¹)	u_L (cm·s ⁻¹)	L_b (mm)	S_u (mm·s ⁻¹)	u_L (cm·s ⁻¹)	L_b (mm)
5	0.8	14.69	5.81	54.21	10.55	11.59	552.04	11.39	-0.60	546.57	11.27	-0.77
	1.0	16.62	3.29	33.95	13.73	14.39	695.02	13.55	-0.41	693.51	13.52	-0.46
	1.2	16.72	0.56	17.46	15.03	15.05	727.49	15.23	-0.26	732.74	15.34	-0.21
	1.4	14.45	4.35	41.68	13.68	13.31	632.60	14.22	0.59	628.11	14.11	0.47
10	0.8	19.23	13.86	126.08	14.21	15.26	784.13	15.44	-0.68	777.31	15.31	-0.68
	1.0	22.51	0.63	23.22	18.47	18.86	1011.92	18.69	-0.40	1008.30	18.62	-0.46
	1.2	21.87	2.49	31.30	19.90	19.35	1025.32	20.29	-0.15	1024.86	20.29	-0.15
	1.4	18.78	7.95	73.90	17.10	16.16	868.90	18.46	0.98	850.31	18.06	0.68
15	0.8	25.31	7.80	74.55	17.71	18.68	1024.31	19.44	-0.57	1012.79	19.23	-0.74
	1.0	29.79	1.92	34.42	23.10	23.17	1330.93	23.57	-0.29	1329.38	23.55	-0.39
	1.2	28.84	6.70	66.78	24.70	23.59	1355.47	25.62	-0.10	1354.88	25.61	-0.11
	1.4	24.16	12.17	111.98	20.38	19.07	1103.79	22.38	1.11	1085.69	22.01	0.80

Summary Results – BFG/COG 7 % H₂ Addition

COG (%)	ϕ	B_{Su} (mm·s ⁻¹)	σ_{Su} (mm·s ⁻¹)	U_{Su} (mm·s ⁻¹)	GRI-Mech 3.0 (cm·s ⁻¹)	Li et al. (cm·s ⁻¹)	Linear Technique			Nonlinear Technique		
							S_u (mm·s ⁻¹)	u_L (cm·s ⁻¹)	L_b (mm)	S_u (mm·s ⁻¹)	u_L (cm·s ⁻¹)	L_b (mm)
5	0.8	15.84	8.15	74.91	12.20	13.42	656.29	13.37	-0.68	649.05	13.22	-0.90
	1.0	20.12	21.74	196.41	15.97	16.72	856.76	16.47	-0.40	853.69	16.41	-0.47
	1.2	19.80	14.34	130.41	17.65	17.64	886.41	18.28	-0.13	885.75	18.27	-0.14
	1.4	16.47	6.33	59.18	16.37	15.86	772.27	17.09	0.42	770.16	17.04	0.37
10	0.8	15.88	13.84	125.40	15.82	17.03	903.23	17.62	-0.55	896.52	17.49	-0.69
	1.0	18.41	2.35	28.03	20.69	21.13	1153.91	21.10	-0.37	1147.33	20.98	-0.44
	1.2	17.35	1.68	23.01	22.49	21.85	1201.85	23.51	-0.14	1203.45	23.54	-0.13
	1.4	15.29	0.55	16.07	19.71	18.59	1002.58	21.03	0.73	993.95	20.84	0.58
15	0.8	26.27	0.60	26.81	19.26	20.36	1111.28	20.94	-0.58	1105.62	20.83	-0.71
	1.0	32.00	15.68	144.49	25.26	25.33	1466.63	25.77	-0.31	1463.27	25.71	-0.36
	1.2	31.24	21.70	197.48	27.24	26.00	1500.66	28.10	-0.07	1498.46	28.05	-0.10
	1.4	25.65	41.10	370.23	22.94	21.41	1226.76	24.61	1.08	1205.69	24.19	0.77

Calculated BFG flame thicknesses, and critical boundary velocity gradients

COG (%)	ϕ	1% H ₂		7% H ₂	
		d_t (mm)	$g_{f/c}$ (s ⁻¹)	d_t (mm)	$g_{f/c}$ (s ⁻¹)
0	0.8	3.08	10.31	1.34	68.48
	1.0	2.72	13.89	1.21	90.59
	1.2	2.44	17.85	1.07	116.54
	1.4	2.44	15.47	1.00	129.04
15	0.8	0.91	170.44	0.77	272.18
	1.0	0.84	222.65	0.72	357.97
	1.2	0.78	258.54	0.66	427.66
	1.4	0.87	193.37	0.70	344.82

B.9 – Modelled BOS Gas Dataset

Test Conditions

Temperature: 303 K
 Pressure: 0.1 MPa
 Fuel Mix:

Fuel Composition (mass fraction)						
Water Mass (g)	H ₂	CO	CO ₂	N ₂	H ₂ O	O ₂
0	0.00042	0.61027	0.20753	0.18093	0.00000	0.00085
0.25	0.00042	0.60434	0.20552	0.17917	0.00971	0.00084
0.5	0.00042	0.59852	0.20354	0.17744	0.01924	0.00083
0.75	0.00041	0.59282	0.20160	0.17575	0.02858	0.00083

Wet BOS Gas flame speeds (Davis et al. mechanism)

ϕ	0 g H ₂ O (cm·s ⁻¹)	0.25 g H ₂ O (cm·s ⁻¹)	0.5 g H ₂ O (cm·s ⁻¹)	0.75 g H ₂ O (cm·s ⁻¹)
0.7	9.55	13.30	15.10	16.22
0.8	11.27	15.92	18.14	19.59
0.9	12.75	18.15	20.80	22.49
1.0	14.00	20.11	23.08	24.97
1.1	14.95	21.74	25.06	27.11
1.2	15.81	23.09	26.63	28.89
1.3	16.46	24.25	27.98	30.29
1.4	16.98	25.12	29.04	31.45
1.5	17.40	25.85	29.83	32.37

BOS/BFG Blends

BOS gas (%)	ϕ	1% BFG H ₂ (cm·s ⁻¹)	3% BFG H ₂ (cm·s ⁻¹)	5% BFG H ₂ (cm·s ⁻¹)	7% BFG H ₂ (cm·s ⁻¹)
5	0.8	3.85	6.18	8.04	9.89
	0.9	4.37	7.00	9.22	11.50
	1.0	4.70	7.62	10.21	12.75
	1.1	4.91	8.09	10.90	13.64
	1.2	4.97	8.32	11.32	14.20
	1.3	4.91	8.32	11.31	14.37
	1.4	4.66	8.14	11.19	14.17
	1.5	4.29	7.61	10.59	13.60
10	0.8	4.50	7.04	9.12	11.12
	0.9	5.08	8.05	10.49	12.83
	1.0	5.50	8.81	11.54	14.18
	1.1	5.75	9.33	12.30	15.17
	1.2	5.85	9.62	12.76	15.80
	1.3	5.80	9.67	12.92	16.08
	1.4	5.59	9.49	12.75	15.97
	1.5	5.28	9.07	12.30	15.49
15	0.8	5.14	7.84	9.99	12.01
	0.9	5.80	8.95	11.47	13.84
	1.0	6.27	9.80	12.62	15.29
	1.1	6.57	10.39	13.47	16.37
	1.2	6.72	10.74	14.01	17.10
	1.3	6.72	10.87	14.26	17.48
	1.4	6.57	10.69	14.21	17.49
	1.5	6.29	10.44	13.86	17.15

Appendix C - Thesis Publications

Daniel Pugh, Anthony Giles, Andrew Hopkins, Tim O'Doherty, Anthony Griffiths, Richard Marsh, Thermal distributive blast furnace gas characterisation, a steelworks case study. SUSTEM 2011. Newcastle. 2011

Daniel Pugh, Anthony Giles, Andrew Hopkins, Tim O'Doherty, Anthony Griffiths, Richard Marsh, Thermal distributive blast furnace gas characterisation, a steelworks case study, Applied Thermal Engineering, Volume 53, Issue 2, 2 May 2013, Pages 358-365.

D.G. Pugh, T. O'Doherty, A.J. Griffiths, P.J. Bowen, A.P. Crayford, R. Marsh, Laminar burning velocity and Markstein Length characterisation of compositionally dynamic blast furnace gas. ASME Turbo Expo Copenhagen 2012. GT2012-69667

D.G. Pugh, T. O'Doherty, A.J. Griffiths, P.J. Bowen, A.P. Crayford, R. Marsh, Sensitivity to change in laminar burning velocity and Markstein length resulting from variable hydrogen fraction in blast furnace gas for changing ambient conditions, International Journal of Hydrogen Energy, Volume 38, Issue 8, 19 March 2013, Pages 3459-3470.

D.G. Pugh, T. O'Doherty, A.J. Griffiths, P.J. Bowen, A.P. Crayford, R. Marsh, Laminar burning velocity and Markstein Length characterisation of steelworks gas blends. International conference on applied energy. 2013. ICAE2013-660